APPENDIX A

RESEARCH DESCRIPTION AND FINDINGS

TABLE OF CONTENTS

Additional supporting materials to Appendix A are given in separate files as follows:

LIST OF FIGURES

LIST OF TABLES

A1. INTRODUCTION

A1.1 Background

A1.1.1 Fiber Reinforced Polymer Composite Materials

Fiber reinforced polymers (FRP) are advanced composites consisting of high strength fibers such as aramid, carbon, glass, or kevlar embedded in a polymer matrix. The fibers are the primary load-carrying components of the composite. The polymer resin provides a medium for stresses to be transferred among individual fibers, protects the fibers from damage and environmental effects, and helps maintain alignment of the fibers. In addition, the polymer matrix strongly influences several mechanical properties of the FRP, such as transverse modulus and strength, shear capacity, and compression properties (Sika, 2003). Two categories of polymers are available: thermosetting (e.g., epoxy, vinylester, and polyester) and thermoplastic (e.g., nylon). A schematic representation of the constituent elements of a unidirectional FRP material is shown in Figure A 1.1.

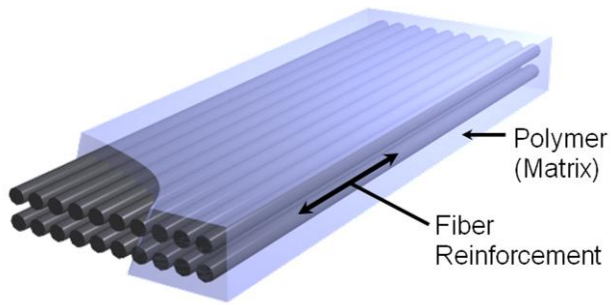

Figure A 1.1 Representation of FRP Material

Composite materials commonly used in civil applications are referred to as carbon fiber based (CFRP), aramid fiber based (AFRP), or glass fiber based (GFRP) depending on the type of fiber from which they are composed. Figure A 1.2 shows the typical range of stress-strain relationships for the three composite fiber types compared to traditional mild steel.

FRP materials can be fabricated in various forms including bars, plates, and sheets. Bars are usually used in new construction where they may be substituted for traditional steel reinforcement. FRP bars and other structural shapes such as prestressing tendons, grid reinforcement, and dowels are fabricated through the process of pultrusion. Pultrusion is a highly automated process in which reinforced fibers and fiber fabrics are pulled through a resin and then extruded into a heated die where the resin is polymerized (Bakis et al., 2002). Plates and sheets are generally used in rehabilitation and retrofit applications. Plates, in particular, are often used as flexural reinforcement for beams and slabs, whereas sheets are most commonly used for shear strengthening and confinement of columns.

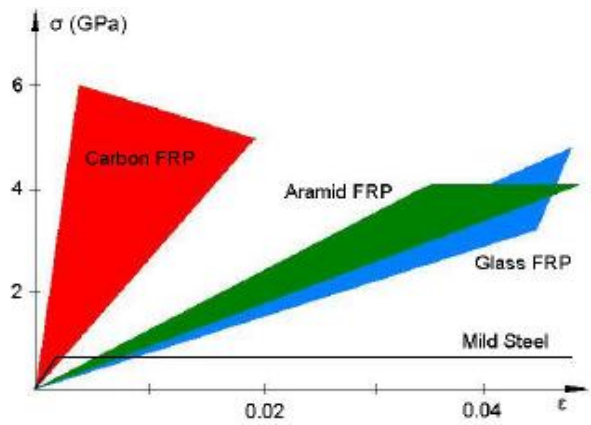

Figure A 1.2 Stress-Strain Relationship of Various FRPs (Sika 2003)

The primary advantage of FRPs are their high strength-to-weight ratio and design versatility. These properties are particularly important in rehabilitation applications because they permit strengthening without significant increase of additional dead weight to the structure. The light weight characteristics of this material also allow it to be applied to a structure without the need for temporary supports. These characteristics of FRP significantly reduce labor costs and strengthening time. Other beneficial properties include corrosion resistance, magnetic transparency, and chemical resistance. There are few drawbacks, for example glass fiber composites can be susceptible to alkaline solutions and ultraviolet radiation if not properly treated. These properties are especially important since most infrastructure problems are related to corrosion of steel reinforcements casued by severe environmental conditions.

A1.1.2 Applications of FRP in Civil Engineering Infrastructures

The use of FRPs in civil infrastructure rehabilitation has increased rapidly in the last two decades. These materials have grown more popular among designers, contractors, and owners due to their advantages over conventional materials, and they have found a wide range of structural applications. FRP materials date back to the early 1940s when they were mainly used in aerospace and naval applications as part of the defense industry. During the late 1970s and early 1980s, the use of FRPs began to emerge in civil engineering infrastructure. By the 1990s, civil engineers were adopting FRPs for use in two major areas: (1) new construction with all-FRP solutions or new composite FRP/concrete systems and (2) repair, strengthening, and rehabilitation of deficient or deteriorated structures.

One of the most common applications of FRP materials in new construction is the use of reinforcing bars. They may be used as an alternative to or in combination with traditional steel reinforcements. Applications of FRP materials have also been developed for highway structures, bridge decks, and concrete-filled FRP shells for drivable piles. FRP materials offer greater strength and stiffness per unit than traditional steel reinforced concrete decks (Bakis et al., 2002). In addition, they provide exceptional durability, substantial reduction or elimination of corrosion, and better surface crack width control (Arya et al., 1995).

Due to the wide spread aging of infrastructure, the greatest potential for FRP materials lies in the rehabilitation and retrofitting of existing structures. Composites for structural strengthening are available today in the form of precured strips or uncured sheets. Precured strips are typically 0.02

to 0.06 in. thick, 2 to 8 in. wide, and made of unidirectional fibers (carbon, glass, aramid) in an epoxy matrix. Uncured sheets typically have a nominal thickness of less than 0.04 inches and are made of unidirectional or bidirectional fibers (often called fabrics) that are either pre-impregnated with resin or impregnated in situ. These fibers are highly conformable to the surface onto which they are bonded (Bakis et al., 2002). Bonding is typically achieved with high-performance epoxy adhesives.

FRP materials can be classified into three categories for retrofit applications: (1) flexural strengthening, (2) confinement of compression members, and (3) shear strengthening. Flexural strengthening of RC members is one of the most common applications, involving epoxy-bonding of FRP sheets to the tensile zone of the member with the direction of fibers parallel to the member axis (Figure A 1.3(a)). Well established analytical procedures can be used to design strengthening systems for beams and columns in flexure, provided that special attention is paid to the bond between the concrete and FRP (Triantafillou, 1998b). This kind of application significantly increases the strength; however, it is usually accompanied by a loss of ductility. Typical failure modes in members strengthened in flexure with FRP are: rupturing of the FRP sheets, failing of concrete in the compressive zone, or peeling of the laminate (Neale, 2000).

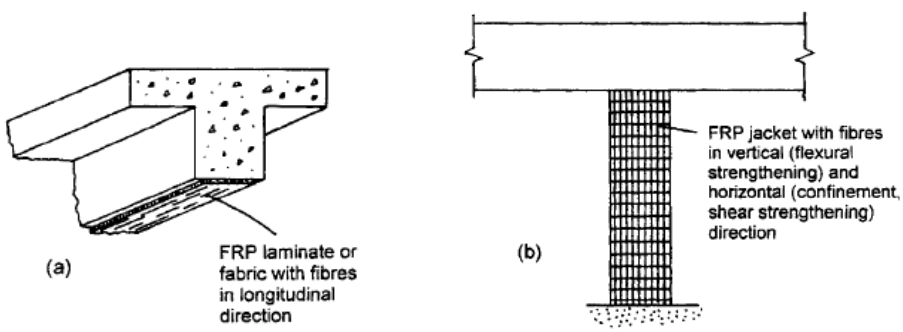

Figure A 1.3 FRP Flexural Strengthening of RC (a) Beam and (b) Column (Triantafillou, 1998b)

Another frequent application of FRP materials is the wrapping of columns (Figure A 1.3(b)) to increase confinement and provide more ductility to the member. This strengthening method is applied in either seismic regions (to enhance the ductility of compression members subjected to seismic loads) or non-seismic regions (to increase the axial capacity of columns subjected to higher vertical loads). In either case, confinement is provided by wrapping RC columns with FRP materials (prefabricated jackets or in situ cured sheets), in which the principal fiber direction is along the circumference of the section (Bakis et al., 2002).

A1.1.3 Shear Strengthening of Concrete Girders with FRP

Various FRP laminates and fabrics offer an alternative to traditional strenghthening techniques for increasing the shear performance of structural members. They considerably increase strength and ductility without significantly affecting the stiffness. Externally bonded FRP materials with fibers parallel to the principal tensile stresses (or as nearly so as possible) have been proven to increase the shear strength of RC elements. FRP shear reinforcement is traditionally attached to a beam by side bonding, U-wrap, or complete wrapping as shown in Figure A 1.4. The FRP may be applied as continuous sheets along the shear span or as discrete strips as shown in Figure A

1.5. The fibers in the FRP may also be oriented at various angles to meet a range of strengthening requirements.

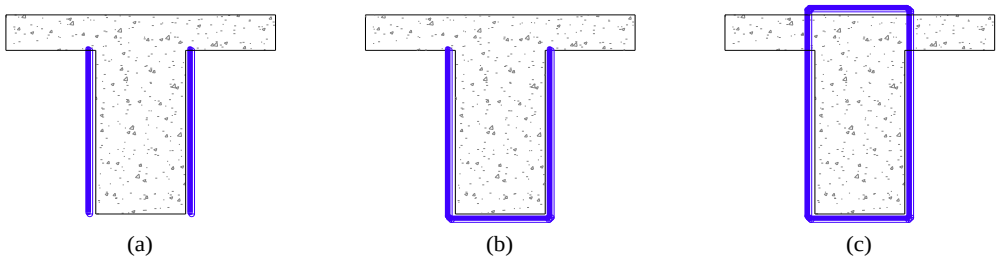

Figure A 1.4 (a) Side bonding, (b) U-wrap, and (c) Complete wrap

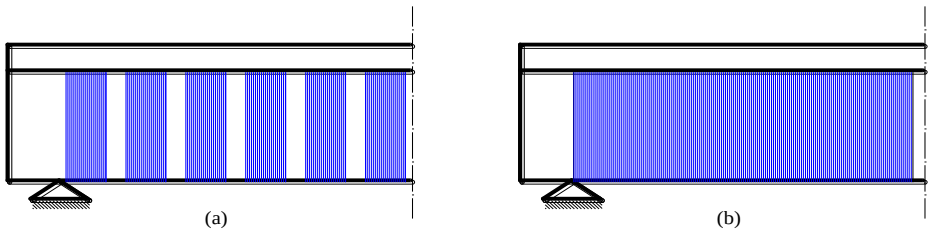

Figure A 1.5 (a) Discrete wraps and (b) Continuous wrap

The effectiveness of the strengthening method depends on the mode of failure (Bakis et al., 2002). The shear failure process of FRP-strengthened RC beams is usually characterized by the development of a single major diagonal shear crack or several diagonal shear cracks, similar to those that develop in normal RC beams without FRP strengthening (Teng et al., 2004). Most experimental results have revealed two main failure modes: (1) tensile rupture of the FRP, starting with the most highly stressed region and propogating along the main shear crack or (2) sequential debonding of the FRP from the concrete substrate starting from the most vulnerable strip (Teng et al., 2004).

The effectiveness of side bonding is limited due to the potential debonding of FRP reinforcement. The U-Wrap configuration is most practical, and its effectiveness in increasing the shear capacity has been investigated by many studies. Complete wrapping has proved to be most effective, but it is not practical from a constructability point of view.

The orientation of FRP fibers can also affect the performance of the strengthening system. Inclined fibers resist the formation of shear cracks, and therefore, are theoretically more effective than vertical fibers for shear strengthening (Denton et al., 2004). The wet lay-up process involves in-situ impregnation of dry fiber/fabric with epoxy resin and the subsequent bonding of these impregnated strips to the pre-treated beam surface (Teng et al., 2004). Corner rounding is commonly used in both U-wrapping and complete wrapping applications to avoid stress concentration at the corners of the beam.

A1.2 Research Objectives

Standard specifications exist for commonly used traditional materials in civil engineering structures. At this time, design specifications for FRP use are still under development. The

results of several experimental investigations have shown that FRP systems can be effective for increasing ductility and strength of structural members such as columns and girders. However, most research has focused on axial and flexural strengthening of members, with less experimental and analytical studies being conducted on the use of FRP systems for shear strengthening of girders. Shear strengthening with FRP is still under investigation, and the results obtained thus far are scarce and sometimes controversial. Even in traditional reinforced concrete members without FRP, the shear design is a complex challenge and uses more empirical methods than axial and flexural design methods. Adding FRP to the equations, with its specific design issues, provides another level of complication in the design. These FRP-related shear design issues and lack of comprehensive analytical models and experimental data are the main motivation for this research project. Thus, a thorough understanding of the shear design problem along with the development of an AASHTO design method for FRP shear strengthening of concrete girders are needed.

As such, the objective of this project is to develop design methods, specifications, and examples for design of FRP systems for strengthening concrete girders in shear. The proposed specifications will be in LRFD format and will be suitable for recommendation to the AASHTO Highway Subcommittee on Bridges and Structures for adoption.

A1.3 Research Plan and Methodology

The following tasks were performed to achieve the objectives presented above.

Task 1 - Reviewed relevant practice, data, existing specifications, and research findings from both foreign and domestic sources on the strengthening of concrete girders in shear using FRP systems containing carbon or glass fibers. Identified FRP systems available for shear strengthening. This information was assembled from both technical literature and unpublished experiences. Information on failure modes, anchorage performance, durability, fatigue, and limitations on applicability of existing design methods were of particular interest.

Task 2 - Identified criteria that influence design of FRP shear strengthening systems using the findings from Task 1. Under this task the collected data were summarized to identify the parameters and topics that are essential to this project. This task has been performed side by side with Task 1 with the following objectives pursued:

(a) *Compiled a* ***comprehensive database*** *encompassing tests carried out worldwide related to FRP shear strengthening.*
(b) *Identified criteria that influence design of FRP shear strengthening systems.*

Task 3 - Compared and evaluated how existing design methods satisfy identified criteria in Task 2. Following the identification and initial review of shear design provisions that account for FRP, a detailed analysis of these provisions and other promising new approaches were conducted.

Task 4 - Prepared an annotated outline of the proposed LRFD design specifications, including discussion of the contents and intent, based on the findings of Tasks 1 through 3. This draft represented a “strawman” of the recommended provisions. It allowed the project panel, as well as the Research Team, to envision these provisions as a final product of this research effort. The

information gathered in Tasks 1 and 2 and synthesized under Task 3 was used to formulate the outline of the recommended provisions.

Task 5 - Recommended design methods, either existing or proposed, for further development. Prepared a detailed work plan for developing design methods. Analytical and experimental components were included in the work plan as needed to validate the design methods.

Task 6 - Submitted an interim report documenting the results of Tasks 1 through 5. Following project panel review of the report, met with the panel to discuss the report and the remaining project tasks. NCHRP approval of the interim report and the work plan developed in Task 5 was required before proceeding.

Task 7 - Developed design methods in accordance with the approved work plan. In this task, the proposed work plan presented to and approved by the NCHRP Panel members was executed. The work plan consisted of developing new shear design methods for FRP-strengthened concrete girders.

Task 8 - Revised the outline of the specifications. The Research Team prepared a revised outline of the recommended specifications and commentary for shear design of FRP-strengthened concrete girders so that they are in accordance with standard practices, and of help to bridge design engineers. Advisory Board members provided input on this task as well.

Task 9 - Prepared detailed design examples for each system to fully illustrate the application of the design methods and the Task 8 specifications. The development of the design examples benefited from the experiences gained on and templates created for NCHRP Projects 12-56 and 12-61. In NCHRP Project 12-56, the test girders were designed to satisfy all service and limit state requirements of the LRFD Bridge Design Specifications. To this end, a MathCad template was prepared for the full implementation of the LRFD specifications. The design examples were written in a clear and concise format so that they facilitate implementation of the new specifications by bridge design engineers.

Tasks 10, 11, and 12 - Prepared a final report documenting the entire research effort and also includes (a) the final draft recommended specifications and commentary, (b) the design methods, and (c) design examples in separate attachments. The overall details of the research are provided in Appendix A. While Tasks 10 and 11 have specific delivery, they were lumped with Task 12.

A2. LITERATURE REVIEW

A2.1 General

A comprehensive and exhaustive collection and review of relevant practice, data, existing specifications, and research findings from both foreign and domestic sources has been conducted as part of Task 1 of this project. The results are presented in this Section.

A2.2 Survey

A survey of the design practices of state departments of transportation (DOTs) was conducted. This survey included both a written questionnaire and either a telephone briefing on the response to the questionnaire or a written response. The objectives of the questionnaire were to determine the status of practice concerning design of concrete girders strengthened in shear using FRP and to provide a vehicle for organizations to express their opinion of the current FRP shear strengthening design methodology. The complete survey questionnaire and results are attached as Additional Material A to Appendix A.

Of the 52 agencies polled, including Washington DC and Puerto Rico, 39 responded to this survey. The survey revealed that only seven (7) state DOTs have experience in the application of FRP for shear strengthening of concrete girders as shown in Figure A 2.1.

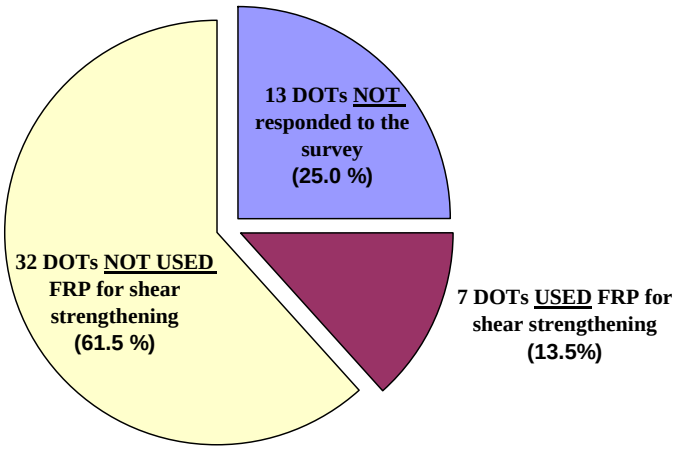

Figure A 2.1 Experience in Using FRP for Shear Strengthening of Concrete Girders by State DOTs

The 32 DOTs that have never used FRP for shear strengthening of concrete girders provided several reasons for not doing so; however, the main reasons were twofold. As shown in Figure A 2.2, fourteen (14) DOTs stated that they had no need for shear strengthening of concrete girders and 12 DOTs expressed concern that there were no proper design specifications or provisions for shear strengthening. Some DOTs considered the use of FRPs less efficient when compared to other strengthening techniques.

For the seven (7) DOTs having experience with FRP applications, it was further asked what kind of design methods were used and what made them choose these methods. Results showed that all seven (7) DOTs used ACI 440.2R-02 (ACI 440, 2002) since it was the only design guideline document available in the US. Some DOTs, such as New York, Oregon, and Pennsylvania, have

made slight modifications to ACI 440.2R-02 (ACI 440, 2002). Design guidelines and specifications provided by FRP manufacturers and course notes from a workshop provided by several organizations were also used by some state DOTs to ensure their designs were properly conducted.

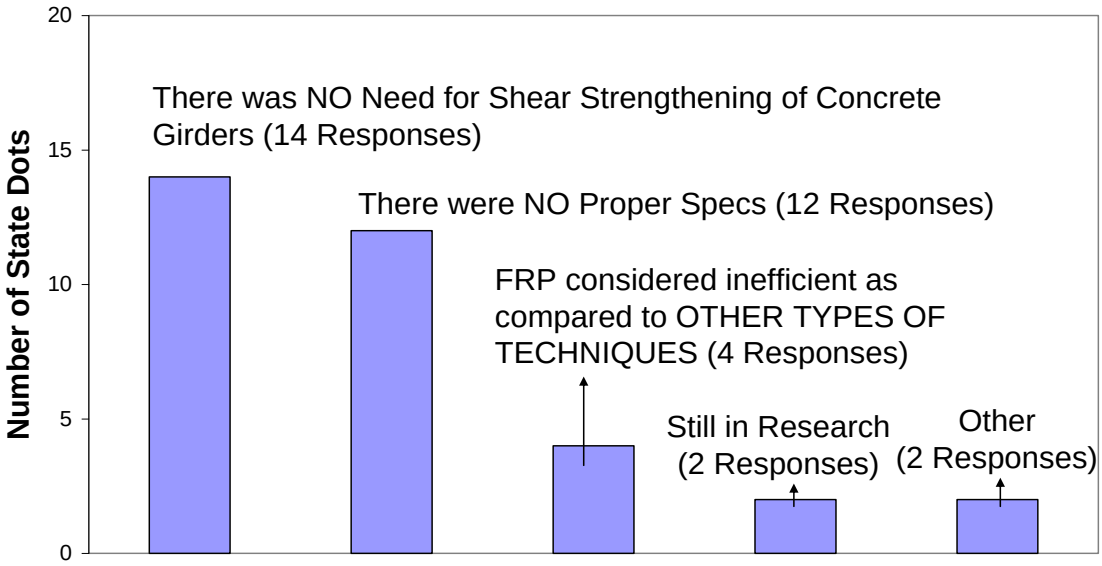

Note: each DOT was allowed to select multiple choices
5 DOTs did not reponded to this question out of 32 DOTs

Figure A 2.2 Reasons for Not Using FRP for Shear-Strengthening of Concrete Girders

The last question in the survey concerned issues to be addressed in future specifications or design examples that can be derived from this study. A list of issues were provided in the survey questionnaire for selection, which included:

(a) Provisions regarding properties of FRP composite materials
(b) Effect of shear-span to depth ratio
(c) Effect of transverse and longitudinal steel reinforcement
(d) In-depth explanation on FRP strengthening schemes
(e) Control of failure modes
(f) Fatigue and durability issues
(g) Prestressed vs. non-prestressed
(h) Effect of anchorage details
(i) Various types of geometry of concrete girders
(j) Beam continuity
(k) Fiber orientations with respect to the longitudinal axis of members
(l) Provisions related to the post-strengthening inspection.
(m) Other issues: please list:

Figure A 2.3 shows that most state DOTs considered provisions regarding properties of FRP composite materials (a) and control of failure modes (e) as the most important issues to be

addressed in future design specifications. An in-depth explanation on FRP strengthening schemes (d) and fatigue and durability issues (f) were also marked as major issues.

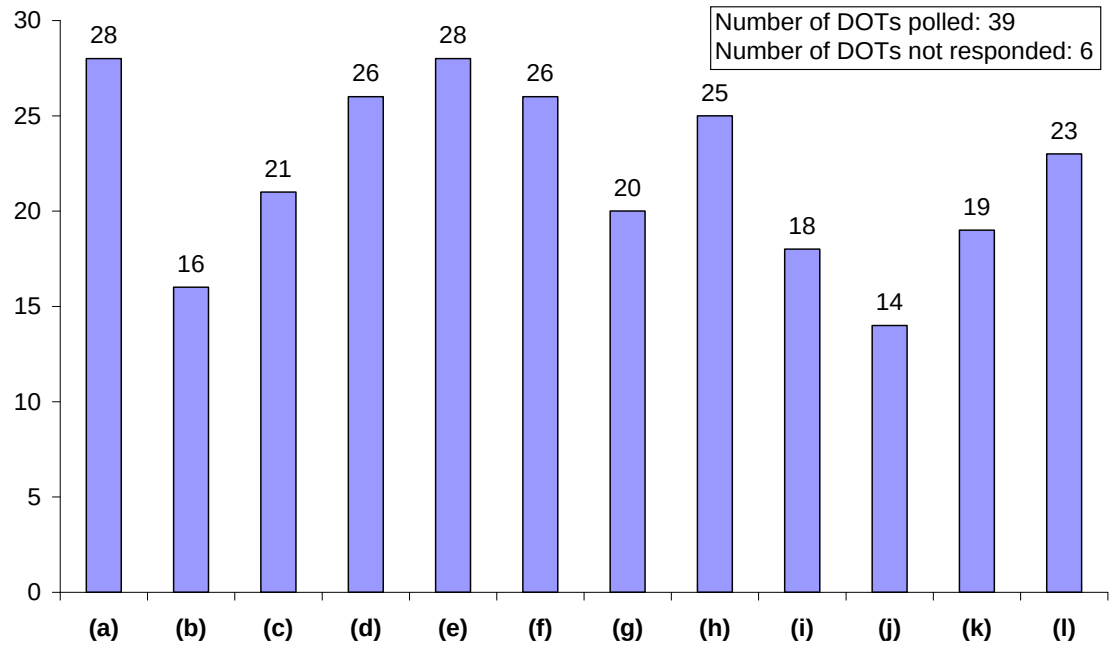

Figure A 2.3 Issues to be Addressed in the Future Specifications

A2.3 Analytical Models

Most existing analytical studies on the shear strength of FRP-strengthened RC beams follow the superposition approach commonly adopted by design codes which define the ultimate shear capacity as the sum of three components: concrete (V_c), internal steel shear reinforcement (V_s), and external FRP shear reinforcement (V_f). Consequently, the shear strength of an FRP-strengthened beam (V_n) is given in the following form:

$$V_n = V_c + V_s + V_f \qquad \text{(A2-1)}$$

Generally, it is assumed that V_c and V_s can be determined from current design guidelines and standards. The contribution of FRP to shear resistance is often assumed to be analogous to that of the steel shear reinforcement based on "Strut-and-Tie" methodology. Much like the steel stirrups, the FRP laminates are considered as ties resisting the tensile stresses along cracks between the concrete struts. However, the effectiveness of the FRP in resisting these tensile stresses is much more complex than that of the internal steel stirrups as it is dependent upon: (1) the bond behavior between concrete and the FRP laminate, (2) the material behavior of the FRP laminate (linear elastic up to failure as opposed to the elasto-plastic nature of steel), (3) FRP laminates geometry (width and effective bond length), (4) failure mode, and (5) level of anchorage provided. Most currently available analytical models express the contribution of FRP to the shear capacity as a function of the effective strain in FRP, ε_{fe}, which is intended to account for the above mentioned parameters. The effective strain of FRP is typically expressed as a fraction of the ultimate tensile strain and is largely dependent on the failure mode which can be either rupture of FRP or debonding of FRP. In the case of FRP rupture, the effective strain is close but

always slightly less than the ultimate tensile strain of FRP due to a non-uniform distribution of strains in the FRP. In the case of debonding, the effective strain in the FRP is much lower than the ultimate tensile strain of FRP. The equations used to calculate the effective strain in FRP, ε_{fe}, have been improved by many researchers as more experimental data has become available. The factors generally considered in determining the effective strain are the stiffness of FRP, the strength of the concrete, the FRP strengthening scheme, and failure mode. This section presents a comprehensive overview of the 17 existing analytical models that have been proposed for predicting the shear contribution of FRP laminates (V_f) to the total shear resistance of a beam (V_n). Each model is presented with units and notation as originally published. The models have been grouped based on commonality in their approaches.

The first group of analytical models includes the first attempts quantifying the shear contribution coming from externally bonded FRP. As such, these two models are based on a limited number of experimental data usually consisting of small-scale test results. Both of these models are based on an assumed shear crack angle (θ) of 45° and therefore the shear crack angle is not a variable of the expressions for the FRP contribution. In addition, neither model attempts to address the interaction between the internal steel reinforcement and externally bonded FRP. Al-Sulaimani et al. (1994) developed the first analytical model for predicting the FRP shear contribution which presented equations for three different strengthening schemes (i.e. shear strips, shear wings, and U-jackets).

$$V_P = \frac{2F_P d}{S_P} = \frac{2\left[\tau_{ave}\frac{t_s h_s}{2}\right]d}{S_P} \quad \text{(for shear strips)} \qquad \text{(A2-2)}$$

$$V_P = 2F_P = 2\left[\tau_{ave}\left(\frac{dh_w}{2}\right)\right] \quad \text{(for shear wings)} \qquad \text{(A2-3)}$$

$$V_P = 2F_P = 2\left[\tau_{ult}\left(\frac{dh_j}{2}\right)\right] \quad \text{(for U-jackets)} \qquad \text{(A2-4)}$$

The shear contribution for FRP strips and wing strengthening schemes were calculated assuming that debonding of the strips or wings would occur when the maximum shear stress (τ_{max}) at the bottom of the strip or wing reached the interface shear strength (τ_{ult}). The interface shear strength was taken to be 508 psi, however, no explanation is given for the bases of this value. The shear stress was assumed to be maximum at the cutoff locations of the strip or wing and the shear distribution was assumed parabolic along the strip as shown in Figure A 2.4. An average shear stresses (τ_{ave}), equal to 174 psi for strips and 116 psi for wings, were established from their experimental results and used in the calculations for the FRP shear contribution.

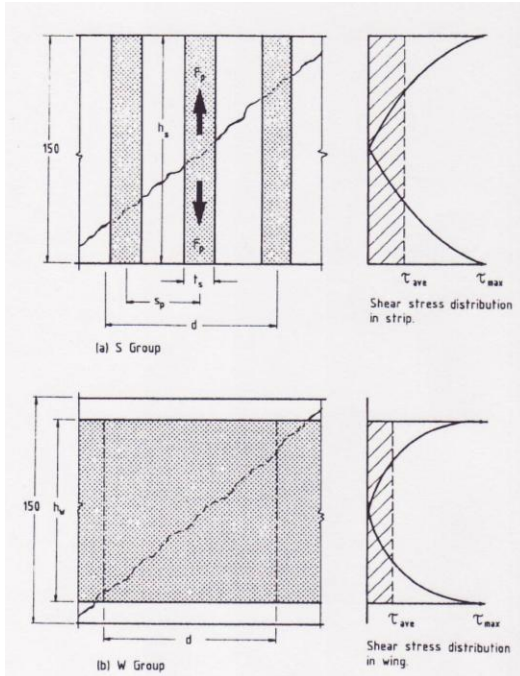

Figure A 2.4 FRP Shear Stress Distribution (Al-Sulaimani et al., 1994)

The FRP shear component for U-jacket strengthening schemes was calculated assuming no debonding occured based on experimental observations. Thus the shear stress distribution was assumed to be uniform along the depth of the wings of the jacket and the full interface shear strength (τ_{ult}) was allowed to be developed. Experimental testing consisted of 16 small-scale rectangular RC beams with transverse steel reinforcement. All specimens were pre-damaged to a predetermined level prior to strengthening to simulate realistic conditions for which such strengthening would be required. Only one type of fiberglass material was used for strengthening in this experimental study, thus the proposed empirical model could not account for the differences in stiffness among the various FRP materials available. In addition, only three strengthening schemes were investigated (i.e. side bonded strips, continuous side bonded wings, and continuous U-jackets), making the proposed model unsuitable for predicting the shear contribution of other strengthening schemes.

Another analytical model, presented by Chajes et al. (1995), was developed from experimental results of 12 test specimens containing no transverse steel reinforcement and tested under four-point bending. Only continuous U-wrapping was investigated with fiber directions of 90° and 45° with respect to the longitudinal axis of the beams. Separate equations were proposed for the two fiber orientations investigated as:

$$V_f = A_f E_f \varepsilon v_{cu} d \qquad \text{(fibers oriented at 0/90 degree)} \qquad \text{(A2-5)}$$

$$V_f = A_f E_f \varepsilon v_{cu} d \sqrt{2} \qquad \text{(fibers oriented at 45/135 degree)} \qquad \text{(A2-6)}$$

Only four of the test specimens were instrumented with strain gages to measure vertical and horizontal strains in the FRP. Based on those measurements, an average value of the vertical strain in the FRP at failure was taken to be εv_{cu} = 0.005 and was recommended for use in the

calculation of the FRP shear contribution. By using this average strain measured at failure, this model could not account for any differences in ultimate strain resulting from the use of different fabrics or wrapping orientations. This model also did not account for strain variation along the width of the FRP. None of the test specimens were pre-cracked (i.e. intentionally loaded to a predetermined level to produce cracking similar to that for which strengthening would be required) prior to strengthening; thus the influence of such pre-existing cracks on the bond performance was not investigated. As such, the performance of the proposed model for predicting the shear capacity of FRP repaired beams is questionable. In no instances was debonding observed in the experimental testing. As a result, the proposed analytical model assumed a perfect bond between the FRP and concrete and did not consider the debonding failure mode.

The second group of analytical models consisted of those based on the determination of an effective FRP strain. All of the models in this group, except that by Hutchinson and Rizkalla (1999), are based on an assumed shear crack angle of 45° and thus the shear crack angle is not a variable of the expressions for the FRP contribution. Triantafillou (1998a) was among the first researchers to propose that the FRP contribution to shear capacity is based on the computation of an effective FRP strain ($\varepsilon_{frp,e}$). In his model, the effective FRP strain ($\varepsilon_{frp,e}$) was obtained from regression of 40 experimental test data collected from various studies (Berset, 1992; Uji, 1992; Dolan et al., 1992; Al-Sulaimani et al., 1994; Ohuchi et al., 1994; Chajes et al., 1995; Malvar, 1995; Sato et al., 1996; and Triantafillou, 1997). His model was the first to recognize that the effective strain in the FRP depends on the development length and bond conditions at the FRP/concrete interface. His model also recognizes that the development length is a function of the axial rigidity ($\rho_{frp}E_{frp}$) of the FRP used. As such, Triantafillou proposed the following expression for calculating the FRP contribution to shear capacity.

$$V_{frp,d} = \rho_{frp} E_{frp} 0.9 b_w d \left(r_1 \frac{\varepsilon_{frp,u}}{\gamma_{frp}} \right) (1 + \cot\beta) \sin\beta \qquad \text{(A2-7)}$$

$$\text{where: } r_1 = \frac{\left(\frac{z_1}{2} + z_2 + \frac{z_3}{2} \right)}{0.9d} \qquad \text{(A2-8)}$$

Curve fitting of the 40 experimental data showed that the effective FRP strain decreases as the axial rigidity of the FRP increases. Thus, as the FRP sheets become thicker and stiffer, debonding dominates over tensile fracture and thus a lower effective strain is developed. Though this model recognizes the effects of debonding on the effective FRP strain and attempts to represent it with a physical model, it also recognizes the inability to determine the bond parameters (z_1, z_2, and z_3) as defined in Figure A 2.5. Thus the author assumes perfect anchorage, and the debonding effect is accounted for in the regression analysis of the experimental data resulting in a more simplified expression.

$$V_{frp,d} = \frac{0.9}{\gamma_{frp}} \rho_{frp} E_{frp} \varepsilon_{frp,e} b_w d \left(1 + \cot\beta\right) \sin\beta \qquad \text{(A2-9)}$$

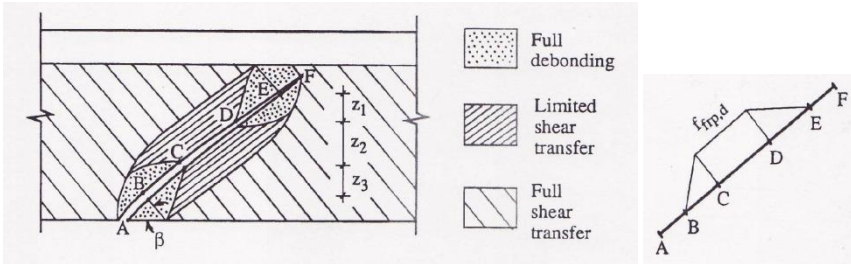

Figure A 2.5 Schematic Illustration of FRP Stress Bearing Mechanisms and Simplified FRP Normal Stress along Diagonal Crack (Triantafillou, 1998a)

All experimental data used in the regression, which included both debonding and FRP rupture failure modes, were found to follow a similar trend and fitted with reasonable accuracy by a single curve as shown in Figure A 2.6.

$$\varepsilon_{frp,e} = 0.0119 - 0.0205\left(\rho_{frp}E_{frp}\right) + 0.0104\left(\rho_{frp}E_{frp}\right)^2 \quad for \quad 0 \le \rho_{frp}E_{frp} \le 1 \tag{A2-10}$$

$$\varepsilon_{frp,e} = -0.00065\left(\rho_{frp}E_{frp}\right) + 0.00245 \quad for \quad \rho_{frp}E_{frp} > 1 \tag{A2-11}$$

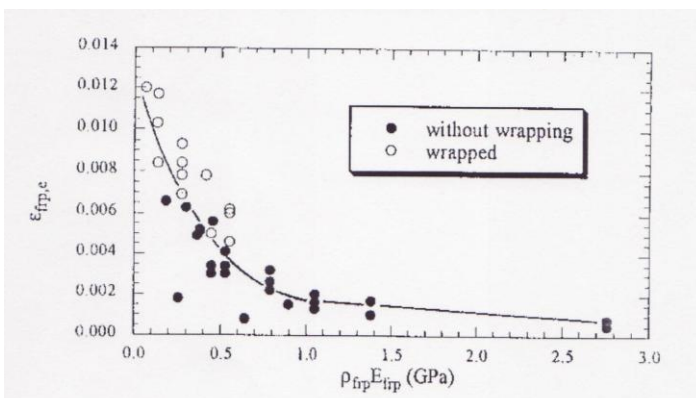

Figure A 2.6 Effective FRP Stain in Terms of $\rho_{frp}E_{frp}$ (Triantafillou, 1998a)

Although the model was developed for continuous sheets, it can be easily modified for use in the case of FRP strips by modifying the FRP reinforcement ratio (ρ_{frp}) to account for the strip width and spacing.

$$\rho_{frp} = \frac{2tw_{frp}}{b_w s_{frp}} \tag{A2-12}$$

This model does not consider any interaction between the stirrups and FRP and thus the FRP contribution is simply added to the existing Eurocode 2 (Eurocode No. 2, 1992) equations for concrete and stirrup shear contributions. A short coming of this model is that it does not account for the difference in ultimate strain among the various types of FRP that could be used for external strengthening.

In 1998, Khalifa et al. (1998) modified Triantafillou's original model (Triantafillou, 1998b) to account for the various types of FRP used and introduced strain limitations due to shear crack

opening and loss of aggregate interlock. Additional experimental data from other studies that had recently become available were added to their database for regression (Araki et al., 1997; Chajes et al., 1995; Funakawa et al., 1997; Ohuchi et al., 1994; Sato et al., 1996; Triantafillou, 1997; Umezu et al., 1997; and Uji, 1992). They proposed a modified effective strain, both for fiber rupture and debonding failure, by introducing a reduction factor *R* for the ultimate tensile stress in the FRP. The reduction factor is a ratio of the effective strain to ultimate strain of the FRP and thus accounts for the various types of FRP used in the experiments. An upper limit of 0.5 is placed on the reduction factor to limit the strain in the FRP to 0.004 to 0.005 to prevent loss of the aggregate interlock mechanism in concrete as a result of excessive crack widths. The shear strength provided by the FRP reinforcement was determined by calculating the force resulting from the tensile stress in the FRP across the assumed crack. This model also recognizes the difference in behavior between debonding and FRP rupture failure modes and presents a separate reduction factor (*R*) for each failure mode.

$$R = 0.5622\left(\rho_f E_f\right)^2 - 1.2188\left(\rho_f E_f\right) + 0.778 \le 0.50 \quad \text{(FRP rupture)} \qquad \text{(A2-13)}$$

$$R = \frac{0.0042\left(f_c^{'}\right)^{2/3} w_{fe}}{\left(E_f t_f\right)^{0.58} \varepsilon_{fu} d_f} \quad \text{(debonding failure)} \qquad \text{(A2-14)}$$

The effective strain in the FRP reinforcement is taken as the lower of the two reduction factors multiplied by the ultimate strain of the FRP material used. The equation presented for the debonding failure mode adopts the concepts of effective bond length (L_e) and average bond stress (τ_{bu}) developed by Maeda et al. (1997). The model also suggests the use of an effective width for calculating the shear capacity governed by the debonding failure mode, recognizing that only the portion of FRP extending past the crack by the effective bond length will be capable of carrying shear. The effective width depends upon the shear crack angle, which is assumed to be 45° in this model, and the FRP surface configuration method as shown in Figure A 2.7.

$$w_{fe} = d_f - L_e \quad \text{(U-jacket configuration)} \qquad \text{(A2-15)}$$

$$w_{fe} = d_f - 2L_e \quad \text{(sheet bonded only on two faces)} \qquad \text{(A2-16)}$$

The expression presented by the authors for the FRP shear contribution, similar to that developed by Triantafillou (Triantafillou, 1998a), is given in ACI format.

$$V_f = \frac{A_f f_{fe}\left(\sin\beta + \cos\beta\right) d_f}{s_f} \qquad \text{(A2-17)}$$

$$\text{where: } f_{fe} = R f_{fu} \qquad \text{(A2-18)}$$

A limitation was imposed by the authors on the FRP spacing in order to prevent the formation of a diagonal crack that does not intercept an FRP strip.

$$s_{f,\max} = w_f + \frac{d}{4} \qquad \text{(A2-19)}$$

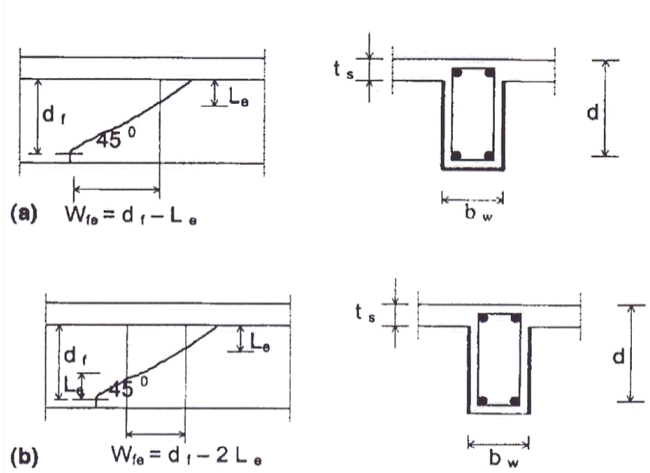

Figure A 2.7 Effective Width of FRP (a) U-Jacket Configuration; (b) FRP Sheet Bonded only on Two Beam Faces (Khalifa et al. 1998)

The authors also recommended a limitation be placed on the total shear strength which can be provided by the combination of stirrups and FRP in order to prevent web crushing of the diagonal compressive struts.

$$V_s + V_f \leq \frac{2\sqrt{f_c'}b_w d}{3} \qquad \text{(A2-20)}$$

Hutchinson and Rizkalla (1999) were the first to propose a model which considers the interaction between the internal steel reinforcement and the externally bonded FRP. Their model included an equation for both the FRP contribution and the steel stirrup contribution assuming that the steel reinforcement does not yield if the member exhibits premature failure due to FRP debonding. This model was developed and calibrated from prestressed girder tests performed by the authors. The experimental program consisted of seven 1:3.5 scaled models of a pretensioned AASHTO bridge girder. Specimens with bent-legged and straight-legged stirrups were investigated to study the effects of the outward force exerted as a result of tensile forces in the vertical and diagonal portions of the bent-legged stirrup causing straightening of the stirrup at the lower flange to web interface as shown in Figure A 2.8.

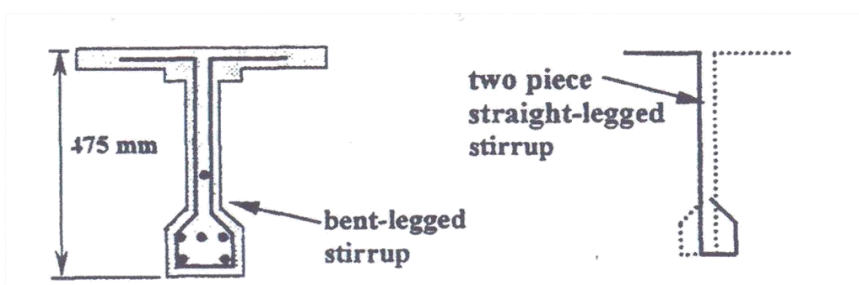

Figure A 2.8 Test Specimen Details (Hutchinson and Rizkalla, 1999)

The study also included a series of rectangular and single-flanged bond specimen tests to determine the influence of surface preparation, concrete surface configuration (shape of the girder), crack orientation, and load-sharing with the embedded steel stirrups on the bond

characteristics between the CFRP sheets and concrete surface as shown in Figure A 2.9. Single-flanged specimens were designed to emulate the lower flange of an AASHTO I-shaped girder. The lower flange of an I-shaped girder caused the FRP to develop tensile forces that subjected the concrete substrate to outward peeling forces as well as shear forces.

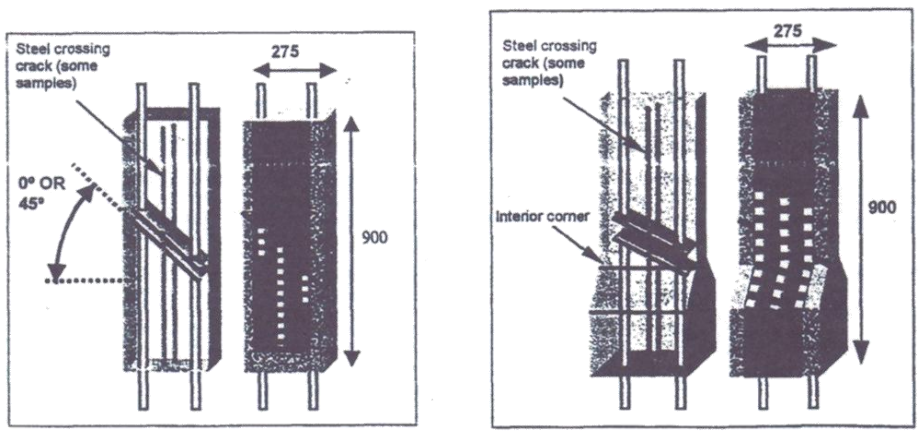

Figure A 2.9 Bond Test Specimen Details (Hutchinson and Rizkalla, 1999)

All test beams were reported to have failed by shear-tension failure occurring in the concrete substrate. It was also reported that the CFRP used for strengthening remained bonded to the concrete over most of the beam at failure. For the I-shaped sections tested in this study, failure typically occurred due to straightening of the FRP sheets resulting in outward peeling forces as well as shear forces in the concrete substrate. Failure generally occurred as a result of shear-tension in the concrete prior to the development of a uniform strain distribution in the FRP. As governed by straightening of the FRP strips, the FRP strain distribution measured just prior to initiation of failure of the beam tests was used to develop a model for calculating the average strain (ε_{fave}) in the FRP sheets at failure as:

$$\varepsilon_{fave} = \varepsilon_{f\max} \frac{\left[(d/2) + 0.5\left(d_f - d/2\right)\right]}{d_f} \qquad \text{(A2-21)}$$

The model assumes a constant maximum strain (ε_{fmax}) in the FRP extending a distance d/2 from the bottom of the effective depth (d_f) and then decreasing to zero at the top of the effective depth (d_f). In this model, d_f refers to the effective depth of the FRP and is measured from the top of the FRP sheets to the centroid of the longitudinal tension reinforcement and d refers to the effective depth of the cross section measured from the extreme compression fiber to the centroid of the longitudinal tension reinforcement as shown in Figure A 2.10.

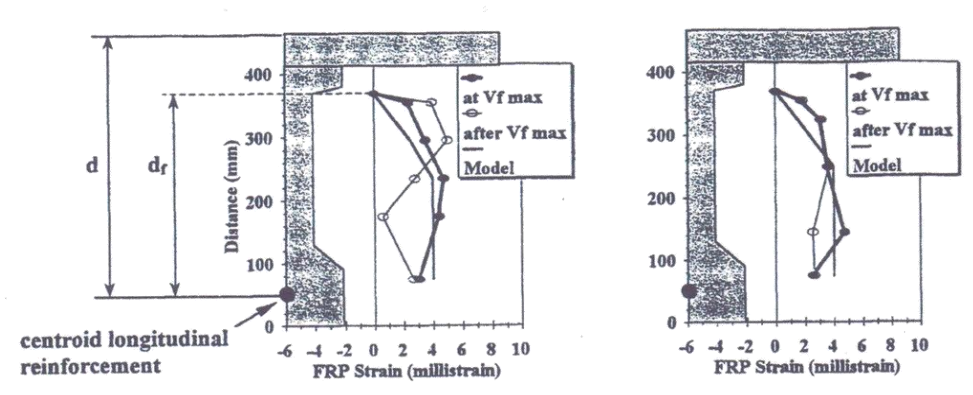

Figure A 2.10 FRP Strain Distribution (Hutchinson and Rizkalla, 1999)

Shear bond tests performed by Maeda et. al. (1997) are used to derive the maximum FRP strain (ε_{fmax}) which was shown to develop over an effective bond length (L_{fe}).

$$\varepsilon_{f\max} = L_{fe} C \tag{A2-22}$$

where: $$L_{fe} = e^{6.134 - 0.580 \ln(t_f E_f)} \tag{A2-23}$$

$$C = constant\ strain\ rate\ of\ 110 \times 10^{-6} mm^{-1}$$

The experimental results showed that just prior to straightening of the FRP sheets, the maximum strain in the FRP (ε_{fmax}) for a single layer of FRP at a 45 degree orientation was 0.004. This value along with the model for effective bond length by Maeda et. al. (1997) is used to calculate the maximum FRP strain for other sheet configurations and stiffnesses. Assuming ε_{fave} is developed in each strip, the shear contribution provided by FRP sheets (V_{fmax}) can be computed (see Figure A 2.11) as:

$$V_{f\max} = \frac{\varepsilon_{fave} E_f 2 n_f t_f w_f d_f}{s_f} \left(\cot\theta + \cot\alpha_f \right) \sin\alpha_f \tag{A2-24}$$

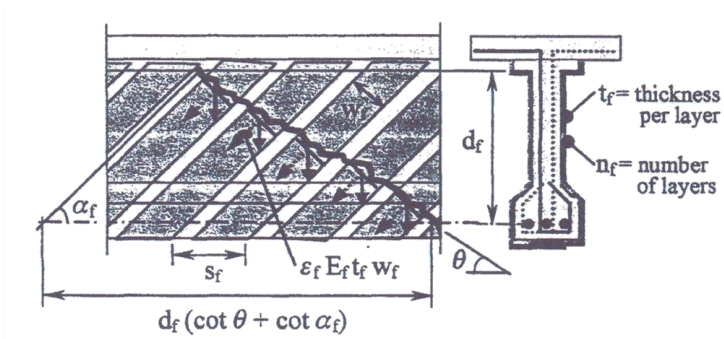

Figure A 2.11 Free-Body Diagram of FRP Shear Strengthening (Hutchinson and Rizkalla, 1999)

All models developed prior to this study assumed that the steel stirrups had reached yielding at the occurrence of failure which may not be the case when FRP is present to help carry the shear forces. Hutchinson and Rizkalla (1999) noted that for I-shaped sections, failure due to

straightening of the FRP at the lower flange-to-web interface typically occurs prior to yielding of the stirrups. Thus, they suggested that the effective stirrup contribution (V_{se}) would be calculated based on an empirical relationship found for the strain in the stirrups (ε_{se}) at the initiation of FRP straightening as:

$$V_{se} = \varepsilon_{se} E_s A_v \frac{d \cot\theta}{s} \qquad \text{(A2-25)}$$

where: $\varepsilon_{se} = \varepsilon_{fave} \sin\alpha_f / \gamma_{fs} \le \varepsilon_{sy}$ (A2-26)

The empirical relationship comes from the ratio of the average vertical strain measured in the FRP to the average strain measured in the stirrups (γ_{fs}) and a value of 1.5 was proposed based on the beam tests conducted. Though this model takes into consideration various crack inclination angles (θ) in its formulations, no direction is given on how the crack inclination angle (θ) is to be determined. One deficiency of this model is that it has been developed and calibrated for prestressed I-shaped girders which typically fail by straightening of the FRP strips and therefore does not take into consideration the FRP rupture failure mode. Some researchers (Chen and Teng, 2003a) also question the validity of the effective bond length equation proposed by Madea et al. (1997) used to determine the maximum FRP strain in this model.

Later, Khalifa and Nanni (2000) proposed a new reduction factor (R) derived for the bond mechanism as shown in Equation A2-27. Six experimental tests on full-scale specimens were conducted in four-point bending to further investigate selected parameters that would help calibrate the new model. The selected parameters were: (1) CFRP amount and distribution (continuous sheets versus strips), (2) wrapping scheme (side bonded versus U-wrap), (3) fiber direction combination (90°-0° versus 90° only), and (4) end anchorage (U-wrap with and without end anchorage).

$$R = \frac{\left(f_c^{'}\right)^{2/3} w_{fe}}{\varepsilon_{fu} d_f}\left[738.93 - 4.06\left(E_f t_f\right)\right] \times 10^{-6} \quad \text{(debonding failure mode)} \qquad \text{(A2-27)}$$

The new model also recommended using a modified effective bond length calculation developed by Miller (1999) instead of the calculation originally proposed by Meada et al. (1997), as shown in Equations A2-28 and A2-29.

$$L_e = -0.00298 t E_f + 3.711 \quad \text{(English)} \qquad \text{(A2-28)}$$

$$L_e = -0.432 t E_f + 94.3 \quad \text{(Metric)} \qquad \text{(A2-29)}$$

The upper limit on the reduction factor (R) was also modified to account for the variety in ultimate strain of the CFRP sheets available as shown in Equation A2-30. The new upper limit is intended to limit the effective strain to a constant value of 0.004 for all FRP types.

$$R = \frac{0.006}{\varepsilon_{fu}} \qquad \text{(A2-30)}$$

According to Triantafillou and Antonopoulos (2000), a short-coming of this model is that FRP rupture is described by an equation that has been derived from test data corresponding to both FRP rupture and debonding. Researchers (Chen and Teng, 2003a) have also questioned the reliability of the model used for calculating the effective bond length which has been based on simple shear tests.

Later in 2000, Triantafillou and Antonopoulos (2000) proposed an updated model which addressed the deficiencies of Triantafillou's original model (Triantafillou, 1998a), accounting for: (1) the nature of FRP fracture which may occur simultaneously or after the peak shear capacity is reached, (2) the difference in behavior between FRP rupture and debonding, and (3) the influence of concrete strength on debonding. The expression for effective strain was calibrated based on the results of over 75 experimental test data from various studies (Berset, 1992; Uji, 1992; Al-Sulaimani et al., 1994; Ohuchi et al., 1994; Chajes et al., 1995; Sato et al., 1996; Antonopoulos, 1996; Miyauchi et al., 1997; Taerwe et al., 1997; Funakawa et al., 1997; Umezu et al., 1997; Araki et al., 1997; Sato et al., 1997a; Ono et al., 1997; and Taljsten, 1997). Experimental results were divided by type of FRP material (CFRP, GFRP, or AFRP) and failure mode (FRP debonding or shear-tension failure combined with or followed by FRP rupture). As previously recommended by Triantafillou (1998a), the effective strain was back calculated from the experimental results and plotted against $E_f\rho_f/f_c^{2/3}$. The $f_c^{2/3}$ is used to account for the influence of concrete tensile strength on the development length of the FRP. Curve fitting of the data is used to derive separate expressions for the effective strain in the cases of FRP debonding, shear-tension failure combined with or followed by CFRP fracture, and shear-tension failure combined with or followed by AFRP fracture as shown in Equations A2-31 through A2-33.

Debonding failure mode:

$$\varepsilon_{f,e} = 0.65\left(\frac{f_c^{2/3}}{E_f\rho_f}\right)\times 10^{-3} \qquad \text{(A2-31)}$$

Shear-tension failure combined with or followed by CFRP fracture:

$$\varepsilon_{f,e} = 0.17\left(\frac{f_c^{2/3}}{E_f\rho_f}\right)^{0.30}\varepsilon_{f,u} \qquad \text{(A2-32)}$$

Shear-tension failure combined with or followed by AFRP fracture:

$$\varepsilon_{f,e} = 0.048\left(\frac{f_c^{2/3}}{E_f\rho_f}\right)^{0.47}\varepsilon_{f,u} \qquad \text{(A2-33)}$$

An upper limit is placed on the effective strain in the FRP to ensure the concrete aggregate interlock mechanism is maintained. A value of $\varepsilon_{max} = 0.005$ is established based on the experimental results where $\varepsilon_{fu} = 0.015$ was determined for CFRP and $\varepsilon_{fu} = 0.035$ was found for AFRP. Equations for determining the contribution of FRP were proposed in Eurocode and ACI formats in this model as shown in Equations A2-34 through A2-36 with an additional reduction factor ($\alpha = 0.8$) used for determining the design FRP effective strain.

$$V_{fd} = 0.9\frac{\varepsilon_{fk,e}}{\gamma_f}E_f\rho_f b_w d\left(1+\cot\beta\right)\sin\beta \qquad \text{(Eurocode format)} \qquad \text{(A2-34)}$$

where: $\varepsilon_{fk,e} = \alpha\varepsilon_{f,e} \le \varepsilon_{\max}$ (A2-35)

$$\phi_f V_f = \phi_f \varepsilon_{f,e,A} E_f \rho_f \left(\sin\beta + \cos\beta\right) bd \quad \text{(ACI format)} \tag{A2-36}$$

where: $\varepsilon_{f,e,A} = 0.9\varepsilon_{f,e} \le \varepsilon_{\max,A} = 0.006$ (A2-37)

This model also suggests limiting the value for the axial rigidity of the FRP $(E_f\rho_f)_{\lim}$ beyond which failure is governed by debonding and the gain in shear capacity is small unless proper mechanical anchorage or full wrapping is used (Triantafillou and Antonopoulos, 2000).

$$\left(E_f \rho_f\right)_{\lim} = \left(\frac{0.65\times10^{-3}\alpha}{\varepsilon_{\max}}\right)^{1/0.56} f_c^{2/3} = 0.018 f_c^{2/3} \tag{A2-38}$$

The authors also suggest a maximum FRP strip spacing for vertically placed strips (i.e., $s_{f,max}$ = 0.8d) such that no diagonal crack may be formed without intercepting at least one FRP strip. As in the case of most other models, this model also does not consider any interaction between the internal steel stirrups and externally bonded FRP. It should be noted that this model was incorporated in the European Bulletin 14 (fib-TG 9.3, 2001).

Chaallal et al. (2002) investigated the relationship between the steel reinforcement ratio and the FRP reinforcement ratio. They concluded that there is an optimum amount of FRP reinforcement needed to achieve the maximum gain in shear resistance, which depends on the steel reinforcement provided. They also reported that the effective FRP strain (ε_{eff}) is a function of the total shear reinforcement ratio ρ_{tot} (i.e., stirrups and FRP) as shown in Equations A2-39 and A2-40. Based on their investigation, they proposed a new model that accounts for the interaction between transverse steel reinforcement and FRP.

$$\varepsilon_{eff} = 3\times10^{-5} \times \rho_{tot}^{-0.6522} \tag{A2-39}$$

where: $\rho_{tot} = n\rho_f + \rho_s$ (A2-40)

This model is developed and calibrated from regression of a total of 14 half-scale RC T-girders tested under a low shear span condition (i.e., a shear span-to-depth ratio (a/d) = 2.0); thus this model takes into consideration deep beam behavior. Deep beams develop arch action which results in a higher concrete contribution (V_c) to the shear resistance. In this model, this effect is accounted for with a deep beam geometry coefficient similar to that formerly presented in ACI 318-99 (ACI 318, 1999) and is developed from regression of the test data based on shear gain concepts as shown in Equations A2-41 and A2-42.

$$V_f = f\left(\frac{a}{d}, \rho_{tot}\right)\left(\frac{A_f}{s_f}\right) E_f \varepsilon_{eff} d_f \tag{A2-41}$$

where: $f\left(\frac{a}{d}, \rho_{tot}\right) = \frac{1+2a/d}{12} + \left(1000\rho_{tot} - 0.6\right) \le 1$ (A2-42)

but greater than $\frac{1+2a/d}{12}$

This model's deficiency is that it has been developed considering test results from a limited number of beams with shear-span-to-depth ratio (a/d) of 2.0. Additional testing is needed to ensure that the proposed deep beam coefficient is valid for other shear span-to-depth ratios

within the deep beam spectrum (a/d < 2.0). The model also gives no consideration to the bond behavior of the FRP to concrete and thus it does not recognize the two different failure modes (i.e. debonding and FRP rupture) or the influence of the concrete strength on the effectiveness of the FRP strengthening scheme.

Pellegrino and Modena (2002) also introduced the effect of the interaction between steel and FRP transverse reinforcements by investigating the influence of the internal shear reinforcement on the inclined cracking patterns and its effect on the bonded FRP. Based on their experimental results, the authors modified the *R* factor originally proposed by Khalifa et al. (1998) to reflect the observed interaction between steel stirrups and externally bonded FRP. The model recognizes the difference in crack patterns between beams with and without transverse steel reinforcement. In a beam without transverse steel reinforcement, only one principal diagonal crack develops while a beam with transverse steel reinforcement develops multiple diagonal shear cracks. As a result, the bond between the concrete and FRP must be developed over a region with multiple diagonal cracks when transverse steel reinforcement is present. The bond characteristics are strongly modified when FRP is attached to cracked concrete. The development length of the FRP is disrupted for each crack, thus the internal transverse steel reinforcement has an effect on the bond conditions between FRP and concrete. To capture this effect, a further reduction factor (R^*) is introduced by the authours which is a function of the ratio between the axial rigidities of the transverse steel and FRP shear reinforcements as:

$$\rho_{s,f} = E_s A_{sw} / E_f A_f \qquad \text{(A2-43)}$$

The new reduction factor (R^*) was calibrated from the experimental results including 11 beams with and without transverse steel reinforcement, as well as, specimens tested by Chaallal et. al. (1998a) and Modena et al. (1999). The focus of the study was directed toward debonding failures, thus only beams with side-bonded CFRP strengthening were considered. The analysis of the test results showed that as the ratio between the axial rigidities of the transverse steel and FRP sheets increases, the effectiveness of the transverse FRP strengthening decreases, which can be expressed as:

$$R^* = -0.53 \ln \rho_{s,f} + 0.29 \quad with \quad 0 \le R^* \le 1 \qquad \text{(A2-44)}$$

This new reduction factor (R^*) is merely applied as a further reduction to Khalifa's model (Khalifa, 1998) for the bond mechanism. Thus the reduction factor used to calculate the shear contribution of FRP sheets is calculated as the lowest of three values:

$$R = lesser\ of \begin{cases} 0.006/\varepsilon_{fu} \\ 0.5622\left(\rho_f E_f\right)^2 - 1.218\rho_f E_f + 0.778 \\ R^* \left\{ 0.0042\left(f_{cm}\right)^{2/3} w_{fe} \Big/ \left[\left(E_f t_f\right)^{0.58} \varepsilon_{fu} d\right] \right\} \end{cases} \qquad \text{(A2-45)}$$

Though the model presents a reasonable attempt to quantify the effects of transverse steel reinforcement on the effectiveness of externally bonded FRP, it is based on a limited number of

test results and should be validated with further experimental study. Since this model is merely a modification of Khalifa's model (Khalifa, 1998), it also exhibits similar deficiencies.

In 2003, Hsu et al. (Hsu et al., 2003 and Zhang and Hsu, 2005) presented an *R* factor modified from that of Khalifa et al. (1998) and added it to the effect of the concrete compressive strength which is known to influence the bond stress between the FRP and concrete. Eleven rectangular RC beams with dimensions of 6 inches by 9 inches were tested in this study to investigate parameters of interest (i.e. various CFRP types and shear reinforcing configurations). The proposed model was based on the test results of this and the existing experimental database. This model introduces two new approaches for determining the reduction factor (*R*), the smaller of which is used to calculate the effective strain (ε_{fe}). The first approach considers the role of concrete compressive strength on the direct-shear behavior between FRP and concrete and is based on curve fitting of the data using $\rho_f E_f / f_c'$ instead of the axial rigidity ($\rho_f E_f$):

$$R = 1.8589\left(\rho_f E_f / f_c'\right)^{-0.7488} \qquad \text{(A2-46)}$$

Because Equation A2-46 is based on a regression study in which the experimental data points are distributed both above and below the best fitting curve, a safety factor of 0.8 was applied to shift the curve down such that it fall below most of data points and thus yields conservative estimates:

$$R = 1.4871\left(\rho_f E_f / f_c'\right)^{-0.7488} \qquad \text{(A2-47)}$$

The authors pointed out that the similar equation proposed by Khalifa (1998), which is claimed to be used to calculate the reduction factor for rupture only, is calibrated from test results including both FRP rupture and debonding failures. It was observed from the experimental data that FRP ruptures occurred when $\rho_f E_f < 0.55$ GPa and that debonding occurred when 0.55 GPa < $\rho_f E_f < 1.2$ GPa. The authors showed that better correlation with the experimental data could be achieved when the concrete compressive strength (f_c') is considered in addition to the FRP axial rigidity ($\rho_f E_f$). The second approach introduces a new reduction factor based on the bonding mechanism which recognizes the dominant role of the concrete compressive strength on the direct shear behavior of the FRP. The ultimate direct shear strength (τ_{max}) is derived from an empirically based design equation which is a function of f_c' as follows:

$$\tau_{\max} = \left(5\times10^{-6}\times f_c'^2\right) - \left(2.73\times10^{-2}\times f_c'\right) + 925.3 \qquad \text{(English)} \qquad \text{(A2-48)}$$

$$\tau_{\max} = \left(7.64\times10^{-4}\times f_c'^2\right) - \left(2.73\times10^{-2}\times f_c'\right) + 6.38 \qquad \text{(Metric)} \qquad \text{(A2-49)}$$

The reduction factor (*R*) is based on an assumed triangular stress distribution along the effective bond length (L_e) in which the maximum stress is given by the empirical design equation for τ_{max} (Figure A 2.12).

$$R = \frac{\tau_{\max} L_e}{2 f_{fu} t_f} \le 1 \qquad \text{(A2-50)}$$

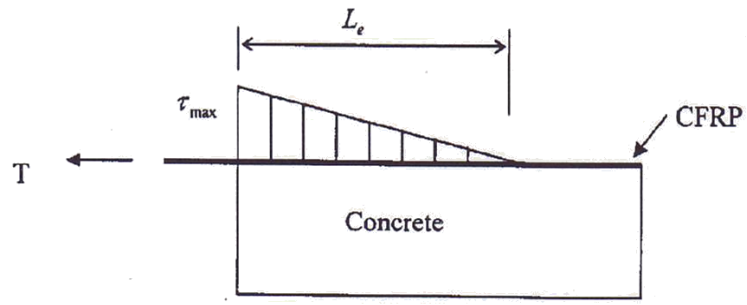

Figure A 2.12 Simplified Stress Distribution along FRP Laminates (Zhang and Hsu, 2005)

The authors suggested an approximate estimate of 2.95 inches for the effective bond length. The FRP shear contribution is thus calculated using the same equation as proposed by Khalifa et al. (1998) but with the newly proposed reduction factors as:

$$V_f = \frac{A_f f_{fe} (\sin\beta + \cos\beta) d_f}{s_f} \quad \text{(A2-51)}$$

where: $f_{fe} = \mathrm{R}\, f_{fu}$ (A2-52)

This model could benefit from further research into better defining the effective development length and ultimate direct shear strength. This model also does not consider the interaction between steel and FRP transverse reinforcements.

The third group of models focused on the non-uniformity of the strain distribution along the height of externally bonded FRP reinforcements. Unlike most models previously discussed in this section, these models do not rely on the assumption of a 45° shear crack and thus the shear crack angle (θ) has been considered as a variable in the expressions for V_f. However, the interaction between the transverse steel reinforcement and externally bonded FRP is not considered by the following models and thus the amount of transverse steel reinforcement is not a variable of the models in this group.

The first model based on extensive experimental work investigating effective stress distribution along externally bonded FRP was developed by Chen and Teng (2003a and 2003b). Specifically, they developed two models to address the debonding and FRP rupture failure modes separately. Their models are based on the assumption that the stress distribution in the FRP along the shear crack is non-uniform as a result of: (1) the variation in shear crack width along its length, (2) linear-elastic nature of FRP, and (3) the bond behavior between FRP and concrete. Since most of the beams strengthened by complete wrapping fail in shear by rupture, and most of those strengthened by U-wrapping or side-bonding fail by debonding of the FRP, one of these two models would apply, depending on the strengthening scheme. The computation of the FRP contribution to shear capacity is based on the truss model as shown in Equation A2-53 and differs for each model only in the means of computing the effective FRP stress ($f_{frp,e}$).

$$V_{frp} = 2 f_{frp,e} t_{frp} w_{frp} \frac{h_{frp,e} (\cot\theta + \cot\beta) \sin\beta}{s_{frp}} \quad \text{(A2-53)}$$

The model uses stress distribution factors developed to reflect the fact that the effective stress at ultimate failure is merely a fraction of the maximum stress achievable for the debonding and FRP rupture limit states, respectively. Since the stress distribution factors have been derived assuming that discrete FRP strips can be treated as an equivalent continuous FRP sheet, the equations are applicable for both discrete strips and continuous wrapping. With a minor modification, this model can be applied to beams for which mechanical anchorage systems are used to prevent or delay debonding. For the debonding limit state, the non-uniform stress distribution in the FRP is accounted for with a stress distribution factor (D_{frp}) applied to the maximum stress in the FRP ($\sigma_{frp,max}$) as shown:

$$f_{frp,e} = D_{frp}\sigma_{frp,\max} \tag{A2-54}$$

where: $$D_{frp} = \frac{\int_{zt}^{zb} \sigma_{frp,z} dz}{h_{frp,e}\sigma_{frp,\max}} \tag{A2-55}$$

Simplified expressions for the maximum stress in the FRP ($\sigma_{frp,max}$) and the stress distribution factor (D_{frp}) were developed by evaluating the bond behavior from simple shear tests like those shown in Figure A 2.13.

The most important aspect of this bond behavior is the effective bond length which is defined as the length of bond beyond which no additional strength can be achieved. The authors have developed models for predicting the effective bond length and bond strength based on experimental data covering a wide range of parameters found in the literature as shown in Equations A2-56 through A2-61.

The maximum stress in the FRP ($\sigma_{frp,max}$) is expected to occur in the region with the longest bond length and is limited by the ultimate bond strength in the case of debonding as shown in Equation A2-62. Assuming the critical shear crack to be a straight line, the maximum bond length (L_{max}) in the FRP can be expected to occur at the bottom end of the shear crack for U-wrap configurations and at mid-height for side bonded configurations.

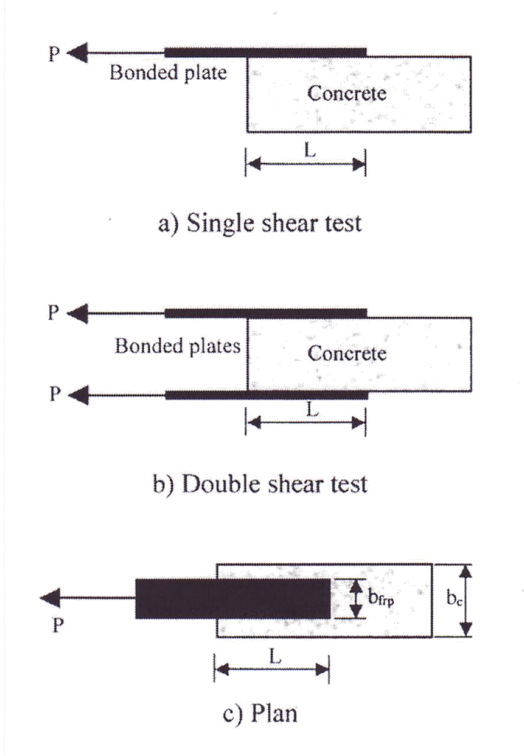

Figure A 2.13 Single and Double Shear Tests (Chen and Teng, 2003a)

$$\sigma_{frp,z} = \min \begin{cases} f_{frp} \\ 0.427\beta_w \beta_{Lz} \sqrt{\dfrac{E_{frp}\sqrt{f_c^{'}}}{t_{frp}}} \end{cases} \tag{A2-56}$$

where: $$\beta_{Lz} = \begin{cases} 1 \quad if \;\; \lambda_z \geq 1 \\ \sin\dfrac{\pi\lambda_z}{2} \quad if \;\; \lambda_z < 1 \end{cases} \tag{A2-57}$$

$$\lambda_z = \frac{L_z}{L_e} \tag{A2-58}$$

$$L_z = \frac{z}{\sin\beta} \tag{A2-59}$$

$$L_e = \sqrt{\frac{E_{frp} t_{frp}}{\sqrt{f_c^{'}}}} \tag{A2-60}$$

$$\beta_w = \sqrt{\frac{2 - w_{frp}/s_{frp}\sin\beta}{1 + w_{frp}/s_{frp}\sin\beta}} \tag{A2-61}$$

$$\sigma_{frp,\max} = \min \begin{cases} f_{frp} \\ 0.427\beta_w \beta_L \sqrt{\dfrac{E_{frp}\sqrt{f_c^{'}}}{t_{frp}}} \end{cases} \tag{A2-62}$$

where: $$\beta_L = \begin{cases} 1 & if\ \lambda \geq 1 \\ \sin\dfrac{\pi\lambda}{2} & if\ \lambda < 1 \end{cases} \tag{A2-63}$$

$$\lambda = \frac{L_{\max}}{L_e} \tag{A2-64}$$

$$L_{\max} = \begin{cases} \dfrac{h_{frp,e}}{\sin\beta} & U-wrap \\ \dfrac{h_{frp,e}}{2\sin\beta} & side\ bonded \end{cases} \tag{A2-65}$$

The stress distribution factor (D_{frp}) for the debonding limit state is thus derived by substituting the above expressions for $\sigma_{frp,z}$ and $\sigma_{frp,max}$ into Equation A2-55 and it can be expressed as:

$$D_{frp} = \begin{cases} \dfrac{2}{\pi\lambda}\dfrac{1-\cos\dfrac{\pi}{2}\lambda}{\sin\dfrac{\pi}{2}\lambda} & if\ \lambda \leq 1 \\ 1-\dfrac{\pi-2}{\pi\lambda} & if\ \lambda > 1 \end{cases} \tag{A2-66}$$

The FRP rupture limit state occurs when the crack width of the critical shear cracks becomes excessive and causes the strain in the FRP to reach its ultimate strain. Fibers in the most highly strained region are torn once they reach their ultimate strength. Rupture propagates along the shear crack as the stresses are redistributed to adjacent fibers which are also torn once they reach their ultimate strength. Thus the strain in the FRP at any instant during the failure process is non-uniform along the shear crack. The resulting analogous assumption that all FRPs intersected by the critical shear crack will reach its ultimate strength, as is often used in the case of steel stirrup reinforcement, is inappropriate and unconservative. As in the case of debonding, the authors use a stress distribution factor (D_{FRP}) to account for the fact that the effective stress in the FRP intersected by a shear crack ($f_{FRP,e}$) is only a fraction of the ultimate tensile strength of the FRP (f_{FRP}), expressed as follows:

$$f_{FRP,e} = D_{FRP}\, f_{FRP} \tag{A2-67}$$

Since this stress distribution was not recognized in most previous studies and because it is difficult to measure during testing when the location of the critical shear crack is unknown prior to failure, limited information is available. The authors consider a normalized strain distribution which can take one of many theoretical shapes developed using Equations A2-68 and A2-69.

$$\bar{\varepsilon}_z = \begin{cases} \dfrac{1-C\bar{z}}{1-C}\bar{z} & 0 \le C < \dfrac{1}{2} \\ 4C\bar{z}\left(1-C\bar{z}\right) & \dfrac{1}{2} \le C \le 1 \end{cases} \tag{A2-68}$$

where: $\bar{z} = \dfrac{z}{z_b}$ (A2-69)

The shape of the strain distribution developed using Equations A2-68 and A2-69 is dependent upon the value of the coefficient C, ranging from parabolic with a maximum strain at mid-height for C=1 to linear when C=0 as shown in Figure A 2.14. The strain distribution factor is taken as the ratio of the average strain to the maximum strain within the effective FRP height as shown in Equations A2-70 through A2-74.

Though the actual strain distribution is not yet known, it varies over a small range for the various values that can be assumed for the coefficient *C* as shown in Figure A 2.15. To simplify the strain distribution model, the authors make the following assumptions:

(1) Partial debonding of the FRP is expected to occur in most cases prior to failure, but the ultimate failure is due to FRP rupture. The FRP will most likely debond across the full height of the beam along the critical shear crack and therefore the strain in the FRP is approximately proportional to the width of the shear crack.

(2) The width of the shear crack can be represented by a linear function starting a zero at the crack tip near the top of the member and increasing toward the bottom of the member.

$$D_{FRP} = \frac{\int_{z_t}^{z_b} \bar{\varepsilon}_z dz}{h_{FRP,e}\,\bar{\varepsilon}_{z,\max}} = \begin{cases} \dfrac{1+\zeta}{2(1-C)} - \dfrac{C}{3(1-C)}\left(1+\zeta+\zeta^2\right) & 0 \le C < \dfrac{1}{2} \\ 2C\left(1+\zeta\right) - \dfrac{4}{3}C^2\left(1+\zeta+\zeta^2\right) & \dfrac{1}{2} < C \le 1 \text{ and } \zeta = \dfrac{1}{2C} \\ \dfrac{3\left(1+\zeta\right) - 2C\left(1+\zeta+\zeta^2\right)}{6\zeta\left(1-C\zeta\right)} & \dfrac{1}{2} < C \le 1 \text{ and } \zeta > \dfrac{1}{2C} \end{cases} \tag{A2-70}$$

where: $h_{FRP,e} = z_b - z_t$ (Figure A 2.16) (A2-71)

$\zeta = z_t / z_b$ (Figure A 2.16) (A2-72)

$z_t = d_{FRP,t}$ (Figure A 2.16) (A2-73)

$z_b = 0.9d$ (Figure A 2.16) (A2-74)

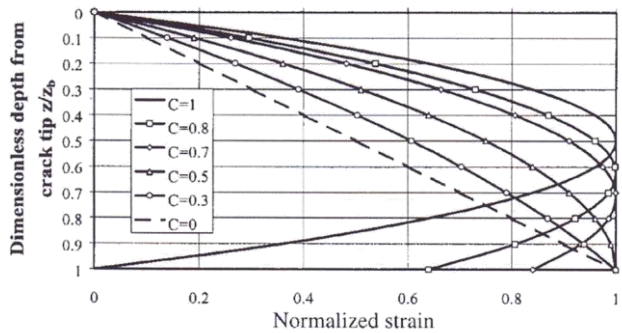

Figure A 2.14 Normalized Strain Distribution in FRP along Shear Crack (Chen and Teng, 2003b)

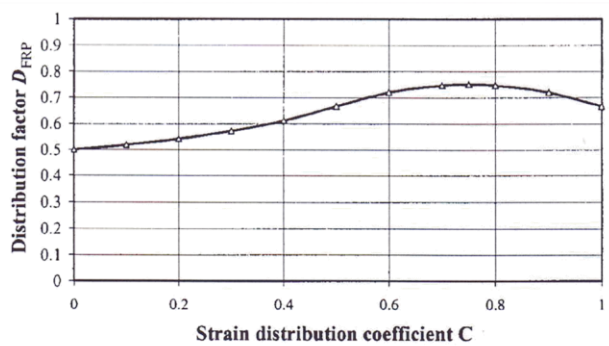

Figure A 2.15 Effect of Strain Distribution Coefficient (*C*) on Distribution Factor (D_{FRP}) (Chen and Teng, 2003b)

Based on the above assumptions, the authors suggest that a linear strain distribution model (C = 0) be used to approximate the actual strain distribution with reasonable accuracy.

$$D_{FRP} = \frac{1+\zeta}{2} \qquad \text{(A2-75)}$$

For both models, the effective FRP height is defined by an upper edge which is 0.1d below the physical upper edge of the FRP and a lower edge which is taken to be at the centroid of the flexural steel reinforcement as shown in Figure A 2.16. This assumption for the effective lower edge is based on (1) the critical shear crack often develops from a vertical flexural crack which changes to a diagonal shear crack only after extending above the flexural steel and (2) forces in the FRP cannot be supported by the concrete cover. The model only needs to be altered to account for the possibility that the lower ends of side-bonded strips are not flush with the soffit of the beam.

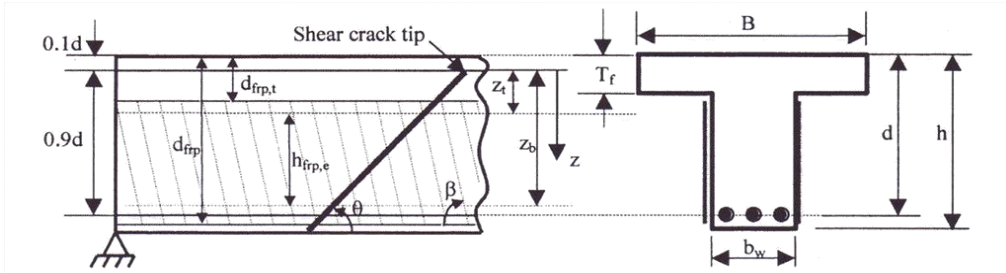

(a) Debonding Limit State

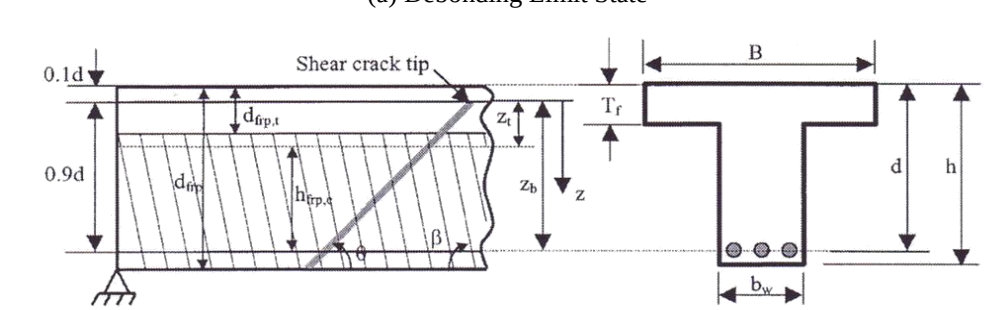

(b) FRP Rupture Limit State

Figure A 2.16 Free-Body Diagram of General Shear Strengthening Schemes (Chen and Teng, 2003a,b)

For practical design, the authors recommend the crack inclination angle be assumed as 45° and the shear contribution of FRP be determined using Equations A2-76 through A2-79. In addition, they recommend that the maximum stress in the FRP, in the case of the debonding limit state, be based on the 95th percentile characteristic value of the bond strength determined from simple shear tests.

$$V_{frp} = 2\frac{f_{frp,ed}}{\gamma_{frp}} t_{frp} w_{frp} \frac{h_{frp,e}\left(\sin\beta + \cos\beta\right)}{s_{frp}} \qquad \text{(A2-76)}$$

where: $f_{frp,ed} = D_{frp}\sigma_{frp,\max}$ (A2-77)

$$\sigma_{frp,\max} = 0.315\beta_w\beta_L\sqrt{\frac{E_{frp}\sqrt{f_c^{'}}}{t_{frp}}} \le f_{frp} \quad \text{(debonding limit state)} \qquad \text{(A2-78)}$$

$$\sigma_{frp,\max} = \begin{cases} 0.8 f_{frp} & if \ \dfrac{f_{frp}}{E_{frp}} \le \varepsilon_{\max} \\ 0.8\varepsilon_{\max} E_{frp} & if \ \dfrac{f_{frp}}{E_{frp}} > \varepsilon_{\max} \end{cases} \quad \text{(FRP rupture limit state)} \qquad \text{(A2-79)}$$

The factor 0.8 used in the FRP rupture limit state in Equation A2-79 reflects the reduction in ultimate tensile strength which can be due to sharp corners of the concrete member if not properly rounded.

An additional limitation is also placed by the authors on the maximum usable strain of FRP (ε_{max}) to control the width of the shear cracks and prevent shear failure without FRP rupture. The authors recommend a value of ε_{max} = 1.5% until greater information can be obtained which can

lead to a more sound proposal. The authors also suggest that only the FRP rupture limit state needs to be checked for complete wrap shear strengthening schemes and only the debonding limit state needs to be checked for side bonded shear strengthening schemes. However, they recommend that both limit states be checked for the case of U-wrap strengthening schemes as both failure modes are a possibility. Since this model was derived based on the assumption that strips could be treated as equivalent continuous sheets, a strip spacing limitation is imposed by the authors to ensure that a sufficient number of strips are intersected by the shear crack thus validating this assumption (see Equation A2-80 and Figure A 2.17). As discussed previously, the bond length is most effective at the lower end of the shear crack for U-wrapped configurations and at mid-height for side bonded configurations. In addition, the strip must be sufficiently deformed to be effective; however, a strip placed near the crack tip will only experience minor deformations and thus will be ineffective.

$$s_{frp} - \frac{w_{frp}}{\sin\beta} \leq \min\begin{cases} \dfrac{h_{frp,e}\left(1+\cot\beta\right)}{2} \\ 300\ mm \end{cases} \qquad \text{(A2-80)}$$

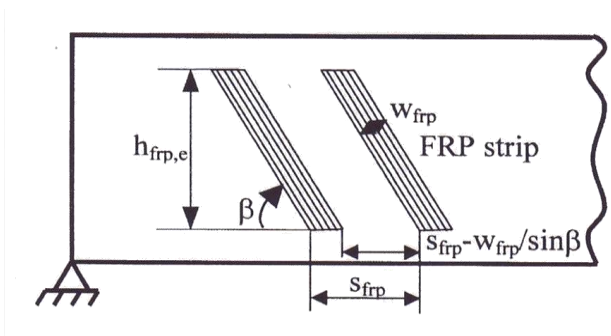

Figure A 2.17 FRP Strengthening Nomenclature (Chen and Teng, 2003a)

The theoretical models and proposed design models were compared with 46 experimental data consisting of debonding failures and 58 experimental data consisting of FRP rupture failures all obtained from the literature (Uji, 1992: Al-Sulaimani et al, 1994; Chajes et al., 1995;, Kage et al., 1997; Sato et al., 1997a; Taerwe et al., 1997; Araki et al., 1997; Funakawa et al.; 1997; Kamiharako et al., 1997; Ono et al., 1997; Umezu et al., 1997; Triantafillou, 1998a; Khalifa et al., 1998; Chaallal et al., 1998b; Mitsui et al., 1998; Kachlakev and Barnes, 1999b; Hutchinson and Rizkalla, 1999; Mutsuyoshi et al., 1999; and Khalifa and Nanni, 2000). The theoretical models proved to be in good agreement with the experimental results and the proposed design model was found to be conservative in all cases except for a few statistical outliers. Although the authors recognized that the internal steel stirrups may not reach yielding if the strains in the FRP at the ultimate limit state are low, no approach is provided to account for this particular circumstance. An argument could also be made for the validity of the expressions for the debonding limit state which was derived based on simple shear tests on small scale specimens. In the case of FRP rupture failure mode, deeper investigation should be pursued to obtain a better understanding of the stress distribution along the shear crack which may not be linear as assumed in the proposed model. Greater accuracy might also be obtained by accounting for a variable shear crack angle instead of the proposed 45° angle.

In 2005, Carolin and Taljsten (2005b) proposed a model to address the linear-elastic and anisotropic nature of the composite, non-uniform strain distribution along the depth of the cross section, and behavior at the service and ultimate limit states. The non-uniform strain distribution along the depth of the cross section is due to the linear elastic behavior of the FRP until failure. Since there is no distinct yield plateau, as in the case of steel reinforcements, assumption of a uniform stress distribution along the FRP would be invalid. Instead, when the most stressed fibers reach or exceed their ultimate capacity they rupture and the forces are redistributed to neighboring fibers. In their model, this non-uniform strain distribution is taken into account with a reduction factor and strain limitations are set on the principal strain in the concrete rather than the fiber strain as used in other models. The model handles the non-uniform strain distribution by deriving an effective strain in the FRP based on an average fiber utilization factor (η). This factor is expressed as the average strain in the fibers over the height of the cross section compared to the strain in the most stressed fiber (ε_{max}) of the cross section. The strain in the fibers along the height depends on the loading conditions and fiber orientation and can be evaluated using engineering mechanics. The average value is obtained by integrating the strains over the height as:

$$\eta = \left(\int_{-h/2}^{h/2} \varepsilon_f \left(y \right) dy \right) \Big/ \left(\varepsilon_{\max} h \right) \qquad \text{(A2-81)}$$

Three different material models are used by the researchers to analyze the sensitivity of the proposed strain distribution with respect to the material models. The first model is based on a reinforced concrete member having the same stiffness in all directions for both tension and compression. It is pointed out that this is not a true reflection of the real material behavior; however, the model is considered to provide the extreme limit for the material model. The second model recognizes the differences in stiffness of cracked concrete related to the reinforcement ratio and type of loading. The third model considers areas of high shear and low flexural forces in which flexural cracks will not be present. The fiber utilization factor for fibers bonded vertically is found to be 0.67 for all loading conditions since they are not affected by the bending moment. However, this is not the case for other fiber configurations as shown in Table A 2.1.

Table A 2.1 Effectiveness Factors (η) for Web-Bonded Fibers

Normalized bending moments m_1/m_2	Fiber direction 45° material models			Fiber direction 90°
	1	2	3	
-2/-1	0.27	0.59	0.52	0.67
-1/0	0.44	0.64	0.62	0.67
0/0	0.67	0.67	0.67	0.67
0/1	0.44	0.64	0.62	0.67
0/2	0.40	0.61	0.57	0.67
0.4/1.25	0.48	0.64	0.64	0.67
1/1	0.36	0.67	0.68	0.67
1/2	0.40	0.64	0.62	0.67
2/3	0.33	0.64	0.56	0.67
-1/1	0.30	0.61	0.56	0.67

Equations for the FRP contribution are derived from anisotropic composites and account for the angle of the fibers as well as the direction of the principal strain (crack inclination). To derive the FRP contribution using the truss analogy, an arbitrary crack path must be defined. Since it is difficult to predetermine the crack orientation angle, three geometric angles are required to define the FRP contribution. The required angles are the crack inclination (α), fiber orientation (β), and the angle between the principal tensile stress and fiber orientation (θ) as shown in Figure A 2.18 and the derived equations shown in Equations A2-82 through A2-85.

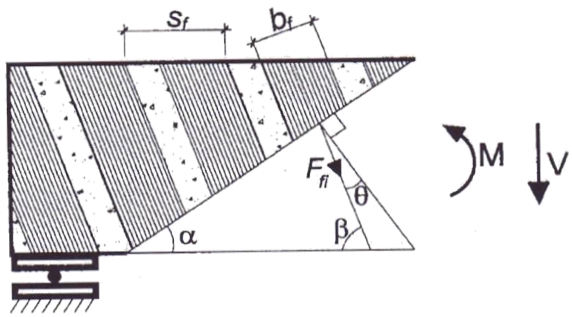

Figure A 2.18 Free-Body Diagram for a Given Strengthening Orientation (Carolin and Taljsten, 2005b)

$$V_f = F_f \sin(\beta) \quad \text{(A2-82)}$$

where: $$F_f = \sum F_{fi} \quad \text{(A2-83)}$$

$$F_{fi} = \sigma_{fe} A_f \quad \text{(A2-84)}$$

$$A_f = t_f z \frac{\cos\theta}{\sin\alpha} \quad \text{(complete wrap)} \quad \text{(A2-85)}$$

$$A_f = t_f z \frac{b_f}{s_f \sin\beta} \frac{\cos\theta}{\sin\alpha} \quad \text{(composite strips)} \quad \text{(A2-86)}$$

$$\sigma_{fe} = \varepsilon_{fe} E_f \quad \text{(A2-87)}$$

$$\varepsilon_{fe} = \eta \varepsilon_{cr} \quad \text{(A2-88)}$$

The contribution of FRP can be determined by Equations A2-89 and A2-90. The effective FRP strain (ε_{fe}) is also a function of the critical strain (ε_{cr}) limited by following miminum critera; i) the ultimate allowable fiber capacity (ε_{fu}), ii) the maximum allowable strain to prevent bond failure (ε_{bond}), iii) the maximum allowable strain to prevent loss of the concrete contribution ($\varepsilon_{c\,max}$) as shown in Equation A2-91. The strain limitations ε_{bond} and $\varepsilon_{c\,max}$ can be determined from ACI 440.2R-08 equations 11-6(a) and 11-6(b) (ACI, 2008).

$$V_f = \eta \varepsilon_{cr} E_f t_f z \frac{\cos\theta}{\sin\alpha} \quad \text{(Complete wrap)} \quad \text{(A2-89)}$$

$$V_f = \eta \varepsilon_{cr} E_f t_f z \frac{b_f}{s_f \sin\beta} \frac{\cos\theta}{\sin\alpha} \quad \text{(Composite strips)} \quad \text{(A2-90)}$$

where: $$\varepsilon_{cr} = \min \begin{Bmatrix} \varepsilon_{fu} \\ \varepsilon_{bond} \cos^2\theta \\ \varepsilon_{c\,\max} \cos^2\theta \end{Bmatrix} \quad \text{(A2-91)}$$

The authors performed 23 experimental beam tests with rectangular cross sections for comparison with the proposed model. Strain measurements over the height of the beam's cross section were normalized with respect to the maximum measured strains and compared with the proposed fiber utilization factor. The experimentally measured strain distributions were found to be in good agreement with the theoretical calculations. The authors suggest that areas of further study include (1) the effects of the aggregate size of the concrete and amount of reinforcement on the maximum allowable concrete strain, (2) the bond characteristics and limitation on strain due to anchorage, which should be based on fracture mechanics, (3) methods for estimating crack risks and crack widths.

The first model accounting for the effects of shear span-to-effective depth ratio was developed by Cao et al. (2005). Test results from 18 beams, tested as part of their study, showed a strong relationship between the shear crack angle (θ) and the shear span-to-effective depth ratio (λ). Shear span-to-effective depth ratios ranging from 1.4 to 3.0 and external FRP reinforcement index ($\omega_{frp} = 2A_{frp}E_{frp}/(bs_{frp}E_c)$) ranging from 0.09 to 1.1% were investigated. All specimens were pre-cracked prior to being strengthened by complete wrapping with discrete strips. In this model, debonding of the most highly stressed FRP strip from the sides of the beam is defined as the lower bound limit state. This limit state is justified since some level of debonding will always precede FRP rupture and loss of aggregate interlock will typically occur prior to FRP rupture which requires large deformations and cracking. Their model took an approach similar to that of Chen and Teng (2003a), deriving a strain distribution factor (D_{frp}) expressed as the ratio of the average strain in the FRP over the effective height to the maximum strain.

$$D_{frp} = \frac{\sum_{i=1}^{n} \varepsilon_{frp,i}}{n\varepsilon_{frp,\max}} \qquad \text{(FRP strips)} \qquad \text{(A2-92)}$$

$$D_{frp} = \frac{\int_0^l \varepsilon_{frp}(x)\,dx}{l\varepsilon_{frp,\max}} \qquad \text{(Continuous sheets)} \qquad \text{(A2-93)}$$

Strain measurements from strain gages placed along the effective height of the FRP were used to determine the strain distribution factor at various load stages. The strain distribution factor was observed to decrease with increase in the shear span-to-depth ratio. This phenomenon is illustrated in Figure A 2.19. Beams with small shear span-to-depth ratios are likely to fail due to diagonal compression failure which leads to fairly uniform shear cracks. As a result, the stress distribution in the FRP intersecting the cracks will be fairly uniform. However, beams with large shear span-to-depth ratios, fail by the formation of flexural shear cracks. These cracks start as flexural cracks along the tension face and then turn into shear cracks as they propagate toward the loading point. This type of cracking pattern is typically wider in the lower part of the beam where the crack first started. As a result, the stress distribution in the FRP intersecting the cracks will be non-uniform.

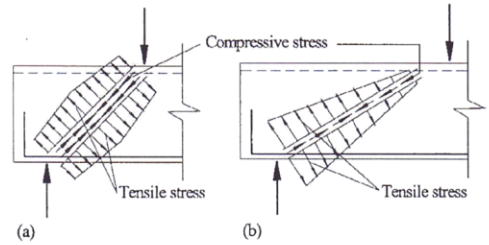

Figure A 2.19 FRP Strain Distribution based on Shear Span-to-Depth Ratio (a) small λ and (b) large λ (Cao et al., 2005)

The following modification was proposed to the original strain distribution factor proposed by Chen and Teng (2003a) to account for the effects of shear span-to-depth ratio.

$$D_{frp} = \left(1 - \frac{\pi - 2}{\lambda_{frp}\pi}\right)(1.2 - 0.1\lambda) \quad for \quad 1.4 < \lambda < 3 \tag{A2-94}$$

The term (1.2 – 0.1λ) is a linear modification of the original factor proposed by Chen and Teng (2003a) to account for shear span-to-depth effects derived from regression of the test results. The critical shear crack angle also depends on the shear span-to-depth ratio. To represent the effects of the critical shear angle, the strain distribution factor can be divided by tan θ.

$$V_{frp} = 2t_{frp}w_{frp}E_{frp}\varepsilon_{frp,\max}\frac{h_{frp}}{s_{frp}}\frac{D_{frp}}{\tan\theta} \tag{A2-95}$$

Alternative expressions for the strain distribution factor and FRP shear contribution are offered by the authors as a reasonable approximation to account for both the shear span-to-depth ratio and shear crack angle effects as follows:.

$$V_{frp} = 2D_{f\theta}t_{frp}w_{frp}E_{frp}\varepsilon_{frp,\max}\frac{h_{frp}}{s_{frp}} \tag{A2-96}$$

where: $$D_{f\theta} = \left(1 - \frac{\pi - 2}{\lambda_{frp}\pi}\right) \times \begin{cases} 1 \quad for\ \lambda \le 1.4 \\ \dfrac{1}{1 - 0.2(\lambda - 1.4)^2} \quad for\ 1.4 < \lambda < 3 \\ 2.05 \quad for\ \lambda \ge 3 \end{cases} \tag{A2-97}$$

The maximum FRP strain at debonding ($\varepsilon_{frp,max}$) in Equation A2-96 is calculated as proposed by Chen and Teng (2003a) only the authors propose that β_L be 1.0 as shown in Equation A2-98 since FRP wrapped around a corner of the beam can provide support to the portions on the sides of the beam to help delay complete debonding even if $L < L_e$.

$$\varepsilon_{frp,\max} = \frac{0.427\beta_w\sqrt[4]{f_c'}}{\sqrt{E_{frp}t_{frp}}} \tag{A2-98}$$

An issue arising from this model is that it is based on empirical strain gage measurements in which some abnormalities were observed in the test results. Since the models are also developed from regression of a limited number of test results, a few abnormalities in strain gage readings could lead to unrealistic strain distribution factors. In the cases where the number of FRP strips crossing the shear crack is small, the measured strains may also not be truly representative of the actual distribution. This model could also benefit from further investigation into the effect of the amount of FRP on the strain distribution factor. The following model is verified for the shear-span-to-depth ratio of 1.4 to 3.0; thus further testing is needed to expand the applicability of the model to other shear span-to-depth ratios. The equations proposed in this model are calibrated from tests in which only shear strengthening with discrete strips and complete wrapping schemes were considered. The authors claim that the models are also applicable to continuous FRP sheets; however, additional testing is needed to verify this as well as investigate other strengthening schemes.

The last group of models consists of theoretical approaches which are mechanics-based and do not rely on experimental results for regression or calibration. The first attempt to use the compression field theory was demonstrated by Malek and Saadatmanesh in (1998). As with the model developed by Chajes et al. (1995), this model assumes no slipping occurs between the FRP and concrete thus complete composite action is developed. The model assumes that the FRP tensile strength reaches when the composite is intersected by the critical shear crack, if sufficient bond length is available. This model also assumes that there are no stress concentrations within the FRP material. This model also introduced the anisotropic behavior of the FRP considering the fiber orientation and used the two-dimensional stress-strain relationship of the composite. The constitutive equations proposed in this model are presented in Equations A2-99 and A2-109.

$$\begin{bmatrix} \sigma_{xx} \\ \sigma_{yy} \\ \tau_{xy} \end{bmatrix} = \begin{bmatrix} \overline{Q_{11}} & \overline{Q_{12}} & \overline{Q_{13}} \\ \overline{Q_{12}} & \overline{Q_{22}} & \overline{Q_{23}} \\ \overline{Q_{13}} & \overline{Q_{23}} & \overline{Q_{33}} \end{bmatrix} \begin{bmatrix} \varepsilon_{xx} \\ \varepsilon_{yy} \\ \gamma_{xy} \end{bmatrix} \tag{A2-99}$$

where:

$$\overline{Q_{11}} = Q_{11}\cos^4(\theta) + 2(Q_{12} + 2Q_{33})\sin^2(\theta)\cos^2(\theta) + Q_{22}\sin^4(\theta) \tag{A2-100}$$

$$\overline{Q_{12}} = Q_{12}\left(\sin^4(\theta) + \cos^4(\theta)\right) + (Q_{11} + Q_{22} - 4Q_{33})\sin^2(\theta)\cos^2(\theta) \tag{A2-101}$$

$$\overline{Q_{22}} = Q_{11}\sin^4(\theta) + 2(Q_{12} + 2Q_{33})\sin^2(\theta)\cos^2(\theta) + Q_{22}\cos^4(\theta) \tag{A2-102}$$

$$\overline{Q_{13}} = (Q_{11} - Q_{12} - 2Q_{33})\sin(\theta)\cos^3(\theta) + (Q_{12} - Q_{22} + 2Q_{33})\sin^3(\theta)\cos(\theta) \tag{A2-103}$$

$$\overline{Q_{23}} = (Q_{11} - Q_{12} - 2Q_{33})\sin^3(\theta)\cos(\theta) + (Q_{12} - Q_{22} + 2Q_{33})\sin(\theta)\cos^3(\theta) \tag{A2-104}$$

$$\overline{Q_{33}} = (Q_{11} + Q_{22} - 2Q_{12} - 2Q_{33})\sin^2(\theta)\cos^2(\theta) + Q_{33}\left(\sin^4(\theta) + \cos^4(\theta)\right) \tag{A2-105}$$

$$Q_{11} = \frac{E_l}{1 - v_{lt}v_{tl}} \tag{A2-106}$$

$$Q_{22} = \frac{E_t}{1 - v_{lt}v_{tl}} \tag{A2-107}$$

$$Q_{12} = v_{tl}\frac{E_l}{1 - v_{lt}v_{tl}} \tag{A2-108}$$

$$Q_{33} = G_{lt} \tag{A2-109}$$

The FRP shear contribution (F_p) is determined as the resultant of the shear and normal stresses in the vertical direction along the shear crack as shown in Equation A2-110. The stirrup contribution (F_v) is calculated using the corresponding stress-strain relationship of steel as shown in Equations A2-111 and A2-112.

$$V_f = F_p = ht_p\left[\overline{Q_{13}}\varepsilon_2 + \overline{Q_{23}}\varepsilon_1 + \frac{\left(\overline{Q_{12}}\varepsilon_2 + \overline{Q_{22}}\varepsilon_1\right)}{\tan\left(\theta_c\right)}\right] \tag{A2-110}$$

where: ε_1 and ε_2 are the strains in the FRP corresponding to a system of coordinates coinciding with the principle directions

$$V_s = F_v = E_s\varepsilon_y A_v \frac{h_v}{\tan\left(\theta_c\right)s} \quad for \quad \varepsilon_y < \frac{F_y}{E_s} \tag{A2-111}$$

$$V_s = F_v = F_y A_v \frac{h_v}{\tan\left(\theta_c\right)s} \quad for \quad \varepsilon_y \geq \frac{F_y}{E_s} \tag{A2-112}$$

The total shear force acting on the beam is assumed to be resisted only by the FRP and steel stirrups. Thus the concrete shear mechanisms (i.e. aggregate interlock and concrete in the compression zone) are not considered in this model. Instead, the authors recommend the concrete contribution to shear capacity (V_c) be determined by ACI 318 provisions (ACI 318, 2008). Therefore, the total force resisted by the FRP and steel stirrups is calculated based on equilibrium of the forces along the crack. The shear crack inclination angle (θ_c) is determined by following a rigorous iteration process until both equilibrium and compatibility requirements are satisfied. The model was developed considering continuous sheets; however, it can be easily modified to predict the behavior of beams strengthened with FRP strips by considering the strip spacing. No experimental testing was used in the calibration of this model; however, experimental tests performed by Norris (1994) were used to evaluate the accuracy of the model for predicting the gain in shear capacity due to externally bonded FRP. A short coming of this theoretical approach is that it is based on the assumption of perfect bond between FRP and concrete and as such the debonding failure mode is not considered.

In 2001, Deniaud and Cheng (2001, 2003, and 2004) proposed a model which combines the strip method and shear friction approach, taking into account the interaction between concrete, transverse steel reinforcement, and FRP. In this model, each FRP strip crossing the web shear crack is evaluated individually to determine the maximum allowable strain based on geometry of the FRP sheets. The geometry of the FRP strips is defined by the bonded length above and below the critical shear crack as well as the anchorage provided at each end of the strip. A free-body diagram is used to evaluate the force and moment equilibrium in each FRP strip. The bond strength and corresponding maximum allowable strain (ε_x) for each FRP strip is evaluated using an interface mean shear stress curve. This curve was developed from best fit regression of simple shear tests conducted by Alexander and Cheng (1997) and Kamel et al. (2000), assuming an effective bond length as proposed by Maeda et al. (1997). As a result, the relationship of bond strength to concrete strength was proposed as (Figure A 2.20):

$$\frac{\tau}{\sqrt{f_c^{'}}} = \left(2 - \frac{L}{L_{eff}}\right)\beta \qquad (L < L_{eff}) \tag{A2-113}$$

$$\frac{\tau}{\sqrt{f_c'}} = \frac{L_{eff}}{L}\beta \qquad (L \geq L_{eff}) \tag{A2-114}$$

where: $L_{eff} = e^{6.134-0.58\ln(tE_{FRP})}$ (A2-115)

The strain distribution was initially assumed to be linear among the fibers along the critical shear crack. However, experimental testing by the authors showed that a relatively uniform strain distribution existed in the FRP fibers along the critical shear crack and thus a uniform strain distribution is assumed in the model. The smallest value of ε_x occurs in the FRP strip closest to the location where the shear crack intersects the web-flange interface because it has the shortest effective bond length. Thus this strip is assumed to be the first to fail, resulting in a sequential progression of debonding of the FRP strips. With each debonding of an FRP strip, the shear forces initially carried by the debonded FRP strip are redistributed to the remaining FRP strips. As the number of remaining FRP strips continues to decrease, the strain (ε_x) increases until a maximum (ε_{max}) is reached. At this point a ratio of the remaining bond width over the initial width (R_L) is determined to reflect the loss in FRP contribution. Analysis showed that the maximum FRP strain (ε_{max}) and remaining bond ratio (R_L) are independent of the concrete crack angle (θ) and not significantly affected by the number and width of FRP strips crossed by the crack. However, the peak load carried by the FRP sheets is strongly tied to the number and width of FRP sheets crossing a crack. A computer program was written for performing a parametric study to generate data for deriving simplified equations for the maximum FRP strain (ε_{max}) and remaining bond area ratio (R_L) as shown in Equations A2-116 and A2-117. Five different parameters were investigated in the formation of the equations for ε_{max} and R_L which include: (1) concrete strength (f_c'), (2) height of FRP sheets (d_{FRP}), (3) stiffness per unit width of FRP sheets ($t \cdot E_{FRP}$), (4) principle fiber direction (α), and (5) anchorage of the FRP sheets.

$$\varepsilon_{\max} = \frac{3\sqrt{f_c'}\,d_{FRP}^{0.16}}{(tE_{FRP})^{0.67}(k_a \sin\alpha)^{0.1}} \leq \varepsilon_{ultFRP} \qquad (\%) \tag{A2-116}$$

$$R_L = 1 - 1.2\exp\left[-\left(\frac{d_{FRP}}{k_e L_{eff}\sin\alpha}\right)^{0.4}\right] \tag{A2-117}$$

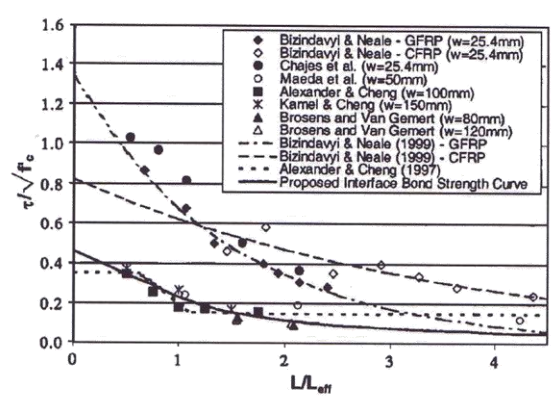

Figure A 2.20 Interface Shear Strength Curves (Deniaud and Cheng, 2004)

In Equations A2-116 and A2-117, the factors k_a and k_e describe the end anchorage conditions as shown in Figure A 2.21. With this method, the effectiveness of any anchorage system can be evaluated with the calibration of appropriate anchorage factors. The maximum FRP strain was found to be strongly dependent on the concrete strength, FRP stiffness, and to a lesser degree, the FRP height, anchorage conditions, and fiber orientation. The remaining bond ratio was found to be dependent on the effective bond length and stiffness of the FRP sheets.

Finally the FRP contribution for a given fiber orientation (α) is expressed as:

$$T_{FRP} = d_{FRP} t E_{FRP} \varepsilon_{\max} R_L \left(\frac{w_{FRP}}{s_{FRP}} \right)^2 \left(\frac{s}{d_s} \sin\alpha + \cos\alpha \right) \sin\alpha \qquad \text{(A2-118)}$$

While the FRP contribution is described by the strip method, the shear friction approach incorporates the interaction between concrete, steel stirrups, and FRP as well as a variable of concrete crack angle (θ).

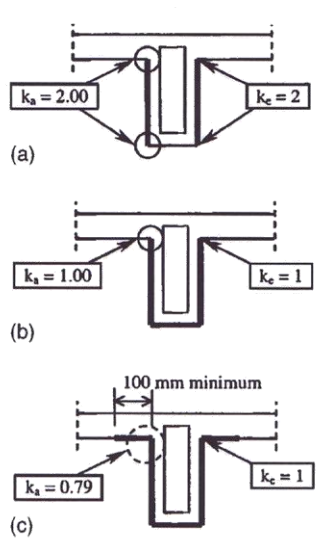

Figure A 2.21 Anchorage Factors for Various Sheet Anchorage and End Conditions (a) FRP on Lateral Faces Only, (b) U-Wrapped, (c) U-Wrapped with Bands Extended underneath Flange (Deniaud and Cheng, 2004)

The shear friction approach is based on the formation of a single diagonal web shear crack along which slippage occurs. Since externally bonded FRP sheets are only activated after cracking in the web has formed, the shear friction model might be well suited for describing the FRP behavior. The strip and shear friction models require evaluation of all potential shear crack paths to find the one which yields the lowest shear capacity. To eliminate the need for an iterative calculation process, a continuous formulation was also derived as:

$$V_r = 0.25 k^2 f_c^{'} b_w h \frac{d_s}{ns} + T_v (n-1) + n T_{FRP} \quad \text{(discrete formulation)} \qquad \text{(A2-119)}$$

$$V_r = k \sqrt{f_c^{'} A_c \left(T_v + T_{FRP} \right) \frac{d_s}{s}} - T_v \quad \text{(continuous formulation)} \qquad \text{(A2-120)}$$

where: $k = 2.1\left(f_c^{'}\right)^{-0.4}$ (A2-121)

$$T_v = A_v f_{vy} \quad \text{(A2-122)}$$

Based on suggestions from Tozser and Loov (1999), an approximation accounting for the effective section of the flange of T-beams and I-beams participating in the shear friction was added to the model. This approximation is based on an assumed angle of 45° to account for the effective section in the flange as shown in Figure A 2.22. Thus the total shear capacity and FRP contribution can be rewritten to account for the effective flange area which participates in shear resistance as:

$$V_r = 0.25k^2 f_c^{'}\left(A_{cf}\tan\theta_f + A_{cw}\tan\theta_w\right) + T_v n_s + T_{FRP} \quad \text{(A2-123)}$$

$$T_{FRP} = d_{FRP} t E_{FRP} \varepsilon_{\max} R_L \left(\frac{w_{FRP}}{s_{FRP}}\right)^2 \left(\frac{\sin\alpha}{\tan\theta_w} + \left(n_s + 1\right)\cos\alpha\right)\sin\alpha \quad \text{(A2-124)}$$

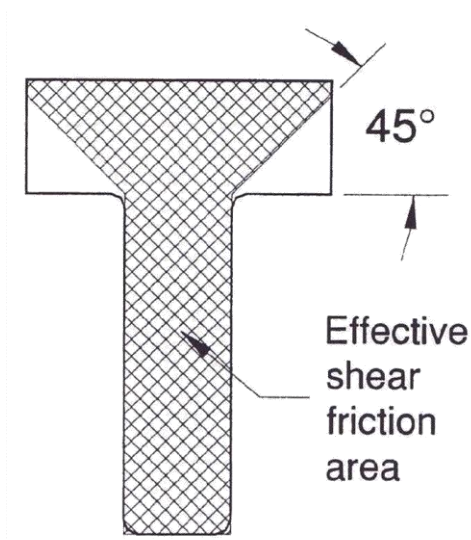

Figure A 2.22 Effective Shear Friction Area (Deniaud and Cheng, 2001)

A total of 35 small-scale and full-scale test data from the literature (Uji, 1992; Al-Sulaimani et al., 1994; Chajes et al., 1995; Sato et al., 1996; Triantafillou, 1998a; Drimoussis and Cheng, 1994; Adey et al., 1998; and Deniaud and Cheng, 2001 and 2003) was used to validate the proposed design model. It is noted that fully wrapped specimens tested by Triantafillou (Triantafillou, 1998a) were not considered in the validation with the justification that full wrapping is not a practical strengthening scheme in field applications. A short-coming of this model is that the maximum FRP strain (ε_{max}) and remaining bond area ratio (R_L) are based on an interface shear strength curve which has been found to be significantly affected by the width of FRP sheets bonded to the concrete block specimens used in the simple shear tests. It was noted that the bond strength increases as the width of the FRP sheets becomes smaller. Thus, multiple interface shear strength curves have been proposed (Alexander and Cheng, 1997; Bizindavyi and Neale, 1999; and Deniaud and Cheng, 2001) with large scatter existing among them based on the data from which they were defined. Further investigation should be conducted to better define the effect of the FRP width bonded to the concrete.

Monti and Liotta (2005 and 2007) developed a closed-form equation based on mechanics rather than regression-based formulas. The model is obtained by defining the generalized constitutive law of an FRP layer bonded to concrete with consideration for the compatibility imposed by the shear crack opening and appropriate boundary conditions. The boundary conditions are dependent upon the strengthening configuration used. This model was developed on the assumptions that (1) shear cracks are evenly spaced along the beam axis, and inclined at an angle (θ), (2) crack depth is equal to the internal lever arm ($z = 0.9d$) at the ultimate limit state, and (3) the resisting shear mechanism is based on the Mörsch's truss model in the case of U-jacketing and complete wrap strengthening schemes and on crack-bridging in the case of side bonding. Using FRP bond-slip relationships, they proposed an analytical expression of the stress field in the FRP sheet crossing a shear crack. This model makes V_f a function of both the strengthening configuration and some basic geometric and mechanical parameters. It provides an expression for the FRP shear strength that is dependent on the type of wrapping. Two failure criterions are considered in the development of the model (i.e. a straight strip/sheet and a strip/sheet wrapped around a corner). For straight strip/sheet configurations, the effective bond length (l_e) and debonding strength (f_{fdd}) are important and can be determined as:

$$l_e = \sqrt{\frac{E_f t_f}{2 f_{ctm}}} \tag{A2-125}$$

where: $$f_{ctm} = 0.27 R_{ck}^{\ 2/3} \tag{A2-126}$$

$$f_{fdd} = \frac{0.80}{\gamma_{f,d}} \sqrt{\frac{2 E_f \Gamma_{Fk}}{t_f}} \tag{A2-127}$$

where: $$\Gamma_{Fk} = 0.03 k_b \sqrt{f_{ck} f_{ctm}} \tag{A2-128}$$

$$k_b = \sqrt{\frac{2 - w_f / \rho_f}{1 + w_f / 400}} \geq 1 \tag{A2-129}$$

$$w_f \leq \min\left(0.9d, hw\right) \sin\left(\theta + \beta\right) / \sin\theta \tag{A2-130}$$

If the available bond length (l_b) is less than the effective bond length (l_e), the debonding strength is reduced as:

$$f_{fdd}\left(l_b\right) = f_{fdd} \frac{l_b}{l_e} \left(2 - \frac{l_b}{l_e}\right) \tag{A2-131}$$

In the case of FRP strips/sheets wrapped around a corner, it was noted that the FRP attains only a fraction of its ultimate strength (f_{fu}). This fractional percentage was found to be a function of the corner radius (r_c) with respect to the beam width (b_w) as determined by:

$$f_{fu}(r_c) = f_{fdd} + \left(\phi_R f_{fu} - f_{fdd}\right) \quad \text{(for } l_b \geq l_e\text{)} \tag{A2-132}$$

$$f_{fu}(l_b, r_c) = f_{fdd}\left(l_b\right) + \left(\phi_R f_{fu} - f_{fdd}\left(l_b\right)\right) \quad \text{(for } l_b < l_e\text{)} \tag{A2-133}$$

where: $$\phi_R = 0.2 + 1.6 \frac{r_c}{b_w} \quad \text{where} \quad 0 \leq \frac{r_c}{b_w} \leq 0.5 \tag{A2-134}$$

The FRP stress profile along the crack ($\sigma_{f,cr}(x)$) is obtained using a generalized stress-slip law, appropriate compatibility equations for the crack width, and appropriate boundary conditions and end restraints. The generalized stress-slip law for both failure criterions are depicted in Figure A 2.23 through Figure A 2.25. In order to provide a closed-form solution, a linear expression is assumed for the crack width compatibility as:

$$w(x) = \alpha x \tag{A2-135}$$

where: α = the crack opening angle

Assuming symmetry at each side of the crack, the slip imposed on the FRP strip/sheet crossing the crack may be expressed as follows.

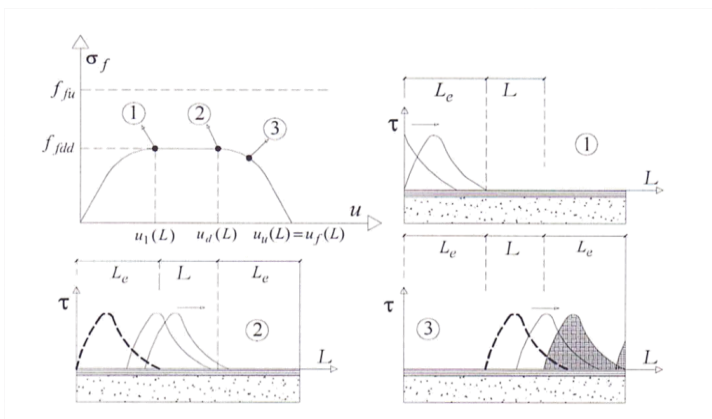

Figure A 2.23 Stress-Slip Law for Straight FRP Strip/Sheet with Free End and Sufficient Bond Length ($l_b \geq l_e$) (Monti and Liotta, 2005)

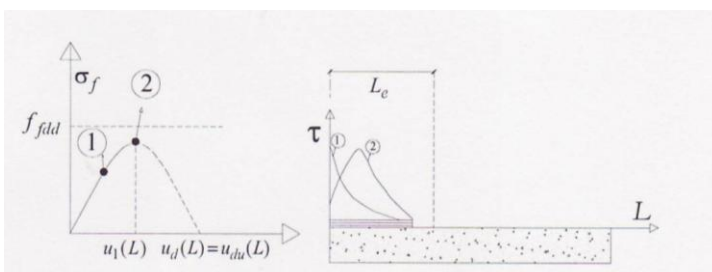

Figure A 2.24 Stress-Slip Law for Straight FRP Strip/Sheet with Free End and Insufficient Bond Length ($l_b < l_e$) (Monti and Liotta, 2005)

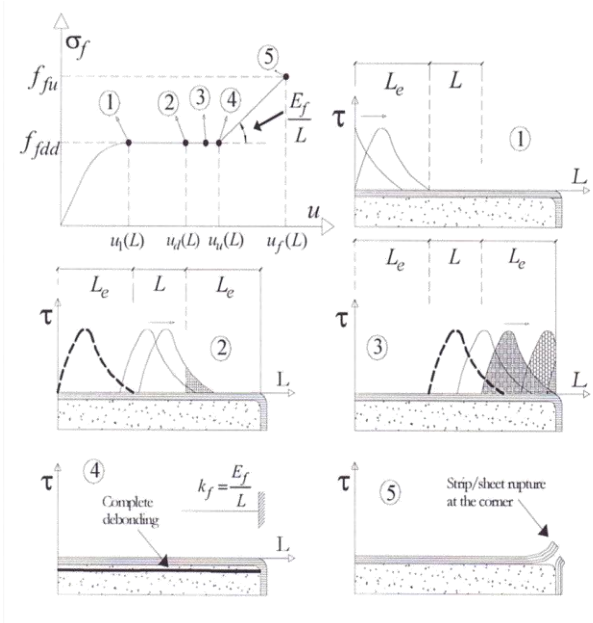

Figure A 2.25 Stress-Slip Law for FRP Strip/Sheet Wrapped Around a Corner (Monti and Liotta, 2005)

$$u(\alpha, x) = \frac{w(x)}{2}\sin(\theta+\beta) = \frac{1}{2}\alpha x \sin(\theta+\beta) \tag{A2-136}$$

Appropriate boundary conditions refer to the available bond length (l_b) on each side of the shear crack which is governed by the adopted strengthening scheme. These boundary conditions are depicted in Figure A 2.26 with the available bond length (l_b) determined as:

$$l_b = \begin{Bmatrix} \min\{l_{b,top}(x), l_{b,bot}(x)\} & S = side\ bonding \\ l_{b,top}(x) & U = U\text{-}jacketing \\ \max\{l_{b,top}(x), l_{b,bot}(x)\} & W = wrapping \end{Bmatrix} \tag{A2-137}$$

The FRP stress profile along the shear crack is thus determined by substituting the compatibility equation $u(\alpha,x)$ and boundary conditions l_b (with recognition for the strengthening scheme adopted) into the constitutive stress-slip law. Figure A 2.27 shows the FRP stress profiles for the three different strengthening schemes when FRP sheets are used. The effective stress in the FRP (σ_{fe}) is then defined in Equation A2-138 as the mean FRP stress profile along the shear crack length defined as z/sinθ.

$$\sigma_{fe}(\alpha) = \frac{1}{z/\sin\theta}\int_0^{z/\sin\theta} \sigma_{f,cr}\left[u(\alpha,x), l_b(x)\right]dx \tag{A2-138}$$

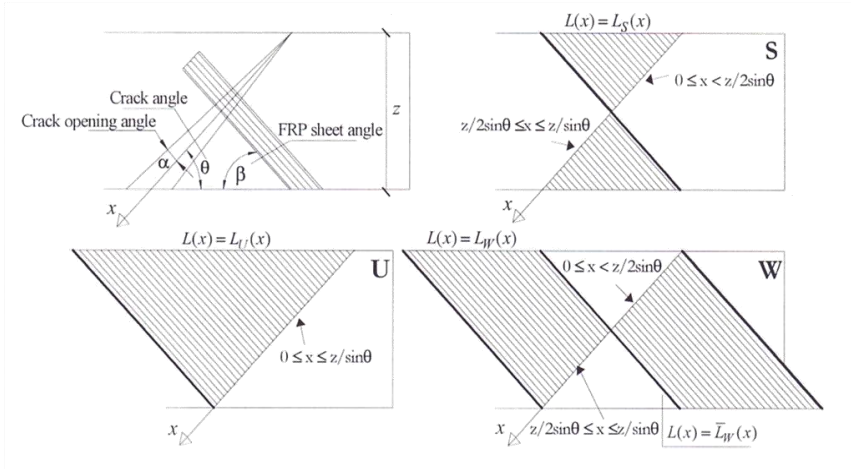

Figure A 2.26 Boundary Conditions for the Three Different Strengthening Schemes (S = side bonded, U = U-jacketing, W = complete wrapping) (Monti and Liotta, 2005)

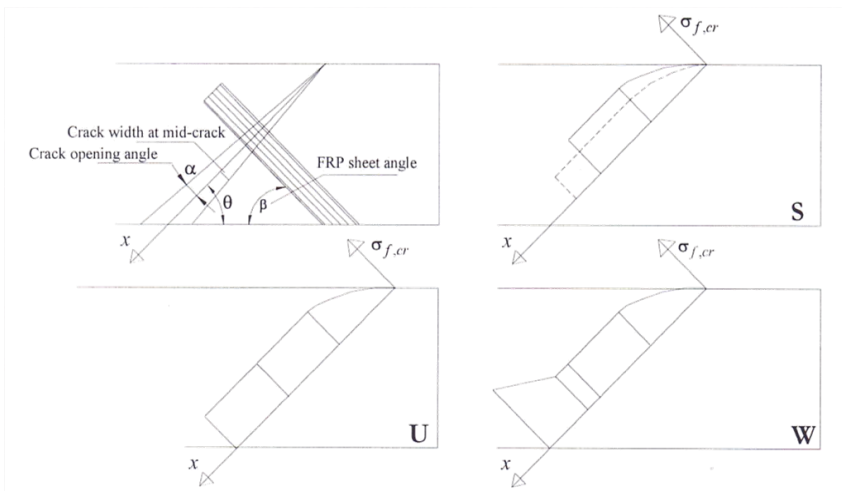

Figure A 2.27 FRP Stress Profiles Along a Shear Crack for the Three Different Strengthening Schemes (S = Side bonded, U = U-Jacketing, W = Complete Wrapping) (Monti and Liotta, 2005)

The effective debonding strength (f_{fed}) used to determine the FRP contribution is then found as the maximum FRP effective stress (σ_{fe}), as shown in Equations A2-139 through A2-143.

$$\frac{d\sigma_{fe}(\alpha)}{d\alpha} = 0 \qquad \text{(A2-139)}$$

side bonded:

$$f_{fed} = f_{fdd}\frac{z_{rid,eq}}{\min\{0.9d, h_w\}}\left(1 - 0.6\sqrt{\frac{l_{eq}}{z_{rid,eq}}}\right)^2 \qquad \text{(A2-140)}$$

where: $$z_{rid,eq} = \min\{0.9d, h_w\} - \left(l_e - \frac{s_f}{f_{fdd}/E_f}\right)\sin\beta \qquad \text{(A2-141)}$$

U-jacketing:

$$f_{fed} = f_{fdd}\left[1-\frac{1}{3}\frac{l_e \sin\beta}{\min\{0.9d, h_w\}}\right] \tag{A2-142}$$

complete wrapping:

$$f_{fed} = f_{fdd}\left[1-\frac{1}{6}\frac{l_e \sin\beta}{\min\{0.9d, h_w\}}\right]+\frac{1}{2}\left(\phi_R f_{fd} - f_{fdd}\right)\left[1-\frac{l_e \sin\beta}{\min\{0.9d, h_w\}}\right] \tag{A2-143}$$

The ultimate shear contributions provided by FRP in the case of u-jacketing and complete wrapping were derived considering the Mörsch resisting mechanism. In the case of side bonded FRP, the ultimate shear resistance is considered to be provided by crack bridging. The final equations for the FRP contribution are proposed as shown in Equations A2-144 and A2-145.

U-jacket and complete wrapping:

$$V_{Rd,f} = \frac{1}{\gamma_{Rd}} 0.9d \cdot f_{fed} \cdot 2t_f \left(\cot\theta + \cot\beta\right)\frac{w_f}{p_f} \tag{A2-144}$$

side bonded:

$$V_{Rd,f} = \frac{1}{\gamma_{Rd}} \min\{0.9d, h_w\}\, f_{fed} \cdot 2t_f \frac{\sin\beta}{\sin\theta}\frac{w_f}{p_f} \tag{A2-145}$$

The authors suggest that FRP shear resistance calculated by this model be added to the concrete and steel stirrup contributions as determined by Eurocode 2 (Eurocode No. 2, 1992). The model was validated with experimental results from 24 beam tests performed by the authors plus 36 tests collected from the literature (Al-Sulaimani et al., 1994; Chajes et al., 1995; Funakawa et al., 1997; Kamiharako et al., 1997; Norris et al., 1997; Taerwe et al., 1997; Umezu et al., 1997; Challal et al., 1998c; Khalifa and Nanni, 2000; Park et al., 2001; Deniaud and Cheng, 2004; Aprile and Benedetti, 2004). Unlike most other models, this model does not rely on the 45° truss assumption and thus the FRP contribution is a function of the shear crack angle (θ). This model has been developed considering only a single shear crack extending through the shear span. This assumption may not lead to reasonable predictions when considering that a band of multiple diagonal cracks usually develop in a typical beam carrying shear forces. This model also does not consider any interaction between the internal steel reinforcement and externally bonded FRP.

Sim et al. (2005) suggested a model using plastic limit theory based on the study by Nielson and Braestrup (1975). In this model, the FRP contribution is determined by means of an upper bound solution technique. This model is developed based on an idealized failure mechanism of the beam in which a plastic hinge is formed at midspan of the beam which is subject to a vertical deflection (u). A linear yield line is assumed between midspan and the support reactions with an angle of rotation (θ). Applying energy conservation theory, the following equilibrium expression is derived.

$$V \cdot u = V_{sp} \cdot u + V_c \cdot u = \left[\left(s_y + \alpha \cdot \gamma_y\right) bd \cot\theta\right] \cdot u + \left[\frac{1}{2}\nu \cdot \sigma_{cu}\left(1-\cos\theta\right)\frac{bd}{\sin\theta}\right] \cdot u \tag{A2-146}$$

where: $s_y = \frac{A_v \cdot f_{sy}}{b \cdot e}$ (A 2-147)

$$\gamma_y = \frac{A_p \cdot f_{py}}{b \cdot t}\left(\sin\beta + \cos\beta\right) \quad \text{(A2-148)}$$

The first term in Equation A2-146 represents the work done by stirrups and FRP under a unit displacement (u), and the second term represents the work done by concrete. This model is only valid if the beam is assumed to be under pure shear which may be appropriate in deep beams where the shear is predominant over flexure. Thus the model is only applicable to members for which the shear-span-to-depth ratio (a/d) is less than 2.0. A strength efficiency factor (α) is suggested to account for the fact that the strength of the FRP bonded to the exterior cannot be fully utilized. The efficiency factor was empirically determined from a series of 10 rectangular RC tests which included one control specimen and nine specimens strengthened with various strengthening schemes. The efficiency factor is suggested to be highly dependent on the physical characteristics of the strengthening material, bond between concrete and the strengthening material, and the strengthening method used. Efficiency factors for the three strengthening materials used in the experimental investigation (CFRP, CFS, and GFRP) were obtained by averaging the test results. The constant, ν, in Equation A2-146 represents the contribution of the concrete compressive strength which, the authors recommend, should be taken as less than 1.0 because the concrete stress in the web should not reach the concrete compressive strength (σ_{cu}). In their study, ν was taken as 0.4 and was justified by the fact that the width of the beam specimens used in calibration of this model were relatively large compared to their depth. The least-upper bound solution is obtained by determining the value of θ for which the derivative of the shear strength (V) with respect to θ equals zero. Using appropriate mathematical implementations, the shear capacity of shear-strengthened beams is derived as follows.

$$\frac{\tau}{\nu\sigma_{cu}} = \frac{\sqrt{a^2+d^2} - (1-2\phi)a}{2d} \quad if \quad \phi < \frac{\sqrt{\left(a^2+d^2\right)} - a}{2\sqrt{\left(a^2+d^2\right)}} = \lambda \quad \text{(A2-149)}$$

$$\frac{\tau}{\nu\sigma_{cu}} = \sqrt{\phi(1-\phi)} \quad if \quad \lambda \le \phi \le \frac{1}{2} \quad \text{(A2-150)}$$

$$\frac{\tau}{\nu\sigma_{cu}} = \frac{1}{2} \quad if \quad \phi > \frac{1}{2} \quad \text{(A2-151)}$$

The validity of the model was checked against the experimental results of Chen and Teng (2003a) and was found to be in good agreement. However, the efficiency factor has been calibrated based only on the author's test results. The author admits that the strength efficiency factor could be improved with further investigations into the characteristics of the FRP, bond properties, and shear-span-to-depth ratio (a/d). In addition, this model is only valid for members with shear-span-to-depth ratio (a/d) less than 2.0 due to the idealized failure mechanism used as the bases of its formulation. As such, this model may not be suitable for typical bridge girders which are considered to carry a more or less uniform load and in which the behavior is more like that of slender beams (a/d > 2.0). Table A 2.2 through A 2.5 summarize the formulations for each analytical model which have been grouped based on the commonality in concepts as discussed above.

A2.4 Current Codes/Guidelines/Specifications

Currently, design procedures for shear strengthening of concrete structures with externally bonded FRP are available in various forms such as codes, guidelines, and specifications provided by several different countries. These documents are introduced briefly in this section along with the core design equations as summarized in Table A 2.6.

American Concrete Institute (ACI) 440.2R-08 (ACI 440, 2008).

ACI 440.2R-08 - Guide for the Design and Construction of Externally Bonded FRP Systems for Strengthening Concrete Structures (ACI 440, 2008) - is the most complete document to date and is based on ACI 318-08 (ACI 318, 2008). ACI 440.2R-08 determines the shear contribution of the FRP shear reinforcement based on failure modes. The FRP shear contribution is limited by an effective strain which establishes the maximum strain achieveable in the FRP as governed by FRP rupture or debonding failure modes. When complete wrapping is used, FRP rupture is the prescribed mode of failure, and the effective strain in the FRP laminate is limited to 0.4% to preclude the loss of aggregate interlock or 75% of the ultimate strain of FRP (empirically based – Priestley et al., 1996). For U-wrap and side bonding applications, both FRP debonding and rupture are potential failure modes. Thus, it is recommended that the shear contribution of FRP based on both failure modes is investigated and the lesser of the two be used. For FRP debonding failure, the effective strain is limited by a bond-reduction coefficient proposed by Khalifa et al. (1998) or 0.4% to preclude the loss of aggregate interlock. Reinforcement limits are also proposed on the total shear reinforcement provided by the combination of externally bonded FRP and internal steel stirrups.

Canadian CAN/CSA S806-02 (CSA S806, 2002).

The CAN/CSA S806-02 Canadian Building Code (CAN/CSA S806, 2002) is a formalized design code addressing externally bonded FRP reinforcement for concrete. The equations of the CAN/CSA S806-02 (CAN/CSA S806, 2002) are based on the simplified method used in the CAN/CSA A23.3-94 (CAN/CSA A23.3, 1994) concrete design code. However, the next edition of CAN/CSA S806 is expected to reflect the method described in the 2004 edition of CAN/CSA A23.3 (CAN/CSA A23.3, 2004). The simplified method used in CAN/CSA A23.3-94 (CAN/CSA A23.3, 1994) is restricted to the usual cases where shear reinforcement including FRP is perpendicular to the longitudinal axis of the beam. The shear contribution of FRP is determined based on failure modes. For failure due to FRP rupture, the strain in FRP is limited to 0.004 similar to that specified in ACI 440.2R-08 (ACI 440, 2008). In the case of bond critical applications the strain in FRP is limited to 0.002.

Canadian CAN/CSA S6-06 (CAN/CSA S6-06, 2006).

The CAN/CSA S6-06 Canadian Bridge Code (CAN/CSA S6-06, 2006) deals with the shear strengthening of concrete with externally-bonded FRPs. In addition, CAN/CSA S6-06 (CSA S6-06, 2006) specifies that the FRP shear strengthening system should consist of U-wraps anchored in the compression zone or complete wrapping of the cross-section. The equations specified in the codes are identical to the ones in ACI 440.2R-02 (ACI 440, 2002).

European fib-TG 9.3 Bulletin 14 (fib-TG9.3, 2001).
European fib-Bulletin 14 (fib-TG9.3, 2001) calculates the FRP contribution to shear capacity (V_{fd}) according to the model proposed by Triantafillou and Antonopulos (2000). This document was produced by fib Task Group 9.3 and represents a combination of guidelines and state-of-the-art reports. Fib-Bulletin 14 recognizes the difference in expected performance between FRP material types as well as preformed and wet lay-up FRP systems. This difference is expressed in the form of various material safety factors. Delamination and debonding are extensively addressed using a simplified bilinear bond model and considering the effects of the loss of composite action between the FRP and concrete substrate. Durability is discussed, but no clear design guidelines are provided to address this issue.

Japanese JSCE Recommendations for Upgrading Concrete Structures with Continuous Fiber Sheets (JSCE, 2001).
Japanese Recommendations (JSCE, 2001) take a performance-based approach to the design of externally bonded FRP materials. In addition to verifying flexural and shear capacity, flexural crack width and protection of the concrete substrate from chloride ion penetration are also considered explicitly.

ISIS Design Manual 4-Strengthening Reinforced Concrete Structures with Externally-Bonded FRP (ISIS, 2001).
This document (ISIS, 2001) provides considerable guidance and a number of design examples for the use of externally bonded FRP based on CAN/CSA S6-06 (CAN/CSA S6-06, 2006) and CAN?CSA S806-02 (CANCSA S806, 2002).

Great Britain Technical Report 55 (Concrete Society, 2004).
This report (Concrete Society, 2004) is similar to fib-Bulletin 14 (fib-TG9.3, 2001) in its approach and scope; however, it addresses more practical construction issues associated with the use of externally bonded FRP materials. Externally bonded FRP strips are treated using a 45° truss analogy similar to other codes and guidelines. The strain in FRP is limited to half of the ultimate design strain for FRP rupture failure. For debonding failure, this report adopted an equation proposed by Neubauer and Rostasy (1997). In all cases, however, the strain is limited to 0.004.

Table A 2.2 Analytical Models Based on Experimentally Determined Limiting Value of FRP Shear Strain/Stress

Author	Year	Equations
Al-Sulaimani et al.	1994	$V_P = \frac{2F_P d}{S_P} = \frac{2\left[\tau_{ave}\frac{t_s h_s}{2}\right]d}{S_P}$ (for shear strips) $V_P = 2F_P = 2\left[\tau_{ave}\left(\frac{dh_w}{2}\right)\right]$ (for shear wings) $V_P = 2F_P = 2\left[\tau_{ult}\left(\frac{dh_j}{2}\right)\right]$ (for U-jackets)
Chages et al.	1995	$V_f = A_f E_f \varepsilon v_{cu} d$ (for FRP oriented at 0/90 degree) $V_f = A_f E_f \varepsilon v_{cu} d\sqrt{2}$ (for FRP oriented at 45/135 degree)

Table A 2.3 Analytical Models Based on an Effective FRP Strain

Author	Year	Equations
Triantafillou	1998a	$V_{frp,d} = \frac{0.9}{\gamma_{frp}} \rho_{frp} E_{frp} \varepsilon_{frp,e} b_w d \left(1+\cot\beta\right)\sin\beta$ $\varepsilon_{frp,e} = 0.0119 - 0.0205\left(\rho_{frp}E_{frp}\right) + 0.0104\left(\rho_{frp}E_{frp}\right)^2$ when $0 \le \rho_{frp}E_{frp} \le 1$ GPa $\varepsilon_{frp,e} = -0.00065\left(\rho_{frp}E_{frp}\right) + 0.00245$ when $\rho_{frp}E_{frp} > 1$ GPa
Khalifa et al.	1998	$V_f = 0.9\rho_{frp}E_{frp}\varepsilon_{fe}b_w d\left(1+\cot\beta\right)\sin\beta$ (Eurocode format) $V_f = \frac{A_f f_{fe}\left(\sin\beta+\cos\beta\right)d_f}{s_f}$ (ACI format) $\varepsilon_{fe} = R\varepsilon_{fu} \qquad f_{fe} = Rf_{fu}$ Based on the effective FRP stress: $R = 0.5622\left(\rho_f E_f\right)^2 - 1.2188\left(\rho_f E_f\right) + 0.778 \le 0.5$ when $\rho_{frp}E_{frp} < 1.1$ GPa Based on bond mechanism: $R = \frac{0.0042\left(f_c^{'}\right)^{2/3} w_{fe}}{\left(E_f t_f\right)^{0.58} \varepsilon_{fu} d_f}$ Effective width: $w_{fe} = d_f$ (complete wrapping) $w_{fe} = d_f - L_e$ (U-wrap) $w_{fe} = d_f - 2L_e$ (side bonded) $s_{f,\max} = w_f + \frac{d}{4} \qquad V_s + V_f \le \frac{2\sqrt{f_c^{'}}b_w d}{3}$
Hutchinson and Rizkalla	1999	$V_n = V_c + V_{se} + V_{f,\max}$ $V_{f\max} = \varepsilon_{fave}E_f 2nt_f w_f \frac{d_f\left(\cot\theta+\cot\alpha_f\right)\sin\alpha_f}{s_f}$ $\varepsilon_{fave} = \varepsilon_{f\max}\frac{\left[d/2+0.5\left(d_f-d/2\right)\right]}{d_f}$ $\varepsilon_{f\max} = L_{fe}C$ $L_{fe} = e^{6.134-0.580\ln\left(t_f E_f\right)}$ and $C = constant\ strain\ rate\ of\ 110\times10^{-6}\,mm^{-1}$ $V_{se} = \varepsilon_{se}E_s A_v \frac{d\cot\theta}{s}$ where $\varepsilon_{se} = \varepsilon_{fave}\sin\alpha_f / \gamma_{fs} \le \varepsilon_{sy}$

Table A 2.3 Analytical Models Based on an Effective FRP Strain (Continued)

Khalifa and Nanni	2000	$V_f = 0.9\rho_{frp}E_{frp}\varepsilon_{fe}b_w d\left(1+\cot\beta\right)\sin\beta$ (Eurocode format) $V_f = \dfrac{A_f\, f_{fe}\left(\sin\beta+\cos\beta\right)d_f}{s_f}$ (ACI format) $\varepsilon_{fe} = R\varepsilon_{fu} \qquad f_{fe} = Rf_{fu}$ R is the least of : $R = 0.5622\left(\rho_f E_f\right)^2 - 1.2188\left(\rho_f E_f\right) + 0.778 \le 0.5$ $R = \dfrac{\left(f_c^{'}\right)^{2/3} w_{fe}}{\varepsilon_{fu} d_f}\left[738.93 - 4.06(t_f E_f)\right]\times 10^{-6}$ $R = \dfrac{0.006}{\varepsilon_{fu}}$
Triantafillou and Antonopoulos	2000	$V_{fd} = 0.9\dfrac{\varepsilon_{fk,e}}{\gamma_f}E_f\rho_f b_w d\left(1+\cot\beta\right)\sin\beta$ (Eurocode format) $\varepsilon_{fk,e} = \alpha\varepsilon_{f,e} \le \varepsilon_{\max} = 0.005 \qquad \alpha = 0.8$ (recommended) $\phi_f V_f = \phi_f \varepsilon_{f,e,A} E_f \rho_f \left(\sin\beta+\cos\beta\right)bd$ (ACI format) $\varepsilon_{f,e,A} = 0.9\varepsilon_{f,e} \le \varepsilon_{\max,A} = 0.006$ $\varepsilon_{f,e} = 0.65\left(\dfrac{f_c^{2/3}}{E_f\rho_f}\right)\times 10^{-3}$ (debonding failure mode) $\varepsilon_{f,e} = 0.17\left(\dfrac{f_c^{2/3}}{E_f\rho_f}\right)^{0.30}\varepsilon_{f,u}$ (shear failure combined with or followed by CFRP fracture) $\varepsilon_{f,e} = 0.048\left(\dfrac{f_c^{2/3}}{E_f\rho_f}\right)^{0.47}\varepsilon_{f,u}$ (shear failure combined with or followed by AFRP fracture) $\left(E_f\rho_f\right)_{\lim} = \left(\dfrac{0.65\times 10^{-3}\alpha}{\varepsilon_{\max}}\right)^{1/0.56} f_c^{2/3} = 0.018 f_c^{2/3}$
Chaallal et al.	2002	$V_f = f\left(\dfrac{a}{d},\rho_{tot}\right)\left(\dfrac{A_f}{S_f}\right)E_f\varepsilon_{eff}d_f$ $\varepsilon_{eff} = 3\times 10^{-5}\times\rho_{tot}^{-0.6522}, \quad \rho_{tot} = n\rho_f + \rho_s$ New deep beam coefficient: $f\left(\dfrac{a}{d},\rho_{tot}\right) = \dfrac{1+2a/d}{12} + \left(1000\rho_{tot} - 0.6\right) \le 1$ but greater than $\dfrac{1+2a/d}{12}$

Table A 2.3 Analytical Models Based on an Effective FRP Strain (Continued)

Pellegrino and Modena	2002	$V_f = 0.9\rho_{frp}E_{frp}\varepsilon_{fe}b_w d\left(1+\cot\beta\right)\sin\beta$ (Eurocode format) $V_f = \dfrac{A_f f_{fe}\left(\sin\beta+\cos\beta\right)d_f}{s_f}$ (ACI format) $\varepsilon_{fe} = R\varepsilon_{fu} \quad f_{fe} = Rf_{fu}$ R is the least of : $R = 0.5622\left(\rho_f E_f\right)^2 - 1.2188\left(\rho_f E_f\right) + 0.778 \le 0.5$ $R = \dfrac{0.006}{\varepsilon_{fu}}$ $R = R^*\left\{0.0042\left(f_{cm}\right)^{2/3} w_{fe} / \left[\left(E_f t_f\right)^{0.58}\varepsilon_{fu} d\right]\right\}$ $0 \le R^* = -0.53\ln\rho_{s,f} + 0.29 \le 1$ $\rho_{s,f} = E_s A_{sw} / E_f A_f$
Hsu et al.	2003	for continuous fiber sheet: $V_f = w_{fe} t_f f_{fe}\sin^2\beta$ for FRP strips: $V_f = \dfrac{A_f f_{fe}\left(\sin\beta+\cos\beta\right)d_f}{s_f}$ $f_{fe} = Rf_{fu}$, $\varepsilon_{fe} = R\varepsilon_{fu}$ Based on model calibration: $R = 1.4871\left(\rho_f E_f / f_c^{'}\right)^{-0.7488}$ Based on bonding mechanism: $R = \dfrac{\tau_{\max} L_e}{2 f_{fu} t_f} \le 1$ $\tau_{\max} = \left(5\times10^{-6}\times f_c^{'2}\right) - \left(2.73\times10^{-2}\times f_c^{'}\right) + 925.3 \quad (English)$ $\tau_{\max} = \left(7.64\times10^{-4}\times f_c^{'2}\right) - \left(2.73\times10^{-2}\times f_c^{'}\right) + 6.38 \quad (Metric)$

Table A 2.4 Analytical Models which Account for Non-uniform Strain Distribution in FRP

Authors	Year	Equations
Chen and Teng	2003 a & b	$V_{frp} = 2\frac{f_{frp,ed}}{\gamma_{frp}} t_{frp} w_{frp} \frac{h_{frp,e}(\sin\beta + \cos\beta)}{s_{frp}}$ $f_{frp,ed} = D_{frp}\sigma_{frp,\max}$ Debonding model: $D_{frp} = \frac{\int_{zt}^{zb} \sigma_{frp,z} dz}{h_{frp,e}\sigma_{frp,\max d}} = \begin{cases} \frac{2}{\pi\lambda}\frac{1-\cos\frac{\pi}{2}\lambda}{\sin\frac{\pi}{2}\lambda} & if\ \lambda \le 1 \\ 1-\frac{\pi-2}{\pi\lambda} & if\ \lambda > 1 \end{cases}$ $\sigma_{frp,\max,d} = 0.315\beta_w\beta_L\sqrt{\frac{E_{frp}}{t_{frp}}\sqrt{f_c^{'}}} \le f_{frp}$ Rupture model: $D_{frp} = \frac{\int_{z_t}^{z_b} \bar{\varepsilon}_z dz}{h_{FRP,e}\bar{\varepsilon}_{z,\max}} = \frac{1+\zeta}{2}$ $\sigma_{frp,\max} = \begin{cases} 0.8 f_{frp} & \text{if} \quad \frac{f_{frp}}{E_{frp}} \le \varepsilon_{\max} \\ 0.8\varepsilon_{\max}E_{FRP} & \text{if} \quad \frac{f_{frp}}{E_{frp}} > \varepsilon_{\max} \end{cases}$ Strip spacing limitation: $s_{frp} - \frac{w_{frp}}{\sin\beta} \le \min\begin{cases} \frac{h_{frp,e}(1+\cot\beta)}{2} \\ 300\ mm \end{cases}$
Carolin and Taljsten	2005b	for complete wrap: $V_f = \eta\varepsilon_{cr}E_f t_f z \frac{\cos\theta}{\sin\alpha}$ for composite strips: $V_f = \eta\varepsilon_{cr}E_f t_f z \frac{b_f}{s_f \sin\beta}\frac{\cos\theta}{\sin\alpha}$ $\eta = \frac{\int_{-h/2}^{h/2} \varepsilon_f(y)dy}{\varepsilon_{\max}h}$ $\varepsilon_{cr} = \min\begin{cases} \varepsilon_{fu} \\ \varepsilon_{bond}\cos^2\theta \\ \varepsilon_{c\max}\cos^2\theta \end{cases}$

Table A 2.4 Analytical Models which Account for Non-uniform Strain Distribution in FRP (Continued)

Cao et al.	2005	$V_{frp} = 2D_{f\theta} t_{frp} w_{frp} E_{frp} \varepsilon_{frp,\max} \dfrac{h_{frp}}{s_{frp}}$ $D_{f\theta} = \left(1 - \dfrac{\pi - 2}{\lambda_{frp}\pi}\right) \times \begin{cases} 1 & for\ \lambda \le 1.4 \\ \dfrac{1}{1 - 0.2(\lambda - 1.4)^2} & for\ 1.4 < \lambda < 3 \\ 2.05 & for\ \lambda \ge 3 \end{cases}$ $\varepsilon_{frp,\max} = \dfrac{0.427\beta_w \sqrt[4]{f_c^{'}}}{\sqrt{E_{frp} t_{frp}}}$

Table A 2.5 Analytical Models Derived from Mechanics Based Approaches Rather than Regression Analysis

Authors	Year	Equations
Malek and Saadatmanesh	1998	$V_f = F_p = ht_p\left[\overline{Q_{13}}\varepsilon_2 + \overline{Q_{23}}\varepsilon_1 + \frac{\left(\overline{Q_{12}}\varepsilon_2 + \overline{Q_{22}}\varepsilon_1\right)}{\tan\left(\theta_c\right)}\right]$ $V_s = F_v = E_s\varepsilon_y A_v \frac{h_v}{\tan\left(\theta_c\right)s} \quad for \quad \varepsilon_y < \frac{F_y}{E_s}$ $V_s = F_v = F_y A_v \frac{h_v}{\tan\left(\theta_c\right)s} \quad for \quad \varepsilon_y \geq \frac{F_y}{E_s}$
Deniaud and Cheng	2001	Discrete formulation: $V_r = 0.25k^2 f_c^{'} b_w h \frac{d_s}{ns} + T_v(n-1) + nT_{FRP}$ $V_r = 0.25k^2 f_c^{'}\left(A_{cf}\tan\theta_f + A_{cw}\tan\theta_w\right) + T_v n_s + T_{FRP}$ (considering flange contribution) Continuous formulation: $V_r = k\sqrt{f_c^{'} A_c\left(T_v + T_{FRP}\right)\frac{d_s}{s}} - T_v$ $k = 2.1\left(f_c^{'}\right)^{-0.4}$ $T_v = A_v f_{vy}$ $T_{FRP} = d_{FRP} t E_{FRP}\varepsilon_{\max} R_L\left(\frac{w_{FRP}}{s_{FRP}}\right)^2\left(\frac{s}{d_s}\sin\alpha + \cos\alpha\right)\sin\alpha$ $T_{FRP} = d_{FRP} t E_{FRP}\varepsilon_{\max} R_L\left(\frac{w_{FRP}}{s_{FRP}}\right)^2\left(\frac{\sin\alpha}{\tan\theta_w} + \left(n_s+1\right)\cos\alpha\right)\sin\alpha$ (considering flange) Maximum allowable strain in FRP: $\varepsilon_{\max} = \frac{3\sqrt{f_c^{'}}\, d_{FRP}^{0.16}}{\left(tE_{FRP}\right)^{0.67}\left(k_a\sin\alpha\right)^{0.1}}(\%) \leq \varepsilon_{ultFRP}$ Remaining bonded width over initial width ratio: $R_L = 1 - 1.2\exp\left[-\left(\frac{d_{FRP}}{k_e L_{eff}\sin\alpha}\right)^{0.4}\right]$

Table A 2.5 Analytical Models Derived from Mechanics Based Approaches Rather than Regression Analysis (Continued)

Monti and Liotta	2005	Side bonding: $V_{Rd,f} = \frac{1}{\gamma_{Rd}} \cdot \min\{0.9d, h_w\} \cdot f_{fed} \cdot 2t_f \cdot \frac{\sin\beta}{\sin\theta} \cdot \frac{w_f}{s_f}$ design effective stress for side bonding: $f_{fed} = f_{fdd} \cdot \frac{z_{rid,eq}}{min\{0.9d, h_w\}} \cdot \left(1 - 0.6\sqrt{\frac{l_{eq}}{z_{rid,eq}}}\right)^2$ $z_{rid,eq} = \min\{0.9d, h_w\} - \left(l_e - \frac{s_f}{f_{fdd}/E_f}\right)\sin\beta$ U-wrap or complete wrapping: $V_{Rd,f} = \frac{1}{\gamma_{Rd}} \cdot 0.9d \cdot f_{fed} \cdot 2t_f \cdot (\cot\theta + \cot\beta) \cdot \frac{w_f}{s_f}$ design effective stress for U-wrapping: $f_{fed} = f_{fdd} \cdot \left[1 - \frac{1}{3}\frac{l_e \sin\beta}{min\{0.9d, h_w\}}\right]$ design effective stress for complete wrapping: $f_{fed} = f_{fdd} \cdot \left[1 - \frac{1}{6}\frac{l_e \sin\beta}{min\{0.9d, h_w\}}\right] + \frac{1}{2}(\phi_R f_{fd} - f_{fdd}) \cdot \left[1 - \frac{l_e \sin\beta}{min\{0.9d, h_w\}}\right]$ $l_e = \sqrt{\frac{E_f t_f}{2 f_{ctm}}}$ where: $f_{ctm} = 0.27 R_{ck}^{2/3}$ $f_{fdd} = \frac{0.80}{\gamma_{f,d}}\sqrt{\frac{2E_f \Gamma_{Fk}}{t_f}}$ where: $\Gamma_{Fk} = 0.03 k_b \sqrt{f_{ck} f_{ctm}}$ $k_b = \sqrt{\frac{2 - w_f/\rho_f}{1 + w_f/400}} \geq 1$ $w_f \leq \min(0.9d, hw)\sin(\theta+\beta)/\sin\theta$ $f_{fdd}(l_b) = f_{fdd}\frac{l_b}{l_e}\left(2 - \frac{l_b}{l_e}\right)$ (for $l_b < l_e$) $\phi_R = 0.2 + 1.6\frac{r_c}{b_w}$ where $0 \leq \frac{r_c}{b_w} \leq 0.5$
Sim et al.	2005	$\frac{\tau}{\nu\sigma_{cu}} = \frac{\sqrt{a^2+d^2} - (1-2\phi)a}{2d}$ *if* $\phi < \frac{\sqrt{(a^2+d^2)} - a}{2\sqrt{(a^2+d^2)}} = \lambda$ $\frac{\tau}{\nu\sigma_{cu}} = \sqrt{\phi(1-\phi)}$ *if* $\lambda \leq \phi \leq \frac{1}{2}$ $\frac{\tau}{\nu\sigma_{cu}} = \frac{1}{2}$ *if* $\phi > \frac{1}{2}$ $\tau = \frac{V}{b \cdot h}$ and $\phi = \frac{A_v \cdot f_{sy}}{b \cdot e \cdot \nu\sigma_{cu}} + \alpha\left(\frac{A_p \cdot f_{sy}}{b \cdot t \cdot \nu\sigma_{cu}}(\sin\beta + \cos\beta)\right)$ $e = stirrup\ spacing$ $t = strengthening\ material\ spacing$

Table A 2.6 Principal Equations of Current Design Guidelines

Codes/Guidelines	Year	Equations
ACI 440.2R-08	2008	$V_n = V_c + V_s + \psi_f V_f$ $V_f = \dfrac{A_{fv} f_{fe} (\sin\alpha + \cos\alpha) d_f}{s_f}$ $f_{fe} = \varepsilon_{fe} E_f$ $\varepsilon_{fe} = 0.004 \le 0.75\varepsilon_{fu}$ for completely wrapped $\varepsilon_{fe} = k_v \varepsilon_{fu}$ for U-wrap or on side $k_v = \dfrac{k_1 k_2 L_e}{11{,}900\varepsilon_{fu}} \le 0.75$ bond reduction coefficient $L_e = \dfrac{23{,}300}{(nt_f E_f)^{0.58}}$ $k_1 = \left(\dfrac{f_c'}{27}\right)^{2/3}$ $k_2 = \begin{cases} \dfrac{d_f - L_e}{d_f} & \text{for U-wraps} \\ \dfrac{d_f - 2L_e}{d_f} & \text{for two sides bonded} \end{cases}$
CSA S806	2002	$V_n = V_c + V_s + V_f$ $V_f = \phi_f \dfrac{A_f E_f \varepsilon_f d_f}{s_f}$ ϕ_F is resistance factor of FRP composites $\varepsilon_f = 4000\mu\varepsilon$ For U-shaped wrap (continuous around the bottom of the web) $\varepsilon_f = 2000\mu\varepsilon$ For side bonding to the web $V_r = V_c + V_s + V_f \le V_C + 0.6\lambda\varphi_C \sqrt{f_c'} b_w d$
fib-TG9.3	2001	$V_{Rd3} = V_{cd} + V_{wd} + V_{fd} \le V_{Rd2,\max}$ $V_{fd} = 0.9 \dfrac{\varepsilon_{fk,e}}{\gamma_f} E_f \rho_f b_w d (\cot\theta + \cot\alpha)\sin\alpha$ $\varepsilon_{fk,e} = \alpha\varepsilon_{fe} \le \varepsilon_{\max}$ for completely wrapped CFRP $\varepsilon_{fe} = 0.17\left(\dfrac{f_c^{2/3}}{E_f \rho_f}\right)^{0.3} \varepsilon_{fu}$ For on side or U-wrapped CFRP $\varepsilon_{fe} = \min\left[0.65\left(\dfrac{f_c^{2/3}}{E_f \rho_f}\right)^{0.56} \times 10^{-3},\ 0.17\left(\dfrac{f_c^{2/3}}{E_f \rho_f}\right)^{0.30} \varepsilon_{fu}\right]$ for completely wrapped AFRP $\varepsilon_{fe} = 0.048\left(\dfrac{f_c^{2/3}}{E_f \rho_f}\right)^{0.47} \varepsilon_{fu}$

Table A 2.6. Principal Equations of Current Design Guidelines (Continued)

Codes/Guidelines	Year	Equations
JSCE	2001	$V_{yd} = V_{cd} + V_{sd} + V_{ped} + V_f$ $V_f = \dfrac{KA_f f_f z(\sin\alpha + \cos\alpha)}{s_f}$ K is shear reinforcing efficiency A_f is total cross sectional area of fiber sheet in space s_f f_{fud} is the design tensile strength of FRP z is the lever arm length set to $d/1.15$ $0.4 \le K = 1.68 - 0.67R \le 0.8$ $R = (\rho_f E_f)^{1/4} \left(\dfrac{f_{fud}}{E_f}\right)^{2/3} \left(\dfrac{1}{f'_{cd}}\right), \; 0.5 \le R \le 2.0$

A2.5 Existing Experimental Investigations

A2.5.1 Review of Behavior of Concrete Structures Strengthened in Shear with FRP Composites

This section provides an exhaustive review of all papers related to reported experimental investigations on shear strengthening with externally bonded FRP. In total, 40 papers and reports have been thoroughly studied to date encompassing approximately 300 tests carried out beginning in 1992 up to June 2006. The review presents paper by paper in chronological order, allowing the reader to understand the evolution of the findings of the research effort, as well as the issues involved as research progressed. For each paper, the review provides information on the objectives, methodology, experimental program, test method, FRP used and its orientation, as well as the strengthening scheme used (configuration). Each review is presented using units contained in the original paper. In addition, whenever necessary, the review provides comments or comparisons with other studies in order to put the results in perspective.

It may be worth noting that the synthesis of this exhaustive review is provided in Section A3 carried out under Task 2 where a synthesis matrix is elaborated and analyzed in terms of various parameters. The detailed numerical data from around 300 tests extracted from the experimental investigations reviewed are also assembled in one-of-a-kind database and presented in Section A3 under Task 2. Both the synthesis matrix and database will be used as the basis for identifying criteria that influence design of FRP shear strengthening systems, a work which will be carried out under Task 2.

Berset (1992)

The first study of shear strengthening with FRP was carried out by Berset (1992). Through a series of tests, he examined the shear behavior of reinforced concrete beams retrofitted with GFRP composite. Six rectangular beams with dimensions 102 mm × 114 mm × 600 mm were tested, targeting the following two parameters: (i) the thickness of the GFRP composite and (ii) the effect of transverse steel. The GFRP composite fabric used was bonded onto the beam sides at an angle of 45°.

The beams with no transverse steel, retrofitted with FRP, failed in shear with debonding of the FRP composite. The gain in shear obtained was a function of the FRP thickness and a 33% to 66%

improvement was attained by increasing FRP thickness. In contrast, the beams containing transverse steel failed in flexure. The model developed by the author is based on the truss analogy. The maximum FRP strain, which is an important variable in the model, is drawn from these tests. This investigation, deemed by the author as exploratory, showed that the FRP retrofit technique may result in an enhancement of shear resistance. In its conclusions, the author drew attention to the scale effect, particularly for small specimens such as the ones considered in this study.

Uji (1992)

Uji (1992) tested eight rectangular concrete beams of dimensions 100 mm × 200 mm × 1300 mm, strengthened with CFRP composite. The investigation targeted the following parameters: (i) the strengthening scheme, i.e., wrapped versus bonded on the sides and (ii) the effect of transverse steel (by studying sections with and without transverse steel reinforcement). The shear ratio (a/d) was fixed at 2.5.

The predominant test beam failure mode was debonding of the composite. The latter never reached more than 30% to 50% of its ultimate resistance. The author observed that FRP strains were greater than those of transverse steel and therefore concluded that the shear capacity is governed by the bonding mechanism at the concrete-FRP interface.

Al Sulaimani et al. (1994)

Al Sulaimani et al. (1994) investigated the behavior of concrete beams that were pre-cracked before being retrofitted in shear with GFRP. Two series of tests were performed, one series with and one without additional strengthening of GFRP in flexure. Each series included eight rectangular 150 mm × 150 mm × 1250 mm beams and considered the following composite configurations: (a) composite in two forms: strips or continuous fabric and (b) composite bonded on the sides or wrapped in a U-configuration.

It was observed that the beams retrofitted with GFRP strips or continuous GFRP fabric without additional strengthening in flexure failed by debonding. The remaining specimens failed in flexure. Devolped cracks followed the same crack pattern initiated during the pre-cracking phase. To evaluate the contribution of the composite, the authors considered the average shear stress at the concrete-FRP interface which was determined to be 1.2 MPa in the case of strips and 0.8 MPa in the case of continuous fabric. The authors concluded that the U-shaped wrap is more effective in preventing debonding.

Chajes et al. (1995)

Chajes et al. (1995) tested twelve T-section beams measuring 63 mm × 190 mm, having a span of 1220 mm, with no transverse steel reinforcement. Three types of FRP were used: glass, aramid, and carbon. The FRP fabric was wrapped around the web in a U shape over the entire beam length at two different angles (0° and 90°) with respect to the longitudinal axis. In the case of CFRP, two more wrap angles were tested: 45° and 135°. The specimens were subjected to four-point loads with a shear ratio a/d of 2.7. All the specimens failed in shear and no debonding of the FRP was observed in any of the specimens. The shear resistance increased by 60% to 150% and the strain measured at failure was approximately $\varepsilon = 0.005$. The latter observation was used

by the authors to evaluate the contribution of FRP to shear resistance. No distinction was made between the different types of FRP fibers or their orientations.

Sato et al. (1996)

Sato et al. (1996) carried out a series of tests on ten rectangular concrete beams measuring 200 mm × 300 mm × 2200 mm, retrofitted in shear with CFRP. The following parameters were studied: (i) the influence of the FRP strengthening scheme, i.e., bonded on the sides versus wrapped in a U pattern and FRP strips versus continuous fabric and (ii) the influence of the transverse steel reinforcement. Test results indicated that specimens with no transverse steel reinforcement failed by debonding of FRP. They also indicated that the gain in resistance due to U-wrapping of FRP is 60% greater compared to FRP bonded onto the sides. In the model presented, the author refers to the bonding mechanism at the concrete-FRP interface to describe the failure mode by debonding.

Miyauchi et al. (1997)

Miyauchi et al. (1997) presented the results of tests performed on a series of seventeen beams strengthened in shear with CFRP. Specimens had a rectangular section of 125 mm × 200 mm and a span between supports of 1400 mm. The experimental program considered the following parameters: (i) the strengthening scheme (CFRP strips with three different spacings versus continuous fabric with one or two layers) and the FRP ratio, (ii) the content ratio of the transverse steel reinforcement, and (iii) the shear span ratio which varied between 1.0 and 3.0. On the basis of these tests, the authors concluded that the rate of increase in the strain on CFRP was greater than that of the strain on steel and proposed a relation which describes the observed interaction. To calculate the contribution of FRP to shear resistance, they adopted the truss analogy by applying a reduction factor of 0.507 to the ultimate FRP stress. It should be noted that only three of the FRP-retrofitted specimens without transverse steel failed in shear. The remaining specimens failed in flexure. Yet the authors developed their calculations on the basis of these latter specimens, which does not appear to make much sense.

Taerwe et al. (1997)

Taerwe et al. (1997) present results of tests conducted on a series of seven rectangular concrete beams measuring 200 mm × 450 mm × 4000 mm, strengthened in shear with CFRP. The following parameters were targeted: (i) the influence of the strengthening scheme (U-wrap versus full wrap), (ii) the spacing of the strengthening additions, and (iii) the influence of the transverse steel ratio. The tests showed that all but one of the strengthened specimens failed by debonding. In the specimen that did not fail by debonding, the FRP wrap fractured after crushing of concrete. Gains in capacity of 20% were achieved. The authors concluded that the contribution of FRP to the shear resistance can be calculated using the truss analogy.

Umezu et al. (1997)

Umezu et al. (1997) conducted a large experimental program on the use of FRP for shear strengthening and retrofit. Twenty-six rectangular concrete beams of various dimensions were tested. For all these tests, the shear ratio was kept constant and equal to 3. Fourteen specimens were retrofitted with aramid (AFRP) and the rest with carbon (CFRP). The full-wrap composite was either continuous or in strip form and was applied over the entire shear span. The authors observed two modes of failure: (i) failure of FRP after crushing of concrete and (ii) simultaneous

rupture of FRP and concrete. As observed by the authors, the latter mode tends to occur with small FRP ratio. In addition, on the basis of the observation that the FRP never reached its full capacity, the authors proposed to apply a reduction factor to the tension resistance of FRP before using the truss analogy model. This factor, which represents the ratio of resistance obtained by tests over resistance obtained with the truss model, assuming that the full capacity of the FRP is attained, decreased when the FRP ratio increased. A maximum value of 0.4 is suggested by the authors for the reduction factor.

Funakawa et al. (1997)

Funakawa et al. (1997) tested five rectangular concrete beams measuring 600 mm × 510 mm × 5060 mm. Three specimens were retrofitted with one, two, or three layers of CFRP fabric full-wrapped over the entire shear span. A fourth specimen was strengthened with AFRP. The last specimen was maintained as control. The specimens strengthened with one and two layers of FRP failed by fracture of the FRP, whereas with three layers, the fracture of the FRP occurred well after rupture of the concrete in compression. From these results, it could be concluded that the FRP contribution to shear resistance increased with the number of FRP layers, and that the combination of aramid and carbon fibers can be effective for enhancing the stiffness of a retrofitted member.

Araki et al. (1997)

Araki et al. (1997) conducted an experimental program on a series of nine rectangular concrete beams measuring 200 mm × 400 mm × 3400 mm. They tested two parameters: (i) the FRP ratio and (ii) the type of fibers, i.e., aramid versus carbon. All strengthened specimens, when tested, reached the maximum load without fracture of the FRP. Specimens showed shear tension failure. In this failure mode, the expansion of shear cracks due to the yielding of stirrups caused failure. In every specimens strengthened with the sheets, rupture of sheets could not be observed when the maximum load was achieved. Fracture occurred after failure of the specimen. FRP strain reached approximately two-thirds of the ultimate strain capacity. The load-deflection curves show that after the formation of the first cracks, the smaller the FRP ratio was, the greater the loss of rigidity. To determine the FRP contribution to shear resistance, the authors used the truss analogy by reducing the tensile resistance of FRP by an estimated factor of 0.60 for carbon and 0.45 for aramid.

Kamiharako et al. (1997)

Kamiharako et al. (1997) presented results of tests carried out on eight rectangular beams. Two series were considered, depending on the dimensions of the specimens: 250 mm × 400 mm × 3000 mm in Series 1, and 400 mm × 600 mm × 3000 mm in Series 2. The parameters studied were: (i) the rigidity of the FRP, which was applied as a full wrap and consisted either of aramid or carbon fibers, (ii) the influence of the resin used; FRP was applied without resin in two specimens in Series 1, and (iii) specimen size. The beams were tested under three-point loads. The a/d ratio depends on the height of the specimen, since the shear span was kept constant at 1000 mm.

All tested beams failed in diagonal tension. The gains in capacity due to FRP varied between 31% and 93%, depending on the rigidity of the FRP and the size of the specimens. As for rigidity, the reported values were greater for carbon than for aramid fibers. Regarding specimen size, the

reported gains were greater in beams of Series 2 (height = 700 mm) than for beams of Series 1. However, it must be noted that the a/d ratio for Series 1 (2.5) is different from that of Series 2 (1.7). This would certainly influence the behavior of the beams, particularly in terms of ultimate resistance. Therefore, the conclusions related to specimen size must be used with great caution. Finally, concerning the influence of resin, the reported results indicated that the gains in capacity due to FRP are nil when the FRP is applied without resin.

Sato et al. (1997a)

Sato et al. (1997a) experimentally investigated the shear resisting behavior of RC beams with CFRP sheets as well as the possibility of utilizing a mechanical anchorage system to address the problem of FRP debonding. The experimental program involved static monotonic testing of three RC T-beams of dimensions 150 mm × 300 mm × 2000 mm with all specimens having identical steel reinforcement. Specimens No. 2 and No. 3 were reinforced with continuous U-wrapped CFRP sheets having fibers oriented at 90 degrees to the longitudinal axis of the beam. The CFRP sheets in specimen No. 3 were anchored by mechanical anchorage. The anchor plate had a width of 50 mm and thickness of 10 mm. The anchor bolts were 10 mm in diameter and spaced 50 mm apart. The failure mode of specimen No. 1 was shear compression failure. The failure mode for specimens No. 2 and No. 3 was shear failure after debonding of the CFRP sheets. Specimens No. 2 and No. 3 showed shear strength gains of 12% and 33% with the use of CFRP sheets, respectively. The ultimate shear strength of specimen No. 3 was greater than that of specimen No. 2. The authors concluded that the use of CFRP sheets with mechanical anchorage is much more effective than that without an anchorage system. They found that by using mechanical anchorage, the ultimate shear strength and shear force when the stirrups yielded increased because the delamination was delayed.

Sato et al. (1997b)

Sato et al. investigated anchoring techniques to develop a shear strengthening technique for avoiding delamination as well as a method for estimating strengthening effectiveness. Specimens were rectangular RC beams measuring 300 mm wide and 500 mm deep. CFRP sheets with a thickness of 0.111 mm were bonded to the concrete surface with epoxy resin. The sheets were anchored by four different methods. Twelve specimens in three series (S, M, and C series, four specimens for each series) were subjected to varying loading conditions, span, and anchoring methods. Specimens in the S series were subjected to monotonic load at the center of the total span. These specimens were designed to fail in shear before flexural yielding of the rebar. More realistic conditions were arranged in the M and C series. These specimens were subjected to an asymmetric load. Monotonic loading was conducted in the M series to observe the shear failure. Cyclic loading was conducted in the C series to observe the improvement in ductility. In the S series, only a 7% increase in shear strength was observed in the non-anchored specimen. Peeling of the CFRP sheets started along the shear crack and gradually propagated along the whole region. The shear strength observed in the specimen with anchoring system type-1 (nail type) was double that of the non-strengthened specimen and rupture of FRP was observed. In the M series, no more than 17% shear strength improvement was observed in the specimens with anchoring systems. The CFRP sheets peeled off, and the anchor bolts sheared off with concrete around them. Each specimen in the C series was subjected to a cyclic load. Shear failure was not observed, but the applied load decreased gradually. The authors concluded that the shear strength of a beam can be improved with CFRP sheets if an adequate anchoring system is provided. They

found that strengthening effectiveness is maintained also under a cyclic load. They also recommended the use of longer anchoring bolts that penetrate the whole web of the beam for type-3 anchoring systems.

Täljsten (1997)

Täljsten et al. (1997) conducted a series of tests on eight concrete rectangular beams measuring 180 mm × 500 mm × 4500 mm. One of the objectives of the program was to study the shear behavior before and after retrofit with CFRP. To this end, two of the three control specimens were tested to failure, retrofitted, and loaded again. The CFRP composite was applied to the sides of the beams at an angle of 45°. The second objective was to evaluate three FRP application systems: (i) hand lay-up, (ii) pre-impregnation in combination with vacuum and heat, and (iii) vacuum injection. The distance between the applied loads was varied so as to ensure rupture by shear. Only three tests out of ten were valid. For example, the specimens which were highly strengthened (two layers of FRP) failed by flexure, which was attributed by the authors to an underestimation of the shear capacity and a resulting under-design of the beams in flexure. The control specimens which were tested to failure before retrofit ruptured by debonding of the FRP at the FRP-concrete interface. The gain in shear resistance reached 100%. In the third beam, fracture of FRP and rupture of concrete occurred simultaneously. Finally, the authors noted that although the hand lay-up method of FRP application was easier and more convenient, the pre-impregnation and vacuum injection systems achieved better quality control.

Chaallal et al. (1998a)

Chaallal et al. (1998a) studied the performance of concrete beams under-designed in shear and retrofitted with CFRP strips bonded onto the sides of the beams. The experimental investigation included a series of eight beams, of rectangular cross section measuring 150 mm × 250 mm × 1300 mm. The parameter studied was the angle of orientation of the CFRP strips: 90° versus 135° with respect to the longitudinal axis. The strengthened specimens failed by debonding of the CFRP strips. The CFRP did not have any effect on the rigidity of the beams in the initial phase of loading. However, their effect became apparent at the formation of the first cracks and multiplied with increasing applied load. In their conclusions, the authors noted that shear strengthening enhanced not only the shear capacity, but also the overall rigidity of the retrofitted beams, by inhibiting the propagation of cracks.

Mitsui et al. (1998)

Mitsui et al. (1998) investigated the influence of the shear span ratio a/d on the shear capacity of concrete beams retrofitted with FRP. They tested six rectangular beams with a cross section of 150 mm × 250 mm, strengthened with a full wrap of CFRP fabric. Two parameters were examined: (i) the a/d ratio (two values were considered, 1.14 and 1.59) and (ii) the state of the beams. The latter parameter refers to the following three cases: (1) pre-loaded beam, lightly cracked and then retrofitted, (2) beam pre-loaded to failure, after which the cracks were repaired with epoxy injection before retrofitting of the beam with FRP, and (3) beam strengthened with FRP with no pre-loading. No debonding was observed in any of the specimens. In all the specimens, the FRP fractured as the beam failed. The measured gain in the shear resistance varied between 30% and 80%. The specimens that were lightly pre-cracked and then retrofitted featured two cracking patterns: one corresponds to the cracks which occurred during the first pre-loading prior to the retrofit and the second corresponding to the cracks due to the second loading

after the retrofit. It was also concluded that the contribution of FRP to the resistance tends to increase with increase in the shear span-to-depth ratio a/d.

Triantafillou (1998a)

Triantafillou (1998a) proposed a model to determine the contribution of FRP to the shear resistance of reinforced concrete beams. The model is based on the truss analogy by adopting the euro-code format. It was obtained by calibration of data collected by the author from the literature and from his own test results. The latter were obtained from a series of tests performed on rectangular concrete beams measuring 70 mm × 110 mm × 1000 mm, without transverse steel, strengthened in shear with CFRP strips. Two variables were tested: the FRP thickness and the angle of orientation (90° and 45°) with respect to the longitudinal axis. In this model, the FRP strain, ε_{FRP}, constitutes the main variable. It is deduced, using the truss analogy, from the measured FRP contribution and then expressed in terms of the axial rigidity of the FRP, $\rho_{FRP}E_{FRP}$. The author noted in particular that the FRP strain decreased as the rigidity increased. He also noted that the gain due to the FRP varies linearly with the rigidity up to an optimum value corresponding to $\rho_{FRP}E_{FRP}$= 0.4 GPa, after which it remains constant. The author suggested that this threshold be used as a design criterion. However, the drawback of this model is that it covers two distinct modes of failure: fracture of FRP and debonding. In addition, the model fails to take concrete resistance into consideration (Khalifa, 1998).

Kachlakev and Barnes (1999a)

Kachlakev and Barnes (1999a) studied the effects of FRP strengthening on the failure modes and performance of RC beams. They also investigated a variety of strengthening schemes to establish a criteria showing the effectiveness of the composite reinforcement. The experimental part of the study involved preparation of 71 RC beams with dimensions 15.2 × 15.2 × 53.3 cm. All specimens were prepared with commercially delivered concrete, having a 28-day compressive strength of 27.5 MPa, and reinforced with one Grade 60 #3 rebar positioned in the center of the beam 51 mm from the bottom. The beams were designed to fail in flexure. Each specimen was tested in flexure using third point loading as described in ASTM C78-94. The beams were divided between two different CFRP systems, and one GFRP system. Strengthening arrangements included: (a) flexural reinforcement only, (b) flexural plus shear reinforcement, (c) shear reinforcement at 45 degrees, and (d) shear reinforcement at 90 degrees. The specimens tested exhibited a variety of failure modes depending on the strengthening scheme, thickness of the laminates, and material (CFRP or GFRP). The majority of failures occurred due to tensile failure of the concrete in the flexural zone as well as tensile failure of the laminate, shearing of the concrete following crushing of the concrete under the loading points, and shearing of the concrete following debonding of the laminate. Increase in the ultimate load carrying capacity of the beams varied from 100 to 400% for the CFRP systems, depending upon the strengthening scheme. For the GFRP systems, an increase ranging from 44 to 162% was observed. The addition of FRP laminates delayed the initial cracking of the concrete by 34 to 110% depending on the strengthening scheme. The beam failure modes showed a strong dependency on the FRP thickness, regardless of fiber orientation. The authors concluded that the ultimate stress of the specimens reinforced for flexure and shear was influenced by the rigidity of the FRP laminates. They also concluded that the optimum amount of FRP reinforcement, which provides maximum strengthening effect, must be established for each FRP system, depending on its thickness and mechanical properties.

Khalifa (1999)

Khalifa (1999) tested a series of twelve concrete rectangular beams measuring 150 mm × 305 mm × 3050 mm, strengthened in shear with FRP. The objective was to study the influence of the following parameters: (i) the presence of internal transverse steel reinforcement, (ii) the shear span ratio a/d (at values of 3 and 4), and (iii) the strengthening configuration. This last parameter referred to the following schemes: (a) unidirectional U-shaped strips with two different widths, (b) unidirectional U-shaped continuous fabric, and (c) bidirectional continuous fabric bonded onto the sides of the beam only. The objective of comparing unidirectional with bidirectional FRP was to evaluate the effect of horizontal fibers on the shear resistance of FRP. The specimens failed in shear by debonding of FRP. Examination of the test results confirmed that the contribution of FRP stabilized beyond a certain level of FRP axial stiffness. In some specimens, a 250% increase in the FRP ratio enhanced the total shear capacity by merely 10%. In the beams with transverse steel, given the applied load, comparison of CFRP strains with corresponding transverse steel strains shows that in presence of CFRP, the steel is less strained. As for the influence of the shear span ratio a/d, only two tests were valid, and these indicated a slight increase in shear capacity as the a/d ratio increased. The following conclusions could be drawn from this study: (1) The contribution of FRP to shear resistance is influenced by the a/d ratio; (2) The contribution of FRP to shear resistance remains constant above a certain FRP ratio; and (3) The contribution of FRP to shear resistance is more significant for beams without transverse steel.

Khalifa et al. (1999a)

Khalifa et al. (1999a) tested nine continuous rectangular beams with a cross section of 150 mm × 305 mm and a span of 2 × 2290 mm, strengthened with CFRP. The parameters of the study included the transverse steel ratio, the FRP ratio, the strengthening configuration, and the orientation of the fibers (unidirectional versus bi-directional). The modes of failure obtained from the tests were out of target in most cases, since most of the specimens failed by slippage of the longitudinal steel reinforcement or by flexure. Failure by debonding occurred only in two specimens. The latter specimens were both without transverse steel; one was strengthened with a U-shaped CFRP wrap and the other with CFRP strips. However, a significant contribution from CFRP, 83% and 135% respectively, was recorded in these cases. Examination of the load-deflection curves of the two valid tests reveals that the effect of the FRP configuration on the contribution of FRP to the shear resistance became apparent only after a certain level of loading. The U-shaped wrap exhibited better performance in providing rigidity. The authors also introduced a small modification to their model describing the debonding mode of failure, first published by Khalifa et al. (1998), to take into consideration the work by Miller (1999) on the FRP-concrete bonding mechanism. The merit of this study stems from its establishment of the fact that, contrary to the case of simple spans (the majority of tests), the strengthened zones of continuous beams experience maximum shear and maximum moment simultaneously.

Khalifa and Nanni (2000)

Khalifa and Nanni (2000) studied the behavior of concrete T-beams without transverse steel reinforcement, retrofitted in shear with different configurations of externally-bonded CFRP. Six 150 mm × 405 mm × 3050 mm beams were tested. The following parameters were considered:

(1) FRP ratio: continuous fabric versus rigid strips
(2) FRP configuration: U wrap versus bonded on the sides
(3) Orientation of the fibers: unidirectional versus bidirectional

(4) Presence or absence of an FRP anchorage: the technique consisting of extending the FRP to a groove made in the compression zone near the web surface, then repairing it by means of a 10 mm diameter FRP rebar glued into the groove with an epoxy paste.

The strengthened beams failed predominantly by debonding. However, the specimen strengthened with a U-wrap anchored to the compression zone by means of an FRP bar failed in flexure. The increase in measured shear capacity was between 35% and 145%. Moreover, the results indicated that the horizontal fibers had no significant effect on the capacity gain, at least in the case of failure by debonding. However, the authors added that such an effect is not to be excluded in the case of deep beams. The following conclusions were drawn from the study:

(1) The contribution of FRP to the shear resistance was significant, particularly when adequate anchorage is provided.
(2) The U-wrap configuration was more effective than FRP bonded onto the sides.
(3) Compared to FRP strips, continuous fabric covered larger areas that could be subject to cracking.
(4) The horizontal fibers did not play a significant role in shear resistance.

Khalifa et al. (2000b)

Khalifa et al. (2000b) investigated the shear performance and modes of failure of simply supported RC T-beams strengthened with two different FRP-based systems, namely, externally bonded CFRP sheets and near-surface mounted (NSM) rods. A series of five 150 mm × 305 mm × 3050 mm T-section beams was retrofitted with a U-wrapped CFRP fabric. Two methods (sandblasting and waterblasting) were used to prepare the concrete surface when externally bonded CFRP sheets were used to investigate the levels of concrete surface roughness. The beams were tested under four-point loads with a shear span ratio a/d = 3.0. All the specimens ruptured forcefully by debonding of the FRP. This was accompanied by delamination of the concrete substrate; the higher the surface roughness, the more dramatic the delamination. Results showed that the capacity gains due to FRP averaged 75%, including all the specimens with different concrete surface treatments. The authors concluded that additional concrete surface roughness beyond that normally prescribed by the manufacturer does not influence the shear capacity of the strengthened beams. The test results also showed that NSM rods as strengthening technique showed their effectiveness in increasing the shear capacity.

Deniaud and Cheng (2001)

Deniaud and Cheng (2001) explored the behavior in shear of T-beams strengthened in shear with CFRP. Eight 140 mm × 600 mm × 3700 mm beams were tested. The following parameters were considered: (i) the spacing of the stirrups, (ii) the type of fiber (carbon versus glass), and (iii) the orientation of the fibers: 90°, 45°/90°, and tri-axial 0°/60°/-60°. In order to collect as large a quantity of data as possible, the tests performed on the specimens were carefully instrumented. All specimens failed by debonding. They also featured similar load-deflection response curves; neither the internal transverse steel reinforcement nor the external FRP affected the initial overall rigidity of the beam. In contrast, both the ultimate capacity and the ductility are clearly influenced by FRP and transverse steel ratios. In this context, the authors noted that the contribution of FRP decreased as the transverse steel ratio increased. Therefore, there is an interaction between internal reinforcement and external strengthening.

Li et al. (2001)

Li et al. (2001) studied the influence of the strengthened height of the beam on the shear capacity. Five rectangular beams measuring 130 mm × 200 mm × 1350 mm were tested. Shear strengthening was implemented using CFRP continuous fabric bonded to the sides of the beam at different heights. CFRP composite was also bonded onto the soffit of the beam. The specimens were carefully prepared before strengthening. The strains were measured at different locations. No failure by debonding was observed. According to the authors, this is attributed to the high quality of the bonding glue. The load-deflection response curves featured two distinct phases. The curves corresponding to the different configurations are quasi-identical in the first phase of loading, which shows that the configuration has no effect on the load. The curves intersected each other as the load increased. However, it was interesting to observe that there was no noticeable difference between the different FRP configurations in the ultimate load. On the basis of this result, the authors suggest that there is no need for FRP to be applied over the entire height of the web. However, the authors did not give an indication on the minimum FRP height required to ensure shear strengthening effectiveness.

De Lorenzis and Nanni (2001a)

De Lorenzis and Nanni (2001a) studied the performance of RC beams strengthened in shear with Near-Surface Mounted (NSM) CFRP rods. A total of 8 T-beams were tested. The cross-sectional dimensions of the beams were 6 inches × 14 inches, and the span was 10 feet. The parameters studied were: (i) spacing of rods, (ii) inclination of rods, (iii) presence of an anchorage in the flange, and (iv) presence of internal steel stirrups. The specimens were tested under four-point loads with a shear span ratio a/d=3. With the exception of the specimen with transverse steel, which failed in flexure, all the specimens strengthened in shear with FRP NSM rods failed in shear. Failure was due either to bonding failure of one or more NSM rods, or to splitting of the concrete cover of the longitudinal reinforcement. Results showed that gains in capacity due to external strengthening can be as high as 106%. Shear capacity of strengthened beams can be increased by decreasing the spacing of the NSM rods, by anchoring rods into the flange, or by changing the inclination of the rods from vertical to 45 degrees. This work shows that the use of NSM FRP rods is an effective technique to enhance the shear capacity of RC beams.

Pellegrino and Modena (2002)

Pellegrino and Modena (2002) studied the influence of transverse steel on the contribution of FRP. To this end, they tested a series of eleven rectangular beams measuring 150 mm × 250 mm × 2700 mm. The parameters studied were: (i) the presence of transverse steel (sections with and without) and (ii) the CFRP ratio. The CFRP fabric used was applied to the sides of the beams in one, two, or three layers. All specimens failed in shear by delamination of the CFRP composite. In the beams without transverse steel, the presence of FRP modified the cracking pattern that is usually observed: near the support, the cracks were inclined more or less horizontally, whereas near the load point, they were inclined at 45°. In the beams containing transverse steel, delamination was more severe and cracks were inclined at angles less than 45°. The authors concluded that in the presence of transverse steel, the contribution of FRP decreased. To take this interaction into consideration, they suggested a partial modification of the model proposed by Khalifa et al. (1998), based on their test results. This modification is a function of the rigidity of the transverse steel rather than of the FRP ratio.

Chaallal et al. (2002)

Chaallal et al. (2002) has presented the results of an experimental program including twenty-eight tests performed on fourteen T-section beams measuring 130 mm × 450 mm × 6000 mm. Two parameters were considered in this study: (i) the spacing of the stirrups and (ii) the number of CFRP layers. The CFRP fabric was applied as a U-wrap over the web. The specimens tested had an a/d ratio of 2 and therefore may be classified as deep beams. The strengthened specimens exhibited rupture of the compression struts followed by rupture of the CFRP near the supports. Such behavior is characteristic of deep beams. In fact, as the CFRP fabric was removed, it was observed that the concrete underneath was completely pulverized. It was clear, in this case, that enhancing the confinement of concrete in compression was the main role played by the FRP. The shear capacity, on the other hand, increased with the number of FRP layers. However, this increase is linked to the transverse steel ratio, as clearly demonstrated by the test results: the higher the ratio, the less significant the contribution of the FRP to the shear resistance. This result led the authors to propose an expression for FRP strain as a function of the global shear reinforcement ratio, that is, including both steel and FRP. The proposed expression was used along with the truss analogy to evaluate the contribution of FRP. Moreover, to extend the expression to the case of slender beams, the authors proposed an additional factor to take into account: the shear span ratio, a/d, as well as the global reinforcement ratio.

Micelli et al. (2002)

Micelli et al. (2002) tested beams extracted from an existing concrete building constructed in 1964. The merit of the study stems from the fact that it considered the performance of FRP used to strengthen an existing structure. Twelve T-beams, two of which were maintained as a control, were tested. The beams had the following dimensions: 152 mm × 381 mm × 2743 mm. They were retrofitted with U-wrapped continuous FRP fabric in one or two layers with and without anchorage. Of the ten strengthened beams, eight were retrofitted with CFRP and the remainder with aramid composite. For the anchorage, the authors used the technique described by Khalifa et al. (2000a). In addition, the small longitudinal steel reinforcement ratio led the authors to strengthen the beams in flexure in order to inhibit any premature failure in flexure. The flexural strengthening was applied to both critical positive and critical negative moment regions. The beams were tested under three-point loads with the load applied at distance a = 2.4d from the support. In the beams with no anchorage, failure occurred by premature debonding of the FRP, accompanied by severe delamination. The gain in shear resistance was 11% to 16%, depending on the number of FRP layers. The beams with anchored FRP achieved higher gains, ranging from 35% to 27%, depending on the number of FRP layers. Failure in this case was caused by loss of anchorage. The addition of a second CFRP layer to the specimens with anchorage did not result in a capacity increase. The authors noted that the gains achieved are small compared to those predicted by theory. This behavior was attributed to deep beam action by the authors, who strongly recommended further investigation into this phenomenon. It must be said that an a/d ratio of 2.4 is at the upper limit of what can be considered as a deep beam. It must also be noted that the resistance of concrete in compression was around 20 MPa. The quality of the concrete substrate could also explain the results obtained. In this context, it would have been interesting to know more details on the state of the concrete substrate and on the surface preparation prior to application of FRP.

Li et al. (2002)
Li et al. (2002) carried out a series of tests on 16 rectangular concrete beams measuring 130 mm × 280 mm × 2700 mm, strengthened in shear with CFRP. The following parameters were studied: (i) the configuration of FRP, which was applied discontinuously over the length on the sides of the beams at different heights, (ii) the spacing of the stirrups, and (iii) the longitudinal steel reinforcement ratio. The strains were measured at various locations (CFRP, transverse steel, concrete and longitudinal steel). The beams were tested under three-point loads with an a/d ratio of 2.9. All the beams ruptured by crushing of concrete under two failure modes: some of them in shear and the other in flexure. The gains due to CFRP varied between 25% and 115%. These gains were proportional to the area of the strengthened surface (the height of the CFRP bonded onto the sides of the beams was one of the parameters studied). Results showed that the presence of transverse steel resulted in a reduction of strength gains. These gains also decreased as the longitudinal reinforcement ratio increased. However, the results which led to this last conclusion are based on specimens which failed in two different modes: in shear and in flexure.

Lees et al. (2002)
Lees et al. (2002) investigated the feasibility of a new strengthening system with FRP, specifically prestressed carbon-FRP straps. This full-wrap system is innovative in the sense that FRP contributes to strength starting from the first stage of loading. In comparison, other strengthening systems, including those with FRP, are passive systems and, therefore, do not influence the shear behavior and particularly concrete contribution before the formation of diagonal cracks. For this investigation, the authors tested two T-beams, one of which was a control beam, with dimensions of 150 mm × 430 mm × 2700 mm. The beams were tested under four-point loads. The strengthened beam ruptured by fracture of the strap. In addition to the gain in capacity (33%) due to the use of this system, the results also included a gain in overall rigidity compared to the control beam. In conclusion, the authors recognized that further work was required to investigate the influence of loading arrangement, pre-stress level, and strap arrangement on the behavior of a strengthened beam.

Czaderski (2002)
Czaderski (2002) tested six T-beams strengthened with L-shaped CFRP plates. The dimensions of the specimens were 150 mm × 430 mm × 3500 mm. The parameters studied were: (i) the type of loading (static loading versus pre-loading with subsequent static loading versus fatigue with subsequent static loading) and (ii) the presence of internal steel stirrups. Two failure modes were observed: (i) shear rupture of the strengthened beam without transverse steel; and (ii) crushing of concrete after yielding of longitudinal steel reinforcement. The latter mode involved the strengthened beams containing transverse steel reinforcement, regardless of the type of applied load. These beams featured a slight increase of 5% in capacity, in contrast to the strengthened beams with no transverse steel, where the gain due to FRP was as high as 95%. The study also presented numerous results on different factors related to strains in CFRP and transverse steel.

Deniaud and Cheng (2003)
Deniaud and Cheng (2003) performed a series of laboratory controlled experiments using concrete beam specimens strengthened externally in shear with FRP sheets. The objective of this investigation was to study the effect of concrete strength, stirrup spacing, height of the beam web, and type of FRP on the behavior of FRP-strengthened concrete beams. The specimen size was

designed to minimize the scale effect, therefore providing a reasonably true behavior of similar real-life structural elements. A T-beam shape was selected to increase the flexural capacity relative to the shear resistance. In addition to the T-shape, two high-strength Dywidag bars with a 26 mm nominal diameter were used as flexural reinforcement. The length of the beams was 3 m. Undeformed closed steel stirrups (6 mm diameter and 520 MPa yield strength) were used with three different spacings: 200 mm, 400 mm, and no stirrups. The beam was designed to provide a flexural capacity between 2 and 3.5 times the shear capacity without FRP contribution. Three types of FRP were used to externally strengthen the web of the beams, including: (1) uniaxial carbon fiber, (2) uniaxial glass fiber, and (3) triaxial (0º/60º/-60º) glass fiber. The glass fibers were applied at a right angle to the longitudinal axis of the beams along the full length of the shear span. The carbon-fiber sheets were placed at a 45º angle to the longitudinal axis of the beams with a width of 50 mm and a gap of 50 mm perpendicular to the direction of the fibers. In all cases, the fibers were extended underneath the flange to provide a minimum anchor length of 100 mm and were wrapped under the web. This series of tests included four beams with a beam height of 400 mm. Since both ends of each beam were tested separately, a total of eight tests were conducted. The test setup consisted of a four-point loading system that created a region of constant moment at midspan. In general, for tests with no FRP (controlled specimens), two major shear cracks were observed within the shear span. The ultimate load was reached when the concrete crack extended upward through the flange near the loading point. The failure of both the uniaxial and triaxial glass-fiber reinforced specimens started to show the same web shear cracks as the controlled specimens; however, following the web shear cracks, a vertical crack was formed on the top of the flange close to the support, and it propagated downward. The glass fiber eventually tore vertically. The unidirectional carbon bands applied at 45º crossed the concrete cracks at nearly right angles and, therefore, was very effective. However, with a gap of 50 mm, these bands generated large shear forces that were transferred to the surrounding concrete. Thus, the sheets peeled off suddenly from the web-face of the beam after the bond strength of the fiber-concrete interface had been reached. The authors concluded that the effectiveness of FRP strengthening to shear contribution is dependent on the amount of internal shear reinforcement. They observed that the composites were less effective when beams were heavily reinforced with internal shear reinforcement.

Diagana et al. (2003)

Diagana et al. (2003) have presented the results of tests conducted on a series of ten rectangular concrete beams measuring 130 mm × 425 mm × 2200 mm. The parameters tested are closely related to the properties of FRP composites: (i) the orientation of the fibers (45° versus 90°) with respect to the beam longitudinal axis, (ii) the configuration of FRP: U-wrap versus full wrap, and (iii) the spacing of the FRP composite application. The composite was made of carbon fibers and was applied discontinuously onto the beam. The beams were tested under three-point loads, with an a/d ratio of 2.1. Gains in capacity due to the CFRP varied between 18% and 61%, depending on the configuration of the FRP and the orientation of the fibers. These gains were greatest for FRP with fibers perpendicular to the plane of cracking and applied in a U-shaped configuration. Two failure modes were observed: debonding of the FRP for U-wrap configuration and fracture of FRP for full wrap.

Taljsten (2003)
Taljsten (2003) tested a series of seven rectangular concrete beams measuring 180 mm × 500 mm × 4500 mm, strengthened in shear with FRP. The beams had no transverse steel. CFRP fabric was used for retrofit and was U-wrapped around the web. The parameters studied included the fiber orientation (45°, 90° and 0°) and FRP thickness. The concrete resistance in compression ranged from 59 to 71 MPa. The beams were tested under four-point loads with an a/d ratio of 2.7. The gains in capacity due to the CFRP were exceptionally high, ranging from 100% to 170%. Only the specimen with the fibers oriented longitudinally to the beam axis recorded a relatively small gain (24%). Most beams failed due to crushing of concrete. One focus of the study was the vertical distribution of the strains in the CFRP composite within the test zone. The author noted that the maximum strain was reached at mid-height of the beam.

Hsu et al. (2003)
Hsu et al. (2003) explored, through a series of five tests, the behavior of rectangular beams with no transverse steel, strengthened in shear with CFRP. The dimensions of the beams were 152 mm × 229 mm × 1067 mm. All the tested parameters were related to the external FRP configuration, as follows: (i) inclination of the CFRP strips (90° versus 45°), (ii) continuous wrap (fabric) versus discontinuous (strips) and (iii) bonding of the FRP composite up to mid-height onto the sides of the beams. The strengthened beams failed in shear by debonding of the FRP. Indeed, except for the beam that was strengthened with FRP fabric wrap, which ruptured by fracture of the FRP, all three other beams failed due to debonding of the CFRP. The gains in capacity due to CFRP varied with the configuration of the FRP. The strips oriented at an angle of 45° showed the best performance improvement (80%), compared to 60% for the strips oriented at an angle of 90° and 33% for the continuous fabric. In this context, it may be worth noting that the FRP strip ratio used was approximately 50% greater than that of the CFRP fabric. As for the FRP partially bonded up to the beam mid-height, the results indicated a capacity gain of 16% due to FRP.

Barros and Dias (2003)
Barros and Dias (2003) assessed the efficiency of two common shear strengthening techniques; that of externally bonded CFRP laminate strips (EBR) and near surface mounted CFRP laminate strips (NSM). This assessment was performed through an experimental program consisting of 20 rectangular RC beams tested in four-point bending under various shear strengthening configurations. Two series of beam geometry were investigated to analyze the influence of beam depth on the effectiveness of the shear strengthening technique. Series A consisted of beams 150 mm × 300 mm with a 1500 mm span length while Series B consisted of beams 150 mm × 150 mm with a 900 mm span length. The two geometric series were further subdivided into two series of longitudinal tensile reinforcement (ρ_{sl}) to evaluate its influence on the shear strengthening performance. Series A10 and B10 had 4ϕ10 mm bars for tensile reinforcement while Series A12 and B12 had 4ϕ12 mm bars for tensile reinforcement. In all series, the shear span to depth ratio was maintained at 2. Within each series, the influence of the strengthening scheme and orientation were assessed by testing: (1) a reference beam without any shear reinforcement, (2) another reference beam with only steel stirrups of ϕ6 mm and 300 mm spacing, (3) a beam with U-shaped strips of wet lay-up CFRP sheets each 25 mm wide and oriented at 90 degrees, (4) a beam with NSM CFRP laminate strips of 1.4×10 mm^2 cross-section oriented at 90 degrees, and (5) a beam with NSM CFRP laminate strips of 1.4×10 mm^2 cross-

section oriented at 45 degrees. The NSM technique was found to be the fastest, easiest, and most effective in shear strengthening. Laminates of 45° orientation were found to be more effective than vertical laminates in the specimens with larger beam depth. Failure modes of the beams strengthened by the NSM technique were also found to be not as fragile as those strengthened by EBR. Test results were also used to appraise the performance of analytical formulations proposed by ACI, fib, and De Lorenzis. In general, the ACI 440 (ACI 440, 2002) and fib-TG9.3 (fib-TG9.3, 2001) formulations were found to overestimate the experimentally determined FRP contributions. The De Lorenzis formulation, which is used to evaluate the NSM technique, was found to predict an FRP contribution of around 61% of the experimental values.

Adhikary et al. (2004)

Adhikary et al. (2004) performed a series of tests on nine rectangular beams measuring 300 mm × 245 mm × 3500 mm, strengthened in shear with CFRP. The parameters of the study are related to the FRP configuration and the fiber type, as follows: (i) kinds of fibers (carbon versus aramid), (ii) wrapping layout (U-wrap versus full wrap) and (iii) anchorage length (anchorage was provided by bonding a certain length of sheet to the top face of the beam). The beams were tested under four-point loads with an a/d ratio of 4.1. With the exception of the beams strengthened with full wrap, which failed in flexure, all other beams (six in total) failed in shear by debonding of FRP or by spalling of concrete. As for resistance, the reported results revealed that the capacity gains due to CFRP and AFRP reached 123% and 118%, respectively. It was concluded that the full-wrap configuration outperformed the U-wrap.

Xue Song et al. (2004)

Xue Song et al. (2004) investigated the effects of externally bonded CFRP sheets in rectangular RC beams with shear deficiencies. The authors addressed the factors that influence the shear capacity of strengthened beams including shear span ratio as well as the amount and distribution of CFRP. They tested sixteen RC beams designed to fail in shear. These members were tested under four-point bending with three different shear span ratios. The beams had a rectangular cross section of 150 mm width and 360 mm height. The specimens were grouped into three series based on the shear span. All specimens consisted of two 16 mm and two 32 mm steel bars as tensile reinforcement. Shear reinforcement consisted of 6 mm steel stirrups spaced at 135 mm through the entire span. The shear capacity of the strengthened beams was about 12.7% and 43.1% higher than the control specimen. Test results indicated that the shear span-to-depth ratio (a/d) is a critical parameter, showing a decreasing trend in FRP strengthening effectiveness with decrease in the shear span-to-depth ratio (a/d). Test results also showed that using an end anchorage system in the CFRP sheets can suspend debonding and significantly enhance the shear capacity. They reported that there were two effects that would influence the ultimate load capacity with increment in CFRP thickness, the first one tended to decrease the tensile load in the CFRP sheets due to the reduction in the average stress in the CFRP sheets. The second one tended to increase it as a result of the increment in CFRP area.

Zhang et al. (2004)

Zhang et al. (2004) studied the behavior of deep beams strengthened in shear with CFRP. They conducted an experimental program of 16 tests on rectangular concrete beams measuring 102 mm × 203 mm × 760 mm. The objectives of the research study were: (i) to evaluate the influence of the a/d ratio on the performance of shear strengthening with FRP and (ii) to compare the

performance of different FRP configurations. The following configurations were successively examined: (a) continuous versus discontinuous (fabric versus strips), (b) fiber orientation (45° versus 90° versus 0°) and (c) FRP application pattern (on the sides only versus U-wrap). The beams were tested under four-point bending with a shear span ratio a/d=1.25, and under three-point bending with an a/d ratio of 1.88. The results showed that, for a given a/d ratio, the gains in capacity due to strengthening depend strongly upon the configuration. Indeed, the beams strengthened with CFRP strips inclined at a 45° angle recorded the highest capacity gains, compared to strips applied at 90°, that is, 200% compared to 179% for a/d = 1.89. Moreover, the beams strengthened with CFRP fabric generally outperformed the beams strengthened with CFRP strips in terms of capacity gain. As for the influence of the a/d ratio, the results showed that the gains were greater for a/d = 1.25, compared to a/d = 1.88. In terms of failure modes, the study indicated that delamination of the CFRP laminates from underneath the concrete surface is the dominant failure mode for all CFRP-strengthened beams.

Cao et al. (2005)

Cao et al. (2005) presented the results of an experimental program encompassing 18 tests, six of which were used as a control. The objective of the investigation was to study the phenomenon of debonding of FRP strips, which can be observed particularly in critical regions of shear strengthening. The beams tested had a rectangular cross-section with the following dimensions: 150 mm × 222 mm × 1700 mm (or 1600 mm for 6 specimens). The parameters studied were: (i) the a/d ratio, considering the following values: 2.9; 2.7; 2.5; 1.8; 14 and (ii) the rigidity of the beam, investigated by varying the spacing and the width of the strips, as well as the type of FRP (carbon or glass). Note also that the test beams were pre-loaded under four-point bending until a diagonal shear crack became apparent, and then fully unloaded. The beams were then strengthened by wrapping FRP strips around the entire cross-section within the test shear span and loaded again up to failure. In general, all test beams exhibited a similar failure process. Local debonding of some FRP strips was initiated at or near the critical shear crack. At a sufficiently high load level, the most highly-stressed strip debonded completely from the side of the beam, although it remained bonded to the top and bottom surfaces of the beam. In terms of capacity gains due to CFRP, the results showed a variation between 18 and 80%, depending on the a/d ratio and the CFRP content. The measuring devices used in the study, particularly those placed on the CFRP strips to measure the strains, yielded interesting conclusions with regards to the strain distribution in the strips located in the critical sections for shear. This distribution was confirmed to be non-uniform, which, according to the authors, must be taken into account for the prediction of CFRP contribution to shear resistance.

Carolin and Taljsten (2005a)

Carolin and Taljsten (2005a) tested a series of 23 rectangular concrete beams having the following dimensions: 180 mm × 440 mm × 4000 mm, strengthened in shear with CFRP. The objective of the study was to examine the influence of CFRP thickness, fiber orientation, and FRP configuration (U-wrap versus full wrap) on the performance of strengthened beams. Some of the beams were pre-cracked before strengthening was applied. Other beams were subjected to fatigue loading after strengthening had been applied. The beams were tested under four-point bending with an a/d ratio of 2.8. The specimens failed in shear according to different modes, depending on FRP configuration, FRP thickness, and fiber orientation. For example, debonding failure was observed for the cases where the fibers were oriented at a 90° angle, whereas FRP

fracture failure occurred when fibers were oriented at 45°. This last failure mode was often associated with a loss of anchorage. Test results also showed that the beams that were pre-loaded, unloaded, strengthened, and loaded again achieved a performance comparable to the strengthened pristine beams, i.e., those which did not have to go through the pre-loading phase. As for fatigue, the results indicated that fatigue-loaded beams tend to have a higher load-bearing capacity when tested to failure, compared to beams without a fatigue history.

Miyajima et al. (2005)

Miyajima et al. (2005) investigated the shear strengthening effect and shear resistance mechanisms provided by the application of CFRP sheets. The cross section of the RC specimens was constructed to 1/8 scale of the original beam they were designed to mimic. The flexural reinforcement ratio of the specimens was 2.03%, similar to that of the original RC beam which was 1.90%. The shear span-to-depth ratio (a/d) was 2.5 so that deep beam behavior would not have any effect on the results. The specimens were designed to fail by shear even after being strengthened by CFRP sheets. It was ensured that the main reinforcement ratio did not exceed the balanced reinforcement ratio. CFRP sheets used for strengthening varied between 50 and 100 mm. Load was applied monotonically at two symmetrical points. All specimens were observed to fail in diagonal shear tension. The authors concluded that the shear resistance mechanism of the CFRP sheets starts around the sheet closes to the crack which starts to spall after the shear cracking has started. However, once the entire area of the sheet providing shear resistance had spalled, the strain in the sheet started to develop again. The maximum load was reached when at least one of the sheets failed. They observed that the reason why the development of the strain in the sheet becomes sluggish is probably attributable to the shift of the bond resistance area of the sheets. They also reported that if the strengthening ratio increases, the cracking load also increases and the cracks start to disperse which results in enlargement of the crack width.

Monti and Liotta (2005)

Monti and Liotta (2005) have presented the results of an experimental investigation involving a series of 24 tests performed on rectangular concrete beams measuring 250 mm × 410 mm × 2800 mm, strengthened in shear with CFRP. A number of different configurations of the composite were tested: (i) surface-bonded FRP versus U-wrap versus full wrap, (ii) fiber orientation (90° versus 45°) and (iii) continuous FRP versus strips at different spacings. The beams were tested under three-point bending with a shear span ratio of a/d = 3.4. The tests showed that rupture by debonding was the predominant mode of failure, accompanied in some cases by opening of a stirrup overlap. The results showed that the gains in shear capacity due to the FRP were greater for a 45° fiber orientation and increased as the spacing of strips was reduced or with a continuous FRP composite. Thus, for example, the beam strengthened with U-shaped FRP strips inclined at an angle of 45° and spaced at only 225 mm achieved a capacity gain of 190%. By comparison, for the beam strengthened with FRP strips bonded onto the sides of the beam at an angle of 90°, the gain obtained was only 5%. In parallel to the experimental study described above, the authors proposed a model for prediction of the contribution of FRP strengthening to shear resistance. The model describes a scenario through which debonding occurs. It is based on the concept of effective bond length and requires a number of factors related to parameters such as FRP configuration. The proposed model was validated with test results achieved by the authors in this study and in other studies reported in the literature.

Sim et al. (2005)
Sim et al. (2005) conducted experimental tests on 10 rectangular RC beams to evaluate the shear strengthening effects of various types of FRP materials (CFRP, CFS, and GFRP). In their study, the strengthening methods of stripping, side wrapping, and complete wrapping were also investigated. Two different fiber orientations (45° and 90°) were also considered for all strengthening methods except for the complete wrap in which only 90° fiber orientation was investigated. All beams were tested in a four-point loading configuration with a shear span-to-depth ratio (a/d) of 1.7. All specimens were observed to fail in a brittle shear failure mode accompanied by debonding of the FRP materials. Improvements in shear capacities ranged between 54% and 73% in most cases. No noticeable difference in the shear strengthening effect was observed among the three different types of strengthening material. However, the fiber orientation was found to be an important factor with greater strength and better control of crack propagation occurring in the case of fibers oriented at 45°. A numerical model was suggested for predicting the shear capacity of FRP strengthened beams based on concrete plasticity theory and an efficiency factor calibrated from the experimental test results. This model was validated against test results by Chen and Teng (Chen and Teng 2003a) and found to be in good agreement.

Bousselham and Chaallal (2006a)
Bousselham and Chaallal (2006a) presented results of 22 tests performed on RC T-beams retrofitted in shear with CFRP layers. The dimensions of the tested specimens are as follows: 152 mm × 350 mm × 3110 mm. The following parameters were investigated: (i) the CFRP ratio (i.e., the number of CFRP layers), (ii) the internal shear steel reinforcement ratio (i.e., spacing), and (iii) the shear span to the beam's depth ratio, a/d (i.e., deep beam effect). All the tested specimens failed in shear, except those of series SB-S2 (slender beams, with steel stirrups spaced at $s = d/4$), which failed in flexure. No specimen failed by debonding, delamination or fracture of the CFRP. The shear failure occurred by crushing of the concrete struts. The results showed that the contribution of the CFRP to the shear resistance is not in proportion to the CFRP thickness (i.e., the stiffness) provided, and depends on whether the strengthened beam is reinforced in shear with internal transverse steel reinforcement. Results also confirmed the influence of the ratio a/d on the behavior of RC beams retrofitted in shear with external FRP.

Bousselham and Chaallal (2006b)
Bousselham and Chaallal (2006b) present results of an experimental investigation involving twelve tests on T-beams (95 mm × 175 mm × 1584 mm) strengthened in shear with CFRP fabrics. The main objective of this study was to evaluate the effect of the following parameters on the shear performance of strengthened RC beams: (i) the CFRP ratio, (ii) the transverse steel reinforcement ratio, and (iii) the type of beams (deep versus slender). All the test specimens failed in shear. No specimen failed by premature debonding, delamination or fracture of the CFRP. The shear failure, which occurred by crushing of concrete struts, was accompanied with a wide open crack in the compression zone. The results clearly indicated that: (i) the gain in shear capacity was significant in slender beams whereas it was very modest in deep beams; (ii) the increase of the CFRP thickness (1L to 2L) achieved an additional gain in capacity for slender specimens, particularly those pertaining to specimens without transverse steel. In deep specimens no noticeable gain was achieved; (iii) the addition of internal transverse steel resulted in a significant decrease of the gain in the slender specimens. The existence of an interaction between

the internal transverse steel and the externally applied CFRP was shown in terms of the gain in the shear capacity as well as of the strains.

Hassan Dirar et al. (2006)

Hassan Dirar et al. (2006) tested four T-beams, three of which (B2, B3, and B4) were fitted with CFRP straps and one (B1) maintained as a control. The dimensions of the beams were 105 mm × 210 mm × 2500 mm. The objective of the study was to examine the effect, if any, of existing cracks on the shear performance of beams retrofitted in shear with FRP. To this end, the authors proceeded as follows: (i) in one beam among the three to be retrofitted, prestress was activated in the straps, with no loading (beam B2); (ii) the two other beams (B3 and B4) were submitted to a pre-loading of 70% of the load capacity, which had been obtained by testing the control beam (B1). They were then unloaded down to 40% of their capacity. The prestress load was then activated in the straps before the beams were finally tested up to failure. Additionally, in beam B4, to evaluate the combined effect of pre-loading and a/d ratio, the load, which was applied after the prestress had been activated, was moved gradually from a shear span of a = 410 mm to a = 820 mm. As far as failure modes are concerned, the results obtained indicated that the specimen B3 suffered a shear failure due to a set of parallel shear cracks emerging from and above the support. This was accompanied by significant damage both to the flange and the end of the beam. In specimen B4, the major shear crack appeared at the outer strap pad with an angle of approximately 34° and ran towards the flange, crossing the middle strap just under the flange. The flange suffered less damage in this specimen than in B3. Test results yielded shear strength increases of 46% and 22% for B3 and B4, respectively. The authors attributed this difference in gain to the more detrimental loading scheme used with B4. As for the influence of pre-loading on shear performance, the results showed that the loading history did not seem to have a pronounced effect on the behavior of RC beams strengthened with CFRP straps.

Pellegrino and Modena (2006)

Pellegrino and Modena (2006) carried out an experimental program on beams with different amounts of transverse steel reinforcement and different amounts of CFRP shear strengthening (U-wraps). The objective of this study was to understand the complex failure mechanisms that characterize the ultimate shear capacity of continuous and simply supported RC members with transverse steel reinforcement and externally bonded FRP sheets. The authors focused their study on the mechanisms of interaction between the external strengthening and internal shear reinforcement. The experimental program involved twelve tests on full-scale rectangular beams that were designed so that their shear ultimate capacity could be reached before flexural failure. The tests were developed with a simply supported load scheme and with a continuous load scheme in which maximum shear and maximum bending moment were simultaneously acting at the support. The following material properties were obtained from ASTM tests for each material: cylindrical compressive strength of the concrete f_c = 41.4 MPa (6.00 ksi); tensile strength of the concrete f_{ct} = 3.76 MPa (0.545 ksi); and yielding strength of the reinforcing steel f_y = 534 MPa (77.45 ksi). The rectangular cross section had overall dimensions of 150 x 300 mm (5.9 x 11.8 in.). The composite material was a unidirectional carbon fiber fabric and was applied in a continuous U-shape with one or two layers. A continuous strengthening with an inclination of 90º was chosen to surely intercept diagonal cracks. Three- or four-point flexural tests were carried out. The load was applied using a 500 kN capacity hydraulic jack with manual controls. Control beams with a continuous load scheme showed a typical mechanism of shear-tensile

failure with the formation of a principal diagonal crack with a subhorizontal direction near the support and the application point of the load and a directional incline of approximately of 45º in the central zone. Control beams with simply supported load scheme showed a similar failure, but the principal diagonal crack developed with almost only one inclination from the bearing to the application point of the load. FRP reinforced beams failed in shear always with peeling off. Longitudinal cracks were present at the upper surface of the beam. These cracks started near the location of the applied load and extend towards the support. Concrete cover splitting developed along the entire height of the beam. The small spacing of stirrups involved an increment in shear strength for continuous beams but did not involve substantial increments in shear resistance for simply supported control beams. Small increments of strength were observed from one to two layers for the FRP-strengthened beams with a continuous static scheme, whereas no increment of strength was observed for the strengthened beams with a simply supported scheme. A general reduction of efficiency of the strengthening technique with U-wrapped FRP sheets was observed when the stirrup spacing decreased for the continuous beams. The authors concluded that there is an interaction between the internal transverse steel reinforcement and the external FRP strengthening for both side bonded sheets and U-wraps. They reported that this interaction is not clearly evidenced in the current recommendations of ACI 440.2R-08 (ACI 440, 2008) in which a strong simplification to calculate the shear resistance, using the simple superposition of single independent contributions of concrete, internal steel reinforcement, and external FRP sheets, is adopted.

Leung et al. (2007)

Leung at al. (2007) focused their investigation on the shear strengthening of concrete beams. They performed a comprehensive experimental study to provide experimental data on the shear capacity of strengthened members with practical sizes and measure the shear capacity of small and large members that are geometrically similar, to determine if the strengthening effect is similar for members of different sizes. In the testing program, a member of three different sizes (180, 360, and 720 mm in depth) was employed. For each member size, the members were retrofitted with two configurations: U-wrapping and full wrapping. Three different sizes of geometrically similar RC beams with S = 2.5D = 6B were tested, where B, D, and S are the beam width, beam depth, and shear span, respectively. For each member size, five specimens were prepared and tested. These included an unstrengthened control, two beams strengthened in shear with U-wrap CFRP strips, and two strengthened with fully wrapped CFRP strips. The thickness, width, and spacing of the CFRP strips were related to the beam dimensions by the following relations: strip thickness = 0.44B/300, strip width = D/9, and strip spacing = D/3. Mild steel was used as internal shear reinforcement, and the shear reinforcement ratio was 0.28% for all the specimens. The beams were overreinforced in flexure to avoid flexural failure. All the specimens were prepared at the same time with the same concrete mix. The average compressive strength from concrete cubes and cylinders, measured at the day of the test, were 30.9 and 27.4 MPa, respectively. All specimens were tested in four-point bending with a Dartec loading system. For most cases, the failure loads for two identical members are found to be close to one another. The exception was the smallest members retrofitted with U-wrap strips (SB-U1 and SB-U2), which failed at 130 and 91.7 kN, respectively. For SB-U1, and all the other specimens repaired in the U configuration, the debonded strips carried with them a thin layer of concrete, indicating a strong adhesive/concrete interface that leads to failure within the concrete. For the beams strengthened by U-wrap strips, there is nearly 60% increase in shear capacity for the small beam, but the large

and midsize beams show only 4-7% increase. The results clearly indicate that the shear strengthening effect for the U configuration is dependent on the member size. On the other hand, the beams strengthened by fully wrapped strips do not show any size effect on the shear capacity. Regardless of member size, the increase in shear capacity was in a similar range of 57-67%. For beams strengthened in the U-wrap configuration, failure was associated with the debonding of FRP strips from the beam while for the beams strengthened by fully wrapped FRP strips, failure was initiated by rupture of the strips. The authors compared the shear contribution of FRP (V_f) from their tests with other reported values in the literature. They searched for factors such as relatively large members to predictions from equations in the design guidelines of ACI (ACI 440, 2002), fib (fib-TG9.3, 2001), and JSCE (JSCE, 2001) and found that for beams strengthened in the U configuration, none of the guidelines can consistently provide conservative estimates of V_f for beams of practical size, although the ACI equations (ACI 440, 2002) were found to be conservative for cases with low volume of steel stirrups.

Gamino et al. (2009)

Gamino et al. (2009) tested eight small-scale RC T-beams with a total depth of 300 mm. Two of the beams were used as control specimens, and the remaining six tests investigated the effects of different FRP materials for shear strengthening with different varying spacing between FRP strips. An anchorage system was used on three of the strengthened specimens, but no details are given on the type or method of anchorage. Results showed an increase in capacity with the use of FRP strengthening and further increase in load capacity for beams in which the anchorage system was used. Shear gains were compared with ACI 440.2R-02 (ACI 440, 2002) and fib-TG9.3 (fib-TG9.3, 2001). ACI 440.2R-02 (ACI 440, 2002) showed the best correlation with the experimental results; however, both specifications were extremely conservative in predicting the FRP contribution. FEM modeling using DIANA 9.1 software was also implemented and was found to present good correlation with the experimental results. The following conclusions were drawn from the test results:

- In shear strengthening using CFRP materials, the anchorage mechanism helps increase the load capacity and ductility
- ACI 440.2R-02 (ACI 440, 2002) guidelines showed better correlation with the experimental results
- DIANA 9.1 software proved capable of simulating the behavior and rupture pattern of the tested beams.

Arteaga et al. (2009)

Arteaga et al. (2009) presented experimental findings from a series of 16 full-scale tests on rectangular RC beams strengthened in shear with FRP. Specimens were 250 mm wide by 420 mm deep with a total span length of 4300 mm. The experimental program consisted of one reference beam and 15 FRP strengthened beams. Test parameters included: (1) FRP configuration (U-wrap or complete wrap), (2) fiber orientation (90 degrees or 45 degrees with respect to the longitudinal axis of the beam), (3) fiber amount (530 g/m^2 or 300 g/m^2), and (4) strengthening type (continuous or discrete FRP strips). Stirrups and applied FRPs were instrumented with strain gauges within the test region. The test procedure used a three point loading configuration in load control. Each beam featured two test regions referred to as long-span and short-span beams. It is noted that this notation does not refer to the span length of the test region, which is constant among all tests, but rather the span of the non-test region.

Experimental results showed increases in the shear capacity in all cases of FRP strengthened specimens in comparison to the reference beam. Test results were normalized with respect to concrete strength to account for differences in the quality of the concrete amongst the beam specimens. Experimentally observed FRP shear contributions were compared to values given by the theoretical models of fib (fib-TG9.3, 2001), CNR (CNR-DT 200/2004, 2004), Chen and Teng (2003a,b), and ACI (ACI 440, 2002). The following conclusions were drawn from the test results:

- Shear strengthening with unidirectional CFRP sheets, significantly enhances the capacity of the beam to resist these stresses, especially for the configuration which completely wrapps a section.
- There is no significant increase in the stiffness of the beams strengthened with CFRP for shear compared to the beams without strengthening.
- The steel stirrups in the cracked area yield before failure, and its capacity is fully used. Therefore it seems valid, at least in this case with low amounts of steel stirrups, that the total shear capacity could be seen as the sum of the contributions coming from concrete, stirrups, and CFRP.
- In the U-wrapped beams, failure occurs by delamination before the ultimate strain of the CFRP.
- All the models, except fib (fib-TG9.3, 2001), are conservative when compared with experimental results (excluding explicit safety factors).
- A deeper study is necessary to assure the stirrups and CFRP contributions model in a general case.

Alrousan et al. (2009)

Alrousan et al. (2009) presented test results of an experimental program consisting of 16 rectangular RC beams with varying depths designed to investigate the size effect. Beam depths of 9 in., 12 in., 15 in., and 18 in. where investigated. None of the beams had steel stirrups. FRP strengthening consisted of 2 in. wide strips with 4 in. wide gaps between strips. All beams were tested in four-point bending configuration with a simply supported span of 4.5 ft. Test results showed that shear strength increases with increases in effective beam depth. Crack openings were also measured using LVDTs, and results showed that crack openings develop at a slower rate as the effective depth increases. Based on test results, the following conclusions were made:

- The use of CFRP composites is an effective technique to enhance the shear capacity of RC beams. The externally bonded CFRP can increase the shear capacity of the beam significantly by 15-19% compared to that of the control beams, depending on the effective depth.
- Beam depth has an influence on the angle of inclination. An increase in primary cracking angle was observed with increase in effective beam depth for the FRP strengthened beams.
- One of the observed failure modes was due to the debonding of more than two CFRP strips. Test results seem to indicate that this mechanism can be prevented by providing a larger bond length (effective depth).

A2.5.2 Review of Anchorage Systems

A2.5.2.1 Existing Analytical Models for Effective Bond Length

Numerous experimental studies have examined the behavior of the bond between concrete and FRP laminates, but effective bond length still cannot be accurately calculated. Since 1994, many theoretical models have been developed to predict the strength of FRP-to-concrete bonds. These models have generally been based on pull-out test results with minimal accounting for the presence of the effective bond length.

Holzenkampfer (1994) investigated the bond strength and ultimate load of steel-to-concrete bonded elements using nonlinear fracture mechanics (NLFM). He demonstrated that sufficiently accurate results could be obtained using a bilinear bond-slip model.

Taljsten (1994) modified Holzenkampfer's (1994) model to take into account the elastic modulus E_c and the thickness t_c of the concrete. This model indicates that as the thickness of the concrete tends to infinity (in the case of deep beams, for instance), the properties of the concrete have no influence on the bond strength at the concrete-composite interface.

Chajes et al. (1996) studied the bond and force transfer mechanism in composite material plates bonded to concrete. Tests were performed using a single-lap shear test specimen and a constant bond length to evaluate the effect of surface preparation, adhesive type, and concrete strength on average bond strength. Their test results indicated that surface preparation can influence ultimate bond strength. They also showed that the concrete surface should be sandblasted followed by an application of a primer to achieve the best possible bond, In addition, they found that the strain distribution in the composite plate along the bonded length decreases at a fairly linear rate with uniform force transfer. Thus, there is an effective bond length for a joint beyond which no further increase in failure load can be achieved.

Karbhari and Engineer (1996) developed a peel test for the investigation of the bond between advanced composites and concrete surfaces. They also developed a methodology for understanding the various mechanisms and modes of interfacial fracture. Their test permits the determination of two components of interfacial fracture energy and allows a quantitative comparison of adhesion mechanisms and energies between systems.

Niedermeier (1996) modified the Holzenkampfer (1994) model and formulated Equation A2-152 to calculate the effective bond length:

$$L_e = \sqrt{\frac{E_f t_f}{4 f_{ctm}}} \qquad \text{(A2-152)}$$

where E_f is the elastic modulus (MPa) and t_f is the thickness (mm) of the FRP. Here, $E_f t_f$ is considered to be the FRP stiffness, and f_{ctm} is the mean tensile strength of the concrete surface (MPa). This model considers the presence of multiple cracks along the beam.

Bizindavyi and Neale (1997) performed an experimental and analytical investigation of transfer lengths of composite laminates bonded to concrete. The observed modes of failure were (1) shearing of the concrete beneath the adhesive layer, (2) cohesive failure at the adhesive layer due to improper bonding procedure, and (3) rupture of the composite coupon. They developed an analytical model based on the shear lag approach. Experimental and analytical results indicated that loads up to approximately two-thirds of the total to be transferred were acceptable.

Using shear tests, Brosens and Van Gemert (1997) investigated the anchoring stresses between concrete and CFRP laminates. Anchoring phenomena involve the increase of stresses including stress concentrations in the anchorage zone due to higher stresses in the CFRP laminates. Shear experiments were performed on two concrete prisms connected by three layers of CFRP laminates glued on two opposite sides. Steel plates were glued on the other sides to allow the application of tensile force. The test specimen was loaded under displacement control. Based on their results, they formulated design equations assuming a triangular shear stress distribution along the CFRP composite. The only parameters needed for this model were tensile strength of concrete and bonding length. These variables could be measured by means of a pull-off test.

Horiguchi and Saeki (1997) used three test methods (tensile, bending, and shear) to investigate the effect of concrete quality on the bond strength of CFRP composite sheets. Three different types of bond tests were conducted for each of the three test methods. The concrete compressive strength was found to have a significant effect on bond behavior, demonstrating that concrete structures should be evaluated by effective bond tests prior to rehabilitation. This work found that the bond strength of a concrete surface with CFRP composites increased with increase of concrete strength.

Maeda et al. (1997) compared the strain distribution in CFRP sheets. Their experimental program involved tensile bond tests with results subjected to finite element analyses. Based on their experimental results, they developed expressions for the average bond strength and the effective bond length (Equation A2-153) along with an expression for ultimate load to cause delamination of the CFRP sheets.

$$L_e = e^{6.13 - 0.58 \ln E_f t_f} \qquad \text{(A2-153)}$$

Using nonlinear fracture mechanics, Neubauer and Rostasy (1997) modified the bond strength model proposed by Holzenkampfer (1994) for steel-strengthened concrete. The authors increased the effective bond length by reducing the constant value of 4 to 2 used in Holzemkampfer's (1994) model in Equation A2-154. They concluded that the bond-slip behavior can be represented by a triangular model for both concrete fracture (failure by crack propagation in the concrete adjacent to the adhesive) and FRP delamination failures (bond failure in the adhesive layer). In this model, the bond demonstrates linear elastic behavior until the peak bond stress is reached.

$$L_e = \sqrt{\frac{E_f t_f}{2 f_{ctm}}} \qquad \text{(A2-154)}$$

Chaallal et al. (1998b) developed a design model based on the assumption that the bond behaves as a Mohr Coulomb material. However, this model is inaccurate since it neglects the influence of the effective bond length. This model was based on limited experimental data and did not include the effect of concrete strength on debonding failure.

Khalifa et al. (1998) developed a design model by modifying the empirical model of Maeda et al. (1997). They related the bond strength to the concrete/sheet interface with concrete strength. This model accounts for the effective bond length using the same equations formulated by Maeda et al. (1997).

Miller and Nanni (1999) quantified the effective bond length by using the linear portion of the strain distribution just before peeling occurs. Maeda et al. (1997) and Brosens and Van Gemert (1997) also reported the linear strain distribution. Using data from their experiments and the work of Maeda et al. (1997), they derived a linear relationship between the effective bond length and the stiffness of the CFRP sheet as:

$$L_e = -0.00298\left(E_f t_f\right) + 3.711 \qquad \text{(A2-155)}$$

Volnyy and Pantelides (1999) attempted to derive the effective bond length using Brosens and Van Gemert's (1997) model in combination with fracture mechanics principles. Unfortunately, their concept of effective bond length was incorrect, and a number of errors crept into the deduction process. The result, therefore, is only an alternative expression of Brosens and Van Gemert's (1997) equations. They suggested a constant value of 0.12% for the maximum tensile strain, *e*, in the CFRP composite.

$$L_e = 2\frac{E_f t_f e}{f_{ctk}} \qquad \text{(A2-156)}$$

where the parameter f_{ctk} is given by

$$f_{ctk} = 0.23 f_c^{2/3} \qquad \text{(A2-157)}$$

Niu and Wu (2000) adopted a linear bond stress-slip model based on linear elastic beam theories to investigate the effects of flexural cracks in concrete on the interfacial shear stresses for several load cases. They developed an energy-based method to predict the initiation of debonding on the retrofit beam and final debonding failure. Their analysis assumed (1) a linear strain distribution throughout the full depth of the section, (2) no slip between the longitudinal reinforcing steel and surrounding concrete, and (3) no slip between the external FRP reinforcement and the concrete surface. Further, they did not account for premature FRP delamination or shear failure and thus assumed that composite action was maintained until failure. Finally, they ignored the tensile strength of the adhesive. Based on previous studies (Bizindavyi and Neale, 1999), the authors proposed Equation A2-158 and suggested that *k* be taken as approximately 0.94 in the equations.

$$L_e = k\sqrt{E_f t_f} \tag{A2-158}$$

By assuming that the debonding strength of a plated beam is affected only by the bond strength at the plate/concrete interface, the fib approach 1 (fib-TG9.3, 2001), based on pull-out tests, models the mechanism of intermediate crack debonding as a plate-to-concrete bonded joint under tension. This approach requires verification of the end anchorage using bond strength models and bond stress-slip and imposition of a strain limitation on the plate to avoid bending between plate ends. The FRP strain corresponding to bond failure is not a fixed value; it is dependent on many parameters such as loading arrangements, behavior of internal reinforcement, and crack distribution. As a result, the use of the strain limitation greatly simplifies the problem of intermediate crack debonding and an equation for the effective bond length was proposed as:

$$L_e = \sqrt{\frac{E_f t_f}{c_2 f_{ctm}}}; c_2 = 2 \tag{A2-159}$$

The fib approach 2 (fib-TG9.3, 2001), a modification of Niedermeier's (1996) model, is based on the bond stress-slip relationship and the envelope line of tensile stresses in FRP. It compares the maximum possible increase in tensile stress (σ_{fd}) within the plate (transferred by bond stress, τ_f) between two subsequent flexural cracks, and the increase is calculated assuming full interaction. Niedermeier (1996) assumed that bond stress between two adjacent cracks occurs in only one direction. This model demonstrates that the force in the plate is dependent on both the anchorage force in the uncracked region and the sum of the bond forces between subsequent flexural cracks caused by beam action. The effective bond length is calculated as:

$$L_e = c_2\sqrt{\frac{E_f t_f}{\sqrt{f_{ck} f_{ctm}}}}; c_2 = 1.44 \tag{A2-160}$$

Chen and Teng (2001) based their model on the nonlinear fracture mechanics (NLFM) solution developed by Yuan and Wu (1999) for predicting bond strength and effective bond length (see Equation A2-160). Their model assumes a triangular bond stress-slip relationship and explicitly recognizes the non-uniform stress distribution in the FRP along a shear crack as determined by the bond strength between FRP strips and concrete. The authors used the cylinder concrete compressive strength for a more practical application. They also demonstrated the importance of b_p/b_c (width ratio of plate to concrete) on the ultimate bond strength.

$$L_e = \sqrt{\frac{E_f t_f}{\sqrt{f_c'}}} \tag{A2-161}$$

Leung (2001) developed a model, based on fracture mechanics principles, for determining the interfacial stress at the plate-to-concrete interface. The model takes into account the effects of applied moment, vertical shear force, crack length, and crack width. This model, however, has only limited application because it only predicts the likelihood of interfacial crack debonding,

providing no failure criterion. This model was verified by finite element analyses only; therefore, it lacks experimental support.

Yang et al. (2001) developed a model based on concrete tensile strength which also treats effective bond length as a constant equal to 3.94 inches.

The Canadian CAN/CSA S806-02, Design and Construction of Building Components with Fibre-Reinforced Polymers (CAN/CSA S806, 2002), represents the only formalized design code addressing the application of externally bonded FRP reinforcement for RC members. According to CAN/CSA S806-02 (CAN/CSA S806, 2002), calculation of the effective bond length is based on a simplified version of the equations developed by Maeda et al. (1997):

$$L_e = \frac{25350}{\left(E_f t_f\right)^{0.58}} \tag{A2-162}$$

The Iso model as shown in Equation A2-163 and the Sato model as shown in Equation A2-164 are contained in JCI (2003) and are direct functions of FRP thickness and stiffness.

$$L_e = 0.125\left(E_f t_f\right)^{0.57} \tag{A2-163}$$

$$L_e = 1.89\left(E_f t_f\right)^{0.4} \tag{A2-164}$$

Based on Popovic's (1973) model by Nakaba et al. (2001), Kanakubo et al. (2003) proposed two different expressions for the calculation of effective bond length. In Equation A2-165, the authors introduce the effect of maximum slippage. For simplicity and design purposes, they proposed a simplified version shown in Equation A2-166.

$$L_e = \sqrt{\frac{2\lambda_f s_e}{k_e}} \tag{A2-165}$$

$$L_e = 0.7\sqrt{\frac{E_f t_f}{\left(f_c'\right)^{0.2}}} \tag{A2-166}$$

where λ_f is the bond length index given by Equation A2-167. The coefficients s_e and k_e are given by the authors and can be taken as 0.428 and 0.354, respectively. The maximum debonding strength is then determined by Equation A2-168.

$$\lambda_f = \frac{E_f t_f}{\tau_{\max}} \tag{A2-167}$$

$$\tau_{\max} = 3.5\left(f_c'\right)^{0.19} \tag{A2-168}$$

Yuan et al. (2003) studied the bond strength between FRPs and concrete using linear elastic fracture mechanics (LEFM) and NLFM. Their LEFM study considered the effect of the widths of both the plate and the concrete member. They also solved the NLFM equations for five different shear stress-slip relationships. Among these relationships, the closest to reality is the linearly ascending then descending relationship. They defined the effective bond length as the value corresponding to 97% of the load carrying capacity, assuming the bond length is infinite and it is expressed as:

$$L_e = a + \frac{1}{2\lambda_1} \ln \frac{\lambda_1 + \lambda_2 \tan(\lambda_2 a)}{\lambda_1 - \lambda_2 \tan(\lambda_2 a)} \tag{A2-169}$$

where the parameters λ_1, λ_2, and a are given as:

$$\lambda_1 = \sqrt{\frac{\tau_{\max}}{s_0 E_f t_f}} \tag{A2-170}$$

$$\lambda_2 = \sqrt{\frac{\tau_{\max}}{(s_f - s_0) E_f t_f}} \tag{A2-171}$$

$$a = \frac{1}{\lambda_2} \sin^{-1}\left[0.99\sqrt{\frac{s_f - s_0}{s_f}}\right] \tag{A2-172}$$

In Equations A2-170 through A2-172, s_f and s_o are the deflection at maximum shear stress and the final deflection at failure, respectively, and they are determined as:

$$s_0 = 0.0195 \beta_w f_{ct} \tag{A2-173}$$

$$s_f = \frac{2G_f}{\tau_{\max}} \tag{A2-174}$$

$$\tau_{\max} = 1.50 \beta_w f_{ct} \tag{A2-175}$$

$$G_f = 0.308 \beta_w^2 \sqrt{f_{ct}} \tag{A2-176}$$

$$\beta_w = \sqrt{\frac{2.25 - b_f / b_c}{1.25 + b_f / b_c}} \tag{A2-177}$$

Aiello and Ombres (2004) proposed a model to analyze the cracking and deformability of plated members. Their model is based on the use of moment-curvature relationships evaluated from analysis of a cracked beam element between two adjacent cracks subjected to constant bending moment. This discrete crack model assumes that all cracks have spacings varying between a minimum value given by the development length, L_b, and a maximum value of $2L_b$. This model

evaluates the crack width, crack spacing, curvature, and beam deflections, accounting for the bond-slip at the plate/concrete interface.

Teng et al. (2004) developed a simple strength model for the intermediate crack debonding failure mode of RC flexural members. This model is a simple modification of the bond strength model of Chen and Teng (2001).

Ueda and Dai (2004) presented a new shear bond model of FRP-concrete interface expressed in Equation A2-178. This model considers effects not only of FRP and concrete mechanical properties, but also of adhesive properties. It is based on a new methodology that eliminates strain gage arrangement on FRP and needs only the FRP strain-slip relationship at the loaded end. The shear bond model is expanded by introducing FRP strain effects on the bond stress-slip relationship so that the model can be applied to short bond length cases. This work concluded that the shear stiffness (shear modulus divided by thickness) of adhesive layers has significant effects on effective bond length. The authors suggested that if α is assigned a constant value of 0.96, a reasonable anchorage strength design is achieved. The authors later modified this expression and developed a new model. Equation A2-179 introduces the concept of fracture energy (G_f):

$$L_e = \frac{9.79\left(E_f t_f\right)^{0.38}}{\left(\frac{G_a}{t_a}\right)^{0.657}\left(f_c'\right)^{0.118}} \ln\left(\frac{1+\alpha}{1-\alpha}\right) \tag{A2-178}$$

$$L_e = \frac{\sqrt{2E_f t_f}}{B\sqrt{G_f}} \ln\frac{1+\alpha}{1-\alpha} \tag{A2-179}$$

where the parameters B and G_f are given by Equations A2-180 and A2-181, respectively.

$$G_f = 0.446\left(\frac{G_a}{t_a}\right)^{-0.352} f_c^{0.236}\left(E_f t_f\right)^{0.023} \tag{A2-180}$$

$$B = 6.846\left(E_f t_f\right)^{0.108}\left(\frac{G_a}{t_a}\right)^{0.833} \tag{A2-181}$$

The approach of Foster and Khomwan (2005) was similar to that of Ueda and Dai (2004); its determination of L_e considers the stiffness of the adhesives. Based on their results, they simplified Ueda and Dai's (2004) equation by introducing a constant that replaces the compressive strength of the concrete as shown in Equation A2-182. The disadvantage of this constant is that it accounts only for a specific range of concrete strengths. They concluded that the effective bond length model is a calibration parameter and will vary for each approach. This work also represented a new approach requiring only the failure load to obtain a good approximation of the stress-slip curve from bond shear tests.

$$L_e = 25\left(E_f t_f\right)^{0.38}\left(G_a / t_a\right)^{-0.66} \tag{A2-182}$$

Lu et al. (2005a) proposed a model on the basis of interfacial fracture energy, regardless of the shape of the bond-slip curve as shown in Equations A2-183 and A2-184. They investigated the average FRP strain, ε_{fe}, at debonding failure using a rigorous FRP-to-concrete interface bond-slip model, and they relied on Neubauer and Rostassy's (1997) definition of the bond length factor β_l.

$$L_e = 1.33\frac{\sqrt{E_f t_f}}{f_t} \tag{A2-183}$$

$$L_e = 0.228\sqrt{E_f t_f} \tag{A2-184}$$

Zhang and Hsu (2005) derived a shear bond model in two steps, (1) model calibration by curve fitting and (2) bond mechanism. Proposed for design purposes, the bond mechanism model assumes a triangular shape distribution for the shear stresses. It also considers the effective bond length as a constant equal to 2.95 inches.

Casas and Pascual (2007) developed a model that represents the behavior of the FRP in the vicinity of a single crack and is therefore representative of the conditions encountered in the specimens used for bonding tests. The authors concluded that in a general case, where the stiffness of the strengthened concrete is much higher than the FRP stiffness, the effective bond length should be calculated as:

$$L_e = \sqrt{\frac{E_f t_f}{g_b}} \tag{A2-185}$$

where g_b is the shear joint stiffness of concrete plus adhesive resin. This is expressed as:

$$g_b = \frac{g_r g_c}{g_r + g_c} \tag{A2-186}$$

where g_r and g_c are the shear joint stiffness for resin and concrete, respectively and can be determined as shown in Equations A2-187 and A2-188, respectively. Here, G_c and G_r are the shear modulus of the resin and concrete. Poisson's ratio for concrete and resin are taken as 0.50 and 0.38, respectively. The resin thickness, t_b, is used in the application of the repair, and the concrete thickness, t_{ce}, can be estimated as in Equation A2-189.

$$g_r = \frac{G_r}{t_b} \tag{A2-187}$$

$$g_c = \frac{G_c}{t_{ce}} \tag{A2-188}$$

$$t_{ce} = w_f + 50.8 \leq \frac{h}{2} \tag{A2-189}$$

Monti and Liotta (2005) developed a model considering all strengthening schemes and failure modes. The model was derived by considering three main steps: (1) a generalized FRP-concrete bond constitutive law is defined, (2) boundary limitations are defined, and (3) the stress field in the FRP crossing a shear crack is analytically determined. This model assumes that cracks are evenly spaced along the beam axis and that crack depth is equal to the internal lever arm (*0.9d*) for the ultimate limit state. It also assumes that the resisting shear mechanism is based on the truss analogy for wrapping and u-jacketing.

The ACI 440.2R-08 (ACI 440, 2008), uses an expression for effective bond length based on the analytical model proposed by Khalifa et al. (1998). This code defines the effective bond length as the length at which the majority of bond stress is maintained. The calculation of the effective bond length is also based on a simplified version of the equations developed by Maeda et al. (1997) as shown in Equation A2-190:

$$L_e = \frac{23300}{\left(nE_f t_f\right)^{0.58}} \tag{A2-190}$$

Ben Ouezdou et al. (2008) proposed a model based on previous experimental studies of effective bond strength in terms of concrete strength, elastic modulus of concrete and FRP, and FRP thickness. They plotted the data to find the relationship between these parameters and effective bond length. By normalizing effective bond length with FRP thickness, they presented it as a function of the dimensionless ratio of the elastic modulus of the FRP to that of the concrete. Because concrete strength is measured more often than the elastic modulus, the authors also proposed a relationship between the effective bond length and the concrete strength as:

$$L_e = 0.012 t_f \left(\frac{E_f}{\sqrt{f_c'}} \right) \tag{A2-191}$$

Technical Report CS-TR55 (Concrete Society, 2004), based on the Neubauer and Rostasy (1997) study, presents the effective bond length as:

$$L_e = 0.7 \sqrt{\frac{E_f t_f}{f_{ctm}}} \tag{A2-192}$$

Eurocode 8-3 (Eurocode 8-3, 2004) presents Equation A2-193 for calculating the effective bond length of shear strengthening:

$$L_e = \sqrt{\frac{E_f t_f}{4\tau_{\max}}} \tag{A2-193}$$

In which, the maximum shear (τ_{max}) is given by:

$$\tau_{\max} = 1.8 f_{ctm} k_b \tag{A2-194}$$

where k_b is the covering coefficient for FRP sheets given by

$$k_b = \sqrt{\frac{1.5}{1 + 0.01 w_f}} \tag{A2-195}$$

Abdelrahman et al. (2009) investigated cracks in concrete and the effect of their orientation on the bond of CFRP sheets. The effective bond length of the CFRP sheets, thickness of fiber sheets, and use of mechanical anchorage were also investigated. The specimens used in this investigation were RC prisms with dimensions of 11.8 x 11.8 x 23.6 inches. Cracks with variable orientation (45, 60, and 90 degrees) were intentionally formed in the specimens during casting. The specimens were loaded in direct tension with U-shaped CFRP sheets bonded to the surface on both sides of the specimen. The mechanical anchorage system consisted of steel plates at the end of the sheets and two or four steel bolts. Strain gages were used at different locations along the bonded length of the CFRP sheet to obtain bond stress away from the crack location, and bond stress versus slip relationships. Depending on the crack orientation, CFRP bonded length, and type of external anchorage system, the failure modes of the tested specimens varied among bond failures, bond-rupture failures, and rupture failures. The authors reported that the ultimate load increased as the angle of the crack inclination decreased. They also reported that mechanical anchorage using two bolts could not prevent bond failure; however, increasing the number of bolts could change the mode of failure to rupture of the sheets. The effective bond length was calculated based on the following expression:

$$L_e = \frac{\sqrt{2 E_f t_f G_f}}{\tau_m} \tag{A2-196}$$

The authors observed the effective bond length to be more than 8.27 inches for one layer of unanchored CFRP sheet with thickness of 0.0046 inches and elastic modulus of 33380 ksi.

Bilotta et al. (2009a) carried out twelve simple shear tests with results presented in an experimental matrix available in the literature. Experimental data was collected in order to allow comparison with theoretical predictions obtained by expressions contained in the CNR-DT200/2004 (2004). Both numerical and experimental studies have showed that dissimilar test set-up can change the experimental results. The tests were performed on CFRP plates and sheets applied on two opposite longitudinal faces of six concrete prisms. Prior to installing FRP reinforcement, the concrete surface was treated by both sand paper and primer. Tests were carried out under a servo-hydraulic testing machine. Several strain gauges were applied along the FRP laminates in order to measure axial strains. Tests with poor results were excluded from analysis by the authors. Comparison between experimental results and theoretical predictions showed good correlation in debonding load values with reference to specimens reinforced by FRP sheets. More scatter was observed in specimens reinforced by FRP plates. As part of this

study they also presented two methods for the calibration of the factor k_G. The first method is based on the procedure proposed by Nigro and Savoia (2005). With reference to each experimental test, k_G, can be computed by using the following expression:

$$k_G = \frac{P_{\max}^2}{b_f^2 \cdot 2E_f t_f k_b \sqrt{f_{ck} f_{ctm}}} \qquad \text{(A2-197)}$$

The mean value, the standard deviation, the coefficient of variation, and the 5-th percentile can be calculated by means of easy statistical relationships assuming a normal distribution for the k_G values obtained from this expression with reference to the number of tests. The second method follows the procedure proposed in EN 1990 (2002). This method uses a correction factor that takes into account all variables not included in the relationship of the theoretical model; such factoring improves the accuracy of the theoretical model by minimizing the differences between the theoretical and experimental results. The authors concluded that Method I confirmed that the k_G values proposed by CNR-DT200/2004 (2004) had not been significantly changed by increasing the experimental data. They also concluded that Method II provided more accurate values for factor k_G, because it provided a higher R-squared value and allowed consideration of the randomness of the material properties. Method II pointed out that significant difference was obtained in terms of k_G values; such results could be explained by considering the large scatter in the experimental results. Based on such consideration, it appeared that two different k_G values should be adopted in the design relationships in order to better predict reinforcement debonding load values.

Bilotta et al. (2009b) discussed the results of 12 cyclic simple shear tests under both monotonic and cyclic actions to investigate the influence of cyclic external actions on the bond between FRP reinforcement and concrete substrate. This study included an additional 16 simple shear tests to investigate the influence of cyclic action on interface behavior at debonding. These tests were performed on 8 concrete prisms with CFRP sheets and plates applied on two opposite longitudinal faces. Tests were carried out using a servo-hydraulic testing machine. Several strain gauges were applied along the FRP laminates in order to measure axial strains during the bonding test. The effective bond length values were calculated according to the relationships suggested by CNR-DT200/2004 (2004), Teng et al. (2001), and fib (fib-TG9.3, 2001). The experimental results showed that the design relationships provided by Teng et al. (2001) and by the main international codes for evaluating the effective bond length values are conservative for both sheet and plate reinforcements. The authors reported that in the case of plates, the effective bond length experimentally evaluated by means of monotonic tests was noticeably lower than theoretically predicted.

Ceroni and Pecce (2009) carried out bond tests on 45 concrete blocks externally strengthened with carbon FRP sheets according to an asymmetric pull-out configuration. The load pattern provided for transfer of the tensile load by gripping the free end of the CFRP sheet and applying compression to the concrete block restrained in a stiff steel frame. Several parameters were investigated such as number of layers, bonded length, and width of the CFRP sheet. This study focused mainly on the effectiveness of three end devices: a CFRP sheet glued transversally to the reinforcement direction, a CFRP bar applied in a groove, and a CFRP fan inserted in a hole in the concrete filled with resin. Most of the specimens failed by debonding at the interface (in some

cases debonding happened superficially). When an anchorage system was used, a greater volume of concrete detached. In conclusion, the FRP fan was found to be the most efficient system with a thicker layer of concrete involved at failure. The experimental results evidenced that the end anchoring devices are more efficient for lower values of the FRP to concrete width ratio.

Diab and Wu (2009) investigated the bond shear strength between BFRP (Basalt fibers) and concrete prisms using double lap shear specimens with different layers of BFRP sheets. For comparison purposes, similar test specimens were made of CFRP and GFRP. The dimensions of the specimens were 3.94 x 3.94 x 17.72 inches. FRP sheets were bonded to both sides of the concrete blocks along the axial direction. A total of 19 specimens were prepared to investigate the bond performance at the FRP-concrete interface. The variables considered were the type of FRP composites and number of layers. Seven strain gauges were mounted on the FRP sheets to monitor debonding deterioration along the FRP-concrete interface. In this study, debonding along the FRP-concrete interface was observed as a predominant failure mode, except for one specimen with glass fibers which failed by debonding along the FRP-concrete interface accompanied with fracture of GFRP. The authors observed that the size of shear failure in concrete depends on the type of fiber. In comparison with bond capacities of different specimens it was observed that the larger stiffness of FRP sheet gave the higher bond load for the same layers. Two layers of BFRP exhibited bond capacity higher than or at least equal to one layer of CFRP.

Kim and Smith (2009) investigated the influence of crack location on the shear strength and behavior of FRP anchors in FRP-to-concrete joint assemblies. Failure modes as well as behavior were described and the effect of crack position was also quantified. A standard single shear test was utilized in this study. All anchors were embedded 1.5 inches. LVDTs and strain gauges were used as measuring instruments. The shear test set-up was mounted in a universal testing machine. This series of tests revealed five failure modes: (1) simultaneous plate debonding and anchor shear failure, (2) simultaneous plate debonding and anchor fan debonding, (3) plate debonding followed by anchor shear failure, (4) plate debonding followed by anchor fan debonding, and (5) plate debonding followed by anchor pull-out. The authors concluded that the strength of the joint depends strongly on the location of the anchor. A significant post-peak reserve strength up to about half the strength of the joint was also observed.

Mahmoudabadi and Mostofinejad (2009) evaluated the effect of both concrete surface treatment and an alternative method affecting the ultimate load capacity of the concrete specimens strengthened with FRP composites. The dimensions of the specimens were 3.94 x 3.94 x 19.69 inch concrete beams. The specimens were prepared according to manufacturer's specification. Concrete surfaces were first ground with a grinding machine. Then the pores of the surface were filled with epoxy. Grooving techniques were also used as an alternative method. Five longitudinal grooves (0.39 inches deep and 0.12 inches wide) were established on select specimens right under the FRP laminates and without any additional surface preparation. Then the grooves were filled with epoxy and the FRP sheet was adhered to the concrete surface. The specimens were tested using a four-point loading setup. 2 LVDTs were used for measuring the midspan displacement of concrete beams. About 30 specimens were loaded up to failure. All surface prepared specimens bonded with FRP laminates failed by intermmediate carck (IC) - debonding starting from the midspan crack. In the specimens with longitudinal grooves, no

debonding was observed until rupture of FRP laminates. As a result of this experimental investigation, it was concluded that the specimens with surface preparation had higher load capacities at ultimate strength compared to non-surface prepared specimens. The specimens with longitudinal grooves instead of surface preparation showed increased ultimate load capacity up to 100%. This is attributed to more contact between FRP laminates and concrete surface, and also to penetration of stress transfer to deeper layers of concrete. The authors concluded that the grooving technique provides full elimination of debonding of FRP laminates from concrete substrate.

Siafas and Donchev (2009) tested eight RC beams strengthened with CFRP attached to the bottom surface of the beams. Several different types of improvement for anchorage of the laminates were investigated. The beams were 7.87 feet long, 3.94 inches wide, and 5.91 inches deep. Five different types of anchorage were investigated: (1) anchorage without additional reinforcement, (2) anchorage with additional bolts, (3) anchorage with additional dowel bars under the laminate, (4) anchorage with preliminary impregnation of the concrete with epoxy resin, and (5) anchorage with epoxy resin and additional GFRP wrapping at the end. The mode of failure was similar for most of the beams (separation of the concrete cover). In case of improvement using bolts, they act very efficiently for preventing development of the delamination at early stages of loading. The authors concluded that: (1) the use of extra epoxy resin for impregnation of the concrete at the anchorage zone of the laminate is not effective because of low cohesion between the structural adhesive and the surface of the epoxy and (2) improvement of the usage of epoxy resin can be obtained using resin with lower viscosity which will allow the resin to penetrate into the concrete and will keep the texture of the surface of the concrete in the same condition as before the application.

A2.5.2.2 Anchorage Systems

This section presents an overview of the existing research studies on various anchorage systems. When a proper anchorage system is not provided, the most common failure mode of FRP-strengthened RC members is debonding of the FRP. Therefore, this section will focus on the effects of anchoring to avoid the debonding of FRP sheets from the concrete surface. Several studies are summarized with a brief description of the specimens used in each.

Various types of anchorage systems have been studied to avoid premature failure due to FRP debonding, including the near surface mounted system (NSM), fiber reinforced polymer (FRP) anchor spikes, additional horizontal strips, and various mechanical anchorage systems. The following sections discuss the research on each system. Existing experimental investigations have proved that anchorage of FRP systems increases the shear contribution provided by FRP composite materials.

Near Surface Mounted (NSM) System

The use of NSM reinforcement, also known as structural repointing, started in the 1940s. These systems were originally intended to strengthen RC members with steel reinforcing bars fastened into preformed grooves on the exterior of a concrete member (Asplund, 1949).

The NSM system described by Khalifa and Nanni (2000) can be used with FRP sheets and precured laminates that are unbonded or fully bonded to concrete. The idea is to embed a bent

portion of the end (or a region near the end) of the FRP reinforcement into the concrete, as shown in Figure A 2.28. In the case of fiber sheets, the bend is created during wet lay-up, and in the case of laminates, it is preformed. This technique requires no surface preparation work apart from cutting the grooves, an operation that demands considerable labor. An NSM system is particularly attractive for strengthening where external reinforcement would be subjected to mechanical and environmental damage (De Lorenzis, 2002).

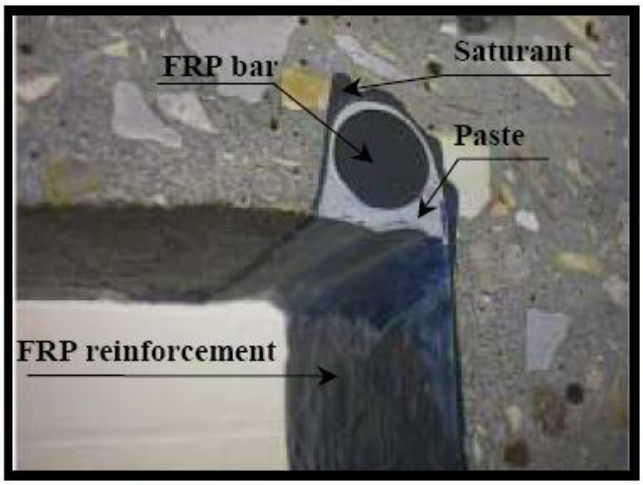

Figure A 2.28 Cross-section of the NSM System (Khalifa et al., 1999)

The FRP reinforcement is anchored by grooving the concrete near the end of the FRP sheet, as shown in Figure A 2.29. The groove must be perpendicular to the fiber direction. Concrete can be grooved using conventional tools. For example, two parallel saw cuts may be made on the concrete surface with a predetermined depth and spaced at a distance equal to the required width of the groove, as shown in Figure A 2.29(a). The concrete between the two cuts is then chipped off.

The groove walls may be roughened by sandblasting, after which the groove is cleaned to remove all loose particles and dust. The concrete surface is then prepared and primed, including the walls of the groove. The FRP reinforcement is bonded to the concrete surface and to the walls of the groove as shown in Figure A 2.29(b). After the resin impregnating the sheet has set, the groove is half filled with a high-viscosity epoxy compatible with the FRP system. The high-viscosity paste ensures easier field execution. An FRP bar is then placed in the groove and lightly pressed in place. This action forces the paste to flow around the sheet and to cover simultaneously part of the bar and the sides of the sheet. The groove is then filled with the same paste, and the surface is leveled.

As a variation of the installation procedure described above, the end of the FRP sheet can be rolled around the bar during the first saturant impregnation, and the bar can be wedged tightly into the groove as shown in Figure A 2.29(c). In this case, the paste is only added as the final step, as illustrated in Figure A 2.29(d). The system can also be applied with or without an FRP bar and can be used to anchor continuous as well as discontinuous sheets.

The NSM system provides an effective solution for cases in which the bonded length of FRP composites is not sufficient to develop its full capacity, or in which anchorage to adjacent members is required. This system is also compatible with the FRP strengthening system and avoids high stress concentration and durability concerns.

Micelli et al. (2002) applied the NSM system to strengthen short shear spans of RC T-joists. This anchorage system increased the shear capacity of the FRP system; however, debonding failure due to anchor pullout was observed.

(a) Cutting the groove

(b) Applying FRP sheet

(c) Inserting an FRP bar

(d) Filling with epoxy

Figure A 2.29 Construction of NSM System

Some of the findings reported by Eshwar et al. (2008) describe the variables affecting the performance of this anchor system. Their research used sixteen RC T-beams externally strengthened using CFRP wet lay-up laminate. The specimen details are shown in Figure A 2.30. The groove size for each specimen was either 1.5 or 2.5 times the anchor bar diameter. Two different anchor locations were tested to represent the situations before and after the re-entrant corner, as shown in Figure A 2.31.

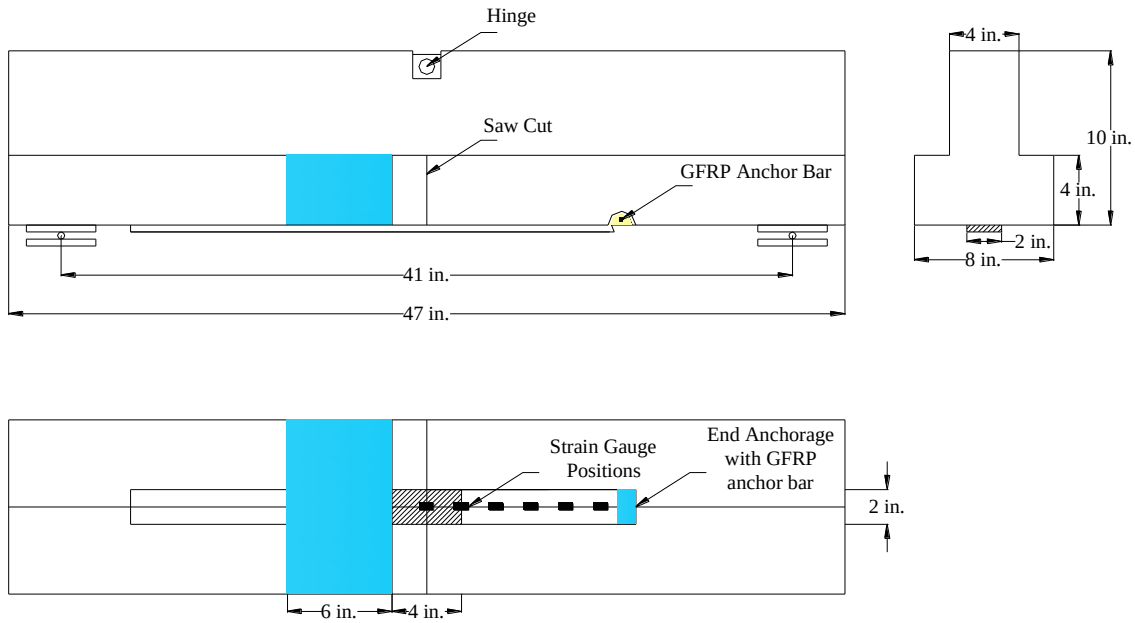

Figure A 2.30 Specimen Details (Eshwar et al., 2008)

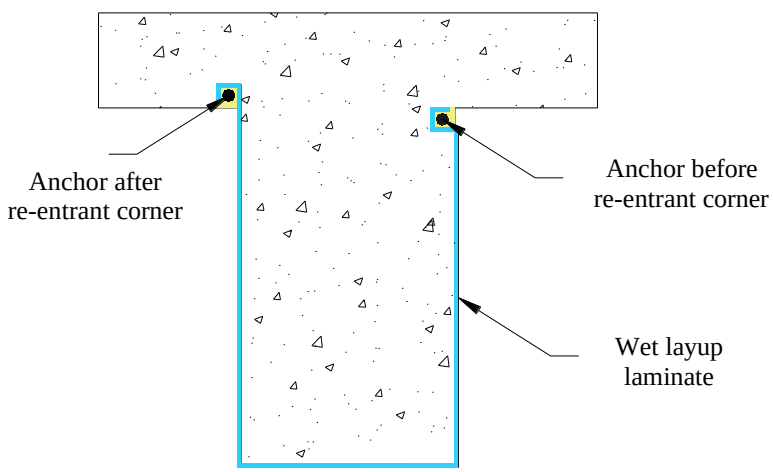

Figure A 2.31 U-Anchor Schemes

The failure mode observed here in all specimens was either anchor pullout or FRP rupture. The failure modes indicate that the end anchor helped to prevent failure of the FRP system. The end anchor location had a significant influence on the ultimate capacity. Specimens with anchors after the re-entrant corner exhibited approximately 40% higher strength than those with anchors before the re-entrant corner, perhaps because, in the latter, the need to press the laminate into the groove induced significant stress concentrations. The performance of externally bonded FRP was found to be improved by 7% to 51% with the use of an NSM anchor (Eshwar et al., 2008).

Groove size influences ultimate capacity when the bar diameter varies. A larger groove appears to reduce stress concentration, leading to higher anchorage capacity. A minimum groove size range should be 1.5 or 2.5 times the bar anchor diameter. A larger groove is more advantageous but less practical because much more concrete would be removed to ease the construction

procedure. A minimum radius of ½ inch should be maintained at the corners of the groove to limit stress concentration and to prevent premature peeling. A GFRP bar with a minimum diameter of 0.4 inches should be used as an end anchor.

Fiber-Reinforced Polymer Anchor Spikes

Fiber anchors offer a new way of anchoring a composite to the reinforced concrete structure. These anchors were originally developed by the Shimizu Corporation in Japan (Jinno and Tsukagishi, 1998). They are made from the same material as the sheet, saturated with epoxy, and inserted immediately after the sheet is placed. This process ensures that the anchors and sheet form a continuous composite unit.

Another system used to prevent the peeling of the FRP strips is GFRP anchor spikes (Eshwar et al., 2003). Each anchor spike consists of a precured fiber portion and a dry fiber portion as shown in Figure A 2.32. The FRP anchor spikes may be constructed in-situ. First, fibers are bundled together and half the fiber length is covered with plastic or duct tape. Second, the uncovered bundled fibers are impregnated and thoroughly saturated with resin. Finally, the saturated fibers are passed through a circular hole in a steel plate or die to obtain the desired diameter of the anchor spikes. The dry fibers are used for bonding purposes and trimmed to the appropriate length according to specific requirements.

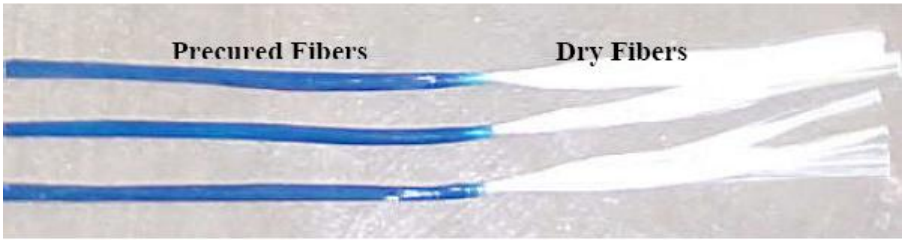

Figure A 2.32 Anchor Spikes

Following surface preparation of the concrete, holes of the desired diameter and depth are drilled and partially filled with saturant. The laminate is then applied, and while it is wet, the precured portion of each spike anchor is inserted into the holes. The dry fibers are spread around the layer in circular fashion, and a layer of saturant is then applied as shown in Figure A 2.33.

Figure A 2.33 Spreading the Dry Fibers

Eshwar et al. (2008) fabricated spike anchors of 0.4 inches in diameter, as shown in Figure A 2.32. Tests were conducted to determine the shear load that the spike anchors could resist prior to

pullout or rupture of the laminate. The specimen details are shown in Figure A 2.34. Spikes were embedded to a depth of 2 and 3 inches to determine the influence of depth on ultimate capacity.

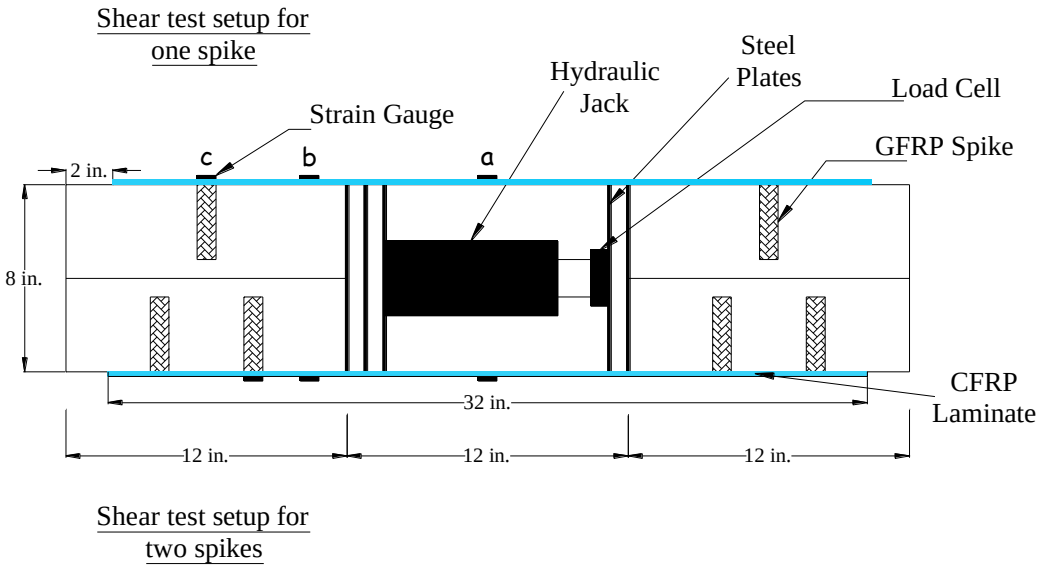

Figure A 2.34 Specimen Details (Eshwar et al., 2008)

Sudden debonding of the FRP from the concrete substrate was observed for some specimens, and gradual debonding was observed for the rest. The use of multiple spike anchors significantly increased the ultimate shear capacity of beams strengthened with FRP. On the other hand, the embedment length of the spikes had little influence on the ultimate capacity of the beams. For design purposes, Eshwar et al. (2008) suggest a spike anchor with a minimum diameter of 0.4 inches and a minimum embedment length of 2 inches when applying these anchors to a concrete substrate. Their work demonstrates that the performance of externally bonded FRP strengthening can be improved by 25% to 200% in terms of ultimate shear with the use of spike anchors.

Orton (2007) found that FRP anchors can allow the FRP sheet to reach its ultimate capacity depending on the number and size used. Figure A 2.35 shows details of the specimens used in this research. Orton (2007) found that carbon FRP anchors increased the strengthening capacity of an FRP sheet by 270%. Depending on the size of the anchor, each spike is able to engage a limited width of the FRP sheet; this is defined as the effective width. For instance, increasing the anchor width by 33% from ⅜ inch to ½ inch increased the effective width of fiber sheets from 2 inches to 3 inches.

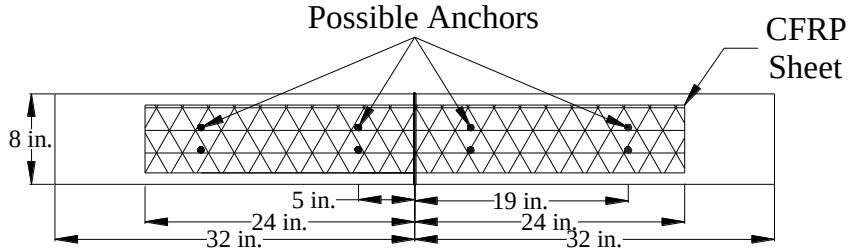

Tests with no height transition

Figure A 2.35 Specimen Details (Orton, 2007)

The anchor bend, described in Figure A 2.36, proved one of the most significant causes of loss of anchor strength. The bend in the anchor resulting from its insertion into the predrilled anchor hole causes a stress concentration that limits anchor capacity and causes it to fracture.

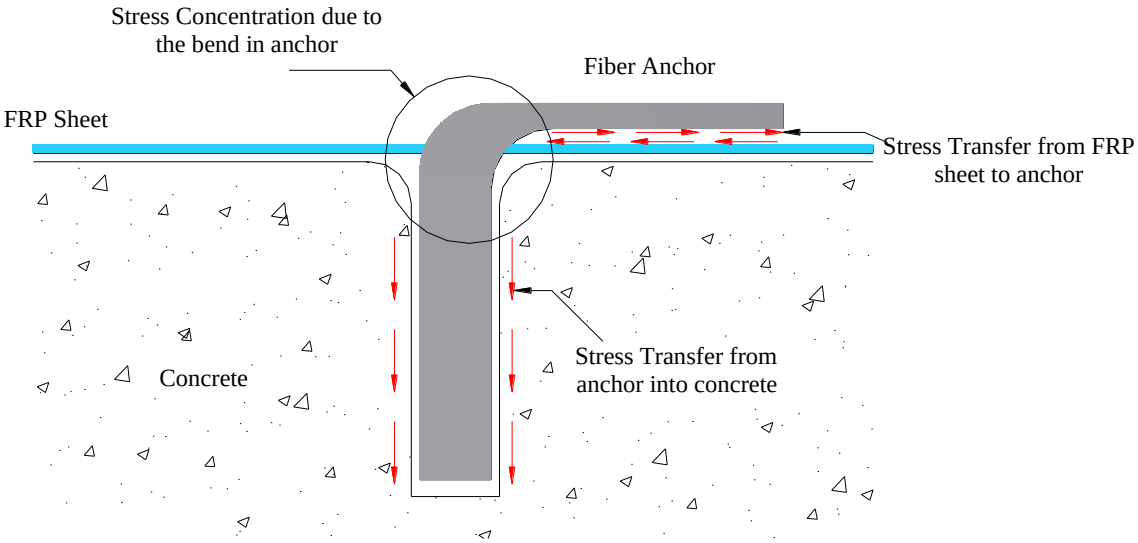

Figure A 2.36 Anchor Bend (Orton, 2007)

Orton's (2007) research also found that concrete surface preparation for the application of the FRP sheet is an insignificant factor because bonding strength between the FRP sheet and the concrete substrate is not critical in developing the ultimate capacity of the FRP sheets.

Niemitz (2008) studied FRP anchors made from FRP sheets by bundling fibers into a roll and splaying the upper end of the anchor so that fibers spread out from the sheet as shown in Figure A 2.37. He reported that such anchors are effective in fastening FRP sheets to RC elements, allowing them to develop their full strength. He also found that FRP anchors provided additional strength to the FRP composite, allowing the FRP sheet to develop its ultimate strength.

Figure A 2.37 FRP Anchor – (Niemitz, 2008)

In the testing conducted by Niemitz (2008), the use of FRP anchors increased the ultimate load capacity of all strengthened specimens. The specimen details and test setup are shown in Figure A 2.38. The ultimate strength of the composite laminate reached in multiple specimens as numerous FRP rupture failures were recorded. The FRP anchor failure modes appeared to be governed by the diameter of the FRP anchor splay, the diameter of the FRP anchor, the spacing

of the anchors, the bond length of the FRP sheet behind the anchor, delamination between the FRP anchor splay and the FRP composite sheet, and FRP anchor pullout.

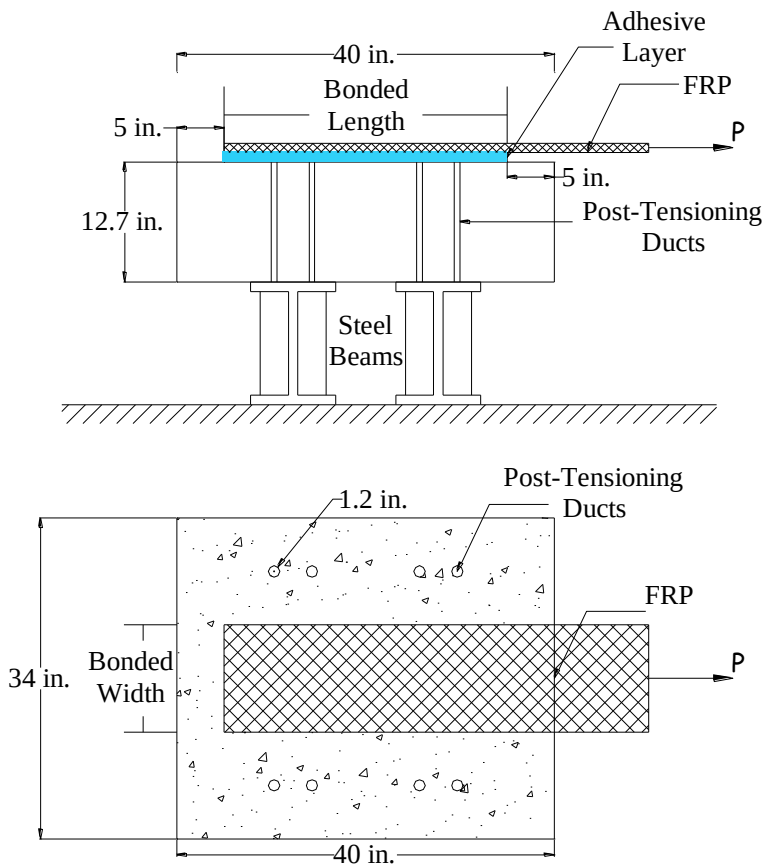

Figure A 2.38 Specimen Details (Niemitz, 2008)

Notably, this research found that the splay diameter determined the effective width of the FRP sheet engaged with an individual anchor. It also determines the diameter of the FRP anchor required to transfer the forces generated in the FRP sheet to the concrete substrate. Therefore, the FRP anchor diameter must be determined in accordance with the width of the FRP laminate to be engaged by each anchor splay. Equation A2-198 was derived and calibrated based on the results of this research:

$$D_A = \sqrt{\frac{4S_A f_{fu} t_p n_p}{35.8\pi}} \qquad \text{(A2-198)}$$

where D_A is the FRP anchor diameter, S_A is the anchor splay diameter, f_{fu} is the FRP ultimate tensile strength in ksi, t_p is the nominal thickness of the FRP sheet, and n_p is the number of FRP plies. All dimensions are measured in inches.

Use of this equation requires selection of an anchor splay diameter which will determine the effective width of the FRP sheet engaged by an individual anchor. This equation is valid only for FRP anchors ranging from ¼ inch to ¾ inch in diameter.

Horizontal FRP Strips

An additional horizontal FRP strip applied on top surface of the vertical FRP strips has also been used to provide end anchorage (e.g., Hutchinson and Rizkalla, 1999; Schnerch, 2001). This technique is very easy to install and no extra labor is required as compared to other anchorage systems.

Schnerch (2001) tested two series of large scale concrete beams strengthened in shear with FRP composites to examine the behavior of FRP shear strengthening on large scale specimens and to investigate parameters to be used for calculation of the shear capacity of all members, regardless of size. The first series of specimens was a full-sized PC I-girder, as shown in Figure A 2.39. The girder consisted of three cross-sectional geometries: a rectangular end block, an intermediate section, and an I-shaped midspan section.

The second series of specimens was an RC T-section which presented a larger web height than those observed in previous research studies, as shown in Figure A 2.40. Thus, these specimens were provided with a larger depth of external FRP shear reinforcement.

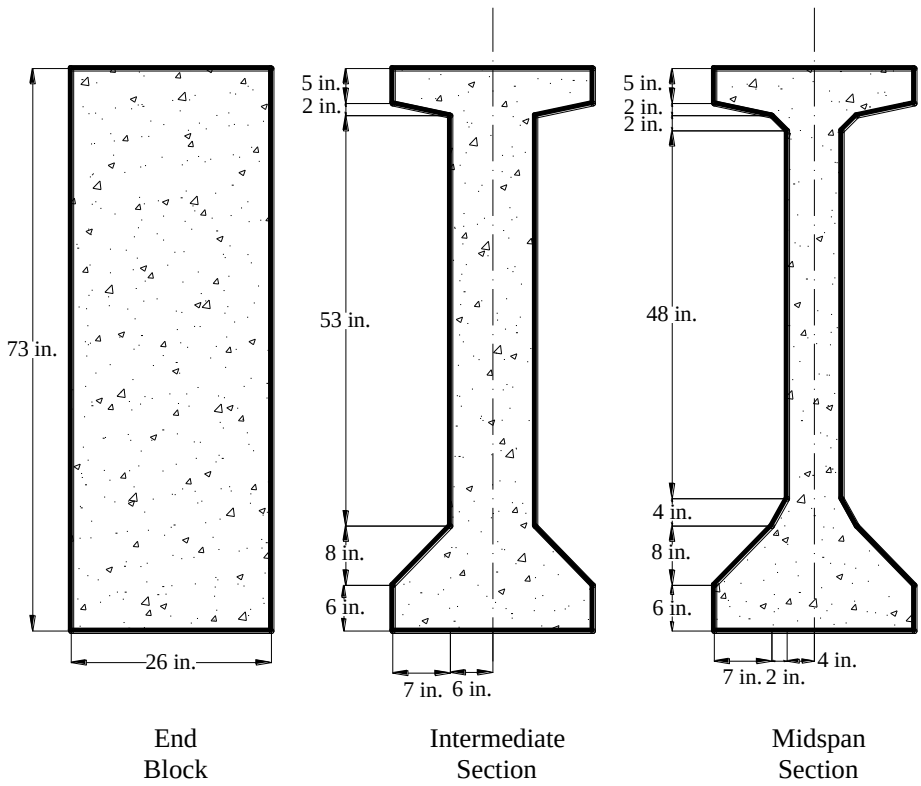

Figure A 2.39 Dimensions of I-Section Girder (Schnerch, 2001)

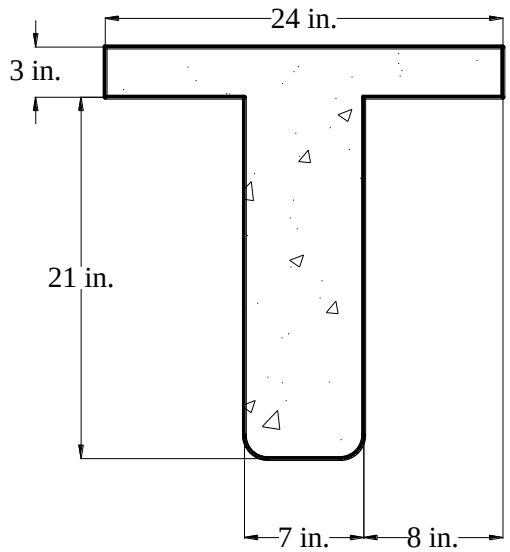

Figure A 2.40 Dimensions of T-Section Beam (Schnerch, 2001)

Schnerch (2001) used the horizontal FRP strips as an anchorage system. Two sheets were placed longitudinally on the prestressed girder beneath the vertical sheets at the top and bottom of the web, as shown in Figure A 2.41. These sheets made visual observation of shear cracking difficult. This anchorage system resulted in debonding, evidence of which was discovered at the interior corner of the bottom flange in sheets affected by the web-shear crack. However, this debonding was largely restrained due to the horizontal strips and did not prevent the FRP sheets from straining significantly. The peeling of the vertical sheets was somewhat restrained by the horizontal sheets because a portion of the horizontal sheet remained bonding to the concrete.

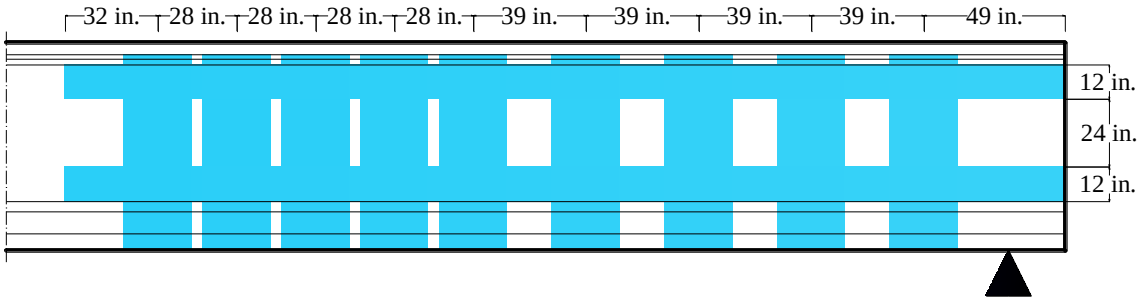

Figure A 2.41 Configuration of External FRP Sheets for the I-Section

In the RC T-beam, an additional horizontal sheet of fibers was placed across the top of the web to anchor the vertical sheets and limit the width of the crack at the top of the web, as shown in Figure A 2.42. This horizontal sheet did not improve the shear capacity of the section. As in the prestressed girders, the addition of this horizontal strip complicated the detection of cracks. Visual evidence of debonding was also difficult to observe, but at later stages of loading a large area of debonding was detected by tapping the sheets.

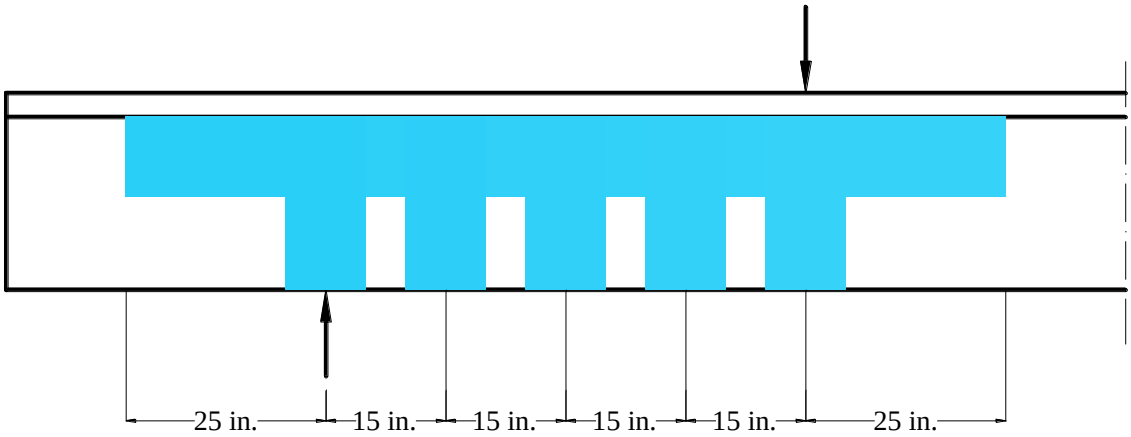

Figure A 2.42 Configuration of external FRP sheets for the T-section

Schnerch's (2001) work showed that this horizontal strip neither prevented debonding, nor did it increase the contribution of the FRP to the shear strength of the beam at failure as mechanical anchorages do. Meanwhile, the test results reported by Hutchinson and Rizkalla (1999) indicated that the shear contribution of FRP increased slightly by 16 % when horizontal strips of FRP were used as anchorage.

Mechanical Anchorages

Mechanical anchorage systems have been used most widely to prevent premature failure due to FRP debonding. Steel angles, steel or FRP composite plates, and anchor bolts are among the most common mechanical anchorage systems. By decreasing stress concentrations in the sheet ends with anchorage plates, or by increasing the bond strength near the ends, debonding failure can be prevented or delayed.

Anchorage of sheet ends with steel plates and bolts has been proved an effective way and can increase the shear capacity of RC members. In the case of U-wraps, Sato et al. (1997b) has shown that mechanical anchoring can increase shear capacities by approximately 20% over that of specimens with no end anchorage. He found, however, that steel mechanical anchors, although effective in the laboratory, were not practical for field application due to drawbacks such as stress concentrations and, in the case of bolting, discontinuity of the FRP at drilling locations.

Sato et al. (1997a) conducted a series of tests using various anchoring methods to develop a shear strengthening technique for beams and a method of estimating strengthening effectiveness. The test results showed that sufficient strength could be achieved only if the CFRP sheets were mechanically anchored. The four methods used to anchor the FRP sheets are shown in Figure A 2.43. Anchoring type 4 is closed strengthening and type 3 is semi-closed strengthening, which consists of lateral plates and bolts. The depth of bolts was 2 inches for type 2 and 5 inches for type 3. The strengthening effectiveness decreases from type 4 to type 1, although repair work becomes easier in this order. Sato et al. concluded that the shear strength of beams can be improved by transverse wrapping of FRP sheets if adequate anchoring is provided by steel plates and bolts and recommended the use of long anchor bolts that penetrate the full web. This anchorage system, however, creates stress concentrations where the anchors are placed.

Discontinuity of the FRP system due to steel bolts may be another disadvantage of this anchorage system.

Matthys (2000) conducted a project to strengthen four continuous RC beams in shear and flexure by supporting them with masonry columns. Bond/anchorage tests indicated a 44% increase in anchorage capacity with the use of steel bolted connections. Mechanical anchorage resulted in a less brittle failure mode due to the transition to an external tensioning system after debonding and increased displacements resulting from CFRP slip.

Schuman (2004a,b,c) conducted a comprehensive study of anchorage systems for shear strengthening of RC beams. He applied a mechanical anchorage system to increase the shear contribution of CFRP systems by embedding anchor rods into the cross-section with various bearing plates, such as the GFRP plate. Although various anchorage systems are possible, the four methods described by Schuman (2004c) can be summarized as (1) complete wrapping through the flange (called complete wrap), (2) FRP laminate extended into the flange, (3) bonded steel anchors with bearing plates (called two-side bonding), and (4) GFRP plate anchors. Figure A 2.44 illustrates two of the methods used by Schuman.

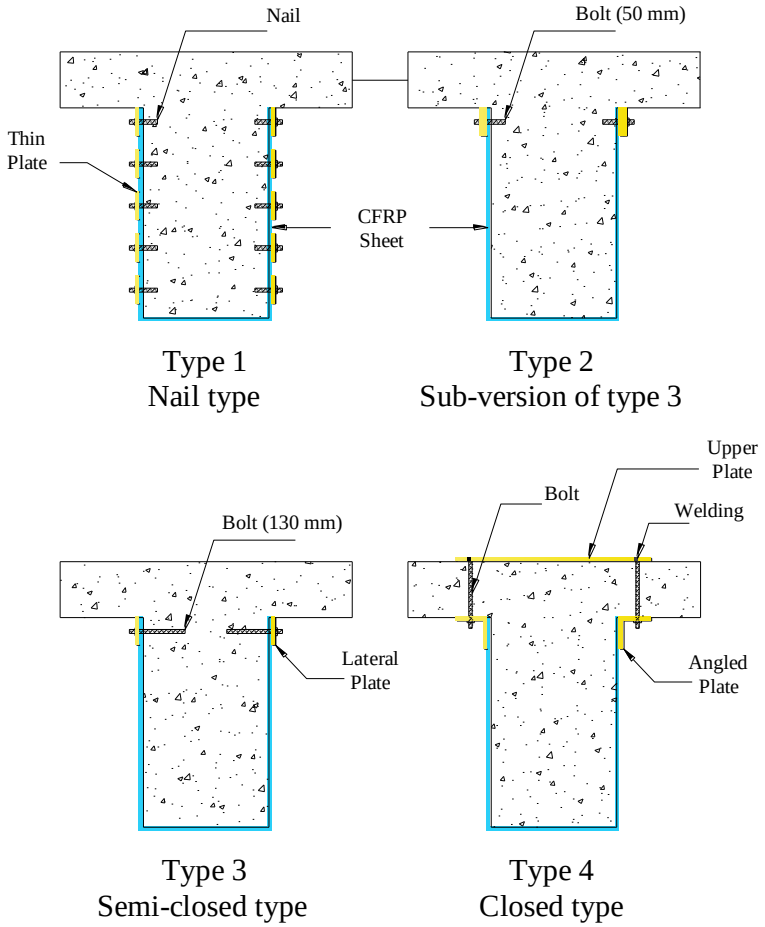

Figure A 2.43 Anchoring Methods of CFRP Sheets by Sato et al. (1997a)

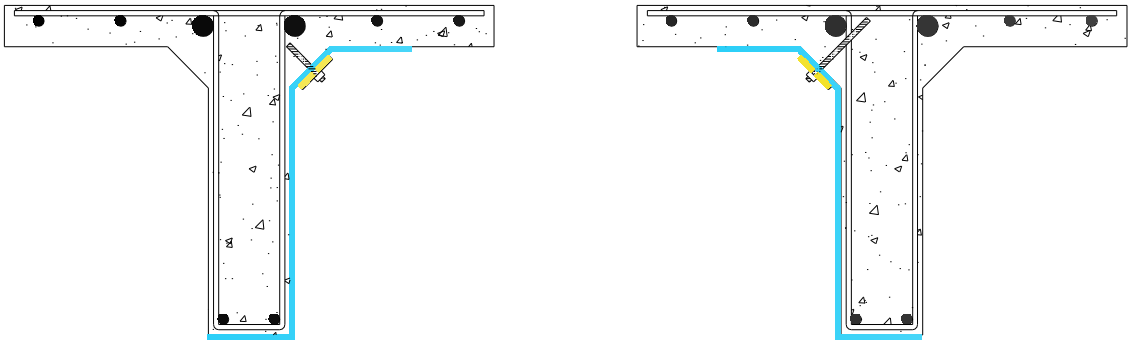

(a) Shallow embedment depth

(b) Deep embedment depth

Figure A 2.44 Specimen Details (Schuman, 2004a,b,c)

The three main purposes of mechanical anchorage are (1) to hold the FRP strip in place after debonding, (2) to provide an additional arch mechanism, and (3) to prevent horizontal shear stress concentration failure at the flange/web intersection. The anchors may provide sufficient capacity and confinement for the formation of an optimum arch. Schuman (2004a,b,c) concluded that if the anchorage is used to increase the capacity for the horizontal shear flow, a concern in flanged sections, then the anchors must be placed across the web/flange intersection. This placement provides additional resistance beyond concrete shear or friction.

Two conclusions of Schuman's (2004a,b,c) research are particularly important. First, the FRP composite alone provides the T-beam with little additional ultimate load and displacement capacity and creates a more brittle failure mode. Second, the use of properly embedded and sized anchors allows the vertical ties to remain intact during failure. These anchors then force a more ductile compression to ensure a shear/flexural failure mode.

Schuman (2004a,b,c) also concluded that short anchors led to an increase in load carrying and displacement capacity. In addition, they caused the CFRP reinforcement to be activated before the steel reinforcement yielded. The application of deeper anchors proved more beneficial effects because the CFRP reinforcement was activated earlier with the delay of yielding in the steel stirrups.

Mechanically fastened FRP laminates (Bank et al., 2004 and Rizzo et al., 2005) consist of precured FRP strips with high longitudinal bearing strength attached to a concrete surface using spaced steel fasteners such as nails or concrete, high-strength wedge anchors. The mechanically fastened FRP technique requires minimum surface preparation because the steel anchor provides the mechanism of load transfer from the composite laminate to the concrete surface.

The precured mechanically fastened FRP laminate was designed, produced, and commercialized as a result of an investigation performed by Lamanna (2002). The objective was the development of a high bearing strength FRP plate (Figure A 2.45). This plate consists of a glass and carbon hybrid pultruded strip embedded in a vinyl ester resin. It is 0.125 inches thick and 4 inches wide. Continuous glass fiber strand mats are used to provide transverse and bearing strength, while standard modulus carbon tows provide longitudinal strength and stiffness.

Figure A 2.45 Pultruded FRP Laminate

Analysis of the parameters influencing the performance of mechanically fastened FRP laminates showed that the use of anchors with a diameter of 3/8 inch or larger guaranteed the bearing failure of the laminate independently from the compressive strength of the concrete.

In addition, the use of wedge anchors (Figure A 2.46) driven into predrilled holes is preferable because the drilling operation can prevent major damage to the concrete around the holes. The use of gap fillers improves the strength and stiffness of the connection. By filling the hole with resin, rigid anchor motions are prevented (Figure A 2.47). The epoxy should be injected to fill the hole at least halfway and to be spread over a small area of concrete around the hole, the FRP composites, and the anchoring accessories, thus filling all gaps of any type.

Figure A 2.46 Concrete Wedge Anchor

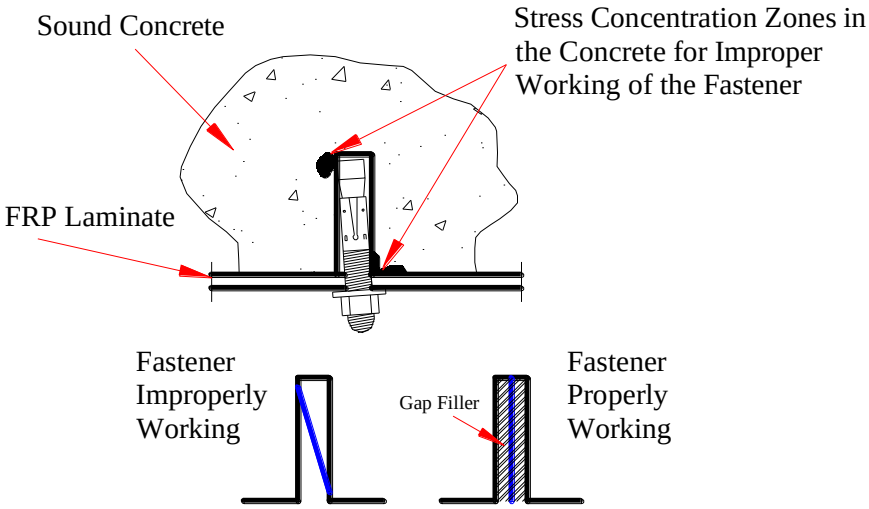

Figure A 2.47 Concrete Wedge Anchor Working Conditions (Rizzo et al., 2005)

The load at failure of the anchor in concrete depends significantly on the embedment length. The embedment length must be chosen to ensure that bearing failure in the FRP laminate occurs before anchor failure. The minimum distance between the edge of the plate and the center line of the first hole should be no less than 2.5 inches.

Rizzo et al. (2005) also recommended that the mechanically fastened FRP plate be improved by replacing the vinyl ester with epoxy resins and by reducing the width of the laminate, better exploiting its capacity.

Bank et al. (2004) focused their research on scaling and anchorage issues. The effect of additional strips, fastener spacing, termination distances, and the use of expansion anchors at the strip ends were considered. This research revealed a number of scaling related issues with the mechanically fastened FRP system. Specifically, multiple strips were not as effective as single strips, and a double row of fasteners at 2 inches on center was found to be less effective than a single row of fasteners at 3 inches on center. In addition, mechanical anchor bolts at the ends of the strip significantly improved performance and delayed the onset of end-delamination failures. The importance of a small termination distance from the support was confirmed in testing. Mechanical expansion anchors delayed the occurrence of end-delamination failures. Fatigue testing to 2 million cycles showed no degradation of the mechanically fastened FRP strengthening system when a single strip with end anchors was tested.

The experimental setup used by Bank et al. (2004) is shown in Figure **A 2.48** (b). This experimental setup placed the simply supported beam into four-point bending through the use of two load points equally spaced from the ends of the beams. The constant moment span was 60 inches, the shear spans were 138 inches each, and the total span length was 336 inches.

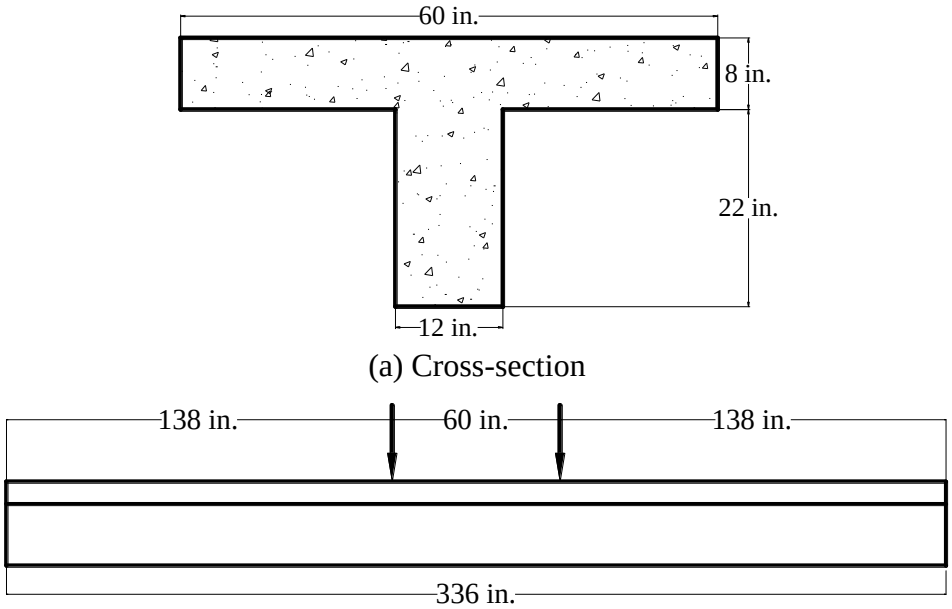

(a) Cross-section

(b) View of experimental setup

Figure A 2.48 Specimen Details (Bank et al., 2004)

El-Sayed et al. (2009) evaluated the performance of the mechanically fastened FRP and developed bearing-slip models to address the mechanically fastened FRP-to-concrete interfacial behavior. They also developed finite element models to address the interfacial behavior between the FRP strips and the concrete substrate for both the mechanically fastened FRP-to-concrete direct shear specimens as well as the mechanically fastened FRP-strengthened RC beams.

In this study, a series of 23 direct shear tests were conducted to address the interfacial behavior of a special hybrid GFRP/CFRP strip mechanically fastened to concrete. Both shot and screwed fasteners were used to install the FRP composites on concrete blocks. The tested specimens were placed in a conventional tensile loading frame. The assembly was designed so that there was direct shear at the FRP-to-concrete interface using the setup described by Bizindavyi and Neale (1999).

For the short fasteners, instant cracks were induced during the fastening process. These cracks weakened the surrounding concrete resulting in the eventual pull-out of the fasteners from the concrete. The use of screwed fasteners was found to be more efficient due to the superior fastener installation which did not damage either the concrete or the FRP strip. The predominant failure mode in the case of the shot fasteners was a bearing failure associated with fastener pullout. In the case of the screwed fasteners, the failure was bearing in the FRP strip. This mode of failure could be changed from FRP bearing to FRP rupture by increasing the number of fasteners.

A2.6 Field Applications

Although there are several field projects related to FRP strengthening systems, most of them are not documented with detailed information. In addition, the main purpose of most of these strengthening projects was for flexural rehabilitation. As a result, only six documented projects directly relate to FRP shear strengthening of concrete bridge girders are presented in this Section.

In-Service Evaluation of a Concrete Bridge FRP Strengthening System (New York State Department of Transportation)

A single span, reinforced concrete T-beam bridge in New York State was strengthened in flexure and shear with externally bonded FRP laminates in November 1999. The bridge was built in 1932 and carries five lanes of traffic without weight-limit restrictions. Strengthening was prompted by cross-sectional losses in the reinforcing bars as a result of corrosion. FRP U-wraps (330 mm width and 483 mm spacing) were applied for shear strengthening along with FRP laminates on the bottom surface of the beams used for flexural strengthening. Design of the FRP strengthening system was based on ACI 440 2R-02 (ACI 440, 2002) provisions.

CFRP Strengthening and Monitoring of the Gröndals Bridge in Sweden

The Gröndals Bridge in Sweden is a prestressed concrete box bridge approximately 400 m in length and a free span of 120 m. The bridge showed significant cracking in service condition. As a result, the bridge required strengthening in several sections in ultimate limit state and service limit state. While strengthening for the ultimate limit state used prestressed Dywidag-stays, the strengthening for the service limit state was carried out by the use of FRP laminates. CFRP laminate strips with a width of 120 mm were applied to the inside walls with steel plate anchorage system to increase the shear strength.

Langevin Bridge-Shear Strengthening Using CFRP Sheets

The Langevin Bridge is a six-span, four-cell, continuous box-girder bridge constructed in Calgary, Canada in 1972. In 2003, the bridge was structurally analyzed and some regions of the bridge were found to be deficient in shear under the current Alberta legal truck (CS-615) load. The analysis of this bridge was complicated by discontinuities in the prestressing tendons as well as irregularities in stirrup spacing. Discontinuities in the prestressing tendons were due to overlapping tendons in splice zones while the irregularities in stirrup spacing were the result of stirrups added during construction. To overcome these challenges, a shear-friction approach was adopted in the analysis of the shear capacity of the bridge. The two external webs were found to be deficient toward the ends of several of the spans. The internal webs were found to be deficient at the right end of span 2 where the internal prestressing tendons are horizontal and thus contribute nothing to the shear resistance. To correct these deficiencies, CFRP sheets were bonded to the inside face of the external webs and to both faces of the interior webs. An optimum fiber orientation of 63 degrees was found based on an assumed average crack angle of 60 degrees. The number of plies and sheet spacing varied depending on the level of shear strengthening required. The design was limited by a fiber strength of 29.7 ksi and material resistance factor of $\phi = 0.5$ as recommended by ISIS Manual #4 (ISIS, 2001). This method of strengthening was considered to be the most cost effective since the shear-friction approach used in the analysis is capable of precisely determining the extent of the regions deficient in shear. Thus, money is not wasted on strengthening regions where it is not needed. No follow-up investigations on the performance of this application have been reported at this time.

Use of Externally Bonded FRP Systems for Rehibilitation of Bridges in Western Canada

The John Hart Bridge in Prince George, British Columbia and the Maryland Bridge in Winnipeg, Manitoba are two bridges in western Canada that have been strengthened in shear with externally bonded CFRP. Since their construction in the early 1960s, truck loads have increased 3-fold and thus the bridges no longer met the ISIS code (ISIS, 2001) requirements for shear strength. The fact that both bridges are located along main arterial roadways and thus must remain accessible to traffic was a major factor in selecting the FRP strengthening method. The John Hart Bridge consists of seven simply supported spans with six I-shaped prestressed concrete AASHTO girders per span. All 42 girders were strengthened using a single diagonal layer of Replark™ CFRP (manufactured by Mitsubishi Corp. of Japan) sheets over a 4 m length at each end. After application, the CFRP sheets were covered with a 0.079 to 0.157 inch thick protective coating. This retrofit was completed within a six week period and is one of the largest strengthening applications of its kind. The Maryland Bridge consists of two sets of five continuous spans with seven I-shaped prestressed concrete AASHTO girders per span. Two of the girder ends were strengthened using the MBrace™ system manufactured by Master Builders Inc. (MBrace, 1998). The other two girder ends were strengthened using the Replark™ system manufactured by Mitsubishi. The strengthening configuration in both cases consisted of vertical CFRP strips wrapped under the bottom flange with a horizontal layer along the web at the top and bottom flanges to prevent debonding. The time required to complete the retrofit was only one week for each pair of girder ends. CFRP strengthening designs for both the John Hart Bridge and Maryland Bridge were based on experimental results on small-scale prestressed I-girders performed by Hutchinson and Rizkalla (1999).

Fatigue of Diagonally Cracked RC Girders Repaired with CFRP

The Willamette River Bridge located near Newberg, Oregon was found to have significant diagonal cracking during an inspection conducted by the Oregon Department of Transportation (ODOT) in late summer of 2001. This RC deck-girder (RCDG) bridge was designed and constructed in 1954 during the highway expansion of the late 1940s through early 1960s. Design provisions during the 1950s relied on a larger allowable concrete stress ($0.02f_c^{'}$ for unanchored and $0.03f_c^{'}$ for anchored longitudinal bars – AASHTO) than permitted by today's design specifications ($0.95\sqrt{f_c^{'}}$ (AASHTO, 2008) and $2\sqrt{f_c^{'}}$ (ACI 318, 2008)). In addition, anchorage requirements for flexural steel were less stringent in the 1950s. Thus, the RCDG bridges designed in the 1950s are under-designed by today's standards. These conditions coupled with increased service loads and volume as well as shrinkage and temperature effects contribute to significant diagonal tension cracking in these types of bridges. Repeated loading from traffic conditions may result in widening of these cracks. The Willamette River Bridge consists of three reinforced concrete approach spans of 55 feet at each end and four steel plate girder spans over water. The approach spans consist of one simple span with five RC deck-girders and two continuous spans with four RC deck girders. The bridge was constructed of concrete with a specified concrete compressive strength of 3300 psi and ASTM A305 reinforcing steel with nominal yield stress of 40 ksi. Diagonal cracking was observed in the concrete approach spans and was repaired using externally bonded CFRP in the fall of 2001. CFRP materials consisted of CF130 unidirectional high-strength carbon-fiber fabric produced by MBrace (MBrace, 1998). Surface preparation prior to application consisted of diamond grinding and epoxy injection of all cracks. Afterwards, 12 inch wide CFRP strips were applied vertically in a U-shape wrapping scheme with a center-to-center spacing of 14 inches. Three years after the CFRP retrofit, the bridge was reinspected and instrumented for monitoring under ambient traffic conditions. No additional cracking was observed during this reinspection. The south approach was selected for instrumentation with strain gages oriented vertically and placed at middepth of the CFRP. These strain gages were monitored for 32.6 days, from which the largest single strain range measured was 34 microstrain. The field investigations provided a baseline for developing equivalent laboratory tests. From the laboratory test results, it was observed that the service-level fatigue loading histories higher than those observed in the field, did not significantly change the ultimate shear capacity. It was further recommended by the researchers, that an open space between adjacent FRP strips be maintained in order to permit observation of diagonal cracking in the girders after repair.

Ebay Island Viaduct: Pilot Project to Comprehensive Carbon Fiber Rehabilitation

The Ebay Island Viaduct Bridge is a 2-1/4 mile long section of westbound Washington State Route 2 that crosses over environmentally sensitive wetlands near the outflow of the Snohomish River into Puget Sound near Everett, Washington. The bridge was built during the late 1960s. After less than thirty years of service, bridge condition inspectors noted that the bottoms of the existing precast concrete webs were manifesting a considerable degree of concrete spalling with accompanying primary steel reinforcement corrosion. In 1999, carbon fiber sheets were bonded to the deteriorated elements to compensate for steel reinforcement loss due to corrosion, which was primarily for flexural strengthening. In addition, carbon fiber sheets were applied with a U-wrap configuration to compensate for the shear capacity loss due to the cross-sectional loss of stirrups caused by corrosion. The carbon fiber repairs have been inspected annually since the

completion of the repair project. No debonding or other deterioration of the carbon fiber plies has been reported through spring 2007.

A2.7 Summary and Concluding Remarks

A comprehensive and exhaustive collection and review has been conducted for relevant practice, data, existing analytical models and specifications, and research findings from both foreign and domestic sources related to the strengthening of concrete girders in shear using FRP systems.

According to the survey results, it appears that there are not many state DOTs that use this technology to strengthen existing bridge girders. Lack of nationally accepted code/provisions was one of the main reasons stated. However, many analytical models and design guidelines exist around the world.

Since the behavior of reinforced concrete beams strengthened in shear with FRP is affected by many factors, the existing analytical models were developed based on different approaches to consider different factors. The approach based on the effective strain of FRP is the most widely accepted method among them. The advantage of this approach is that the design equations are generally much simpler than those developed based on other approaches such as facture mechanics and bond-slip behavior. However, as a disadvantage, the design equations based on effective strain concepts rely on a limited number of experimental results and lack explanation of the shear resistance mechanisms for the FRP shear strengthening system.

A3. DESIGN PARAMETERS OF FRP STRENGTHENING

A3.1 General

Parameters affecting the behavior of externally bonded FRP for shear strengthening must first be identified in order to develop appropriate design equations. In this section, the parameters were identified using the experimental results collected in the literature review of this NCHRP project. This task was organized into three successive parts: (1) synthesize the previous experimental work described previously in Section A2 in a matrix format; (2) develop an exhaustive and detailed database for data analysis; and (3) identify criteria and parameters that influence design. Both the synthesis matrix (qualitative) and the database (quantitative) were used as the basis for identifying the criteria that influence the design of FRP shear strengthening systems.

A3.2 Synthesis Matrix Describing Previous Experimental Work

The specific objective of this task was to synthesize the exhaustive review of published experimental work carried out in Section A2 on the shear strengthening of reinforced concrete beams with externally bonded FRP. This synthesis was presented in an original and convenient matrix form which allows for qualitative identification of the parameters that influence shear behavior and/or were not sufficiently covered in previous studies. Most of these parameters are related to various characteristics of the test specimens, such as geometry, test beam type, concrete type, steel and FRP materials used, and strengthening scheme.

The original matrix developed some years ago by Bousselham and Chaallal (2004) has been: (1) updated by including all published work on the subject, (2) extended by encompassing additional parameters needed for the present study, such as type of loading (fatigue versus static) and type of system (simply supported versus a continuously supported system where the maximum shear and the maximum moment occur simultaneously), and (3) enhanced by the addition of other strengthening systems such as near-surface mounted (NSM) reinforcing bars or prestressed straps. The resulting synthesis matrix is presented in Section 2 of the main body of this report.

As mentioned above, this synthesis provides a valuable source of information on parameters not sufficiently covered in the literature (and therefore not included in the database). In particular, it helps to identify areas which should be considered for further investigations and/or experimental work. The influence of fatigue, prestress, pre-cracking, and type of support (simple versus continuous) are examples of areas where the synthesis matrix can provide insight in the absence of sufficient data. These influences will be discussed in Section A3.4 which discusses the identification of criteria that influence design.

A3.3 Experimental Database

The specific objective of this task was to gather all relevant, detailed, and specific numerical data from tests carried out worldwide and related to FRP shear strengthening. These data have been scrutinized and compiled into a tabular format so that they can be conveniently used to identify the parameters that influence design of externally bonded FRP systems. These detailed data were also used to: (1) develop an experimental program to be carried out as part of this NCHRP project, and (2) develop and calibrate shear design provisions for girders retrofitted in shear with externally bonded FRP.

The resulting database is presented in Additional Material B to Appendix. It should be realized that the construction of this one-of-a-kind database required substantial effort from the project team, not only for its compilation, but also for the verification of the reported data. The data had to be consistent across all the tests covered. In this context, it must be noted that many tests were rejected because their results were irrelevant, incomplete, or dubious.

The data in the database includes the dimensions of the test specimens (beam span, shear span, width, depth, and flange), the mechanical properties of the concrete, the transverse and longitudinal steel reinforcement properties (mechanical, area, and spacing), the FRP composite properties (type, mechanical, thickness, and scheme), total shear resistance, the increase in shear due to the FRP composite, and the mode of failure.

The database has been thoroughly verified and checked and now encompasses more than 500 tests carried out worldwide.

A3.4 Identify Parameters that Influence Design of FRP-Strengthened Systems

A3.4.1 General and Scope

Parameters influencing shear resistance mechanisms and hence system design were identified from review of experimental data reported in the literature on shear strengthening with FRP. This identification was based on knowledge of the shear behavior of conventional RC structures as well as state of the art information regarding the behavior of RC elements retrofitted in shear with FRP.

The following parameters and criteria were successively subjected to qualitative and quantitative analysis: (a) the influence of mechanical and geometric properties of the FRP, (b) the effect of transverse steel reinforcement ratio, (c) the effect of longitudinal steel reinforcement ratio, (d) the effect of shear span-to-depth ratio or type of beams (slender versus deep), and (e) the scale factor or size effect of the specimens. Other parameters and criteria which were not sufficiently documented, but which have been found important for design, were also qualitatively examined in light of the few research studies available in the literature. These parameters included the effects of: (a) concrete strength, (b) fatigue, (c) anchorage details, (d) pre-cracking, and (e) prestress.

The effects of failure modes is implicitly considered since, as indicated subsequently, the analysis was performed by discretization of the various failure modes. The failure modes considered were: (a) shear failure due to debonding, including delamination, which clearly represents an important frequently observed failure mode and (b) shear failure due to rupture of the FRP. Other shear failure modes, generally due to diagonal concrete crushing, but occasionally to concrete splitting, were not considered in the analyses. Results for tests which failed in flexure were also disregarded.

A3.4.2 Influence of FRP Properties

A3.4.2.1 Background

The synthesis matrix (Section 2 of the main body of the report) indicates that CFRP sheets are used in almost all cases for testing the performance of RC beams strengthened in shear with FRP. Although more costly than the other types of FRPs, the choice of carbon fibers is probably motivated by the many performance advantages offered by these fibers compared to FRP with fibers such as glass or aramid. Because most available experimental data are related to CFRP, research in this area will probably continue to favor the use of CFRP composites for future investigations and projects.

Though alternative strengthening methods exist, externally bonded FRP systems are the most widely utilized systems for shear strengthening of RC test specimens (96% of reported tests using externally bonded FRP systems) and probably in practice as well. Flexural or shear strengthening with NSM FRP bars have shown great promise for anchoring capacity compared to externally bonded FRP strips (Rizkalla et al., 2003). However, despite their enhanced anchorage performance, very few studies have been performed using NSM techniques for shear strengthening, with the exception of the work by De Lorenzis and Nanni (2001a,b). The same is true of shear strengthening with FRP straps (Lees et al., 2002), which also offers some advantages, particularly with regards to FRP anchorage problems.

Externally bonded FRP strengthening systems exhibit a large variety of configurations: (i) complete wrap, U-wrap, or side bonding (bonded on the beam sides only), (ii) continuous or discontinuous (strips), and (iii) fibers oriented at angles of 90º or 45º. This variety has added to the complexity of the problem by increasing the already-large number of parameters to be studied. Consideration for the mechanical properties of the FRP has been the primary focus of the scientific community. Only recently have other parameters which play a major role in the shear resistance mechanism been identified and included in various studies. The influence of the transverse steel reinforcement and shear span-to-depth ratio are two examples of such parameters. It is important for future research to include these parameters that have not been well documented. It is believed that the parameters related to the properties of FRP are sufficiently documented at this stage. All the results have shown that FRP with fibers oriented at a 45º angle outperforms FRP with fibers oriented at a 90º angle in terms of shear resistance. Moreover, it has been established that, compared to discontinuous FRP systems, continuous FRP fabric provides the advantage of intercepting all diagonal cracks present. However, the use of continuous fabric inhibits examination of the state of the structure and its in-service changes over time, which is needed for maintenance and repair.

A3.4.2.2 Assessment

To assess the effectiveness of externally bonded FRP, The data are first analyzed in terms of the gain in shear resistance due to FRP, defined by $V_f / V_{control}$, as well as the FRP shear stress, expressed by V_f / bd_f. Here, V_u is the experimental shear capacity of a beam, V_f is the experimental shear contribution provided by FRP ($V_u - V_{u,control}$), b is the width of the beam web, and d_f is the effective depth of the beam. The gain was deliberately chosen because it is a pure experimental quantity, and thus is uncontaminated by effects that would be difficult to evaluate

(Bousselham and Chaallal, 2004). In addition to the gain due to FRP, the FRP shear stress expressed as V_f/bd_f, was also used for analysis.

Figure A 3.1 and Figure A 3.2 present the variations of shear force gain $V_f/V_{control}$ and FRP shear strength V_f/bd_f, respectively, in terms of a function of FRP rigidity expressed with respect to the compressive strength of concrete $\left(E_f\rho_f/f_c'^{2/3}\right)$ for all beams in the experimental database.

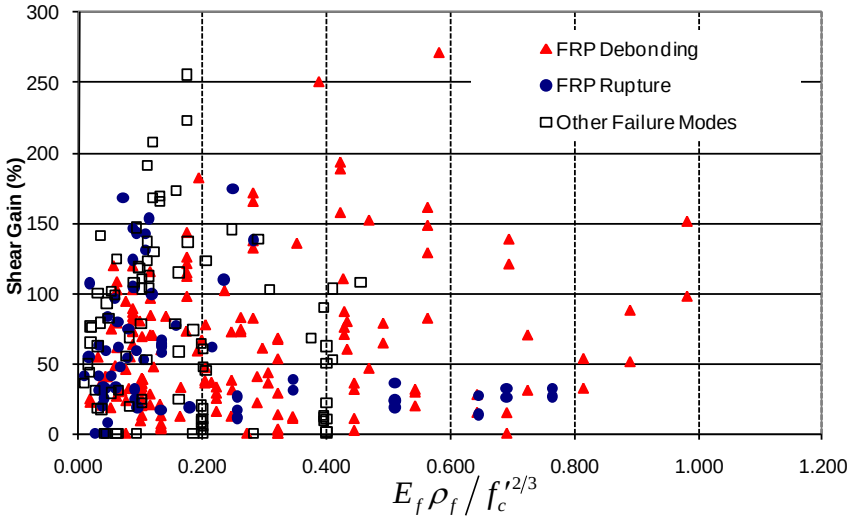

Figure A 3.1 Shear Force Gain (%), $V_f/V_{control}$ in Terms of $E_f\rho_f/f_c'^{2/3}$ (E_f : ksi and f_c' : psi)

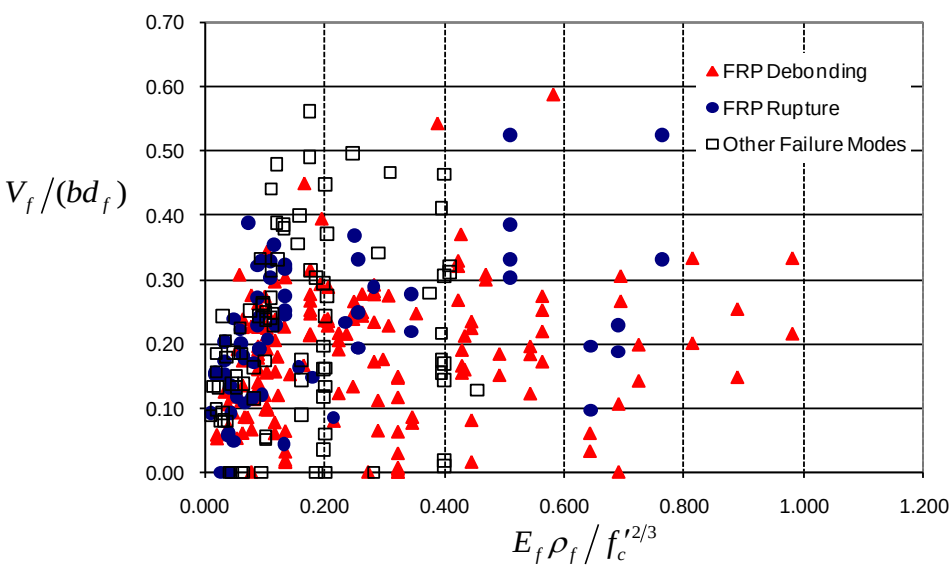

Figure A 3.2 FRP Shear Strength, V_f/bd_f in Terms of $E_f\rho_f/f_c'^{2/3}$ (E_f : ksi and f_c' : psi)

Figure A 3.1 and Figure A 3.2 show that the shear gain and FRP shear strength are generally smaller in beams which failed by FRP debonding when compared to beams which failed by FRP rupture and other failure modes. Furthermore, the shear gain and FRP shear strength tend to increase as the rigidity of FRP, $E_f \rho_f / f_c'^{2/3}$ increases. However, Figure A 3.1 and Figure A 3.2 exhibit a high degree of data point scatter, which appears to reflect the large number of parameters (some of them coupled) that can influence the shear gain to various extents.

Figure A 3.3 shows the variation of the effective FRP strain (ε_{fe}) with respect to a function of FRP rigidity relative to the compressive strength of concrete $\left(E_f \rho_f / f_c'^{2/3}\right)$ for all beams in the experimental database. The effective FRP strain (ε_{fe}) was determined based on the traditional truss analogy using the following expression:

$$\varepsilon_{fe} = V_f \Big/ \left(b_w d_f E_f \rho_f \left(1+\cot\beta\right)\sin\beta\right) \qquad \text{(A3-1)}$$

where: b_w = the width of the web

d_f = the effective height of the beam section

β = the angle of inclination of the FRP with respect to the longitudinal axis of the beam.

The term $\left(E_f \rho_f / f_c'^{2/3}\right)$ was used because it simultaneously includes the effects of: (1) the amount of FRP expressed in terms of the FRP ratio ($\rho_f = A_f / (b_w s_f)$), (2) the fiber type expressed in terms of the modulus of elasticity of FRP (E_f), and (3) the compressive strength of concrete (f_c') which is a major factor influencing the bond performance of FRP strengthening. The term $\left(E_f \rho_f / f_c'^{2/3}\right)$ is of prime importance for evaluating the contribution of FRP to shear resistance, as established in the European design guidelines (*fib*-TG 9.3, 2001). This term includes all the factors affecting the behavior of the materials at the FRP-concrete interface. The same term is used in many design methods to calculate the contribution of FRP to shear resistance (ACI 440.2R-08, 2008; Chen and Teng, 2001; Khalifa and Nanni, 2000; and Deniaud and Cheng, 2004).

From Figure A 3.3, it can be observed that the effective FRP strain decreases as FRP stiffness increases. Figure A 3.3 also clearly shows that the effective strains in beams failing by FRP debonding are likely to be smaller than those in beams failing by FRP rupture or other failure modes. This observation confirms results reported by other researchers (Bousselham and Chaallal, 2004; Khalifa and Nanni, 2000; and Triantafillou and Antonopoulos 2000).

Figure A 3.4 shows the variation in the ratio of the effective FRP strain to the ultimate FRP strain ($R = \varepsilon_{fe} / \varepsilon_{fu}$) with respect to $E_f \rho_f / f_c'^{2/3}$. This ratio is an indicator of how effectively an FRP strengthening system is used. Figure A 3.4 also shows the same trends as shown in Figure A 3.3. In all cases, the effective strains are shown to be only a modest fraction of the ultimate FRP strain. Although Figure A 3.3 and Figure A 3.4 show better relationship between the parameters as compared to Figure A 3.1 and Figure A 3.2, they still exhibit a high degree of scatter.

Therefore, it is necessary to refine the analysis further which will be presented in the later sections.

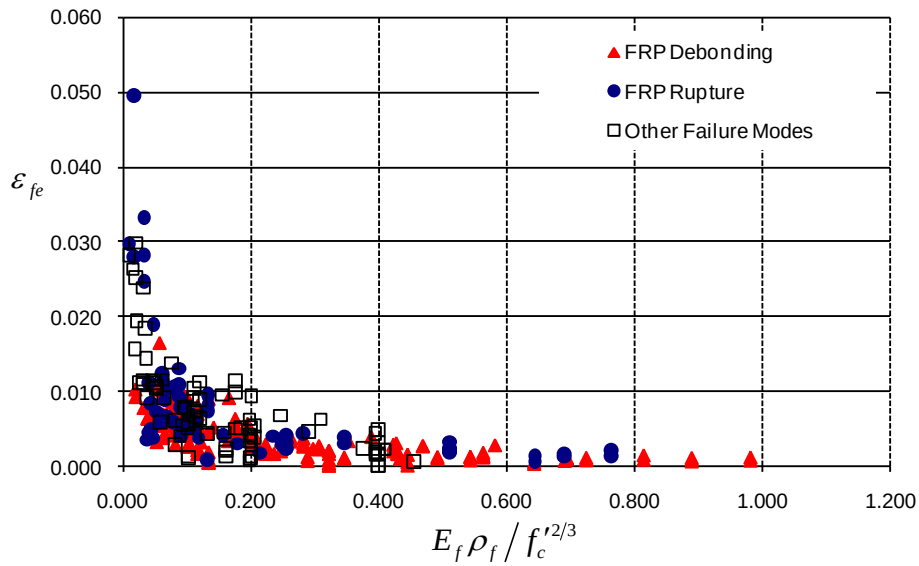

Figure A 3.3 Effective Strain of FRP in Terms of $E_f \rho_f / f_c'^{2/3}$ (E_f : ksi and f_c' : psi)

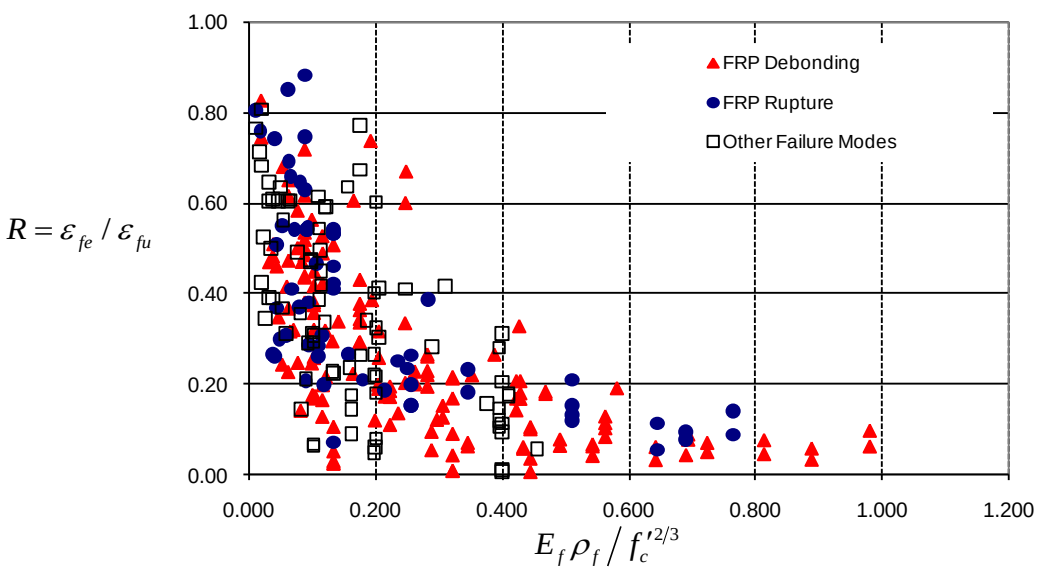

Figure A 3.4 Ratio of Effective FRP Strain to Ultimate FRP Strain, $R = \varepsilon_{fe} / \varepsilon_{fu}$, in terms of $E_f \rho_f / f_c'^{2/3}$ (E_f : ksi and f_c' : psi)

A3.4.3 Effect of Internal Transverse Steel Reinforcement

A3.4.3.1 Background

Many recent studies have shown that the contribution of externally bonded FRP to shear resistance is less in beams containing internal transverse steel than in the same retrofitted beams

without internal transverse steel (Li et al., 2002; Pellegrino and Modena, 2002; Chaallal et al., 2002; Bousselham and Chaallal, 2004; and Czaderski, 2002). This interaction was clearly observed in a recent study by Bousselham and Chaallal (2006a, 2006b), not only in terms of resistance, but also in terms of strains. The study also showed that for a given load, the transverse steel reinforcement was less stressed in FRP-retrofitted beams than in beams that were not retrofitted. However, the resistance mechanisms involved have yet to be explained. Therefore, obtaining a better understanding of these mechanisms through additional experimental and theoretical investigations may well be warranted, because such studies should result in more rational and well-founded models for the shear resistance of RC beams retrofitted with FRP.

A3.4.3.2 Assessment

The influence of transverse steel reinforcement on the contribution of FRP to shear resistance has been documented by many research studies (Bousselham and Chaallal, 2004; Pellegrino and Modena, 2002; Chaallal et al., 2002; Czaderski, 2002; and Li et al., 2002). More recently, this phenomenon has been further demonstrated through monitoring of the variation of strains in FRP and in transverse steel under increasing load (Bousselham and Chaallal, 2006a; 2006b). This influence is confirmed, at a much larger scale, in the present study which encompasses the data from all research studies reported in the literature.

Figures A 3.5 through A 3.8 present the shear gain, FRP shear strength, effective strain, and ratio of the effective strain to the ultimate strains in terms of $E_f \rho_f / f_c'^{2/3}$. In the figures, the data are grouped into three different series. Series 1 represents the beams without transverse steel reinforcement (ρ_v= 0). Series 2 represents the beams with transverse steel reinforcement ratio less than or equal to 0.006 ($\rho_v \leq$ 0.006). Series 3 represents the beams with transverse steel reinforcement ratio between 0.006 and 0.0012 (0.006<$\rho_v \leq$ 0.0012). It can be clearly observed from the figures that the effectiveness of FRP shear strengthening decreases as the transverse reinforcement ratio increases. In other words, the shear gain, FRP shear strength, effective strain, and ratio of the effective strain to the ultimate strains of the beams without transverse reinforcement are greater than those of the beams with transverse reinforcement.

In fact, it is necessary to analyze in more detail the data presented in Figures A 3.5 through A 3.8 in terms of failure modes, which where found to be a major parameter influencing the effectiveness of FRP strengthening systems as discussed in Section A3.4.2.

Figure A 3.9 and Figure A 3.10 present the ratio of the effective strain to the ultimate strain of FRP of the beams failed by FRP debonding and FRP rupture, respectively. In these figures, Series 1 represents the beams without transverse steel reinforcement (ρ_v= 0). Series 2 represents the beams with transverse steel reinforcement ratio less than or equal to 0.006 ($\rho_v \leq$ 0.006). Series 3 represents the beams with transverse steel reinforcement ratio between 0.006 and 0.0012 (0.006<$\rho_v \leq$ 0.0012). The other failure modes were not considered in this analysis since failure modes other than FRP debonding and FRP rupture (i.e. concrete crushing) should be avoided when designing FRP shear strengthening systems because the effectiveness of the system cannot be fully achieved with such failure modes.

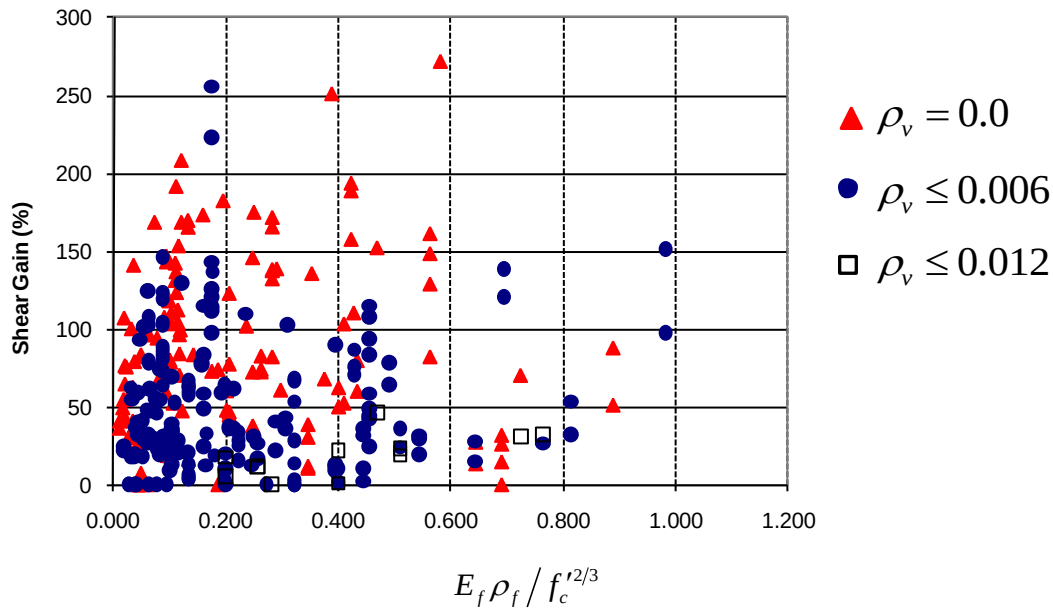

Figure A 3.5 Shear Force Gain, $V_f / V_{control}$ in Terms of $E_f \rho_f / f_c'^{2/3}$ (E_f : ksi and f_c' : psi)

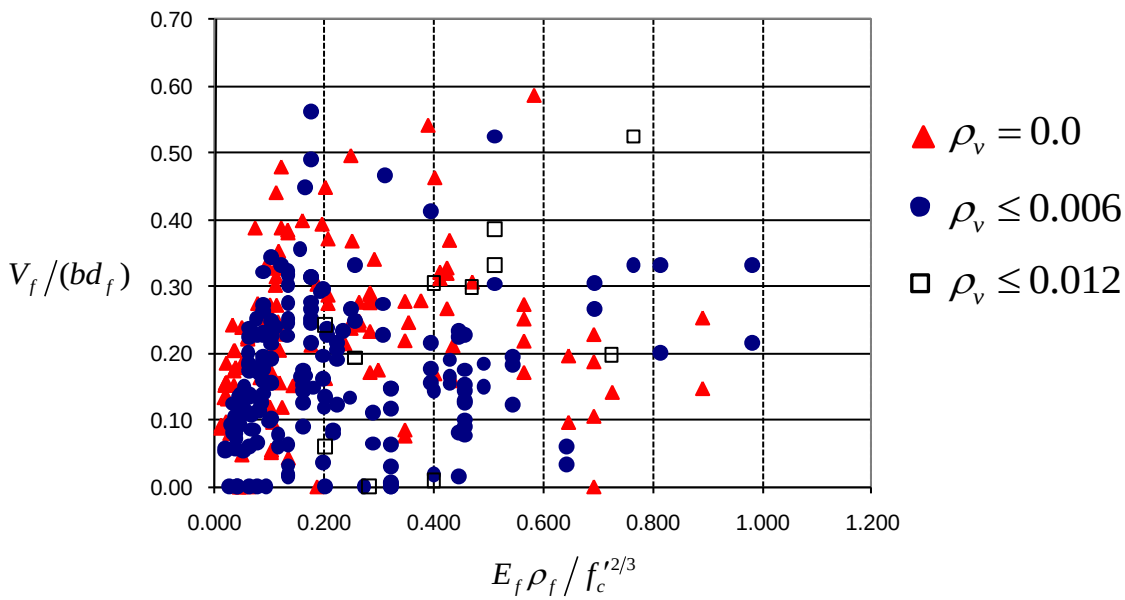

Figure A 3.6 FRP Shear Strength, V_f / bd_f in Terms of $E_f \rho_f / f_c'^{2/3}$ (E_f : ksi and f_c' : psi)

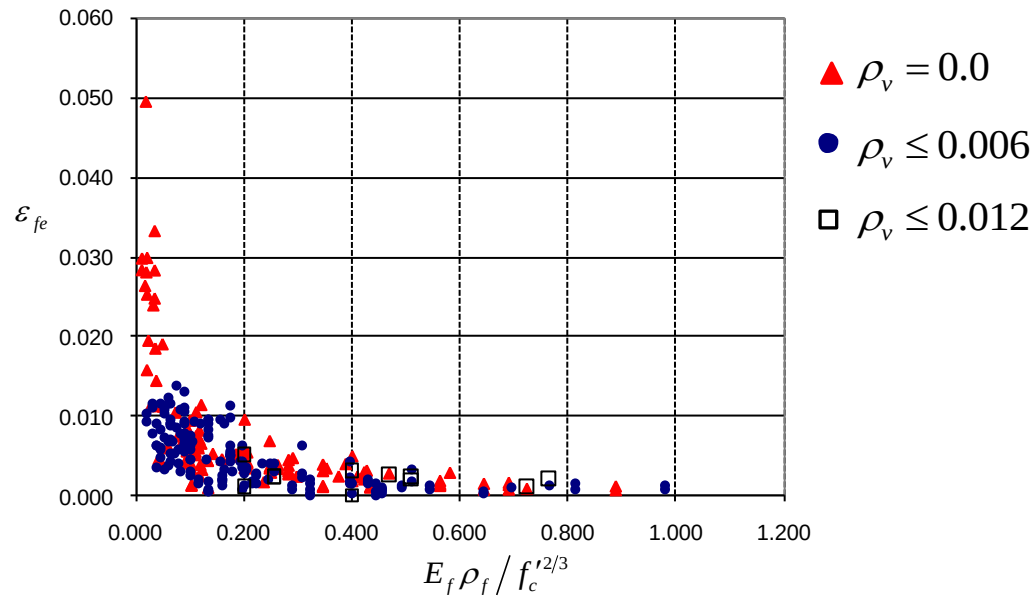

Figure A 3.7 Effective Strain of FRP in Terms of $E_f \rho_f / f_c'^{2/3}$ (E_f : ksi and f_c' : psi)

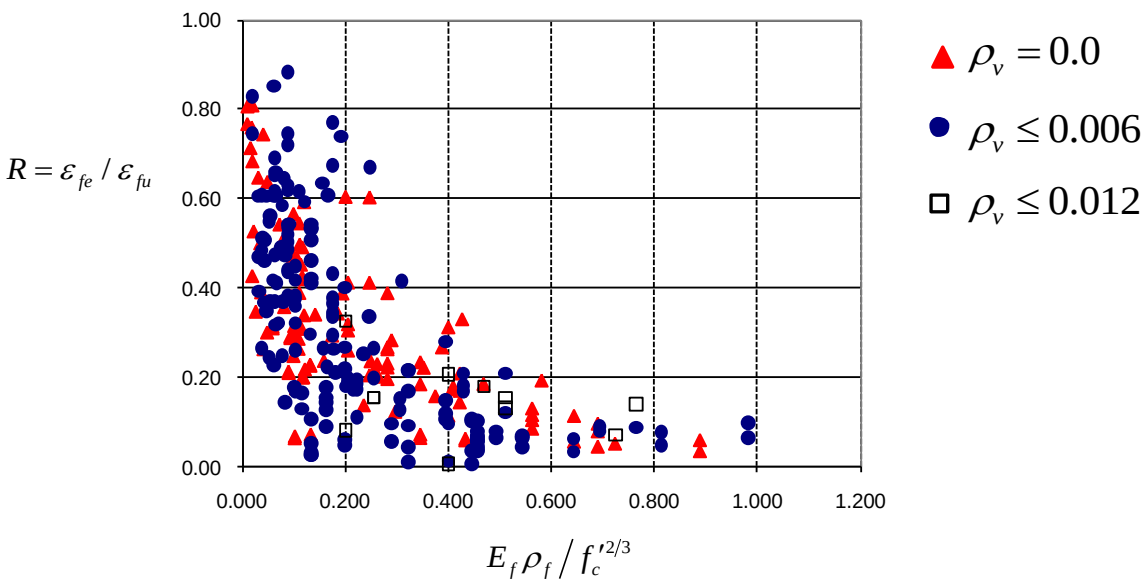

Figure A 3.8 Ratio of Effective FRP Strain to Ultimate FRP Strain, $R = \varepsilon_{fe} / \varepsilon_{fu}$, in terms of $E_f \rho_f / f_c'^{2/3}$ (E_f : ksi and f_c' : psi)

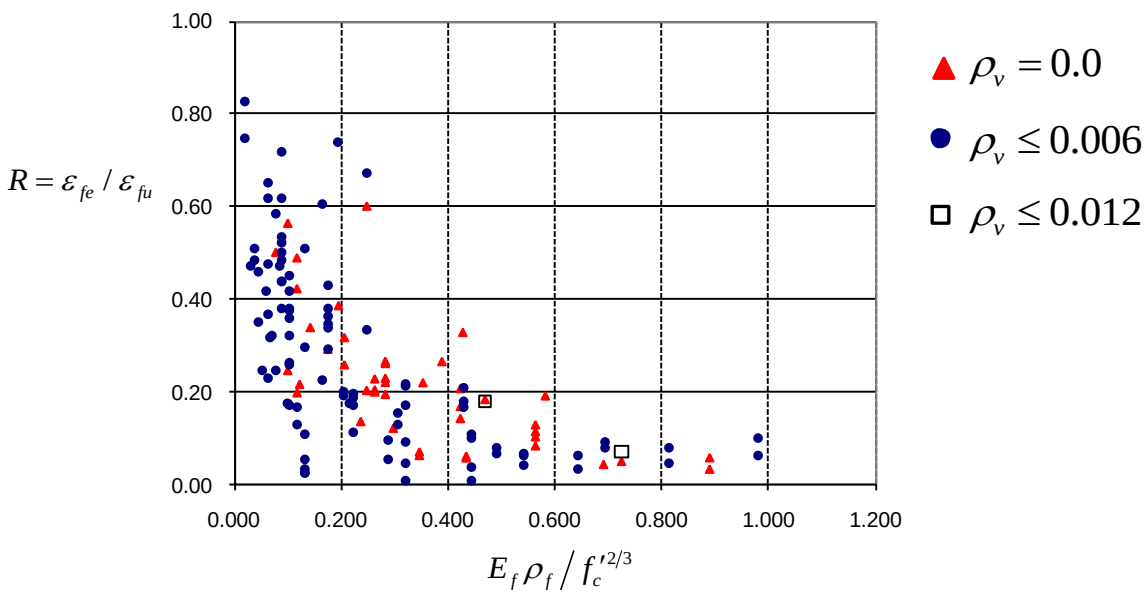

Figure A 3.9 Ratio of Effective FRP Strain to Ultimate FRP Strain, $R = \varepsilon_{fe} / \varepsilon_{fu}$, in terms of $E_f \rho_f / f_c'^{2/3}$ (E_f : ksi and f_c' : psi) - Beams Failed by FRP Debonding

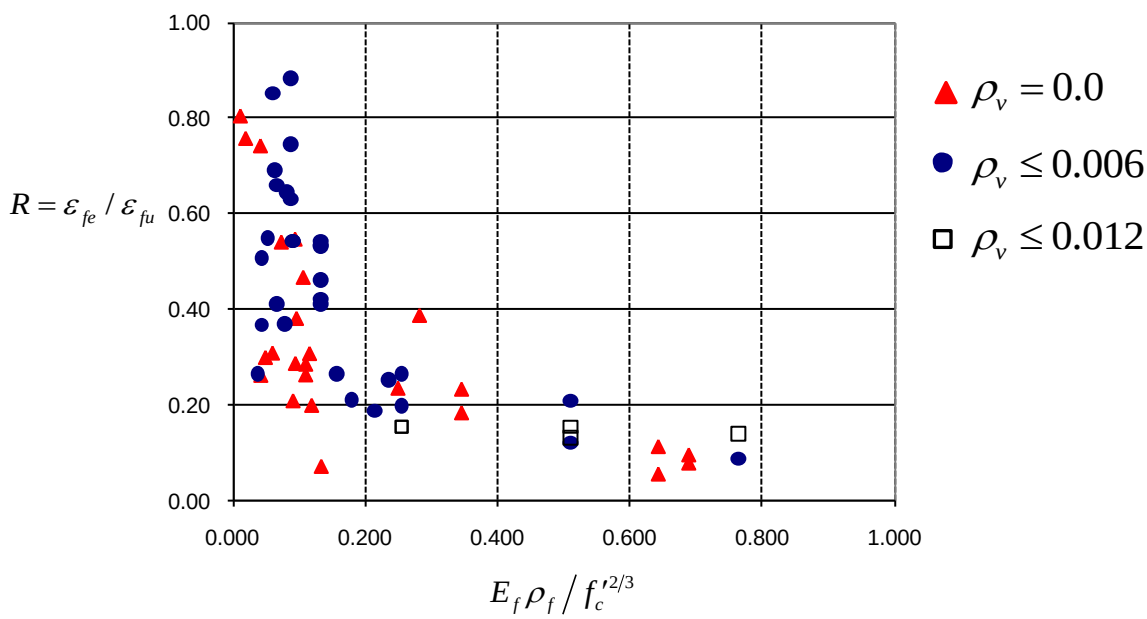

Figure A 3.10 Ratio of Effective FRP Strain to Ultimate FRP Strain, $R = \varepsilon_{fe} / \varepsilon_{fu}$, in terms of $E_f \rho_f / f_c'^{2/3}$ (E_f : ksi and f_c' : psi) - Beams Failed by FRP Rupture

As shown in Figure A 3.9, the ratio of the effective strain to the ultimate FRP strain of the beams without transverse steel reinforcement is generally greater than those beams with transverse steel reinforcement when the beams failed by FRP debonding. This trend, however, is not observed in Figure A 3.10, which presents the results of the beams failed by FRP rupture. Thus, it can be said

that the effect of transverse reinforcement is significant when beams fail by FRP debonding while it is not when beams fail by FRP rupture.

The influence of transverse steel reinforcement on the contribution of FRP to shear resistance is now shown by experimental evidence. However, the resistance mechanisms involved remain to be explained. Therefore, obtaining a better understanding of these mechanisms through additional experimental and theoretical investigations may well be warranted, as this would result in a more rational and well-founded model of the shear resistance of RC beams retrofitted with FRP.

A3.4.4 Scale Effect

A3.4.4.1 Background

The majority of the available experimental data are for rectangular beams. However, a T-section is more representative of the shape used in practical applications. The synthesis matrix reveals that most tests were performed on small-scale specimens rather than full-scale bridge girders. However, numerous studies on the influence of the depth of an RC beam on its shear behavior have shown that the shear resistance decreases as the beam size increases for beams without shear reinforcement (ACI-ASCE Committee 445, 1998). This phenomenon of decreasing shear strength with increasing beam depth, referred to as the *scale effect*, is considered one of the major parameters affecting shear. For this reason, most concrete standards, except those in North America, have introduced correction factors for size in their formulae for the contribution of the concrete to shear resistance. Therefore, it is also desirable to determine if this scale effect also influences RC beams strengthened in shear with externally bonded FRP. The preliminary investigation performed by Bousselham and Chaallal (2004) showed such an effect. Indeed, analysis of the test results reported in the literature on shear strengthening showed a tendency for a decrease in the gain of shear resistance due to FRP as the height of the specimen increased (Bousselham and Chaallal, 2004; Leung et al., 2007). The predictive models for the contribution of FRP to shear strength proposed in the literature are largely based on test results which were mostly obtained from small-scale testing. Therefore, the scale effect is likely to have a direct impact on the reliability of these models which may yield rather optimistic strength predictions. As a consequence, a more in-depth investigation of this major shear parameter, with stringent control of all other interacting parameters, was desirable.

A3.4.4.2 Assessment

Figure A 3.11 and Figure A 3.12 present shear gain due to FRP in terms of $E_f \rho_f / f_c'^{2/3}$ for the beams failed by FRP debonding and FRP rupture, respectively. In these figures, the data are grouped into three different series. Series 1 represents the beams with a depth of 10 inches or less (d ≤ 10 in.). Series 2 represents the beams with a depth between 10 inches and 20 inches (10 in. < d ≤ 20 in.). Series 3 represents the beams with a depth between 20 inches and 33 inches (20 in. < d ≤ 33 in.).

As shown in Figure A 3.11, the shear gain due to FRP is greater in the beams with a depth of 10 inches or less than the beams with a depth greater than 10 inches for beams failing by FRP deboning. However, this trend is not observed in the case of the beams failed by FRP rupture as shown in Figure A 3.12. This observation implies that the FRP-concrete interface bond behavior

is significantly affected by the beam depth. Thus, this phenomenon should be carefully investigated. The similar observation can be made in Figure A 3.13 and Figure A 3.14, which present the shear strength of FRP in terms of $E_f \rho_f / f_c'^{2/3}$ for the beams failed by FRP debonding and FRP rupture, respectively.

However, the trends shown in the previous figures are not observed in Figure A 3.15 and Figure A 3.16, which present the effective strain of FRP in terms of $E_f \rho_f / f_c'^{2/3}$, and Figure A 3.17 and Figure A 3.18, which present the ratio of the effective strain of FRP to the ultimate strain of FRP in terms of $E_f \rho_f / f_c'^{2/3}$. This is because the other test parameters are coupled with the effects of beam depth. Thus, other graphs were generated by introducing a function of the total shear reinforcement ratio, the concrete strength, and the depth of beams ($\left[\left(E_f \rho_f + E_s \rho_v\right) / \sqrt{f_c'}\right]\sqrt{d}$) in order to see the coupled effects of several parameters affecting the shear behavior of FRP strengthened beams revealed in the previous discussions. In fact, the function includes the amount of FRP shear reinforcement, the amount of transverse steel reinforcement (stirrups), the concrete strength, and the beam depth.

Using the function, $\left[\left(E_f \rho_f + E_s \rho_v\right) / \sqrt{f_c'}\right]\sqrt{d}$, Figures A 3.19 through A 3.22 were plotted, in which the same trend can be observed as in Figures A 3.15 through A 3.18. In other words, the effectiveness of FRP shear strengthening decreases as the value of $\left[\left(E_f \rho_f + E_s \rho_v\right) / \sqrt{f_c'}\right]\sqrt{d}$ increases, which confirms all the previous discussions made in the previous sections in the case of FRP debonding failure. To increase the value of $\left[\left(E_f \rho_f + E_s \rho_v\right) / \sqrt{f_c'}\right]\sqrt{d}$, either the shear reinforcement (FRP and/or stirrups) or the depth of beams should increase. This confirms the previous discussion about the effects of FRP properties, transverse reinforcement, and the depth of beams. Therefore, it is recommended using such function which accounts for the coupled effects of various parameters when developing design equations for beams with FRP debonding failure.

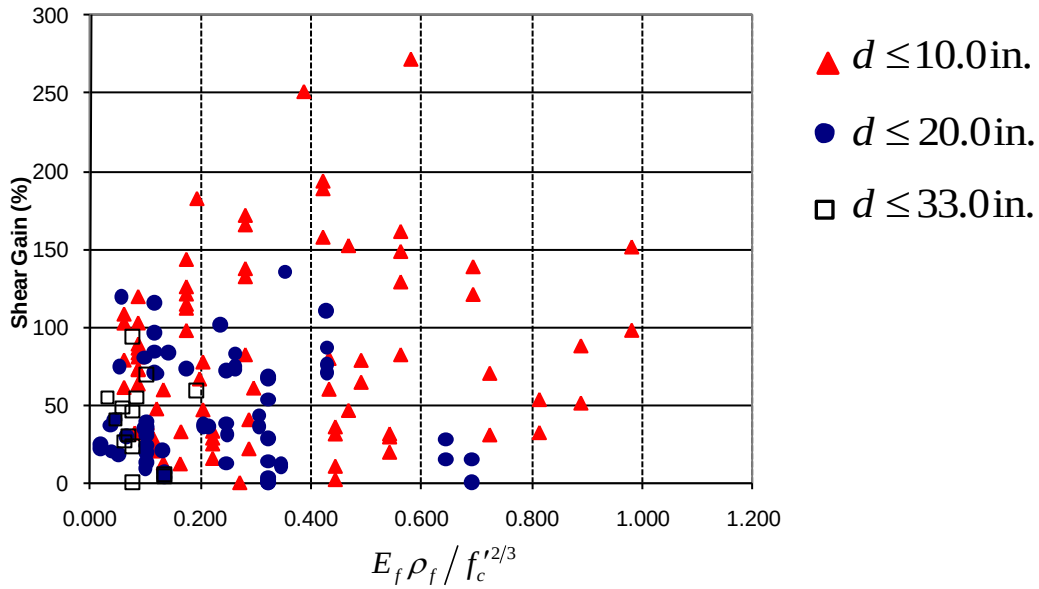

Figure A 3.11 Shear Gain (%) Due to FRP in terms of $E_f \rho_f / f_c'^{2/3}$ (E_f : ksi and f_c' : psi) - Beams Failed by FRP Debonding

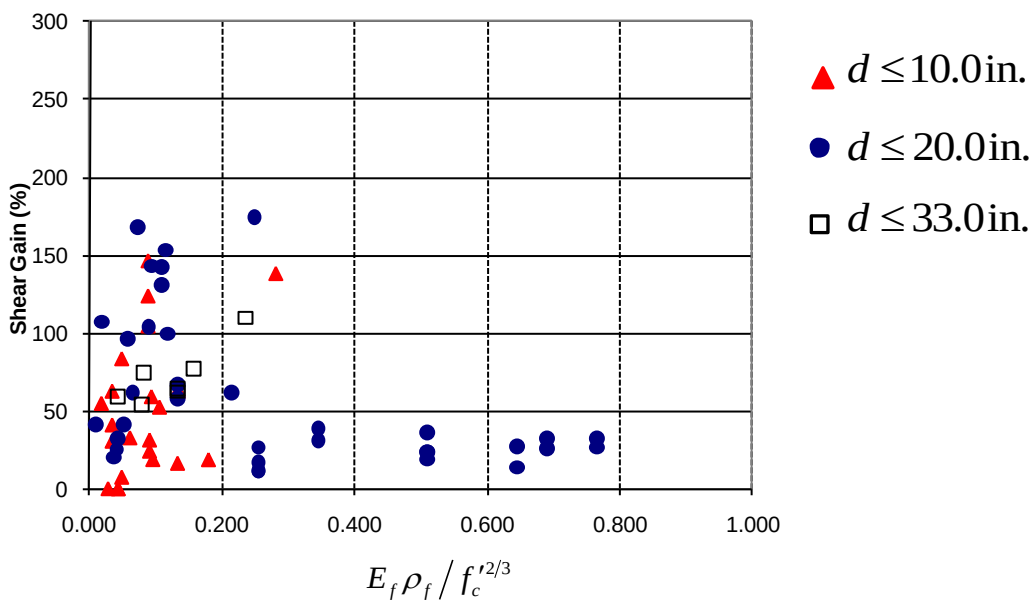

Figure A 3.12 Shear Gain (%) Due to FRP in terms of $E_f \rho_f / f_c'^{2/3}$ (E_f : ksi and f_c' : psi) - Beams Failed by FRP Rupture

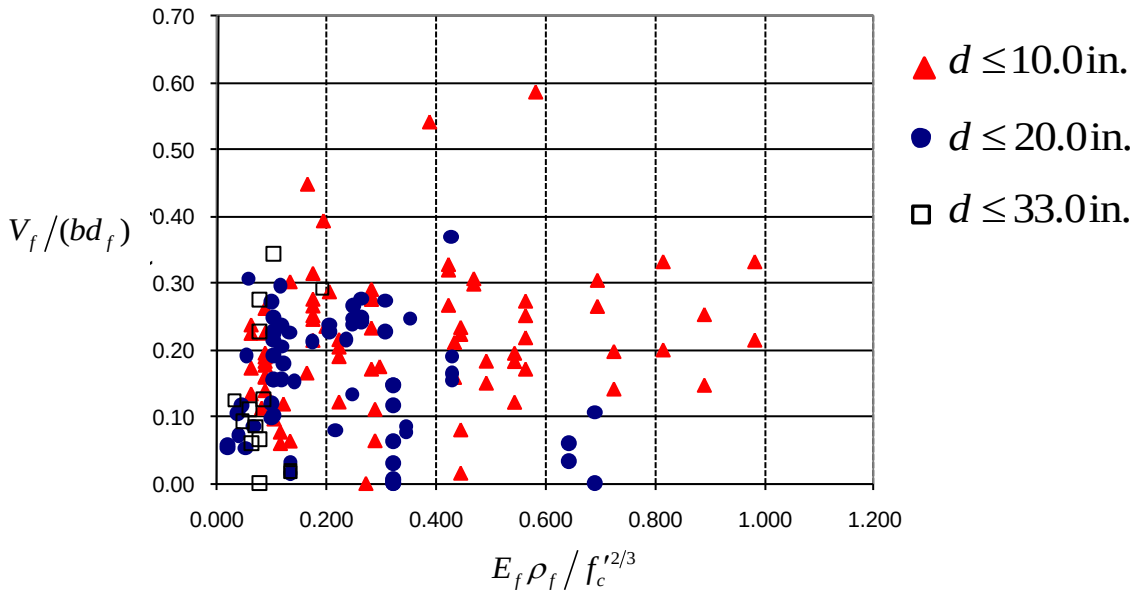

Figure A 3.13 FRP Shear Strength, V_f/bd_f in Terms of $E_f\rho_f/f_c'^{2/3}$ (E_f : ksi and f_c' : psi) - Beams Failed by FRP Debonding

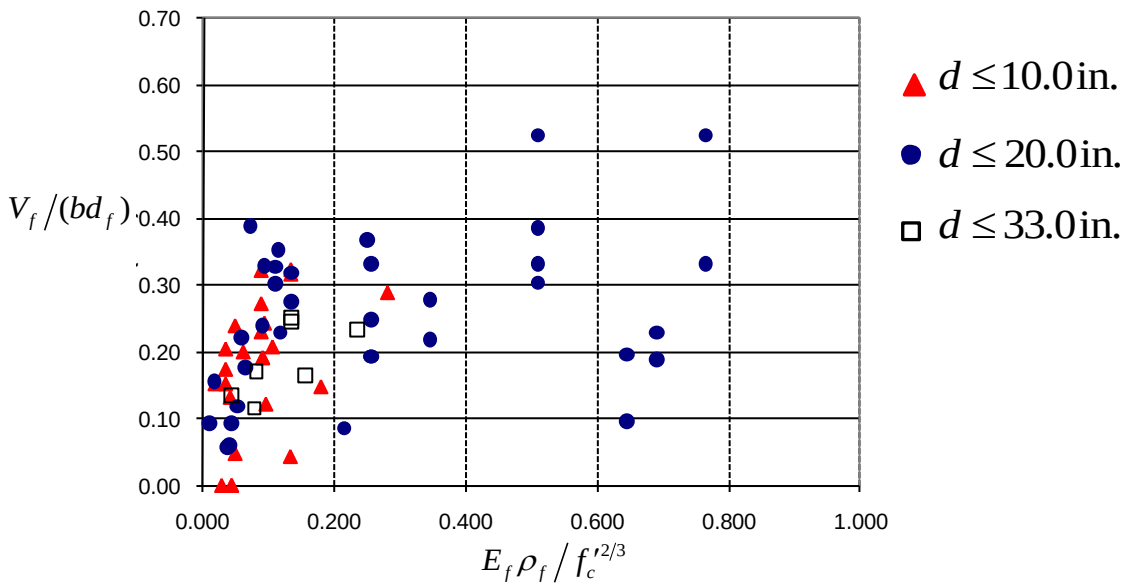

Figure A 3.14 FRP Shear Strength, V_f/bd_f in Terms of $E_f\rho_f/f_c'^{2/3}$ (E_f : ksi and f_c' : psi) - Beams Failed by FRP Rupture

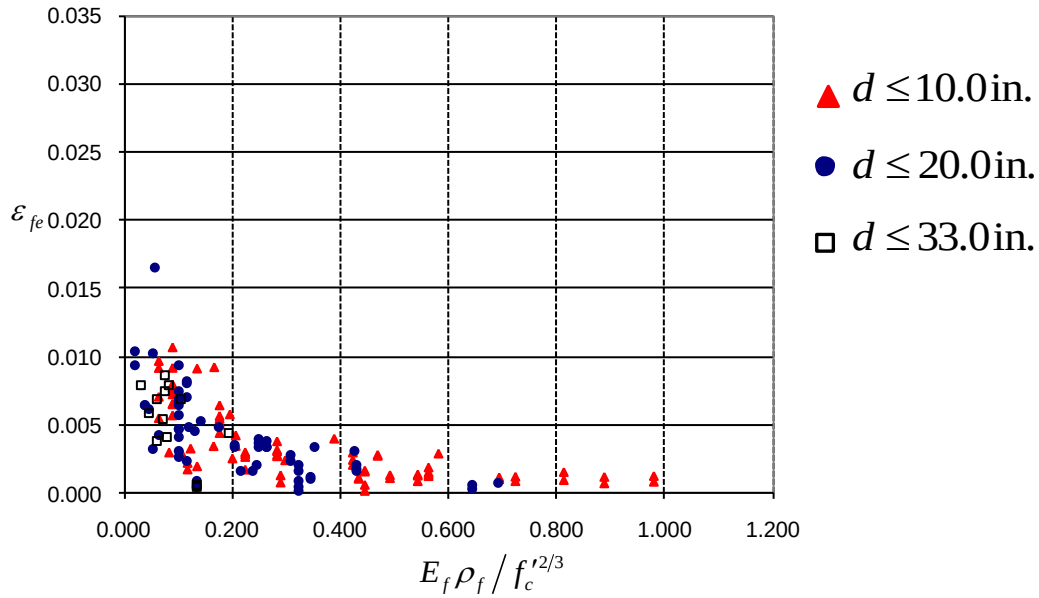

Figure A 3.15 Effective Strain of FRP in Terms of $E_f \rho_f / f_c'^{2/3}$ (E_f : ksi and f_c' : psi) - Beams Failed by FRP Debonding

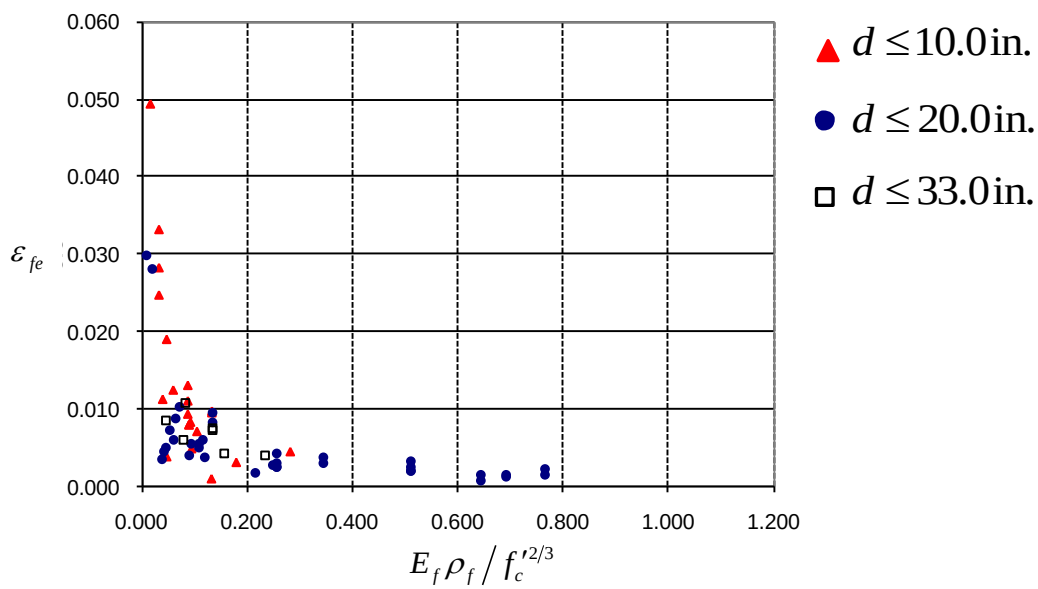

Figure A 3.16 Effective Strain of FRP in Terms of $E_f \rho_f / f_c'^{2/3}$ (E_f : ksi and f_c' : psi) - Beams Failed by FRP Rupture

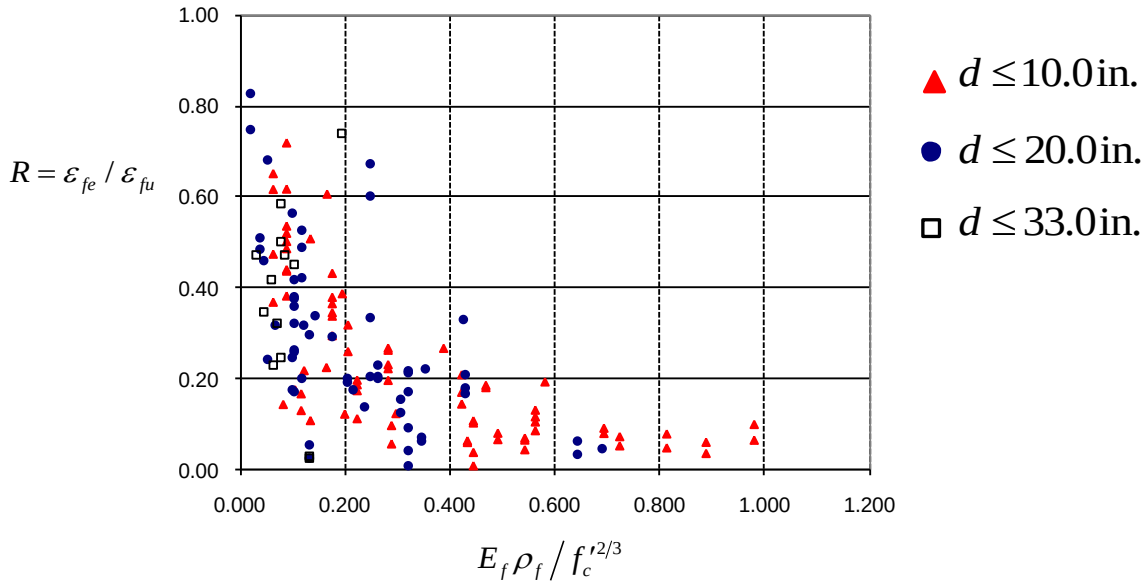

Figure A 3.17 Ratio of Effective FRP Strain to Ultimate FRP Strain, $R = \varepsilon_{fe} / \varepsilon_{fu}$, in terms of $E_f \rho_f / f_c'^{2/3}$ (E_f : ksi and f_c' : psi) - Beams Failed by FRP Debonding

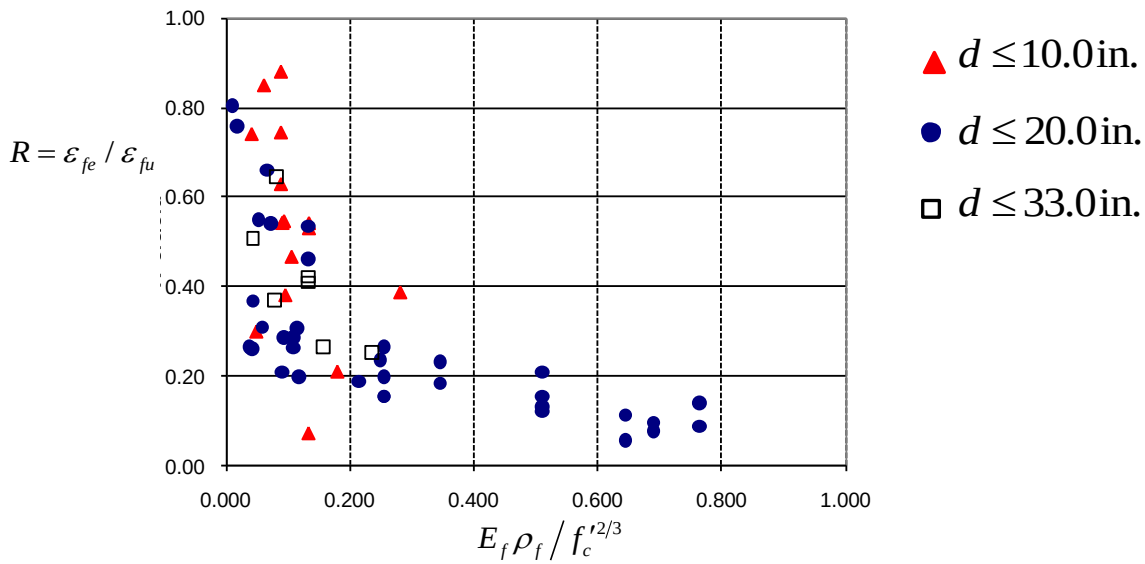

Figure A 3.18 Ratio of Effective FRP Strain to Ultimate FRP Strain, $R = \varepsilon_{fe} / \varepsilon_{fu}$, in terms of $E_f \rho_f / f_c'^{2/3}$ (E_f : ksi and f_c' : psi) - Beams Failed by FRP Rupture

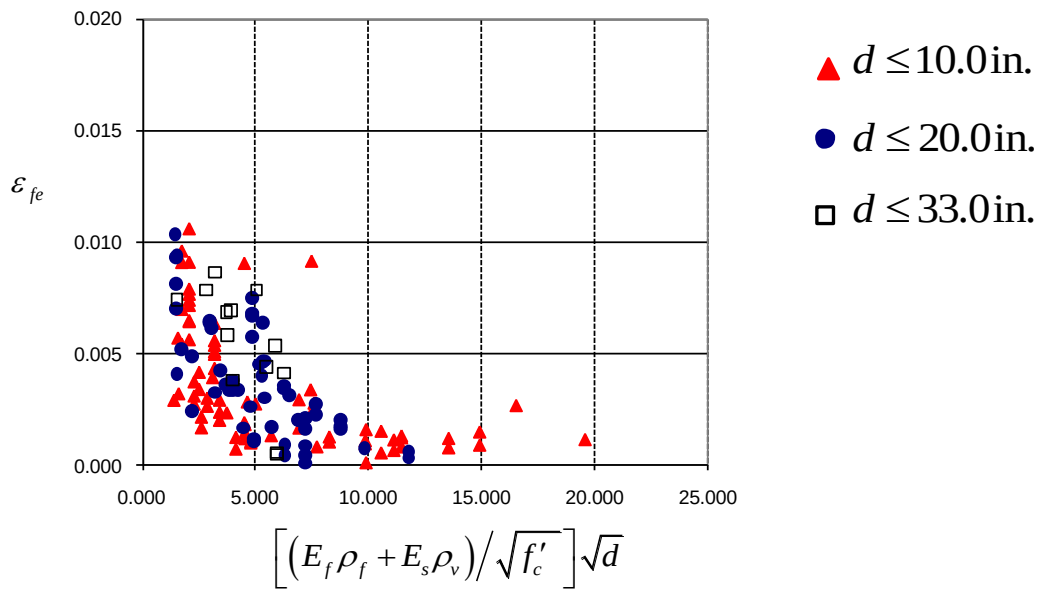

Figure A 3.19 Effective Strain of FRP in Terms of $\left[\left(E_f\rho_f + E_s\rho_v\right)/\sqrt{f_c'}\right]\sqrt{d}$ (E_f, E_s : ksi; f_c' : psi; and d : in.) - Beams Failed by FRP Debonding

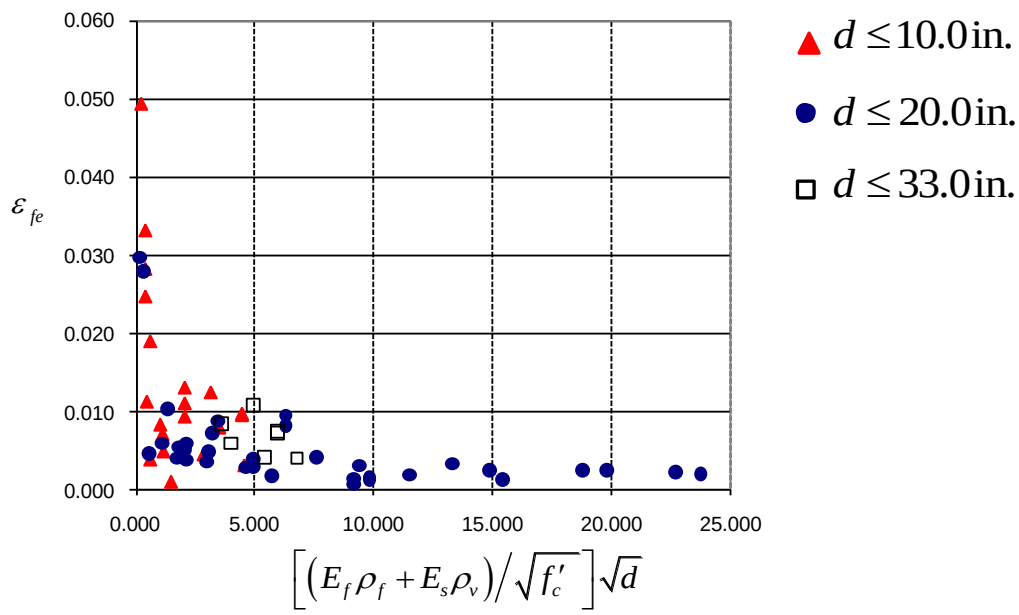

Figure A 3.20 Effective Strain of FRP in Terms of $\left[\left(E_f\rho_f + E_s\rho_v\right)/\sqrt{f_c'}\right]\sqrt{d}$ (E_f, E_s : ksi; f_c' : psi; and d : in.) - Beams Failed by FRP Rupture

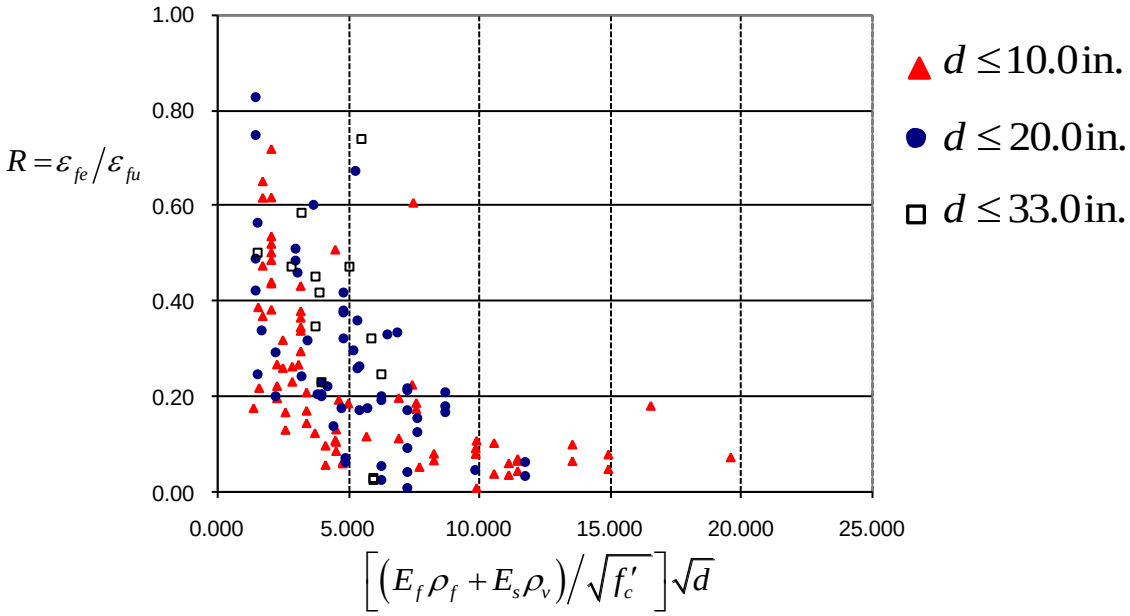

Figure A 3.21 Ratio of Effective FRP Strain to Ultimate FRP Strain, $R = \varepsilon_{fe} / \varepsilon_{fu}$, in terms of $\left[\left(E_f \rho_f + E_s \rho_v \right) / \sqrt{f_c'} \right] \sqrt{d}$ (E_f, E_s : ksi; f_c' : psi; and d : in.) - Beams Failed by FRP Debonding

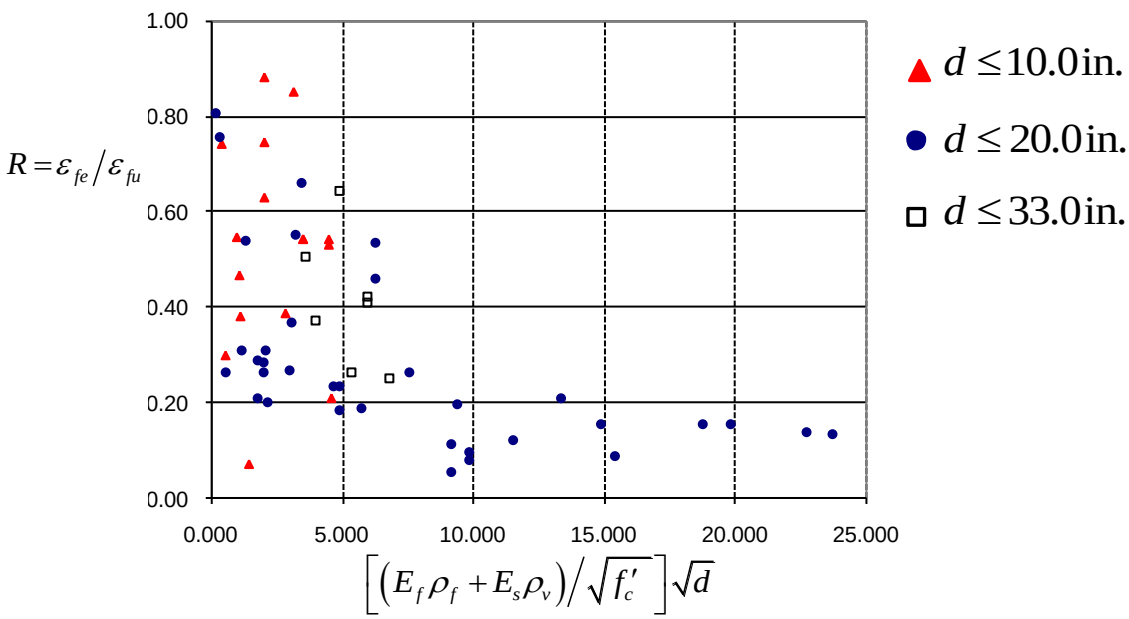

Figure A 3.22 Ratio of Effective FRP Strain to Ultimate FRP Strain, $R = \varepsilon_{fe} / \varepsilon_{fu}$, in terms of $\left[\left(E_f \rho_f + E_s \rho_v \right) / \sqrt{f_c'} \right] \sqrt{d}$ (E_f, E_s : ksi; f_c' : psi; and d : in.) - Beams Failed by FRP Rupture

A3.4.5 Effect of Shear Span-to-Depth Ratio (Slender vs. Deep Beam)

A3.4.5.1 Background

The majority of the available experimental data concerns beams that can be classified as slender. However, the shear behavior of RC beams depends largely on the shear span-to-depth ratio, defined as the shear span (*a*) divided by the effective beam depth (*d*). This ratio (*a/d*) is used to distinguish between slender and deep beams. In this context, it is important to know whether shear strengthening with externally applied FRP offers the same performance for both slender and deep beams. The literature reports some test results on the shear performance of deep beams retrofitted in shear with FRP (Zhang et al., 2004, and Chaallal et al., 2002). However, these tests involve deep beams only, and they fail to provide a basis for comparison between the shear performance of deep beams and slender beams. Recently, Bousselham and Chaallal (2006b) studied the influence of the *a/d* ratio by considering both slender beams (*a/d = 3.0*) and deep beams (*a/d = 1.5*). The results obtained in this study indicate that the gain in shear resistance due to FRP is superior for slender beams. This result is probably attributed to the arch action exhibited by deep beams. Thus, the shear contribution of externally bonded FRP, like that of the internal transverse steel, is less significant in deep beams than in slender beams.

A3.4.5.2 Assessment

Figures A 3.23 through A 3.30 present the shear gain due to FRP, shear strength of FRP, the effective strain of FRP, and the ratio of the effective strain to the ultimate FRP strain in terms of $\left[\left(E_f\rho_f + E_s\rho_v\right)\Big/\sqrt{f_c'}\,\right]\sqrt{d}$ for the two separate failure modes (FRP debonding and FRP rupture). In the figures, Series 1 represent the deep beams of which shear span-to-depth ratio (a/d ratio) is less than or equal to 2.5 ($a/d \leq 2.5$). Series 2 represents slender beam tests of which the a/d ratio was between 2.5 and 4.0 ($2.5 < a/d \leq 4.0$). Series 3 represent the slender beams of which the a/d ratio was between 4.0 and 5.0 ($4.0 < a/d \leq 5.0$).

It is clearly shown in the figures that FRP shear strengthening is more effective in slender beams than in deep beams regardless of failure modes. Thus, the future design equations for the bridge girders should be developed based on a set of data excluding the results of deep beams.

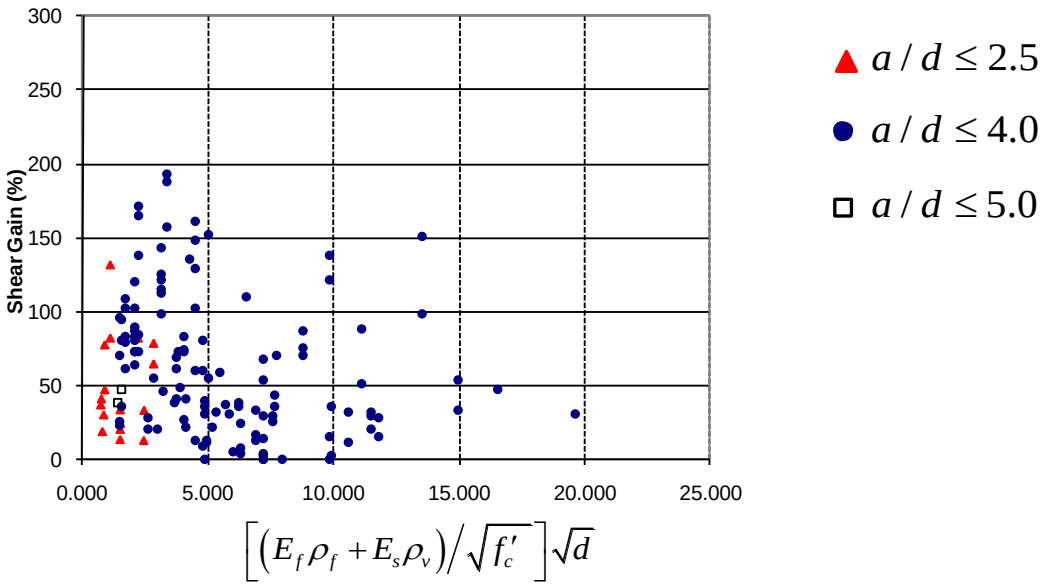

Figure A 3.23 Shear Gain (%) Due to FRP in terms of $\left[\left(E_f\rho_f + E_s\rho_v\right)/\sqrt{f_c'}\right]\sqrt{d}$ (E_f, E_s: ksi; f_c': psi; and d: in.) - Beams Failed by FRP Debonding

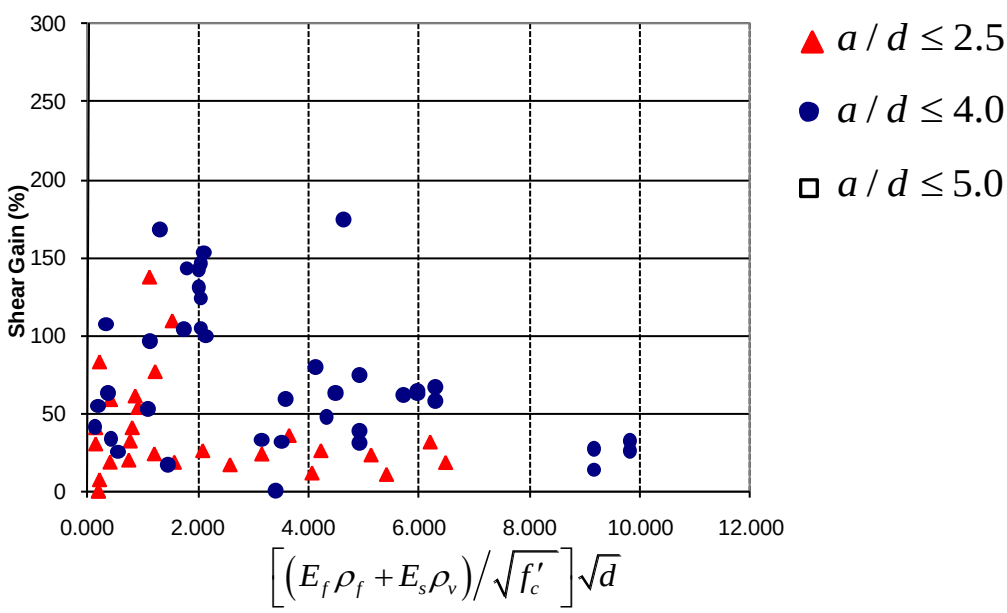

Figure A 3.24 Shear Gain (%) Due to FRP in terms of $\left[\left(E_f\rho_f + E_s\rho_v\right)/\sqrt{f_c'}\right]\sqrt{d}$ (E_f, E_s: ksi; f_c': psi; and d: in.) - Beams Failed by FRP Rupture

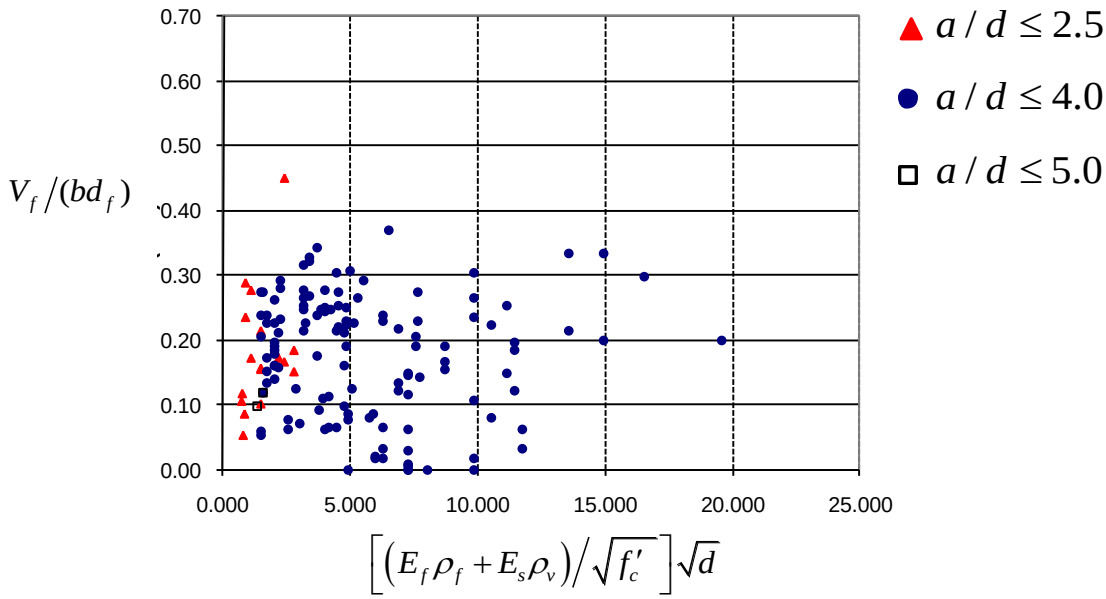

Figure A 3.25 Shear Strength of FRP in terms of $\left[\left(E_f\rho_f + E_s\rho_v\right)/\sqrt{f_c'}\right]\sqrt{d}$ **(**E_f**,** E_s**: ksi;** f_c'**: psi; and** d**: in.) - Beams Failed by FRP Debonding**

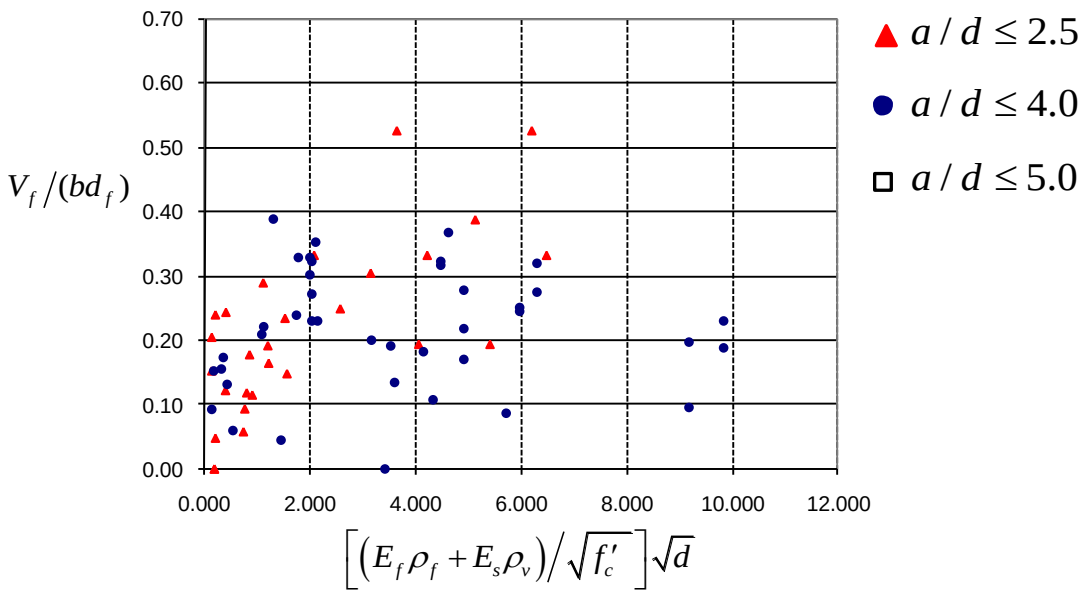

Figure A 3.26 Shear Strength of FRP in terms of $\left[\left(E_f\rho_f + E_s\rho_v\right)/\sqrt{f_c'}\right]\sqrt{d}$ **(**E_f**,** E_s**: ksi;** f_c'**: psi; and** d**: in.) - Beams Failed by FRP Rupture**

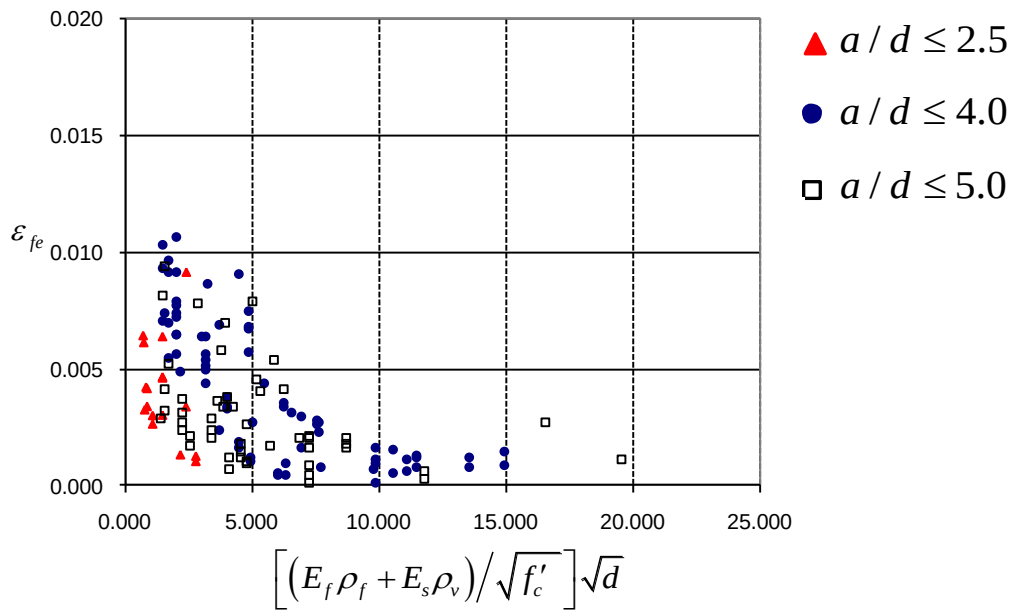

Figure A 3.27 Effective Strain of FRP in Terms of $\left[\left(E_f\rho_f + E_s\rho_v\right)/\sqrt{f_c'}\right]\sqrt{d}$ (E_f, E_s : ksi; f_c' : psi; and d : in.) - Beams Failed by FRP Debonding

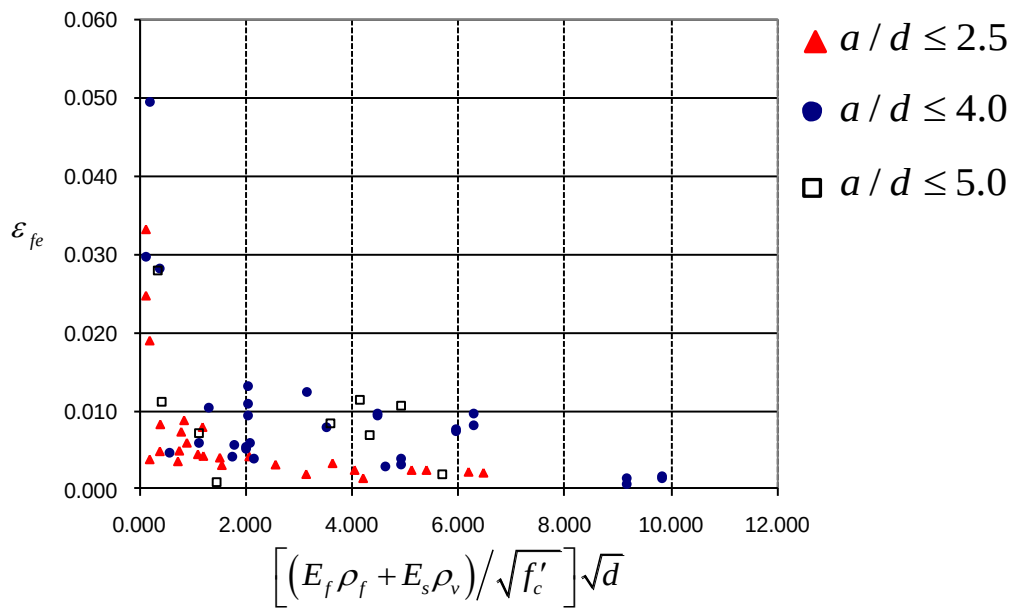

Figure A 3.28 Effective Strain of FRP in Terms of $\left[\left(E_f\rho_f + E_s\rho_v\right)/\sqrt{f_c'}\right]\sqrt{d}$ (E_f, E_s : ksi; f_c' : psi; and d : in.) - Beams Failed by FRP Rupture

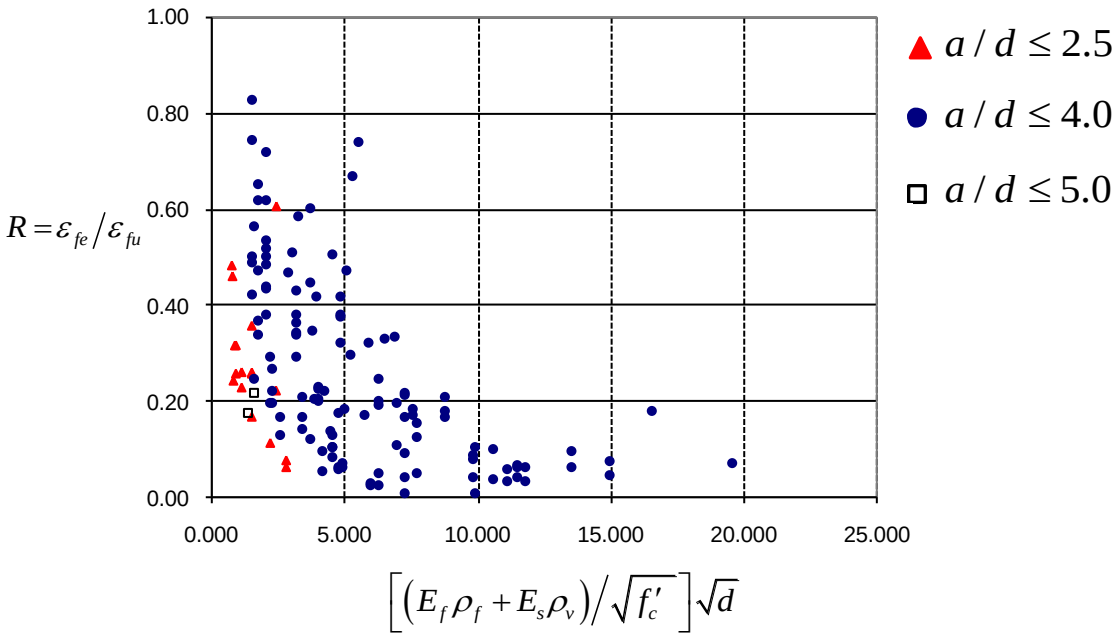

Figure A 3.29 Ratio of Effective FRP Strain to Ultimate FRP Strain, $R = \varepsilon_{fe} / \varepsilon_{fu}$, in terms of $\left[\left(E_f \rho_f + E_s \rho_v \right) / \sqrt{f_c'} \right] \sqrt{d}$ (E_f, E_s : ksi; f_c' : psi; and d : in.) - Beams Failed by FRP Deonding

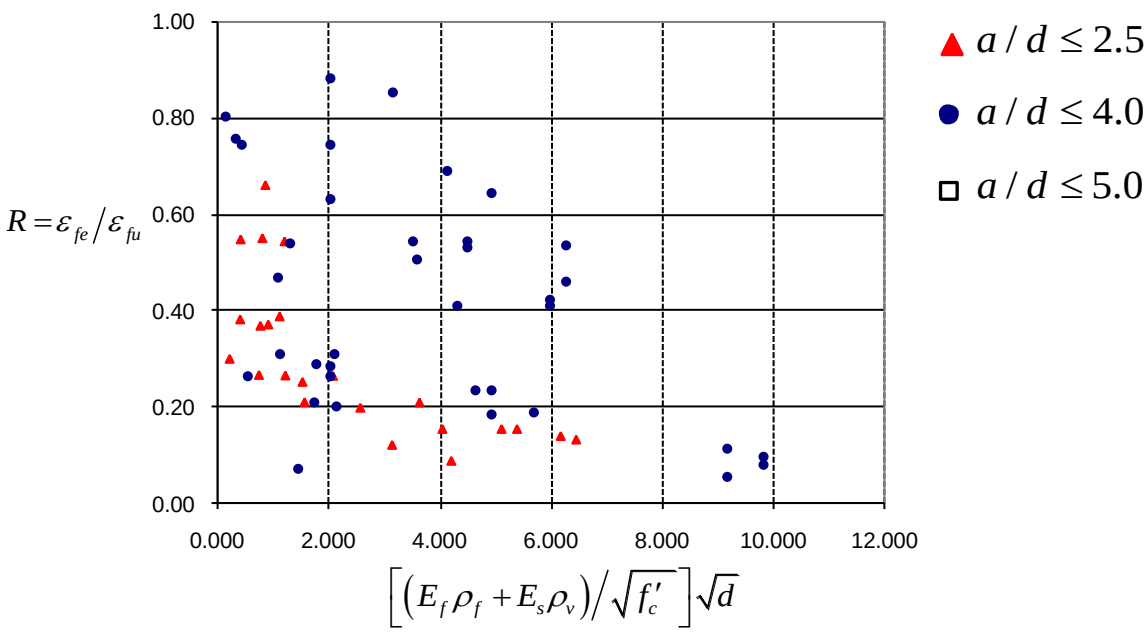

Figure A 3.30 Ratio of Effective FRP Strain to Ultimate FRP Strain, $R = \varepsilon_{fe} / \varepsilon_{fu}$, in terms of $\left[\left(E_f \rho_f + E_s \rho_v \right) / \sqrt{f_c'} \right] \sqrt{d}$ (E_f, E_s : ksi; f_c' : psi; and d : in.) - Beams Failed by FRP Rupture

A3.4.6 Influence of Parameters not Fully Documented - Qualitative Assessment

A3.4.6.1 Influence of FRP Configuration and Anchorage

The effect of the FRP configuration (side bonding, U-wrap, or complete wrap), determined from examination of the database information, is illustrated in Figure A 3.31. In Figure A 3.31, the following can be observed: (a) debonding is the dominant mode of failure for beams strengthened in shear with FRP bonded on the sides only, (b) in contrast, for beams retrofitted with complete FRP wrap and U-wraps with anchorage systems, debonding almost never occurs, and (c) in the case of beams retrofitted with U-wraps, 65% failed by debonding and 35 % failed by other failure modes such as diagonal tension failure in the web, shear compression failure in the compression zone, and flexural failure. A debonding type of failure is obviously related to the absence of sufficient anchorage in the case of FRP bonded on the sides only. However, the use of a complete wrap is often not practically feasible, in particular, for T-section beams or beams with slab or decks. In this context, the U-wrap configuration may present a necessary practical compromise.

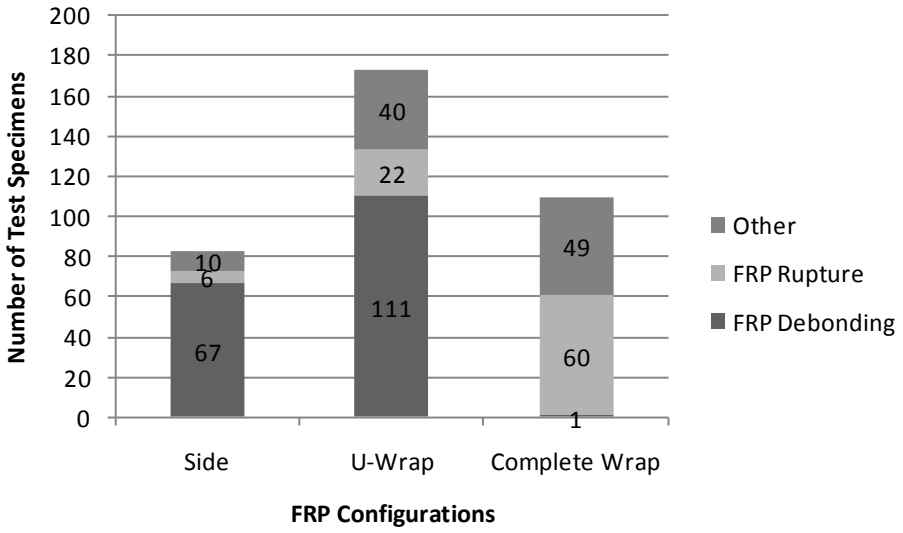

Figure A 3.31 Modes of Failure Related to Strengthening Scheme

A3.4.6.2 Influence of Concrete Strength

Concrete strength has an influence on the performance of shear strengthening with FRP from both the local and the global points of view. From the local point of view, this influence impacts the bonding performance at the FRP-concrete interface. A higher concrete strength will delay, if not inhibit altogether, failure by debonding. From the global point of view, this influence is linked to the failure scenarios proposed, that can differ depending on the concrete strength. A low concrete strength will inhibit early crushing of concrete in the compression zone or in the diagonal struts (Bousselham and Chaallal, 2006a) while it will decrease bond strength at the FRP-concrete interface. However, despite its importance with regards to the performance of shear strengthening with FRP, the effect of concrete strength has not been systematically studied. It is interesting to note, though, that the guidelines for the design of RC structures strengthened with externally applied FRP take into account the concrete strength when calculating the

contribution of FRP to shear resistance (ACI 440.2R-08, 2008; and *fib*-TG 9.3, 2001), either for the determination of the effective FRP strain or to prevent premature crushing of concrete. Therefore, it may be useful to document this influence analytically and experimentally. In this context, the range in concrete strengths tested needs to be representative of the conditions prevailing in practice for existing bridge structures.

A3.4.6.3 Influence of Fatigue

Shear fatigue behavior of RC beams is affected by its constituents (concrete and reinforcement) and the interaction between the two. Numerous research studies on fatigue behavior of concrete structures have been performed with focus on plain concrete beams and reinforcing steel. For example, Chang and Kesler (1958) conducted fatigue tests on concrete beams without shear reinforcement while shear fatigue of concrete beams with stirrups was investigated by Hawkins (1974), Ueda et al. (1981), Ueda and Okamura (1983), as well as, Kwak and Park (2001). Teng et al. (1998) reported fatigue test results of deep beams. Bond fatigue between concrete and reinforcing bars was studied by Rehm and Eligehausen (1979) and Balazs (1991). Fatigue of reinforcing bars was studied by Halgason and Hanson (1974), Corley et al. (1978) and Kreger et al. (1989).

On the other hand, there is limited research on fatigue behavior of concrete structures strengthened with externally bonded FRP laminates. Moreover, most studies on fatigue behavior of FRP strengthened concrete structures have focused on flexural strengthening (Muszynski and Sierakowski, 1996; Papakonstantiou et al., 2001; Senthilnath et al., 2001; Lopez-Anido et al., 2003; Breña and Gussenhoven, 2005; Ekenel and Myers, 2005) with only limited studies on shear strengthened fatigue response. Table A 3.1 summarizes the experimental parameters of select research studies investigating the fatigue behavior of concrete structures strengthened in either flexure or shear with FRP. A summary of research studies on fatigue performance of FRP shear strengthened RC beams is also presented.

Harries (2005) presented a review paper on fatigue behavior of FRP-strengthened members to identify the debonding problem in fatigue. He discussed the effects of different specimen loading geometry, particularly shear span-to-depth ratios, type and geometry of FRP strengthening system, and specimen size in the context of their relation to debonding behavior and their effects on observed S-N behavior of RC beams subject to flexural fatigue. FRP strengthening is known to reduce the strain in the internal reinforcement under static service loads. However, fatigue behavior of FRP-strengthened RC beams is controlled by the behavior of the internal reinforcement and appears to be only moderately improved over the unstrengthened beam. Harries (2005) highlighted the variability of actual stress range in both the internal steel and the FRP bond interface, when establishing accurate S-N relationships. Shear span-to-depth ratio and the shear-to-moment ratio both affect the debonding response and consequently the apparent S-N behavior. Most importantly, he reported that applications prone to “intermediate crack induced” debonding appear to be more critical in terms of their fatigue behavior than those experiencing “end peel” debonding. This issue is of great importance to the present study.

Table A 3.1 Noteworthy Fatigue Tests for FRP-Strengthened Concrete Beams

Reference	Beam Type	Strengthening Type	FRP Type	No. of Cycles	Frequency	Load Range (% of Ultimate Capacity)
Ekenel and Myers (2009)	RC	Flexure	Carbon	2M	2 Hz	33 % ~ 63 %
Senthilnath et al. (2001)	RC	Flexure	Carbon	2M	3 Hz	31 % ~ 58 %
Aidoo et al. (2004)	RC-T	Flexure	Carbon	1.4M	1 Hz	2 % ~ 52 % (low stress) 12 % ~ 65 % (high stress)
Papakonstantinou et al. (2001)	RC-T	Flexure	Glass	6M	2- 3 Hz	3 % ~ 40 % (low stress) 3 % ~ 80 % (high stress)
Czaderski and Motavalli (2004)	RC-T	Shear	Carbon*	5M	4.4 Hz	39 % ~ 59 %
Williams and Higgins (2008)**	RC-T	Shear	Carbon	1M	1-1.25 Hz	4 % ~ 40 % 4 % ~ 75 % 8 % ~ 51 %
Chaallal et al. (2009)	RC-T	Shear	Carbon	5M	2 Hz	35 % ~ 65 %

* L-Shaped Plate
** Consideration was taken to limit measured strains of the internal steel reinforcing to ensure levels were below the fatigue limit of 24 ksi at 1 million cycles.

Harries and Aidoo (2005) reported on the deterioration of FRP-concrete bond under cyclic loads at a stress range as low as 4% of the FRP strength. They conducted three large-scale and two full-scale test specimens. The 9,150 mm long full-scale specimens were 825 mm deept T-beams with 927 mm wide flange and 343 mm wide web. The 4,750 mm long, large-scale specimens were rectangular section with 254 mm depth and 152 mm width. They observed that the current design recommendations and “accepted practice” generally neglect this detrimental effect. The clear effects of bond deterioration under fatigue loading were demonstrated for large-scale laboratory specimens and in full-scale specimens recovered from a forty-year old interstate highway bridge. They suggested additional limit states be considered when even relatively small fatigue loads are present. Harries and Aidoo (2006) followed up their earlier study by indicating that the ACI 440.2R-02 (ACI 440, 2002) recommendations for mitigating debonding failures of externally bonded FRP as inadequate to effectively mitigate intermediate crack-induced debonding in flexural members.

Hoult and Lees (2005) proposed a shear retrofitting method using external CFRP straps for RC beams. The straps were mounted on steel pads at the top and bottom of the T-beam, and were run through special holes in the flange. The specimens were 280 mm deep with 250 mm wide flange and 105 mm wide web. The shear span was 750 mm. Clearly, the straps are uniquely different from the system used in the present study. The straps continued to provide effective shear

enhancement after 1 million cycles of fatigue loading between 50-80% of the ultimate strength of the strengthened beam.

Rasheed et al. (2006) emphasized the importance of controlling the prestressing strand-stress range in pre-cracked prestressed concrete girders in the FRP strengthening process to avoid long-term fatigue failures. They indicated that FRP develops higher strains across cracks relieving strand stresses at these critical locations.

Rosenboom and Rizkalla (2005) chose the fatigue load range to simulate typical loading of an actual bridge under the effect of the increased service loading conditions. They tested seven prestressed concrete bridge girders taken from two decommissioned bridges in Eastern North Carolina, both of which were erected in the 1960s. The 9,140 mm long C-Channel prestressed girders were 775 mm wide and 484 mm deep. The load range varied between a minimum load equivalent to the dead load and a maximum load equivalent to the combined dead and increased live load. The minimum load, in addition to the girder's own weight, included a load producing a moment equivalent to the moment due to an asphalt wearing surface, typically, used for these types of bridges. The service load was determined based on a truck configuration specified by AASHTO HS-15 type loading. The study concluded that strengthening using CFRP materials can reduce the stress ratio in the prestressing strands due to their effectiveness in controlling crack widths and increasing the overall stiffness. The most fatigue critical component in a CFRP strengthened prestressed concrete bridge girder were determined to be the prestressing strands. In order to prevent premature rupture of the strands due to the increased live load, the stress ratio should be kept within acceptable limits.

Budek et al. (2007) tested fatigue of under-strengthened shear-critical RC beams reinforced with external CFRP stirrups that were mounted as near-surface reinforcement. Although they determined the usefulness of the proposed system, it is not directly relevant to the present study.

Iwashita et al. (2007) examined the bonding behavior of FRP sheets on concrete blocks under fatigue loading. The bonded area for each specimen was 50 mm x 200 mm. The fatigue behavior of bonding surface between FRP sheets and concrete was characterized by the conducted P–S–N diagram representing the relationship among the probability of FRP debonding (P), the bond stress amplitudes (S), and the number of cycles (N) at debonding on a semi-logarithmic scale. Three phases of debonding were characterized as micro-debonding at the initiation phase, FRP-concrete interfacial debonding, and the macro-debonding, which is the complete debonding. The authors concluded that the upper limit of the maximum load ratio is about 20–30% when the debonding is not occurred after 2 million loading cycles. Moreover, during cyclic loading, the FRP strains at the initiation of debonding are considerably smaller than the case of static loading. In the fatigue testing, effective bond length increases gradually, and finally, FRP debonding occurs. These are two important considerations for the ensuing study.

Williams and Higgins (2008) reported on three full-size girder specimens repaired with bonded carbon fiber laminate for shear strengthening that were tested in the laboratory under repeated loads and compared with two non-fatigued specimens. The specimens had a height of 1,219 mm with a stem width of 356 mm and a deck portion 914 mm wide by 152 mm thick. Laboratory fatigue loading produced localized debonding along the FRP termination locations at the stem-

deck interface, and the fatigue loading did not significantly alter the ultimate shear capacity of the specimens.

Ekenel and Myers (2005) studied the fatigue behavior of RC girders strengthened with carbon FRP for flexural applications. Nine 1,829 mm long RC beams with 254 mm wide and 165 mm deep rectangular sections were tested. The load range was established to simulate service load stresses within 33-63% of the ultimate capacity of the beams. The tests were accompanied by other factors such as freeze–thaw, extreme temperature, ultraviolet light exposure, and relative humidity cycles. All beams survived 2 million fatigue cycles without showing significant bond degradation between composite and substrate. However, significant flexural stiffness degradation was observed in the conditioned specimens.

Yun et al. (2008) compared the behavior of the FRP-concrete bond interface in a double-face shear-type bond test (direct pullout test) under fatigue conditions. The tests included a gage length of 140 mm, in between two 400 mm bonded specimens. They studied externally bonded FRP, near-surface mounted FRP, fiber anchored FRP, and a newly developed hybrid bonded FRP system. They noted that in all bonding systems, the first cycle dissipates more energy than subsequent cycles due to the more significant initial micro-cracking that occurs. The slip increase is also much faster in the earlier cycles than that in the later cycles. They reported that fatigue conditioning did not alter the residual strength of the specimens, while the total slip increased with the fatigue load level.

Most recently, Chaallal et al. (2009) tested six specimens under fatigue loading between 35% and 65% of the respective static capacity. Half of the beams had no internal shear reinforcement, while the other half were equipped with internal transverse steel reinforcement. In each group, three specimens were tested with zero, one and two layers of continuously wrapped CFRP. The tests were conducted up to 5 million cycles at a frequency of 2 Hz. However, the main conclusions of the tests regarding the survivability of the specimens are questionable because the predicted capacities were as much as 50% off from the measured capacity, and therefore the load range was much lower than what was intended.

Dai et al. (2005) conducted static and fatigue tests on FRP strengthened specimens with frost damage experienced concrete. The tests included 60 mm x 190 mm FRP-concrete bonded area. They reported that the initial frost damage did not shorten the fatigue life of FRP/concrete joints if a same relative tensile stress level was kept in the FRP sheets where the relative tensile stress level was defined as a ratio of the applied tensile force in FRP sheets for the fatigue tests to the maximum static pull-out achieved in each test series.

O'Neill et al. (2007) reported on a limited number of fatigue tests on adhesive systems used for externally bonded FRP application. Tests included 25.4 mm square bonded area. They concluded that the degradation of FRP-retrofitted concrete beams under fatigue loading is more a function of the adhesive bond line rather than the FRP or the concrete substrate. The study suggested a reduction factor for allowable FRP strain associated with fatigue, as a function of the adhesive stiffness and the expected fatigue stress range. In particular, the study recommended using a stiffer adhesive for lower stress ranges and a softer adhesive for a higher stress range.

A3.4.6.4 Influence of Pre-Cracking

Almost all the experimental investigations conducted so far have concerned the shear performance of strengthened RC beams that had not been pre-loaded (pre-cracked) prior to their retrofit. However, external strengthening with FRP is most suitable for existing in-service structures that often are pre-cracked, if not slightly-damaged. The few investigations carried out, so far, on RC beams that were pre-cracked prior to their strengthening indicate that pre-loading does not affect the shear performance of retrofitted beams (Czaderski, 2002; Carolin and Taljsten, 2005a, and Hassan Dirar et al., 2006). However, this finding may need to be confirmed by further tests.

A3.4.6.5 Influence of Prestress

According to fib-T.G 9.3 (2001), "less than 10% of the bridges that have been FRP-strengthened so far are pre-stressed." This seems rather surprising given the number of bridge superstructures made of pre-stressed concrete (PC). To our knowledge, the only study dealing with PC beams strengthened in shear with FRP was performed by Hutchinson and Rizkalla (1999). The study reported that the prediction by the shear equations proposed by the authors based on ACI 318 was in good agreement with the test results of seven prestressed concrete beams strengthened with CFRP strips. Because most bridge girders are made of prestressed concrete, further studies dealing with prestressed concrete are needed.

A3.4.6.6 Influence of Structural Continuity

The ACI 440 Committee (ACI 440, 2008) makes the following observation regarding the effective FRP strain to be used for determining the FRP contribution to shear resistance, "the methodology for determining the bond reduction coefficient κ_υ specified in ACI 440.2R-08 (ACI 440, 2008) has been validated for members in regions of high shear and low moment, such as monotonically-loaded simply supported beams." Therefore, it may be important to examine the shear response for areas subjected to a combination of high flexural and shear stresses. This is the case for multi-span bridge girders, which constitute an important type of bridge girder often encountered in practice. The literature includes very few tests performed on continuous beams (Khalifa et al., 1999a; Mitsui et al., 1998; and Miyauchi et al. 1997). However, the results of these studies did not provide an insight to the behavior of the web near this stress field.

A3.5 Conclusions and Recommendations

A thorough and exhaustive state-of-the-art review of research studies dedicated to the shear strengthening of RC beams with FRP has been presented. These include:

- A detailed description of various investigations in terms of the parameters studied, the geometric characteristics of the specimens tested, and the type and configuration of FRP used. A matrix synthesizing these research studies is also presented in Section 2 of the main body of the report and qualitatively analyzed.
- An in-depth analysis of the experimental data available in the literature was needed in order to identify the major parameters and criteria that influence the behavior and hence the design of RC beams strengthened in shear with FRP. To this end, the database created by Bousselham and Chaallal (2004) has been greatly enhanced and updated. It now encompasses more than 260 tests carried out worldwide (excluding all tests that were rejected for valid reasoning) and includes all the variables that may influence the shear behavior of FRP-strengthened beams (Additional Material B). It is important to realize that

the data used in this analysis were collected from different sources and often include many variables acting simultaneously. In addition, shear by its nature is a complex problem and involves numerous parameters which often interact among themselves. Therefore, this part of the investigation called for a great deal of caution both in the manipulation of the data and in the interpretation of the analytical results. This need for caution also explains the choice of the shear gain as an analytical criterion as well as the FRP shear stress, the distinction made between slender and deep beams, the distinction made between failure by debonding and by other modes of shear failure reported in the literature, and finally the decoupling whenever possible of the major parameters.

The following observations are made based on this comprehensive study.

- The majority of the beam specimens tested are rectangular, often of relatively small size, not preloaded when retrofitted, and tested under static loads;
- The influence of FRP characteristics, including the configuration (continuous versus discontinuous and complete wrap versus U-wrap or side bonding) and the angle of inclination of the fibers (45° versus 90°), is well-documented and well-covered by existing studies;
- In contrast, only recently have other parameters been investigated with limited attention and interest, although they play a major role in the shear resistance mechanism. Specimen size (Bousselham and Chaallal, 2006c), pre-loading (Czaderski, 2002; Carolin and Taljsten, 2005a; and Hassan Dirar et al., 2006), and shear fatigue (Czaderski, 2002; and Carolin and Taljsten, 2005a) are examples of such parameters. As for the transverse steel reinforcement parameter, which has been increasingly covered in recent tests, its influence on shear resistance is now clearly established. However, the resistance mechanisms associated with the phenomenon are still not fully understood;
- Evidence shows a distinct lack of strain measurements for the various components (FRP, steel, concrete);
- There is lack of rational explanations for the mechanisms involved, and consequenctly, it is difficult to develop more scientifically rational and well-founded models. In this context, Bousselham and Chaallal (2006a,b), when comparing the shear resistance due to FRP using results from tests where the shear resistance was predicted using existing guidelines and design methods, it was concluded that the major aspects of shear strengthening are still not captured by these theoretical predictions.

The above observations lead to the following recommendations:

- Additional experimental investigations, aimed to clarify: (a) the influence of transverse steel reinforcement, with emphasis on the mechanisms which can explain the experimentally observed interaction between external FRP shear strengthening and internal transverse steel reinforcement; (b) the effect of specimen size, in order to evaluate the influence of this parameter on the contribution of FRP to shear resistance, especially since the available experimental data are derived mainly from relatively small specimens; (c) the effect of fatigue loading, particularly with regards to the performance of the anchorage of the FRP, and the consequent risk of debonding that may result; (d) the shear performance of RC beams strengthened with FRP while preloaded (pre-cracked); (e) the effect of prestress on the performance of beams retrofitted in shear with FRP;

- These investigations should be studied in a more systematic way and be performed in a more global parametric study to maintain better control of the variables involved;
- The number of control specimens should be chosen to allow for the generation of more reliable, purely experimental data for the contributions of concrete, the transverse steel reinforcement, and FRP to shear resistance;
- The importance of well distributed and reliable instrumentation and measurement must be emphasized. In view of the lack of recorded strain data, the strains in the different components (concrete, FRP, longitudinal and transverse steel reinforcement) should be carefully and thoroughly monitored. The instrumentation should be designed and selected so that the experimental data will shed light on the understanding of shear resistance mechanisms involved. This will also help to validate the numerical simulations that are planned as part of this study and consequently will lead to the development of rational and accurate design methods and guidelines.
- Regarding the properties of the beams to be tested, focus should be on AASHTO type, at least for the majority of the tests. As for the FRP composite, it does not appear a priority to include this parameter in the experimental investigation. However, the fact that most available data are related to CFRP may justify the use of these types of FRP. With regard to the FRP configuration, the use of U-wrap offers many advantages: on one hand, it provides better failure mode performance compared to FRP bonded on two sides, and on the other hand, the U-wrap scheme is easier to install and more practical than the complete wrap scheme.

A4. EVALUATION AND SELECTION OF MODELS FOR V_f

This section makes a comparative evaluation of existing models for the FRP contribution to shear resistance, V_f, and then presents the proposed relationships for V_f that stem from this study. More specifically, Section A4.2 presents models for V_f that have been proposed by researchers and a brief summary of the experimental basis of each of these models. Section A4.3 does the same for V_f relationships that have been incorporated into committee guidelines and code specifications. Section A4.4 presents an overview of the multiple shear design provisions in the AASHTO LRFD Bridge Design Specifications (AASHTO, 2008), and then identifies where V_f relationships could be added to these specifications (as outlined in Attachment A of this report). Section A4.5 provides a summary of the experimental database that was used in evaluating existing models for V_f, while Section A4.6 gives the results of this evaluation. Section A4.7 presents the selection and justification of V_f relationships for use in the AASHTO LRFD Bridge Design Specifications (AASHTO, 2008). Section A4.8 provides a summary of the key observations, the results of the assessments, and the proposed V_f relationships.

A4.1 Introduction

This introduction provides a brief summary of factors to be considered in the development of relationships for V_f for use in the AASHTO LRFD Bridge Design Specifications (AASHTO, 2008). Some of these considerations include the results of experiments which have illustrated how many other factors affect the contribution of FRP reinforcement to shear capacity and that any calibration of model must deal with significant uncertainties in other contributions to shear resistance as well as the deficiencies of existing experimental databases to calibrate design provisions.

The results from experimental studies show that the effectiveness of FRP in providing shear resistance depends on many factors including the modes of failure; the two most common being rupture of the FRP and debonding of the FRP from the concrete surface which is considered to include tearing of the outer concrete from its core. The mode of failure is strongly controlled by the attachment scheme. FRP rupture usually occurs in beams with full wrapping and in many cases of beams with U-jacketing particularly when an anchorage system is used in combination with this U-jacketing. FRP debonding typically governs in beams with side bonding (without full anchorage) and in most cases of U-jacketing without anchorage of the free ends. The contribution of FRP to shear resistance has also been shown in experiments to be influenced by FRP stiffness, amount and orientation of this reinforcement, rupture strength, orientation, adhesive resistance, type of anchorage system, strength of concrete, presence of shear cracking, presence of steel shear reinforcement, shape of section, and other factors. Experiments have further demonstrated that the provided FRP contribution was more difficult to predict for debonding than for rupture failures. The above suggests that it is not possible to develop simple relationships that well predict the FRP contribution to shear resistance, V_f, and that there may need to be at least two relationships: one in which rupture failures are expected and another more conservative relationship where debonding and other modes of failure are expected.

In codes of practice, the total shear resistance in a reinforced concrete beam without FRP reinforcement is expressed as the sum of the contribution of concrete, V_c, and the contribution of shear reinforcement, V_s. Consistent with this structure, it is most common to account for the contribution of the FRP reinforcement through the addition of a third item, V_f. This approach assumes that there is not a strong interaction between the shear strength provided by FRP reinforcement and the contributions of V_c and V_s for the many different types of regions that need to be strengthened in shear. If there is a strong interaction, then V_f must be selected to be conservative when the interactions have a negative effect on its contribution, or this interaction must be directly accounted for in the expression for V_f. Another difficulty in the development of an appropriate relationships for V_f is that it must be calibrated by the ratio of measured to calculated nominal strength V_{test}/V_n where $V_n = V_c + V_s$. For one reason, this is a challenge because of the large number of factors that significantly influence V_c and V_s that are not accounted for in codes. Consequently, this V_{test}/V_n may be much higher in a situation when the FRP reinforcement was shown to be ineffective (based on companion shear test one with and one without FRP reinforcement) in a situation in which the FRP reinforcement was shown to be effective. The multitude of relationships for V_c and V_s in the AASHTO LRFD specifications (AASHTO, 2008) further complicates this calibration.

A significant number of experimental research programs have been conducted worldwide to understand the shear strength contribution of FRP reinforcements. From these programs, numerous models, both empirical and semi-empirical, have been derived. Unfortunately, the types of members that have been tested in laboratories do not well represent the types of members in the field that need FRP shear strengthening, and consequently these models may not be reliable for members that are outside of the range of the experimental testing program(s) on which they are based. Most experiments have been on small, stocky, simply-supported members that have rectangular cross-sections, do not contain shear reinforcement and were not pre-cracked in shear. The size and shape of cross-sections are particularly important since the effectiveness of FRP strengthening depends on the development length of FRP reinforcements and the anchorage scheme as often controlled by member size and shape. Consequently, any calibration of provisions requires careful review and selection of the results from the available experimental test data.

A4.2 Analytical Models for V_f

This section presents an overview of existing analytical models that predict the contribution to shear resistance of FRP laminates, V_f. Each of these methods is presented using the form of relationship, units and notation as used by the authors of each model. The authors' form was preserved so as to present different possible structures for the V_f expressions for consideration for the LRFD specifications. Nearly all of the expressions for V_f are independent of the system of units. When otherwise, the units are clearly identified in the presentation of the author's model. While the models use a total of more than 50 different variables, there is a significant common core of variables as listed below.

- $a/d = \lambda$ = shear span to depth ratio
- $A_f = A_F = A_{fv}$ = area of FRP reinforcement (may be total area of a strip or area per unit length)

- b_w = web width
- d = depth of member (distance from tension reinforcement to extreme compression fiber)
- $d_f = h_{frp}$ = depth of section over which FRP shear reinforcement is distributed
- $E_f = E_{frp} = E_F = E_{fu}$ = stiffness of FRP reinforcement
- E_s = stiffness of transverse steel reinforcement
- $f'_c = f'_{cd}$ = compressive strength of concrete
- $f_{fe} = f_{frp,ed}$ = effective stress in FRP shear reinforcement
- $R = \varepsilon_{frp,e}/\varepsilon_{fu}$ = ratio of effective to ultimate strain in FRP reinforcement
- s = spacing of shear reinforcement
- $s_f = s_{frp} = s_{FRP} = s_F$ = spacing of FRP shear reinforcement
- $t_f = t_{frp}$ = thickness of FRP shear reinforcement
- $w_f = w_{fe} = w_{frp} = w_{FRP}$ = width of FRP shear reinforcement strip
- $V_f = V_{frp,d} = V_{fd}$ = shear strength contribution of FRP shear reinforcement
- $\alpha = \alpha_f = \beta$ = angle between FRP reinforcement fibers and longitudinal axis of the beam
- $\gamma_{frp} = \gamma_b$ = safety factor (value greater than 1.0; commonly used method in European practice)
- $\varepsilon_{frp} = \varepsilon_{fe} = \varepsilon_{frp,e} = \varepsilon_F = \varepsilon_{fd,e}$ = effective strain in FRP shear reinforcement
- ε_{fu} = ultimate tensile strain in FRP shear reinforcement at rupture
- θ = shear crack angle
- $\rho_{frp} = \rho_f$ = ratio of FRP shear reinforcement = $2nt_f w_f / b_w s_f$
- ρ_s = ratio of transverse steel reinforcement = $A_v / b_w s$

The general formulation of equations used by researchers and in codes of practice to calculate the FRP contribution to shear resistance, V_f, has the same structure as that for steel shear reinforcement, V_s. This general form for V_f is shown in Equation A4-1

$$V_f = \frac{A_f E_f \varepsilon_{fe} d_f}{s_f}\left(\cot\theta_c \sin\beta + \cos\beta\right) \qquad \text{(A4-1)}$$

in which the reliable stress capacity of the FRP, called the effective stress (f_{fe}), is equal to the stiffness of the FRP (E_f) multiplied by an effective strain (ε_{fe}). A_f is the area of FRP reinforcement over a member length equal to the longitudinal spacing (s_f) of these strips and d_f is the effective depth of the FRP reinforcement. The expression in the brackets is used to account for the effect of the angle of the shear crack θ_c and the orientation of the FRP reinforcement where β is the angle between FRP reinforcement fibers and the longitudinal axis of the beam. With the typical assumptions that θ_c is 45 degrees and that vertical FRP reinforcement strips are used, the expression in the brackets collapses to 1.0.

It is possible to rewrite Equation A4-1 in an even more general form by expressing the quantity of FRP reinforcement by its ratio ρ_f. The area of FRP reinforcement in the spacing s_f is computed as $A_f = 2nt_f w_f$ in which n is the number of FRP layers, t_f is the thickness of a single

FRP layer, and w_f is the width of a FRP strip. The FRP shear reinforcement ratio is then $\rho_f = A_f / (b_w s_f)$ as shown in Equation A4-2(a) and Equation A4-2(b) in which the effective stress $f_{fe} = E_f \varepsilon_{fe}$.

$$V_f = \rho_f E_f \varepsilon_{fe} b_w d_f \left(\cot\theta_c \sin\beta + \cos\beta\right) \quad \text{(A4-2a)}$$

$$V_f = \rho_f f_{fe} b_w d_f \left(\cot\theta_c \sin\beta + \cos\beta\right) \quad \text{(A4-2b)}$$

With the use of this general formulation, the relationships for V_f differ in three principal ways: (i) the consideration of the crack angle θ_c, (ii) the effective FRP depth d_f, and (iii) the effective FRP strain ε_{fe} or stress f_{fe}. Most models assume that the shear crack angle is 45° and thereby set $cot\,\theta_c = 1$. Some models, such as those by Pellegrino and Modena (2002), Cao et al. (2005), and Carolin and Taljsten (2005b), account for a variable angle in their equation. While a few models provide a detailed expression for evaluating d_f that accounts for the FRP configuration and attachment scheme, d_f is taken in most models as simply $d_f = 0.9d$, where d is the depth from the top of the section to the centroid of the longitudinal tension steel reinforcement. This is equivalent to how the shear depth, d_v, may be taken in the AASHTO LRFD specifications (AASHTO, 2008).

The primary difference between existing relationships for V_f is in how the effective FRP strain ε_{fe} or stress f_{fe} is determined. An effective strain (or stress) being considered as the ultimate strain (ε_{fu}) in the FRP is not always reached at a crack; this is due to debonding/anchorage failures or non-uniform strain distribution in the FRP along a shear crack. Non-uniform strain distribution also exists for the internal transverse steel reinforcement, but the plastic deformation capacity of stirrups ensures that all stirrups intersecting a shear crack can reach their yield strength before a shear failure occurs. FRP has close to a linear elastic response and thus differences in crack widths and spacings along a critical diagonal line will lead to non-uniform distributions of both FRP strain and stress. A further consideration is that when rupture first occurs at a point in the FRP sheet, the energy released in this FRP rupture leads to a ripping line of rupture across the rest of the FRP strip.

The effective strain at the point of shear failure is influenced by many factors including the failure mechanism (debonding or rupture), strengthening scheme (side bonding, U-jacket, or full wrap), effective bond length, strain distribution in the FRP sheet, and the limit of shear crack width. Different approaches are adopted in different models. Some models simply use a constant fixed value for the effective strain or a fixed fraction of the ultimate strain. Most models provide detailed expressions that consider a selection or all of the above factors in which the effective strain is taken as a functional fraction of the ultimate strain, $\varepsilon_{fe} = R \times \varepsilon_{fu}$. The axial stiffness of FRP ($\rho_f E_f$), concrete strength (f'_c), and anchorage conditions are three key parameters used in the calculation of the effective strain and thereby the relationship for V_f.

A description of 17 models proposed by researchers is now presented.

A4.2.1 Al-Sulaimani et al. (1994)

Al-Sulaimani et al. (1994) proposed a set of equations for the FRP contribution to the shear capacity of beams that were damaged to predetermined amounts prior to being repaired with FRP. Tests were carried out with different FRP wrapping schemes.

For shear repair with FRP strips, Group S:

V_p is calculated with the assumption that the strips will peel when the maximum shear stress, τ_{max}, at the bottom of the strip reaches the interface shear strength, τ_{ult}.

$$V_p = \frac{2F_p d}{S_p} = \frac{2\left[\tau_{ave}\left(\frac{t_s h_s}{2}\right)\right]d}{S_p} \quad where\ t_s = the\ width\ of\ a\ strip\ and\ h_s = depth\ of\ a\ strip$$

For shear repair with FRP wings, Group W:

V_p is calculated in the same manner as Group S.

$$V_p = 2F_p = 2\left[\tau_{ave}\left(\frac{dh_w}{2}\right)\right],\ where\ h_w = depth\ of\ a\ wing$$

For shear repair with the FRP jacket, Group J:

V_p is calculated under the assumption that no peeling of the jacket occurs.

$$V_p = 2F_p = 2\left[\tau_{ult}\left(\frac{dh_f}{2}\right)\right] where\ h_f = depth\ of\ a\ jacket$$

Experimental Basis: Al-Sulaimani et al. (1994) tested 16 RC beams 150 x 150 x 1250 mm. The reinforcement included three 12 mm diameter high tension steel bars in the bottom of the beam and two 6 mm diameter bars in the top of the beam. The web reinforcement consisted of 6 mm diameter closed stirrups spaced at 200 mm center-to-center. The bonding schemes included 3 mm thick fiberglass plates used as shear strips, shear wings, and U-jackets. All beams were tested as simply supported beams with a span of 1200 mm and a shear span of 400 mm.

A4.2.2 Chajes et al. (1995)

Chajes et al. (1995) proposed that the contribution of FRP reinforcement to shear capacity be calculated in the same manner as is the contribution of transverse steel reinforcement.

$$V_s = \frac{A_v f_y (\sin\alpha + \cos\alpha) d}{s}$$

where: α is the angle between the longitudinal axis of the transverse reinforcement and beam. In their version of this equation, Chajes et al. (1995) adopted a linear stress-strain relationship for the FRP reinforcement, assuming that failure occurs in the concrete, and that there is perfect bond between the FRP and the concrete. Thereby,

$$V_f = A_f E_f \varepsilon v_{cu} d \quad \text{for FRP oriented at 0/90 degrees, and}$$
$$V_f = A_f E_f \varepsilon v_{cu} d \sqrt{2} \quad \text{for FRP oriented at 45/135 degrees}$$

where: εv_{cu} is the ultimate vertical tensile strain of concrete which was taken as 0.005. The format of these equations also assumes that the FRP reinforcement is continuous rather than in strips and thereby A_f is the area of FRP reinforcement per unit length.

Experimental Basis: This model was based on experiments on 8 reinforced concrete T-beams in which Aramid, E-glass or graphite fabric with 45 or 90 degree orientations were used. The FRP reinforcement was completely wrapped and there was no pre-cracking or transverse steel reinforcement.

A4.2.3 Triantafillou (1998a) and Triantafillou and Antonopoulos (2000)

Triantafillou (1998a) also used a model that was similar in format to that used for steel reinforcement but incorporated an effective FRP strain that decreases as the axial rigidity of the FRP increases. A relationship between FRP axial rigidity, $\rho_{frp} E_{frp}$, and effective strain $\varepsilon_{frp,e}$ was derived from experimental test data. Two equations for effective strain were developed. The equations for V_f and effective strain $\varepsilon_{frp,e}$ are given below.

$$V_{frp,d} = \frac{0.9}{\gamma_{frp}} \rho_{frp} E_{frp} \varepsilon_{frp,e} b_w d (1 + \cot\beta) \sin\beta$$
$$\varepsilon_{frp,e} = 0.0119 - 0.0205(\rho_{frp} E_{frp}) + 0.0104(\rho_{frp} E_{frp})^2 \text{ when } 0 \le \rho_{frp} E_{frp} \le 1\text{GPa}$$

Experimental Basis: Triantafillou (1998a) tested 9 rectangular RC beams reinforced in shear with side bonded carbon FRP reinforcement at a 90 degree orientation. There was no pre-cracking or transverse steel reinforcement. To supplement these test results, a database of 33 other tests on reinforced concrete beams strengthened in shear with FRP reinforcement was used. This database included beams reinforced with AFRP, GFRP, and CFRP laminates. Complete Wrap, U-wrap and two-side bonding were used to strengthen the beams using either 45 or 90 degree orientations.

$$\varepsilon_{frp,e} = -0.00065(\rho_{frp} E_{frp}) + 0.00245 \text{ when } \rho_{frp} E_{frp} > 1 \text{ GPa}$$

Later in 2000, an updated model was proposed by Triantafillou and Antonopoulos (2000) in which the expression for effective strain was calibrated based on the results of over 75 experiments. This model was incorporated in the European fib-TG 9.3 Bulletin 14 (fib-TG9.3, 2001), as will be presented in section 4.2.3.

A4.2.4 Malek and Saadatmanesh (1998)

The proposed model by Malek and Saadatmanesh (1998) was developed using truss analogy and compression field theory. When analyzing reinforced concrete beams with web-bonded composite plates, the stress-strain relationship in one of the composite plates can be represented by a matrix. The stress-strain relationship can be simplified by calculating the stresses in the composite plate when the system of coordinates coincides with the principle directions. The resulting shear and normal stresses in the plate along the crack in the vertical direction, F_p, is given as follows:

$$V_f = F_p = ht_p\left[Q_{13}\varepsilon_2 + Q_{23}\varepsilon_1 + \frac{Q_{12}\varepsilon_2 + Q_{22}\varepsilon_1}{\tan(\theta_c)}\right]$$

Along the same crack, the vertical force carried by the steel stirrups is calculated using the following equations:

$$V_s = F_v = E_s\varepsilon_y A_v \frac{h_v}{\tan(\theta_c)s}, \quad for\ \varepsilon_y < \frac{F_y}{E_s}$$

$$V_s = F_v = F_y A_v \frac{h_v}{\tan(\theta_c)s}, \quad for\ \varepsilon_y \geq \frac{F_y}{E_s}$$

Experimental Basis: Several tests were conducted on concrete beams strengthened with web-bonded CFRP. Different fiber orientations (±45º) along with different types of carbon fabrics were tested. In each test, two beams were used; one was not repaired and served as the control while the other beam was repaired with CFRP.

A4.2.5 Khalifa et al. (1998) and Khalifa and Nanni (2000)

Khalifa et al. (1998) and Khalifa and Nanni (2000) developed two related models. Only the second model is presented, as Khalifa and Nanni (2000) considered the 2000 model to be an improvement to their 1998 model. Their method is similar to that of Triantafillou (1998a) except that a different approach is taken for evaluating the effective strain. In the development of their mode, they took experimental values of V_f, set them equal to Triantifillou's (1998a) equation and then back calculated the effective strain. To eliminate the effects of various types of the FRP sheets, the ratio of the effective strain to the ultimate strain, R, was plotted with respect to the FRP axial rigidity, $\rho_f E_f$. From this plot, a best fit polynomial was derived.

$$R = 0.5622(\rho_f E_f)^2 - 1.2188(\rho_f E_f) + 0.778 \leq 0.5 \text{ when } \rho_f E_f < 1.1\,\text{Gpa}$$

The 1.1 GPa limit on the axial rigidity was an observation made from all the available data and the 0.5 limit on R had the effect of limiting the strain on the FRP sheets to 0.004-0.005. In the later paper, this reduction factor for FRP strength was proposed to coincide with a fracture failure mode with a limit of $\rho_f E_f < 0.7$ GPa. Another R factor was proposed based on the bond mechanism as given as:

$$R = 0.0042(f_{cm})^{2/3} w_{fe} / \left[(E_f t_f)^{0.58} \varepsilon_{fu} d\right]$$

Later Miller (1999) modified the above equation and proposed an equation based on experimental and analytical results as:

$$R = \frac{(f_c^{'})^{2/3} w_{fe}}{\varepsilon_{fu} d_f} \left[738.93 - 4.06(t_f E_f)\right] \times 10^{-6}$$

The R is also restricted by the following equation to limit the shear crack width.

$$R = \frac{0.006}{\varepsilon_{fu}} \quad \text{(based on limiting the shear crack width)}$$

Thus, the reduction factor R may be assumed as the lowest of three values given above.

Experimental Basis: For their initial study and analytical model, Khalifa et al. (1998) used a database of 48 test results that consisted of non pre-cracked reinforced concrete beams with rectangular cross sections. CFRP reinforcement was used with 45 and 90 degree fiber orientations, complete wrap, u-jacketing and side-bonded, continuous sheets and strips, and single and double plies. In the later paper (Khalifa et al., 1999b), they also considered the results of their own tests, which were done on 6 reinforced concrete beams with rectangular cross sections. These beams had CFRP reinforcement and used 0- and 90-degree fiber orientations, complete wrap and u-jacketing, continuous sheets and strips, and single and double plies.

A4.2.6 Hutchinson and Rizkalla (1999)

Hutchinson and Rizkalla (1999) provided the only analytical model based on pre-tensioned concrete girder tests. The contribution of FRP to shear resistance was also modeled after that provided by transverse steel reinforcement and is given as:

$$V_{f,\max} = \varepsilon_{f,ave} E_f 2nt_f w_f \frac{d_f (\cot\theta + \cot\alpha_f)\sin\alpha_f}{s_f}$$

The average FRP strain for I-shaped sections, $\varepsilon_{f,ave,}$ is taken as

$$\varepsilon_{f,ave} = \varepsilon_{f,\max} \frac{\left\lfloor d/2 + 0.5(d_f - d/2)\right\rfloor}{d_f}$$

where: $\varepsilon_{f,max}$ is the maximum strain in the FRP and can be taken as 0.004. This strain was modeled from a FRP failure mode of peeling which was observed in the tested I-girders. The equation is based on a constant strain $\varepsilon_{f,max}$, extending $d/2$ from to the bottom of d_f and decreasing to zero at the top of d_f. For other effective strains, related to different failure modes, Hutchinson and Rizkalla (1999) referred to Triantafillou (1998a) and Khalifa et al. (1998).

Experimental Basis: The tests consisted of seven pre-tensioned concrete I-girders reinforced with CFRP jacket oriented at 45° and 90°. The test beams were 10 m long and 1:3.5 scale model of AASHTO type I-shaped bridge girders. All test beams had a depth of 415 mm with a top slab of 480 mm in width and 60 mm in depth. The concrete compressive strength at the time of testing ranged from 44 to 55 MPa. The test beams were pre-tensioned using 7-wire steel strands with a diameter of 0.5 inches and an ultimate tensile strength of 1860 MPa.

A4.2.7 Chaallal et al. (2002)

Chaallal et al. (2002) investigated the influence of amount of transverse steel reinforcement on the effectiveness of FRP reinforcement. They found that the amount of steel shear reinforcement influenced the effective FRP strain. Thus, they suggested that the optimum number of FRP layers to achieve the maximum gain in shear resistance depends on the amount of internal shear steel reinforcement. They also compared the measured FRP strains to strains calculated using Triantifillou (1998a)'s equations. They attributed the difference between the measured and the calculated strains to the fact that the Triantifillou (1998a)'s equations were based on the test results of small-scale slender beams, which is not the case for the girders used in Chaallal et al.'s (2002) test. Based on the regression analysis of the measured values, the following equation was recommended:

$$\varepsilon_{fe} = 3\times10^{-5}\times\rho_{tot}^{-0.6522}, \qquad \rho_{tot} = n\rho_f + \rho_s$$

where: ρ_{tot} is the total shear reinforcement ratio and n is the ratio of the FRP elastic modulus to the steel elastic modulus. Note that in computing ρ_{tot} and ε_{fe}, the ratio $\rho_f = A_{vf}$ per unit length divided by shear area = $2t_f/bd$. Similarly, $\rho_s = A_{sv}$ per unit length $/bd = A_{sv}/s_v bd$; both the ratio ρ_f and ρ_s have the dimension of $(\text{inch})^{-1}$. Chaallal et al. (2002) observed that the addition of CFRP layers modified the behavior of the beam from deep to slender. Thus the deep beam coefficient, f(a/d)=(1+2a/d)/12, as defined in the ACI 318-99 (ACI 318, 1999), was suggested to be included in the calculation of the shear gain due to the CFRP warp. It was also observed that the beam coefficient had a trend of increasing as the total shear reinforcement ratio increased. As a result, a simplified linear relationship was proposed as:

New deep beam coefficient: $$f\left(\frac{a}{d},\rho_{tot}\right) = \frac{1+2a/d}{12} + \left(1000\rho_{tot} - 0.6\right) \le 1$$

The contribution to shear capacity of the CFRP was based on the strut-and-tie model and used a coefficient to account for the beneficial effects of strut action.

$$V_f = f\left(\frac{a}{d}\right)\left(\frac{A_f}{s_f}\right)E_f\,\varepsilon_{fe}\,d_f$$

Experimental Basis: Chaallal et al. (2002) tested 12 RC beams that were half-scale T-section girders in which steel shear reinforcement was used. Multi-layer and fully wrapped CFRP reinforcement with a 90 degree fiber orientation was used.

A4.2.8 Chen and Teng (2003a,b)

Chen and Teng (2003a,b) proposed two different analytical models, one for each of the failure modes of FRP rupture and FRP debonding. Both models use the same relationship for evaluating the FRP contribution to shear capacity.

$$V_{frp} = 2\frac{f_{frp,ed}}{\gamma_b} t_{frp} w_{frp} \frac{h_{frp}(\sin\beta + \cos\beta)}{s_{frp}}$$

The only difference between these two models is the way of computing the effective FRP stress ($f_{fpr,ed}$).

A4.2.8.1 FRP debonding model

The effective design stress in the debonding model is the product of a stress distribution factor and the maximum stress in FRP reinforcement at a crack location.

$$f_{frp,ed} = D_{frp}\sigma_{frp,\max,d}\,, \quad D_{frp} = \text{ strain distribution factor}$$

$$\sigma_{frp,\max,d} = 0.315\beta_w\beta_L\sqrt{\frac{E_{frp}}{t_{frp}}\sqrt{f_c^{'}}} \le f_{frp}$$

where: D_{frp} is a ratio of the stress along the FRP sheet intersecting the shear crack at the ultimate limit state, and the product of the height of the FRP and the ultimate tensile capacity of the FRP. The maximum FRP design strain, $\sigma_{frp,max,d}$, is based on the maximum stress being located where FRP has the longest bond length at the debonding failure. Maximum FRP design stress is then limited by ultimate bond length unless rupture controls. The β_L factor incorporates the effect of bond length for different bonding schemes and the β_W factor accounts for the effect of FRP-to-concrete width ratio of the specimen.

Experimental Basis: Chen and Teng (2003a) used a database of previous tests results to develop their FRP debonding model. The database consisted of 46 RC rectangular and T-shaped beams. The bonding schemes tested used U-jacketing and side bonding with 45 and 90 degree main fiber orientations and only beams that failed by debonding of the FRP were considered. The beams were not pre-cracked, and transverse steel reinforcement was used.

A4.2.8.2 FRP Rupture model

The design stress in the rupture model is given as:

$$f_{frp,ed} = D_{frp}\sigma_{frp,\max}, \quad D_{frp} = \text{ strain distribution factor}$$

$$\sigma_{frp,\max} = \begin{cases} 0.8 f_{frp} & \text{if } \dfrac{f_{frp}}{E_{frp}} \le \varepsilon_{\max} \\ 0.8\varepsilon_{\max} E_{FRP} & \text{if } \dfrac{f_{frp}}{E_{frp}} > \varepsilon_{\max} \end{cases}$$

For the strain distribution, D_{frp}, for which there is little experimental data, a lower bound value of 0.5 was given and used in the database to simplify calculations and provide conservative results. The 0.8 factor in the maximum design stress of FRP was a reduction factor to account for the difference in strength from standard tensile tests using flat coupons and ε_{max} which was set at 1.5% until further research is done.

Experimental Basis: Chen and Teng (2003b) used a database of 58 reinforced concrete rectangular and T-shaped beam tests. U-jacketing and complete wrap strengthening schemes were used in these tests. The results were only considered for specimens that failed by FRP rupture. The database included beams with and without transverse steel reinforcement.

A4.2.9 Pellegrino and Modena (2002)

Pellegrino and Modena (2002) proposed a relationship to account for an observed decrease in the effectiveness of the FRP reinforcement with an increasing amount of transverse steel reinforcement. They employed Khalifa et al.'s (1998) effective strain model for R based on the bond mechanism that had been modified by Miller (1999). Pellegrino and Modena (2002) added an additional R^* value which acted as an additional reduction factor when transverse steel reinforcement is present. The least of the following R factors were used to calculate the effective stress used in the equation given by Khalifa et al. (1998) for the contribution of FRP to shear contribution:

$$R = 0.5622(\rho_f E_f)^2 - 1.2188(\rho_f E_f) + 0.778 \le 0.5 \text{ or}$$

$$R = \frac{0.006}{\varepsilon_{fu}} \text{ or}$$

$$R = R^* \left\{ 0.0042 (f_{cm})^{2/3} w_{fe} / \left[(E_f t_f)^{0.58} \varepsilon_{fu} d \right] \right\}$$

$$0 \le R^* = -0.53 \ln \rho_{s,f} + 0.29 \le 1$$

where: $\rho_{s,f}$ is the stiffness ratio between the transverse steel reinforcement and the FRP shear reinforcement.

Experimental Basis: Pellegrino and Modena (2002) tested 11 rectangular RC beams with and without transverse steel reinforcement. The FRP was side bonded, multi-layered and at a 90-degree fiber orientation.

A4.2.10 Hsu et al. (2003)

Hsu et al. (2003) proposed a new *R* factor to be used in the calculation of the contribution of FRP to shear strength. The equation for the FRP contribution is similar to steel shear. Hsu et al. (2003) generated a new *R* factor based on the bonding mechanism as well as a new *R* factor based on the model calibration of their test results. The equations can be found below:

$$V_f = \frac{A_f E_f \varepsilon_{fe} (\sin\beta + \cos\beta) d_f}{s_f}$$

$$\varepsilon = R\varepsilon_{fu}$$

R value based on model calibration:

$$R = 1.48712(\rho_f E_f / f'_c)^{-.7499}$$

R value based on bonding mechanism:

$$R = \frac{\tau_{\max} L_e}{2 f_{fu} t_f} \leq 1$$

$$\tau_{\max} = 5x10^{-6} f'_c - 2.73x10^{-2} f'_c + 925.3$$

The maximum shear stress given by this equation occurs when the concrete is at failure. The distribution of stress can be simplified as a triangular shape along the effective length in order to derive an *R* factor based on the bonding mechanism.

Experimental Basis: Hsu et al. (2003) tested a total of 15 beams. Of the ten beams tested for flexural strength in a three-point bending test, six were 9'-6" x 6" x 12" and four were 11'-4" x 6" x 9". The first six beams were designed to be under-reinforced, while the final four beams were designed to be over-reinforced. The remaining five beams were tested for shear strength and had dimensions of 4' x 6" x 9". These beams were designed to fail in shear either before or after CFRP strengthening. The CFRP strips were 2" wide and 1/20" thick.

A4.2.11 Deniaud and Cheng (2001)

The proposed analytical model by Deniaud and Cheng (2001) is based on a strip method and shear friction approach. This model describes the interaction between the concrete, steel stirrups, and FRP. In the strip method, each FRP strip is evaluated to determine the maximum allowable strain from the geometry of the FRP sheets. The shear friction approach uses the following equation to find the shear strength along a plane crossing n spaces and n-1 stirrups where the first two terms account for the concrete and steel contributions and the last term for the FRP contribution.

$$V_r = 0.25k^2 f_c' b_w h \frac{d_s}{ns} + T_v(n-1) + nT_{FRP}$$

The governing shear strength of a beam is then taken by the lowest shear strength among all of the potential failure planes. The equation for effect of FRP, T_{FRP}, is:

$$T_{FRP} = d_f t_f E_f \varepsilon_{\max} R_L \left(\frac{w_{FRP}}{s_{FRP}} \right)^2 \left(\frac{s}{d_s} \sin\alpha + \cos\alpha \right) \sin\alpha$$

It is necessary to note that the width and spacing of the FRP bands, w_{FRP} and s_{FRP} , are perpendicular to the direction of the principal fibers, but not along the longitudinal direction of the beam as is done for the other methods. ε_{max} and R_L terms are defined by the following equations:

Maximum allowable strain in FRP: $\varepsilon_{\max} = \dfrac{3\sqrt{f_c^{'}}\, d_f^{0.16}}{\left(t_f E_f\right)^{0.67} \left(k_a \sin\alpha\right)^{0.1}} (\%)$

Remaining bonded width over initial width ratio: $R_L = 1 - 1.2 \exp\left[-\left(\dfrac{d_f}{k_e L_{eff} \sin\alpha} \right)^{0.4} \right]$

where: k_a is the coefficient accounting for anchorage conditions, and k_e is the coefficient describing the number of bonded ends.

Experimental Basis: Deniaud and Cheng (2001b)'s model was developed using a database of 35 test results. The shear test specimens ranged from small to full-scale where the FRP wrapping scheme was either two-side bonding or U-wrap.

A4.2.12 Cao et al. (2005)

This was the first analytical model to consider the effects of pre-cracking. The test results showed a strong relationship between the shear crack angle θ and the shear span-to-effective depth ratio λ. Since λ also has a significant effect on the strain distribution factor, D_{frp}, a modified distribution factor, $D_{f\theta} = D_{frp}/tan\theta$, was developed to represent the effects of both the strain distribution factor as well as the shear crack angle. The simplification for design purposes is given below in terms of λ:

$$D_{f\theta} = \left(1 - \frac{\pi - 2}{\lambda_{frp} \pi} \right) \times \begin{cases} 1 & \text{for } \lambda \le 1.4 \\ \dfrac{1}{1 - 0.2(\lambda - 1.4)^2} & \text{for } 1.4 < \lambda < 3 \\ 2.05 & \text{for } \lambda \ge 3 \end{cases}$$

where: λ_{frp} is the normalized FRP bond length.

Using an approach similar to Chen and Teng (2003a), the maximum FRP strain at debonding is given as:

$$\varepsilon_{f,\max} = \frac{0.427\beta_w \sqrt{f_c^{'}} L_e}{E_f t_f}$$

Meanwhile, the FRP contribution to shear strength is given as:

$$V_f = 2D_{f\theta} t_f w_f E_f \varepsilon_{f,\max} \frac{0.9d}{s_f}$$

Experimental Basis: Cao et al. (2005) performed tests involving 12 pre-cracked reinforced concrete beams with rectangular cross-sections. They used complete wrapped, CFRP and GFRP strips at a 90-degree fiber orientation.

A4.2.13 Zhang and Hsu (2005)

Zhang and Hsu (2005) presented a modified *R* factor from Khalifa et al. (1998). Using the same equation for the contribution of FRP to shear strength, similar to that of steel shear, Zhang and Hsu (2005) proposed a different *R* factor based on bonding mechanism and a new *R* factor based on model calibration from their test results. The equations are given below:

$$V_f = \frac{A_f f_{fe} (\sin\beta + \cos\beta) d_f}{s_f}$$

$$f_{fe} = R f_{fu}, \ \varepsilon_{fe} = R\varepsilon_{fu}$$

$$R = 1.4871 \left(\rho_f E_f / f_c^{'}\right)^{-0.7488}$$ from model calibration through comparison with experimental results

$$R = \frac{\tau_{\max} L_e}{2 f_{fu} t_f} \le 1$$ based on bonding mechanism

Instead of using a polynomial as a best fit, as done by Khalifa et al. (1998), Zhang and Hsu (2005) used a power regression line on a plot of the strain reduction vs. the axial rigidity and compressive strength. In a previous study, Hsu et al. (1997) found that concrete compressive strength played a significant role and proposed the following empirical formula for the ultimate direct shear strength:

$$\tau_{\max} = (7.64 \times 10^{-4} \times f_c^{'2}) - (2.73 \times 10^{-2} \times f_c^{'}) + 6.38 \text{ (unit: MPa)}$$

The relationship between concrete and shear stress, combined with a shear stress distribution which was modeled as a triangle over the effective length, gives the *R* factor above based on the bonding mechanism.

Experimental Basis: Zhang and Hsu (2005) tested 11 RC beams with rectangular cross-sections and without steel shear reinforcement or pre-cracking. They tested specimens with only CFRP strips at 0, 45, and 90 degree fiber orientations.

A4.2.14 Carolin and Taljsten (2005b)

Carolin and Taljsten's (2005b) analytical model is given below

$$V_f = \eta \varepsilon_{cr} E_f t_f r_f z \frac{\cos\theta}{\sin\alpha}$$

where: η is the average fiber utilization (0.60, value authors suggest), $\theta = \alpha + \beta - 90$, α is the angle of the crack inclination, β is the FRP fiber orientation, and ε_{cr} is the critical FRP strain

$$\varepsilon_{cr} = \min \begin{cases} \varepsilon_{fu} \\ \varepsilon_{bond} \cos^2\theta \\ \varepsilon_{c\max} \cos^2\theta \end{cases}$$

where: ε_{fu} is the ultimate tensile strain of the FRP, ε_{bond} is the maximum allowable strain without achieving anchorage failure, and ε_{cmax} is the maximum strain to achieve the concrete contribution. Values were not given in the database for the later two terms and the authors did not provide a way of estimating them, so ε_{fu} was used.

Experimental Basis: This model was derived from a database 23 RC beams with rectangular cross-sections, with and without steel shear reinforcement. The database consisted of specimens with CFRP reinforcement that included full wrapping, two-side bonding, and with 45 and 90 degree fiber orientations.

A4.2.15 Monti and Liotta (2005)

Monti and Liotta (2005) proposed an analytical expression of the stress field in the FRP sheet crossing a shear crack. In this model, V_f is a function of both the adopted strengthening configuration and some basic geometric and mechanical parameters. This model provides expressions for the FRP shear strength that are dependent on the type of wrapping.

$$V_f = \frac{1}{\gamma_{Rd}} \cdot min\{0.9d, h_w\} \cdot f_{fed} \cdot 2t_f \cdot \frac{sin\,\beta}{sin\,\theta} \cdot \frac{w_f}{s_f}$$

$$V_f = \frac{1}{\gamma_{Rd}} \cdot 0.9d \cdot f_{fed} \cdot 2t_f \cdot (cot\,\theta + cot\,\beta) \cdot \frac{w_f}{s_f}$$

where: γ_{Rd} is the partial coefficient; h_w is the depth of the web in case of T sections; f_{fed} is the design effective stress of the FRP.

In the case of side-bonding, the design effective stress is given as:

$$f_{fed} = f_{fdd} \cdot \frac{z_{rid,eq}}{min\{0.9d, h_w\}} \cdot \left(1 - 0.6\sqrt{\frac{l_{eq}}{z_{rid,eq}}}\right)^2$$

where: $z_{rid,eq} = z_{rid} + l_{eq}, z_{rid} = min\{0.9d, h_w\} - l_e \sin\beta$, $l_{eq} = \frac{slip}{f_{fdd} / E_f} \sin\beta$

In the case of U-jacking, the design effective stress is given as:

$$f_{fed} = f_{fdd} \cdot \left[1 - \frac{1}{3} \frac{l_e \sin\beta}{min\{0.9d, h_w\}}\right]$$

In the case of wrapping, the design effective stress is given as:

$$f_{fed} = f_{fdd} \cdot \left[1 - \frac{1}{6} \frac{l_e \sin\beta}{min\{0.9d, h_w\}}\right] + \frac{1}{2}(\phi_R f_{fd} - f_{fdd}) \cdot \left[1 - \frac{l_e \sin\beta}{min\{0.9d, h_w\}}\right]$$

In above equations, f_{fdd} is the debonding strength, f_{fd} is the design ultimate strength, l_e is the effective bond length, and ϕ_R is a coefficient accounting for the influence of the rounding radius on the ultimate strength of FRP in the case of wrapping.

Experimental Basis: Monti and Liotta (2005) tested 24 beam specimens strengthened with FRP in shear. The beam cross-sections were rectangular with a width of 250 mm wide and an overall height of 450 mm. The concrete mean compressive cubic strength was 13.3 MPa. Side-bonding, U-jacketing, and full wrapping were used in the application of the FRP reinforcement. All strips/sheets were in a single layer of CFRP that had a thickness of 0.22 mm and an elastic modulus of 390 GPa.

A4.2.16 Pellegrino et al. (2008)

Pellegrino et al. (2008) continued to expand the experimental database on effective bond length, L_e. They contributed new tests that cover a wide range of FRP axial rigidities. From these tests, a new L_e equation is proposed that takes into account a new value of constant c_2 and a superior limit.

$$L_e = (n_f E_f t_f)^{1/2} / (c_2 f_{ctm})^{1/2} \text{ with } L_e \leq 140 \text{ mm and } c_2 = 21.5$$

The influence of FRP stiffness on maximum bond/shear stress, slip at peak bond strength, and slip at ultimate peak stress was also compared to previous models. From the experimental results, a new relationship for FRP stiffness at the maximum bond/shear stress can be found.

$$\tau_{\max} = 3.1(n_f t_f E_f)^{0.32}$$

New values for s_{peak} were found experimentally to be lower than the earlier proposed models while the new values for $_{sult}$ were higher than previous models. This led to the following equations for both s_{peak} and s_{ult}.

$$s_{peak} = \frac{0.075}{(n_f t_f E_f)^{0.2}}$$

$$s_{ult} = \frac{10.5}{(n_f t_f E_f)^{0.6}}$$

Experimental Basis: The tests consisted of thirty-nine specimens tested in double-shear and bending setups. The double shear test setup consisted of two concrete prisms 100mm x 100mm x 300mm, connected through two CFRP strips 50mm wide and externally bonded to two opposite sides of the concrete prisms. The bending tests also consisted of two concrete prisms of the same dimensions connected through a CFRP strip externally bonded to the lower side of the prisms.

A4.3 Models for V_f in Current Guidelines and Code Specifications

Provisions for evaluating the contribution of FRP shear reinforcement to shear capacity have been incorporated into codes of practice and other documents of professional organizations. Unlike the models proposed by individual researchers, these selected relationships for V_f would be expected to have considered a broader range of application and been calibrated by a larger database of test results. Unfortunately, it is typically difficult to trace what database has been used for these calibrations which may explain some of the large differences in the strengths predicted by the different methods as will be illustrated in section A4.6.

A4.3.1 Canadian Standards Association S806-02 (CAN/CSA S806, 2002)

Canadian Standards Association S806-02 (CAN/CSA S806, 2002) specifies the shear capacity provided by FRP sheets as:

$$V_f = \frac{\phi_F A_F E_F \varepsilon_F d_f}{s_F}$$

where: ϕ_F is resistance factor of FRP composites.

In the absence of more precise information, the value of effective strain ε_F may be conservatively assumed to be as follows:

- for U-shaped wrap continuous around the bottom of the web, $\varepsilon_F = 4000\mu\varepsilon$
- for side bonding to the web (and only in cases where sufficient development length cannot be provided), $\varepsilon_F = 2000\mu\varepsilon$.

A4.3.2 ACI 440.2R-08 (ACI 440, 2008)

ACI 440.2R-08 (ACI 440, 2008) determines the shear contribution of the FRP shear reinforcement by calculating the force resulting from the tensile stress in the FRP across an assumed 45° crack. The shear capacity provided by FRP is given as

$$V_f = \frac{A_{fv} f_{fe} (\sin\alpha + \cos\alpha) d_f}{s_f}$$

where: $A_{fv} = 2nt_f w_f$ is area of FRP with spacing s_f.

The effective stress in the FRP shear reinforcement at ultimate is directly proportional to the effective strain ε_{fe} in FRP at ultimate as follow:

$$f_{fe} = \varepsilon_{fe} E_f$$

The effective strain ε_{fe} is then determined according to different configurations of FRP laminates used for shear strengthening of reinforced concrete members. For completely wrapped members, the effective strain is given as follows:

$$\varepsilon_{fe} = 0.004 \le 0.75\varepsilon_{fu}$$

where: ε_{fu} is the design rupture strain of FRP reinforcement.

For bonded U-wraps or bonded face plies, the effective strain is calculated using the following equations:

$$\varepsilon_{fe} = k_v \varepsilon_{fu} \le 0.004$$

$$k_v = \frac{k_1 k_2 L_e}{11{,}900\varepsilon_{fu}} \le 0.75 \text{ (SI)}$$

$$L_e = \frac{23{,}300}{(nt_f E_f)^{0.58}} \text{ (SI)}$$

$$k_1 = \left(\frac{f_c'}{27}\right)^{2/3} \text{ (SI)}$$

$$k_2 = \begin{cases} \dfrac{d_f - L_e}{d_f} & for\, U\text{-}wraps \\ \dfrac{d_f - 2L_e}{d_f} & for\, two\ sides\ bonded \end{cases}$$

A4.3.3 European fib-TG 9.3 Bulletin 14 (fib-TG9.3, 2001)

European fib-TG 9.3 Bulletin 14 (fib-TG9.3, 2001) calculates the FRP contribution to shear capacity (V_{fd}) using the following equation:

$$V_{fd} = 0.9\varepsilon_{fd,e} E_{fu} \rho_f b_w d(\cot\theta + \cot\alpha)\sin\alpha$$

The design value of the effective FRP strain, $\varepsilon_{fd,e}$, may be approximated by multiplying the mean value of the effective FRP strain, $\varepsilon_{f,e}$, by a reduction factor, k, as:

$$\varepsilon_{fd,e} = k\varepsilon_{f,e} \qquad \text{k = 0.8}$$

The mean value of the effective FRP strain, $\varepsilon_{f,e}$, is given for different FRP types and different configurations of FRP as given below.

For fully wrapped (or properly anchored) CFRP:

$$\varepsilon_{f,e} = 0.17\left(\frac{f_{cm}^{2/3}}{E_{fu}\rho_f}\right)^{0.30} \varepsilon_{fu}$$

For Side or U-shaped CFRP jackets:

$$\varepsilon_{f,e} = min\left[0.65\left(\frac{f_{cm}^{2/3}}{E_{fu}\rho_f}\right)^{0.56} \times 10^{-3}, \quad 0.17\left(\frac{f_{cm}^{2/3}}{E_{fu}\rho_f}\right)^{0.30} \varepsilon_{fu}\right]$$

For fully wrapped AFRP:

$$\varepsilon_{f,e} = 0.048\left(\frac{f_{cm}^{2/3}}{E_{fu}\rho_f}\right)^{0..47} \varepsilon_{fu}$$

Note that in all equations, f_{cm} is in MPa and E_{fu} is in GPa.

A4.3.4 D4.3.4 Japanese JSCE Recommendations (JSCE, 2001)

Japanese JSCE Recommendations (JSCE, 2001) calculate the FRP contribution to shear capacity, V_{fd}, as:

$$V_{fd} = K\frac{A_f f_{fud} z(\sin\alpha_f + \cos\alpha_f)}{s_f}$$

where: K is shear reinforcing efficiency, A_f is total cross-sectional area of fiber sheet in space s_f, f_{fud} is the design tensile strength of FRP, z is the lever arm length set to d/1.15, and α_f is the angle between principal fiber orientation and longitudinal axis of the member.

The shear reinforcing efficiency (K) is expressed in terms of the elastic modulus (E_f) and the amount of FRP (ρ_f) as given below.

$K = 1.68 - 0.67R$, however, $0.4 \le K \le 0.8$

$$R = (\rho_f E_f)^{1/4} \left(\frac{f_{fud}}{E_f} \right)^{2/3} \left(\frac{1}{f'_{cd}} \right)^{1/3}, \text{ however, } 0.5 \le R \le 2.0$$

In the above equations, f_{fud} is in MPa and E_f is in GPa.

A4.4 AASHTO LRFD Shear Design Provisions (AASHTO, 2008)

As described in the introduction to this section , the selected expression for V_f will need to be calibrated to work with existing AASHTO LRFD relationships (AASHTO, 2008) for V_c and V_s so that the resulting average bias and COV (Coefficient of Variation) of the ratio of V_{test}/V_n (where $V_n = V_c + V_s + V_f$) produces the needed level of reliability – as presented later in Section A7. A challenge to this calibration is that there are multiple approaches in the AASHTO LRFD Specifications (AASHTO, 2008) for calculating the V_c and V_s contributions to shear resistance. These approaches are summarized below. The selected method for the calibration of selected relationships for V_f is presented at the end of Section A4.4. It is the expectation that the final location for V_f within the AASHTO LRFD specifications (AASHTO, 2008) will be determined based on discussions with AASHTO subcommittees and that an additional calibration may be required after that determination.

The AASHTO LRFD Bridge Design Specifications (AASHTO, 2008) provide six different methods for evaluating the shear capacity of members. Five of these are sectional design procedures, and one is for the design by the strut-and-tie methods. The range of applicability of each of these methods and key relationships are provided below. These relationships are provided in multiple units, in ksi units as currently used in the AASHTO LRFD specifications (AASHTO, 2008), in the often more familiar psi units which is the system for which many of these relationships were derived, and finally in MPa units which is the unit of choice for nearly all of the models for V_f that have been proposed by researchers, incorporated into design guidelines and codes, and used in the database of test results.

A4.4.1 Simplified Method for Non-Prestressed Sections (Article 5.8.3.4.1)

This method is applicable to beams that are less than 16 inches deep with or without steel shear reinforcements, beams greater than 16 inches when minimum shear reinforcement is provided, and footings when the point of zero shear to face of column/wall is less than $3d_v$.

This method is essentially equivalent to the approach in the AASHTO Standard Specifications for Highway Bridges (AASHTO, 2002) and ACI 318-08 (ACI 318, 2008) for evaluating the shear capacity of non-prestressed sections for which the basic concrete stress at ultimate is taken as $2\sqrt{f'_c}$ (psi) and a 45 degree truss (θ = 45) is used for calculating the contribution of steel stirrup reinforcement. With these values, the basic relationships for this approach are determined as given below.

$V_c = 0.0316\beta\sqrt{f'_c}b_v d_v$ (5.8.3.3-1), where $\beta = 2$ and therefore $V_c = 0.0632\sqrt{f'_c}b_v d_v$ (f'_c in ksi)

This is equivalent to $V_c = 2\sqrt{f'_c}b_v d_v$ (f'_c in psi) and $V_c = 0.167\sqrt{f'_c}b_v d_v$ (f'_c in MPa)

$V_s = \dfrac{A_v f_y d_v(\cot\theta + \cot\alpha)\sin\alpha}{s}$ (5.8.3.3-4), with $\theta = 45°$ & $\alpha = 90°$ then $V_s = \dfrac{A_v f_y d_v}{s}$

A4.4.2 Article 5.8.3.4.2 General Procedure (Article 5.8.3.4.2)

This method is applicable to all prestressed and non-prestressed sections where it is appropriate to assume that plane sections remain plane.

In this method, V_c and V_s are functions of β and θ where these in turn are functions of the calculated strain in the longitudinal tension reinforcement. The strain in the longitudinal reinforcement is taken as the demand on this reinforcement divided by its axial stiffness. This demand considers the actions of Shear (V_u), and the coincident Moment (M_u), Axial Load (N_u), and prestressing force ($A_{ps}f_{po}$). The reinforcement consists of both non-prestresssed and prestressed reinforcements.

The relationships for β and θ, as presented below, were derived from the Modified Compression Field Theory (MCFT), and introduced in the AASHTO LRFD specifications in 2007 (AASHTO, 2007). The parameter β controls the contribution of the concrete to shear resistance and this is limited by the interface transfer resistance along shear cracks. The contribution of the stirrups to resistance is based on the parallel chord truss model where the angle of diagonal compression, θ, is based on the calculated state of strain in the web of the beam as influenced by the applied forces acting on the section and the non-linear material response characteristics. To derive these simplified expressions from the MCFT, it was necessary to make several assumptions, including that:

- the strain at peak compressive stress is -0.002
- the transverse (vertical) strain at the ultimate limit state is 0.002
- the maximum size of the aggregate is 19 mm (0.75 inches)
- a parabolic stress strain response of the concrete in compression
- a 12 inch crack spacing in members with minimum transverse shear reinforcement

In the general procedure, V_c and V_s are evaluated by 5.8.3.3-1 and 5.8.3.3-4.

$$V_c = 0.0316\beta\sqrt{f'_c}b_v d_v \quad (5.8.3.3\text{-}1) \text{ and } V_s = \frac{A_v f_y d_v(\cot\theta + \cot\alpha)\sin\alpha}{s} \quad (5.8.3.3\text{-}4)$$

where

$\beta = \dfrac{4.8}{(1+750\varepsilon_s)}$ for members with minimum steel shear reinforcement

$\beta = \dfrac{4.8}{(1+750\varepsilon_s)}\dfrac{51}{(39+s_{xe})}$ for members without minimum steel shear reinforcement

$\theta = 29 + 3500\varepsilon_s$ for all members, and where

$$\varepsilon_s = \frac{\left(\frac{|M_u|}{d_v} + 0.5N_u + |V_u - V_p| - A_{ps} f_{po} \right)}{E_s A_s + E_p A_{ps}}$$

A4.4.3 Appendix B5 General Procedure

This method is also applicable to all prestressed and non-prestressed sections where it is appropriate to assume that plane sections remain plane. It was the previous General Procedure and differs from the new method in Article 5.8.3.4.2 (just presented) in that β and θ are found through tables as a function of the longitudinal strain, depth, and normalized level of shear stress (v/f'_c). The values for β and θ as given in these tables differ to some degree to what is calculated by the equations in Article 5.8.3.4.2. In this approach, the longitudinal strain is evaluated as that at mid-depth of the beam, and the angle of diagonal compression is considered in evaluating the influence of shear demand on longitudinal straining. This approach is maintained in an appendix to the AASHTO LRFD Bridge Design Specifications (AASHTO, 2008). The main relations and tables for this approach are given below.

To obtain values for β and θ from Table A 4.1 ($A_v \geq A_{v,min}$), it is necessary to compute the shear design stress ratio (v/f'_c) and the longitudinal strain ε_x at mid-depth. The longitudinal strain ε_x may be taken as one-half of the strain in the longitudinal tension reinforcement, ε_t, as computed below

$$\varepsilon_x = \frac{\varepsilon_t}{2} = \frac{M_u / d_v + 0.5N_u + 0.5(V_u - V_p)cot(\theta) - A_{ps} f_{po}}{2(E_s A_s + E_p A_{ps})} \leq 0.002$$

To obtain values for β and θ when $A_v < A_{v,min}$, Table A 4.2 is used. The column of Table A 4.2 is based on the value of the longitudinal strain at mid-depth, ε_x, as computed above, and the row is determined using the spacing of the layers of crack control reinforcement s_{xe} as

$$s_{xe} = \frac{1.38 s_x}{0.63 + a_g} \ (in.)$$

where: a_g is the maximum aggregate size in inches.

Table A 4.1 Determination of β and θ for Members with at least Minimum Shear Reinforcement

$\frac{v_u}{f_c'}$	$\varepsilon_x \times 1{,}000$								
	≤−0.20	≤−0.10	≤−0.05	≤0	≤0.125	≤0.25	≤0.50	≤0.75	≤1.00
≤0.075	22.3 6.32	20.4 4.75	21.0 4.10	21.8 3.75	24.3 3.24	26.6 2.94	30.5 2.59	33.7 2.38	36.4 2.23
≤0.100	18.1 3.79	20.4 3.38	21.4 3.24	22.5 3.14	24.9 2.91	27.1 2.75	30.8 2.50	34.0 2.32	36.7 2.18
≤0.125	19.9 3.18	21.9 2.99	22.8 2.94	23.7 2.87	25.9 2.74	27.9 2.62	31.4 2.42	34.4 2.26	37.0 2.13
≤0.150	21.6 2.88	23.3 2.79	24.2 2.78	25.0 2.72	26.9 2.60	28.8 2.52	32.1 2.36	34.9 2.21	37.3 2.08
≤0.175	23.2 2.73	24.7 2.66	25.5 2.65	26.2 2.60	28.0 2.52	29.7 2.44	32.7 2.28	35.2 2.14	36.8 1.96
≤0.200	24.7 2.63	26.1 2.59	26.7 2.52	27.4 2.51	29.0 2.43	30.6 2.37	32.8 2.14	34.5 1.94	36.1 1.79
≤0.225	26.1 2.53	27.3 2.45	27.9 2.42	28.5 2.40	30.0 2.34	30.8 2.14	32.3 1.86	34.0 1.73	35.7 1.64
≤0.250	27.5 2.39	28.6 2.39	29.1 2.33	29.7 2.33	30.6 2.12	31.3 1.93	32.8 1.70	34.3 1.58	35.8 1.50

Table A 4.2 Determination of β and θ for Members with less than Minimum Shear Reinforcement

s_{xe} (in.)	$\varepsilon_x \times 1000$										
	≤–0.20	≤–0.10	≤–0.05	≤0	≤0.125	≤0.25	≤0.50	≤0.75	≤1.00	≤1.50	≤2.00
≤5	25.4 6.36	25.5 6.06	25.9 5.56	26.4 5.15	27.7 4.41	28.9 3.91	30.9 3.26	32.4 2.86	33.7 2.58	35.6 2.21	37.2 1.96
≤10	27.6 5.78	27.6 5.78	28.3 5.38	29.3 4.89	31.6 4.05	33.5 3.52	36.3 2.88	38.4 2.50	40.1 2.23	42.7 1.88	44.7 1.65
≤15	29.5 5.34	29.5 5.34	29.7 5.27	31.1 4.73	34.1 3.82	36.5 3.28	39.9 2.64	42.4 2.26	44.4 2.01	47.4 1.68	49.7 1.46
≤20	31.2 4.99	31.2 4.99	31.2 4.99	32.3 4.61	36.0 3.65	38.8 3.09	42.7 2.46	45.5 2.09	47.6 1.85	50.9 1.52	53.4 1.31
≤30	34.1 4.46	34.1 4.46	34.1 4.46	34.2 4.43	38.9 3.39	42.3 2.82	46.9 2.19	50.1 1.84	52.6 1.60	56.3 1.30	59.0 1.10
≤40	36.6 4.06	36.6 4.06	36.6 4.06	36.6 4.06	41.2 3.20	45.0 2.62	50.2 2.00	53.7 1.66	56.3 1.43	60.2 1.14	63.0 0.95
≤60	40.8 3.50	40.8 3.50	40.8 3.50	40.8 3.50	44.5 2.92	49.2 2.32	55.1 1.72	58.9 1.40	61.8 1.18	65.8 0.92	68.6 0.75
≤80	44.3 3.10	44.3 3.10	44.3 3.10	44.3 3.10	47.1 2.71	52.3 2.11	58.7 1.52	62.8 1.21	65.7 1.01	69.7 0.76	72.4 0.62

If ε_x is negative, then the member is uncracked and the axial stiffness of the uncracked concrete needs to be considered as follows

$$\varepsilon_x = \frac{M_u / d_v + 0.5N_u + 0.5(V_u - V_p)cot(\theta) - A_{ps} f_{po}}{2(E_s A_s + E_p A_{ps} + A_{ct} E_c)}$$

where A_{ct} is the area of the concrete beneath mid-depth.

A4.4.4 Simplified Procedure for Prestressed and Nonprestressed Sections (Article 5.8.3.4.3)
This procedure is applicable to all beams that are not subjected to axial tension and that contain the minimum level of steel shear reinforcement. This method is similar to the AASHTO Standard Specifications for Highway Bridges (AASHTO, 2002) and ACI 318-08 (ACI 318, 2008), but where a new relationship has been introduced for web-shear strength (V_{cw}) and the contributions of the steel shear reinforcement (V_s) is based on a variable angle truss model. The nominal shear strength, V_n, is the sum of the concrete contribution, V_c, and shear reinforcement contribution, V_s, as given below.

$$V_n = V_c + V_s \quad (in., ksi)$$

The concrete contribution V_c is taken as the smaller of V_{cw}, the resistance to web-shear cracking, and V_{ci}, the resistance to flexure-shear cracking, as given below.

$$V_{cw} = (0.06\sqrt{f'_c} + 0.30 f_{pc}) b_v d_v + V_p \quad (in., ksi)$$

$$V_{ci} = 0.02\sqrt{f'_c} b_v d_v + V_d + \frac{V_i M_{cre}}{M_{max}} \geq 0.06\sqrt{f_c^{'}} b_v d_v \quad (in., ksi)$$

where: $M_{cr} = \frac{I}{y_t}(0.19\sqrt{f_c^{'}} + f_{pe} - f_d)\,(in.,ksi)$

$$V_{cw} = (3.5\sqrt{f_c^{'}} + 0.3 f_{pc}) b_w d + V_p \quad (in., psi)$$

$$V_{ci} = 0.6\sqrt{f_c^{'}} b_w d + V_d + \frac{V_i M_{cr}}{M_{\max}} \quad (in., psi)$$

where: $M_{cr} = \frac{I}{y_t}(6\sqrt{f_c^{'}} + f_{pe} - f_d)\,(in., psi)$

The contribution of the steel shear reinforcement, V_s, is calculated as:

$$V_s = \frac{A_v f_y d_v \cot\theta}{s} \quad (in., ksi)$$

where: $cot\,\theta$ can be derived from Mohr's circle or stress to consider the effects of prestressing on cracking stress, as follows:

$$\cot\theta = \begin{cases} 1.0, \text{if } V_{ci} \text{ is less than } V_{cw}; \\ 1.0 + 3\dfrac{f_{pc}}{\sqrt{f_c^{'}}} \le 1.8(\text{ksi, in}), \text{ if } V_{ci} \text{ is greater } V_{cw}. \end{cases}$$

A4.4.5 Shear and Torsion for Segmental Box Girder Bridges (Article 5.8.6.5)
This approach is applicable to post-tensioned box-girder bridges where is it appropriate to assume that plane sections remain plane. For non-prestressed sections, it is the same as the simplified approach in Article 5.8.3.4.1 as given in A4.4.1. For prestressed section, V_c is modified as follows.

$$V_c = 0.0632K\sqrt{f'_c}b_v d_v \text{ , where } K = \sqrt{1 + \frac{f_{pc}}{0.0632\sqrt{f'_c}}} \le 2.0 \, (f'_c \text{ in ksi})$$

$$V_c = 2K\sqrt{f'_c}b_v d_v \text{ , where } K = \sqrt{1 + \frac{f_{pc}}{2\sqrt{f'_c}}} \le 2.0 \, (f'_c \text{ in psi})$$

where: f_{pc} is the unfactored compressive stress in concrete after prestress losses have occurred either at the centroid of the cross-section resisting transient loads or at the junction of the web and flange where the centroid lies in the flange. The contribution of the steel shear reinforcement is based on a 45 degree parallel chord truss.

A4.4.6 Strut-and-Tie Model (Article 5.6.3)
This design methodology is to be used when it is not reasonable to assume that plane sections will remain plane, such as in the end regions of beams in which the shear span-to-depth ratio (*a/d*) is less than 2.

A4.4.7 Selection of Model for V_c and V_s to Use in Assessment
Given the multitude of methods for evaluating the contributions of V_c and V_s to shear capacity in the AASHTO LRFD Specifications (AASHTO, 2008) and the interdependencies between V_c and V_s for each of these methods, it is expectated that the location or locations for V_f in the AASHTO LRFD specifications (AASHTO, 2008) will be determined through discussions with AASHTO subcommittees, and that upon this some recalibration of the expression for V_f will be needed. Regardless, and for the purpose of this project, a base model for V_c and V_s needs to be selected to complete all of the steps for a calibration. The selected model is that in Articles 5.8.3.4.1 (Simplified Procedure for Nonprestressed Sections), in Article 5.8.3.4.2 (General Procedure) when minimum steel shear reinforcement is provided or when the member depth or maximum spacing of distributed longitudinal reinforcement is less than 12 inches, and in Article 5.8.3.4.3 (Simplified Method for Prestressed and Nonprestressed Sections). In all cases, it may only be used when $d_v/b \le 4$ so to guard against the development of diagonal compression failures driving by tearing of the web by the FRP reinforcement as discussed in A4.8. The selected model is that of the simplified procedure presented in A4.4.1 and given by the following:

$V_c = 0.0316\beta\sqrt{f'_c}b_v d_v$ (5.8.3.3-1)

where: $\beta = 2$ and therefore $V_c = 0.0632\sqrt{f'_c}b_v d_v$ (f'_c in ksi)

This is equivalent to $V_c = 2\sqrt{f'_c}b_v d_v$ (f'_c in psi) and $V_c = 0.167\sqrt{f'_c}b_v d_v$ (f'_c in MPa)

$$V_s = \frac{A_v f_y d_v(\cot\theta + \cot\alpha)\sin\alpha}{s} \text{ (5.8.3.3-4), with } \theta = 45° \& \alpha = 90° \text{ then } V_s = \frac{A_v f_y d_v}{s}$$

While this method is not applicable to members greater than 16 inches in depth that do not contain shear reinforcement, the relationship provided for V_c is identical to that in the General Procedure (Section A4.4.2) which is applicable to such members when distributed horizontal reinforcement is placed on 12 inch centers and the strain in the longitudinal reinforcement is less than 0.00187. This usually conservative but not unrealistic assumption is made for the purpose of this evaluation.

$$\beta = \frac{4.8}{(1+750\varepsilon_s)}\frac{51}{(39+s_{xe})} = \frac{4.8}{(1+750(0.00187))}\frac{51}{(39+12)} = 2.00$$

A4.5 Experimental Database of Test Results

Prior to making a comparative assessment of the different methods for calculating V_f, it is essential to begin with a critical review of the experimental test data. This review led to only a segment of the total test data being subsequently used in the comparative evaluation. This section will present a discussion of the experimental test data, criteria for the selection of a subset of the data to be used for the comparative evaluation of the models for V_f, and the effect of this criteria on the available data for the evaluations.

The collected database consisted of 410 beams with FRP reinforcement and 132 associated control beams. Of the 410 beams with FRP reinforcements, 50 could not be further considered for use due to missing information, such as sufficient details to define the amount of FRP used, the total shear strength, V_{test}, or the experimentally measured strength provided by the FRP, $V_{f,test} = V_{test} - V_{control}$. The left side of Table A 4.3 presents a summary of key characteristics of the control beams (CBs) and the remaining 360 beams with FRP reinforcements. As shown, a slight majority of the beams had steel shear reinforcements, most beams were more than 300 mm (11.8 in.) deep, few were more than 500 mm (19.7 in.) deep, and the majority of the beams would be considered slender with a shear span to depth ratio (*a/d* ratio) greater than 2.5.

A critical examination of the control beams and beams with FRP reinforcements was made in order to only use test data in the evaluation and calibration of relationship for V_f that were considered relevant and would not unwisely skew these assessments. The right side of Table A 4.3 presents a summary of key features of the final database of 266 beams that were considered "valid" to calibrate the proposed relationships for V_f in the LRFD specifications as completed in A4.7. This breakdown includes the number of beams with FRP reinforcements in which FRP debonding, FRP rupture, and other modes of failure were observed. The rationale used for

eliminating test results to use in the calibration of these specifications, and a description of this data, and the associated control beams is given below.

Table A 4.3 Number of Beams in Complete and Valid Experimental Databases

	All Beams		Valid Beams Only				
	CB	FRP	CB	FRP	Deb	RuP	Other
All	132	360	125	266	128	62	76
No Av	59	157	59	118	47	29	42
With Av	73	203	66	148	81	33	34
h ≥ 300 mm	96	263	89	199	100	46	53
h ≥ 500 mm	18	51	18	49	14	19	16
a/d ≥ 2.5	94	270	88	226	116	45	65

The initial and subsequently abandoned approach for creating this evaluation database was to establish rigid acceptance criteria so that the selected database would most represent the types of members in the field and that beam shear, as opposed to arch action, was ensured. However, when applying a combination of suitable criteria, the number of beams left in the database for calibration was unacceptably low. Thereby, the evaluation database was selected through a beam by beam elimination methodology. For each test result, key parameters were calculated including more than a dozen geometric parameters such as reinforcement percentage, the measured effectiveness of the FRP reinforcement in terms of effective strain, $R = \varepsilon_{fe} / \varepsilon_{fu}$, as well as effective strength ratios of $V_{f,test}/V_{f,models}$ and V_{test}/V_n (where $V_n = V_c + V_s$ + selected V_f models), and the latter both for the test beam with FRP reinforcement and the associated control beam. Several plots where tables were then simultaneously displayed, such as V_{test}/V_n versus beam height, so that the effect of eliminating individual data points on V_f model selection and calibration could be readily seen. Some of the primary considerations for elimination are given below.

- If the ratio of V_{test}/V_n of the control beam was less than about 0.7, then it was then the case that the ratio of V_{test}/V_n of the associated beams with FRP reinforcement was usually low. Thus, even through $V_{f,test}$ in this situation may have been useful for selection of the model for V_f, the overall ratio of V_{test}/V_n was not appropriate to consider for the calibration of V_f for use in combination with V_c and V_s in the AASHTO LRFD specifications (AASHTO, 2008).
- If members with a/d ratios less than two had high ratios of V_{test}/V_n ratios, as these would shift the mean upwards and attribute a great safety in the application of V_f models than would be expected for slender beams (a/d > 2.5).
- Very low concrete strength when the ratio of $V_{f,test}/V_{f,models}$ and V_{test}/V_n was outside of usual ranges.
- Low ratios of V_{test}/V_n (less than about 1) when shear failures were not observed. Results were included when moderate (1-2) or higher (> 2) V_{test}/V_n ratios were measured even if non-shear modes of failure were reported. This is reasonable for the following reason. If the FRP shear reinforcement performed so effectively that the flexural capacity of the member was reached,

then the effectiveness of the FRP shear strengthened beam is at least the reported ratio of V_{test}/V_n and then this test result provides a lower bound estimate of strength gain and should be included.

- For similar reasons as in the previous point, beam results were eliminated when the ratio of V_{test}/V_n was low for members in which the ratio of the spacing the steel shear reinforcement to depth of the beam *s/d* exceeded 0.75 and not if the ratios were moderate or high.
- While it was originally anticipated that the overall depth of the beam (*h*) would be a significant factor for data elimination, whereby tests from small beams with very high V_{test}/V_n ratios were eliminated, an examination of the data indicated that applying a strict criteria for elimination based on height was not needed.

The above provides a general description of the type of member by member elimination approach was applied to produce a 266 member database of "valid" test results for calibration of V_f for use in the AASHTO LRFD Bridge Design Specifications (AASHTO, 2008). This approach was considered to preserve as much of the test data as possible for model calibration and validation.

The distribution of test parameters in this "valid" set of test beams with FRP reinforcements, as broadly given in Table A 4.3 is more fully presented in Figure A 4.1 and with respect to the following parameters:
(a) overall depth of beam or height (*h*)
(b) shear span to depth ratio (*a/d*)
(c) ratio of spacing of steel shear reinforcement to depth of beam (*s/d*)
(d) axial rigidity of provided FRP reinforcement ($\rho_f E_f$)
(e) strength of provided FRP reinforcement ($\rho_f f_{fu}$)
(f) normalized shear stress at failure ($V_{test}/(b_v d_v (f'_c)^{0.5})$)
(g) amount of provided steel shear reinforcement ($\rho_v f_y$)
(h) compressive strength of concrete (f'_c)

As shown, the distribution of test parameters values does not well represent the types of members that would be used in the field. Most bridge beams are large and slender, contain flanges and web reinforcement, and a large portion of them are continuous. One of the effects of this is that the experimental database is only useful for evaluating shear behavior near simple supports where there is little moment action on the section. Many other observations can be made from Figure A4.1 on the features of the database, including:

- Figure A 4.1(a): only 13 test beams are greater than 24 inches in depth, the majority of which are test results from this project
- Figure A 4.1(b): nearly one-half of the beams have an a/d ratio between 2.5 and 3
- Figure A 4.1(c): about one-third of the beams have a s/d ratio of 0.75 or greater, which is well above that acceptable in the AASHTO LRFD specifications (AASHTO, 2008)
- Figure A 4.1(d&e): the majority of the testing has been on beams in which a lighter level and strength of FRP reinforcement was provided

- Figure A 4.1(f): the majority of the shear test strength at failure are well less than one-half of the maximum AASHTO LRFD (AASHTO, 2008) shear design stress
- Figure A 4.1(g): in cases where steel shear reinforcement has been provided, the amount (or strength) of the provided reinforcement has been low to modest, only exceeding a couple times the minimum required level of shear reinforcement
- Figure A 4.1(h): very limited test data is available on members cast with higher strength concretes

	min (in.)	max (in.)	height (count)
1	0	6	20
2	6	12	127
3	12	18	70
4	18	24	36
5	24	30	2
6	30	40	11

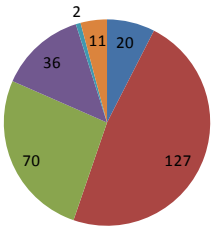

(a) overall depth of beams or height (h)

	min	max	a/d ratio (count)
1	0	1.5	3
2	1.5	2	9
3	2	2.5	28
4	2.5	3	124
5	3	4	92
6	4	5	10

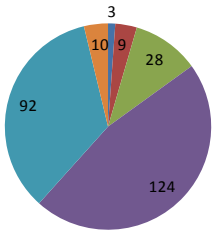

(b) shear span-to-depth ratio (*a/d*)

	min	max	s/d ratio (count)
1	0	0.25	2
2	0.25	0.5	45
3	0.5	0.75	43
4	0.75	1	20
5	1	2	10
6	2	3	28

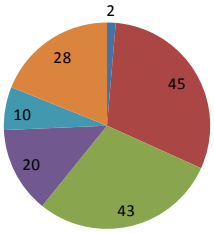

(c) ratio of spacing to depth of steel shear reinforcement (*s/d*)

	min (ksi)	max (ksi)	pfEf (count)
1	0	25	72
2	25	50	83
3	50	75	44
4	75	100	17
5	100	200	35
6	200	300	14

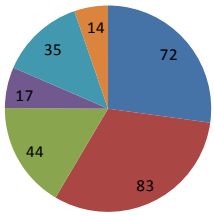

(d) axial rigidity of provided reinforcement ($\rho_f E_f$)

	min (ksi)	max (ksi)	pf(ffu) (count)
1	0	0.25	32
2	0.25	0.5	60
3	0.5	0.75	58
4	0.75	1	20
5	1	2	56
6	2	7	40

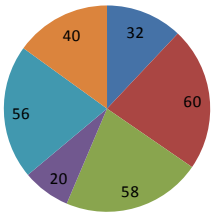

(e) axial strength of provided FRP reinforcement ($\rho_f f_{fu}$)

	min	max	vt/sqrt(f'c) (count)
1	0	4	8
2	4	6	76
3	6	8	78
4	8	10	36
5	10	12	30
6	12	22	38

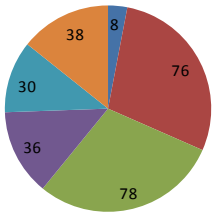

(f) normalized shear stress at failure ($V_{test}/(b_v d_v (f'_c)^{0.5})$)

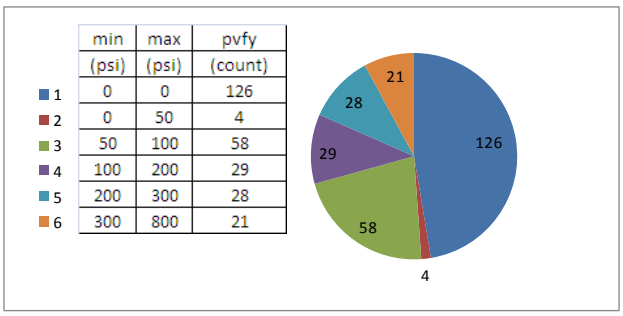

(g) amount of provided steel shear reinforcement ($\rho_v f_y$)

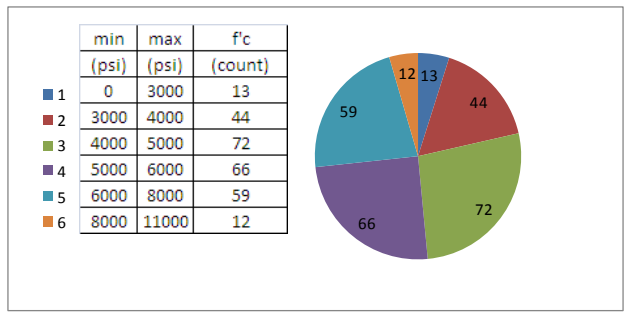

(h) compressive strength of concrete (f'_c)

Figure A 4.1 Distribution of Test Data as a Function of Key Parameters

A4.6 Comparative Evaluation of Analytical Models

This section uses the evaluation database presented in Section A4.5 to make a comparative assessment of the accuracy of 21 existing analytical models. These models are: (1) Al-Sulaimani et al., 1994; (2) Chajes et al., 1995; (3) Triantafillou 1998a and Triantafillo and Antonopoulos 2000; (4) Malek and Saadatmanesh, 1998; (5) Khalifa et al., 1998; (6) Khalifa and Nanni, 2000; (7) Hutchinson and Rizkalla, 1999; (8) Chaallal et al., 2002; (9) Chen and Teng, 2003a,b; (10) Pellegrino and Modena, 2002; (11) Hsu et al., 2003; (12) Cao et al., 2005; (13) Deniaud and Cheng, 2001; (14) Zhang and Hsu, 2005; (15) Carolin and Taljsten, 2005b; (16) Monti and Liotta, 2005; (17) Pellegrino et al., 2008; (18) European fib-TG9.3, 2001; (19) Japanese JSCE Recommendation, 2001, (20) CSA S806-02, 2002; (21) ACI 440.2R-08, 2008.

All models employ the parallel short truss model for evaluating the contribution of FRP reinforcements, as presented below.

$$V_f = \frac{A_f f_{fe} d_f (\cot\theta + \cot\alpha)\sin\alpha}{s}$$

or

$$V_f = \rho_f f_{fe} b_v d_f (\cot\theta + \cot\alpha)\sin\alpha$$

In the application of this relationship in this study, the angle of diagonal compression (θ) was taken as 45°, which is a common assumption used in US design practice. With this, and for a given amount and angle (α) of FRP shear reinforcement, the parameter that controls the FRP contribution to shear resistance is the average effective FRP reinforcement stress (f_{fe}) at the point of maximum shear capacity. Given the close to linear relationship between the stress and strain in the FRP reinforcement up to close to the ultimate capacity, this effective may be taken as $f_{fe} = E_f \varepsilon_{fe}$ where ε_{fe} is the effective strain in the FRP reinforcement at the ultimate shear limit state. Thus, researchers who have examined the FRP contribution to shear capacity have focused on developing relationships for the effective strain ε_{fe} as a function of identified variables of greatest influence. Due to the wide range in FRP ultimate stress levels, and the even greater variation in FRP material stiffness, E_f, many researchers have selected to develop relationships that define this effective strain as a fraction of the effective strain at ultimate, $\varepsilon_{fe} = R\,\varepsilon_{fu}$.

Thereby, and prior to comparing the effectiveness of various models and relationship for calculating V_f, it is useful to examine the experimentally measured effective strain, $\varepsilon_{fe,test}$ and R_{test} as a function of key test parameters for selected segments of the test data. This is presented in the seven plots in Figure A 4.2 in which effects on $\varepsilon_{fe,test}$ are examined and Figure A 4.3 in which effects on $R_{f,test}$ are examined. The key test parameters being presented are:

(a) axial stiffness of provided FRP reinforcement ($\rho_f E_f$)
(b) shear span-to-depth ratio (a/d)
(c) overall height (h)
(d) strength of provided FRP reinforcement ($\rho_f f_{fu}$)
(e) concrete compressive strength (f'_c)
(f) normalized shear stress at failure ($v_{test}/f'_c = V_{test}/(b_v d_v f'_c)$)
(g) level of provide steel shear reinforcement ($\rho_v f_y$)

Six types of markers are used in each of these plots to distinguish between the following segments of the test data:

- Hollow Red Square: no steel shear reinforcement (no Av) and a debonding (Deb) mode of failure
- Hollow Blue Circle: no steel shear reinforcement (no Av) and a rupture (Rup) mode of failure
  Hollow Orange Triangle: no steel shear reinforcement (no Av) and other (Other) mode of failure
  Solid Red Square: with steel shear reinforcement (w. Av) and a debonding (Deb) mode of failure
  Solid Blue Circle: with steel shear reinforcement (w. Av) and a rupture (Rup) mode of failure
- Solid Orange Triangle: with steel shear reinforcement (w. Av) and other (Other) mode of failure

In the plots in Figure A 4.2, $\varepsilon_{fe,test} = \dfrac{V_{f,test}}{\rho_f b_w d_f E_f}$

In the plots in Figure A 4.3, R = $\varepsilon_{fe,test}/\varepsilon_{fu}$.

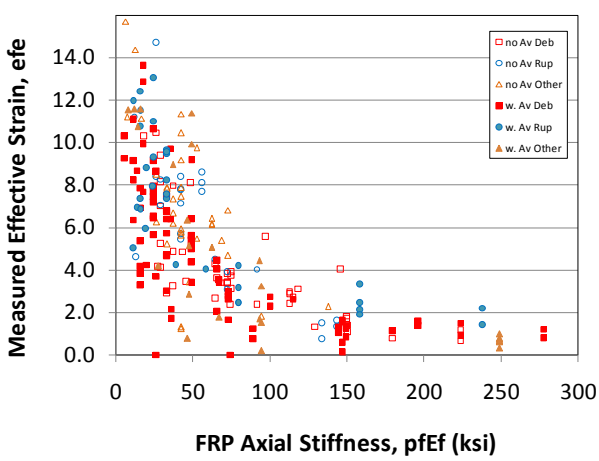

(a) axial stiffness of provided FRP reinforcement ($\rho_f E_f$)

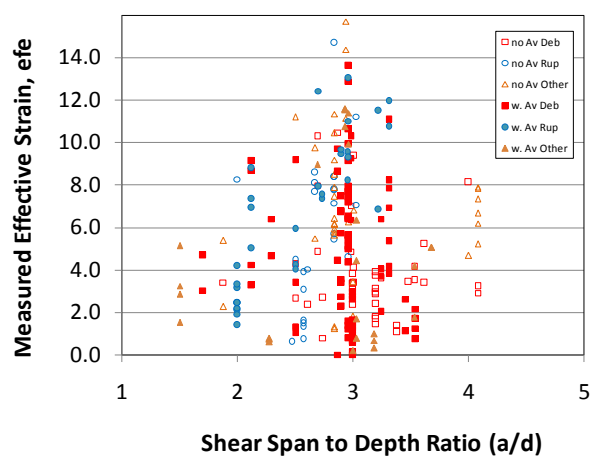

(b) shear span-to-depth ratio (a/d)

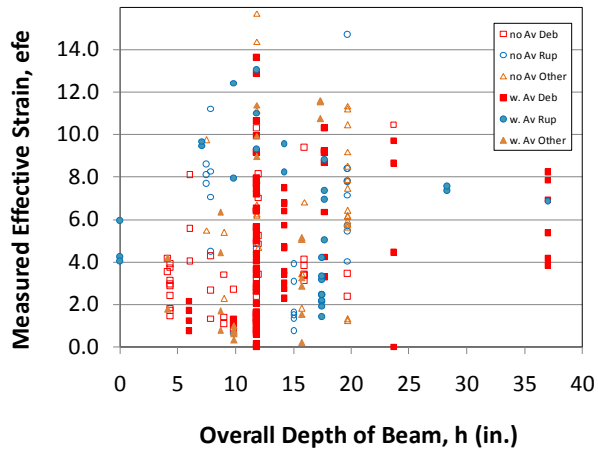

(c) overall height (h)

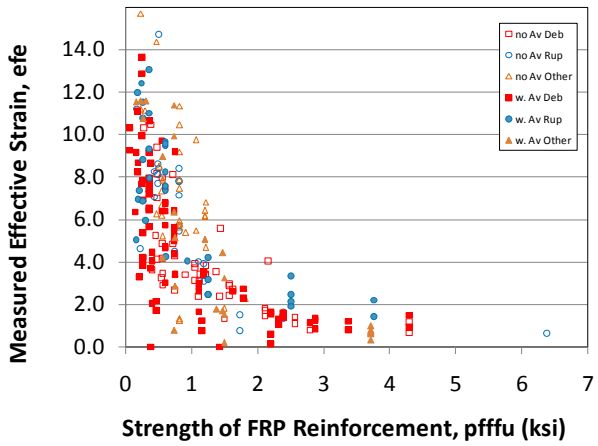

(d) strength of provided FRP reinforcement ($\rho_f f_{fu}$)

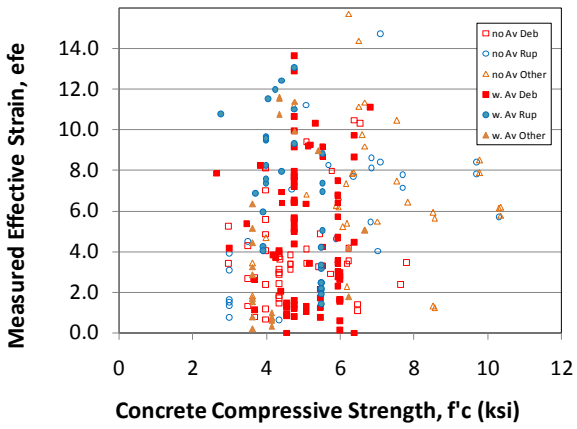

(e) concrete compressive strength (f'_c)

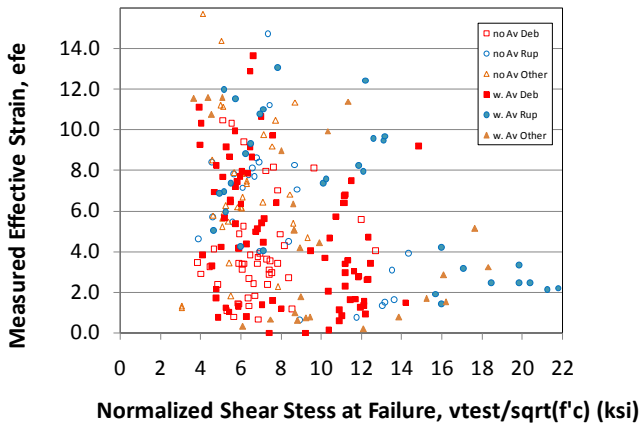

(f) normalized shear stress at failure ($v_{test}/f'_c = V_{test}/(b_v d_v f'_c)$)

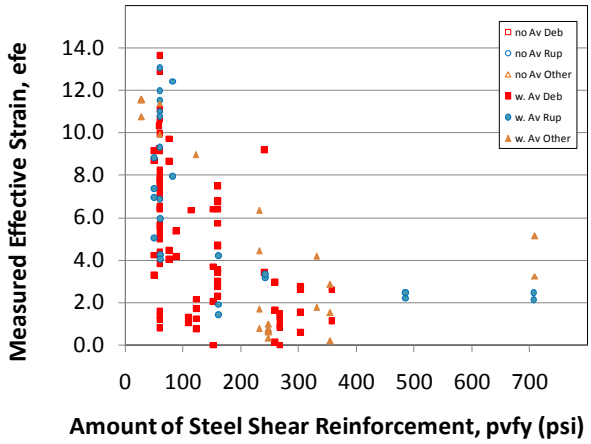

(g) level of provide steel shear reinforcement ($\rho_v f_y$)

Figure A 4.2 Effective Strain Distribution of Test Data as a Function of Key Parameters

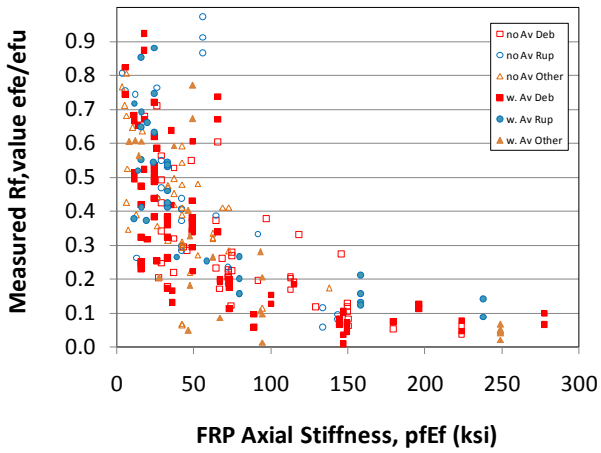

(a) axial stiffness of provided FRP reinforcement ($\rho_f E_f$)

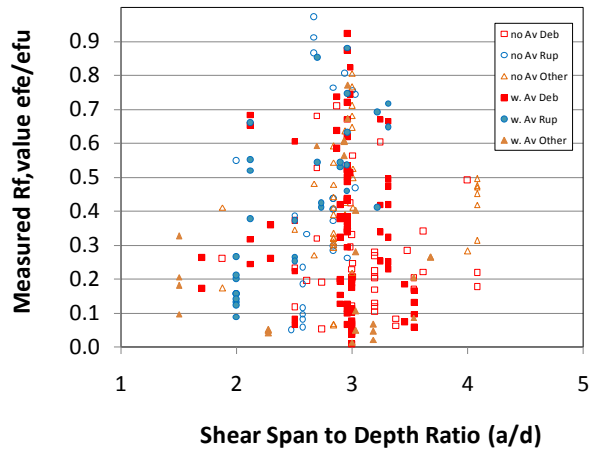

(b) shear span-to-depth ratio (a/d)

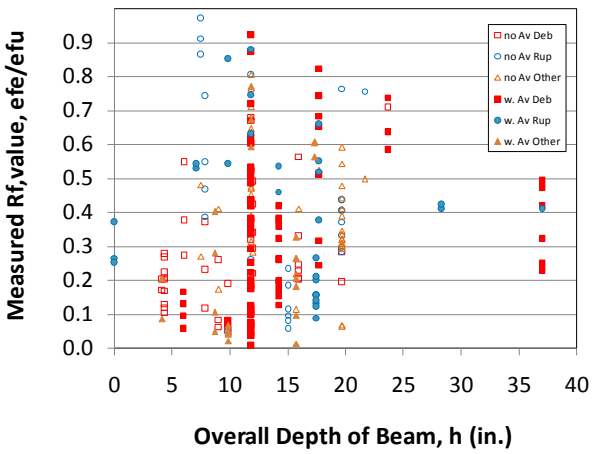

(c) overall height (h)

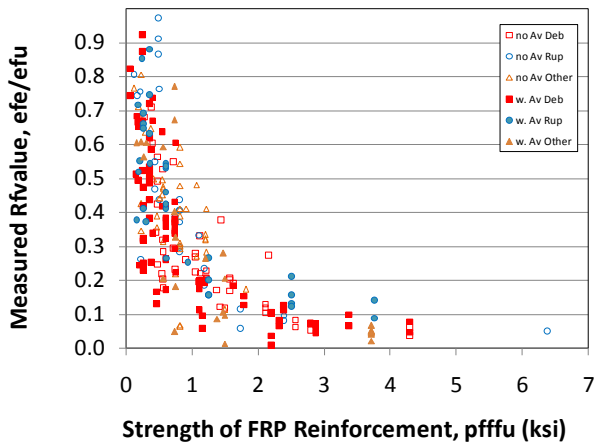

(d) strength of provided FRP reinforcement ($\rho_f f_{fu}$)

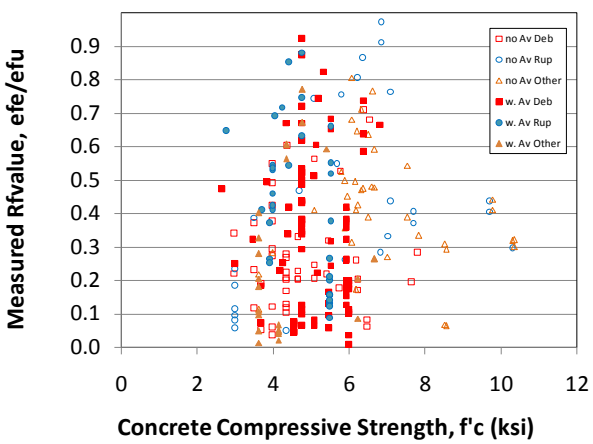

(e) concrete compressive strength (f'_c)

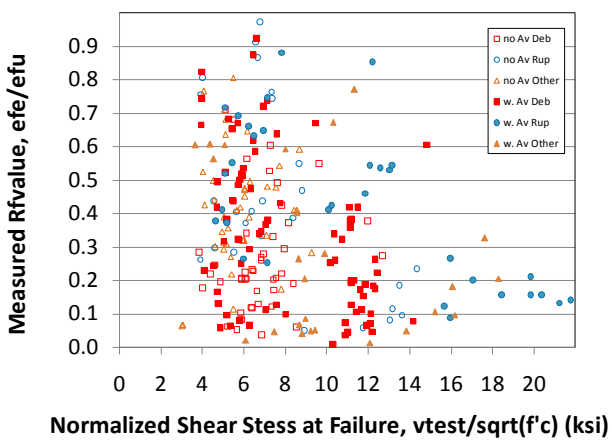

(f) normalized shear stress at failure ($v_{test}/f'_c = V_{test}/(b_v d_v f'_c)$)

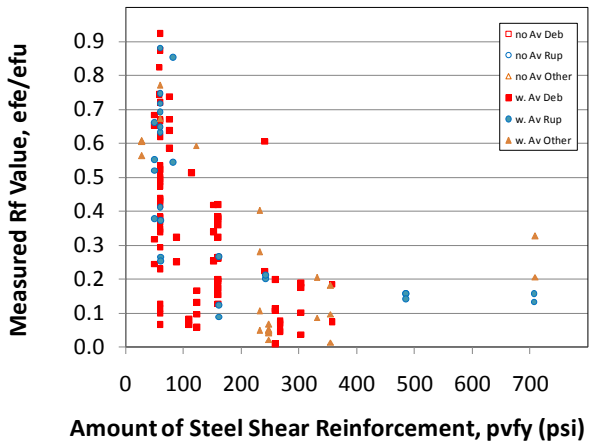

(g) level of provide steel shear reinforcement ($\rho_v f_y$)

Figure A 4.3 R_f-Distribution of Test Data as a Function of Key Parameters

A very large number of important observations can be made examining these figures. A key observation is that the factors most influencing both measured effective strain (ε_{fe}) and ratio of the measured effective to ultimate strain ($R_f = \varepsilon_{fe}/\varepsilon_{fu}$) are shown to be the axial stiffness and strength of the provided FRP reinforcement and the provided amount of steel shear reinforcements, as illustrated in (a), (d), and (g) of Figures A4.2 and A4.3. No significant trend was observed for any of the modes of failure for the influence of height, *a/d* ratio, concrete strength, or the normalized shear stress at failure.

Table A 4.4 presents a summary of the calculated ratios of $V_{f,test}/V_f$ for each of the 21 examined relationships for V_f, of which 17 were those proposed by researchers and 4 were from codes and guidelines. This table is identical to Table 2.10 from the main body of the report in which the following observations were made.

Table A 4.4 Comparative Assessment of Models for V_f

Model Affiliation	Al-Sulaimani et al.	Chajes et al.	Triantafillou and Antonopoulos	Malek and Saadatmanesh	Kalifa et al.	Kalifa and Nanni	Hutchinson and Rizkalla	Challal et al.	Chen and Teng	Pellegino and Modena	Hsu et al.	Deniaud and Cheng	Cao et al.	Zhang and Hsu	Carolin and Taljsten	Monti and Liotta	Pelligrino and Modena	fib-TG9.3	JSCE	CSA S806	ACI 440
Year	1994	1995	2000	1998a	1998	2000	1999	2002	2003a,b	2002	2003	2001b	2005	2005	2005b	2005	2006	2001	2001	2002	2008
Model #	1	2	3	4	5	6	7	8	9	10	11	12	13	14	15	16	17	18	19	20	21
1.) All Beams																					
Mean	0.23	1.10	0.84	0.34	1.46	1.49	1.90	1.16	1.68	3.56	1.30	8.39	0.75	1.19	1.15	1.67	0.41	1.24	0.52	1.46	1.65
COV	0.67	1.05	1.10	0.81	1.05	1.03	1.01	0.77	0.64	2.29	0.89	1.71	0.71	0.59	0.81	0.75	0.73	0.60	0.76	0.99	0.96
Num	324	324	324	324	315	317	324	324	324	244	244	324	324	324	324	324	324	317	324	324	317
2.) All "Valid" Beams (those used in LRFD Vf Model Calibration)																					
Mean	0.25	1.23	0.98	0.38	1.53	1.57	2.10	1.18	1.83	3.24	1.39	9.30	0.78	1.30	1.25	1.84	0.44	1.35	0.57	1.61	1.78
COV	0.62	0.94	0.56	0.73	0.97	0.95	0.91	0.67	0.57	1.34	0.89	1.71	0.57	0.53	0.73	0.66	0.67	0.50	0.66	0.89	0.88
Num	251	251	251	251	244	244	251	251	251	187	187	251	251	251	251	251	251	244	251	251	244
3.) "Valid" Beams: MoF = Rupture																					
Mean	0.24	0.88	0.81	0.32	1.25	1.32	1.53	1.07	1.48	2.73	1.35	8.85	0.62	1.22	1.08	1.58	0.38	1.17	0.48	1.18	1.35
COV	0.69	0.70	0.38	0.69	0.57	0.69	0.68	0.62	0.45	1.16	0.79	1.33	0.52	0.44	0.69	0.51	0.63	0.43	0.59	0.67	0.61
Num	126	126	126	126	125	125	126	126	126	94	94	126	126	126	126	126	126	125	126	126	125
4.) "Valid" Beams: MoF = Debonding																					
Mean	0.22	1.60	1.19	0.49	2.14	2.07	2.73	1.43	2.23	4.85	1.92	15.70	1.01	1.64	1.65	2.31	0.56	1.58	0.73	2.09	2.36
COV	0.45	1.00	0.62	0.77	1.18	1.18	0.96	0.67	0.57	1.31	1.03	1.63	0.49	0.56	0.77	0.73	0.73	0.48	0.72	0.94	1.00
Num	61	61	61	61	58	58	61	61	61	40	40	61	61	61	61	61	61	58	61	61	58
5.) "Valid" Beams: MoF = Other																					
Mean	0.30	1.55	1.12	0.37	1.51	1.62	2.63	1.18	2.12	2.91	1.05	4.08	0.89	1.15	1.23	1.89	0.42	1.52	0.58	2.00	2.10
COV	0.53	0.82	0.53	0.56	0.72	0.66	0.80	0.66	0.54	1.35	0.35	1.29	0.53	0.52	0.56	0.64	0.50	0.50	0.55	0.78	0.73
Num	64	64	64	64	61	61	64	64	64	53	53	64	64	64	64	64	64	61	64	64	61
6.) "Valid" Beams: No Av																					
Mean	0.30	1.48	1.14	0.41	1.74	1.92	2.54	1.01	2.06	1.89	1.22	4.31	0.83	1.23	1.36	1.89	0.47	1.49	0.62	1.94	2.15
COV	0.61	1.00	0.59	0.77	1.16	1.04	0.97	0.53	0.58	1.08	0.76	1.21	0.56	0.41	0.77	0.68	0.70	0.44	0.69	0.95	0.96
Num	114	114	114	114	108	108	114	114	114	108	108	114	114	114	114	114	114	108	114	114	108
7.) "Valid" Beam: With Av																					
Mean	0.21	1.01	0.85	0.35	1.36	1.30	1.74	1.33	1.63	5.08	1.62	13.45	0.74	1.37	1.16	1.80	0.41	1.25	0.52	1.33	1.48
COV	0.54	0.71	0.44	0.67	0.58	0.62	0.68	0.70	0.51	1.13	0.96	1.49	0.56	0.59	0.67	0.64	0.63	0.53	0.61	0.67	0.62
Num	137	137	137	137	136	136	137	137	137	79	79	137	137	137	137	137	137	136	137	137	136
8.) "Valid" Beams: MoF = Debonding: No Av																					
Mean	0.31	0.82	0.87	0.30	1.38	1.62	1.43	0.91	1.53	1.42	1.18	5.21	0.63	1.22	1.00	1.62	0.39	1.27	0.47	1.10	1.42
COV	0.71	0.77	0.40	0.73	0.65	0.74	0.75	0.47	0.49	0.65	0.52	0.77	0.57	0.40	0.73	0.55	0.71	0.42	0.60	0.75	0.67
Num	47	47	47	47	46	46	47	47	47	46	46	47	47	47	47	47	47	46	47	47	46
9.) "Valid" Beams: MoF = Rupture: No Av																					
Mean	0.22	1.95	1.36	0.57	2.45	2.55	3.33	1.10	2.37	2.67	1.53	5.62	0.94	1.34	1.90	2.08	0.62	1.61	0.79	2.55	2.88
COV	0.39	1.09	0.73	0.86	1.47	1.35	1.05	0.61	0.67	1.34	1.06	1.50	0.60	0.43	0.86	0.90	0.78	0.54	0.84	1.03	1.13
Num	29	29	29	29	26	26	29	29	29	26	26	29	29	29	29	29	29	26	29	29	26
10.) "Valid" Beams: MoF = Other: No Av																					
Mean	0.33	1.96	1.30	0.42	1.68	1.84	3.31	1.05	2.48	1.93	1.05	2.20	1.01	1.16	1.40	2.07	0.45	1.69	0.66	2.51	2.56
COV	0.50	0.67	0.43	0.33	0.69	0.60	0.65	0.48	0.42	0.64	0.30	0.48	0.41	0.38	0.33	0.51	0.36	0.32	0.37	0.64	0.64
Num	38	38	38	38	36	36	38	38	38	36	36	38	38	38	38	38	38	36	38	38	36
11.) "Valid" Beams: MoF = Debonding: With Av																					
Mean	0.19	0.92	0.77	0.34	1.17	1.14	1.59	1.16	1.44	3.99	1.52	11.02	0.61	1.22	1.12	1.56	0.38	1.11	0.48	1.22	1.31
COV	0.50	0.65	0.36	0.66	0.49	0.55	0.64	0.65	0.42	0.99	0.89	1.28	0.48	0.46	0.66	0.48	0.57	0.43	0.58	0.63	0.55
Num	79	79	79	79	79	79	79	79	79	48	48	79	79	79	79	79	79	79	79	79	79
12.) "Valid" Beams: MoF = Rupture: With Av																					
Mean	0.22	1.28	1.03	0.43	1.89	1.68	2.19	1.72	2.11	8.91	2.64	24.84	1.07	1.91	1.42	2.51	0.51	1.56	0.66	1.68	1.94
COV	0.50	0.57	0.32	0.53	0.48	0.57	0.54	0.62	0.42	0.92	0.89	1.27	0.39	0.56	0.53	0.59	0.62	0.43	0.48	0.52	0.53
Num	32	32	32	32	32	32	32	32	32	14	14	32	32	32	32	32	32	32	32	32	32
13.) "Valid" Beams: MoF = Other: With Av																					
Mean	0.27	0.96	0.86	0.29	1.26	1.30	1.63	1.36	1.60	5.00	1.07	6.82	0.72	1.13	0.97	1.63	0.38	1.28	0.47	1.25	1.44
COV	0.56	0.97	0.64	0.89	0.73	0.73	0.93	0.76	0.69	1.24	0.44	1.07	0.69	0.69	0.89	0.83	0.67	0.74	0.80	0.90	0.77
Num	26	26	26	26	25	25	26	26	26	17	17	26	26	26	26	26	26	25	26	26	25

The average and COV of the strength ratios ($V_{f,\,test}/V_f$) are first presented for the entire dataset (All Beams) and then for only those test results considered useful (or valid) for calibrating provisions to be used in codes of practice including the AASHTO LRFD Bridge Design Specifications (AASHTO, 2008). The remaining segments are further separated according to the Mode of Failure (MoF), the use of steel shear reinforcement (No Av or with Av), and by combinations of these two. As apparent for each segment, there is a very wide variation in the average strength ratio and generally the COVs are large. This is not unexpected for the 17 models proposed by various researchers for two reasons: (i) researchers typically derived their models to provide a best fit with a relatively small number of tests, often only ones that they personally conducted, and (ii) unlike with the use of steel shear reinforcement, there is a very wide range in types and effectiveness of FRP including stiffness (E_f), ultimate strength (f_{fu}), means of application, anchorage, orientation, and other factors. Consequently, it is to be expected that individual models would perform much better (reasonable strength ratio and lower COV) for some segments of the test data than others. This is evident for example in exploring the COV for the model by Khalifa et al. (1998) in which the COV for members with observed rupture failures without and with steel shear reinforcement is 1.47 and 0.48 respectively. The following more specific observations were made:

(1) As presented in Table A 4.4, the mean values of $V_{f,\,test}/V_{f,\mathrm{cal}}$ range from 0.38 to 3.24, with significant scatter as given by the COV values of 0.53 to 1.34. This is far more scatter than for most of the very empirical relationships in codes of practice including the concrete contribution to shear resistance V_c. This is suspected to be as a result of the variety of FRP strengthening systems, methods of application, and sensitivity to other factors that influence the general shear behavior of structural concrete members.

(2) As $\rho_f f_{fu}$ increases, the strength ratio $V_{f,\,test}/V_{f,\,cal}$ exhibits a decreasing trend for nearly all reviewed methods. This suggests that all methods are more conservative for low values of $\rho_f E_f$ and generally become less conservative when higher levels of FRP reinforcement are used.

(3) The mean strength ratio $V_{f,\,test}/V_{f,\,cal}$ is typically more conservative for those members that failed due to rupture of the FRP reinforcement. This was not the case for models of Chaallal et al. (2002) and Zhang and Hsu (2005) in which the mean strength ratio for $V_{f,\,test}/V_{f,\,cal}$ were quite similar for both these modes of failure.

(4) The models by Zhang and Hsu (2005) and fib-TG9.3 (2001) were observed to better predict the capacities for both debonding and rupture failures. These two models provide the mean values around 1.10 for both debonding and rupture. Fib-TG9.3 (2001) gives smaller COV values than Zhang and Hsu (2005).

(5) For simplicity, fixed values of effective strains are used in three models, Chajes et al., 1995 (0.005), Hutchinson and Rizkalla, 1999 (between 0.6 and 0.9 times 0.004), CSA S806-02, 2002 (0.004 and 0.002). For cases of rupture failure, these models were quite conservative with mean strength ratios for Chajes et al. (1995) of 1.75, for Hutchinson and Rizkalla (1999) of 2.91, and for CSA S806-02 (2002) of 2.23; all with similarly high COV values around 0.90. This suggests that a fixed value of effective strain around 0.004 is conservative for rupture failure. The results for debonding failure suggests that if a fixed value of effective strain is used for debonding

failure, then it should be less than 0.004. The results from these three models suggest that the value of the effective strain should depend on other parameters.

(6) The means strength ratio for $V_{f,\,test}/V_{f,\,cal}$ associated with the JSCE (2001) is particularly low. The explanation is because the JSCE Recommends (2001) that the effective stress in FRP is between 0.4 and 0.8 times the rupture stress of FRP, which leads to high predictions of the shear contribution of FRP.

(7) Four models, Triantafillou (1998a), Khalifa et al. (1998), Pellegrino and Modena (2002), and fib-TG9.3 (2001), were developed following the same strategy of modifying the effective strain equation. Fib-TG9.3 (2001) gives quite good results compared to others, and this method may be promising in future applications. Pellegrino and Modena (2002) modified Khalifa et al. (1998)'s R factor by introducing a new factor R^* to account for the effects of inclined cracks and steel shear reinforcement, but it is found that R^* should be zero for specimens with large amounts of transverse reinforcement ratio. This suggests that FRP is not an effective means of strengthening members with significant amounts of steel shear reinforcement. The explanation for this has not been presented by the authors.

Due to the complexity and variety of methods to evaluate V_f, it is useful to directly compare the calculated FRP contributions to shear capacities by different methods using specific examples, such as the one now presented. Consider a member that has a rectangular cross-section with a width of 7.09 inches, a height of 19.69 inches, and a shear span-to-depth ratio of 3.5. FRP shear reinforcement consists of CFRP sheets externally bonded with fibers oriented at 90 degrees in a U-wrap configuration over a height of 17.32 inches. The concrete compressive strength is 8,557 psi, the modulus of elasticity of the CFRP sheet is 33,939 ksi, and the ultimate tensile strength of the CFRP sheet is 653 ksi. Steel shear reinforcement is used and consists of 8M bars (A_v = 0.22 in.^{2}) with a yield strength of 64 ksi. The spacing of the steel stirrups is 11.8 inches. Figure A 4.4 shows the relationship between the calculated shear stress capacity provided by the FRP reinforcement ($V_f\,/b_v d_f$) as a function of the axial rigidity of the FRP reinforcement ($\rho_f E_f$) for 15 of the previously discussed models. In the calculations the shear crack angle is assumed to be 45 degree.

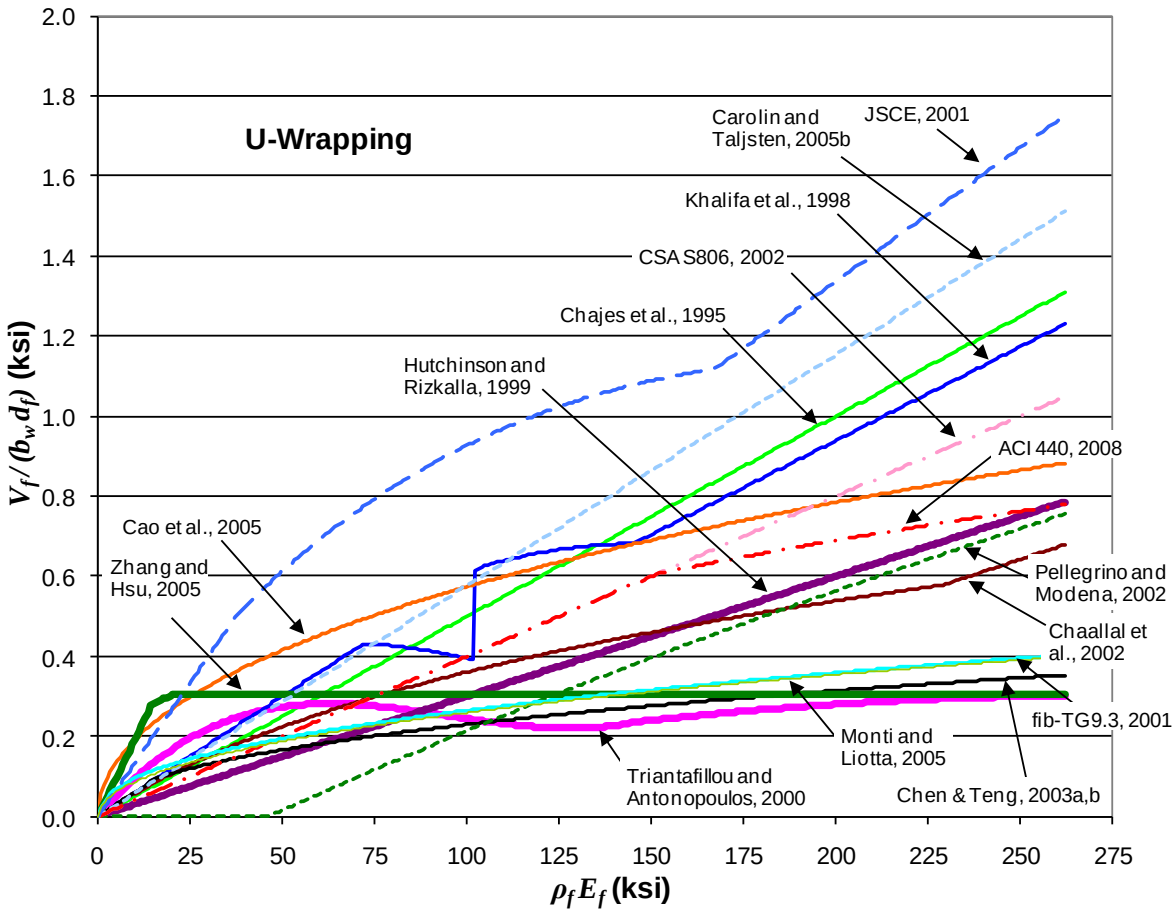

Figure A 4.4 Comparison of Capacity Provided by Different FRP Models

The comparisons presented in Figure A 4.4 illustrate that there are very significant differences in the magnitude of the strength calculated by the various models for V_f for a given level of FRP reinforcement for a specific member. The model in the JSCE Recommendations (2001) was observed to be the least conservative while the model by fib-TG9.3 (2001) was the most conservative. In about half the models, there was a linear increase in the calculated value of V_f with FRP rigidity, while in the other half there was either a limit placed on the FRP contribution to shear resistance or V_f increased less than in proportion to the FRP rigidity, particularly after $\rho_f E_f$ > 1.0 GPa. Not including the JSCE model since it is at an extreme, the ratio of the maximum to minimum calculated contribution of V_f was around 2.5 at $\rho_f E_f$ = 109 ksi and 5 at $\rho_f E_f$ = 261 ksi. This magnitude of the range in calculated V_f values by the different models is indicative of the complexity of the resistance mechanism, sensitivity of the provided strengthening to types of tests used for the calibration of models, and lack of maturity of models.

Relationships for V_f in codes and guidelines are expected to consider a wider range of test results than is typically considered for an individual study. Therefore, it is to be expected that there would be a more uniform average strength ratio and COV across all segments of the test data for the code/guidelines case. This can be observed to be generally true with the model proposed by fib-TG9.3 (2001) which exhibited the most uniform performance. Models 3, 9, 13, and 14 also demonstrated similar performance across a broad range in categories.

As previously identified, models 3, 9, 13, 14, and 18 were observed to provide the lowest COV of strength ratios ($V_{f,test}/V_f$) across a wide range of segments of the database. These are the models by:

Triantafillou and Antonopoulos (2000): Model 3
Chen and Teng (2003a,b): Model 9
Cao et al. (2005): Model 13
Zhang and Hsu (2005): Model 14
European fib-TG9.3 Bulletin 14 (2001) (from Triantafillou and Antonopoulos, 2000): Model 18

This determination of the most effective models is useful for identifying features for inclusion in a V_f model for the AASHTO LRFD specifications (AASHTO, 2008). Selected features of these five most effective models include consideration of:

- axial stiffness of FRP reinforcement, $\rho_f E_f$
- compressive strength of concrete (f'_c)
- mode of failure (debonding or rupture)
- type of FRP application (full wrap, side bonding, or U-wrap)
- development length available for FRP (L_e)
- bond strength between FRP and concrete (τ_{max})

The selection of a suitable model for V_f for use in design must consider the following:

1) Complexity of Relationship for Evaluation
There is little merit and considerable danger in proposing a model that may be incorrectly evaluated in a significant percentage of situations. The majority of available models for V_f are much more complex than most formula in codes of practice and not considered to be suitable for use in practice.

2) Availability and Reliability of Model Parameter Data
The relatively complex models proposed by most researchers take advantage of the measurable features of the test beam and FRP application, including for instance the development length of the FRP reinforcement. While this is obviously useful for developing models with improved accuracy, the selection of design provisions must consider what is practical to assume and available for the designer to know or specify. The selection of parameters to include in a V_f relationship for use in the AASHTO LRFD specification (AASHTO, 2008) should also consider that FRP shear reinforcement is most likely to be used for strengthening of an existing and potentially old structure for which full design details are not known.

3) Calibration with Full Shear Strength Ratio Considering Specific V_c and V_s Relationships
A comparative evaluation of V_f models, as presented in Section 2.3, can be conducted using the strength ratios of $V_{f,test}/V_f$. However, the selected relationship for V_f to include in a code of practice must be calibrated based on the bias (strength ratio) and COV of the $V_{n,test}/V_n$ ratio where $V_n = V_c + V_s + V_f$. This is necessary in order to achieve the needed level of design safety as determined through a reliability study as presented in Section A7.

A4.7 Selection and Evaluation of V_f Relationships for Use in LRFD Specifications

A4.7.1 Selection of Factors Controlling V_f Contribution

Section A4.3 presented a large range in the forms of relationships for V_f. An assessment of the accuracy of these models was made in Section A4.6 using a large experimental database that included the text completed in this research program. There was a significant difference in the success of models depending on mode of failure and level of shear reinforcement. As expected, models were more effective at predicting the capacity of members with similar reinforcement characteristics and modes of failure from which they were derived. This illustrates that it is useful to have two different models for V_f, one for members in which sufficient anchorage is provided so that the contribution of the FRP is expected to be controlled by FRP rupture. The other in which there is not expected to be this level of sufficient anchorage, and then failure is expected to be a result of debonding or another mode of failure.

Consistent with how the capacity provided by steel shear reinforcement is considered in the AASHTO LRFD Specifications (AASHTO, 2008), the contribution of FRP stirrup reinforcement can be evaluated from the following relationship.

$$V_f = \frac{A_f f_{fe} d_f (\cot\theta + \cot\alpha)\sin\alpha}{s}$$

where: f_{fe} is the effective stress in the FRP reinforcement at the ultimate limit state. This stress may be taken as $f_{fe} = E_f \varepsilon_{fe}$ where ε_{fe} is the effective strain in the FRP reinforcement at the ultimate limit state and therefore:

$$V_f = \frac{A_f E_f \varepsilon_{fe} d_f (\cot\theta + \cot\alpha)\sin\alpha}{s_f}$$

in which: $A_f = 2n_f t_f w_f$, n_f is the number of layers of FRP reinforcement on each face of the web, t_f is the thickness of one layer of FRP reinforcement, and w_f is the width of the strip of FRP reinforcement. The terms t_f, w_f, and s_f have little meaning when continuous FRP reinforcement is provided, and therefore it is more clear to express V_f in terms of the ratio of provided FRP reinforcement (ρ_f) so that:

$$V_f = \rho_f E_f \varepsilon_{fe} b_w d_f (\cot\theta + \cot\alpha)\sin\alpha$$

where: $\rho_f = \dfrac{2n_f t_f w_f}{s_f}$

Based on the measured performance of models for V_f as presented in section A4.6, it was decided to use two relationships for V_f: one when full anchorage is provided such that the capacity is expected to be limited by FRP rupture, and a second when full anchorage is not provided and other modes of failure, such as debonding, are expected.

A primary variable that controls the contribution of the FRP reinforcement for both rupture and non-rupture failures is the axial rigidity ($\rho_f E_f$) of the provided FRP reinforcement. This was observed by other researchers and commonly used in models for V_f. As part of this project, the contractor considered the influence of other factors in combination with $\rho_f E_f$ on both R and ε_{fe}, but no combination was identified that resulted in modestly lower coefficients of variation (COV). Thereby, to keep the evaluation of R and ε_{fe} as simple as possible, it was selected to make these V_f relationships to be solely a function of the axial rigidity of the provided FRP reinforcement ($\rho_f E_f$).

Based on the success of previous models and stemming from an iterative evaluating of model structure on COV of V_{test}/V_n ratios, it was selected to take the effective strain as a fraction of the rupture strain (ε_{fe} = R ε_{fu}) and to limit this strain when full-anchorage is not provided (non-rupture failures likely) to 0.012. The selection and calibration of R_f as functions of $\rho_f E_f$ is now presented.

A4.7.2 Measured R for Full Anchorage Condition (Rupture Failures)

The influence of $\rho_f E_f$ on both the measured effective strain in the FRP reinforcement (ε_{fe}) at shear capacity and on the ratio R_f of the measured effective to ultimate strain, was illustrated in Section A4.6. The latter is represented in Figure A 4.5. In these calculations,

$$\varepsilon_{fe,test} = \frac{V_{f,test}}{\rho_f b_w d_f E_f} \quad \text{and} \quad R_f = \frac{\varepsilon_{fe,test}}{\varepsilon_{fu}}$$

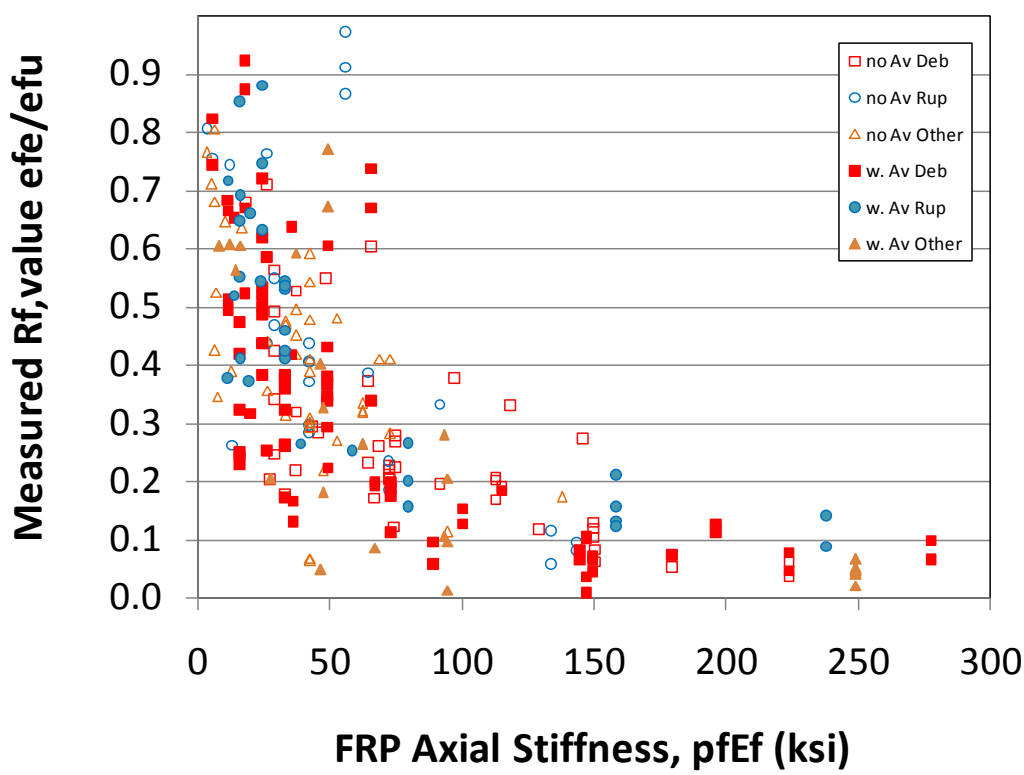

Figure A 4.5 Relationship between measured R_f and Axial Rigidity of FRP, $\rho_f E_f$

A4.7.3 Calibration of V_f Relationships

Until this point of the report, the evaluation and selection of suitable relationships for V_f have only considered the ability of relationships for V_f, to predict the strength increase in beam shear capacity due to the addition of FRP reinforcement over the measured strength of identical control beams that did not have FRP reinforcements, $V_{f,test} = V_{test} - V_{control}$. This is considered to be the most appropriate means of evaluating and selecting a suitable form of relationship for V_f as has been just completed in the previous sections. However, just as the code expression for V_s cannot be justified and calibrated by examining the strength gain in beams due to the addition of steel shear reinforcement, the relationship for V_f must also be selected based on the ratios of measured V_{test}/V_n where $V_n = V_c + V_s + V_f$ so that the combination of the bias ($\lambda = \mu$ – nominal) and COV produces the code specified level of reliability, which for the AASHTO LRFD specifications (AASHTO, 2008) uses a β_r value of 3.5.

The selected relationships for V_f are now presented. This is followed by the results of the statistical assessments of V_{test}/V_n and then by an examination of the influence of key beam variables on these ratios.

Based on the results of statistical assessments (including the reliability study) and considerations of simplicity as presented in Section A4.6, the following expressions are proposed for determining the effective strain (ε_{fe}) for use in the AASHTO LRFD Bridge Design Specifications (AASHTO, 2008).

When "full-anchorage" is provided such that the shear resistance at shear failure is expected to be controlled by FRP rupture:

$$\varepsilon_{fe} = R\varepsilon_{fu} \quad where \quad \varepsilon_{fu} = f_{fu}/E_f \quad and$$

$$R = 4(\rho_f E_f)^{-.67} \leq 1.0$$

where: $\rho_f E_f$ is in ksi units and limited to 300 ksi

$$R = 0.143(\rho_f E_f)^{-.67} \leq 1.0$$

where: $\rho_f E_f$ is in GPa units and limited to 2.07 GPa

Comparison of this expression with the test data yields an average strength ratio (bias) of 1.68 with a corresponding COV of 0.33, which provides close to the needed target reliability.

When "full-anchorage" is not provided, it is likely that the shear capacity will be controlled by FRP debonding or another mode of failure before FRP rupture can be achieved:

$$\varepsilon_{fe} = R\varepsilon_{fu} \leq 0.012 \quad where \quad \varepsilon_{fu} = f_{fu}/E_f \quad and$$

$$R = 3(\rho_f E_f)^{-.67} \leq 1.0$$

where: $\rho_f E_f$ is in ksi units and limited to 300 ksi

$$R = 0.107(\rho_f E_f)^{-.67} \leq 1.0$$

where: $\rho_f E_f$ is in GPa units and limited to 2.07 GPa

Comparison of this expression with the test data yields an average strength ratio (bias) of 1.44 and a corresponding COV of 0.25, which provides close to the needed target reliability.

Table A 4.5 presents the mean and distribution of V_{test}/V_n ratios for the selected valid set of beam test results.

Table A 4.5 Assessment of Suggested V_f Model

	Rupture Failures			Non-Rupture Failures (Debonding and Other)				
Vtest/Vn Ratios	All	No Av	W Av	All	Deb No Av	Deb W. Av	Other No Av	Other W. Av
Mean	1.683	1.676	1.689	1.440	1.492	1.422	1.528	1.302
COV	0.334	0.361	0.310	0.269	0.266	0.269	0.225	0.305
Min	0.844	0.844	0.920	0.635	0.896	0.808	0.771	0.635
Max	2.740	2.740	2.480	3.031	3.031	2.744	2.238	2.310
Count	62	29	33	204	47	81	42	34

As presented, there are relatively similar Mean and COV values in V_{test}/V_n ratio for cases in which rupture failures were reported (V_f based on $R = 4(\rho_f E_f)^{-0.67}$) for full anchorage conditions for members with and without shear reinforcement. This is also the case for situations in which debonding and other modes of failure were reported (V_f based on $R = 3(\rho_f E_f)^{-0.67}$). The number of beams in each category (listed beside Count) indicates that the number of beams demonstrating each mode of failure, with and without shear reinforcement, is similar (ranging from 29 to 47 members) but for Debonding failures for members in which there were 81 test beams available for the assessment.

Figure A 4.6 illustrates the pattern of measured strength ratios (V_{test}/V_n) for all valid beams for the six categories of members in Table A 4.5 and as used in section A4.6. The markers used to identify each of these categories are the same as used in A4.6 as given below:

Hollow Red Square: no steel shear reinforcement (no Av) and a debonding (Deb) mode of failure
Hollow Blue Circle: no steel shear reinforcement (no Av) and a rupture (Rup) mode of failure
Hollow Orange Triangle: no steel shear reinforcement (no Av) and other (Other) mode of failure
Solid Red Square: with steel shear reinforcement (w. Av) and a debonding (Deb) mode of failure Solid Blue Circle: with steel shear reinforcement (w. Av) and a rupture (Rup) mode of failure
Solid Orange Triangle: with steel shear reinforcement (w. Av) and other (Other) mode of failure

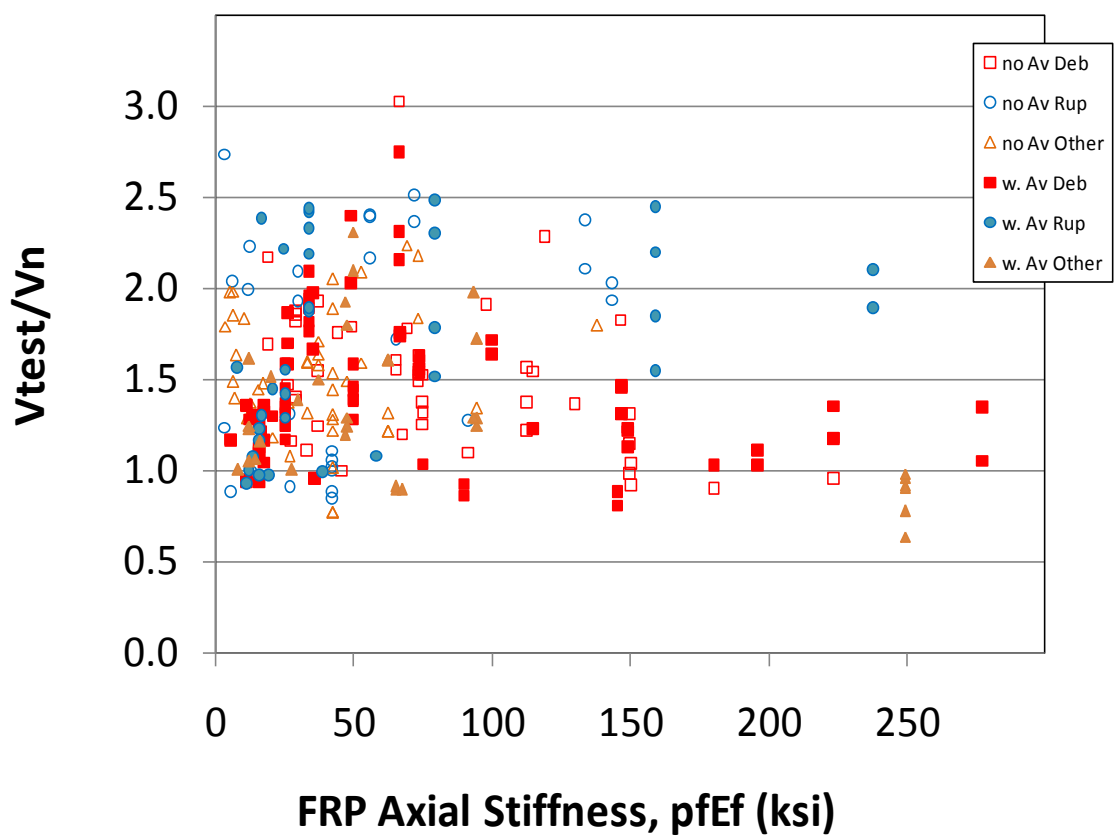

Figure A 4.6 V_{test}/V_n Ratio versus $\rho_f E_f$

It is also important to examine that there are no significant trends in the ratio of V_{test}/V_n with other key test parameters or it would indicate that it may be important to account for these in the relationships for determining V_f. The plots in Figure A 4.7 present these ratios as a function of shear span to depth ratio (a/d), overall depth (h), strength of FRP reinforcement ($\rho_f f_{fu}$), concrete strength (f'_c), normalized shear stress at failure ($v_{test}/f'_c = V_{test}/(b_v d_v f'_c)$), and the level of provided steel shear reinforcement ($\rho_v f_y$).

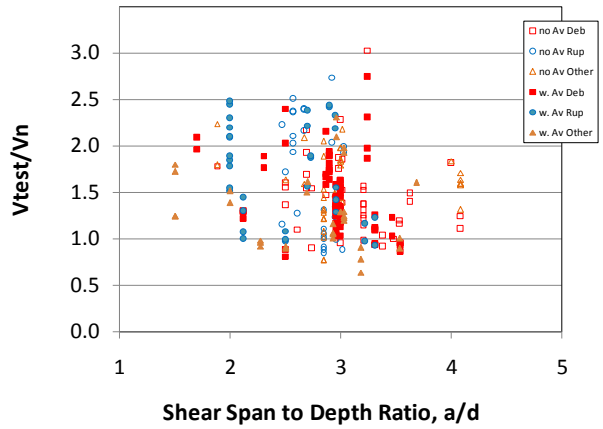

(a) Shear Span to Depth Ratio (*a/d*)

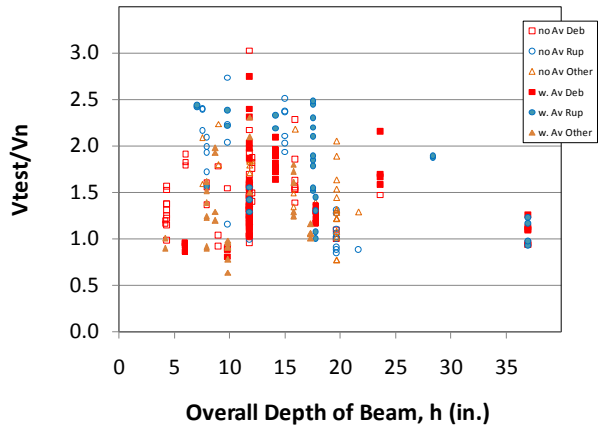

(b) Overall Depth of Beam (*h*)

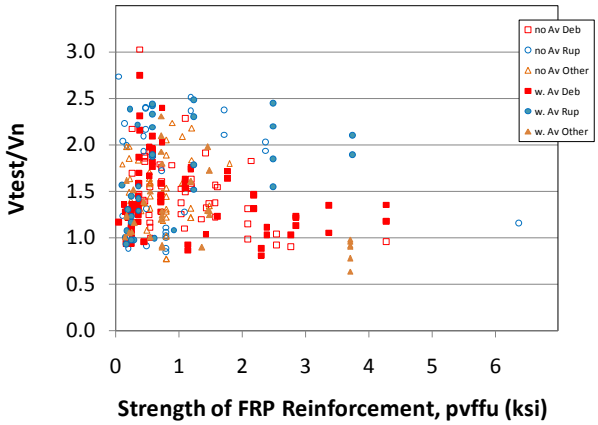

(c) Strength of FRP Reinforcement ($\rho_f f_{fu}$)

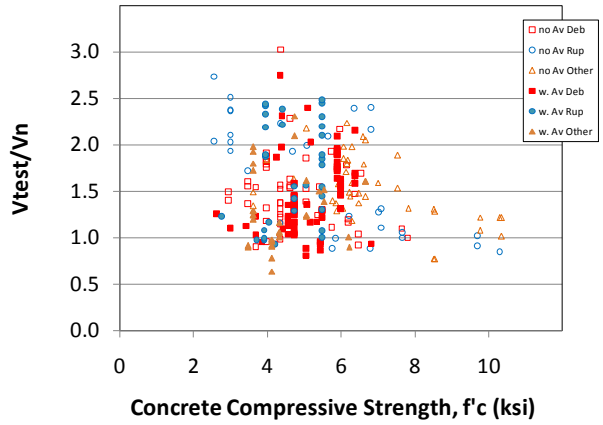

(d) Concrete Compressive Strength (f'_c)

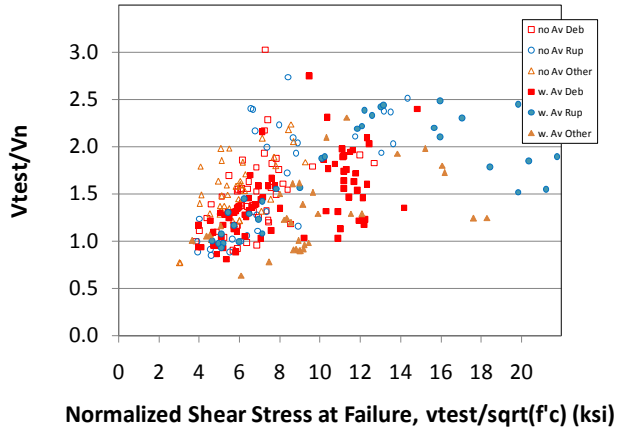

(e) Normalized Shear Stress at Failure

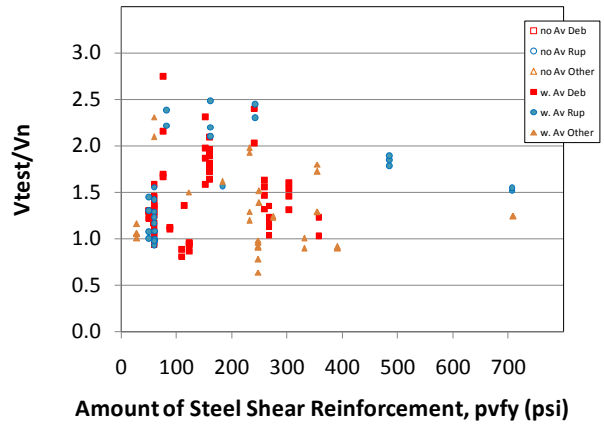

(f) Strength of Steel Shear Reinf. ($\rho_v f_y$)

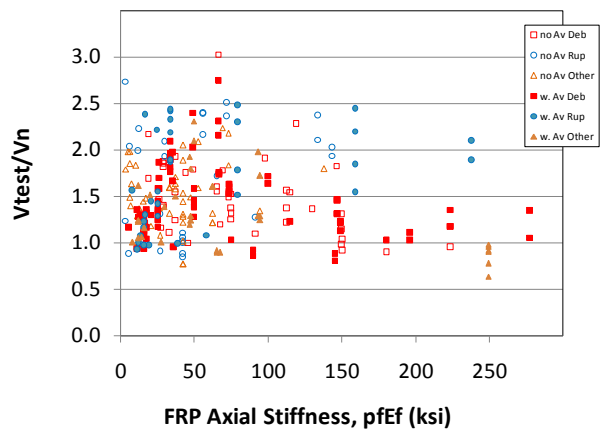

(g) FRP Axial Stiffness ($\rho_f E_f$)

Figure A 4.7 V_{test}/V_n Ratio as a Function of Key Parameters

As shown, there is essentially no trend in the measured strength ratios (V_{test}/V_n) with the shear span to depth ratio (a/d) or the overall depth of the member (h). While there appears to be a downward trend with increasing strengths of FRP reinforcement ($\rho_f f_{fu}$), concrete compressive strength (f'_c), and strength of steel shear reinforcement ($\rho_v f_y$), the number of values at the right end of this trend was not considered sufficient to warrant adjusting the relationships for V_f to account for these potential effects. If additional data in the future verifies such trends, then adjustments to these relationships may be warranted.

A4.8 Application of V_f to Stocky and Slender Cross Sections: Modes of shear Failure

As indicated in the main body of the report, and as further described in Section A5.3, the application of FRP reinforcements on precast I-shaped sections with "slender webs" did not provide significant or reliable FRP contributions to shear capacity, V_f, and on occasion resulted in a decrease in strength relative to that of the member which did not have FRP shear reinforcement. When this was observed in the early part of the experimental research program on I-shaped beams, changes in the experimental setup and girder details were made to address what was hoped to be a phenomena associated with some avoidable FRP reinforcement detail. To the contrary, and after repeated tests demonstrated similar effects, it was concluded that the reason that the application of FRP shear reinforcements did not lead to strength gains was due to breakdown in the diagonal compressive capacity of slender webs when stiff, well bonded FRP reinforcements are glued to the surface of these webs. While the members experiencing this web capacity breakdown were all prestressed, it has been concluded that this breakdown was due to the slenderness of the webs and not the effect of prestressing. Consequently, the relationships for V_f that have been proposed in this study are suitable for cross-sections without slender webs for both prestressed and non-prestressed members. Based on an examination of strength gains as a function of the ratio of depth to web width (d/b_w), the relationships proposed for V_f are considered justifiable for members with a web slenderness of $d/b_w \leq 4$, and should not be used otherwise. It is anticipated that the use of near surface mounted FRP is expected to avoid the breakdown of slender webs, but that examination was beyond the scope of this study.

A description of modes of shear failure in reinforced and prestressed concrete beams is now presented to explain the web breakdown phenomena. This begins with a description of how shear is carried on concrete structures, and mechanisms of shear resistance. This is provided in sufficient detail so that the criticality of ensuring adequate diagonal compressive strength in webs and the mathematical relationships for defining these stresses can be fully understood. Figure A 4.8(a) presents the flow of forces in the web of a girder. As shown, shear is carried by a field of diagonal compression that is lifted by bands of stirrups across cracks in the same manner as forces flow in a parallel chord truss model. This model has been at the basis of evaluating the steel shear reinforcement contribution to shear capacity since the late 1800s. The equilibrium relationships for the section described in Figures A4.7(c) and A4.7 (d) subjected to only shear are also presented. These relationships are expressed so that the critical material stress level in the concrete, longitudinal steel reinforcement, and steel shear reinforcements are all given as a function of the level of applied shear.

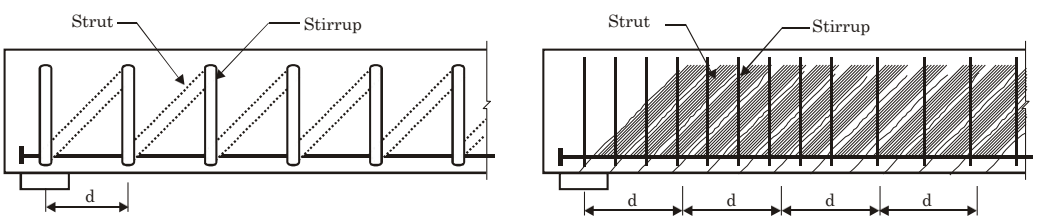

(a) Flow of Forces in a Prestessed and Non-Prestressed Beams

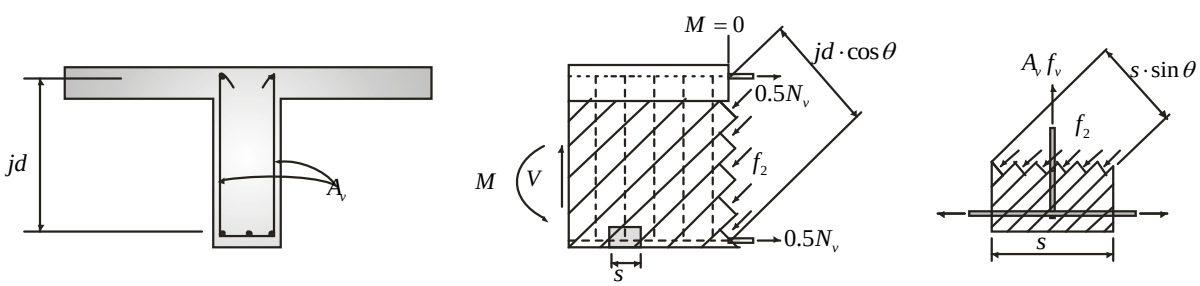

(b) Cross section

(c) Diagonal stresses and longitudinal equilibrium

(d) Force in stirrup

Equilibrium equations: $f_2 = \dfrac{V}{b_w jd}\left(\tan\theta + \cot\theta\right)$, $\quad N_v = V\cot\theta$, $\quad \dfrac{A_v f_v}{s} = \dfrac{V}{jd}\tan\theta$

Figure A 4.8 Flow of Shear Forces in Structural Concrete Beams

The equilibrium relationships that can be derived from Figure A 4.8 are as follows:

$$f_2 = \frac{V}{b_w jd}\left(\tan\theta + \frac{1}{\tan\theta}\right);\ f_\ell = \frac{V}{A_\ell \tan\theta};\ f_v = \frac{V\tan\theta\,(s)}{jd(A_v)}$$

where: the flexural lever arm *jd* may be taken as the shear depth d_v.

For a member subjected to a given level of shear, there are four unknowns (f_2, f_ℓ, f_v, and θ) but only three equations. This led Morsch to correctly conclude that it was not possible to solve for the state of stress in a member subjected to shear based on equilibrium alone. Therefore, some assumptions were needed to develop shear design provisions. While all code bodies from around the world have assumed that the steel shear reinforcement will yield at ultimate ($f_v = f_y$), they have frequently made different assumptions to address other aspects of the incompleteness of the understanding of how shear is carried. In ACI 318 (ACI, 2008) and the AASHTO Standard Specifications (AASHTO, 2007), it was assumed that the angle of diagonal compression was 45°, and to avoid a diagonal compression failure (f_2 reaching diagonal compressive strength $f_{2,max}$), the maximum design shear on the section was controlled by limiting the contribution of steel shear reinforcement to an effective shear stress in psi units of $8\sqrt{f'_c}$. By contrast, a plasticity approach was taken in Europe in which the capacity of the truss was considered to be equal to that in which a plastic mechanism could be developed that consisted of stirrups yielding and the diagonal compressive stress in the concrete reaching a selected stress state, often taken as approximately 60% of the compressive strength of plain concrete. This allowed for the angle of diagonal compression to be directly solved and eliminated the need to guard against a diagonal compression failure through a limitation on the design shear stress.

The barrier to determining the angle of diagonal compression, θ, and thereby enabling the direct determination of stresses in a section due to an imposed shear, was overcome with the development of the Compression Field Theory (CFT). This theory considered strain compatibility—the non-linear behavior of diagonally cracked concrete materials—and used the assumption on coincidence of principal angles of strain and stress, to directly solve for θ and thereby all other states in the member due to the effects of shear. This approach was enhanced with the creation of the Modified Compression Field Theory (MCFT), from which the general procedure of the AASHTO LRFD Bridge Design Specifications (AASHTO, 2008) was derived, to consider the contribution of the concrete in tension, f_1, that acts perpendicularly to the direction of principal compression in the web of a beam. The MCFT includes the use of a check of the local equilibrium at a crack face to ensure that this average tensile stress contribution of the concrete can be transmitted and, when necessary, limits this stress by the interface shear transfer resistance capacity across cracks. The contribution of this concrete in tension is the basis of the V_c contribution to resistance in the general procedures of the AASHTO LRFD specifications (AASHTO, 2008).

The purpose of this rather long preceding discussion was to illustrate that shear in prestressed and non-prestressed beams induces diagonal compression in the web of beams that must be controlled by some means to prevent diagonal compression failures. This basic concern has largely been neglected by the U.S. educational and design communities because the limitations on V_s eliminated the need for this consideration. By contrast, the European and the general procedures of the AASHTO LRFD (AASHTO, 2008) shear design provisions impose more complete and accurate considerations to guard against diagonal compression failures.

With this as background, the potentially destructive effects of FRP reinforcement on the breakdown of the diagonal compressive strength and also interface shear transfer resistance are

clear. When diagonal cracking develops in members, significant diagonal tensile strain occurs. If vertical FRP reinforcements with only unidirectional fibers are effectively bonded to the surface of slender or thin webs, then they will constrain vertical expansion and more freely allow longitudinal expansion. Since the direction of principal tension in the cracked concrete and the constraints introduced by the FRP reinforcements are at significant angles to one another, this will induce significant localized shear and tensile stresses in the concrete near cracks. Due to the very strong bond between the FRP and the concrete, out of plane tension in the concrete and tearing of the concrete from the core of web can result. In thin and slender webs, this can result in breakdown in the diagonal compressive strength and thereby no strength gain or a reduction in shear capacity can result.

A4.9 Summary

A4.9.1 Types of Members in Evaluation Database

The members in the evaluation database do not well reflect the types of bridge members for which FRP reinforcement would be used. The members in the experimental database are mostly reinforced concrete, small, stocky, simply supported, of rectangular cross-sections, and not pre-cracked in shear. By contrast, most bridge members are large, slender, and have flanges. Additionally, most of the shear span-to-depth ratios of the test beams were very close to 2.5 whereas most members in the field are more slender such that the $M_u/V_u d_v$ (equivalent to a/d) at many design sections, particularly for continuous members, is considerably more than 2.5. In addition, FRP strengthening is most likely to be used in existing members if they are pre-cracked in shear. Because of these differences, the selection and calibration of relationships for V_f need to be more than a statistical exercise.

A4.9.2 Inaccuracy in All Examined Models

None of the models that were examined were able to provide reliable estimates of shear strengthening effect, V_f, for all of the members in the database. The scatter of the predictions captured by the COVs was amongst the highest as is seen in existing empirical code provisions for other types of strength evaluations. This indicates that the mechanisms of FRP strengthening are still poorly understood. This is further exemplified by the large differences in the strength predictions by the examined models for individual beams and on average.

It was also observed that some models were much more effective than others, namely:

- Model 3: Triantafillou and Antonopoulos (2000)
- Model 9: Chen and Teng (2003a,b)
- Model 13: Cao et al. (2005)
- Model 14: Zhang and Hsu (2005)
- Model 18: European fib-TG9.3 Bulletin 14 (2001) (from Triantafillou and Antonopoulos, 2000)

A4.9.3 Proposed Method for Evaluating the FRP Contribution to Shear Resistance

A brief summary of the proposed methology for evaluating V_f is given below.

$$V_f = \rho_f E_f \varepsilon_{fe} b_w d_f (\cot\theta + \cot\alpha)\sin\alpha$$

where: α is the angle of the FRP strips relative to the longitudinal axis.

- For Full Anchorage (Rupture Failures Expected)

$$\varepsilon_{fe} = R\varepsilon_{fu} \quad where \quad \varepsilon_{fu} = f_{fu}/E_f \quad and$$
$$R = 4(\rho_f E_f)^{-.67} \leq 1.0$$

where: $\rho_f E_f$ is in ksi units and limited to 300 ksi

- For Other Anchorage (Non-Rupture Failures more likely)

$$\varepsilon_{fe} = R\varepsilon_{fu} \leq 0.012 \quad where \quad \varepsilon_{fu} = f_{fu}/E_f \quad and$$
$$R = 3(\rho_f E_f)^{-.67} \leq 1.0$$

where: $\rho_f E_f$ is in ksi units and limited to 300 ksi

A5. EXPERIMENTAL WORK

A5.1 Overall Experimental Program

The experimental program was designed to address issues identified in Sections A1 through A4, which constituted Phase I of this research project. The primary focus was to investigate parameters which affected the shear behavior of FRP strengthened girders that have not been fully investigated in the existing experimental database. These parameters include the effects of: (1) pre-cracking, (2) negative moments, (3) long-term conditions such as fatigue loading and corrosion of internal steel reinforcement, and (4) prestressing. In addition, most prior experimental work was conducted on small-scale specimens, the results of which have been used as the basis for the current design equations adopted in most codes/guidelines/specifications. Thus an objective of the experimental program was also to expand the current experimental database with results for full-scale specimens that could be used to evaluate the reliability of existing design equations. The results of this experimental program, in addition to the existing experimental database, were used in the development of new design equations for predicting the contribution of externally bonded FRP to shear strength.

The experimental work was mainly divided into full-scale RC T-beams and AASHTO type prestressed I-girders. This section presents the experimental program and discussion of the experimental results for both.

A5.2 RC T-Beams

A5.2.1 General

The objective of the experimental program was to investigate the shear performance of full-scale RC T-beams strengthened with externally bonded FRP sheets. The experimental program consisted of a total of 15 tests performed on 8 full-scale RC beams. Each beam (except for the last beam which was designed for fatigue testing) was designed to provide two distinct test regions, from here on referred to as specimens. The principal parameters investigated were the effects of: (1) the transverse steel reinforcement index, (2) pre-cracking, (3) different mechanical anchorage systems, (4) different fiber orientations (45° and 90° relative to the longitudinal axis of the beams), (5) negative moment, (6) environmental conditioning (corrosion damage), and (7) fatigue loading.

A5.2.2 Test Matrix

The test matrix was designed to investigate the test parameters addressed in the previous section. Table A 5.1 presents the test matrix used in this study. The nomenclature of the specimen names indicates the stirrup spacing in inches (8 or 12), the strengthening configuration (S90 = strips at 90° to the longitudinal axis, and S45 = strips at 45°), the presence and type of mechanical anchorage (NA = no anchorage, DMA = discontinuous mechanical anchorage, SDMA = sandwich discontinuous mechanical anchorage, and HA = additional horizontal strips), the presence of pre-existing cracks (PC), testing under negative moment conditions (HM), and fatigue loading conditions (Ftg).

To investigate the effects of different amounts of transverse steel reinforcement (stirrups hereafter), two different stirrup spacings were chosen to simulate moderate and low levels of

transverse reinforcement. The design for moderate transverse reinforcement (stirrups spaced at 8 inches) met the minimum requirement of the AASHTO LRFD specification (2008) for transverse reinforcement. The design for low transverse reinforcement (stirrups spaced at 12 inches) did not meet the AASHTO LRFD specification (2008) requirement.

Beam 1 consisted of specimens RC-8-Control and RC-12-Control. Therefore, it was constructed with stirrups spaced at 8 inches on one end and 12 inches on the other end. The two tests performed on this beam provide a benchmark for comparison with the other tests and thus, no FRP strengthening was provided.

Beam 2 consisted of specimens RC-8-S90-NA and RC-8-S90-DMA and therefore was constructed with stirrups spaced at 8 inches along its full length. Both test regions were strengthened with FRP strips at 90°. Specimen RC-8-S90-NA was strengthened with only FRP strips, whereas RC-8-S90-DMA was strengthened with FRP strips as well as a discontinuous mechanical anchorage system.

Beam 3 consisted of specimens RC-12-S90-NA and RC-12-S90-DMA and therefore was constructed with stirrups spaced at 12 inches throughout its length. Both test regions were strengthened with FRP strips at 90°. Specimen RC-12-S90-NA was strengthened with only FRP strips, whereas RC-12-S90-DMA was strengthened with FRP strips as well as a discontinuous mechanical anchorage system.

Beam 4 consisted of specimens RC-12-S90-HA-PC and RC-12-S90-SDMA-PC and therefore was constructed with stirrups spaced at 12 inches throughout its length. Both test regions were pre-cracked under a specified loading of 60% of the anticipated shear capacity prior to being strengthened with FRP strips at 90°. Specimen RC-12-S90- HA-PC was strengthened with FRP strips and additional horizontal FRP strips for anchorage, whereas RC-12-S90- SDMA-PC was strengthened with FRP strips and a sandwich discontinuous mechanical anchorage system.

Beam 5 consisted of specimens RC-12-S90-SDMA-Cor and RC-12-S45-NA and therefore was constructed with stirrups spaced at 12 inches throughout its length. Specimen RC-12-S90-SDMA-Cor was conditioned under an accelerated corrosion process (discussed in detail in Section A5.2.8) prior to being strengthened with FRP strips at 90° and a sandwich discontinuous mechanical anchorage system. This specimen provided a performance evaluation for FRP shear strengthening of a corrosion damaged beam. Meanwhile, specimen RC-12-S45-NA was strengthened with FRP strips at 45° to the longitudinal axis of the beam without a mechanical anchorage system.

Beam 6 consisted of specimens RC-12-S45-HA and RC-12-S45-SDMA and therefore was constructed with stirrups spaced at 12 inches along the full length. Both test regions were strengthened with FRP strips at 45°. Specimen RC-12-S45-HA was strengthened with FRP strips and additional horizontal FRP strips for anchorage, whereas RC-12-S45-SDMA was strengthened with FRP strips and a sandwich discontinuous mechanical anchorage system.

Beam 7 was designed to investigate the behavior of an FRP shear strengthening system in negative moment regions. Beam 7 consisted of specimens RC-12-S90-HM and RC-12-S90-

SDMA-HM and therefore was constructed with stirrups spaced at 12 inches along its full length. Both test regions were strengthened with FRP strips at 90°. Specimen RC-12-S90-NA-HM was strengthened with FRP strips without a mechanical anchorage system, whereas RC-12-S90-SDMA was strengthened with FRP strips and a sandwich discontinuous mechanical anchorage system.

Beam 8 was designed to investigate the performance of FRP shear strengthening under fatigue loading. Beam 8 consisted of only specimen RC-12-S90-NA-Ftg and was constructed with stirrups spaced at 12 inches along its full length. The specimen was strengthened with FRP strips at 90° without a mechanical anchorage system.

Table A 5.1 Test matrix for RC T-Beams

T-Beam I.D.	Test I.D.	Test Parameters				
		Pre-Existing Cracks	Strengthening Scheme	Anchorage Type	Shear Reinforcement	
					ρ_v*	ρ_f**
1	RC-8-Control	No	No	Without Anchorage	0.0015 (#3@ 8 in. spacing) (To Specs)	0
	RC-12-Control				0.0010 (#3@12 in. spacing) (Deficient)	0
2	RC-8-S90-NA	No	Strip/90	No Mechanical Anchorage	0.0015 (#3@8 in.)	0.00048
	RC-8-S90-DMA			Discontinuous Mechanical Anchorage		
3	RC-12-S90-NA	No	Strip/90	No Mechanical Anchorage	0.0010 (#3@12 in.)	0.00048
	RC-12-S90-DMA			Discontinuous Mechanical Anchorage		
4	RC-12-S90-HA-PC	Yes	Strip/90	Horizontal Strips	0.0010 (#3@12 in.)	0.00048
	RC-12-S90-SDMA-PC	Yes	Strip/90	Sandwich Discontinues Mechanical Anchorage	0.0010 (#3@12 in.)	0.00048
5	RC-12-S90-SDMA-Cor	No	Strip/45	Sandwich Discontinues Mechanical Anchorage	0.0010 (#3@12 in.)	0.00048
	RC-12-S45-NA			Without Anchorage		0.00034
6	RC-12-S45-HA	No	Strip/45	Horizontal Strips	0.0010 (#3@12 in.)	0.00034
	RC-12-S45-SDMA	No	Strip/45	Sandwich Discontinues Mechanical Anchorage	0.0010 (#3@12 in.)	0.00034
7	RC-12-S90-NA-HM	No	Strip/90	No Mechanical Anchorage	0.0010 (#3@12 in.)	0.00048
	RC-12-S90-SDMA-HM	No	Strip/90	Sandwich Discontinuous Mechanical Anchorage	0.0010 (#3@12 in.)	0.00048
8	RC-12-S90-NA-Ftg	No	Strip/90	No Mechanical Anchorage	0.0010 (#3@12 in.)	0.00048

* ρ_v = transverse steel reinforcement (stirrups) ratio = $A_v / b_w s$

** ρ_f = External FRP shear reinforcement ratio = $A_f / b_w s_f = 2 t_f w_f / b_w s_f$

A5.2.3 Beam Details

A5.2.3.1 Beam Design

The test beams were designed to mimic the geometry of beams used in a bridge located in Troy, New York (Hag-Elsafi et al. 2001a) which is one of very few examples in wich an extensive field investigation using externally bonded FRP strengthening was used. This bridge is a 42 feet long by 120 feet wide RC structure consisting of 26 simply-supported T-beams spaced at 4.5 feet on center with an integral concrete deck. The bridge was built in 1932 and since then has suffered from severe corrosion damage. The RC T-beams of the bridge have been strengthened in shear and flexure with externally bonded CFRP laminates. These repairs have been monitored through strain gages placed on the internal steel reinforcement and CFRP laminates. A typical beam section of the Troy Bridge had a total depth of 37.5 inches, including a 7 inch deep flange and 18 inch wide web. The main flexural reinforcement consisted of eight 1.25 inch square steel reinforcing bars. The cross section of these bars was measured when they were exposed for the mounting of strain gages during the repair program conducted by NYDOT. Figure A 5.1 shows the cross section of the T-beams as presented in the report published by Hag-Elsafi et al. (2001a). To recreate this cross sectional layout as closely as possible, the T-beams for the experimental program should have cross-sectional dimensions and reinforcement scheme as detailed in Figure A 5.2.

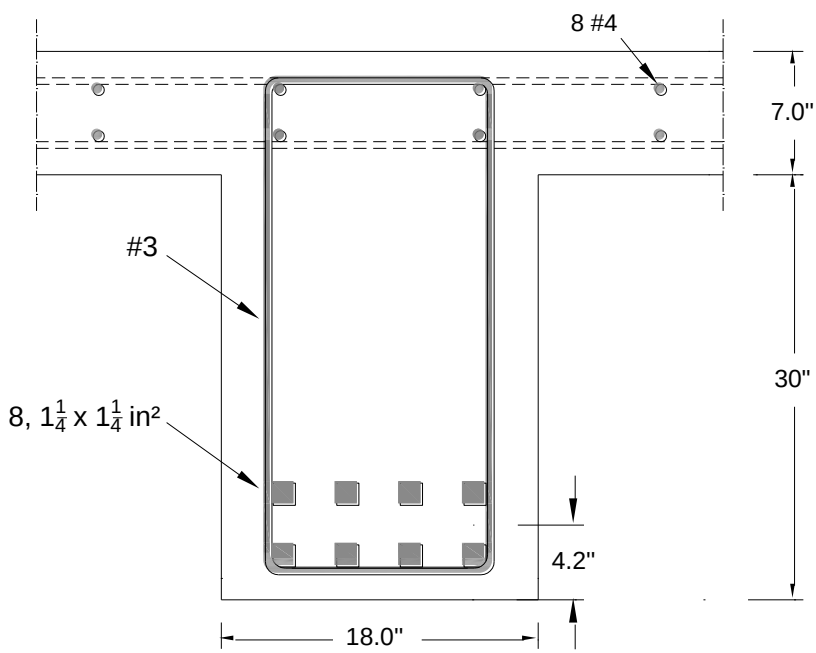

Figure A 5.1 Cross Section of Typical Beams in Troy Bridge (Hag-Elsafi et al. 2001a)

However, because the beams of the Troy Bridge were fabricated in 1932, the concrete and steel properties are quite different from those used today. Material properties for the concrete and steel used in the Troy Bridge were not properly documented. The researchers of NYDOT conservatively assumed the yield strength of the steel reinforcement (f_y) to be 30 ksi and the concrete strength (f'_c) to be 3 ksi. These material properties are not readily available from today's manufacturers; therefore, more common materials (f_y = 40 ksi and f'_c = 4 ksi) were used to construct the test beams. In addition, the longitudinal reinforcement of the Troy beams

consists of 1.25 inch square steel bars that are no longer manufactured. To maintain the same area of steel and same number of bars found in the Troy Bridge, eight #11 bars should be used.

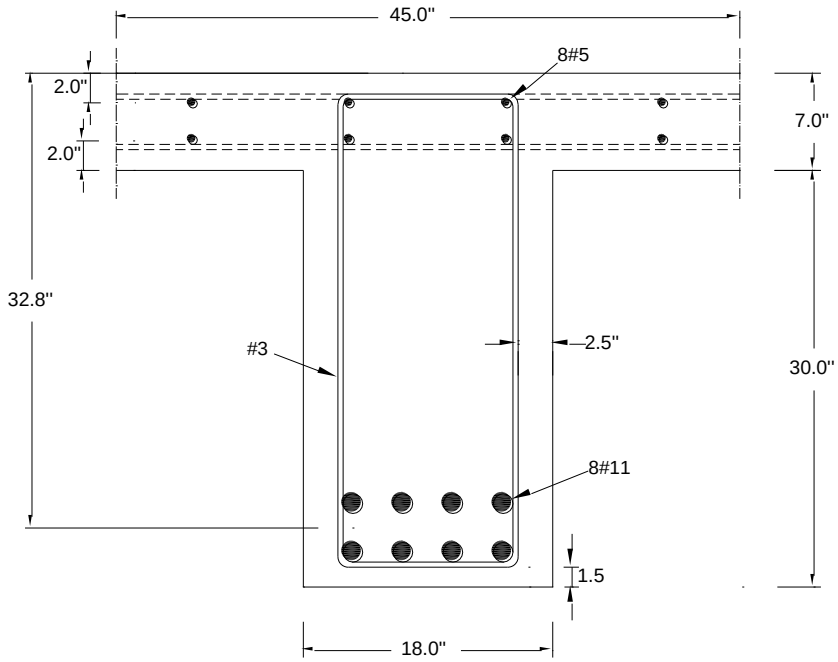

Figure A 5.2 Equivalent Cross-Section Modeled on Troy Bridge Beams

The geometry of the cross section of the test beams exactly reproduced that of the Troy Bridge. According to AASHTO-LRFD design specifications (AASHTO, 2008), the effective width of the flange was calculated as the smallest of:

1) $b \le \frac{l}{4} \Rightarrow b \le \frac{42\text{ ft}}{4} = 10.5\text{ ft} = 126\text{ in.}$
2) $b_{ti} \le 6 \cdot t_f = 6 \times 7\text{ in.} = 42\text{ in.} \;\Rightarrow\; b \le (42\text{ in.} \times 2) + 18\text{ in.} = 102\text{ in.}$
3) $b_{ti} \le \frac{l_n}{2} \;\Rightarrow\; b = \frac{36\text{ in.}}{2} \cdot 2 + 18\text{ in.} = 54\text{ in.}$ (controls)

where: b = effective flange width, b_{ti} = effective overhanging flange width on each side of the web, l = span of the beam, and l_n = clear distance to the next web

This value (54 in.) was compared to the values of the effective width of the flange estimated by NYDOT researchers in 1999 and 2001 (Hag-Elsafi et al. 2001b) based on the results of load testing under truck loads. Their measurements (44.3 to 46.6 inches) are close to those obtained analytically, thus validating their accuracy. Assuming the measured values to be more reliable, an effective width of 45 inches was chosen for the design of the test beams; however, due to the limitations of the test set-up, an effective width of 42 inches was finally selected for the test beams.

The cross section was analyzed according to the ACI 318-08 (ACI 318, 2008) and AASHTO LRFD (AASHTO, 2008) design codes. The Response 2000 software (Collins and Mitchell, 1997), which is based on the modified compression field theory, was also used to analyze the behavior of the cross section. The analysis showed that twelve #11 Grade 60 reinforcing bars in two layers near the tension face were needed to provide adequate flexural reinforcement to prevent flexural failure. The transverse reinforcement was designed to ensure shear failure prior to flexural failure and thus required the use of #3 stirrups at moderate (8 in.) and large (12 in.) spacings as described previously. Grade 40 steel was used for the transverse reinforcement, similar to that used in the Troy Bridge. The final cross section design is shown in Figure A 5.3.

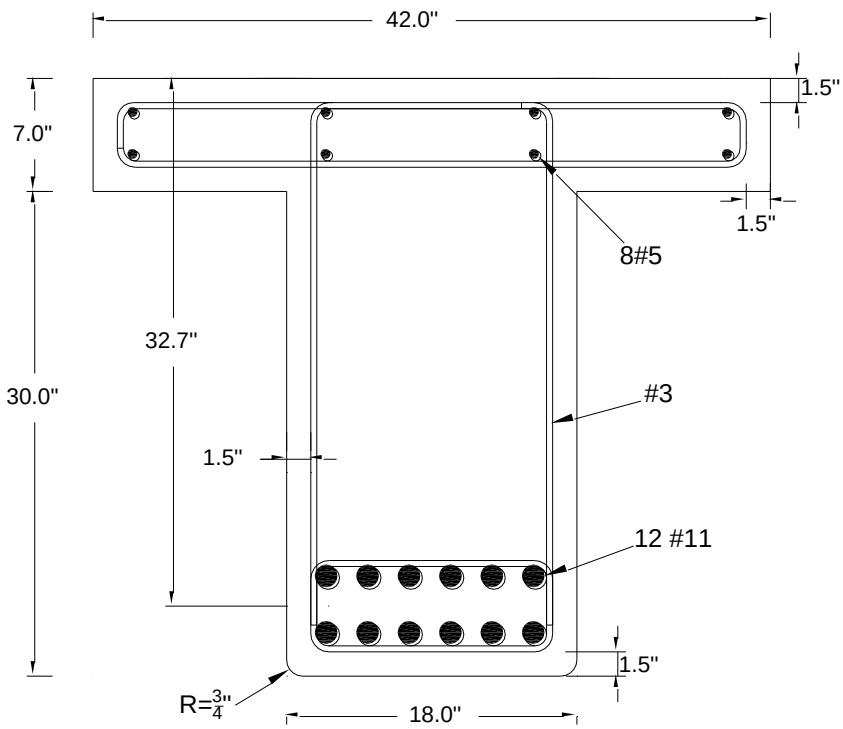

Figure A 5.3 Cross-Section of Test Beams

A5.2.3.2 Reinforcement Details

The length of Beams 1 through 7 was 37 feet while Beam 8 was only 28 feet long. The total height of all test beams was 37 inches. Beams 1 through 7 had two distinct test regions while Beam 8 had only one test region. Each test region was 9 feet in length from center line of the end support to center line of the reaction frame. Longitudinal reinforcements consisted of twelve #11 Grade 60 reinforcing bars for tension reinforcement and eight #5 Grade 60 reinforcing bars for compression reinforcement. The stirrups in the test region were #3 Grade 40 reinforcing bars, and the center-to-center spacing was either 8 inches or 12 inches depending on the specimen. Additional stirrups at a reduced spacing of 4 inches were provided at both ends to prevent failure near support regions. The reinforcement details of all beams are presented in Figures A 5.4 through A 5.7.

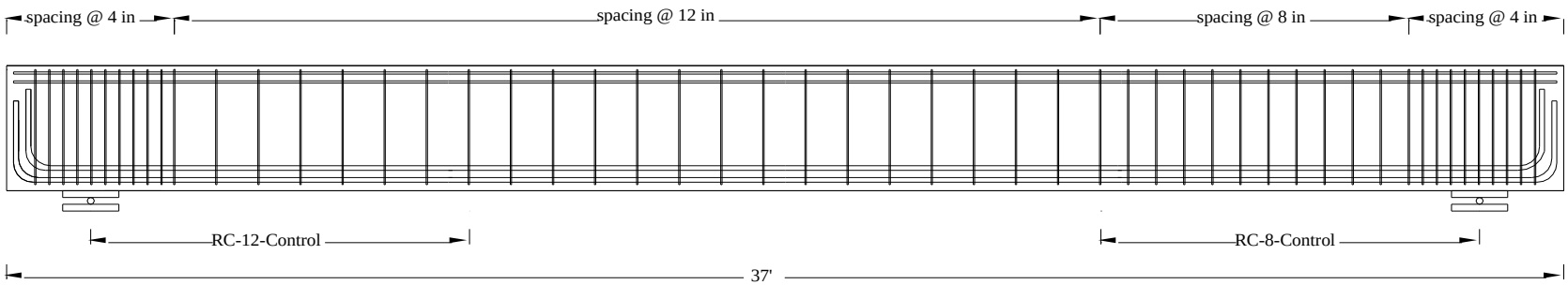

Figure A 5.4 Reinforcement Details - Beam 1

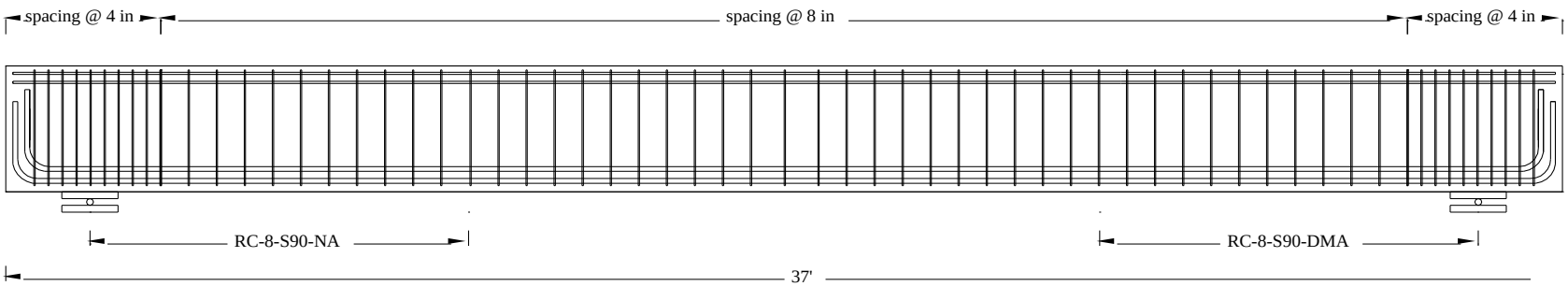

Figure A 5.5 Reinforcement Details - Beam 2

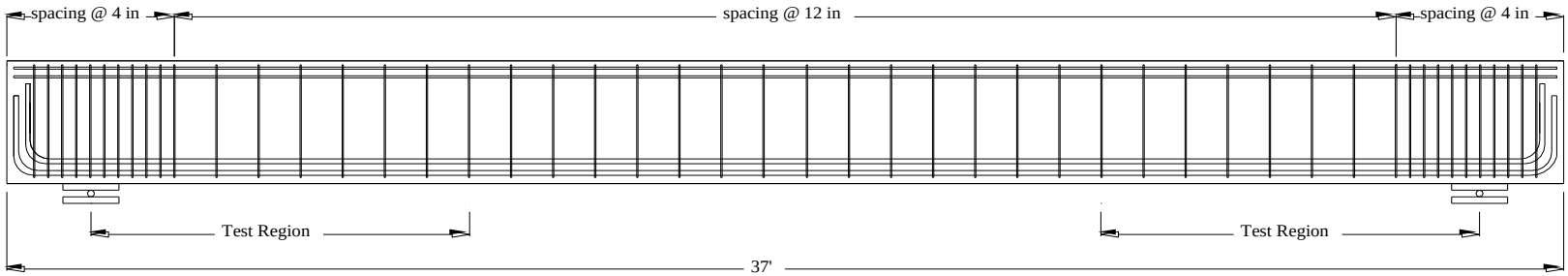

Figure A 5.6 Reinforcement Details - Beams 3, 4, 5, 6, and 7

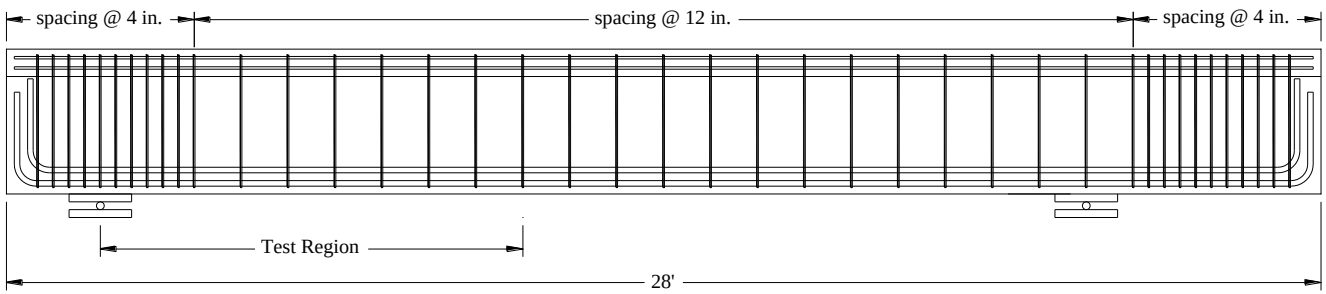

Figure A 5.7 Reinforcement Details - Beam 8

A5.2.3.3 FRP Strengthening Details

All specimens, except for the control specimens, were strengthened with one-ply of CFRP applied as discrete strips that were U-wrapped along the test region. Each strip was 10 inches wide with center-to-center spacing of 15 inches for fibers oriented at 90° and 21.21 inches for fibers oriented at 45°. Some applications also included a mechanical anchorage system. The FRP strips have been labeled #1 through #6, with #1 being closest to the reaction point and #6 being closest to the support. This pattern is the same for all test specimens strengthened with FRP. The FRP strengthening details of all specimens are provided in Figures A 5.8 through A 5.15.

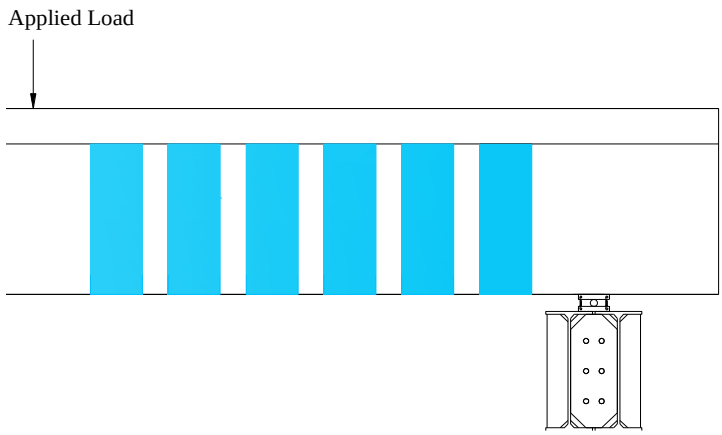

Figure A 5.8 FRP Application Details - Beams with 90 ° Fiber Orientation without Mechanical Anchorage System - RC-8-S90-NA, RC-12-S90-NA, and RC-12-S90-NA-Ftg

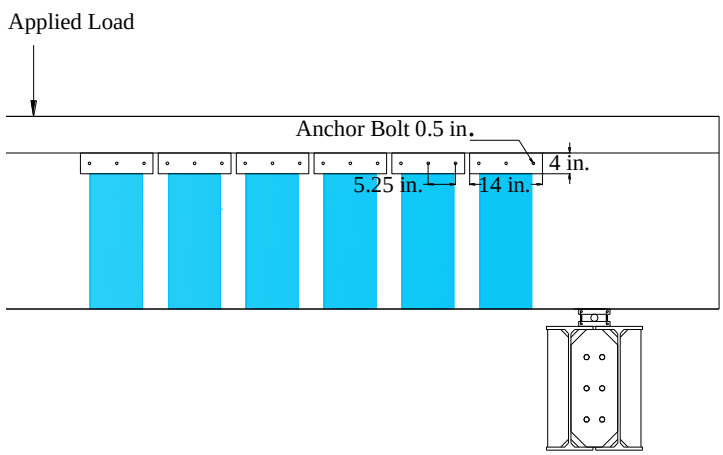

Figure A 5.9 FRP Application Details - Beams with 90 ° Fiber Orientation with a Mechanical Anchorage System - RC-8-S90-DMA, RC-12-S90-DMA, RC-12-S90-SDMA-PC, RC-12-SDMA-Cor

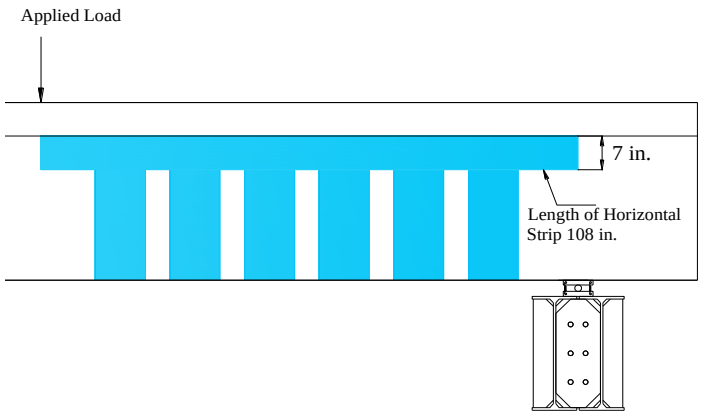

Figure A 5.10 FRP Application Details - Beams with 90 ° Fiber Orientation with Horizontal FRP Strips - RC-12-S90-HA-PC

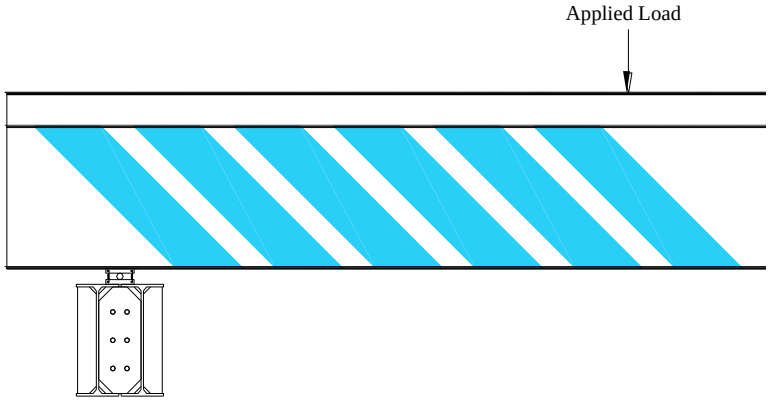

Figure A 5.11 FRP Application Details - Beams with 45 ° Fiber Orientation without Mechanical Anchorage Systems- RC-12-S45-NA

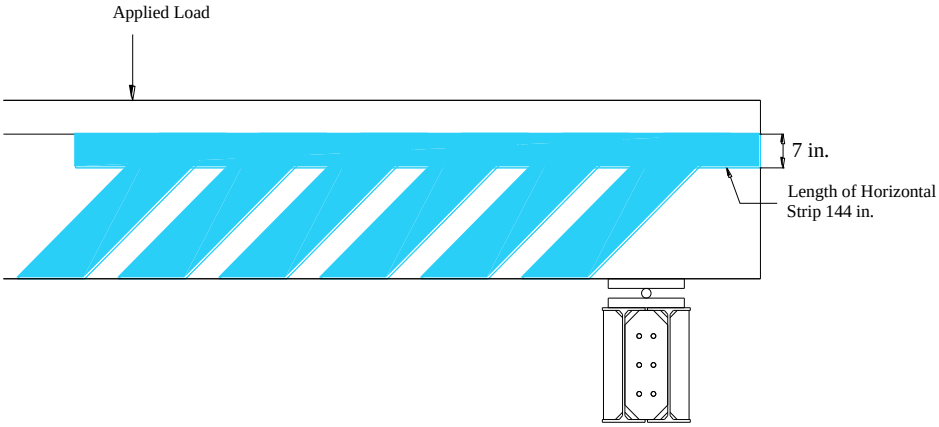

Figure A 5.12 FRP Application Details - Beams with 45 ° Fiber Orientation with Horizontal FRP Strips - RC-12-S45-HA

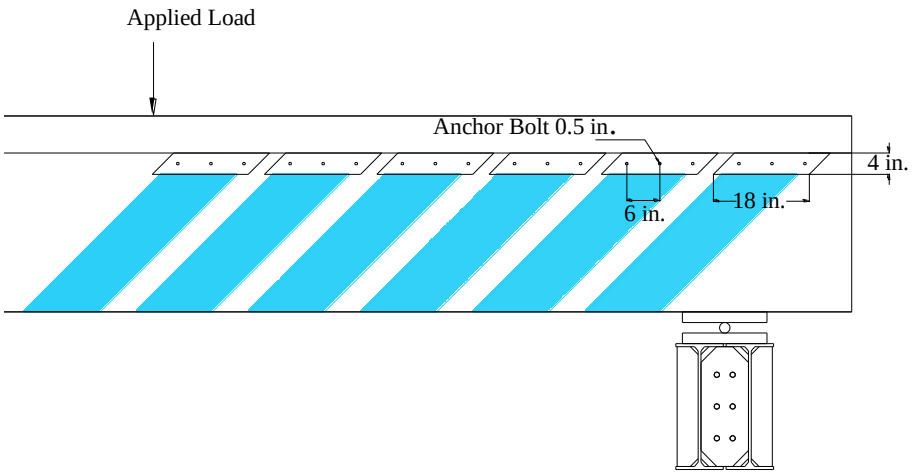

Figure A 5.13 FRP Application Details - Beams with 45 ° Fiber Orientation with Mechanical Anchorage Systems - RC-12-S45-HA

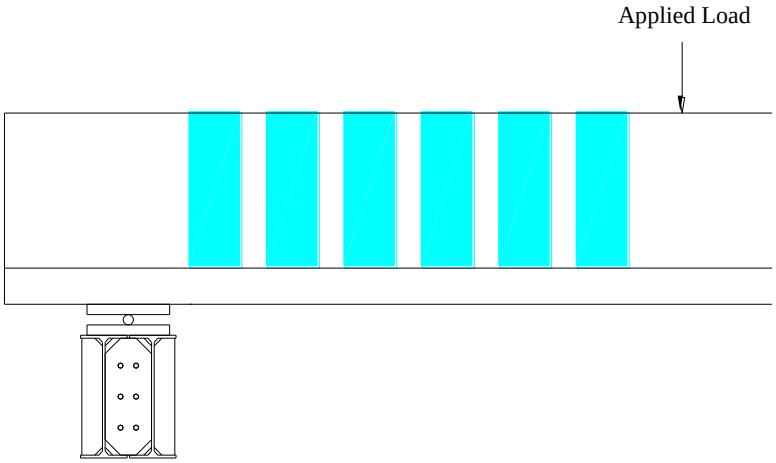

Figure A 5.14 FRP Application Details - Beams with 45 ° Fiber Orientation without Mechanical Anchorage Systems Subjected to Negative Moment- RC-12-S90-NA-HM

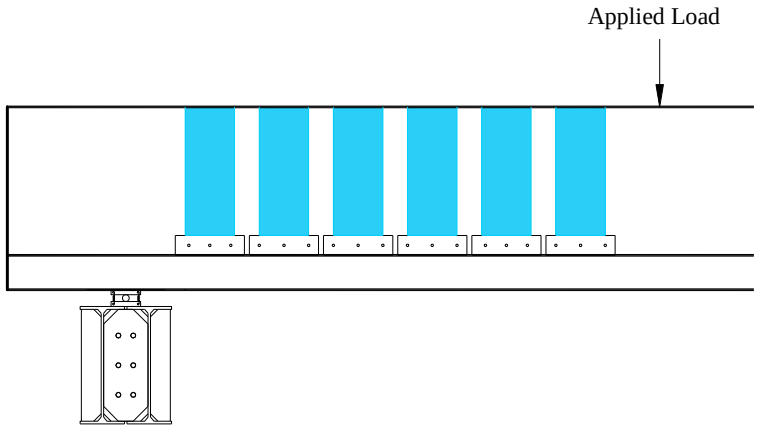

Figure A 5.15 FRP Application Details - Beams with 45 ° Fiber Orientation with Mechanical Anchorage Systems Subjected to Negative Moment- RC-12-S90-SDMA-HM

A5.2.4 Materials Used

A5.2.4.1 Concrete

The concrete used in this study was provided by a local plant with an expected 28-day target strength of 4,000 psi. Due to the large cross-sectional dimensions, only one beam could be cast at a time, but the same concrete mix design was used for all test beams which included a maximum aggregate size of 1 inch. During each casting, 12 standard cylinders (6 inches in diameter and 12 inches in height) were cast to monitor the concrete strength for each beam in accordance with ASTM C39/C39M (2005). Table A 5.2 reports the concrete compressive strengths at the time of testing for each specimen.

Table A 5.2 Compressive Strength of Concrete

T-Beam I.D.	Test I.D.	Compressive Strength at Time of Testing (psi)
1	RC-8-Control	2,800
	RC-12-Control	2,880
2	RC-8-S90-NA	3,060
	RC-8-S90-DMA	3,450
3	RC-12-S90-NA	4,190
	RC-12-S90-DMA	4,420
4	RC-12-S90-HA-PC	2,650
	RC-12-S90-SDMA-PC	2,780
5	RC-12-S90-SDMA-Cor	6,180
	RC-12-S45-NA	6,050
6	RC-12-S45-HA	3,850
	RC-12-S45-SDMA	4,230
7	RC-12-S90-NA-HM	3,710
	RC-12-S90-SDMA-HM	4,060
8	RC-12-S90-NA-Ftg	4,730

A5.2.4.2 Steel Reinforcement

Shear reinforcement for the test specimens consisted of #3 reinforcing bars of Grade 40 (web) and Grade 60 (flange) steel. All longitudinal reinforcement was Grade 60 steel, with #5 bars for compression reinforcement in the top flange and #11 bars for flexural tension reinforcement. All steel reinforcement was tested in accordance with ASTM A370 (2008) to obtain the mechanical properties which are summarized in Table A 5.3.

Although Grade 40 steel was specified for the web reinforcement, a yield stress of approximately 60 ksi was obtained from testing of coupons (see Figure A 5.28). Based on these results, the stress-strain relationship of the steel reinforcement was developed as shown in Equation A 5-1. This relationship was used in the analysis of the test results.

Table A 5.3 Mechanical properties of steel reinforcement

Bar Size	Grade	Yield Strength (ksi)	Ultimate Strength (ksi)
#3 (Stirrups in the web)	40	59.8	91.8
#3 (Stirrups in the flange)	60	77.7	106.1
#5 (Flexural compression steel)	60	66.2	99.4
#11 (Flexural tension steel)	60	70.9	108.1

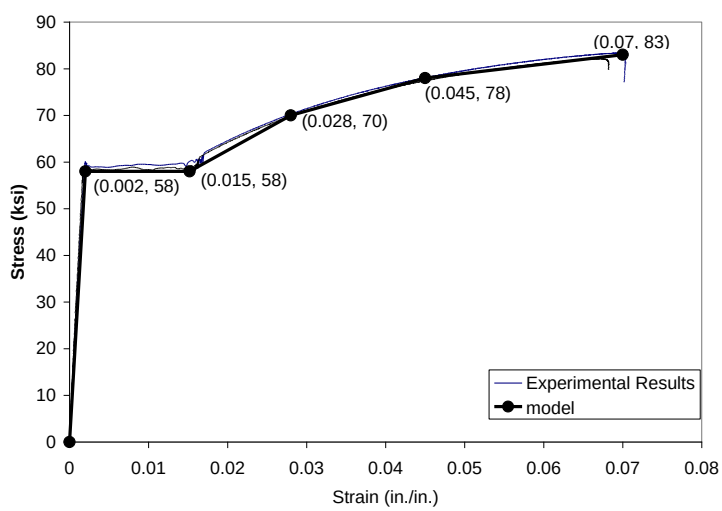

Figure A 5.16 Stress-strain relationship for Grade 40 steel used for Stirrups

$f_s = E_s \varepsilon_s$ (ksi); $E_s = 29{,}000$ ksi when $\varepsilon_s \le 0.002$ (A5-1a)

$f_s = 58$ (ksi) when $0.002 < \varepsilon_s \le 0.015$ (A5-1b)

$f_s = 923\varepsilon_s + 43.75$ (ksi) when $0.015 < \varepsilon_s \le 0.028$ (A5-1c)

$f_s = 471\varepsilon_s + 56.82$ (ksi) when $0.028 < \varepsilon_s \le 0.045$ (A5-1d)

$f_s = 200\varepsilon_s + 69$ (ksi) when $0.045 < \varepsilon_s \le 0.07$ (A5-1e)

A5.2.4.3 CFRP Composites

FRP Sheets

Carbon fiber reinforced polymer (CFRP) sheets were provided by Mbrace Systems® (MBrace, 1998), and the mechanical properties provided by the manufacturer are shown in Table A 5.4. The FRP sheets were applied to a small area outside of the test region (Figure A 5.17), a so called pull-off test region, using the same materials and methods used for the application of FRP in the test region. Three direct pull-off tests, performed in accordance with ASTM D4541-03 (2003), were conducted for each specimen to obtain the FRP-concrete interface bond strength. All test results showed that bond strength was greater than the minimum requirement of 200 psi specified by ACI 440.2R-08 (2008), as shown in Table A 5.5.

.

Table A 5.4 Mechanical properties of FRP strips

	Manufacturer's Data
Design Strength, ksi	550
Design Strain, in./in.	0.017
Elastic Modulus, ksi	33,000

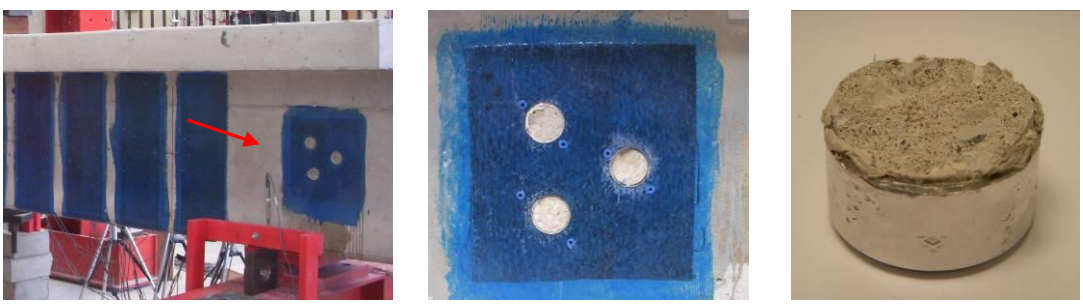

(a) Sampling area for pull-off tests (b) FRP sheets on the sampling area after pull-off tests (c) Pull-off specimen showing failure modes

Figure A 5.17 Pull-Off Test – Test Region, FRP Sheets After Testing, and Pull-Off Specimen

Table A 5.5 Pull-Off Test Results

Test I.D.	Bond Strength Pull-off Test (psi)			Average (psi)
	#1	#2	#3	
RC-8-S90-NA	378	458	462	433
RC-8-S90-DMA	211	363	374	316
RC-12-S90-NA	498	471	363	444
RC-12-S90-DMA	322	274	319	305
RC-12-S90-HA-PC	227	344	362	311
RC-12-S90-SDMA-PC	315	356	256	309
RC-12-S90-SDMA-Cor	528	508	517	517
RC-12-S45-NA	523	449	333	435
RC-12-S45-HA	295	326	372	331
RC-12-S45-SDMA	306	365	349	340
RC-12-S90-NA-HM	403	376	381	387
RC-12-S90-SDMA-HM	464	469	437	457
RC-12-S90-NA-Ftg	406	122*	333	369

*Data was not used in the calculation of average bond strength because failure occurred at the FRP-concrete interface due to inappropriate application of the bonding material.

Epoxy Resins

The fiber sheets were bonded to the concrete surface using primer, putty, and saturant. All resins were provided by MBrace® (MBrace, 1998). Table A 5.6 summarizes the mechanical properties of these products, as specified by the manufacturer.

Table A 5.6 Summary of Mechanical Properties of Resins

	Modulus of Elasticity (ksi)	Ultimate Tensile Strength (psi)	Tensile Rupture Strain (%)	Glass Transition Temp. (ºF)
Primer	105	2,500	40	171
Putty	260	2,200	7	168
Saturant	440	8,000	3.5	163

CFRP Plates for Mechanical Anchorage

The FRP laminates used as plates for the mechanical anchorage system consisted of pre-cured glass and carbon hybrid pultruded strips embedded in a vinyl ester resin. The pre-cured laminate had a thickness of 0.127 inches and width of 4 inches. Table A 5.7 summarizes the mechanical properties of the laminates. These FRP laminate plates were attached to the surface of the beam with epoxy saturant and concrete wedge anchors.

Table A 5.7 Mechanical properties of laminates (Rizzo et al. 2005)

Properties	Strength/Capacity
Stress at Failure (ksi)	121
Modulus of Elasticity (ksi)	8,992
Open Hole Tensile Strength (ksi)	121
Uncostrained Bearing Capacity (kips)	53

A5.2.4.4 Concrete Wedge Anchor for Mechanical Anchorage Systems

The fastening system chosen for the CFRP plates used as mechanical anchorage consisted of commercially available steel wedge anchors. The anchors for specimen RC-8-S90-DMA were provided by Red Head® while the anchors used in all other specimens were provided by Thunderstud®. Both were 0.5 inches in nominal diameter and 4 inches in embedment length. Technical data provided by the manufacturers are shown in Table A 5.8.

Table A 5.8 Wedge Anchor Properties

Anchor Type	Anchor Diameter (in.)	Embed. Depth (in.)	Torque (ft/lb)	Mechanical Properties for 4,000 psi Concrete	
				Tension (lb)	Shear (lb)
Red Head®	1/2	4	55	9,640	7,240
Thunderstud®	1/2	4	50/60	10,175	9,377

A5.2.5 Beam Fabrication

A5.2.5.1 Construction of the Beams

All test beams were constructed in the Highbay Structures Laboratory at Missouri S&T. Steel form-work was used to cast the beams. The steel cage was assembled from reinforcement that was pre-bent by the manufacturer to the desired geometry and shipped to the laboratory. To set up the external shear strengthening system, it was necessary to leave holes in the flange by placing PVC pipes in the formwork so that the Dywidag bars could pass through. To reduce the amount of surface preparation prior to the application of FRP, the soffit of the beam was cast with rounded corners, having a 0.75 inch radius, using plastic chamfer strips. Due to the large dimensions of the T-beams, it was possible to cast only one beam at a time. After casting, the top surface of the beams was covered with plastic sheeting and a wet surface was maintained for seven days to retain moisture for proper curing. Cylinders were cured in the same environment as the test beams by placing them underneath the same plastic sheeting. Pictures showing the construction process are presented in Figure A 5.18.

(a) Steel cage assembly

(b) Formwork

(c) Concrete pouring

(d) Constructed T-Beam

Figure A 5.18 Beam Construction Process

A5.2.5.2 FRP Application

Prior to application of the FRP sheets, the concrete surface was prepared using a concrete grinder with a revolving head in accordance with ICRI 03732 (1997). Grinding was only performed on the surfaces where the sheets were to be applied on both sides of the beam (Figure A 5.19(a)). After grinding, the surface was cleaned using a vacuum and compressed air to remove all dust and fine particles that might impair the bond of FRP. The concrete surface was then coated with a layer of epoxy-based primer using a short nap roller (Figure A 5.19 (b)). The function of the primer was to penetrate the fine pore structure of the concrete in order to achieve high bond strength between the FRP sheets and the concrete surface. To fill the small holes and level the surface, a thin layer of epoxy-based putty was then applied using a putty knife (Figure A 5.19 (c)). Then, a coat of saturant was applied to the beam surface using a short nap roller (Figure A 5.19 (d)). FRP sheets cut to the required length were then pressed into place in the desired location and with the appropriate orientation on the concrete surface. A ribbed steel roller was rolled over the surface of the FRP sheets to impregnate the fibers with saturant. Finally, an overcoat of the same saturant was applied to the surface of the FRP sheets (Figure A 5.19 (e)).

(a) Surface preparation | (b) Applying primer | (c) Applying putty

(d) Applying first coat of saturant | (e) Applying FRP sheets and second coat of saturant

Figure A 5.19 FRP Application Process

A5.2.5.3 Anchorage Systems

Anchorage systems can be used to enhance the shear contribution of FRP by preventing premature failure due to FRP debonding. Three different types of anchorage systems were used including: (1) discontinuous mechanical anchorage systems (DMA), (2) sandwich discontinuous mechanical anchorage systems (SDMA), and (3) additional horizontal FRP strips.

Discontinuous Mechanical Anchorage System (DMA)

This system consisted of two CFRP pre-cured laminate plates bonded to each FRP strip with epoxy resin and anchored firmly in place with concrete wedge anchors. The mechanical anchorage was applied in several steps: (1) cutting and pre-drilling of the plates to the desired geometry as shown in Figure A 5.20; (2) drilling of 4.5 inch deep holes in the appropriate locations along the concrete web with a hammer drill and ½ inch diameter bit; (3) cleaning of the holes and surface with compressed air to remove any dust that might impair the bond of the saturant; (4) setting the fasteners in the holes by driving them with a hammer; (5) mixing and application of saturant to one side of each plate using a short nap roller; and (6) positioning of the plates and fixing them in place with washers and nuts tightened to a controlled torque. Geometric details of the anchorage system are shown in Figure A 5.14.

(a) Cutting the plates (b) Drilling the plates

Figure A 5.20 FRP plate preparation

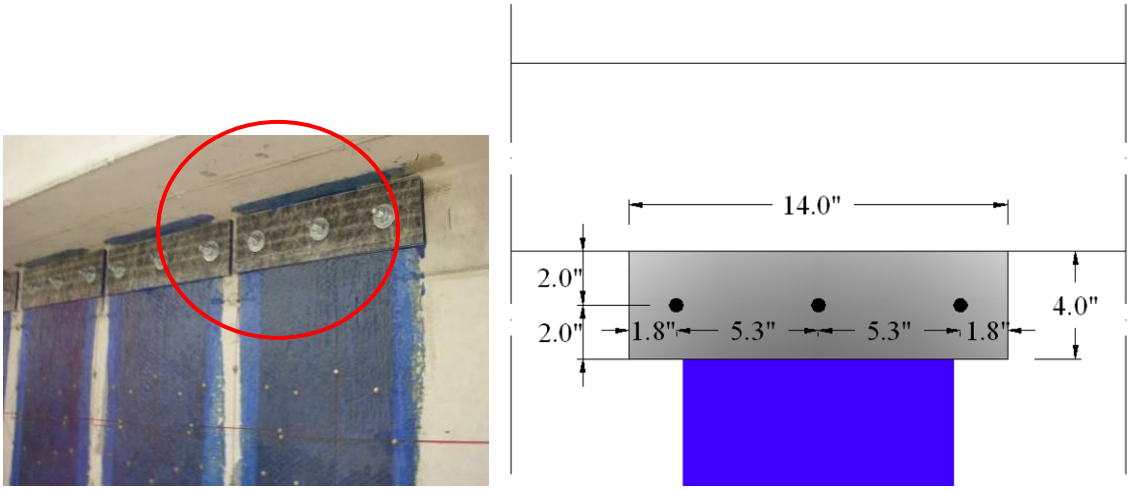

Figure A 5.21 Details of Discontinuous Mechanical Anchorage

<u>Sandwich Discontinuous Mechanical Anchorage System (SDMA)</u>

The sandwich discontinuous mechanical anchorage system (SDMA) is similar to the DMA with the only difference being that the FRP strips are wrapped around the first FRP plate and secured tightly by overlapping it with the second FRP plate for better anchorage as detailed in Figure A 5.22.

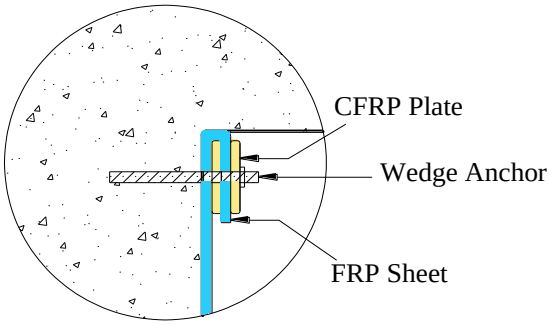

Figure A 5.22 Details of Sandwich Discontinuous Mechanical Anchorage

Construction of this mechanical anchorage system was also slightly different from the processes for DMA. First, the FRP sheets and FRP plates were cut to the required length. A coat of saturant was then applied to the FRP sheet where the anchorage would be located, as shown in Figure A 5.23(a). The FRP plate was then set in the saturant and centered appropriately as shown in Figure A 5.23(b). An additional coat of saturant was applied to the plate as shown in Figure A 5.23(c). The FRP sheet was then folded to wrap the plate as shown in Figure A 5.23(d) and a ribbed steel roller was used to impregnate the fibers with saturant as shown in Figure A 5.23(e). Another coat of saturant was applied to the sheet to obtain a better bond between the plates and the FRP sheet, as shown in Figure A 5.23(f). The second plate was then set in the saturant and squared appropriately with the first plate as shown in Figure A 5.23(g). To ensure a good bond between these elements, the plates were secured with screws, as shown in Figure A 5.23(h), and steel plates or concrete blocks were placed on top to help compress them together while the saturant was allowed to dry as shown in Figure A 5.23(i). After securing the mechanical anchorage plates to the FRP sheets, the FRP application was conducted following the same procedure detailed in Section A5.2.5.2. Figure A 5.24 shows a beam with this mechanical anchorage system.

Additional Horizontal FRP Strips

This anchorage system is composed of an extra FRP composite strip parallel to the longitudinal axis of the beam covering all the free edges of the vertical FRP strips where debonding usually initiates, as shown in Figure A 5.25. The appropriate width of the horizontal strips was determined to be 7 inches based on predictions of the effective bond length of the vertical FRP strips using currently available bond models. The length was 108 inches in order to span the full length of the test region. This anchorage system was installed immediately after the application of the vertical FRP sheets to obtain better bond between the vertical and horizontal FRP sheets.

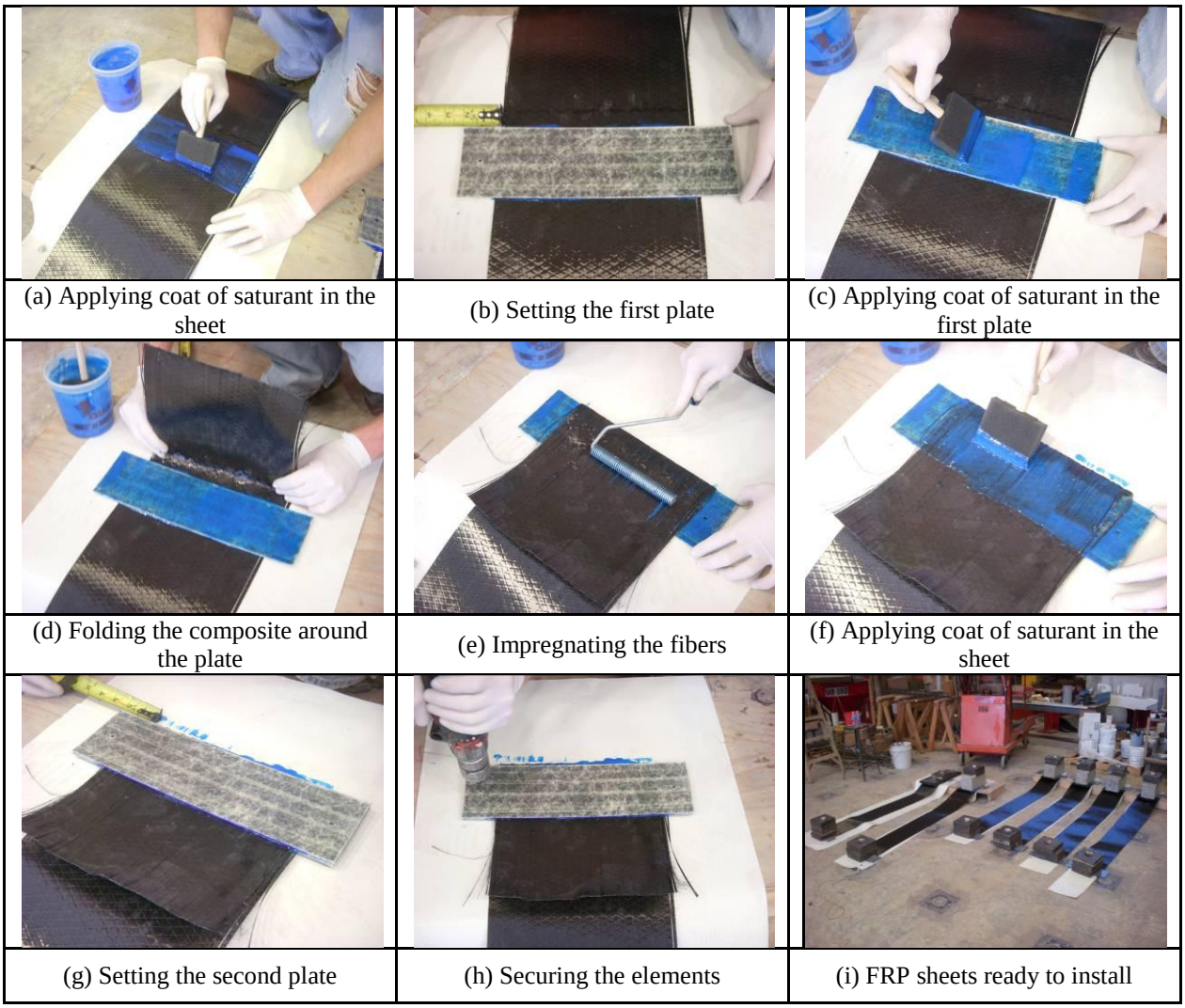

(a) Applying coat of saturant in the sheet	(b) Setting the first plate	(c) Applying coat of saturant in the first plate
(d) Folding the composite around the plate	(e) Impregnating the fibers	(f) Applying coat of saturant in the sheet
(g) Setting the second plate	(h) Securing the elements	(i) FRP sheets ready to install

Figure A 5.23 Construction of Mechanical Anchorage Systems

Figure A 5.24 A Test Beam with Sandwich Mechanical Anchorage System

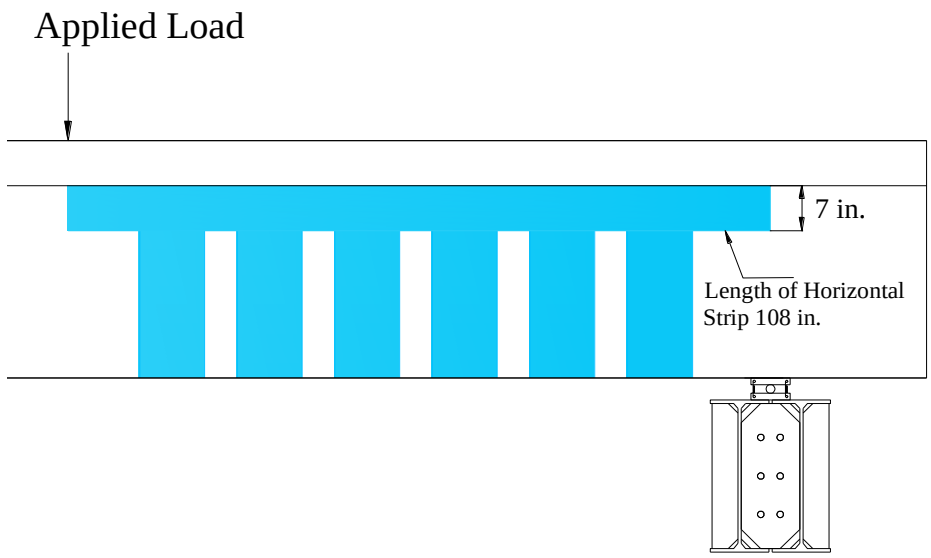

Figure A 5.25 An Example of Additional Horizontal FRP Strips - RC-12-PC-S90-HS

A5.2.6 Test Set-Up

All specimens were tested under simply supported conditions subjected to a three-point loading. The maximum compression capacity of the actuators available in the Highbay Structures Laboratory was inadequate to cause specimen failure in a three point loading scheme with concentrated downward loading at point B, as shown in Figure A 5.26(a). Therefore, the test set-up was modified as shown in Figure A 5.26(b). This test set-up used the reaction force to generate the required shear force. It significantly reduced the load required by the actuators by a function related to the distance between the reaction frame and the loading point.

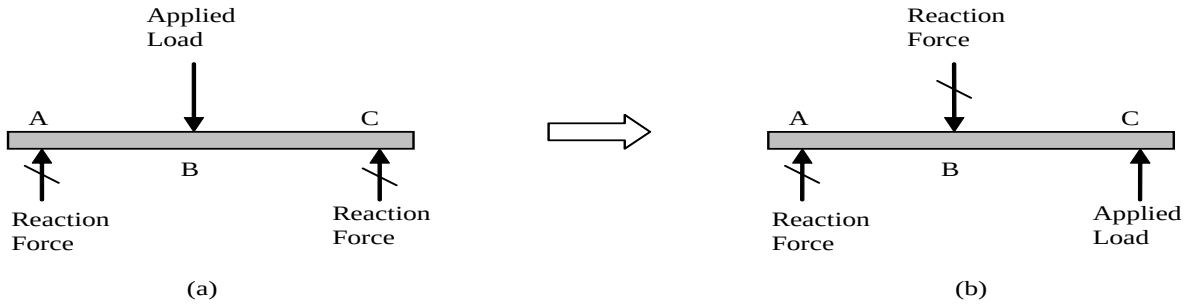

Figure A 5.26 Test Set-up Scheme

Two actuators with 110-kips of tensile capacity were used to apply load to the beam, as shown in Figure A 5.27 and Figure A 5.28. They pull upward on the beam to simulate the concept illustrated in Figure A 5.26(b). The loading and reaction frame assemblies were designed to withstand at least three times the anticipated maximum load and reaction force applied to the corresponding frames. The tests were performed under deformation control, and the load was applied in a series of loading steps until failure. Electronic measurements of strain and deformation were recorded throughout the entire loading history of the specimens while hand measurements of strain and crack pattern formations were taken at pauses between each loading step. Measurement devices are described in greater details in Section A5.2.7.

Each beam consisted of two test regions. The total beam length was 37 feet, with a simply supported span length of 24 feet. The middle reaction was 9 feet from the support, giving a shear span-to-depth ratio of 3.3. The advantage of this configuration was that one test beam could be used for testing two specimens by moving the supports and relocating the cantilever portion. Thus, two distinct tests were performed on each beam as follows: (1) The left test region of the beam was tested first until shear failure occurred, (2) the supports, loading and reaction frames were moved such that the right test region was subjected to the same loading conditions as the left test region, and (3) the right test region was tested. In addition, external shear reinforcement was provided to protect the right test region from premature failure during testing of the left test region. The external reinforcement consisted of two HSS steel members placed on top and bottom of the beam, connected by two #11 Dywidag bars having yield stress of 75 ksi (see Figure A 5.27). Based on this test set-up the shear force in the test region is about 5/3 larger than the shear force outside the test region.

For Beam 7 which was used for the investigation on the effects of negative moment, the test beam was placed upside down as shown in Figure A 5.29 and the same concept was used to apply the shear force to load the beam up to failure.

A5.2.7 Instrumentation

The specimens were instrumented with several measurement devices to monitor global and local deformation and strains. A load cell was also used to measure the force at the reaction point and thus to calculate the shear force in the test region. All devices were connected to a data acquisition system capable of recording data from up to 120 channels. In this section, the overall instrumentation scheme is presented while detailed information on each specimen can be found in Additional Material C to Appendix.

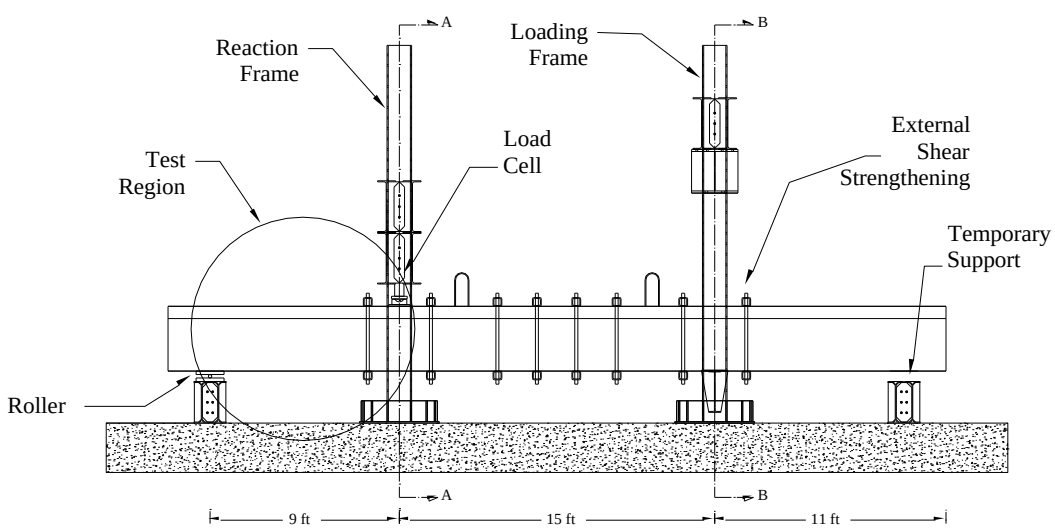

Figure A 5.27 Details of test set-up (section A-A and B-B are shown in Figure A 5.28)

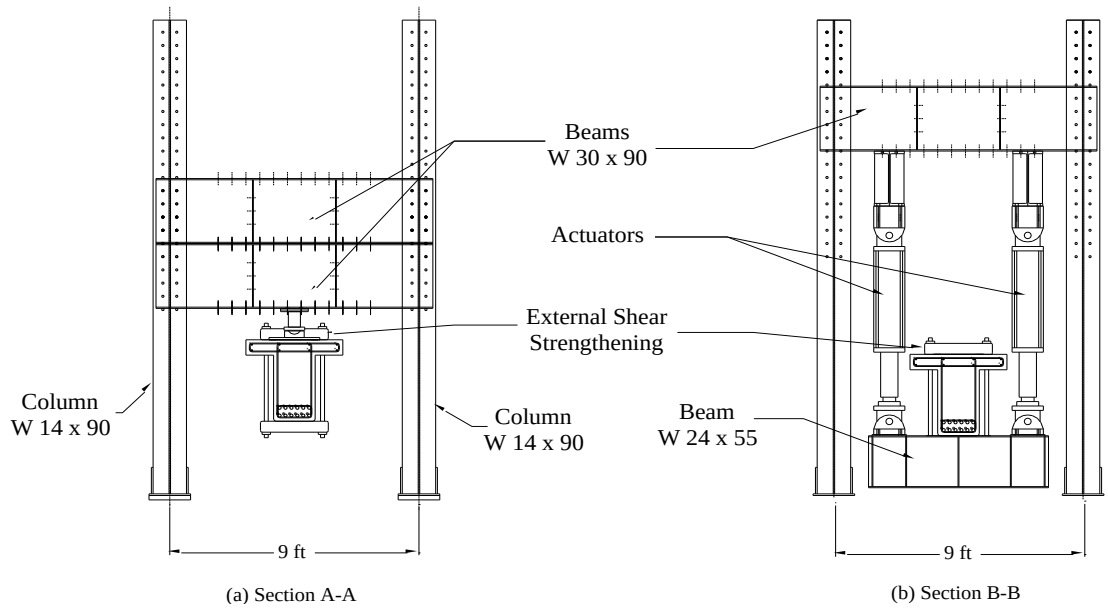

Figure A 5.28 Details of (a) reaction and (b) loading frame

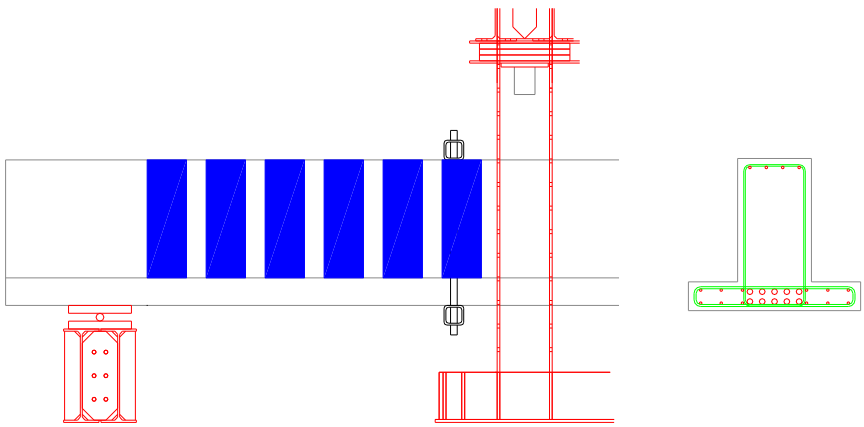

Figure A 5.29 Test Set-Up for Beam 8 - RC-12-S90-NA-HM and RC-12-S90-SDMA-HM

A5.2.7.1 Local Deformations and Strains

Electric resistance strain gages were used to monitor local strains of stirrups within the test regions. Two or three strain gages were installed on each stirrup within the test regions depending on the specimens. An example is presented in Figure A 5.30 while Additional Material C to Appendix presents the locations of the strain gages for all specimens in more detail.

In addition, strain gages were placed in various locations along the longitudinal tension and compression reinforcement to monitor flexural strains at various locations along the shear span. The positions of the strain gages on the longitudinal reinforcement were identical for all specimens except for Beam 8 and they are shown in Figure A 5.31.

On the specimens strengthened with FRP, six strain gages were attached directly to each FRP strip on the same side of the beam where strain gages were installed on stirrups. The use of strain gages at various locations on the FRP allowed monitoring of the strain distribution over the FRP strips. The position of the strain gages on the FRP sheets was almost identical for all the specimens, with and without mechanical anchorage, as shown in Figure A 5.32. More detailed information on the locations of strain gages on FRP strips for all specimens are provide in Additional Material C.

During the course of testing, some specimens were instrumented with strain gages along cracks that developed during testing. These strain gages were used to monitor the strain variation in the FRP along the cracks as shown in Figure A 5.33.

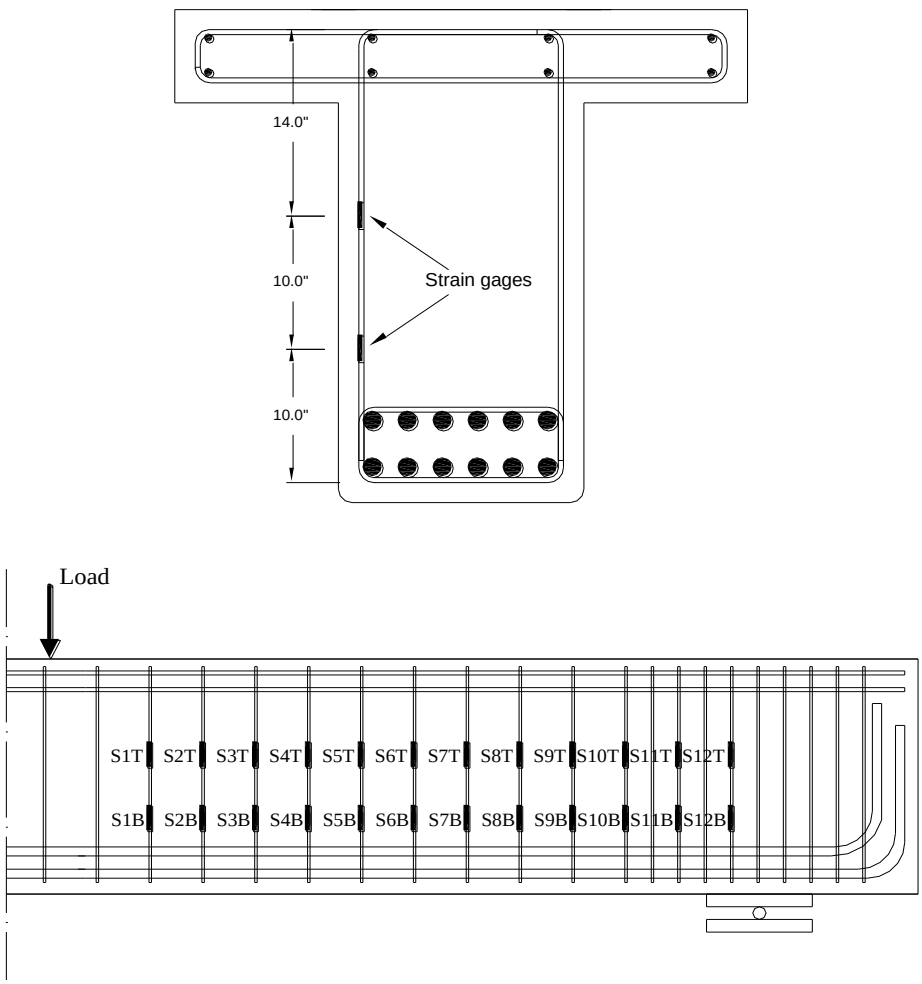

Figure A 5.30 Location of Strain Gages on the Stirrup in the Test Region for Specimen RC-8-S90-NA

During testing of specimens with mechanical anchorage systems, the behavior of the mechanical anchorage system was monitored by strain gages applied on the CFRP plates. The plates located on strips #3 and #4 were instrumented with strain gages because higher stresses were found at those locations during previous tests of RC-8-S90-NA and RC-12-S90-NA specimens. Two

strain gages were placed on each plate and oriented horizontally and vertically. Details are shown in Figure A 5.34.

Strain gages are also installed on the additional horizontal FRP strips as shown in Figure A 5.35.

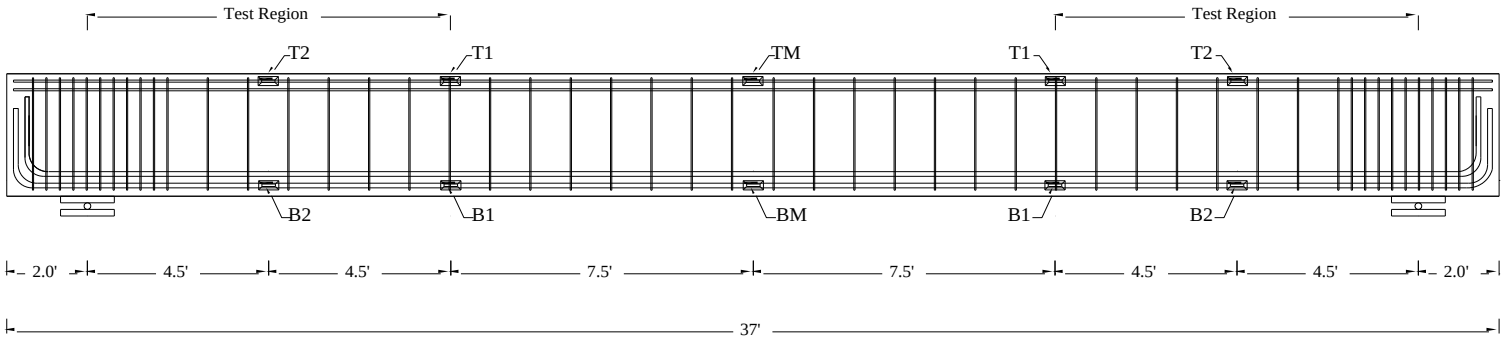

Figure A 5.31 Location of Strain Gages on Longitudinal Reinforcement

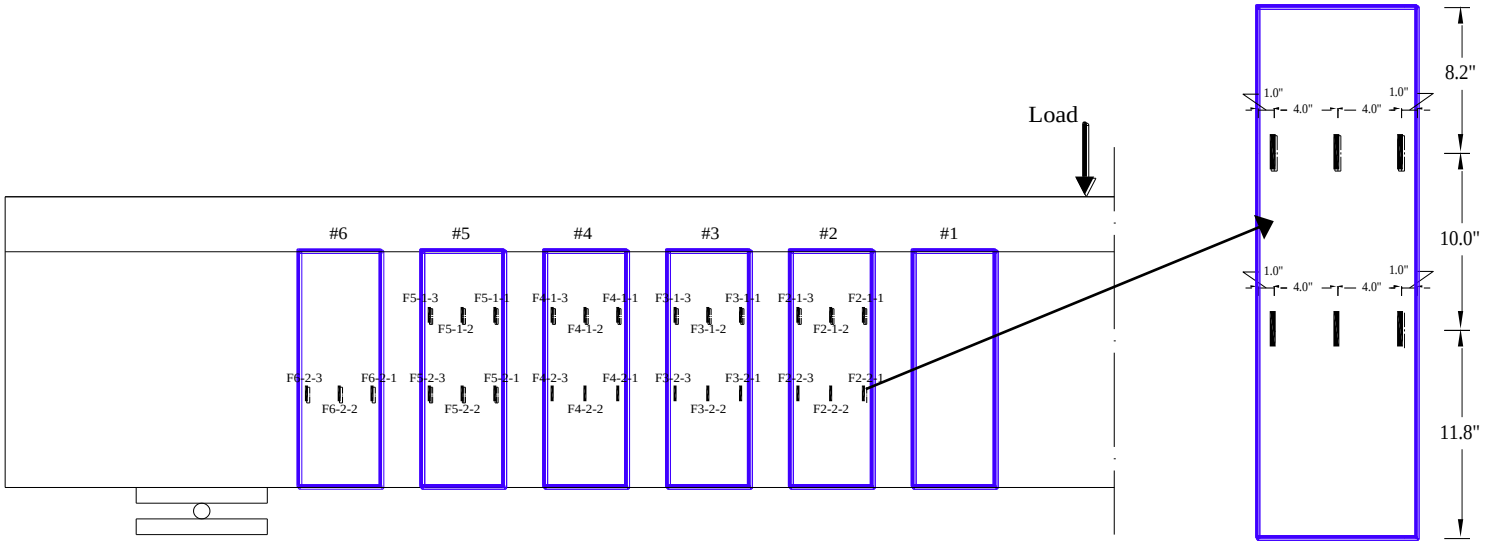

Figure A 5.32 Location of Strain Gages on FRP Strips

216

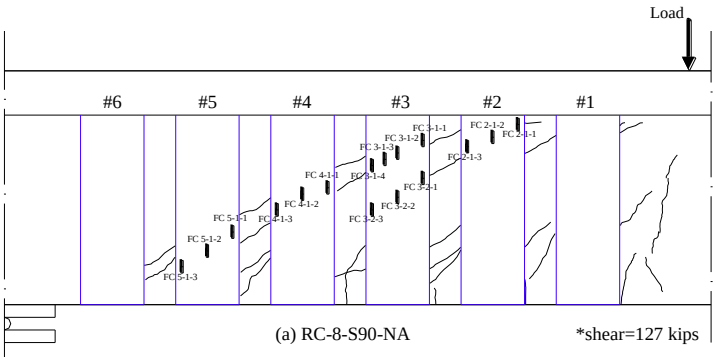

Figure A 5.33 Location of strain gages on FRP along cracks

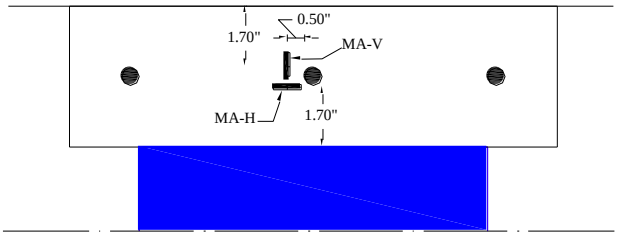

Figure A 5.34 Strain Gages on CFRP Plates of Mechanical Anchorage Systems

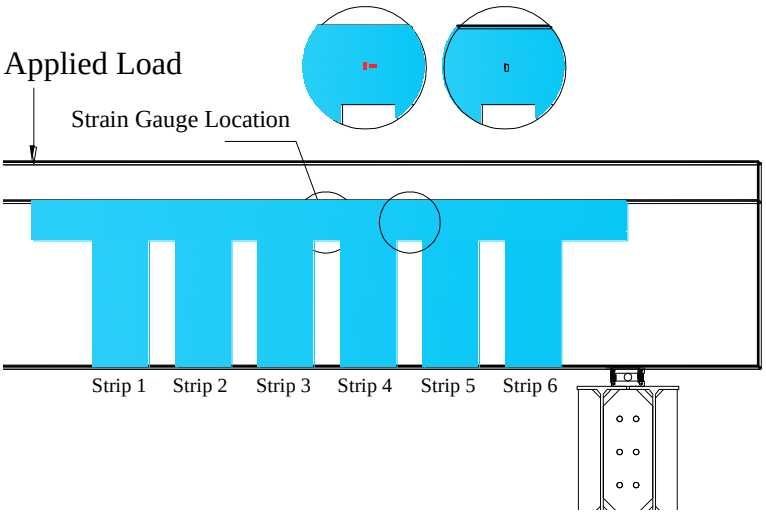

Figure A 5.35 Strain Gages on Additional Horizontal FRP Strips

A5.2.7.2 Global Deformations.

A total of 21 linear variable displacement transducers (LVDTs) were used to represent four strain rosettes and thus to measure global strains in the web of the test regions, as shown in Figure A 5.36.

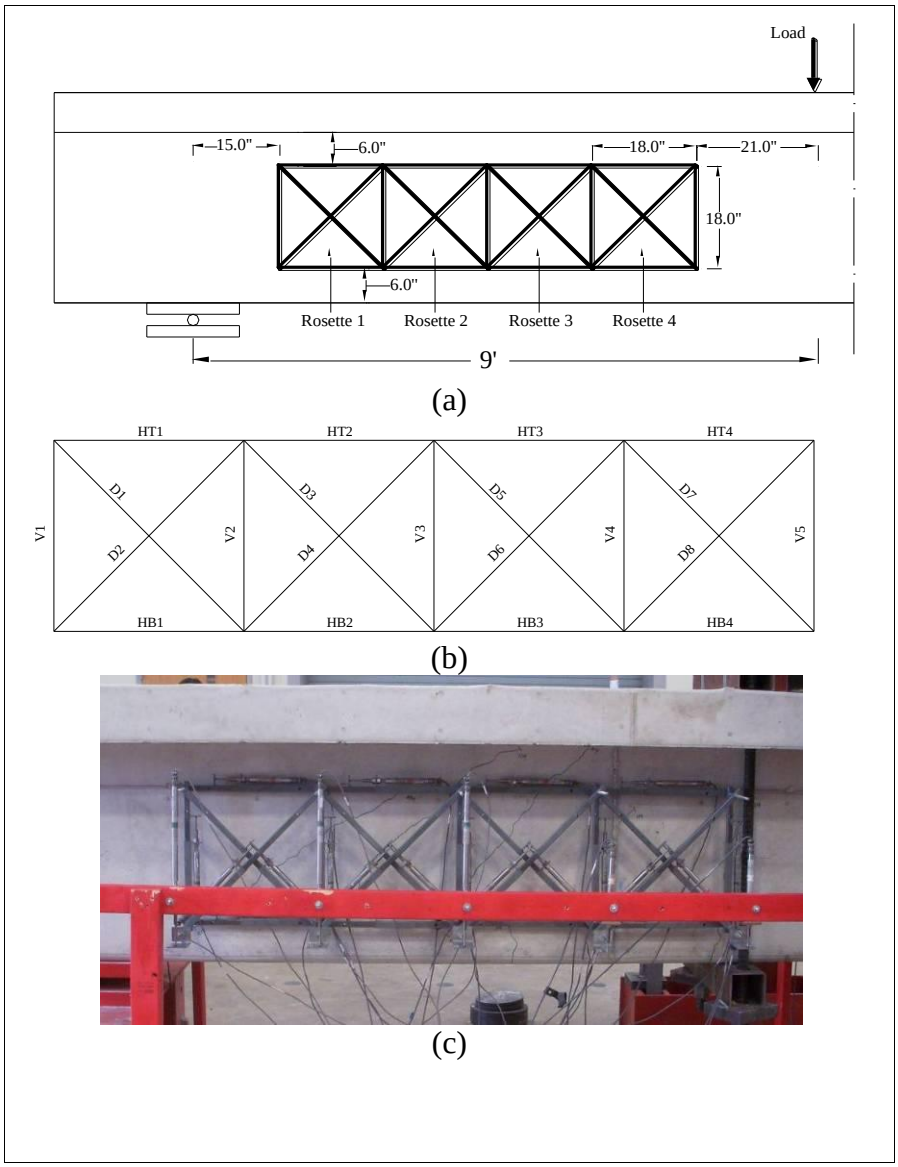

Figure A 5.36 LVDT Rosette: (a) Dimensions, (b) Denomination, and (c) Picture

Global strains in the web of the test specimens were also measured using Demec gages attached to the concrete or to the FRP surface with epoxy-based bonding material. These gages formed a rosette, as shown in Figure A 5.37. In order to compare the global vertical strain of the beam surface with the strain measured in the stirrups, the horizontal alignment of the Demec gage rosettes correspond to the position of the stirrups, and the vertical alignment corresponds to the mid-height of the web. Thus, the horizontal arrangement of the Demec gage rosettes along the test region changed within the RC-8 series and RC-12 series. Figure A 5.37 and Figure A 5.38

show, as an example, the placement of the Demec gages on the two control specimens which is the sames for the specimens strengthened with FRP.

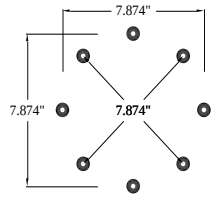

Figure A 5.37 - Demec Gages Rosette

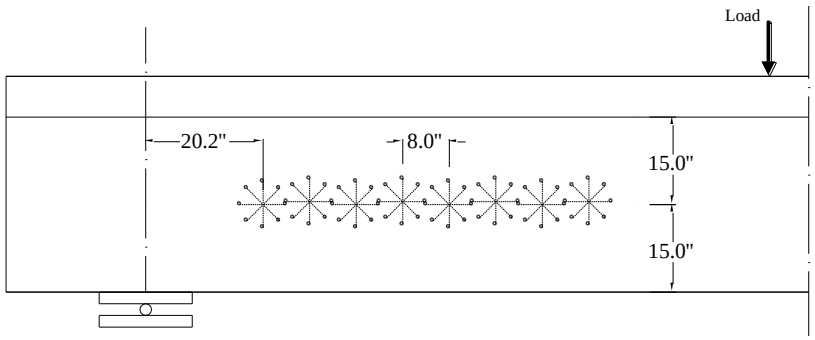

(a)

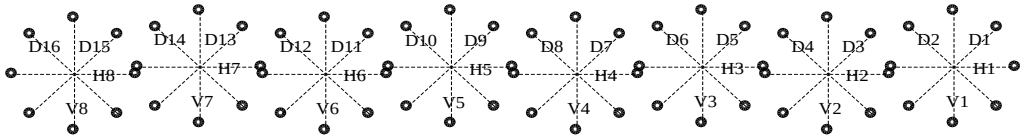

(b)

Figure A 5.38 RC-8 series: Demec gages rosettes (a) arrangement and (b) nomenclature

String transducers and LVDTs were also used to monitor vertical deflection and horizontal deformation of the test specimens. In the test region, five LVDTs (DF) were placed vertically along the bottom of the beam to measure the deflection at different locations. Two additional LVDTs were placed horizontally at 2.5 inches from the top side of the flange (CVT) and at 2 inches from the bottom side of the web (CVB) at the reaction point location. These two LVDTs were used to measure the curvature at the region of maximum bending moment. Another LVDT was located vertically on the support (DFROL) to monitor any possible deformation in the support. Figure A 5.40 shows the position of these devices.

Three string transducers were then placed at the loading point (Figure A 5.41) to measure vertical displacement of the test specimen and any possible rotation. Several LVDTs were also placed at various locations along the beam to monitor global displacement of the specimen, as shown in Figure A 5.42. In addition, an inclinometer (INCL) was placed at the far end of the beam to monitor inclination during the tests.

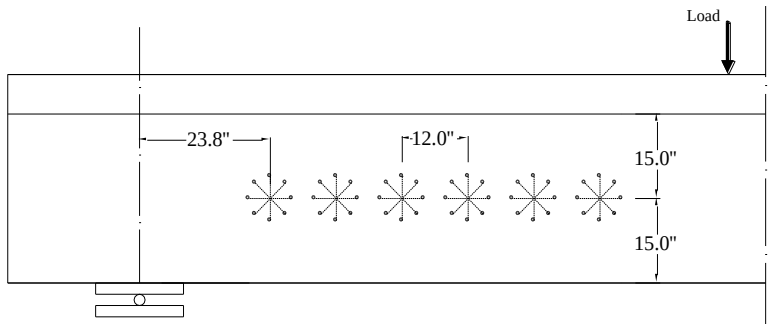

(a)

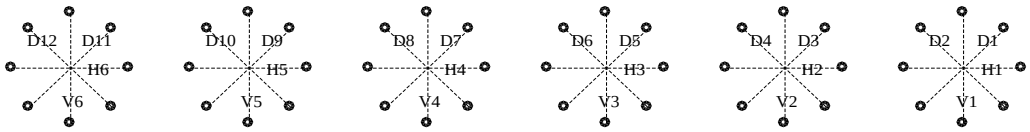

(b)

Figure A 5.39 RC-12 series: Demec gages rosettes (a) arrangement and (b) nomenclature

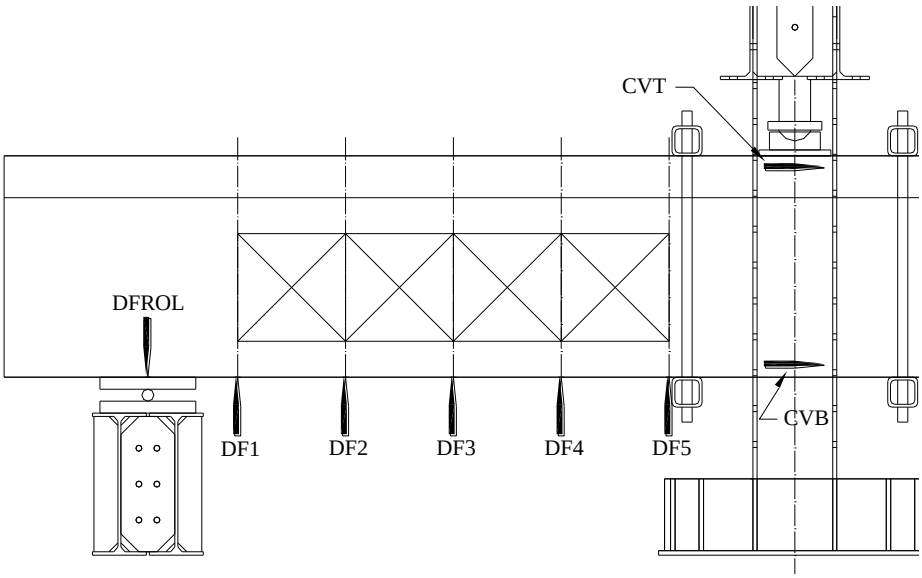

Figure A 5.40 LVDTs in the Test Region

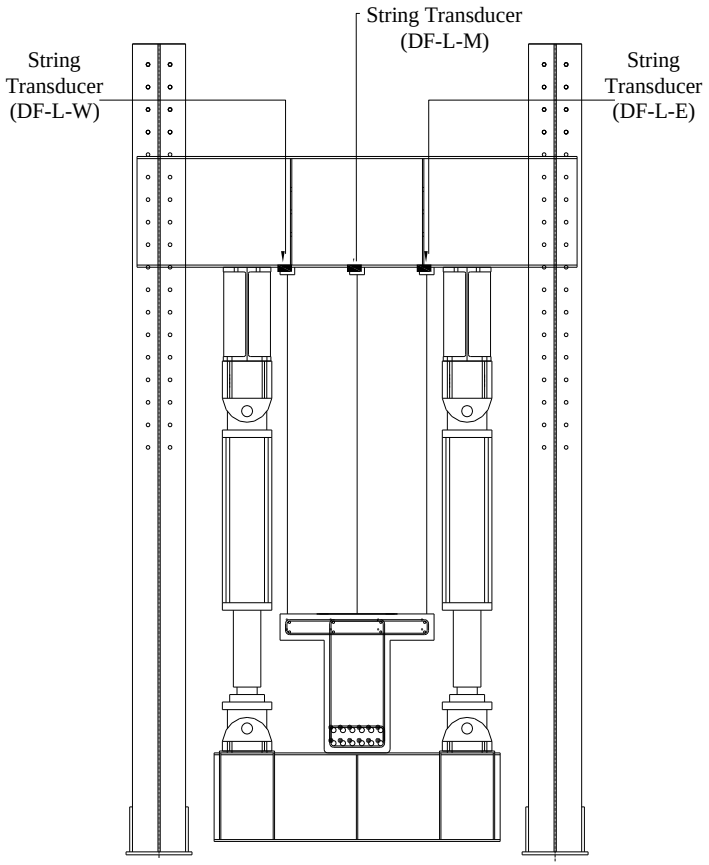

Figure A 5.41 String Transducers at Loading Point

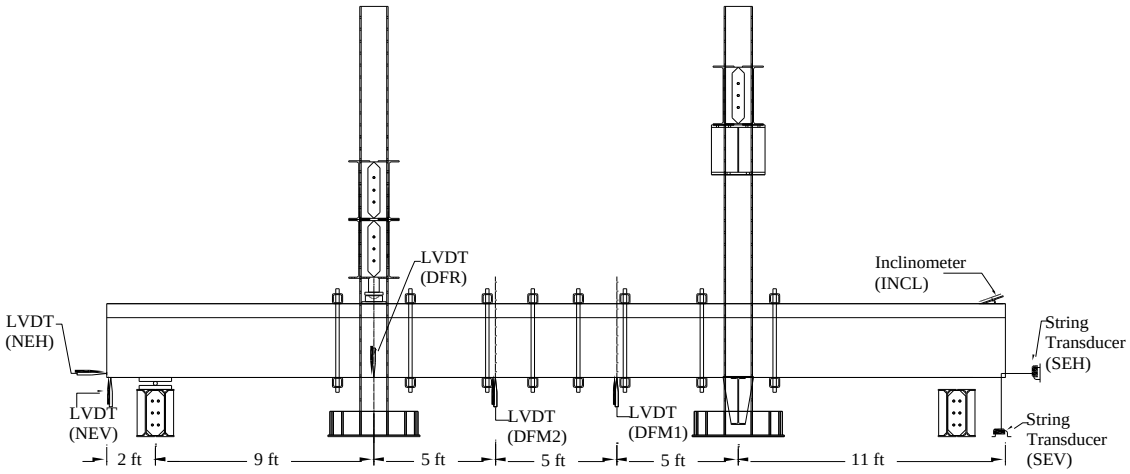

Figure A 5.42 Deflections and Elongation Measurements along the Test Beam

A5.2.8 Accelerated Corrosion Process

Specimen RC-12-S90-SDMA-Cor was tested to investigate the effectiveness of FRP shear strengthening applied to beams showing slight corrosion of internal steel reinforcement. Reinforced concrete beams may experience corrosion-related problems during their service life. When there is severe corrosion damage such as spalling of concrete and significant loss of cross-sectional area of the internal steel reinforcement, proper measures should be sought to restore the cross- section, which occasionally require extensive formwork and labor. Meanwhile, FRP strengthening, without the extensive cross-sectional restoration work, could be an immediate and efficient repair method when the symptoms such as cracking and rust formation at the surface of concrete are detected at the early state of corrosion development. It should be noted that the cracking pattern due to the corrosion of internal steel reinforcement is quite different than the pre-cracking due to shear force, which was another test parameter considered in other beams of this project.

Specimen RC-12-S90-SDMA-Cor was subjected to an accelerated corrosion process for 31 days using the galvanic cell concept to induce corrosion damage which was visually perceptible. The accelerated corrosion process consisted of applying a constant current of 6 Am and wet-dry cycles with saline solution. A DC power supply was connected to the stirrups within the test region to apply a constant current. The schematic drawing of the accelerated corrosion process is presented in Figure A 5.43.

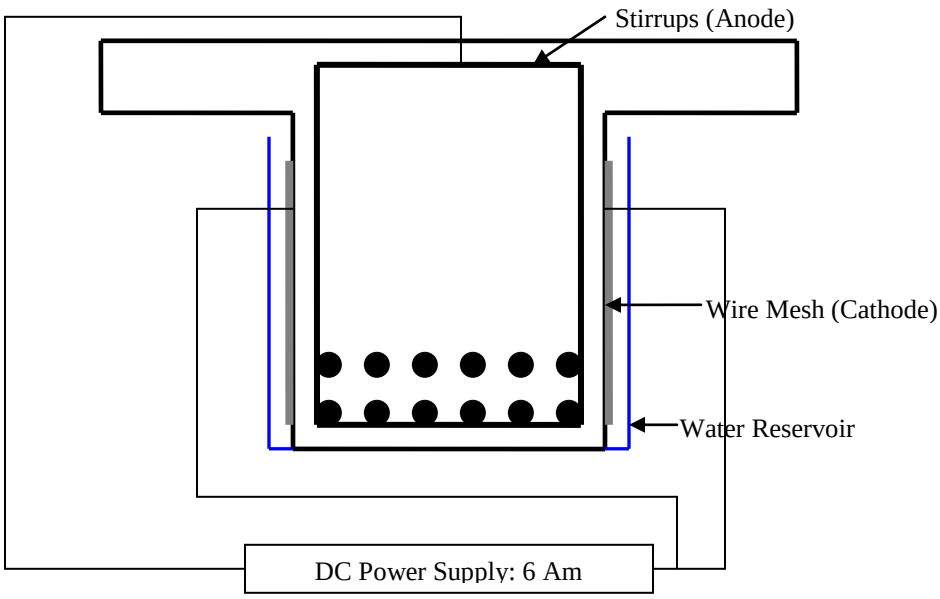

Figure A 5.43 Schematic of Accelerated Corrosion Process

Accelerated corrosion damage was visible as cracks and rust formation on the surface of the beam along the stirrups and longitudinal reinforcement as shown in Figure A 5.44. The measured crack widths ranged between 0.0015 and 0.002 inches. Specimen RC-12-S90-SDMA-Cor was then strengthened in shear with FRP and tested up to failure.

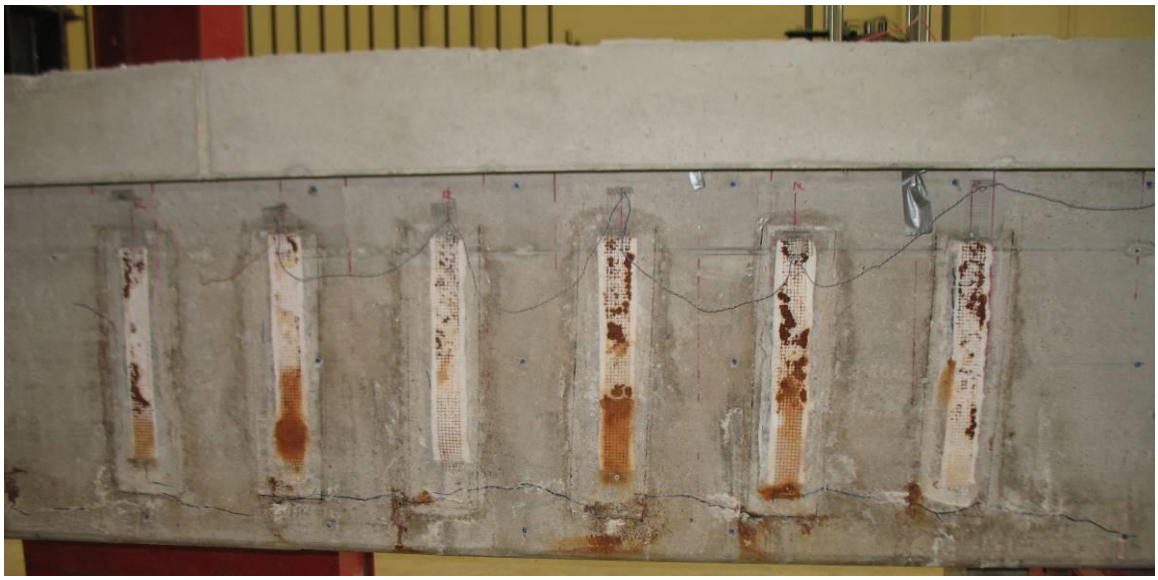

(a) Before Grinding Off the Rust

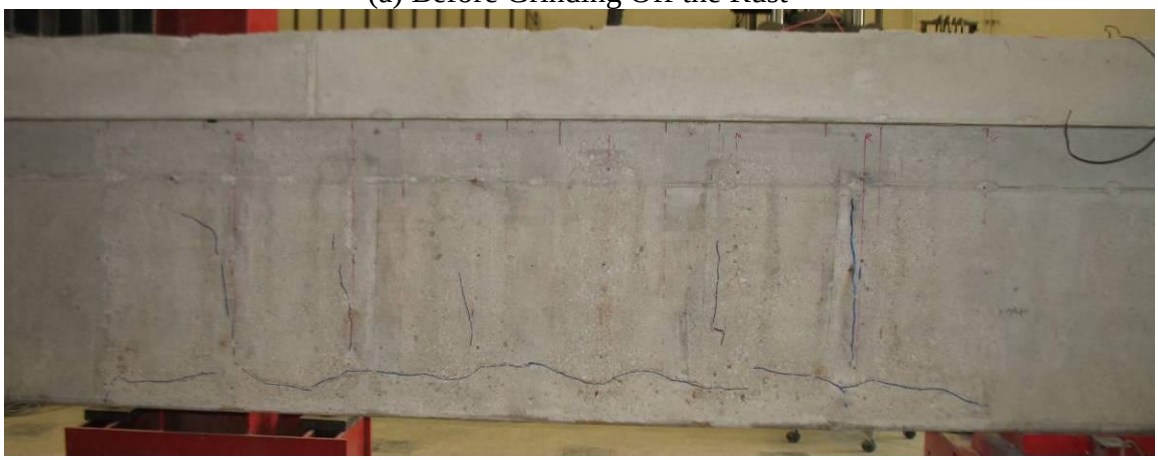

(b) After Grinding Off the Rust

Figure A 5.44 Specimen RC-12-S90-SDMA-Cor

A5.2.9 Fatigue Test Protocol

A5.2.9.1 Selection of Strengthening Configurations

Of the two types of specimens (anchored and un-anchored), given that only one fatigue test was proposed for the project, the decision was made to install the un-anchored FRP system. The following reasons were considered: (1) an un-anchored system is more universally accepted and utilized, (2) the anchoring mechanism used in this project may not be the ideal system, (3) testing of an anchored system may not yield conclusive results on the performance of the FRP-concrete bond and FRP strengthening system, and (4) if and when debonding initiates during the fatigue tests of the un-anchored system, one can revisit the usefulness of continuing the fatigue test with the un-anchored system, and perhaps ridding the specimen of the un-anchored FRP system and equipping it with the anchored system for further fatigue loading. This latter reasoning, however, was not exercised in the present study.

Based on the discussion presented above, the specimen for fatigue testing was determined to be identical to specimen RC-12-S90-NA, which will serve as a reference specimen for the fatigue results.

A5.2.9.2 Loading Protocol

The specimen was first loaded up to 60% of its strengthened capacity and was subsequently unloaded to determine its signature stiffness at virgin state. Fatigue loading followed in installments of approximately 500,000 cycles at a frequency of 1 Hz between 30% and 60% of the capacity of the strengthened specimen. After each 500,000 cycles, a static loading and unloading was carried out to about 60% of the shear capacity of the FRP strengthened beam to monitor degradation of stiffness as a result of fatigue loading.

Previous studies have applied fatigue loads at a frequency range of 1 to 5 Hz. Barnes and Mays (1999) suggested keeping the frequency below 3 Hz to avoid the hysteresis effect. Emberson and Mays (1996) reported that frequencies more than 2 Hz may cause RC beams to start a successive cycle before being fully recovered from the previous one. Senthilnath et al. (2001) reported that higher frequencies could produce undesirable heating of the beam. The natural frequency of the test beams of this study is about 4.95 Hz, and thus the frequency of less than 2 Hz would not cause any resonance. The frequency of 1 Hz was selected based on the expected deformation and the capacity of the actuator.

A5.2.10 Results and Discussion

A5.2.10.1 Overall Behavior

Table A 5.9 presents concrete compressive strengths at the time of testing ($f_c^{'}$), the shear force at diagonal cracking (V_{cr}), the maximum shear force at failure ($V_{n,\exp}$), and the ultimate failure mode for all specimens. Overall, the data in Table A 5.9 indicates that the use of externally bonded FRP increased the shear capacity of the specimens, and the use of mechanical anchorage systems provided additional shear strength. However, no direct comparison of shear strength can be made at this point, because the concrete strength of each specimen is different. Rather, the discussion has focuses on cracking load, crack patterns, and failure modes in this section. An in-depth discussion of shear strength gain and normalization of concrete strength is presented in Section A5.2.10.3; while the effects of each test parameters are discussed in detail in Sections A5.2.10.4 through A5.2.10.10. The performance of anchorage systems tested in this study is discussed in detail in Section A5.4.

Table A 5.9 Summary of Experimental Results

Beam I.D.	Concrete strength $f_c^{'}$ (psi)	Shear Force at cracking V_{cr} (kips)	Ultimate Shear Capacity $V_{n,\exp}$ (kips)	Failure Mode
RC-8-Control	2,800	58	153	Shear Failure (Diagonal Tension)
RC-12-Control	2,880	59	124	Shear Failure (Diagonal Tension)
RC-8-S90-NA	3,060	68	191	FRP Debonding
RC-8-S90-DMA	3,450	57	212	FRP Debonding
RC-12-S90-NA	4,190	70	172	FRP Debonding
RC-12-S90-DMA	4,420	70	205	FRP Debonding
RC-12-S90-HA-PC	2,650	61	187	FRP Debonding
RC-12-S90-SDMA-PC	2,780	61	214	FRP Rupture
RC-12-S90-SDMA-Cor	6,180	91	268	FRP Rupture
RC-12-S45-NA	6,050	91	217	FRP Debonding
RC-12-S45-HA	3,850	92	181	FRP Debonding
RC-12-S45-SDMA	4,230	89	203	FRP Rupture
RC-12-S90-NA-HM	3,710	96	186	FRP Rupture
RC-12-S90-SDMA-HM	4,060	94	229	FRP Rupture
RC-12-S90-NA-Ftg	4730	60	143	FRP Debonding Due to Fatigue Loading

Cracking Load

The shear cracking loads presented in Table A 5.9 were determined from the relationships between shear force and shear strain derived from the strain measurements of the LVDT Rosette. An example is presented in Figure A 5.45, while the relationships of shear force and shear strain for all specimens is presented in Additional Material E to Appendix. As indicated in Table A 5.9 and the figures in Additional Material E to Appendix, the cracking load is not affected by FRP strengthening but is strongly influenced by the concrete strength.

Cracking Pattern

Crack patterns at different loading stages of all specimens are presented in Additional Material H to Appendix. In all specimens, flexural cracking was observed at the maximum moment region prior to the initiation of shear cracking in the web. However, as the load was increased, two or three major diagonal shear cracks formed in the web. These cracks propagated into the top flange resulting in the ultimate failure of the specimens.

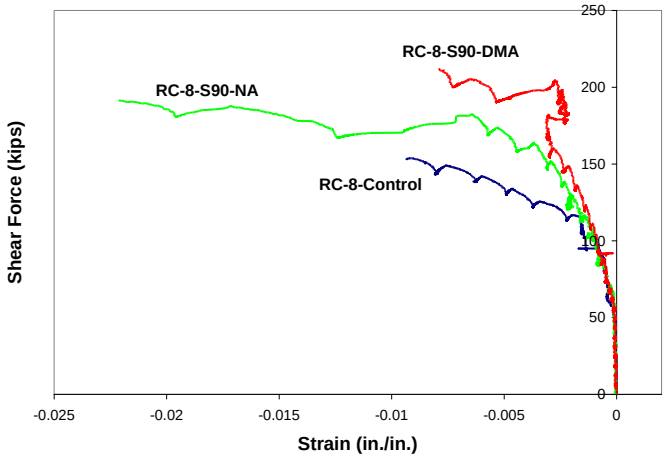

(a) RC-8 series

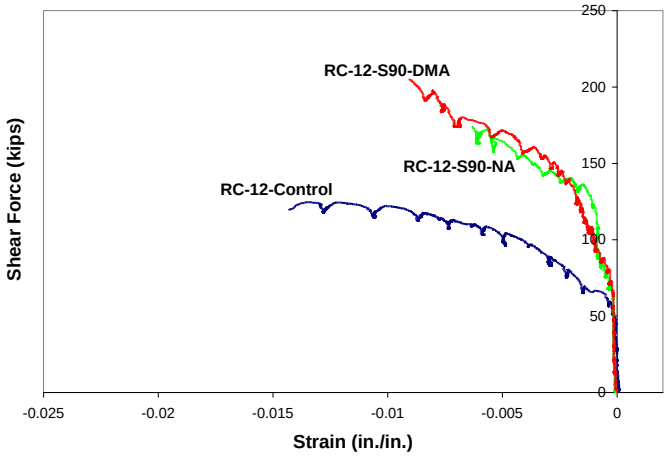

(b) RC-12 series

Figure A 5.45 Shear Force versus Shear Strain Measured from LVDT Rosette 3

Failure Modes

The control specimens without FRP strengthening (RC-8-Control and RC-12-Control) failed when the diagonal web cracks reached the top flange as shown in Additional Material M to Appendix. The FRP strengthened specimens without anchorage systems (RC-8-S90-NA, RC-12-S90-NA, and RC-12-S45-NA) failed mainly due to the debonding of FRP as shown in the figures in Additional Material M to Appendix. The FRP strengthened specimens with discontinuous mechanical anchorage systems (RC-8-S90-DMA, RC-12-S90-DMA) failed due to debonding of FRP (see the figures in Additional Material M to Appendix); however, the FRP debonding in these specimens was delayed because of the mechanical anchorage systems as compared to the cases in the FRP strengthened beams without mechanical anchorage systems. As a result, the ultimate shear strengths of the FRP strengthened specimens with discontinuous mechanical anchorage were greater than those of the FRP strengthened specimens without mechanical anchorage systems.

The FRP strengthened specimens with additional horizontal FRP strips (RC-12-S90-HA-PC, and RC-12-S45-HA) failed mainly due to the debonding of FRP as shown in the figures in

Additional Material M to Appendix; however, the additional horizontal FRP strips helped to delay the debonding of FRP, resulting in a shear strength increase as compared to the FRP strengthened specimens without mechanical anchorage systems.

The FRP strengthened specimens with sandwich discontinuous mechanical anchorage systems (RC-12-S90-SDMA-PC, RC-12-S90-SDMA-Cor, and RC-12-S45-SDMA) failed mainly due to the rupture of FRP as shown in the figures in Additional Material M to Appendix; thus, the increase in shear strength was significant as compared to the specimens with other types of anchorage systems. This result indicated that the sandwich discontinuous mechanical anchorage systems provided the best performance among the anchorage systems considered in this study.

For the FRP strengthened specimens subjected to the negative moment (RC-12-S90-NA-HM and RC-12-S90-SDMA-HM), failure occurred due to rupture of FRP regardless of the use of mechanical anchorage systems as shown in the figures in Additional Material M to Appendix.

The FRP strengthened specimen subjected to fatigue loading (RC-12-S90-NA-Ftg) experienced debonding of FRP at a very early stage of fatigue loading and the area of FRP debonding spread gradually until eventually all FRP strips crossing the critical shear cracks were debonded at the end of fatigue loading as shown in the figures in Additional Material M to Appendix. As a result, the failure mode of the specimen was similar to the control specimens without FRP strengthening.

The performance and failure modes of the anchorage systems are discussed in significant detail in Section A5.4.

A5.2.10.2 Contribution of Various Shear Components

The total shear resistance can be considered as the sum of the contributions from concrete, stirrups, and FRP sheets:

$$V_{n,\exp} = V_c + V_s + V_f \qquad \text{(A5-2)}$$

where $V_{n,\exp}$ is the experimentally determined ultimate shear resistance (see Table A 5.9), V_c is the contribution of concrete, V_s is the contribution of stirrups, and V_f is the contribution of FRP. Analysis of the shear contributions coming from each component is based on free body diagrams of a part of the specimens separated along the critical crack that resulted in failure of the specimens. Details of this procedure are described below.

<u>Free Body Diagrams for Each Specimen.</u>

Free body diagrams were drawn based on crack patterns at the time of failure. The critical crack, defined as the widest crack, was used to separate the specimen into two parts. For instance, Figure A 5.46 and Figure A 5.47 show the specimens at failure and the corresponding free body diagrams of RC-8-Control and RC-8-S90-NA. The stirrups and FRP strips crossing the critical crack are the only ones considered to resist the shear force applied to the specimen. Therefore, only these stirrups and FRP strips were used to calculate the shear contribution of stirrups and FRP strips.

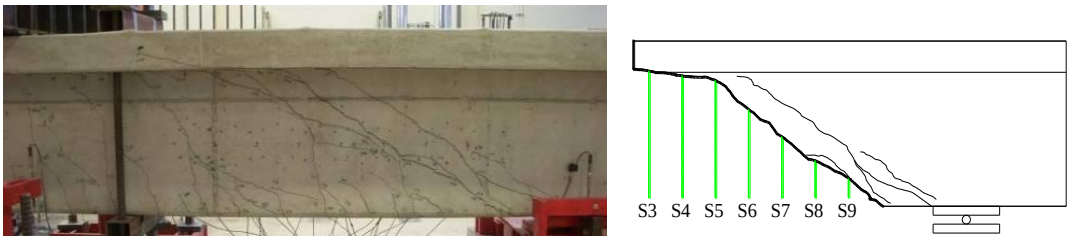

Figure A 5.46 Free Body Diagram of RC-8-Control

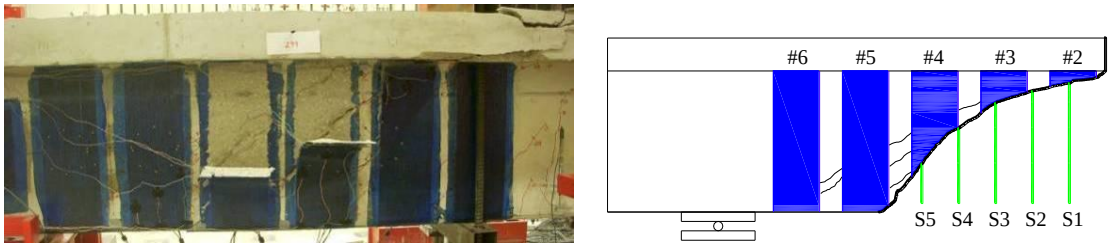

Figure A 5.47 Free Body Diagram of RC-8-S90-NA

Calculation of Contribution of Stirrups (V_s).

Strains recorded by gages installed on the stirrups were used to calculate the shear force carried by those stirrups. As previously described in Section A5.2.7, two or three strain gages, depending on the specimens, were installed on each stirrup within the test region. As an example, Figure A 5.48 shows the strains recorded by two strain gages for two generic stirrups of specimen RC-8-Control. The strain recordings for all specimens are presented in Additional Material E to Appendix. The majority of the strain gages installed on the stirrups (about 95%) were properly working throughout the course of the test.

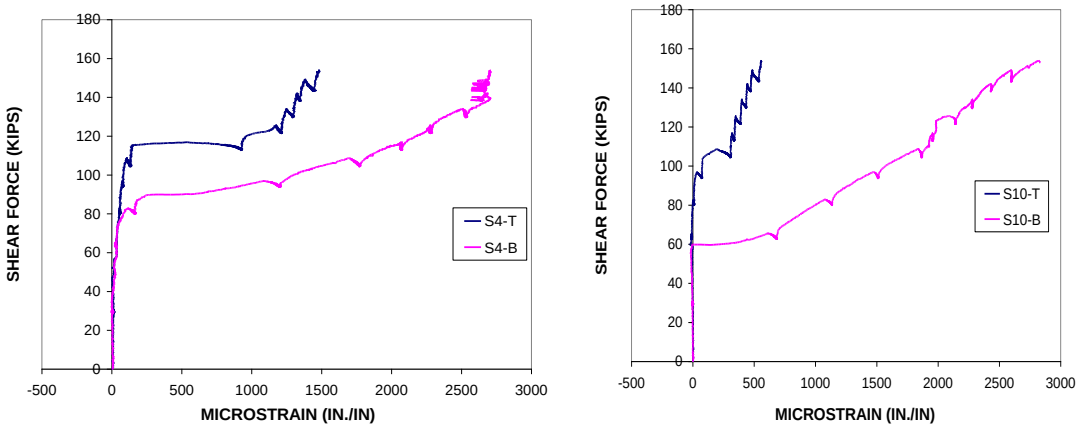

(a) (b)

Figure A 5.48 Strains in (a) Stirrup #4 and (b) Stirrup #10 (RC-8-Control)

Figure A 5.48 shows that the strain levels registered by two strain gages in a stirrup can be different depending on their locations relative to the web shear cracks. However, analysis of strain levels at various crack locations suggests that the strain level is higher at strain gages closest to shear cracks. At this location, therefore, the gage provides a more realistic

representation of the actual strain values in the stirrups. For this reason, the strain gages showing higher strain values were used to compute the force in each stirrup.

The shear force carried by stirrups crossed by the critical diagonal crack was calculated using the following equation:

$$V_s = \sum A_{vi} f_{vi} \qquad \text{(A5-3)}$$

where A_{vi} = area of the cross section of the ith stirrup in the free-body-diagram, f_{vi} = stress in i^{th} stirrup in the free body diagram (determined using the proposed stress-strain relationship of the stirrups explained in Section A3.4.2).

<u>Calculation of Contribution of FRP (V_f).</u>
The strain values measured by strain gages installed on each FRP strip (see Section A5.2.7) were used to calculate the shear force carried by each FRP strip. The strain values on the FRP strips for all the specimens are provided in Additional Material F to Appendix. Similar to the strains in the stirrups, the strain values in the FRP are also very sensitive to the locations of the strain gages relative to the diagonal cracks. Therefore, the force carried by an FRP strip was calculated using the strain values registered by the three strain gages located closest to the critical crack, as shown in Figure A 5.49. All strain gages installed on the FRP sheets were properly working during testing. The total shear force carried by the FRP was computed using the following equation:

$$V_f = \sum A_{fi} f_{fi} = \sum A_{fi} E_f \varepsilon_{fi,ave} \qquad \text{(A5-4)}$$

where A_{fi} = area of ith FRP strip in the free-body-diagram, f_{fi} = stress in i^{th} strip in the free-body-diagram, E_f = modulus of elasticity of the FRP strips, and $\varepsilon_{fi,ave}$ = average strain of FRP.

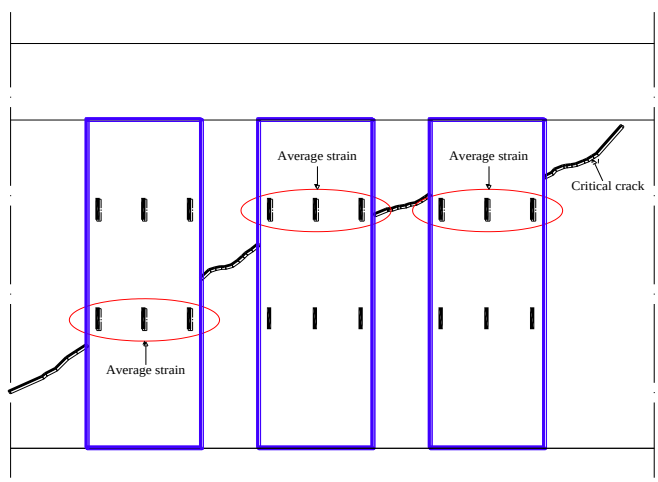

Figure A 5.49 Example of Evaluation of Average FRP Strain

Calculation of Contribution of Concrete (V_c).

The shear contribution of the concrete was calculated by subtracting the contributions of the stirrups and FRP from the total shear resistance measured during the tests:

$$V_c = V_{n-\exp} - V_s - V_f \qquad \text{(A5-5)}$$

The shear contribution of concrete can be attributed to (1) aggregate interlocking, (2) dowel action of longitudinal reinforcement, and (3) shear force carried in the compression zone of the member. However, this work combines all these contributions in V_c, and investigation of the interaction among them is beyond the scope of this study.

Shear Component Diagram.

Based on the calculations described above, the following shear diagrams were drawn for all test specimens. In all these diagrams, the horizontal axis represents the shear force applied to the test specimens and the vertical axis represents the shear contribution of each component.For all specimens, the diagrams show that the contributions of stirrups and FRP sheets are minimal before shear cracking.

At cracking load, the contribution of stirrups (V_s) in the control specimen exhibits a steep jump, implying that the stirrups started taking shear force (see Figure A 5.50(a) and Figure A 5.51(a)). Meanwhile, the stirrups in the FRP-strengthened specimens showed a relatively gradual increase in shear contribution as compared to the cases of the control specimens, and the contribution of FRP significantly increased after the stirrups yielded. In addition, it can be observed in the pre-cracked FRP specimens that the contributions of stirrups and FRP started immediately with application of the load (see Figure A 5.51(d) and (e)). Detailed discussion of the contribution of each component is presented in the following sections.

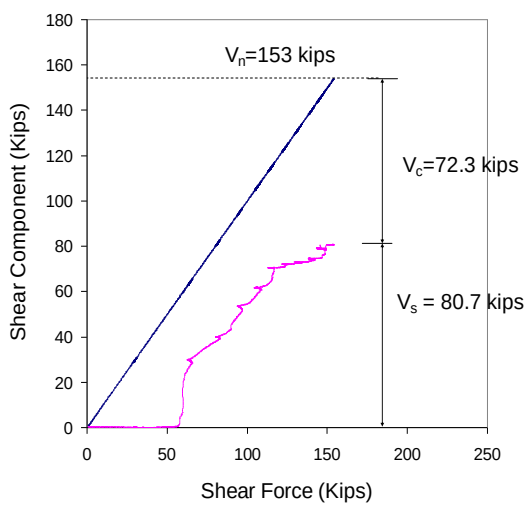

(a) RC-8-Control

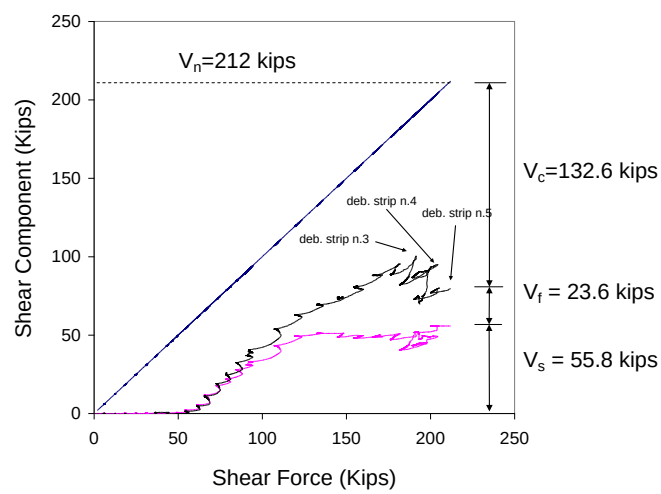

(b) RC-8-S90-NA

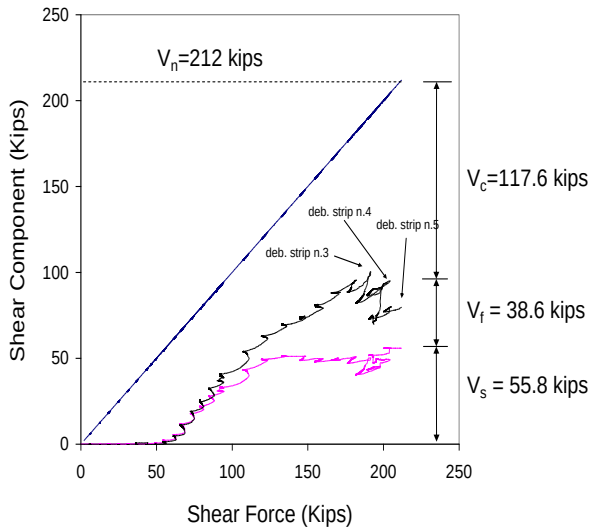

(c) RC-8-S90-DMA

Figure A 5.50 Shear Component Diagrams – RC-8 series

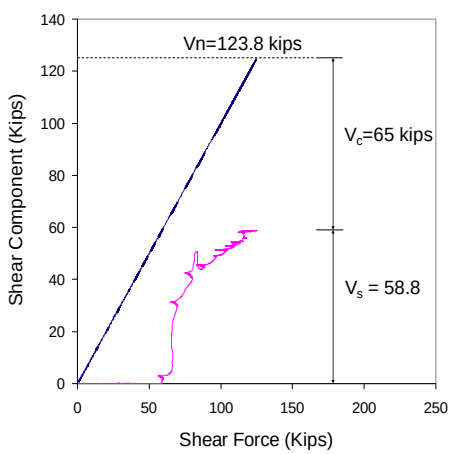

(a) RC-12-Control

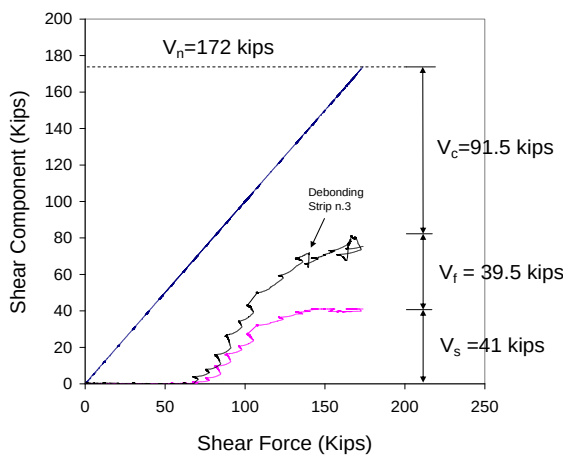

(b) RC-12-S90-NA

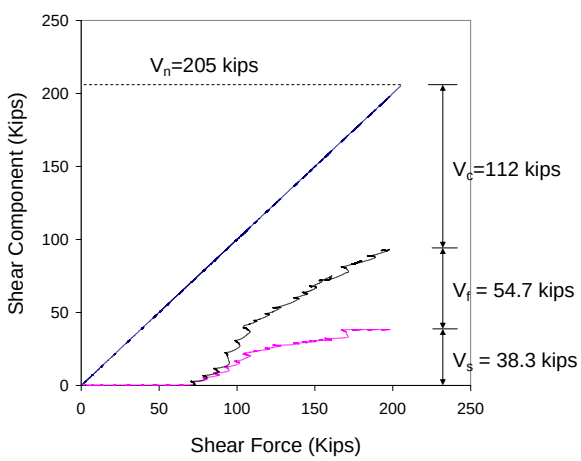

(c) RC-12-S90-DMA

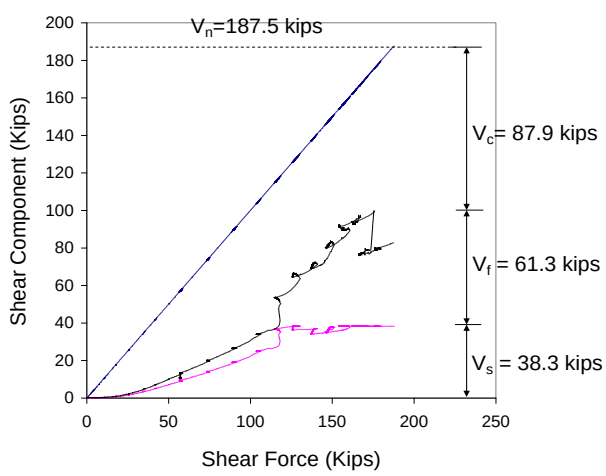

(d) RC-12-S90-HS-PC

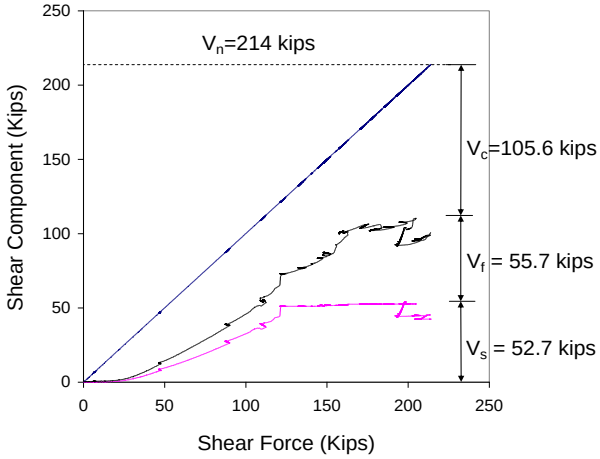

(e) RC-12-S90-SDMA-PC

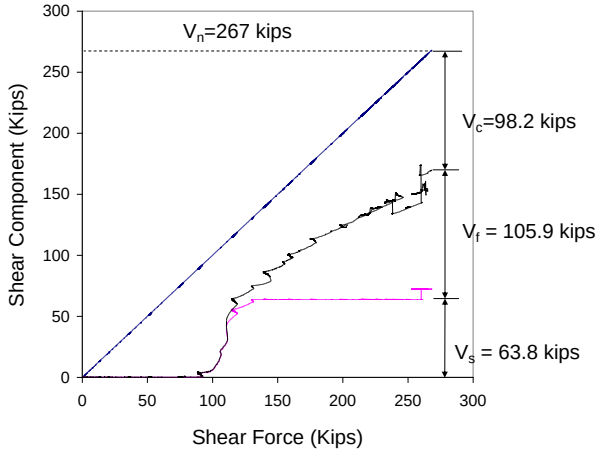

(f) RC-12-S90-SDMA-Cor

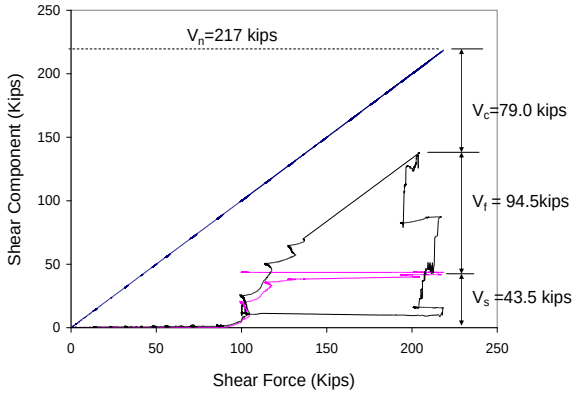

(g) RC-12-S45-NA

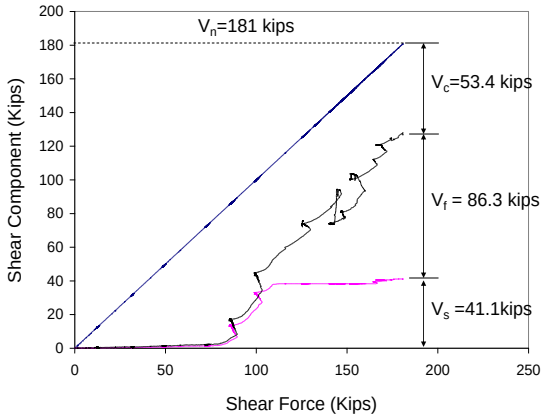

(h) RC-12-S45-HS

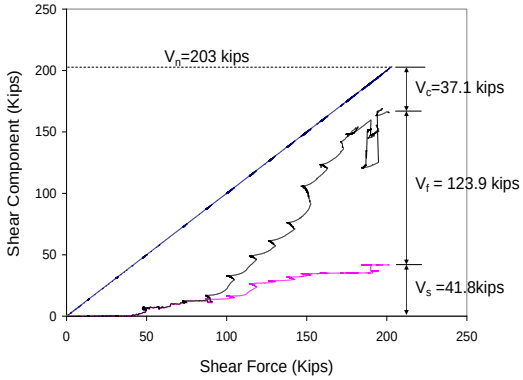

(i) RC-12-S45-SDMA

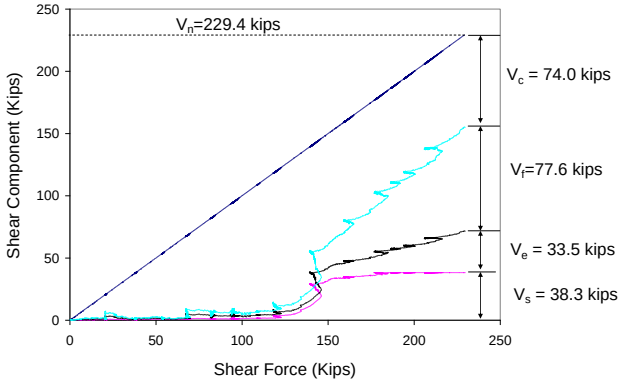

(j) RC-12-S90-SDMA-HM

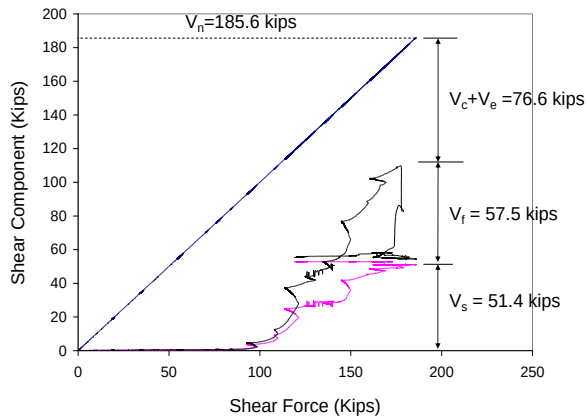

RC-12-S90-NA-HM

Figure A 5.51 Shear Component Diagrams – RC-12 Series

A5.2.10.3 Normalized Concrete Strength and Actual Shear Strength Gain

The shear contribution of concrete (V_c) cannot be directly compared among all test specimens due to differences in concrete strength as shown in Table A 5.9. In order to compare the shear contributions of concrete (V_c) and shear strength in the FRP-strengthened specimens with those of the corresponding control specimens, the concrete strength and shear strength must be normalized as follows:

$$V_{n,normalized} = \frac{V_{c,\exp}}{\sqrt{\dfrac{f'_{c,spec}}{f'_{c,control}}}} + V_s + V_f \qquad \text{(A5-6)}$$

where $V_{c,exp}$ = contribution of the concrete derived from the shear component analysis, $f'_{c,spec}$ = concrete strength of test specimens strengthened with FRP, and $f'_{c,control}$ = concrete compressive strength of the control specimens.

The actual shear strength gain of the specimens strengthened with FRP is defined as the difference between the normalized shear strength of FRP-strengthened specimens and that of the corresponding control specimens. As a result, the actual shear gain does not necessarily reflect the shear strength gain only due to FRP. Rather, it includes the changes in the contribution of concrete and stirrups due to the application of FRP, i.e., the interaction among the shear components.

The actual shear gains of all specimens are presented in Table A 5.10. Overall, the results presented in Table A 5.10 show that FRP strengthening increased the shear capacity, and its effectiveness depends on the variables considered. Discussions on the test variables considered in this experimental program will be presented in the following sections.

A5.2.10.4 Effects of Transverse Steel Reinforcement

The effects of transverse steel reinforcement on the behavior of RC beams strengthened in shear with FRP are discussed in this section, by comparing the behavior of RC-8-Series and RC-12-

Series specimens (i.e., RC-8-Control vs. RC-12-Control, RC-8-S90-NA vs. RC-12-S90-NA, and RC-8-S90-DMA vs. RC-12-S90-DMA).

Figure A 5.52 presents the load-displacement responses of the specimens to be discussed. As shown in Figure A 5.52(a), the behavior of the two control specimens, RC-8-Control and RC-12-Control appeared to be slightly different. However, the behavior of the specimens strengthened with FRP, as shown in Figure A 5.52(b) and (c), are almost identical whether or not mechanical anchorage systems are used. This implies that the behavior of the FRP strengthened beams was governed by FRP. Thus, the failure of FRP, either by debonding or rupture, was the cause of failure in the beams. Again, the shear strength of the beams obtained from the tests cannot be directly compared due to the differences in concrete compressive strength; thus, the normalization of concrete strength had to be used to obtain the actual shear strength gain as discussed in Section A5.2.10.3.

Table A 5.10 Nominal Shear Strength and Shear Gain Calculations based on Normalized Concrete Strength

	f'_c (psi)	$V_{n,test}$ (kips)	V_c (kips)	V_s (kips)	V_f (kips)	$V_{n,norm}$ (kips)	Actual Shear Gain (kips)	Shear Gain (%)
RC-8-Control	2800	153	72.3	80.7	-	153	-	-
RC-12-Control	2880	123.8	65	58.8	-	123.8	-	-
RC-8-S90-NA	3000	191.3	86.6	63.8	41	188.5	**35.5**	**23.2**
RC-8-S90-DMA	3450	212	132.6	55.8	23.6	198.9	**47.3**	**30.9**
RC-12-S90-NA	4190	172	91.5	41	39.5	156.4	**32.6**	**26.3**
RC-12-S90-DMA	4420	205	112	38.3	54.7	183.4	**59.6**	**48.1**
RC-12-S90-SDMA-PC	2780	214	117.8	37.2	59	216.1	**92.3**	**74.6**
RC-12-S90-HA-PC	2650	187.5	87.9	38.3	61.3	191.2	**67.4**	**54.5**
RC-12-S90-SDMA-Cor	6180	267.9	98.2	63.8	105.9	236.7	**112.9**	**91.1**
RC-12-S45-NA	6050	217	79	43.5	94.5	191	**67.2**	**54**
RC-12-S45-HA	3850	181.3	53.4	41.1	86.3	173.6	**49.8**	**40.2**
RC-12-S45-SDMA	4230	203	37.1	41.8	123.9	196.3	**72.5**	**58.6**
RC-12-S90-NA-HM	3710	185.6	27.6	103.2	54.8	182.3	**58.5**	**47.3**
RC-12-S90-SDMA-HM	4060	229.3	44.3	86.6	84.4	222.3	**98.5**	**80.4**
RC-12-S90-NA-Ftg	4730	-	-	-	-	-	-	-

f'_c : Concrete strength at the time of testing
$V_{n,test}$: Measured Shear Strength
V_c: Shear contribution of concrete
V_s: Shear contribution of stirrups
V_f: Shear contribution of FRP
$V_{n,norm}$: Normalized Shear Strength

Considering the actual shear strength gain as shown inTable A 5.10, reveals that FRP shear strengthening was more effective for RC-12-S90-DMA than for RC-8-S90-DMA. Meanwhile, there was minimal difference in the actual shear strength gain between RC-8-S90-NA and RC-12-S90-NA. In other words, it can be said that the FRP shear strengthening system used in the test program seemed to be more effective for the beams with 12 inch stirrup spacing than the beams with 8 inch stirrup spacing when mechanical anchorage systems were used. This trend, however, was not observed when mechanical anchorage systems were not used.

Another way of determining the effectiveness of FRP shear strengthening is to compare effective strains or the ratio of effective strains to ultimate FRP strain as discussed in Section A3.4.2.2.

Figure A 5.53 presents the ratio of the effective strains to the ultimate FRP strains of RC-8-Series and RC-12-Series specimens. Figure A 5.53 clearly shows that the effectiveness of FRP shear strengthening is greater in RC-12-Series than in RC-8-Series when mechanical anchorage systems were used; while there is no significant difference between the two specimens when mechanical anchorage systems were not used. These results confirm the previous observations made from the actual shear strength gain.

Previous research studies and analysis of the existing data performed in this project, as discussed in Section A3.4.3, show that the effectiveness of FRP shear strengthening decreases with increase in the amount of stirrups. Thus, the observations made in this project seem to be consistent with previous research studies and analysis results of the existing experimental database.

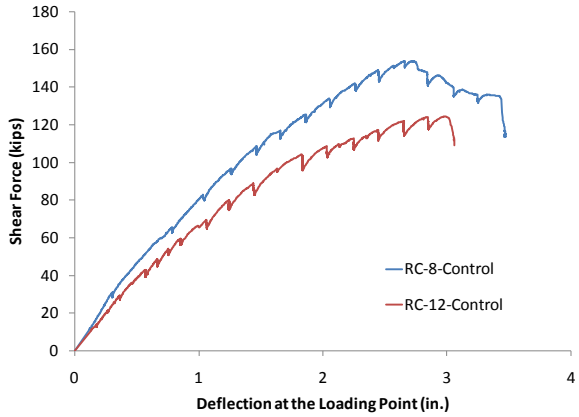

(a) Control Specimens

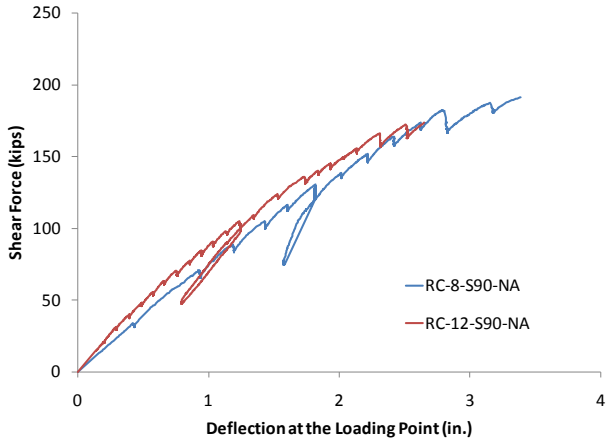

(b) Specimens without Mechanical Anchorage

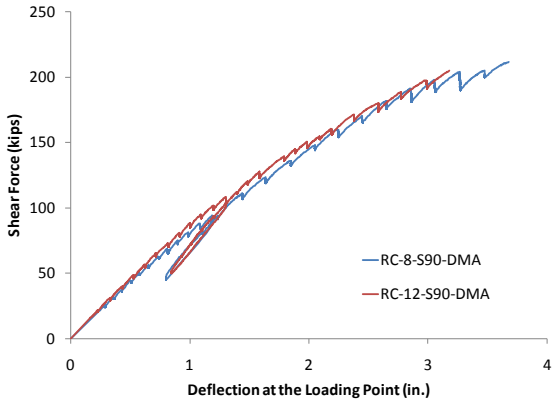

(c) Specimens with Mechanical Anchorage

Figure A 5.52 Comparisons of Shear Force vs. Deflection at the Loading Point between RC-8-Series and RC-12-Series

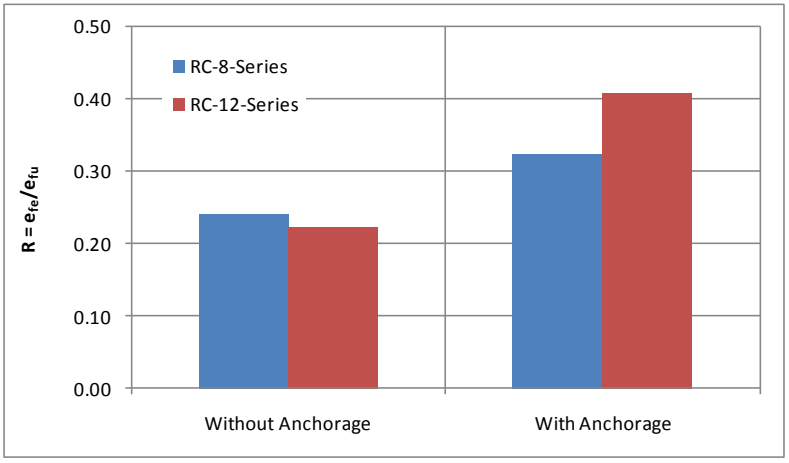

Figure A 5.53 Comparison of the Ratio of Effective Strain to Ultimate FRP Strain between RC-8-Series and RC-12-Series

However, it should be noted here that the failure of specimen RC-8-S90-DMA occurred prematurely possibly due to the incomplete bonding between FRP sheets used for shear strengthening and the FRP plates used for mechanical anchorage (see Section A5.4.2 for more details about the performance of the mechanical anchorage systems tested in this project). As a result, the mechanical anchorage systems in RC-8-S90-DMA did not keep the FRP sheets from debonding; thus could make a significant contribution to the shear strength increase. This can also explain the fact that the measured contribution of FRP (V_f) at failure was smaller in RC-8-S90-DMA than RC-8-S90-NA. Figure A 5.54(a) shows the variations in the contribution of FRP for specimens RC-8-S90-NA and RC-8-S90-DMA while Figure A 5.54(b) shows the variations in the contribution of FRP for specimens RC-12-S90-NA and RC-12-S90-DMA. As shown in Figure A 5.54(a), the contribution of FRP in specimen RC-8-S90-DMA reached its peak value before failure, which is greater than the maximum contribution of FRP in specimen RC-8-S90-NA, and decreased due to the debonding of FRP strips. As a result, the contribution of FRP at failure in specimen RC-8-S90-DMA becomes smaller than that of specimen RC-8-S90-NA.

It can be reasonably speculated that if the mechanical anchorage system used in RC-8-S90-DMA had performed properly, as in RC-12-S90-DMA, the actual contribution of FRP in RC-8-S90-DMA would have been much higher. As a result, the actual shear strength gain of RC-8-S90-DMA would have been similar to the actual strength gain of RC-12-S90-DMA. However, this result would not be consistent with the previous research results and the findings from the analysis of the existing experimental database. In order to investigate this contradiction, interaction between FRP shear strength and internal transverse steel reinforcement was investigated. Figure A 5.55 presents the variation of the contributions of stirrups in RC-8-Series and RC-12-Series specimens during the entire loading history. As shown in Figure A 5.55, the shear contribution of stirrups decreased when FRP was used as external shear strengthening. Further decrease in the contribution of stirrups can be observed when anchorage systems were used. Thus, it can be said that there exist an interaction between the contributions of FRP and stirrups. This also explains why there are significant differences between the measured contribution of FRP and the actual shear strength gain. The decrease in the contribution of stirrups is primarily contributed to the change in crack angle. Figure A 5.56 and Figure A 5.57 present the photographs of the specimens at failure and the free-body diagrams drawn based on

the photographs. The free-body diagrams were used for the analysis of shear contributions of each component. It can be found from the observation on the figures that the number of stirrups bridging over the critical cracks decreases with the use of FRP. Therefore, the contribution of stirrups decreases as presented in Figure A 5.55. This could be one of the reasons why the effectiveness of FRP shear strengthening decreases with the use of more stirrups. In addition, it can be observed in Figure A 5.55 that the slopes of the stirrup contribution curves of the control specimens are much steeper than those of specimens with FRP strengthening. This implies that FRP strengthening decreases the contribution of stirrups, eventually delaying the yielding of stirrups in some cases. In conclusion, it can be said that the effects of transverse reinforcement (stirrups) were not observed in the tests performed in this project. However, the test results were based on a very limited number of specimens; thus, it is not proper to draw generalized conclusions from such results.

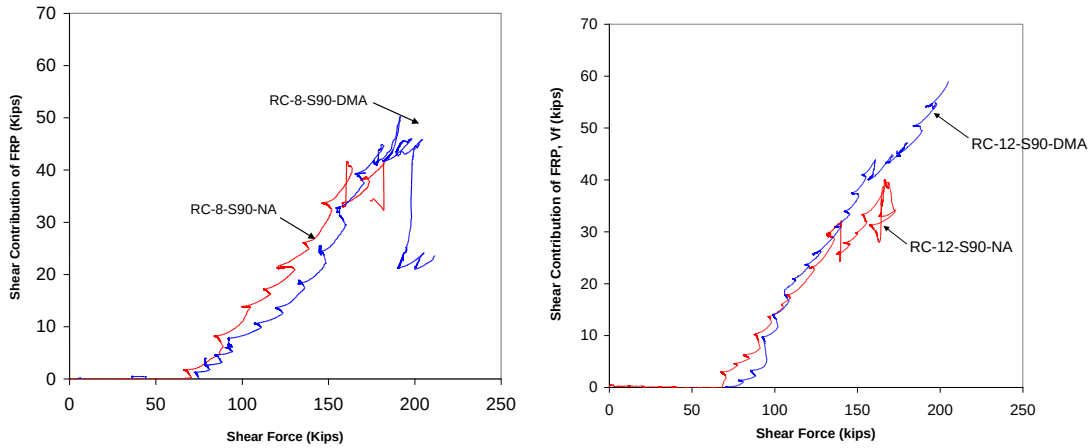

(a) RC-8 series (b) RC-12 series

Figure A 5.54 Shear Contribution of FRP in RC-8-Series and RC-12-Series Specimens

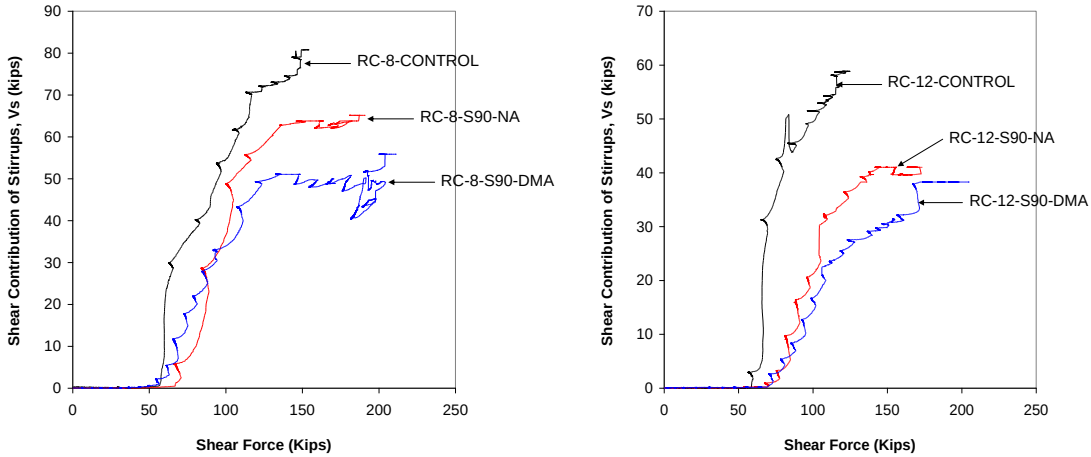

(a) RC-8 series (b) RC-12 series

Figure A 5.55 Shear Contribution of Stirrups in RC-8-Series and RC-12-Series

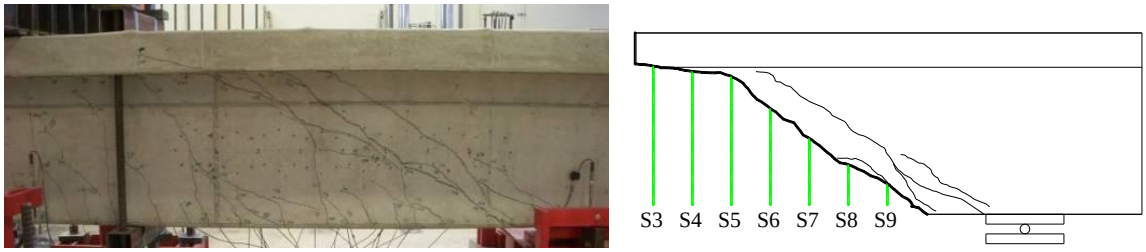

Figure A 5.56 Free Body Diagram of RC-8-Control

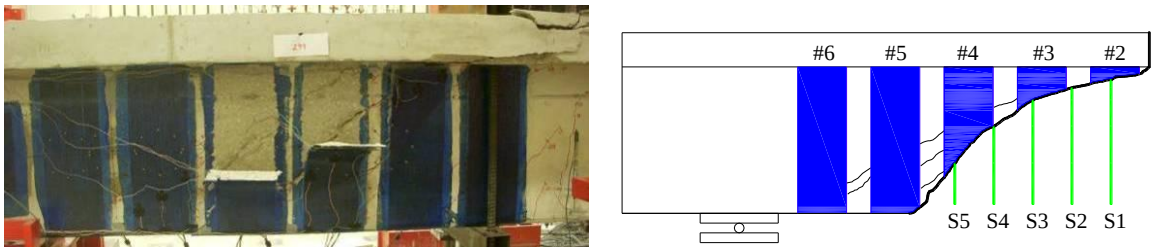

Figure A 5.57 Free Body Diagram of RC-8-S90-NA

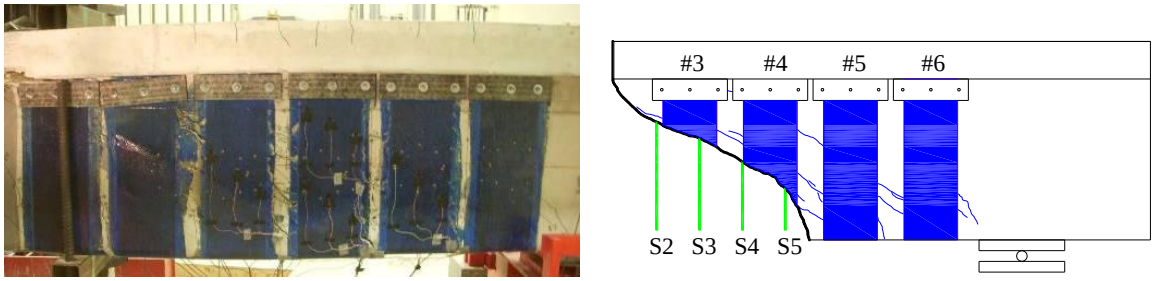

Figure A 5.58 Free Body Diagram of RC-8-S90-DMA

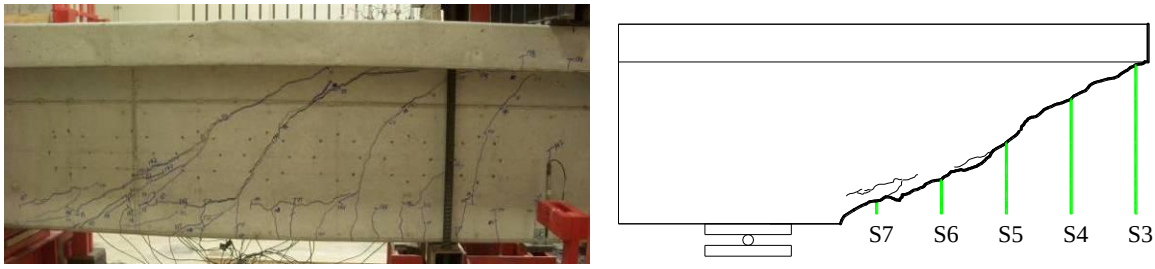

Figure A 5.59 Free Body Diagram of RC-12-S90-Control

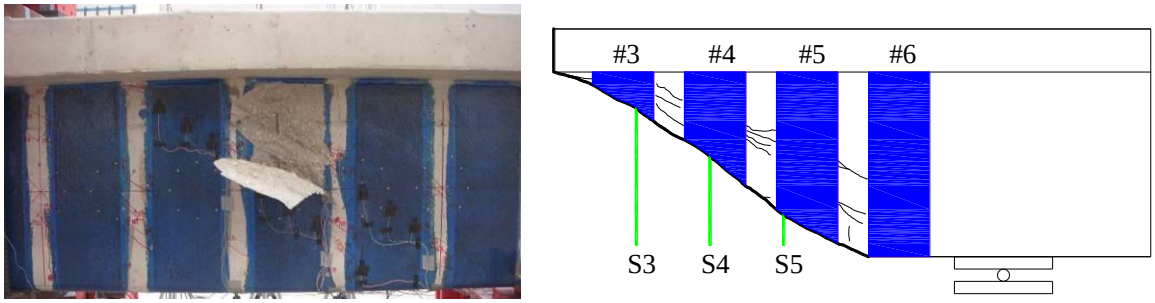

Figure A 5.60 Free Body Diagram of RC-12-S90-NA

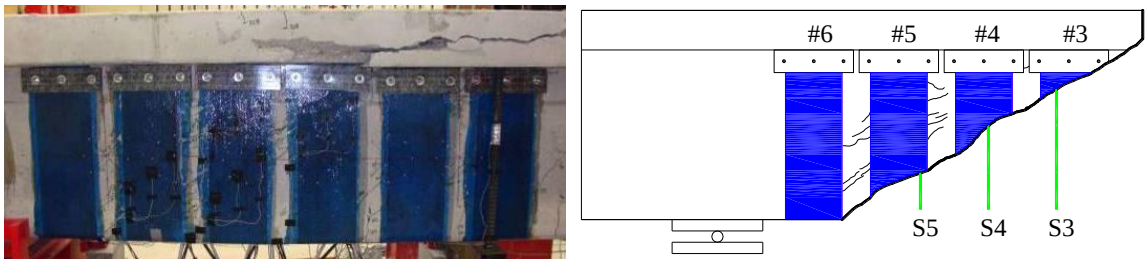

Figure A 5.61 Free Body Diagram of RC-12-S90-DMA

Meanwhile, it was found from the test results that there exists an interaction between the stirrups and FRP, which could be key to the understanding of why FRP strengthening is less effective when more stirrups are used as reported by other research studies and the analytical study on the existing experimental database performed in this project.

A5.2.10.5 Effects of Pre-Existing Cracks

Two tests including specimens RC-12-S90-HA-PC and RC-12-S90-SDMA-PC have been performed to evaluate the effects of pre-existing cracks. As shown in Figure A 5.62, Specimen RC-12-S90-HA-PC was loaded up to 91 kips while Specimen RC-12-S90-SDMA-PC was loaded up to 75 kips of shear force. As a result, two major diagonal cracks were generated as shown in Figure A 5.63 and Figure A 5.64.

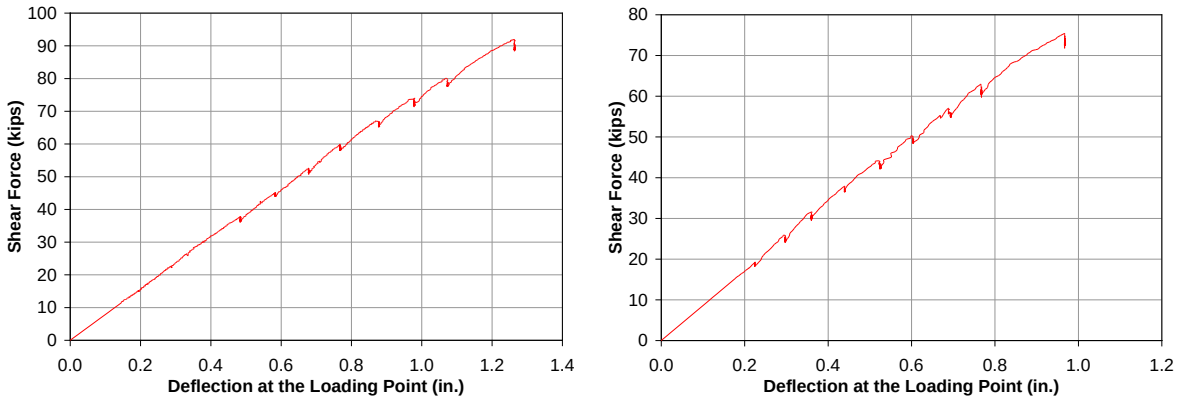

(a) RC-12-S90-HA-PC (b) RC-12-S90-SDMA-PC

Figure A 5.62 Shear Force vs Deflection at the Loading Point during the Pre-Cracking Procedure in the Web of Specimen RC-12-S90-HA-PC and RC-12-S90-HA-PC

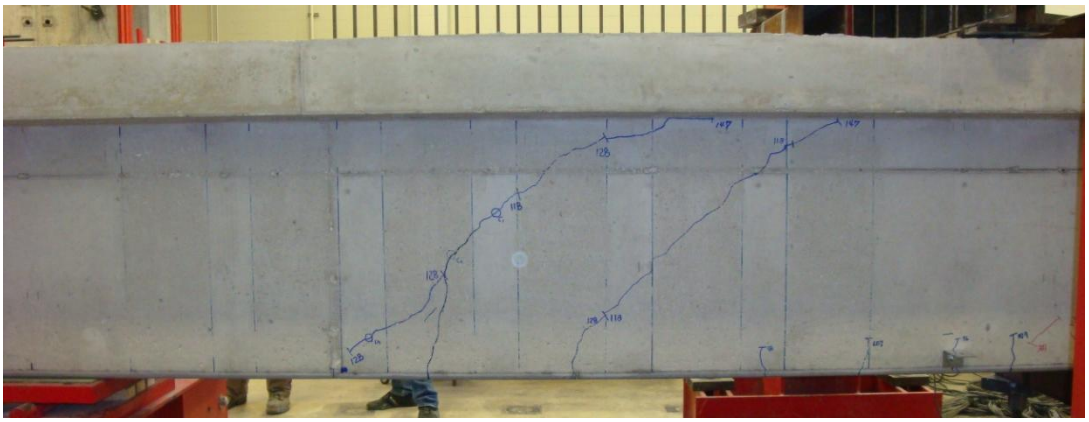

Figure A 5.63 A Photograph of RC-12-S90-HA-PC Taken after the Pre-Cracking Test

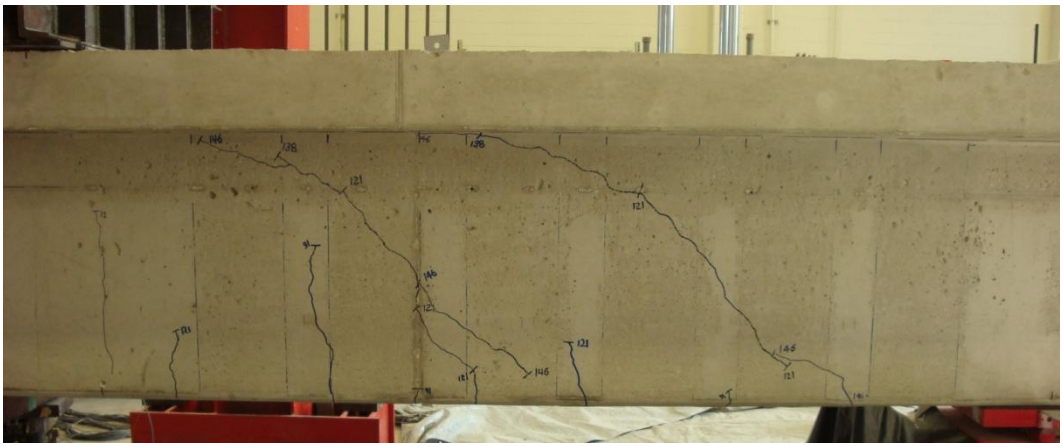

Figure A 5.64 A Photograph of RC-12-S90-SDMA-PC Taken after the Pre-Cracking Test

Specimen RC-12-S90-HA-PC and RC-12-S90-SDMA-PC were then strengthened with FRP and tested up to failure. Figure A 5.51 present the shear contribution of each component (i.e. V_c, V_f, and V_s) observed from the failure tests of the specimens. It can be observed that the shear contribution of stirrups and FRP in the specimens with pre-existing cracks (see Figure A 5.51(d) and (e)) increased gradually from a very early state of the loading history as compared to the other specimens which exhibited a sudden increase in shear contribution of FRP and stirrups at a later stage in the loading history. This resulted in the yielding of all stirrups bridging over the critical cracks at a lower shear force as compared to the other specimens without pre-existing cracks.

The behavior of FRP strengthening of the specimens with pre-existing cracks was also slightly different than that of the specimens without pre-existing cracks. The variation in the contribution of FRP for specimens with pre-existing cracks is compared to the variations in contribution of FRP for specimens without pre-existing cracks in Figure A 5.65. As shown in Figure A 5.65, the contribution of FRP in the specimens without pre-existing cracks (RC-12-S90-NA and RC-12-S90-DMA) varied almost linearly up to failure of the specimens while the specimens with pre-existing cracks exhibited a steep jump of the contribution of FRP when the second major diagonal shear cracks developed.

Overall, it was observed that the behavior of stirrups and FRP strips is influenced by the existence of diagonal shear cracks. The failure of the specimens was due to the debonding of additional horizontal strips for Specimen RC-12-S90-HA-PC and the rupture of FRP sheets for RC-12-S90-SDMA-PC. However, the impact of pre-existing cracks on the shear performance of FRP strengthened beams cannot be conclusively determined from this study since there were no reference specimens for comaprison. Meanwhile, there are experimental studies on RC beams with pre-existing cracks (Czaderski, 2002; Carolin and Taljsten, 2005a, and Hassan Dirar et al., 2006) showing that the existence of pre-existing cracks did not affect the shear strength of FRP strengthened RC beams.

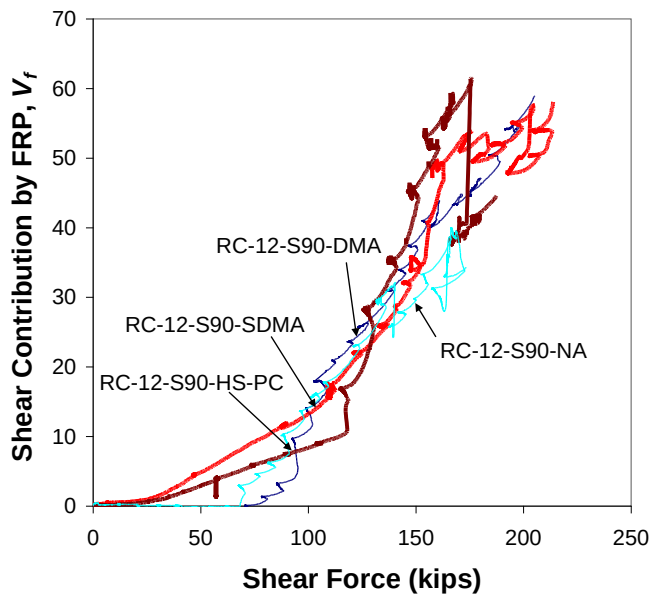

Figure A 5.65 Comparison of Shear Contribution of FRP between Specimens with Pre-Existing Cracks and Specimens without Pre-Existing Cracks

A5.2.10.6 Effects of Fiber Orientations

The objective of testing Specimens RC-12-S45-NA, RC-12-S45-HA, and RC-12-S45-SDMA, was to evaluate the effects of fiber orientation. The beams were strengthened in shear using externally boned FRP sheets with a fiber orientation of 45° relative to the longitudinal axis of the beams; while previous beams were strengthened with a fiber orientation of 90°.
Specimen RC-12-S45-NA was strengthened with FRP strips at 45° without any mechanical anchorage system. Beam RC-12-S45-HA was strengthened with FRP strips at 45° and an additional horizontal FRP strip at the top for mechanical anchorage. Specimen RC-12-S45-SDMA was strengthened with FRP strips at 45° and the sandwich plate discontinuous mechanical anchorage system. Specimens RC-12-S45-NA and RC-12-S45-HA failed due to the debonding of FRP sheets. Specimen RC-12-S45-SDMA failed due to the rupture of FRP sheets while the mechanical anchorage system was not damaged until failure. The photographs taken at the failure of these specimens are provided in Additional Material M to Appendix.

The test results from these specimens are summarized in Table A 5.11 along with the test results of the previously tested beams. The actual shear gains in Table A 5.11 were calculated using the normalized shear strength, which takes into account the differences in concrete strength. To

evaluate the effects of fiber orientation, the specimens with similar mechanical anchorage schemes had to be compared, i.e., RC-12-S90-NA vs. RC-12-S45-NA, RC-12-S90-HA-PC vs. RC-12-S45-HA, and RC-12-S90-SDMA-PC vs. RC-12-S45-SDMA. However, a direct comparison is meaningless without further normalization to account for the fact that the specimens strengthened with 45° orientation have a lower FRP reinforcement ratio than those strengthened with a 90° orientation. Maintaining a constant FRP reinforcement ratio would have resulted in insufficient spacing to observe crack propagation between FRP strips for the 45° orientation. In addition, such tight spacing of the FRP strips would have been equivalent to a continuous FRP strengthening scheme. Thus it was deemed necessary to maintain the spacing between FRP strips which results in a reduction of the FRP reinforcement ratio for the 45° orientation. Table A 5.11 presents the results after normalization to account for both differences in concrete strength and FRP reinforcement ratio. The results from Table A 5.11 show that the fibers oriented at 45° with respect to the longitudinal axis of the beams appeared to be more effective than the fibers oriented at 90° as one might expect.

Table A 5.11 Comparisons of Tests Results between Specimens of 45° Fiber Orientation and Specimens of 90° Fiber Orientation

	f'_c (psi)	$V_{n,yest}$ (kips)	V_c (kips)	V_s (kips)	V_f (kips)	$V_{n,norm}$ (kips)
RC-12-S90-NA	4190	172	91.5	41	39.5	156.4
RC-12-S45-NA	6240	217	79	43.5	94.5/0.7*=135	257.5
RC-12-S90-HA-PC	2650	187	87.9	38.3	61.3	191.2
RC-12-S45-HA	3850	181	53.4	41.1	86.3/0.7*=123	217.5
RC-12-S90-SDMA-PC	2780	214	117.8	37.2	59	216.1
RC-12-S45-SDMA	4230	203	37.1	41.8	123.9/0.7*=177	255.9

*0.7 is the ratio of the FRP reinforcement ratio of the specimens with 45° orientation to that of the specimens with 90° orientation.

A5.2.10.7 Effects of Anchorage Systems

Three different types of anchorage systems were used in this test program, (1) discontinuous mechanical anchorage (DMA), (2) sandwich discontinuous mechanical anchorage (SDMA), and additional horizontal FRP strips (HA). The performance of these mechanical anchorage systems is discussed in detail in Section A5.4 while this section briefly presents the contribution of FRP (V_f). Figure A 5.66 compares the shear contribution of FRP among the specimens with different anchorage systems and it clearly shows that SDMA performed best, followed by HA and DMA.

A5.2.10.8 Effects of FRP Strengthening in Negative Moment Region

Specimens RC-12-S90-NA-HM and RC-12-S90-SDMA-HM were tested to evaluate the effects of FRP strengthening in negative moment regions. Therefore, the beam was cast and tested upside down as shown in Figure A 5.29 to induce tension stresses in the flange. Specimen RC-12-S90-NA-HM was strengthened without mechanical anchorage systems. The failure was initiated due to the debonding of FRP sheets (see Additional Material M to Appendix). Specimen RC-12-S90-SDMA-HM was strengthened with sandwich discontinuous mechanical anchorage systems. The failure was initiated due to the rupture of FRP sheets (see Additional Material M to Appendix).

Figure A 5.67 shows the shear force versus deflections at the loading points of Specimens RC-12-S90-NA-HM and RC-12-S90-SDMA-HM and the corresponding reference beams (RC-12-S90-NA for RC-12-S90-NA-HM and RC-12-S90-SDMA-PC for RC-12-S90-SDMA-HM). As shown in Figure A 5.67, the shear strength of the specimens subjected to the negative moment appeared slightly greater than that of the corresponding control beams. Pellegrino and Modena (2006) also made similar observation in their experimental study investigating the effectiveness of FRP shear strengthening on continuous beams.

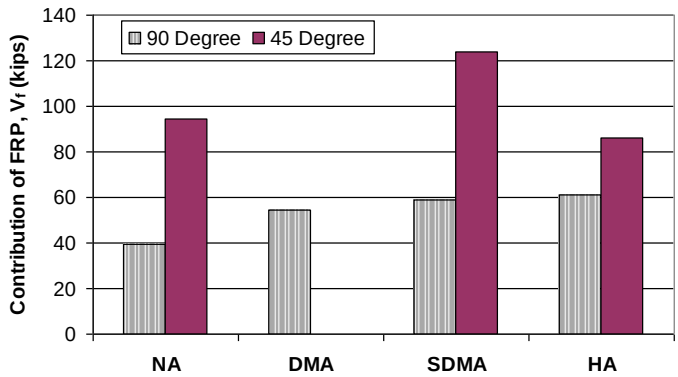

Figure A 5.66 Comparison of Contribution of FRP to the Shear Strength among the Specimens with Different Anchorage Systems

A5.2.10.9 Effects of FRP Strengthening for Corrosion-Damaged Beams

Specimen RC-12-S90-SDMA-Cor was used to investigate the effects of corroded internal steel reinforcement on the effectiveness of FRP shear strengthening. Specimen RC-12-S90-SDMA-Cor was subjected to the accelerated corrosion process as described in Section A5.2.8 and then strengthened in shear with FRP. The damage level due to the corrosion of internal steel reinforcement was also presented in Section A5.2.8. Figure A 5.68 shows the shear force versus deflection at the loading point of Specimen RC-12-S90-SDMA-Cor and the corresponding reference beam RC-12-S90-SDMA-PC.

It is interesting to see in Figure A 5.68 that the shear strength of RC-12-S90-SDMA-Cor was greater than that of RC-12-S90-SDMA. A higher concrete strength for RC-12-S90-SDMA-Cor can partially explain such results, but the increase in shear strength is mainly contributed to the difference in cracking patterns. For the reference beam, RC-12-S90-SDMA-PC, the critical shear crack crossed over two FRP strips whereas in the case of RC-12-S90-SDMA-Cor, four FRP strips bridged the critical shear crack. The cracks in the accelerated corrosion specimen consisted of web shear cracks merged into the pre-existing cracks along the longitudinal reinforcement developed by the accelerated corrosion process, as shown in Figure A 5.69. As a result, the contribution of FRP was greater in the case of RC-12-S90-SDMA-Cor than RC-12-S90-SDMA-PC as shown in Table A 5.9. It is hard to make generalized conclusions from a single test; however, the results of this test prove that shear strengthening with externally bonded FRP sheets can still be effective for repair of RC beams with slight corrosion-damage.

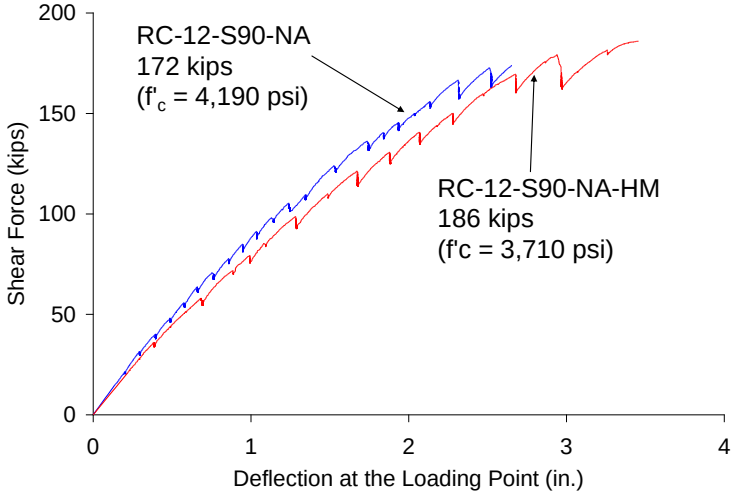

(a) RC-12-S90-NA-HM vs RC-12-S90-NA

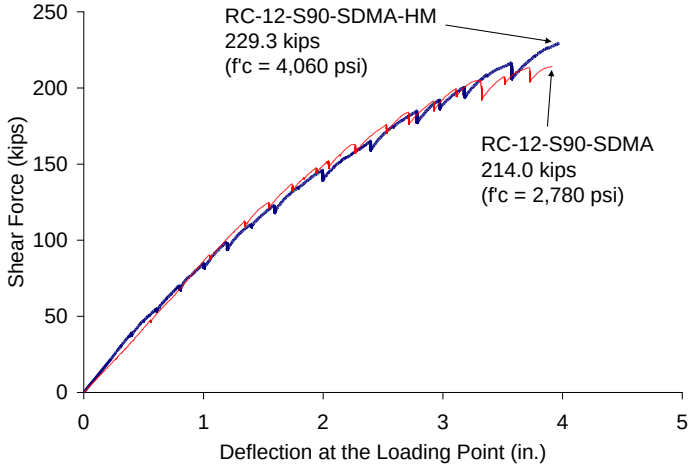

(b) RC-12-S90-SDMA-HM vs RC-12-S90-SDMA-PC

Figure A 5.67 Shear Force vs. Deflection at the Loading Points of Beams RC-12-S90-NA-HM and RC-12-S90-SDMA-HM.

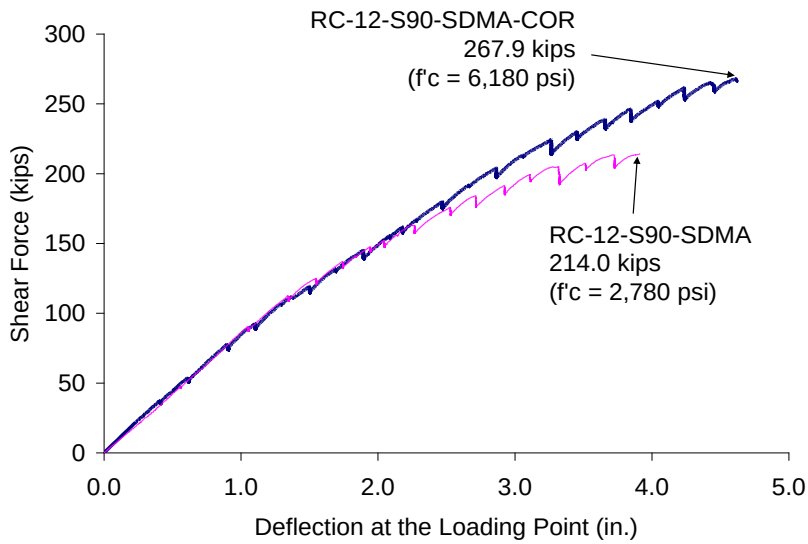

Figure A 5.68 Shear Force vs. Deflection at the Loading Point of Specimen RC-12-S90-SDMA-Cor

(a) RC-12-S90-SDMA-PC

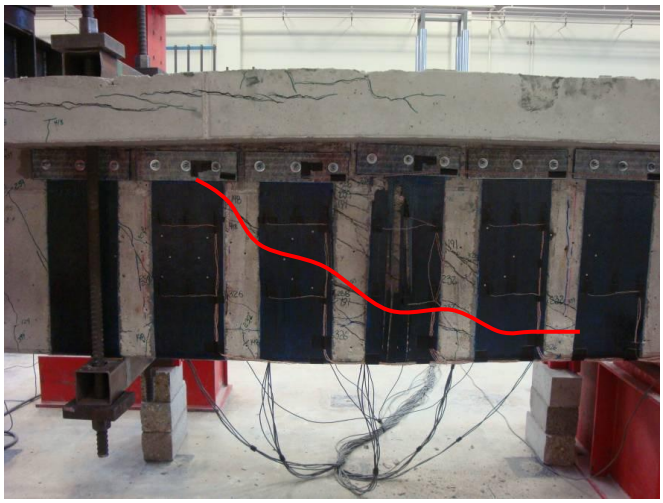

(b) RC-12-S90-SDMA-Cor

Figure A 5.69 Critical Shear Cracks of Beams RC-12-S90-SDMA-PC and RC-12-S90-SDMA-Cor

A5.2.10.10 Effects of Cyclic Loading on FRP Shear Strengthening

Figure A 5.70 shows the load range applied for the fatigue tests. The figure does not show any high fluctuation in the load, validating the test procedure. Given the change in the stiffness of the specimen, minimal drift from the target load range is observed beginning after about one million cycles of fatigue loading.

Figure A 5.71 shows the damage growth in terms of accumulated deflections under the load point at the middle of the cross section. Both minimum and maximum deflections are captured. The figure clearly shows a steady damage growth in the specimen, with periods of high damage

resulting perhaps from debonding of FRP. Such periods can be observed between 1 and 1.5 million cycles of loading. The upper limit of deflection increases by about 173% while the lower limit increases by about 134%. The range between the minimum and maximum deflection does not change significantly, as depicted in Figure A 5.71, indicating a moderate loss of stiffness.

Figures A 5.73 through A 5.78 show the strains at the top middle and bottom middle portions of FRP strips No. 1 through 6, moving away from the load point. On each FRP strip, three strain gages are mounted at the top 1/3 and another three at the bottom 1/3. The representative strain gages on the six FRP strips are numbered as S26, S29, S32, S35, S38, S41, S44, S47, S50, S53, S56, and S59. Except for the farthest FRP strip, almost all strips indicate some debonding from as early as 300,000 cycles, although significant debonding may be inferred at about 1 million cycles. In most cases, the strain at the top of the strip was larger than that at the bottom throughout most of the fatigue load history.

Figure A 5.79 shows the load-deflection curves for the static loading and unloading prior to each series of 500,000 cycles of fatigue loading and the residual strength test at the conclusion of fatigue testing. A moderate loss of stiffness is apparent from the load-deflection responses.

Subsequently, the static stiffness degradation of the specimen is captured in Figure A 5.80, indicating a 32% loss of stiffness between the virgin specimen and that after 2 million cycles of loading. The stiffness in this figure is calculated based on the initial slope of the load-deflection curves in the previous figure. A significant drop in the stiffness is noted after the first 1.5 million cycles of loading, primarily due to the debonding of FRP strips.

Figures A 5.81 through A 5.84 show the development of crack propogation for the specimen, noted after each static test, from the initial static test of the virgin specimen through the residual strength test after the 2 million cycles of fatigue loading. Figures A 5.81 through A 5.84 similarly depict the debonding patterns for the six FRP strips on the west side of the specimen, corresponding to the crack patterns. Identification of debonded areas was made by tapping of the FRP strips after each static loading. Table A 5.12 quantifies the debonded areas as a percentage of the FRP strip area.

Figure A 5.85 shows the complete peeling of FRP strips 3 and 4 on the west side of the specimen after about 1.5 million cycles of fatigue loading. The photograph clearly shows the splitting of FRP strips prior to complete peel off. Figure A 5.86 shows the peel off and splitting of FRP strips 4 and 5 on the east side of the specimen at about the same time as the earlier photograph.

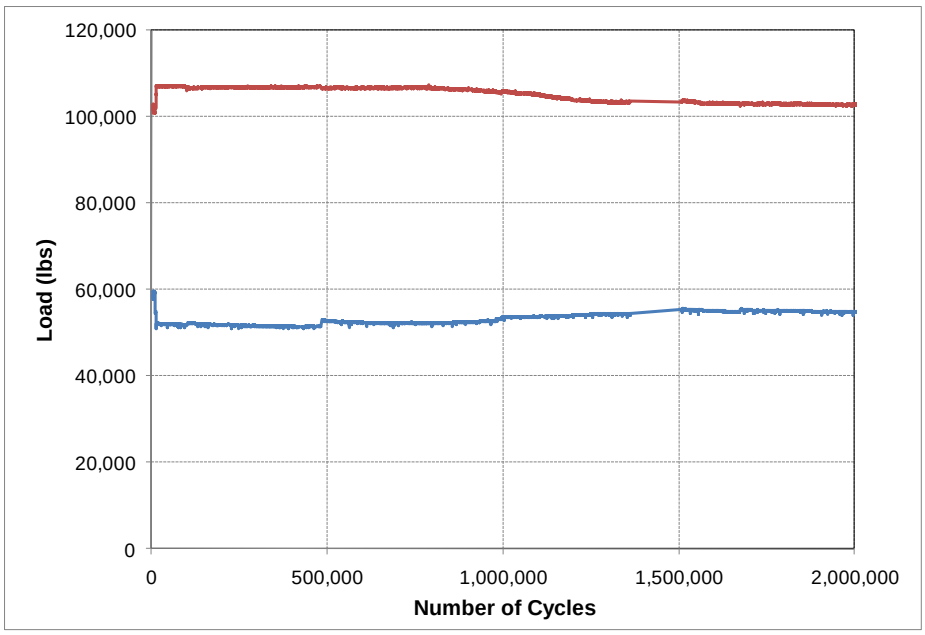

Figure A 5.70 Maximum and Minimum Load Range in Fatigue Tests

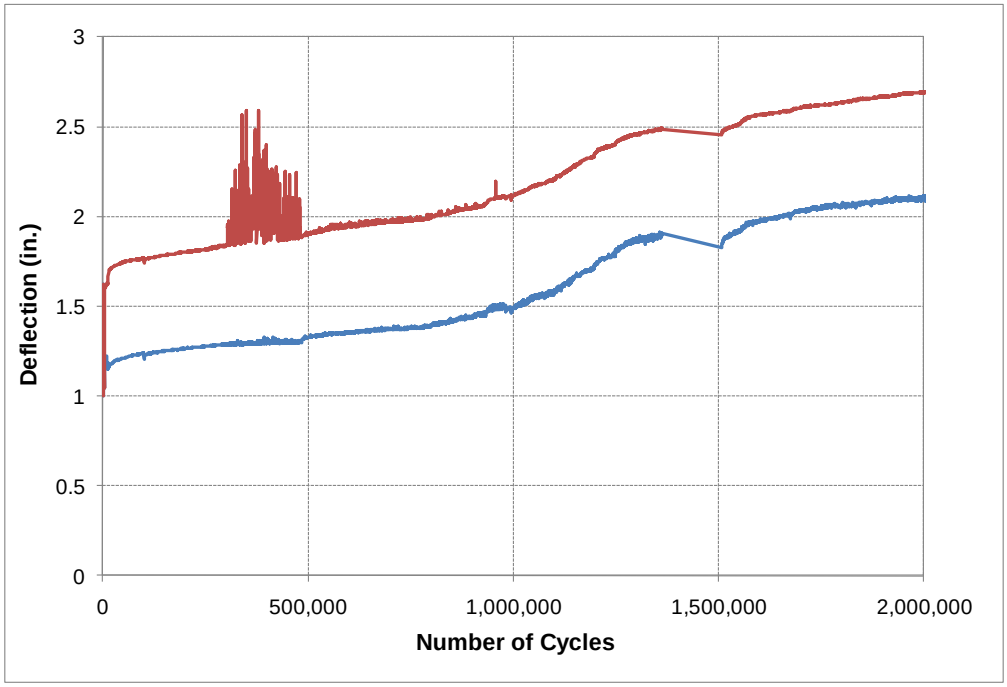

Figure A 5.71 Growth of Maximum and Minimum Deflections at Load Point

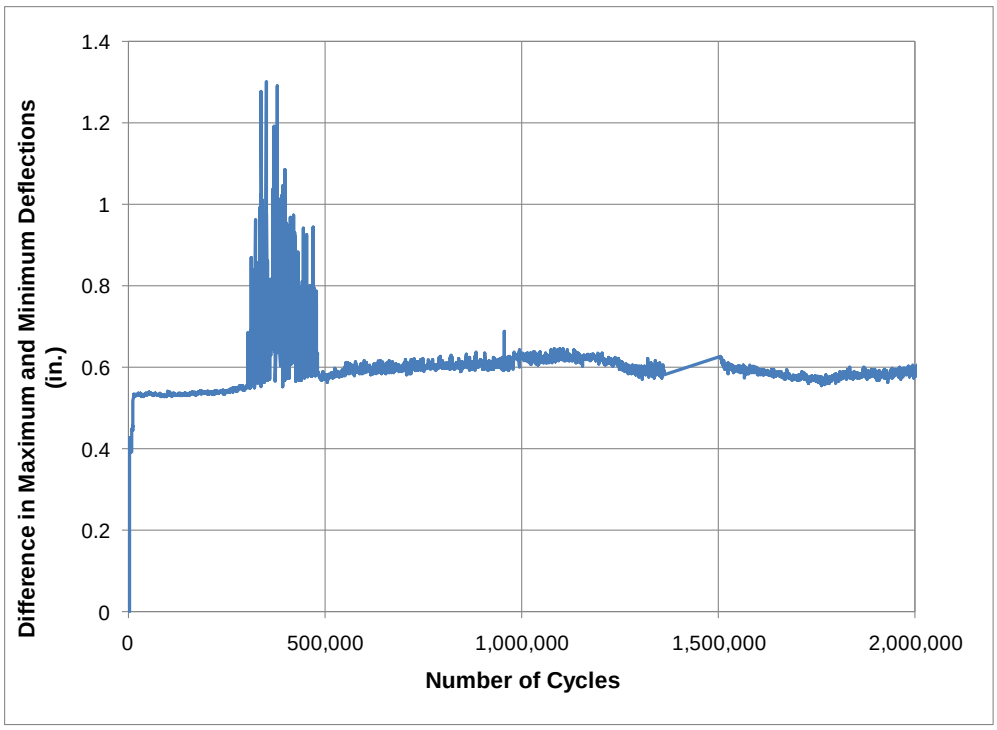

Figure A 5.72 Difference between the Maximum and Minimum Deflections at Load Point

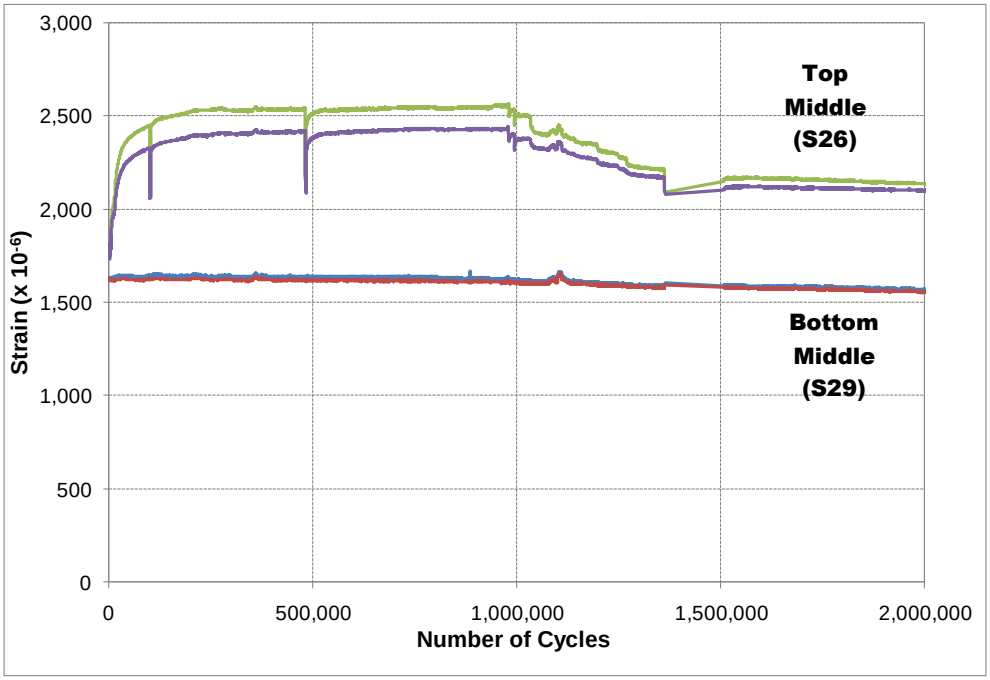

Figure A 5.73 Maximum and Minimum Strain Range at the Top and Bottom for FRP Strip 1

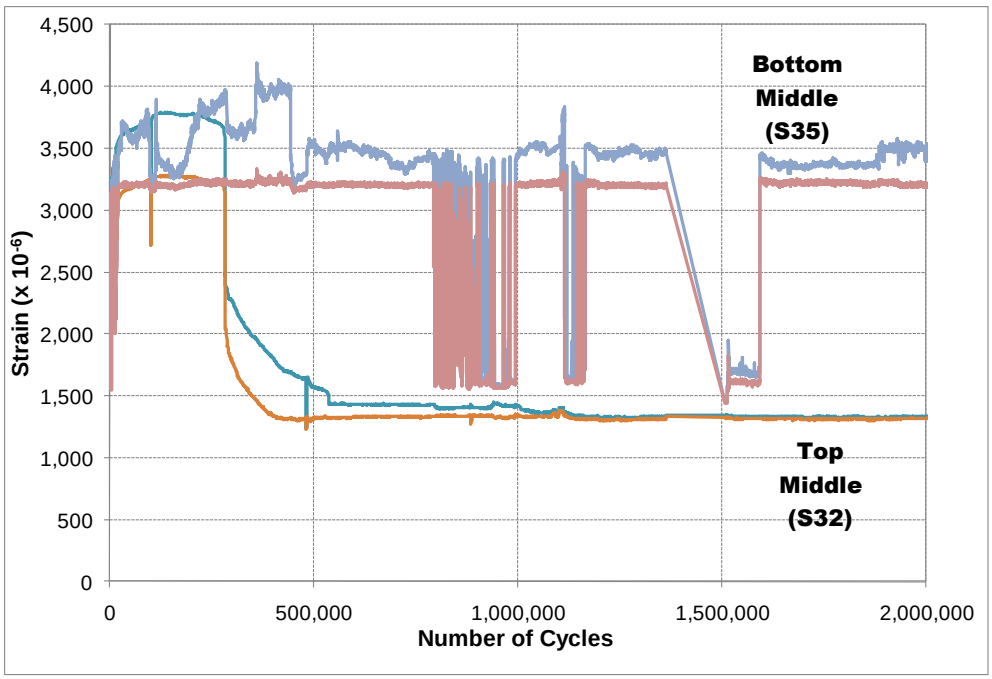

Figure A 5.74 Maximum and Minimum Strain Range at the Top and Bottom for FRP Strip 2

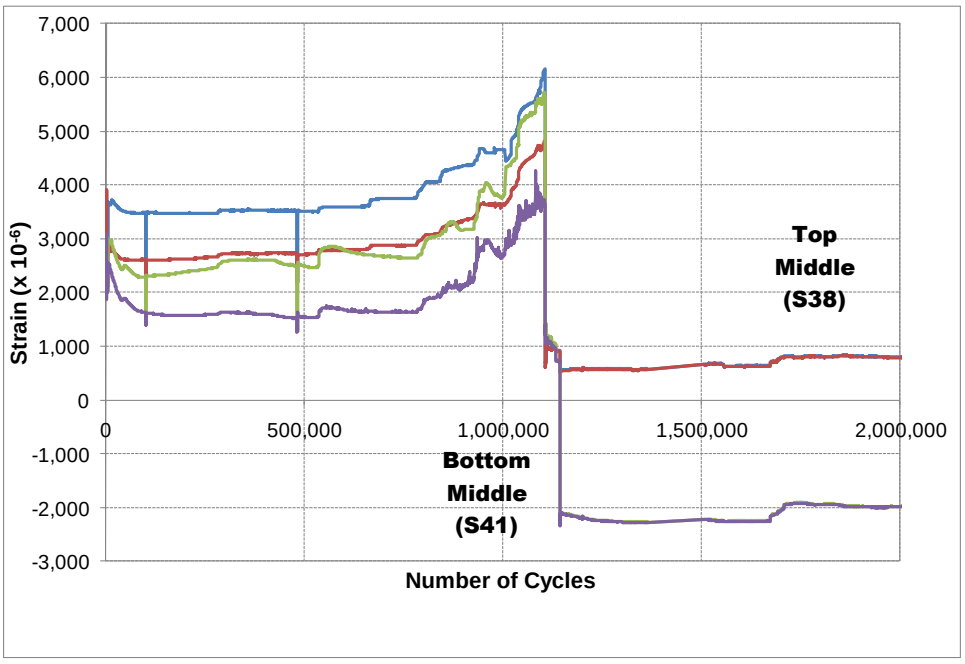

Figure A 5.75 Maximum and Minimum Strain Range at the Top and Bottom for FRP Strip 3

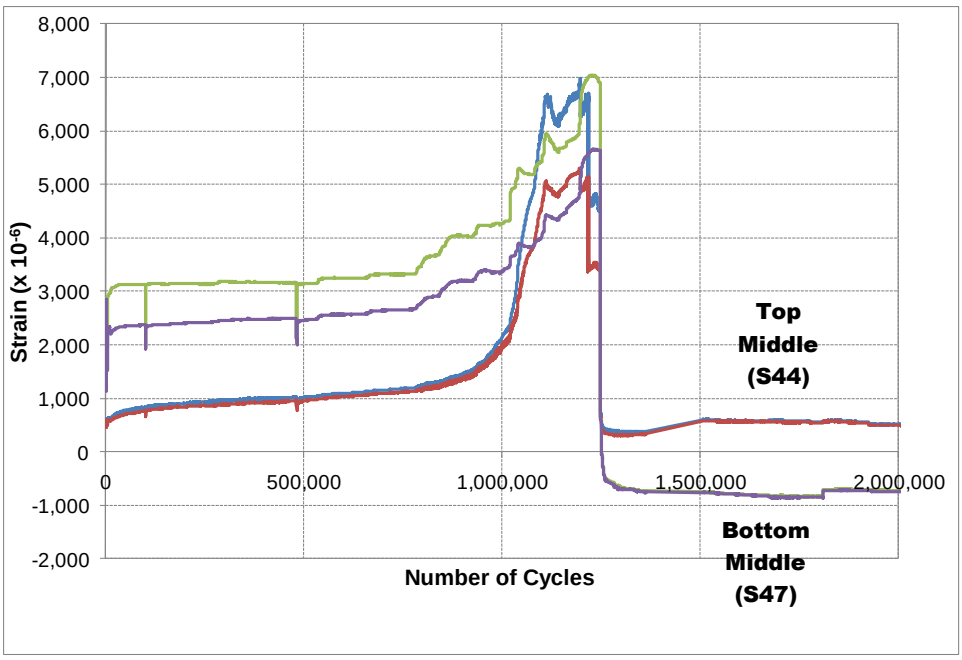

Figure A 5.76 Maximum and Minimum Strain Range at the Top and Bottom for FRP Strip 4

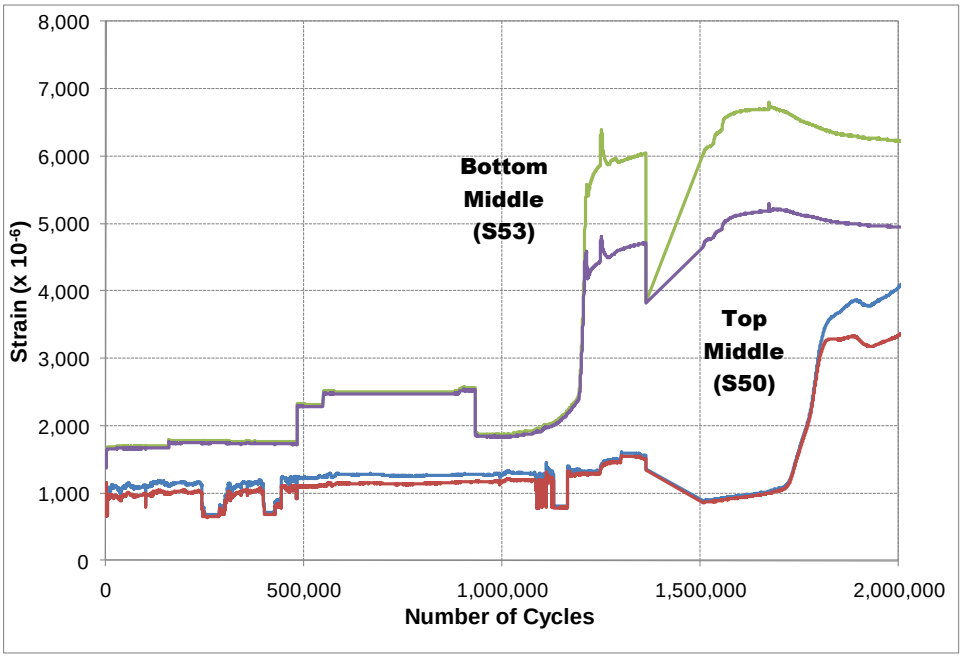

Figure A 5.77 Maximum and Minimum Strain Range at the Top and Bottom for FRP Strip 5

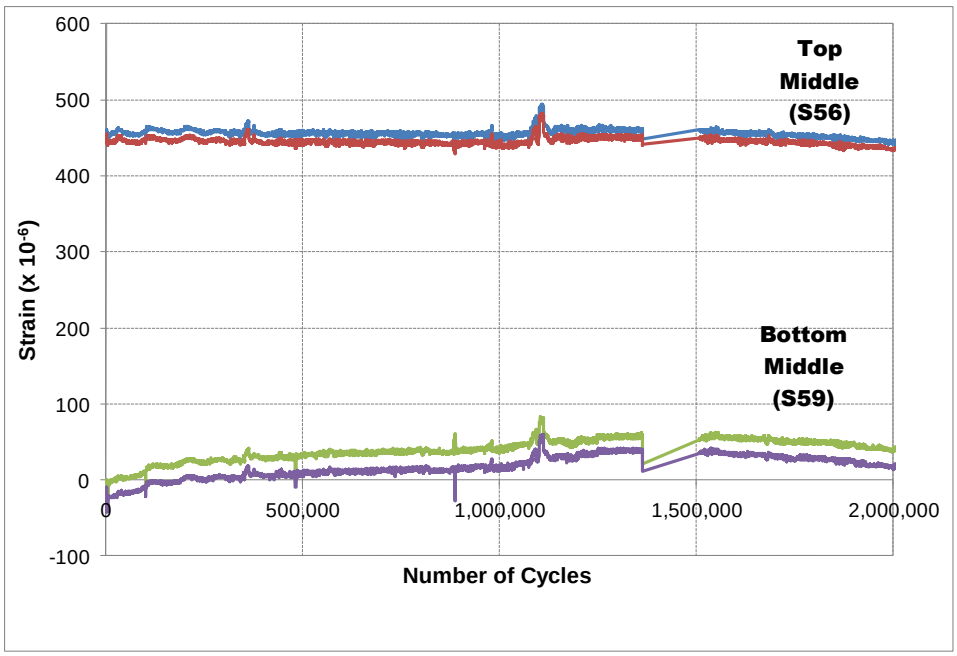

Figure A 5.78 Maximum and Minimum Strain Range at the Top and Bottom for FRP Strip 6

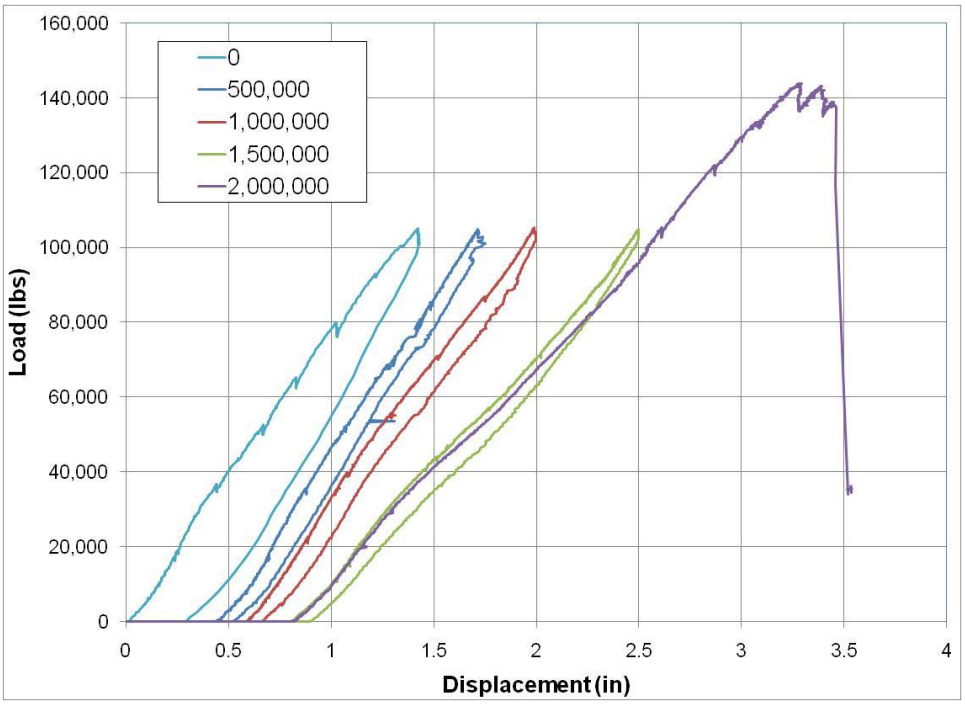

Figure A 5.79 Load-Deflection Response Curves for Static Loading and Unloading of Specimen

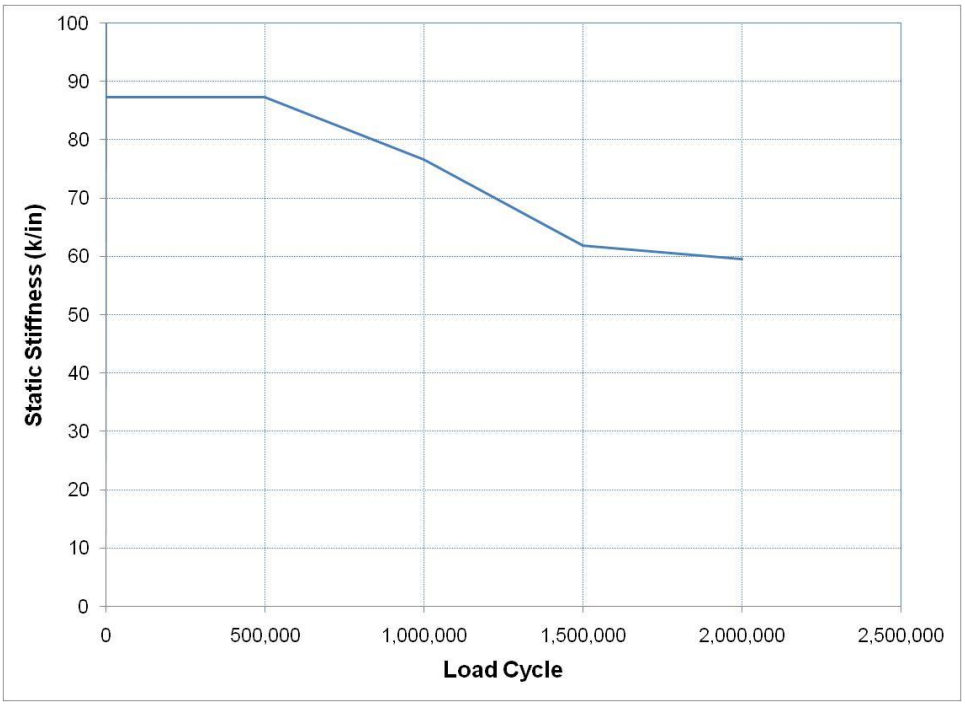

Figure A 5.80 Static Stiffness Degradation

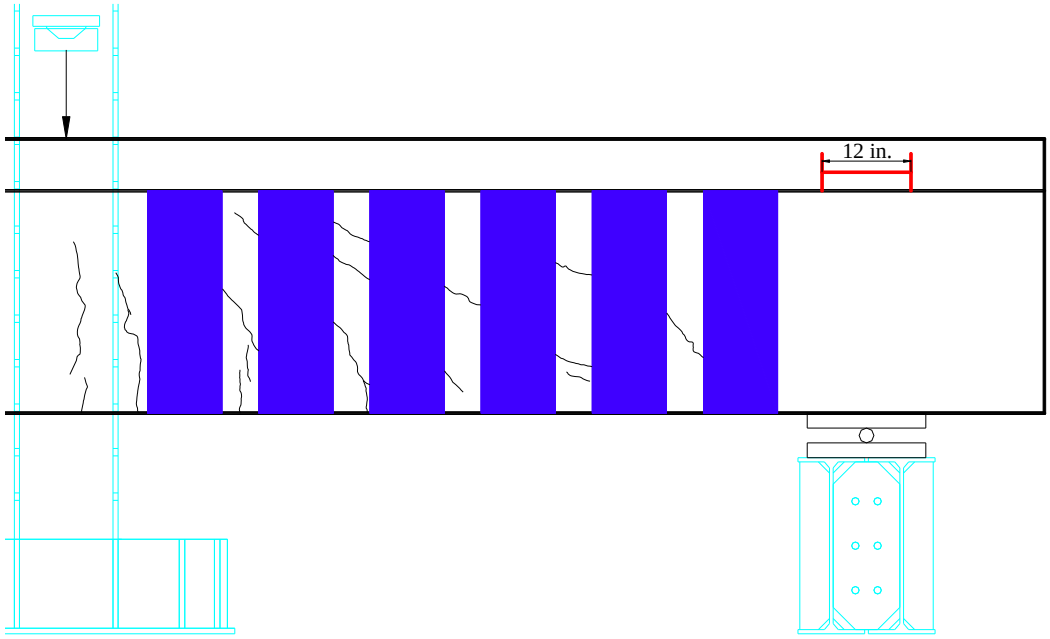

Figure A 5.81 Crack Pattern after Initial Static Test

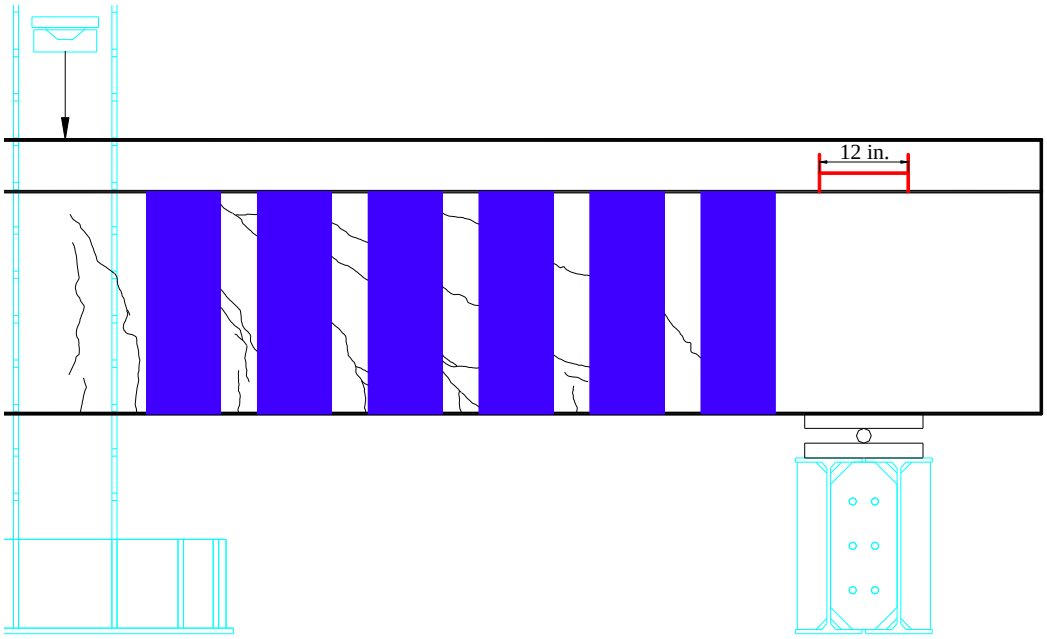

Figure A 5.82 Crack Pattern after Second Static Test (488,477 Cycles)

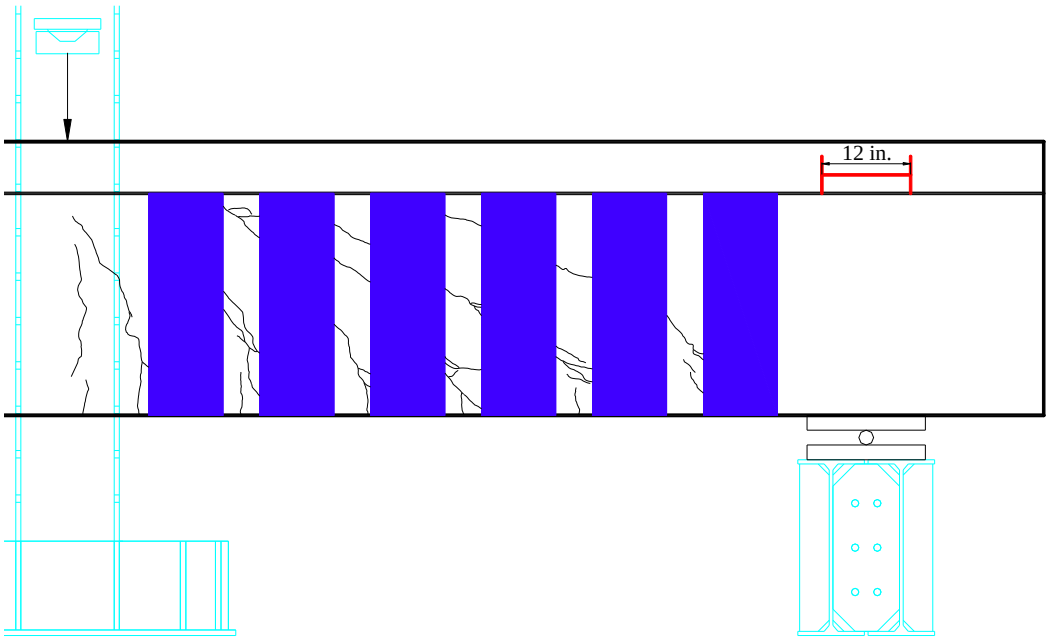

Figure A 5.83 Crack Pattern after Third Static Test (988,768 Cycles)

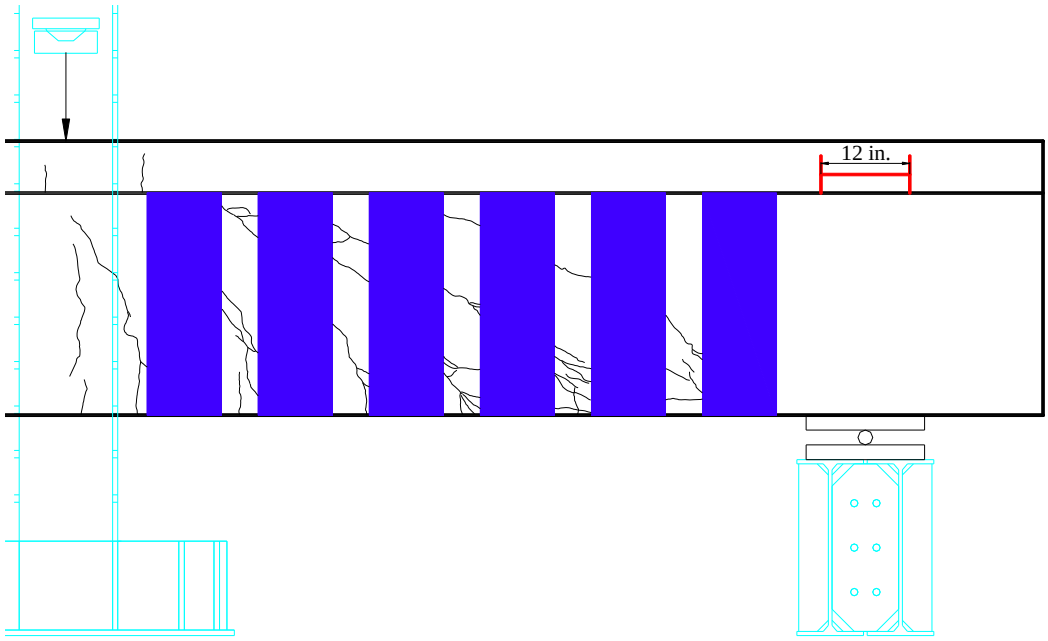

Figure A 5.84 Crack Pattern after Fourth Static Test (1,545,375 Cycles)

Table A 5.12 Debonded Areas of FRP Strips

	Strip 1	Strip 2	Strip 3	Strip 4	Strip 5	Strip 6
Static Test 2	-	19%	-	-	-	-
Static Test 3	-	19%	34%	-	-	-
Static Test 4	-	19%	92%	94%	-	-
Residual Strength Test	-	19%	92%	94%	55%	-

Note: Total Area of a strip is 300 in^2

Figure A 5.85 Complete Peeling of FRP Strips 3 and 4 after 1.5 Million Cycles (West side)

Figure A 5.86 Peeling of FRP Strips 4 and 5 on the East Side

It should be noted that the FRP-strengthened RC specimen was subjected to 2 million cycles of fatigue loading between 30% and 60% of the strengthened capacity, which translates to about 48 % and 86% of the un-strengthened beam. While debonding begins after about 350,000 cycles and grows steadily over the course of the fatigue test, it is important to note that the specimen survived the 2 million fatigue cycles without failure. A similar un-strengthened specimen is not expected to have survived such a high level of fatigue loading, because the stress range in the steel reinforcement would have been above its yield strength. However, for all practical purposes, after 1.0 million cycles, one can consider the specimen as the ones without any FRP shear strengthening. As clear from both static and fatigue testing, and as expected, the FRP strips delayed the onset of yielding in the stirrups, and also resulted in higher overall performance for the RC specimen, albeit debonding of FRP occurred at well below the 2 million cycles. It should be noted that because some yielding of the stirrups occurred during the initial static test, cracks were allowed to grow without bound and thus FRP bond was fully engaged and severly worked during fatigue loading. However, other fatigue test performed by Williams and Higgins (2008) reported much better bond performance when loading ranges were maintained at a range such that stirrups would not yield.

The fatigue behavior of the beam followed that of the FRP-concrete bond interface, as discussed extensively by Harries (2005). Proper anchorage of FRP is expected to delay the debonding and improve its performance. It is also important to note the effect of crack opening in RC on the debonding of FRP strips and the fatigue behavior of FRP-strengthened RC beam. This behavior is expected to be quite different in the case of PC girders.

Overall, from the single fatigue test in this study, as well as a number of fatigue tests that were reported earlier from the literature, one can conclude the following:

(a) if stresses in the shear stirrups are below the yielding strength, the FRP strengthening can help further delay the yielding, thus preventing the fatigue failure of the girder in shear; and
(b) if the stirrups have already yielded under existing service loads, while it would be unlikely that the stresses drop considerably by adding the FRP strengthening system, FRP could still help contain the stresses and prevent catastrophic failure of the girder.

Therefore, it is important to consider shear strengthening of a concrete girder using FRP within an overall strengthening plan, which includes consideration of the flexural capacity. When a girder is deficient in shear, strengthening may not require increasing the flexural capacity of the girder, but rather bringing up the shear resistance to an acceptable level. As a design philosophy, limiting the stress in the stirrups to the yield strength can provide an assurance that shear fatigue failure of the girder would not occur.

A5.2.10.11 Strain Distribution of FRP

Vertical strains in the test region were measured using LVDTs (see Figure A 5.87). The results are plotted for multiple load levels in Figure A 5.87 and Figure A 5.88 indicating that vertical strains are not uniform over the shear span. Since FRP sheets were bonded to the concrete, the vertical strains of FRP, aligned with fiber direction, also appeared to be non-uniform prior to debonding of FRP, as shown in Figure A 5.89 and Figure A 5.90. In fact, the FRP strain distribution becomes more complex after debonding, showing irregular distribution over the

shear span; however, Figures D 5.89 and D 5.90 only show the distribution of FRP strains at loading steps prior to the initial debonding of FRP.

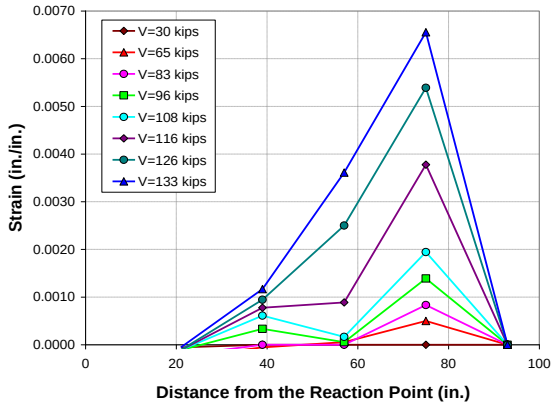

(a) RC-8-Control

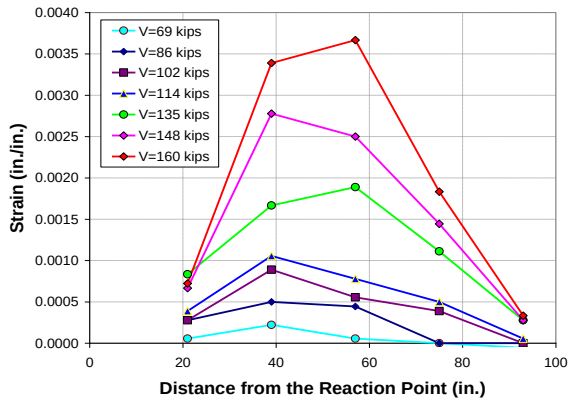

(b) RC-8-S90-NA

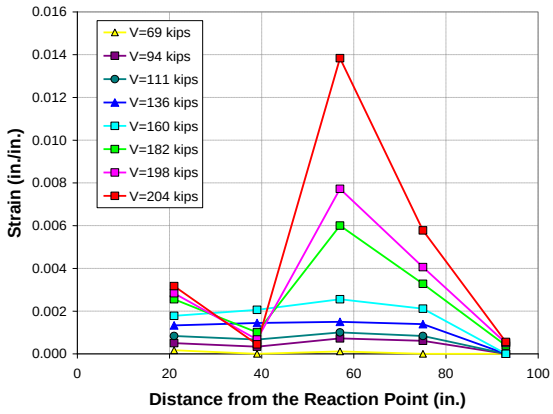

(c) RC-8-S90-DMA

Figure A 5.87 Vertical Strain Distribution over Shear Span Measured by LVDTs (RC-8 series)

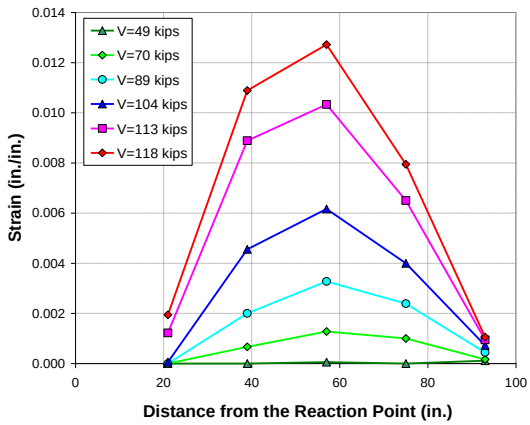

(a) RC-12-Control

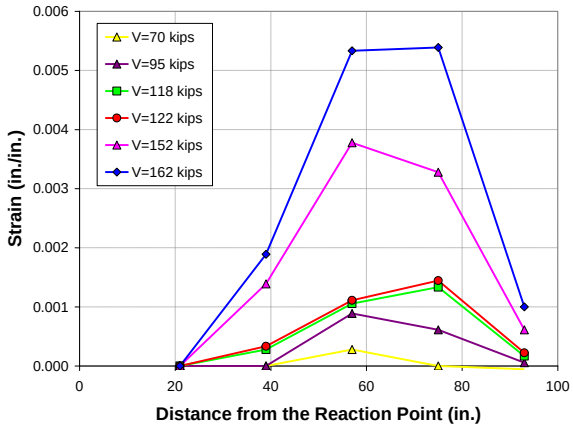

(b) RC-12-S90-NA

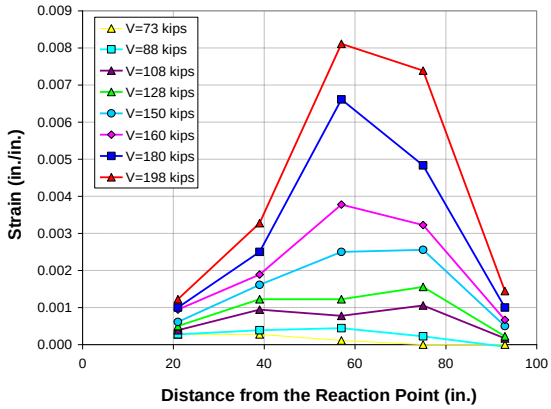

(c) RC-12-S90-DMA

Figure A 5.88 Vertical Strain Distribution over Shear Span Measured by LVDTs (RC-12 series)

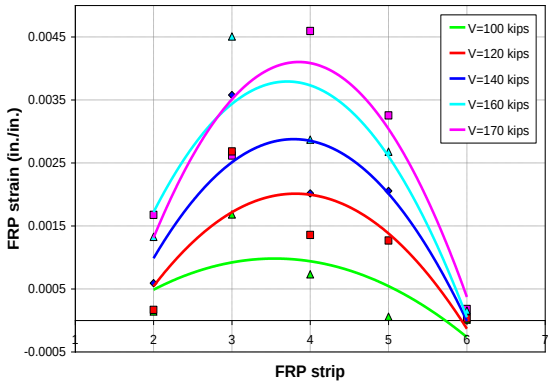

(a) RC-8-S90-NA

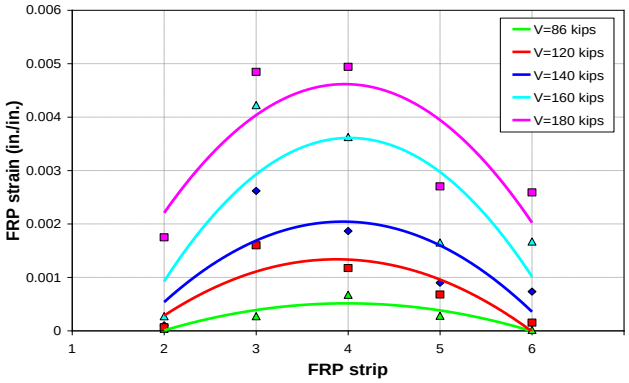

(b) RC-8-S90-DMA

Figure A 5.89 FRP Strain Distribution over Shear Span Measured by Strain Gages (RC-8 Series)

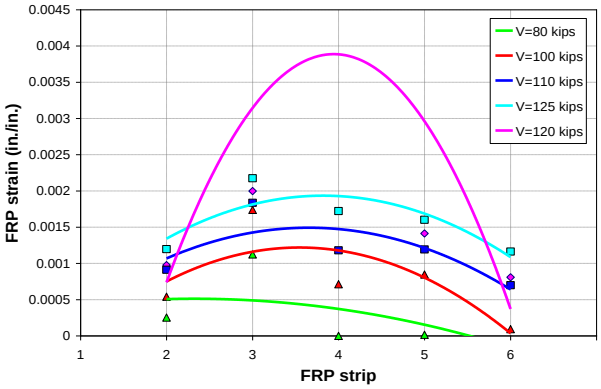

(a) RC-12-S90-NA

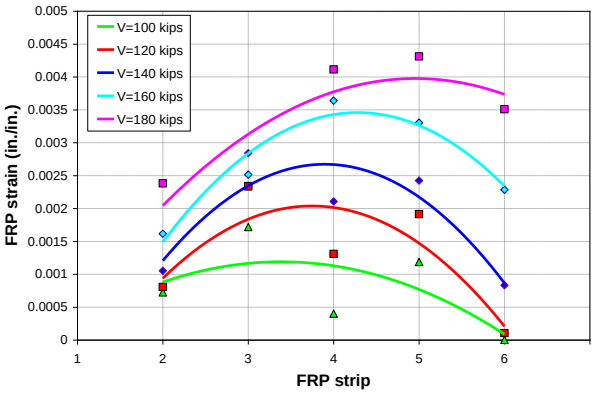

(b) RC-12-S90-DMA

Figure A 5.90 FRP Strain Distribution over Shear Span Measured by Strain Gages (RC-12 Series)

Many researchers (Cao et al. 2005, Monti and Liotta, 2007) have attempted to model the FRP strain distribution in order to predict the strain level of FRP and the shear forces carried by each FRP sheet in the shear span. However, based on the non-uniform strain distribution, the performance of their analytical models did not appear more accurate than other analytical models using simple equations based on effective strain (stress) concepts (Tumialan, 2007) as discussed in Section A4. The limited accuracy of these models may be due to the effects of various parameters on FRP strain distribution. These parameters include the stiffness of the top and bottom flanges, longitudinal and transverse steel reinforcement ratio, and quality of bond between FRP and concrete including the use of mechanical anchorage. Thus more comprehensive experimental and analytical work is required to fully understand the distribution of strains.

The simplest and most widely accepted way of predicting the shear contribution of FRP is to use the truss analogy, which is also used to calculate the shear contribution of stirrups. It is commonly assumed that stirrups yield at failure and thus that the yield strength of the stirrup can reasonably predict the shear contribution of transverse reinforcement. However, FRP strains are not uniform, as shown in Figure A 5.89 and Figure A 5.90. An average value of FRP strain must be assumed if the truss analogy is to be used. The average strain level is referred to as the effective strain in many existing analytical models and code/specifications. In this study, effective strain was calculated based on actual shear gain (discussed in Section A5.2.8.3).

A5.2.10.12 Effective Strain of FRP Sheets

Most currently available analytical models express the contribution of FRP to the shear capacity as a function of the effective strain of FRP (ε_{fe}). The effective strain is typically expressed as a fraction of the ultimate strain and represents the average strain experienced by the FRP strips at ultimate shear capacity of the strengthened member.

The effective strain (ε_{fe}) was calculated using Equation A5-7 and assuming V_f as the actual shear gain experienced by the FRP strengthened specimens:

$$V_f = \frac{A_f f_{fe} d_f}{s_f}(\sin\beta + \cos\beta) = \frac{A_f E_f \varepsilon_{fe} d_f}{s_f}(\sin\beta + \cos\beta) \qquad \text{(A5-7)}$$

where $A_f = 2n_f t_f w_f$ is the area of transverse FRP reinforcement covering two sides of the beam, n_f is number of FRP plies, t_f is the FRP reinforcement thickness, w_f is the width of the strip, s_f is the spacing between the strips (defined as the distance from the centerline of one strip to the center line of an adjacent strip), and β is the angle between the orientation of the fibers and the horizontal axis of the beam.

Effective strains were calculated not only for the test specimens in this study but also for the specimens included in the experimental database. Figure A 5.91 plots the results against the rigidity of FRP over the compressive strength of concrete ($E_f t_f / \sqrt{f_c'}$). Since the effective strain of FRP is largely dependent on the failure mode, the effective strains drawn from the database were grouped in this figure by the failure mode of the test specimen, i.e., either as debonding or rupture of the FRP strips.

According to Figure A 5.91, the effective strain decreases as the rigidity of FRP increases. The effective strains of the specimens tested in this study are similar to those drawn from the database with respect to FRP rigidity, implying that the effectiveness of FRP shear strengthening on full-scale RC beams can be regarded as much as that verified through small-scale experimental results.

The concept of effective strain is used for the development of design equations that is presented in a significant detail in Chapter 3.2 of this report.

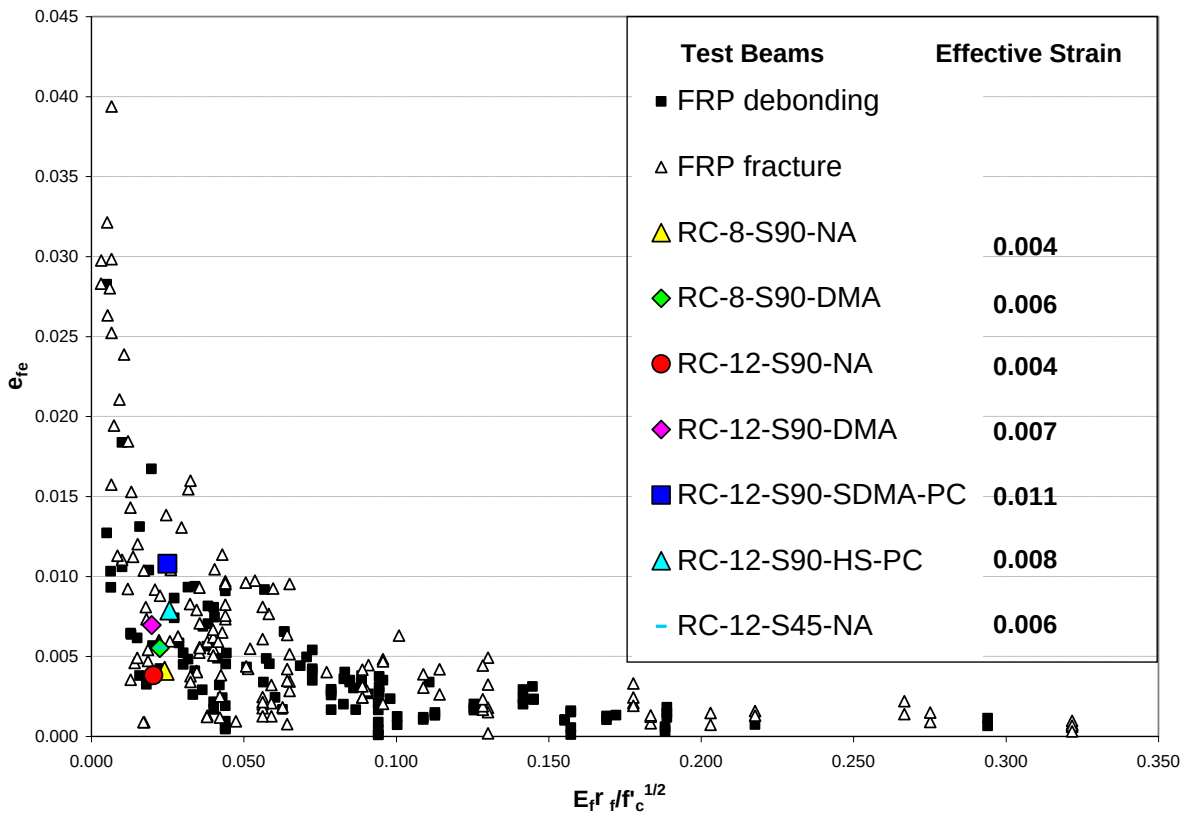

Figure A 5.91 FRP Effective Strain vs FRP Rigidity

A5.2.11 Summary and Conclusions

A total of 15 specimens were tested to investigate the behavior of RC T-beams strengthened in shear with externally bonded FRP sheets. The test parameters included the amount of internal transverse reinforcement, different anchorage systems, orientations of fibers with respect to the longitudinal axis of the test beams, existence of diagonal cracks in the web prior to strengthening, existence of corrosion damage, negative moment region vs. positive region, and effects of fatigue loading.

The test results showed that the differences in the amount of internal transverse steel reinforcement (stirrups) used in the RC-8-Series and RC-12-Series beams did not significantly changed the shear strength gain. However, it was found that there is an interaction between the contribution of FRP and the contribution of stirrups.

Among the three different types of anchorage systems, the sandwich discontinuous mechanical anchorage systems (SDMA) performed best, showing rupture of FRP sheets. Meanwhile, the specimens with discontinuous mechanical anchorage systems (DMA) and horizontal additional FRP strips (HA) showed an increase in shear strength as compared to the specimens with no anchorage systems.

The fibers oriented at 45° with respect to the longitudinal axis of the beams appeared to be more effective than the fibers oriented at 90°.

The effects of negative moment did not appear to influence the behavior of the beams as compared to specimens tested under positive moment conditions.

It was also shown that beams with slight corrosion damage can be effectively repaired in shear by externally bonded FRP sheets.

For the beams with pre-existing cracks, the stirrups were found to yield at a lower shear force than beams without pre-existing cracks. However, the presence of pre-existing cracks did not change the ultimate failure modes of the beams. Thus, the existence of pre-existing cracks does not seem to have a negative impact on the effectiveness of FRP shear strengthening.

From the single fatigue test in this study, as well as a number of fatigue tests that were reported earlier from the literature, one can conclude the following:

(a) if stresses in the shear stirrups are below the yielding strength, the FRP strengthening can help further delay the yielding, thus preventing the fatigue failure of the girder in shear; and
(b) if the stirrups have already yielded under existing service loads, while it would be unlikely that the stresses drop considerably by adding the FRP strengthening system, FRP could still help contain the stresses and prevent catastrophic failure of the girder.

Therefore, it is important to consider shear strengthening of a concrete girder using FRP within an overall strengthening plan, which includes consideration of the flexural capacity. When a girder is deficient in shear, strengthening may not require increasing the flexural capacity of the girder, but rather bringing up the shear resistance to an acceptable level. As a design philosophy, limiting the stress in the stirrups to the yield strength can provide an assurance that shear fatigue failure of the girder would not occur.

A5.3 PC Girders

A5.3.1 General

The objective of the PC girder testing was to investigate and extend the current state of knowledge for FRP shear strengthening of RC beams using full-scale AASHTO type PC girders. The experimental study presented herein was designed to address the very limited prior research data available on the use of FRP for shear strengthening of PC girders. Therefore, no baseline results are available for comparison with the results obtained from the present study. In addition, some investigation into the geometry effects has been pursued since PC girders typically have a thin web with stiff top and bottom flanges which is not the case in most RC beams. As such, the failure modes of PC girders are more significantly affected by the geometry of the cross-section.

Although the information acquired from the previous research studies are very limited, it can be observed that: (1) the effectiveness of FRP shear strengthening can be affected by the size of the test girders in the case of PC girders, (2) use of mechanical anchorage systems can greatly affect the effectiveness of FRP shear strengthening systems, and (3) cross-sectional shape can be a critical parameter affecting shear behavior of PC girders strengthened in shear with FRP.

A5.3.2 Test Matrix

The test matrix for the PC girders was selected to investigate the above mentioned observations and draw conclusions from the limited number of full-scale tests as shown in Table A 5.13. The test parameters in Table A 5.13 include:

- Size of test girders (Type 4 vs. Type 3)
- Stiffness of top and bottom flanges (cross-sectional type)
- Effects of pre-existing damage (pre-cracking)
- FRP strengthening scheme (fibers oriented at 90° versus 45°)
- Types of mechanical anchorage used to avoid premature failure due to debonding of FRP
- Transverse steel reinforcement (stirrups) ratio

The first three test parameters were also considered in the RC T-beam tests, but the last two test parameters are more relevant to the PC girder testing and thus have been incorporated in the experimental program during the course of the project. The cross-sectional properties of the PC girders are presented in Figures A 5.92 through A 5.97.

Table A 5.13 PC Girder Test Matrix

MoDOT Standard	Girder	Test I.D.	Test Parameters							
			Cross-Section Type	Pre-Existing Cracks	Strengthening Scheme	Anchorage Type	Steel Shear Reinforcement	FRP Shear Reinforcement	Shear Span (ft)	Shear Span-to-Depth Ratio (a/d)
Type 4	1	T4-12-Control	I	No	None	None	#3 @ 12" (ρ_v = 0.0031)	ρ_f = 0	9	2.9
		T4-18-Control	I	No	None	None	#3 @ 18" (ρ_v = 0.0020)	ρ_f = 0	9	2.9
	2	T4-18-S90-NA	I	No	Strips/90	None	#3 @ 18" (ρ_v = 0.0020)	ρ_f = 0.0014	9	2.9
		T4-18-S90-CMA	II	No	Strips/90	Continuous CFRP Plates	#3 @ 18" (ρ_v = 0.0020)	ρ_f = 0.0014	12	2.9
	3	T4-18-S90-DMA	II	No	Strips/90	Discontinuous CFRP Plates	#3 @ 18" (ρ_v = 0.0020)	ρ_f = 0.0014	12	2.9
		T4-18-S45-DMA	II	No	Strips/45	Discontinuous CFRP Plates	#3 @ 18" (ρ_v = 0.0020)	ρ_f = 0.0010	12	2.9
	4	T4-12-Control-Deck	II	No	None	None	#3 @ 12" (ρ_v = 0.0031)	ρ_f = 0	12	2.9
		T4-12-S90-SDMA	II	No	Strips/90	Discontinuous Sandwich CFRP Plates	#3 @ 12" (ρ_v = 0.0031)	ρ_f = 0.0014	12	2.9
Type 3	5	T3-12-Control	III	No	None	None	#3 @ 12" (ρ_v = 0.0031)	ρ_f = 0	12	3.4
		T3-12-S90-NA	III	No	Strips/90	None	#3 @ 12" (ρ_v = 0.0031)	ρ_f = 0.0014	12	3.4
	6	T3-12-S90-NA-PC	III	Yes	Strips/90	None	#3 @ 12" (ρ_v = 0.0031)	ρ_f = 0.0014	12	3.4
		T3-12-S90-DMA	III	No	Strips/90	Discontinuous CFRP Plates	#3 @ 12" (ρ_v = 0.0031)	ρ_f = 0.0014	12	3.4
	7	T3-18-Control	IV	No	None	None	#3 @ 18" (ρ_v = 0.0020)	ρ_f = 0	12	3.4
		T3-18-S90-NA	IV	No	Strips/90	None	#3 @ 18" (ρ_v = 0.0020)	ρ_f = 0.0014	12	3.4
	8	T3-18-S90-HS	IV	No	Strips/90	Horizontal FRP Strips	#3 @ 18" (ρ_v = 0.0020)	ρ_f = 0.0014	12	3.4
		T3-18-S90-SDMA	IV	No	Strips/90	Discontinuous Sandwich CFRP Plates	#3 @ 18" (ρ_v = 0.0020)	ρ_f = 0.0014	12	3.4

A5.3.3 Girder Details

All PC girders were designed with considerations for both the AASHTO LRFD (AASHTO, 2008) and ACI (ACI 318, 2008) design guidelines. Girder geometry and strand patterns were based on standard I-girders used by the Missouri Department of Transportation (MoDOT). All PC girders were designed with the intention of shear failure being the governing failure mode. A layer analysis (Collins and Mitchell, 1997) which incorporates both equilibrium and strain compatibility together with appropriate constitutive material laws was used for achieving the most accurate prediction of the girder's flexural capacity. Shear capacities were checked according to both ACI (ACI 318, 2008) and AASHTO LRFD (AASHTO, 2008) design specifications with FRP contributions predicted using ACI 440 design guidelines (ACI 440.2R-08). The design software RESPONSE 2000 (Collins and Mitchell, 1997) was also used as a design tool for evaluating the expected shear and flexural capacities. The constitutive material laws used included: Thorenfeldt's model (1987) for concrete in compression, the modified Ramberg-Osgood function (Mattock, 1979) for the stress-strain relationship of the prestressing strands, and an elastic-perfectly plastic stress-strain relationship for mild steel.

The final design of the first series of PC I-girders is presented in Figure A 5.92(a). The cross-sectional shape was a MoDOT Type 4 section and a total of four girders were constructed based on this design. Designs for both moderate and low level of shear reinforcement were developed to investigate the influence of the internal steel shear reinforcement on behavior. The low case is a stirrup spacing of 18 inches on center and represents a girder that is insufficiently reinforced for shear as governed by the ACI (ACI 318, 2008) and AASHTO LRFD (AASHTO, 2008) design guidelines for minimum shear reinforcement requirements. The moderate case is a stirrup spacing of 12 inches on center and represents a girder that meets the above mentioned shear reinforcement requirements. It should be noted that the area provided by the double-legged #3 stirrups is significantly greater than the minimum cross-sectional area requirements specified by the ACI (ACI 318, 2008) and AASHTO LRFD (AASHTO, 2008) design specifications. A deck slab was added (Figure A 5.92(b)) after initial testing resulted in undesirable failure modes as will be discussed in later sections. For ease of construction, the deck slab was designed to have the same width as the top flange of the beam as shown in Figure A 5.92(b). The depth of the deck slab was determined to be 12 inches based on a parametric study to ensure shear failure prior to flexural failure. To ensure composite action between the girder and deck slab, the horizontal shear transferring steel (shear studs) were designed according to AASHTO LRFD Bridge Design Specifications (AASHTO, 2008). The shear studs were added by drilling holes in the top of the girders and setting #5 reinforcing bars with a concrete epoxy. The end result was a 13 inch wide by 12 inch deep deck slab with #5 shear studs spaced at 12 inches on center as shown in Figure A 5.92(b).

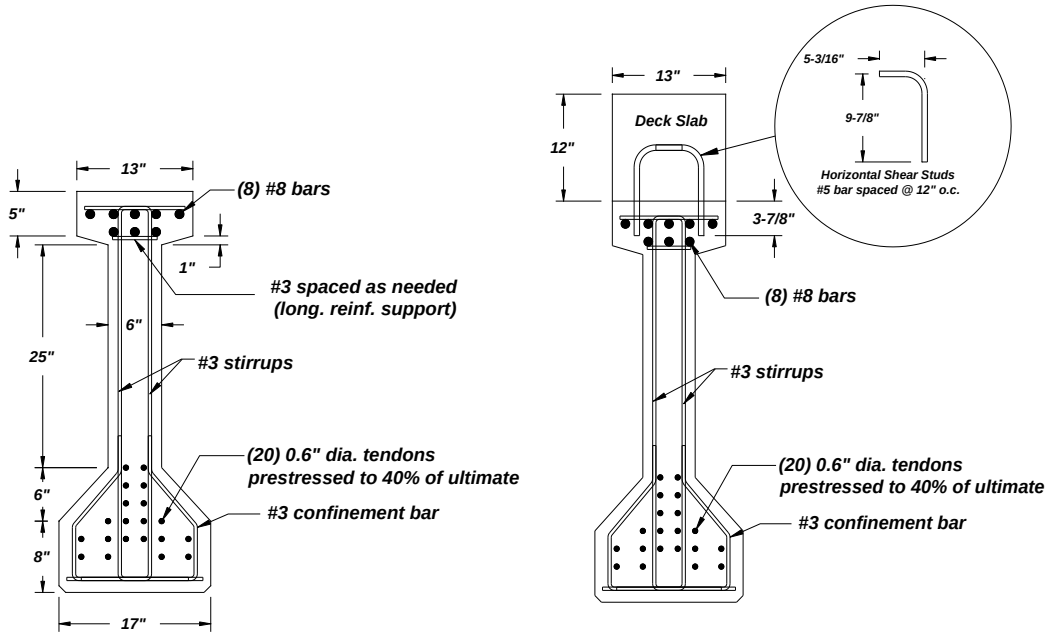

(a) Cross-Section Type I (MoDOT Type 4) (b) Cross-Section Type II (MoDOT Type 4)

Figure A 5.92 Cross-Section Details

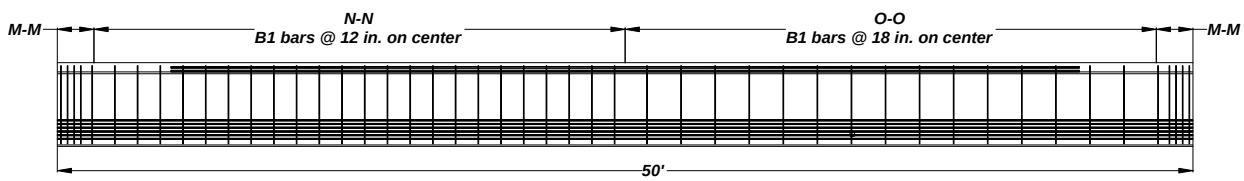

Figure A 5.93 Elevation Details

As a result of the premature failure issues encountered during testing of the MoDOT Type 4 girders, a new design was developed featuring a MoDOT Type 3 section geometry. Detailing of the new cross-section and reinforcement layout are depicted in Figure A 5.94. The new design was a partially prestressed section, meaning it would have both prestressing tendons and mild steel reinforcement in the tension flange. The use of partial prestressing ensures an adequate level of flexural reinforcement while also making sure that the initial prestressing load does not overstress the concrete resulting in cracking. Steel shear reinforcement design corresponds to the moderate case with stirrups at 12 inch spacing on centers.

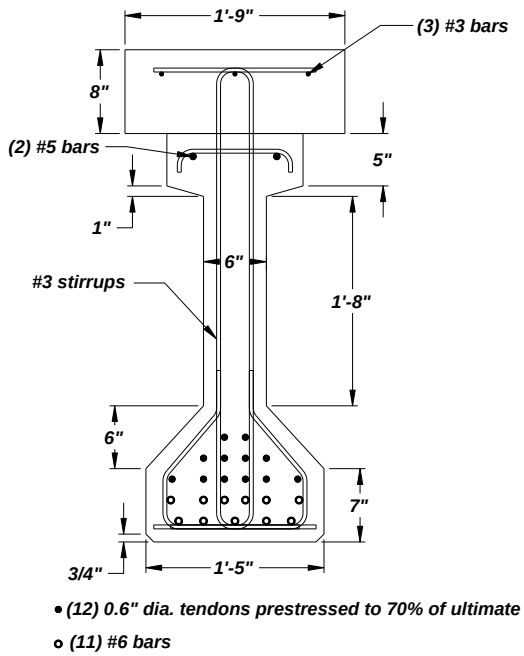

Figure A 5.94 Cross-Section Type III (MoDOT Type 3) Detail

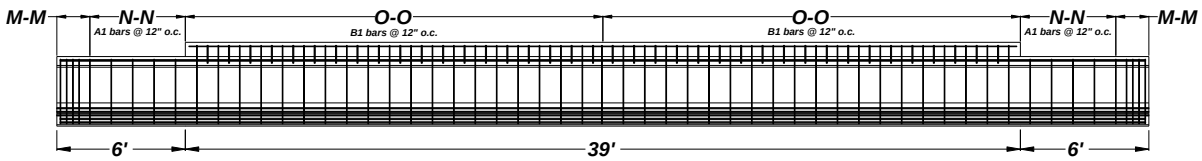

Figure A 5.95 Elevation Details

Testing of the newly designed MoDOT Type 3 girders resulted in additional undesirable failure modes and the need for a new girder design. The new design featured the same MoDOT Type 3 section, but a different reinforcement layout and deck slab width as shown in Figure A 5.96. Since the geometry of the cross-section is common among the state DOTs and has already been used in previous testing, it was not considered reasonable to change it for the new design. Unlike the previous MoDOT Type 3 girder design, the new design was fully prestressed on the tension face. However, in order to ensure the flexural capacity would be much greater than the ultimate shear capacity, the tendons had to be stressed to a level such that the extreme fiber stresses of the concrete in tension would exceed those recommended for serviceability requirements by the ACI (ACI 318, 2008) and AASHTO LRFD (AASHTO, 2008) design specifications. As a result, some cracking of concrete at transfer of the prestressing force would be imminent. Additional bonded reinforcement was provided in the top flange of the girder to help resist the tensile stresses resulting from the prestressing force. This approach to meeting the serviceability requirements is more desirable as it allows for a fully prestressed section for monitoring the behavior of PC girders strengthened with FRP for shear, which is the focus of our study. This allowed us to use a tendon arrangement and initial stressing force adequate for providing a level of flexural strength that would ensure shear failure even with FRP shear strengthening and mechanical anchorage. In the new girder design, additional steel reinforcement was also added to the deck slab to provide

confinement. This modification provides increased flexural capacity and helps to prevent the undesirable flange failure experienced in previous tests. The stirrup spacing was also increased from 12 inches to 18 inches, corresponding to the low shear reinforcement case.

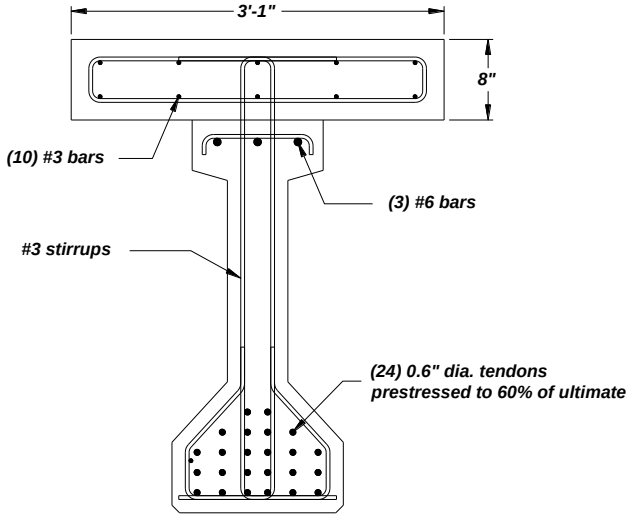

Figure A 5.96 Cross-Section Type IV (MoDOT Type 3) Detail

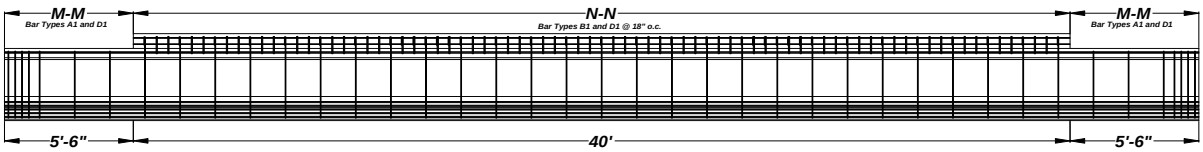

Figure A 5.97 Elevation Details

A5.3.4 Materials Used

The mechanical properties of various materials used in the PC girder testing, such as concrete, steel, and FRP composite materials, are summarized in this section.

A5.3.4.1 Concrete

The concrete mix design chosen for the PC girders is shown in Table A 5.14. This mix design was developed by the local precast plant (Egyptian Concrete Company) and has been used by the company for many years to produce similar girders for MoDOT. The compressive strength of the concrete used in construction of the girders was periodically evaluated in accordance with ASTM C 39 (2005), and the results are summarized in Table A 5.15. As shown in Table A 5.15, the 28-day strength ranged between 8890 and 10660 psi even though MoDOT only specifies 7 ksi as a 28-day target strength. These strength values correspond to high strength concrete while concrete with strength of 7 ksi is usually regarded as regular strength concrete. Thus, the behavior of prestressed concrete girders made from these two different strength concretes will vary. However, it was considered more reasonable to use a concrete mix design typically used in practice (i.e., the high strength mix provided by Egyptian Concrete) in order to more accurately reflect existing bridge conditions.

Table A 5.14 Concrete Mix Design

Cement (Type I)	27 lb/ft^3
Sand (Mississippi River Sand)	112 lb/ft^3
Fine Aggregate (Derby Doe Run Dolomite)	43 lb/ft^3
Coarse Aggregate (Derby Doe Run Dolomite)	67 lb/ft^3
Water Cement Ratio	0.31
Percent Air (%)	6.0

Table A 5.15 Compressive Strength of Concrete

MoDOT Standard	Girder I.D.	Test I.D.	Compressive Strength of Girder at Time of Testing (psi)	Age of Girder at Time of Testing (days)	Compressive Strength of Deck Slab at Time of Testing (psi)
Type 4	1	T4-18-Control	9930	124	N/A
		T4-12-Control	9970	143	N/A
	2	T4-18-S90-NA	10020	172	N/A
		T4-18-S90-CMA	10120	227	5240
	3	T4-18-S90-DMA	10160	257	7370
		T4-18-S45-DMA	10190	276	7840
	4	T4-12-Control-Deck	10660	571	10730
		T4-12-S90-SDMA	10330	585	10810
Type 3	5	T3-12-Control	8890	12	8520
		T3-12-S90-NA	8910	18	8760
	6	T3-12-S90-NA-PC	9470	30	8670
		T3-12-S90-DMA	10380	39	9700
	7	T3-18-Control	9590	33	9820
		T3-18-S90-NA	10120	41	10030
	8	T3-18-S90-HS	10190	100	10900
		T3-18-S90-SDMA	10430	107	11280

A5.3.4.2 Steel

Steel reinforcements were tested as per ASTM A370 (2008) in order to determine their mechanical properties. Mechanical properties for the tendons and all mild steel reinforcements are provided in Table A 5.16.

Table A 5.16 Mechanical Properties of Steel Reinforcement

Reinforcement Type	Grade	Yield Strength (ksi)	Ultimate Strength (ksi)	Modulus of Elasticity (ksi)
# 3 (Stirrups)	60	65	99	26,000
#5 (Flexural compression steel)	60			
# 6 (Flexural compression steel)	60	78	98	25,800
# 6 (Flexural tension steel)	60	78	98	25,800
# 8 (Flexural compression steel)	60	66	103	29,700
0.6 in. seven-wire strand	270		291	29,100

A5.3.4.3 FRP Composite Material

Refer to Section A5.2.4.3.

A5.3.4.4 Epoxy Resins

Refer to Section A5.2.4.3.

A5.3.4.5 CFRP Plates for Mechanical Anchorage

Refer to Section A5.2.4.3.

A5.3.4.6 Concrete Wedge Anchor for Mechanical Anchorage

The fastening system chosen for the CFRP plates used a mechanical anchorage for the FRP strips consisting of commercially available steel wedge anchors. The anchors for Girder T4-18-S90-CMA were provided by Thunderstud®. Technical data provided by the manufacturers are shown in Table A 5.8.

A5.3.5 Girder Fabrication

A5.3.5.1 Construction of Girders

All prestressed concrete girders were constructed at a local precast plant (Egyptian Concrete Company). Construction of the PC I-girders began with instrumentation of the steel reinforcement with strain gages. Stirrup and confinement reinforcement were bent into the desired shape according to the design drawings. A portion of the stirrup and confinement bars were delivered to the Missouri S&T High-bay Structures Laboratory for strain gage installation. These instrumented stirrup and confinement bars were positioned within the predetermined test regions of the girder during fabrication of the steel cage. Strain gages were also installed at several locations along the longitudinal reinforcement with the intent of measuring prestress losses and curvature strains at the point of loading (maximum moment). Strain gage locations vary between the different girder designs. A sacrificial #3 reinforcement bar was positioned within the bottom flange of all fully prestressed girders for the placement of strain gages. This dummy reinforcement bar was positioned at the centroid of the tensile reinforcement. All strain

gages were connected to lead wires which were routed to the ends of the girder. Once the steel cage was assembled and the prestressing tendons were tensioned to the design forces, the prefabricated steel forms were put into position. The concrete was produced on site at the precast plant and placed using specialized equipment. Concrete cylinders were made for material testing. The concrete was vibrated using both stick and external form vibrators. After completely filling the forms with concrete, the top surface was finished smooth and covered with a tarp. The girders were then allowed to set for two days under steam curing. After two days of curing, the forms were removed and concrete cylinders were tested to determine the concrete strength. If sufficient concrete strength was reached, the tendons were cut at the ends of the girders to transfer the prestressing force to the concrete. The construction procedures are presented in Figure A 5.98.

(a) Steel Cage Assembly

(b) Prestress Tendon Layout

(c) Adding Forms to Steel Assembly

(d) Concrete Pouring

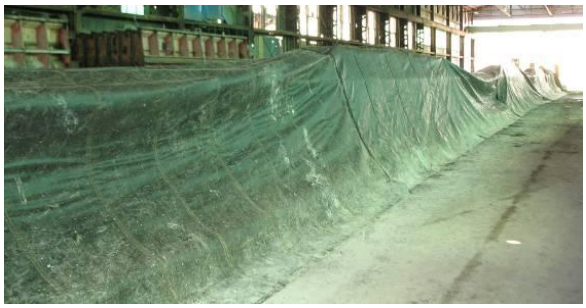

(e) Steam Curing

(f) Tendon Cutting

Figure A 5.98 Construction Procedure of Prestressed Concrete Girders

A5.3.5.2 FRP Application

Before application of the FRP sheets, the concrete surface was sandblasted in accordance with ICRI 03732 (1997) as shown in Figure A 5.99 and the sharp corners were smoothed to a radius of 1 inch with a power grinder.

Figure A 5.99 Sandblasting of Test Girders

Then, FRP sheets were applied using a wet-layup technique as shown in Figure A 5.100. First, a coat of primer is applied to ensure a good bond between the sheets and concrete surface. Putty was applied to fill any holes, providing an even surface for FRP application. Then, saturant was used to saturate the fibers and apply them to the concrete surface. The FRP sheets were applied in a U-wrap configuration oriented at either 90° or 45° relative to the longitudinal axis of the girder depending on the strengthening scheme to be investigated.

One piece of FRP was also applied in a small area outside of the test region, so called a bond test sampling area, (Figure A 5.101) using the same materials and methods used for the application of FRP in the test region. Direct pull-off bond strength tests were conducted on three spots within this sampling area in order to obtain the FRP-concrete interface bond strength in accordance with ASTM D4541-03 (2003).

(a) Applying Primer

(b) Applying Putty

(c) Applying First Coat of Saturant

(d) Applying FRP Sheets

(e) Applying Second Coat of Saturant

Figure A 5.100 FRP Application Procedures

Figure A 5.101 Sampling Area for Pull-Off Tests

A5.3.5.3 Anchorage Systems

In this project, four different anchorage systems were investigated: (1) additional horizontal FRP strips, (2) continuous pre-cured CFRP plates anchored in place with concrete wedge anchors, (3) discontinuous pre-cured CFRP plates anchored in place with bolts running through the web, and

(4) discontinuous pre-cured CFRP plates with sandwich wrapped ends and anchored in place with bolts running through the web.

Horizontal FRP Strip

This anchorage system is composed of extra FRP composite strips parallel to the longitudinal axis of the beam and covering all the edges of the vertical FRP strips as well as along the interface of the web and bottom flange (locations where debonding is known to initiate). This anchorage system was installed immediately after the application of the vertical FRP sheets for shear strengthening to obtain a better bond between the vertical and horizontal FRP sheets.

Continuous Mechanical Anachorage

This mechanical anchorage configuration consisted of a single continuous CFRP plate (150 inches long) bonded to the FRP strips with resin and anchored firmly in place with concrete wedge anchors. Thunderstud® concrete wedge anchors (0.5 inches in diameter with a two inch embedment length) were used for this specimen. Anchor spacing was as shown in Figure A 5.102(b).

Discontinuous Mechanical Anchorage

Several configurations were used for this anchorage system. Anchor spacing, anchor diameter, embedment length of anchors, length of plates, and epoxy curing times were varied from specimen to specimen. In general, for the PC girders, two CFRP plates were bonded to the strips with FRP resin and anchored firmly in place with steel bolts passing through the web, as shown in Figure A 5.102(c).

Sandwich Panel Discontinuous Mechanical Anchorage

This system is similar to the previous discontinuous mechanical anchorage; the only difference being that better anchorage of the FRP strips is obtained by wrapping the FRP composite around the first plate and overlapping it with the second plate to form a three-layer connection as shown in Figure A 5.102(d).

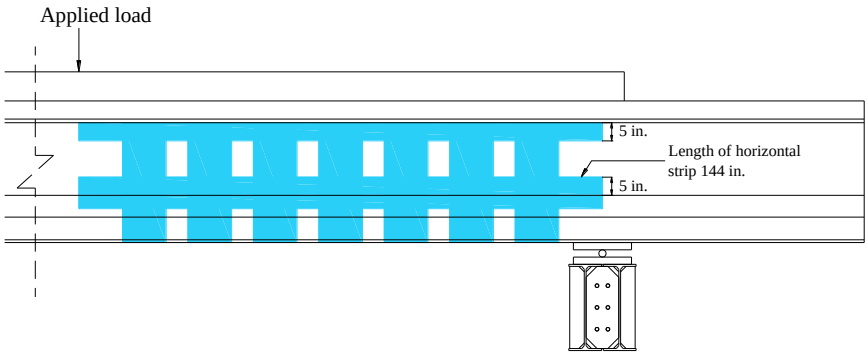

(a) Horizontal FRP Strips

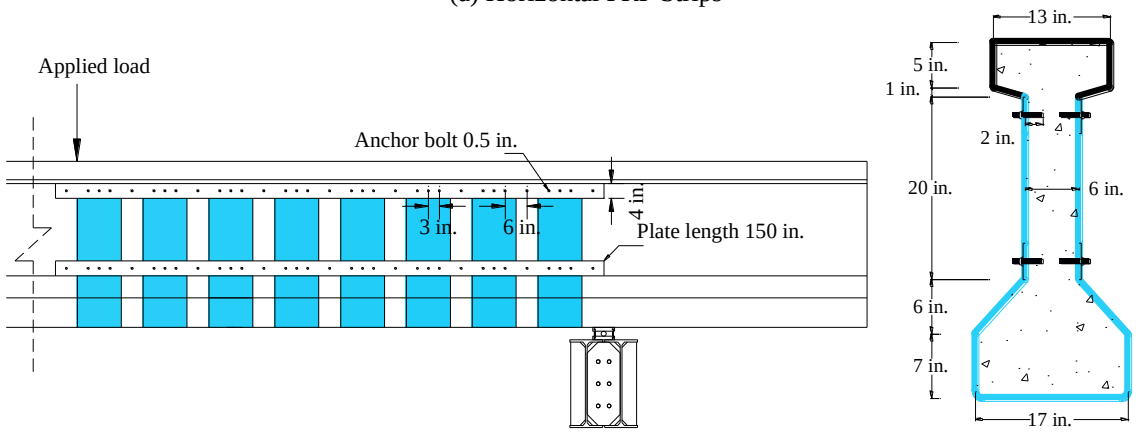

(b) Continuous Mechanical Anchorage

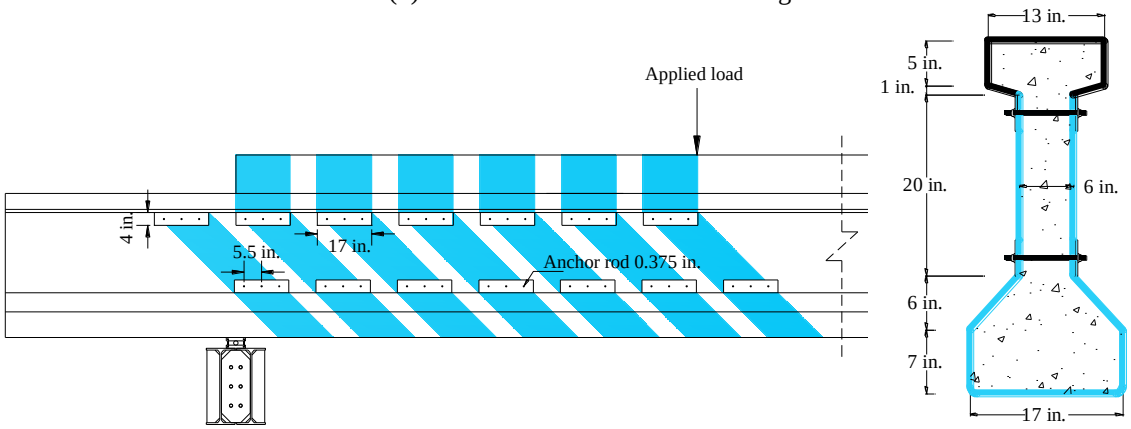

(c) Discontinuous Mechanical Anchorage

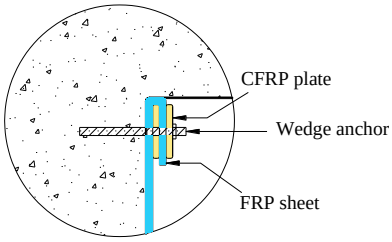

(d) Discontinuous Mechanical Anchorage (Sandwich Panel)

Figure A 5.102 Mechanical Anchorage Systems

A5.3.6 Test Set-up

The test setup for the PC girders was a three point static loading configuration with each girder being designed to have two test regions, one on each end of the girder. The second test region is tested by relocating the supports and loading frame accordingly.

A pair of hydraulic actuators working in parallel, each with 110 kips of force capacity, were necessary to produce the required shear forces. The hydraulic actuators to be used for testing were incapable of applying enough force to fail the girders by applying load at the midspan loading point (point B as shown in Figure A 5.103(a)). Instead, the actuators were used to apply an upward force at the far end reaction (point C as shown in Figure A 5.103(b)). A reaction frame located at point B is used to resist the upward force supplied by the actuators and thus induces the shear force required to fail the test girders.

Applying load in this manner significantly reduces the demand on the hydraulic actuators making testing of the large-scale girders possible. The loading and reaction frame assemblies were designed to withstand forces at least three times those anticipated to occur during testing. Additional external shear reinforcement, consisting of Dywidag bars and hollow steel tube sections, was designed to prevent failure from occurring outside the designated test region and to help preserve the second test region for later testing.

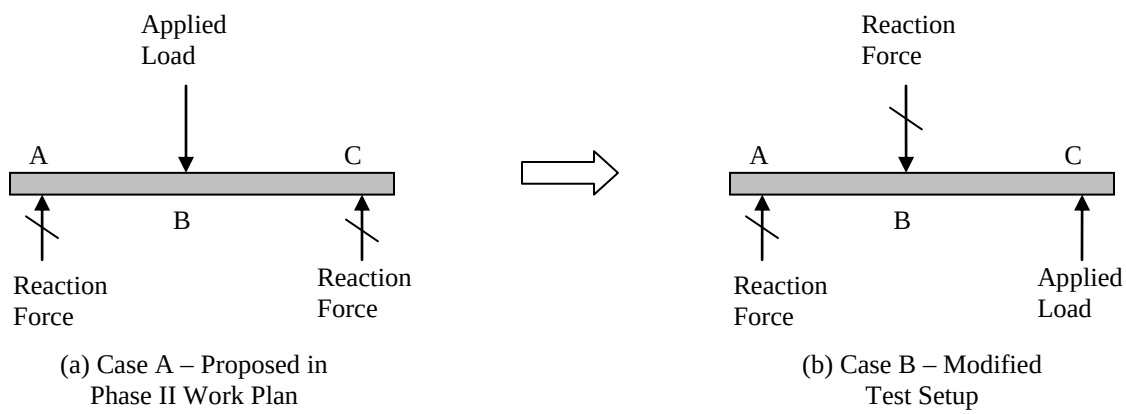

(a) Case A – Proposed in Phase II Work Plan

(b) Case B – Modified Test Setup

Figure A 5.103 Schematic Comparison between Test Setup of Phase II Work Plan and Modified One

The performance and safety of the test setup used for full-scale prestressed concrete girder testing was verified through preliminary testing. Deformations and stability/stiffness of each part of the test setup assembly were closely monitored while a prestressed concrete girder was subjected to 70% of the anticipated shear cracking load. Bearing plates in the reaction frame and the roller at one of the supports were discovered to have inadequate stiffness and were correctly modified prior to full-scale testing.

Slight modifications were made to the test setup throughout the course of the experimental program as different issues, which will be discussed later, were encountered. In some cases, the loading frame had to be moved to increase the lever arm of the actuators in order to avoid exceeding the maximum force capacity of the actuators. Other modifications include: (1) increasing the shear span of the test region, (2) additions and modifications to the external shear

strengthening system, and in some cases (3) use of a hand pump in parallel with the actuators was necessary. Details of the test setup for each experimental test are depicted in Figure A 5.104.

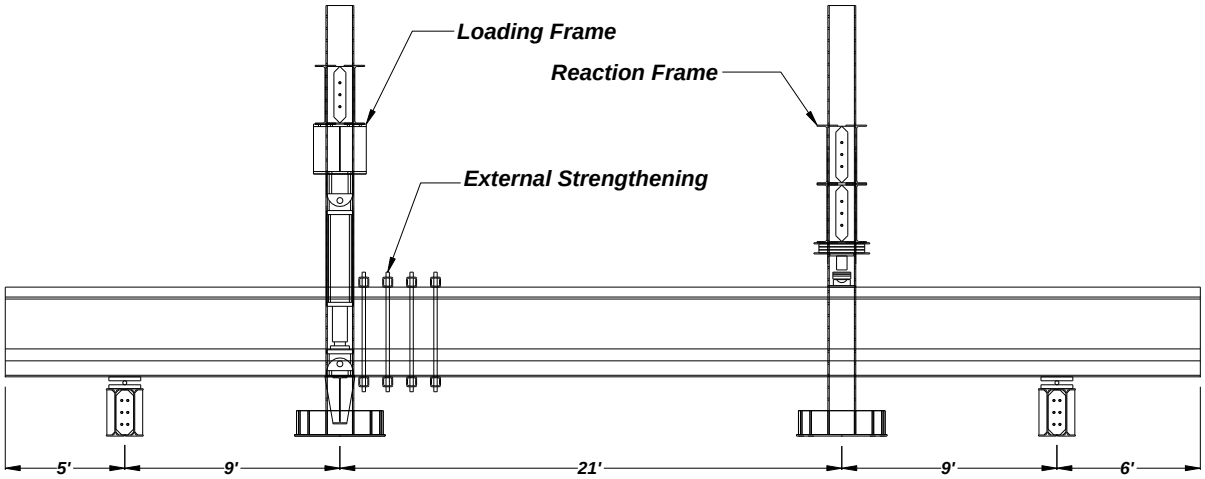

(a) Test Setup Type I (T4-12-Control, T4-18-Control, T4-18-S90-NA)

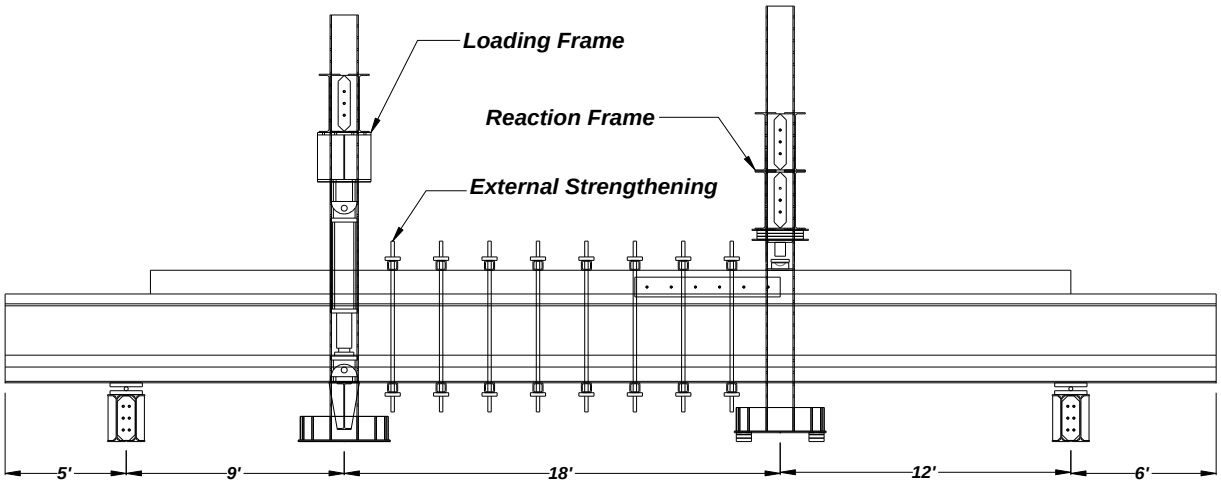

(b) Test Setup Type II (T4-18-S90-CMA, T4-18-S90-DMA, T4-18-S45-DMA)

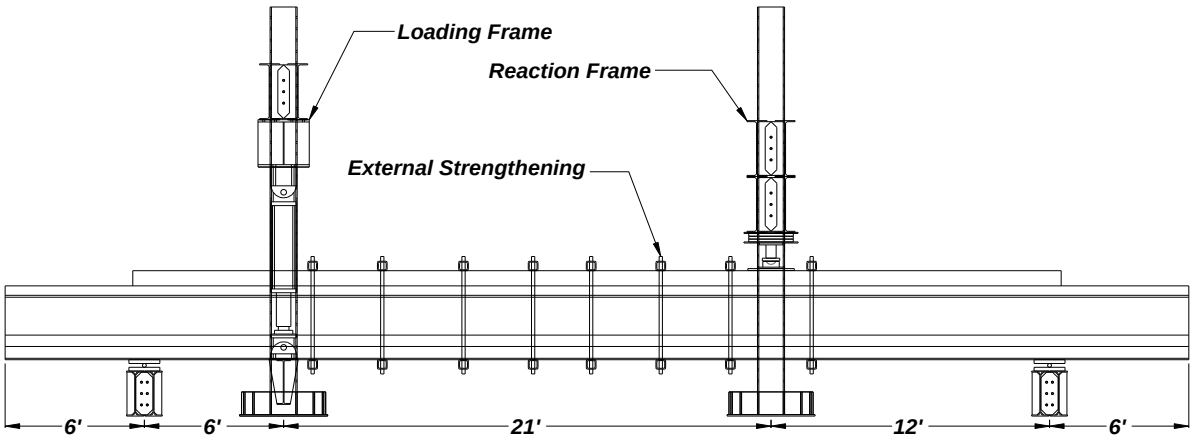

(c) Test Setup Type III (T3-12-S90-NA, T3-12-S90-NA-PC, T3-12-S90-DMA, T3-18-S90-NA, T3-18-S90-HS, T3-18-S90-SDMA)

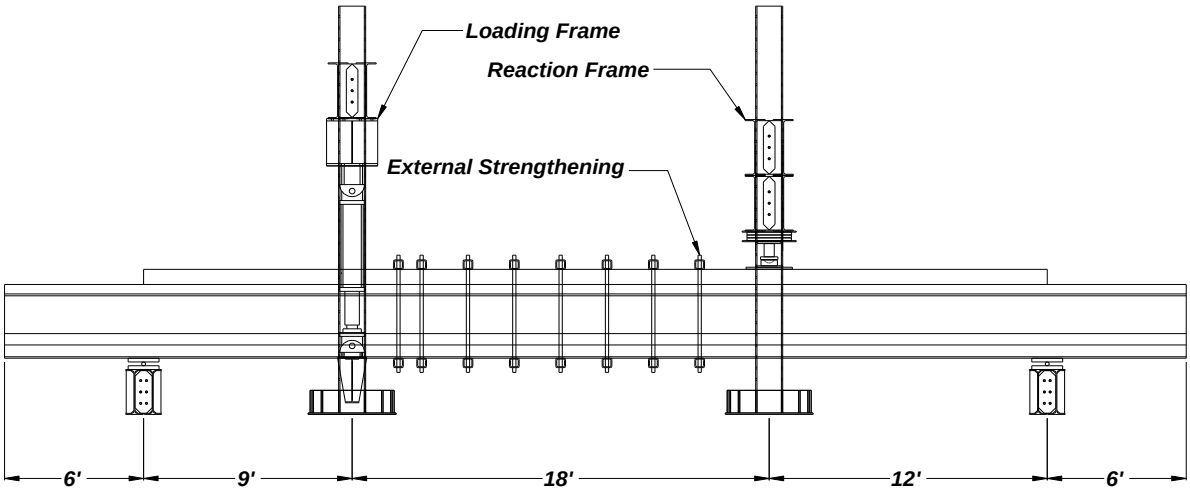

(d) Test Setup Type IV (T3-12-Control)

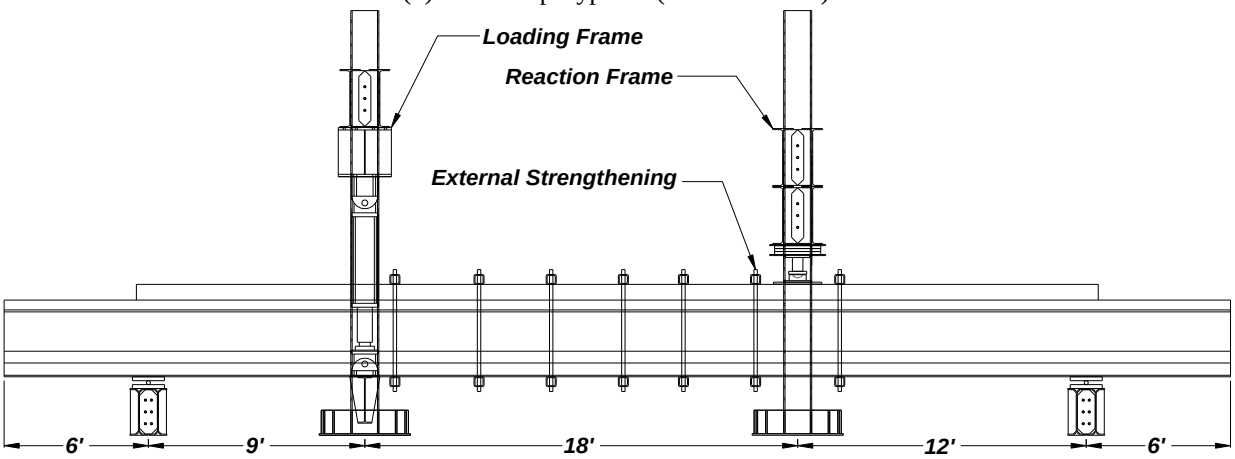

(e) Test Setup Type V (T3-18-Control)

Figure A 5.104 Test Setup Configurations

A5.3.7 Instrumentation

Global and localized deformations were measured using a combination of strain gages, linear variable displacement transducers (LVDT), string transducers, Demec mechanical strain gages, and inclinometer. Load was measured by a load cell at both the reaction frame (point B in Figure A 5.103(b)) and by the actuators at the loading frame (point C in Figure A 5.103(b)).

A5.3.7.1 Local Deformations and Strains

Electric resistance strain gages were installed on the stirrups, confinement bars, and longitudinal reinforcement to monitor local strains within the test regions. Strain gages on the longitudinal reinforcement are also used to measure prestress losses and to monitor flexural behavior (yielding or concrete crushing) at the maximum moment region. In addition, Demec gage points were glued on the surface of the girders along the center of gravity of the prestressing strands as a secondary measure of prestress losses. Strain gages were also installed on the mechanical anchorage systems and at various locations along the FRP strips to monitor strain variation along the width and height of the FRP strips. These gages were also used to monitor the progression of delamination/debonding of the FRP. Figure A 5.105 shows the generalized location of strain measurements on the internal steel reinforcement. Greater detail is provided in Additional Material D to Appendix.

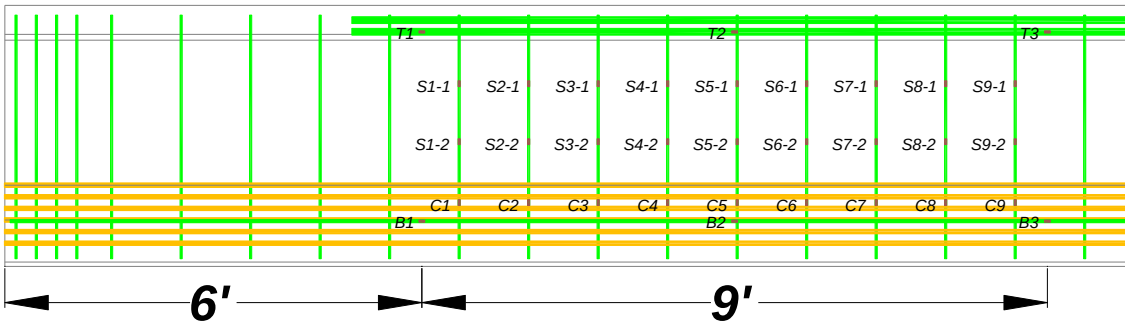

(a) Strain Gages on Steel Reinforcement for Type 4 Girders with Moderate Shear Reinforcement
(T4-12-Control, T4-12-Control-Deck, T4-12-S90-SDMA)

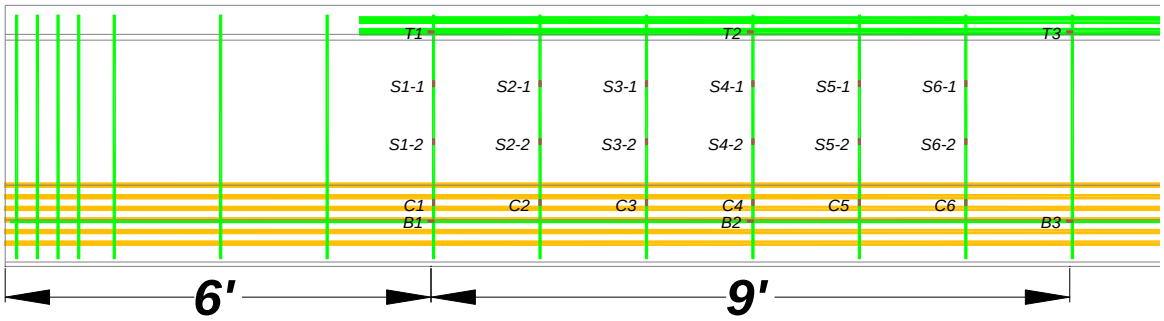

(b) Strain Gages on Steel Reinforcement for Type 4 Girders with Low Shear Reinforcement
(T4-18-Control, T4-18-S90-NA, T4-18-S90-CMA, T4-18-S90-DMA, T4-18-S45-DMA)

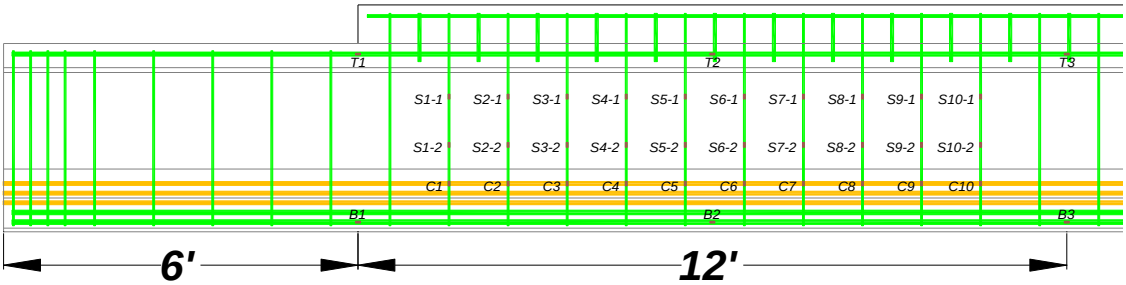

(c) Strain Gages on Steel Reinforcement for Type 3 Girders with Moderate Shear Reinforcement
(T3-12-Control, T3-12-S90-NA, T3-12-S90-NA-PC, T3-12-S90-DMA)

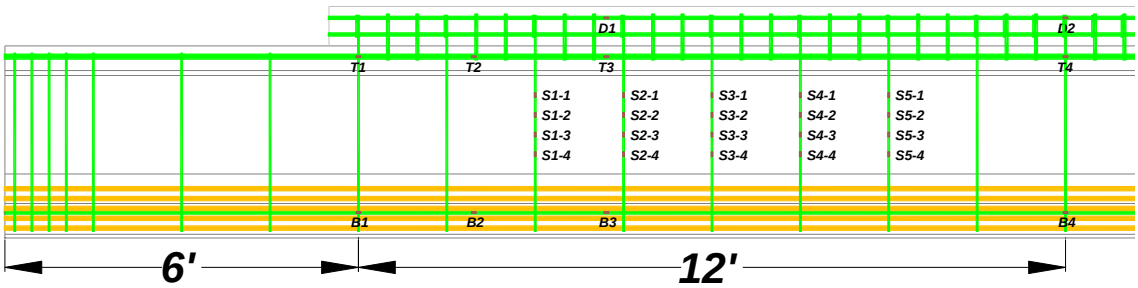

(d) Strain Gages on Steel Reinforcement for Type 3 Girders with Low Shear Reinforcement
(T3-18-Control, T3-18-S90-NA, T3-18-S90-HS, T3-18-S90-SDMA)

Figure A 5.105 Strain Gage Patterns for Internal Steel Reinforcement

Strain gages placed on the FRP strengthening and mechanical anchorage systems vary among the test specimens and thus cannot be concisely shown here. Instead, their location and orientation are detailed in Additional Material D to Appendix.

A5.3.7.2 Global Deformations

A strain rosette consisting of 21 linear variable displacement transducers (LVDTs) was anchored to the web of each test girder to measure shear strains within the test region for the purpose of determining the principal strains and their orientation. A similar system consisting of Demec gages glued to the opposite side of the web were used as a secondary measure for evaluating the principal strains and their orientations. Additional string transducers and LVDTs were also used to monitor deformations at critical points along the test girders. Figure A 5.106 shows the location and nomenclature of the LVDT rosettes and deflection measurements recorded during each test. Figure A 5.107 shows the arrangement of the Demec strain rosettes for each test specimen.

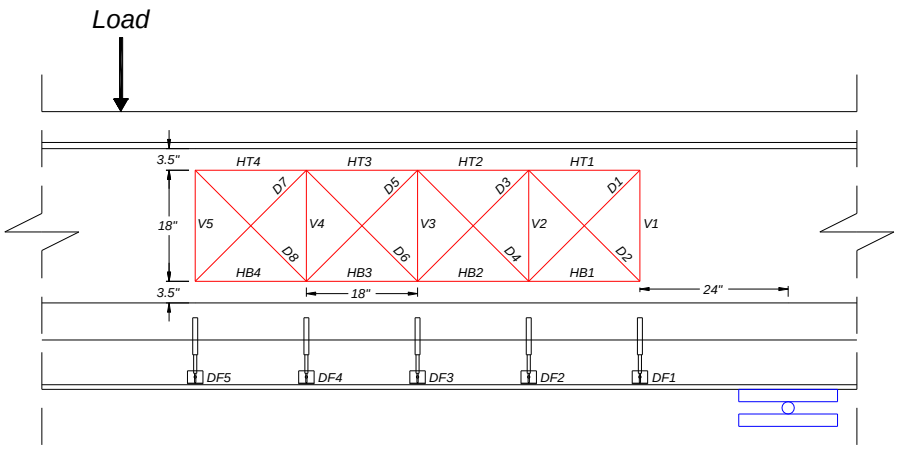

(a) T4-12-Control, T4-18-Control, T4-18-S90-NA

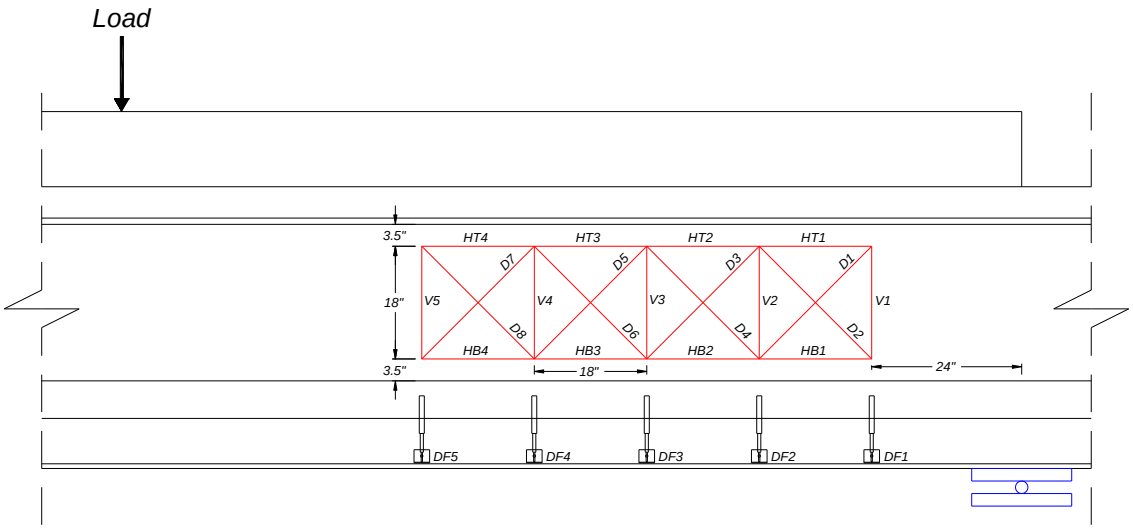

(b) T4-18-S90-CMA, T4-18-S90-DMA, T4-18-S45-DMA, T4-12-Control-Deck, T4-12-S90-SDMA

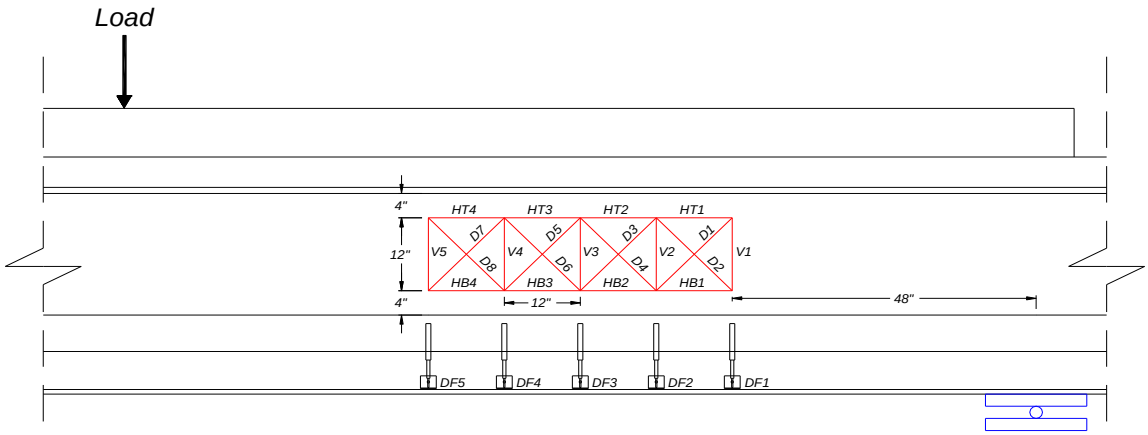

(c) T3-18-Control, T3-18-S90-NA, T3-18-S90-HS, T3-18-S90-SDMA

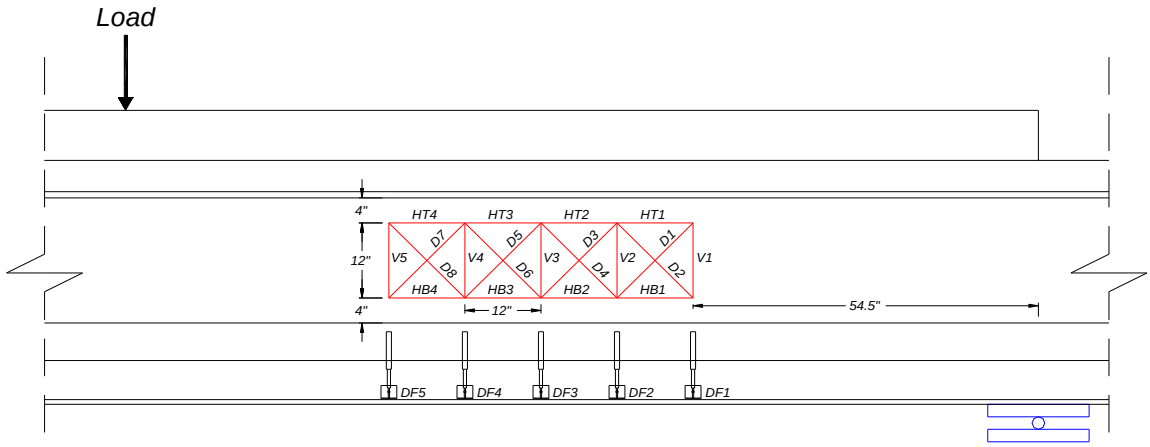

(d) T3-12-Control, T3-12-S90-NA, T3-12-S90-NA-PC, T3-12-S90-DMA

Figure A 5.106 LVDT Strain Rosettes and Deflection Measurements in Test Region

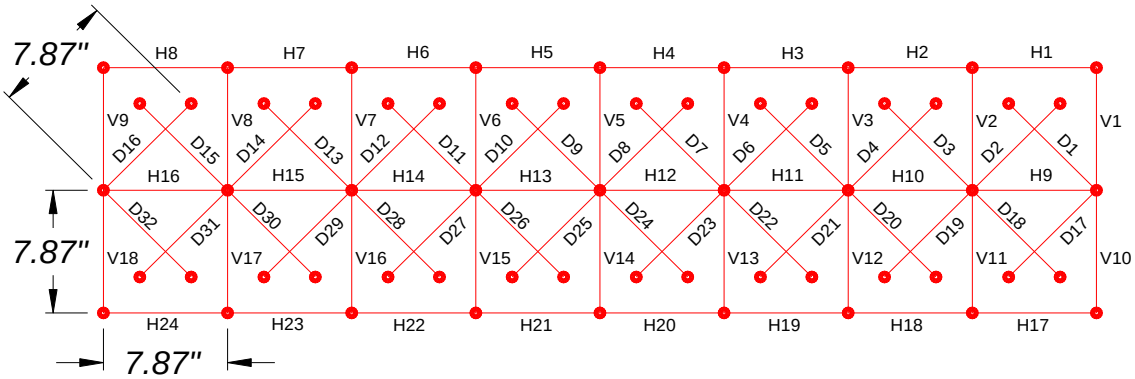

(a) Demec Point Pattern 1
(T4-18-Control, T4-12-Control, T4-18-S90-NA, T4-18-S90-CMA, T4-18-S90-DMA, T4-18-S45-DMA)

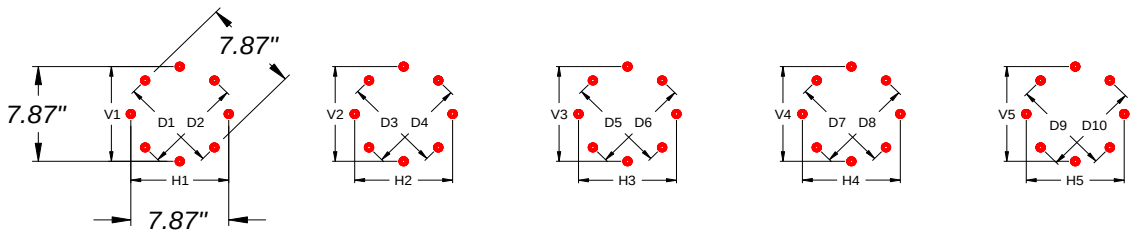

(b) Demec Point Pattern 2
(T4-12-Control-Deck, T4-12-S90-SDMA, T3-12-Control, T3-12-S90-NA, T3-12-S90-NA-PC, T3-12-S90-DMA, T3-18-Control, T3-18-S90-NA, T3-18-S90-HS, T3-18-S90-SDMA)

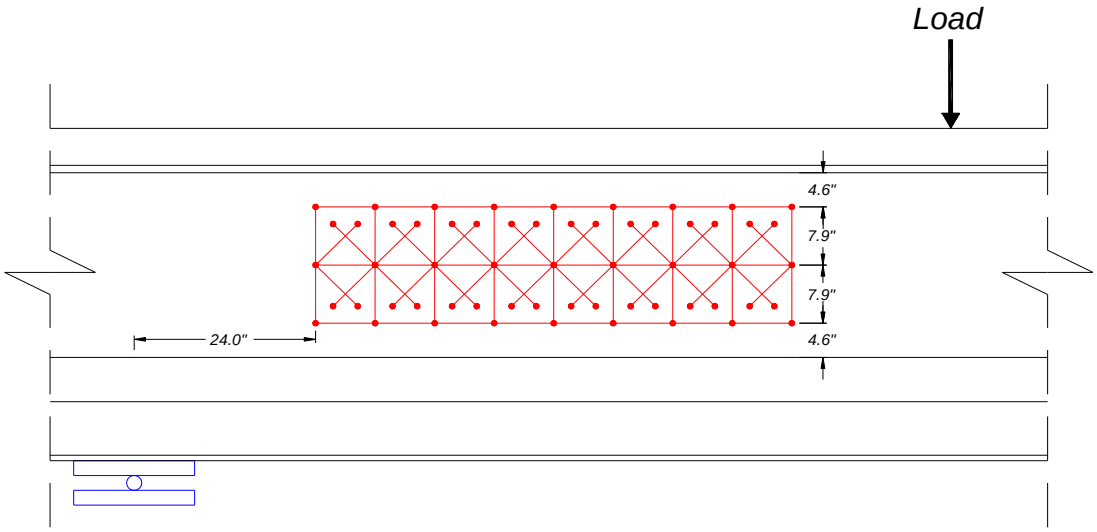

(c) Demec Point Arrangement
(T4-18-Control, T4-12-Control, T4-18-S90-NA, T4-18-S90-CMA, T4-18-S90-DMA, T4-18-S45-DMA)

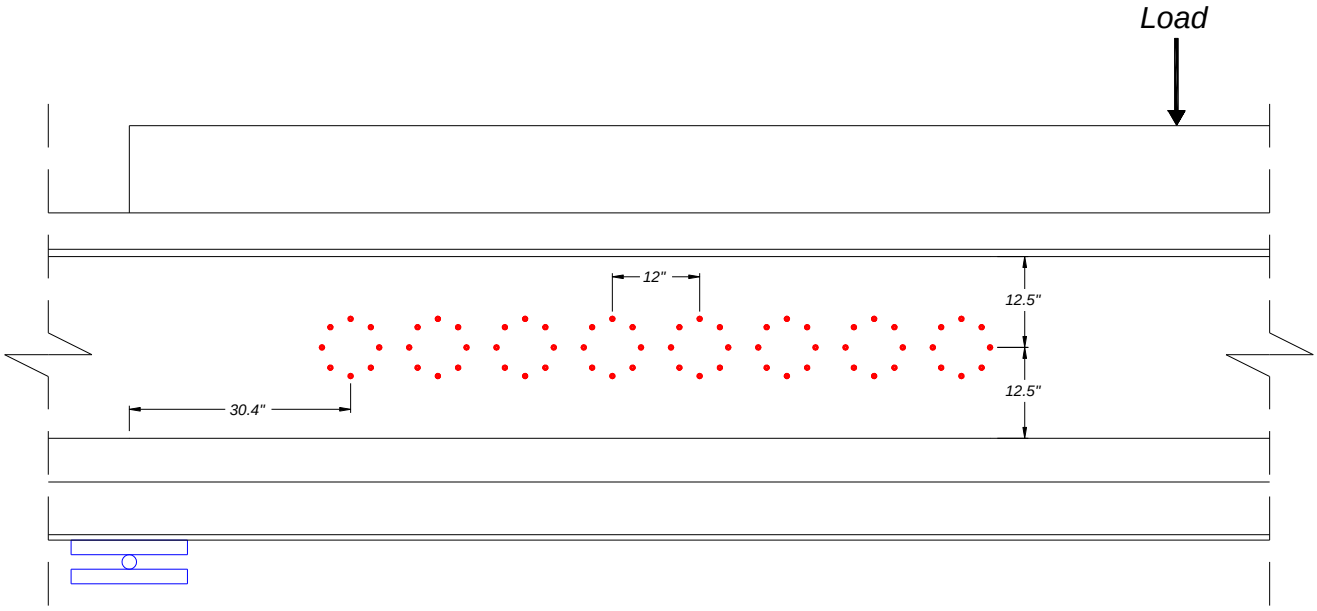

(d) Demec Point Arrangement
(T4-12-Control-Deck, T4-12-S90-SDMA)

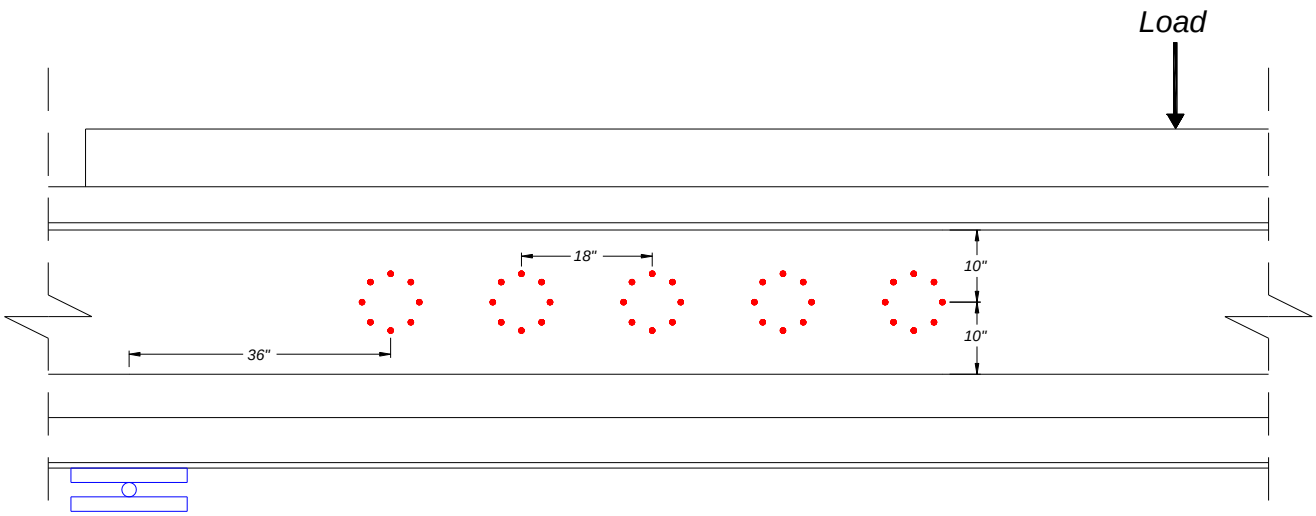

(e) Demec Point Arrangement
(T3-18-Control, T3-18-S90-NA, T3-18-S90-HS, T3-18-S90-SDMA)

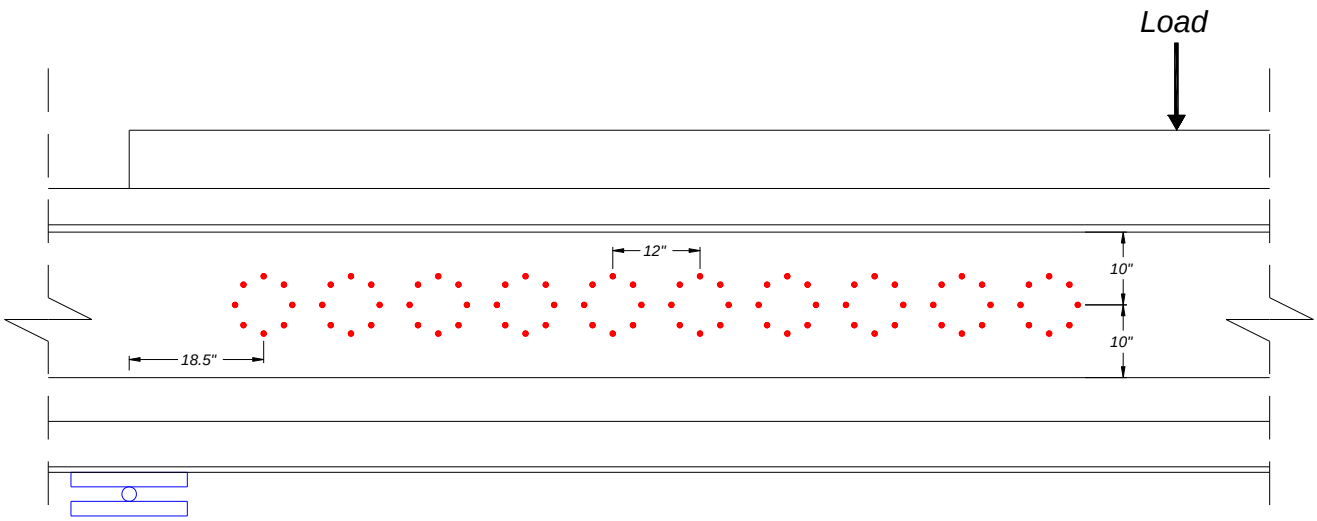

(f) Demec Point Arrangement
(T3-12-Control, T3-12-S90-NA, T3-12-S90-NA-PC, T3-12-S90-DMA)

Figure A 5.107 Demec Strain Rosettes

Two LVDTs (denominated as CVT and CVB) where anchored horizontally along the top and bottom flanges at the reaction corresponding to the point of maximum moment. These LVDTs were used to measure the curvature which could then be used to evaluate the flexural behavior in case flexure was the governing failure mode. Additional LVDTs were placed at the support and reaction frame (denominated as DFROL and DFR) to monitor the rigidity of the test setup during loading. Three string transducers (denominated as DF-L-W, DF-L-M, and DF-L-E) were used at the loading point to measure vertical displacement. The outside string transducers (denominated as DF-L-W and DF-L-E) were also used to monitor and correct for any rotation that might be induced by the use of two actuators for the loading procedure. Additional measurements from LVDTs, string transducers, and an inclonometer were taken throughout the girders outside of the immediate test region for redundancy. The arrangement and nomenclature of these measurements can be found in Additional Material D to Appendix.

A5.3.8 Results and Discussions

A5.3.8.1 Overall Behavior

Table A 5.17 presents concrete compressive strengths at the time of testing ($f_c^{'}$), shear forces measured at three critical stages (cracking, yielding, and ultimate), the failure modes observed, and the shear crack angles measured for each test specimen.

Table A 5.17 Summary of Experimental Results

MoDOT Standard	Test I.D.	Cross-Section Type	Girder Concrete Strength f_c' (psi)	Shear Force at Cracking (kips)	Shear Force at Yielding (kips)	Shear Force at Ultimate (kips)	Ultimate Failure Mode	Shear Crack Angle (deg.)
Type 4	T4-12-Control	I	9970	139	N/A	202	TF	32.0
	T4-18-Control	I	9930	140	185	206	TF	26.0
	T4-18-S90-NA	I	10020	149	193	193	D + TF	21.0
	T4-18-S90-CMA	II	10120	136	N/A	229	D + MA + TF	25.0
	T4-18-S90-DMA	II	10160	161	N/A	244	D + LR + TF	24.0
	T4-18-S45-DMA	II	10190	161	N/A	255	D + TF	32.0
	T4-12-Control-Deck	II	10660	141	228	245	TF	26.0
	T4-12-S90-SDMA	II	10330	108	206	258	TF	30.0
Type 3	T3-12-Control	III	8890	126	233	253	SC	23.0
	T3-12-S90-NA	III	8910	130	229	271	D + WC	22.0
	T3-12-S90-NA-PC	III	9470	N/A	236	239	D + WC	21.0
	T3-12-S90-DMA	III	10380	115	N/A	249	SC	25.0
	T3-18-Control	IV	9590	120	167	252	DT	21.0
	T3-18-S90-NA	IV	10120	153	164	216	D + DT	15.0
	T3-18-S90-HS	IV	10190	133	163	221	D + DT	26.0
	T3-18-S90-SDMA	IV	10430	141	235	235	D + DT	33.0

Note: TF = horizontal failure along the top flange, D = debonding of FRP, LR = localized rupture of FRP, DT = diagonal shear-tension failure, WC = web crushing failure, MA = mechanical anchorage failure, SC = stress concentration failure at reaction point

Shear forces at cracking correspond to the first observation of cracks in the web and also correlate with the point at which steel stirrups and FRP begin to take load. Shear forces at yielding correspond to the applied shear force at which all stirrups along the critical shear crack reached their yielding point. As seen in Table A 5.17, not all specimens experienced full yielding of all stirrups along the critical shear crack prior to failure. It should be noted however, that this yielding criteria is determined based on strain gage measurements on the transverse steel reinforcement. These measurements can be faulted based on proximity of the gage to the critical crack or damage sustained to the gage during construction of the girder. The ultimate shear force is the maximum shear reached during each test. Shear forces in the test region of the PC girders produced a region consisting of multiple shear cracks at various orientations. The shear crack angles presented in Table A 5.17 are the average orientation angles for the critical cracks along

which failure is believed to have occurred. These critical cracks also correspond to the failure plane along which a shear component analysis was conducted. It should also be noted that all the critical crack angles were found to be less than 45° as is often assumed by most analytical models and design specifications.

Since the shape of the girders were observed to have a significant effect on the mode of failure of the test girders, it is most useful to compare the overall behavior of members with the same cross-sectional shape. Among the girders in cross-section type I, it can be seen that the shear force at initiation of cracking is fairly consistent with an average value of 143 kips. The ultimate shear force among these three specimens is also fairly consistent, implying that an increase in transverse steel or addition of externally bonded FRP has no effect on increasing the performance of such girders. However, if one defines failure by yielding of the transverse steel, as is typically done for serviceability considerations, then an increase in shear capacity is realized. In this case, T4-18-Control (control specimen with stirrups at 18 inches) reached yielding of the stirrups at a shear force of 185 kips while T4-18-S90-NA reached a shear force of 193 kips at yielding of the stirrups. Thus an increase in shear capacity of 8 kips can be contributed to the FRP strengthening. Meanwhile, T4-12-Control (control specimen with stirrups at 12 inches) did not experience full yielding of all stirrups and thus failure is limited by the peak shear force of 202 kips. Some increase in stiffness was also achieved with the application of FRP as well as in the case of increase transverse steel reinforcement as shown in Figure A 5.108.

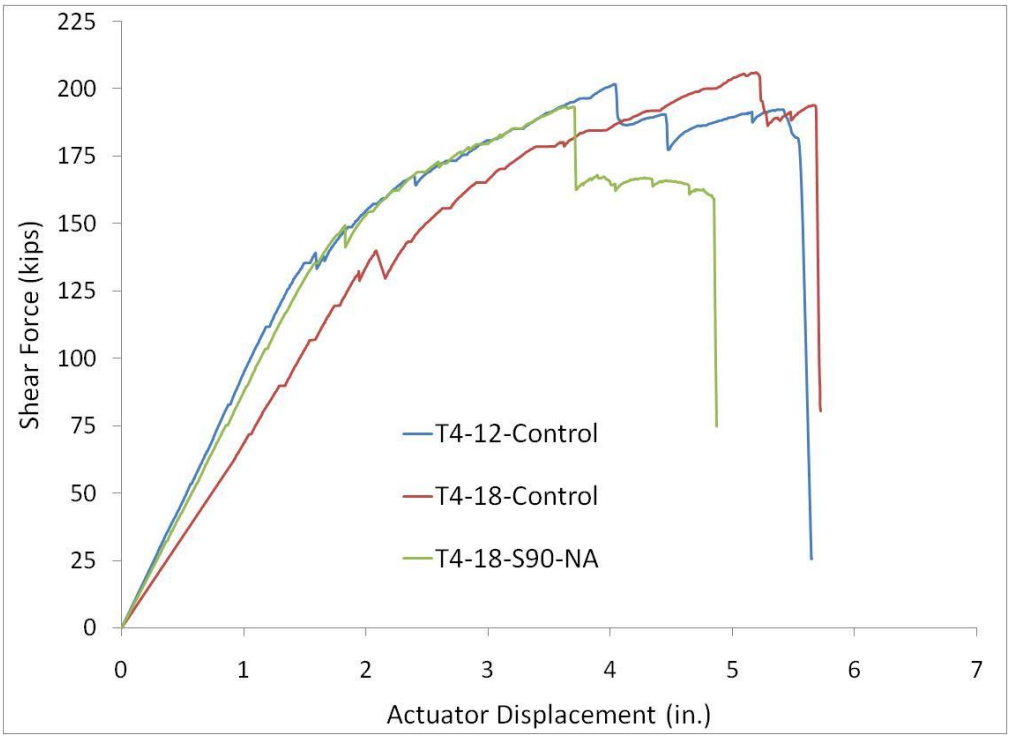

Figure A 5.108 Load-Displacement Response (Cross-section Type I)

Within cross-section type II, a testament to the effectiveness of the various mechanical anchorage schemes and fiber orientations is observed by comparison of the ultimate shear forces. Specimen T4-18-S90-CMA was limited to an ultimate shear force of 229 kips as a result of debonding and mechanical anchorage failure. Meanwhile, the mechanical anchorage system of

specimen T4-18-S90-DMA proved to limit debonding to a lesser degree, and in localized regions, FRP rupture was achieved. As such, a higher shear force of 244 kips was achieved resulting in a net increase of 15 kips. By orienting the FRP fibers at a 45° angle with the same mechanical anchorage system, an additional 11 kips was achieved for a total shear force of 255 kips by specimen T4-18-S45-DMA. Increasing the transverse steel reinforcement (T4-12-Control-Deck) without FRP strengthening resulted in an ultimate shear strength equivalent to that of a mechanically anchored FRP strengthened girder with low transverse steel reinforcement (T4-18-S90-DMA). Adding FRP and mechanical anchorage to a girder with moderate transverse steel reinforcement (T4-12-S90-SDMA), resulted in the highest ultimate shear capacity of 258 kips. Load-displacement responses for the specimens of cross-sectional type II are shown in Figure A 5.109.

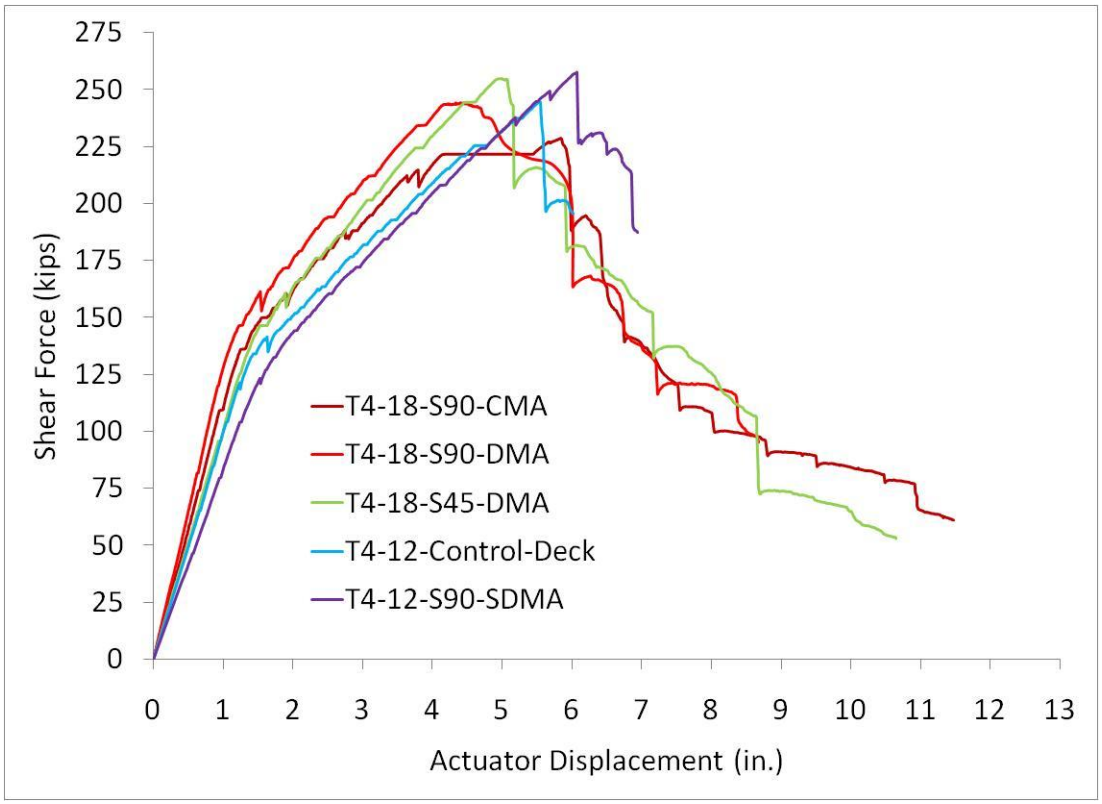

Figure A 5.109 Load-Displacement Response (Cross-section Type II)

Among the test results of girders with cross-section type III, no general trends can be observed due to the undesirable failure modes as explained in Section A 5.3.8.3. As can be seen from the test results, a great deal of scatter is introduced by failure modes related to high stress concentrations under contact loads and web crushing failure which are both unpredictable in nature. Load-displacement responses for the specimens of cross-sectional type III are shown in Figure A 5.110.

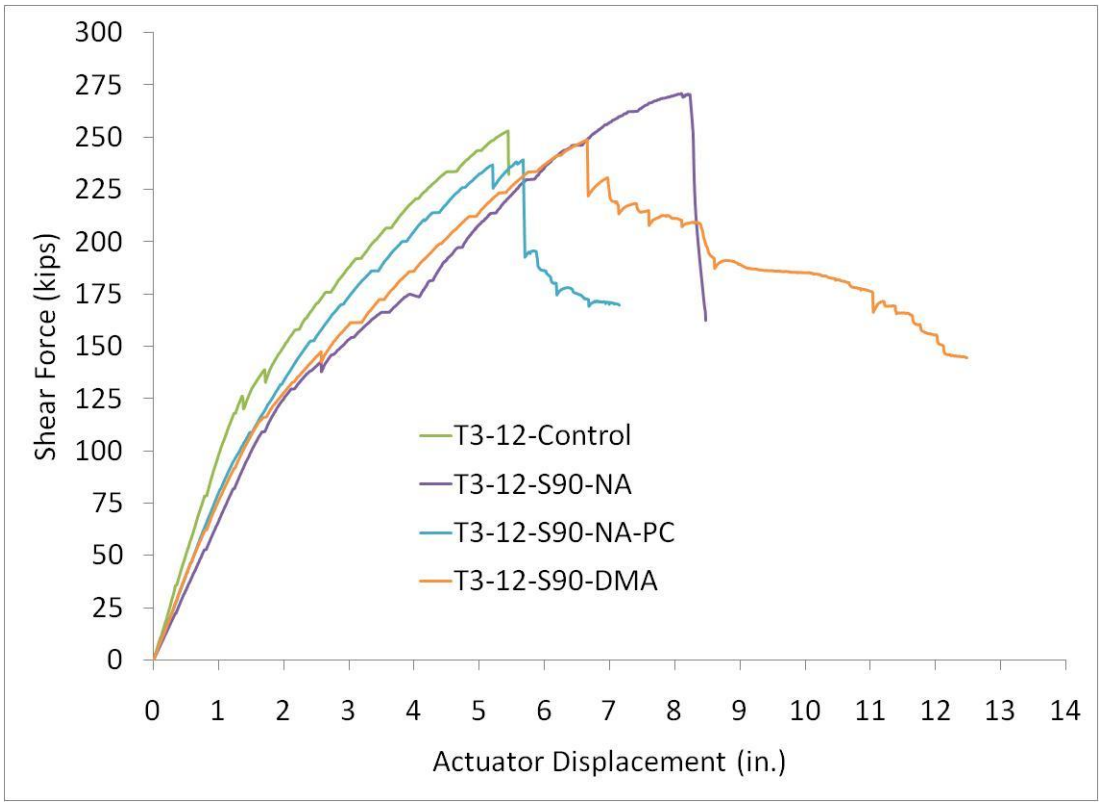

Figure A 5.110 Load-Displacement Response (Cross-section Type III)

Cross-sectional type IV specimens show an increasing trend in shear capacity with increasing anchorage performance provided by the different mechanical anchorage systems investigated. However, all FRP strengthened specimens failed at a lower ultimate shear force than the corresponding control specimen (T3-18-Control), which is a phenomenon that cannot be explained. Despite this anomaly, the test results show that the horizontal strips (T3-18-S90-HS) provided sufficient mechanical anchorage to increase the shear capacity by 5 kips over the non-mechanically anchored FRP strengthened specimen (T3-18-S90-NA). Likewise, the discontinuous sandwich plate mechanical anchorage system was able to provide an additional 14 kips of shear resistance as compared to the horizontal strip system. Load-displacement responses for the specimens of cross-sectional type IV are shown in Figure A 5.111.

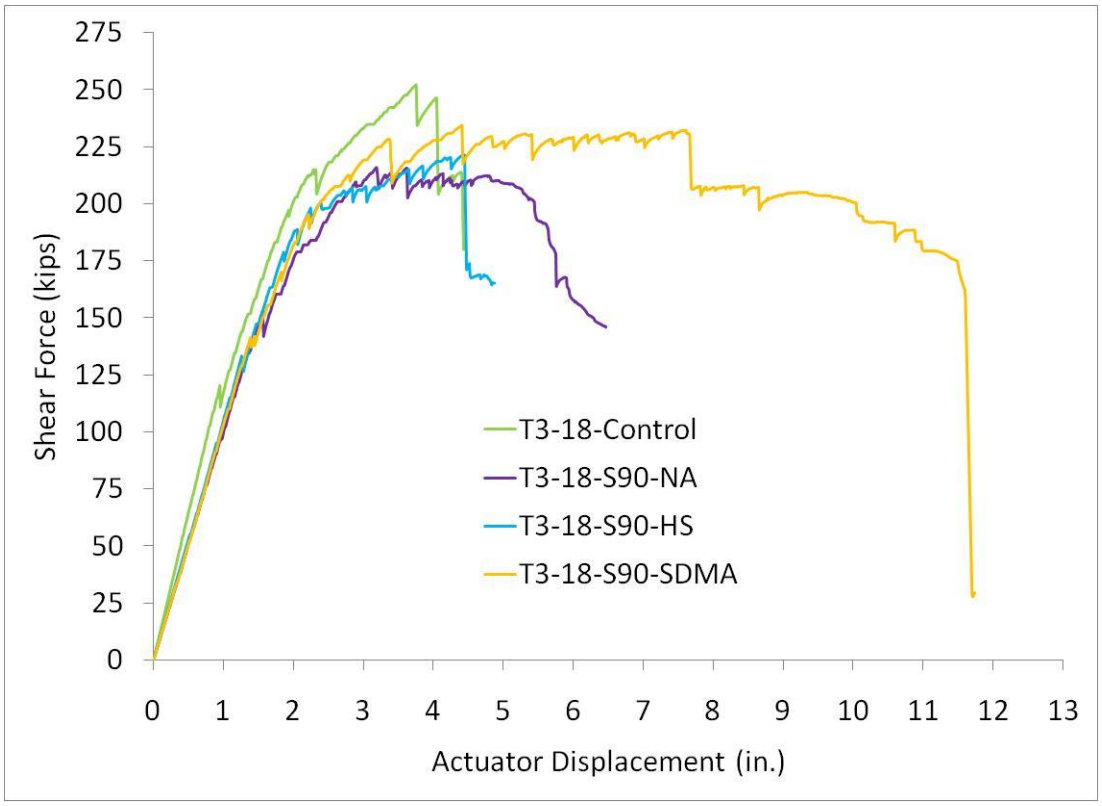

Figure A 5.111 Load-Displacement Response (Cross-section Type IV)

A5.3.8.2 Failure Modes

As seen in Table A 5.17, a variety of failure modes were observed in the PC girder testing. Failure modes include: (1) horizontal failure along the top flange, (2) debonding of FRP, (3) localized rupture of FRP, (4) diagonal shear tension, (5) web crushing, (6) mechanical anchorage failure, and (7) failure due to high stress concentrations localized at the reaction point. Some of the test specimens exhibited multiple failure modes either at the same time or in a sequential manner. Each of these failure modes will be discussed within the context of the specimens in which they were observed.

For the MoDOT Type 4 specimens (Figure A 5.92), shear cracks in the web propagated toward the top flange at which point they turned and ran horizontally along the longitudinal compression reinforcement located at the interface between the web and top flange. The maximum shear force carried by all MoDOT Type 4 girders was ultimately governed by a failure plane created by the horizontal cracks along the top flange (failure mode - TF). This failure mode is believed to be caused by the moderate amount of longitudinal steel in the top flange designed to give the girders adequate flexural capacity to ensure shear failure. However, the small amount of concrete provided by the narrow top flange and thin web offer little confinement and thus the large compression stresses in the top flange result in buckling of the longitudinal reinforcement. This failure mode was observed near the reaction point in the first three test specimens (T4-12-Control, T4-18-Control, and T4-18-S90-NA) as shown in Figure A 5.112. With this type of failure, externally bonded FRP shear strengthening is ineffective as seen by the test results of Girder T4-18-S90-NA (see Figure A 5.112(c)). In an attempt to prevent this type of failure mode, subsequent Type 4 girder tests were modified by increasing the shear span, adding a 12 inch

deep deck slab, and in some cases providing a complete wrap FRP strengthening system for better confinement. These modifications proved to postpone this behavior; however, ultimate failure was always characterized by buckling of the longitudinal compression reinforcement producing a horizontal cracking plane along the top flange as shown in Figure A 5.112.

(a) T4-12-Control

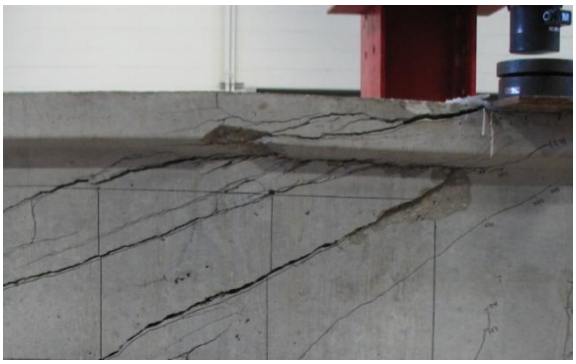

(b) T4-18-Control

(c) T4-18-S90-NA

(d) T4-18-S90-CMA

(e) T4-18-S90-DMA

(f) T4-18-S45-DMA

(g) T4-12-Control-Deck

(h) T4-12-S90-SDMA

Figure A 5.112 Horizontal Failure Plane along Top Flange of MoDOT Type 4 Girders

For the MoDOT Type 4 specimens strengthened in shear with FRP, the horizontal top flange failure was generally preceded by debonding of the FRP (failure mode - D). In two extreme cases, ultimate failure was accompanied by failure of the mechanical anchorage (T4-18-S90-CMA) (failure mode – MA) as shown in Figure A 5.112(d) and localized rupture of the FRP (T4-18-S90-DMA) (failure mode – LR) as shown in Figure A 5.112(e). The continuous plate and anchor bolt system used in T4-18-S90-CMA appeared to be ineffective and failed due to buckling of the continuous CFRP plate followed by pull-out of the concrete anchor bolts (see Figure A 5.113). This failure mode is described in more detail in Section A5.4 of this report.

Figure A 5.113 Mechanical Anchorage Failure of T4-18-S90-CMA

For the MoDOT Type 3 specimens, failure due to web crushing (failure mode – WC) or high stress concentrations near the reaction point (failure mode – SC) were observed when a moderate level of transverse steel reinforcement was provided (stirrups spaced at 12 inches). The control specimen of this group ultimately failed at the top flange near the reaction point. This failure is best explained as a buildup of high stress concentrations due to a combination of diagonal compression stresses, flexural compression stresses, and contact stresses induced by the reaction frame. In an attempt to prevent this failure mode in subsequent tests, additional external strengthening was added near the point load reaction as shown in Figure A 5.104(c). For the specimens strengthened with FRP without mechanical anchorage, a web crushing failure mode was observed as a result of spalling of the concrete cover associated with debonding of the FRP as shown in Figure A 5.114. The loss in concrete cover results in a significant loss in web thickness for I-shaped PC girders.

(a) T3-12-S90-NA (b) T3-12-S90-NA-PC

Figure A 5.114 Web Crushing Failure Mode

(a) T3-12-S90-NA (b) T3-12-S90-NA-PC

Figure A 5.115 Close-Up of Debonded FRP Sheet with Spalled Concrete Cover Attached

To understand this failure mode, it is first necessary to understand the bond behavior between FRP sheets and concrete. Numerous research studies have been conducted on this topic as described in Section A2.5.2. However, most research has focused on simple shear test as shown in Figure A 5.116, in which the maximum shear stress and effective bond length (L_e) were experimentally determined. Debonding occurs first within the effective bond length (L_e), resulting from debonding of a very thin layer of concrete rather than debonding at the FRP/concrete interfaces.

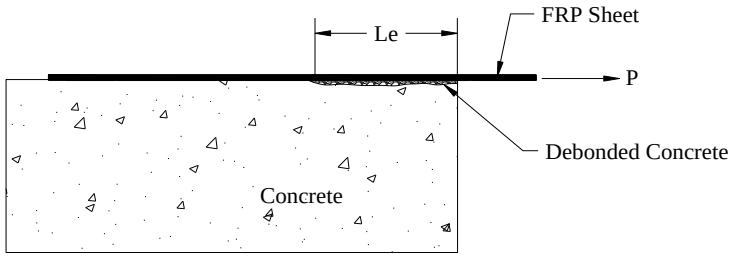

Figure A 5.116 Schematic of Shear Test for Effective Bond Tests

The common form of the equation for determining the maximum normal force that can be carried by the FRP sheet is

$$P_u = \tau_{\max} b_f L_e \qquad \text{(A5-8)}$$

However, the knowledge accumulated from simple shear tests is not directly applicable to shear problems and thus must be modified as shown in Figure A 5.117. Figure A 5.117 presents three different models for debonding based on crack spacing. Unlike the simple shear test used in the previous research studies, a large piece of concrete is debonded as shown in Figure A 5.114 and Figure A 5.115 in the PC girder tests, due to the damage from the compression forces and aggregate interlocking near the cracks. Thus, the debonding lines, as shown in Figure A 5.117, can be assumed as a parabolic line based on the observations. It can also be assumed that the debonding of concrete cover occurs within the effective bond length and the debonding strength is dependent on the concrete tensile strength since the debonding does not occur at the FRP/concrete interface.

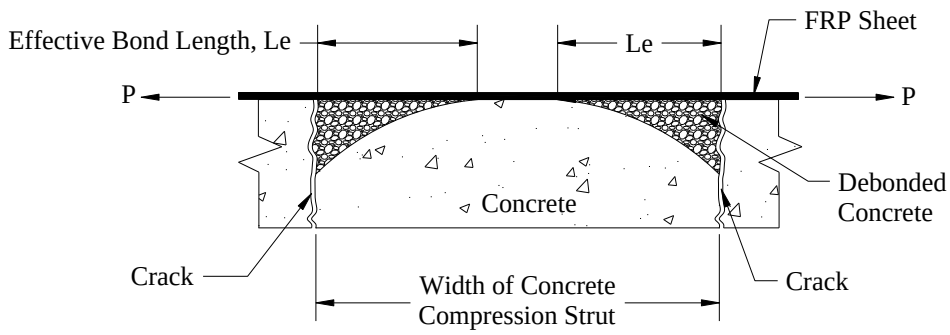

(a) Crack Spacing Wider than 2Le

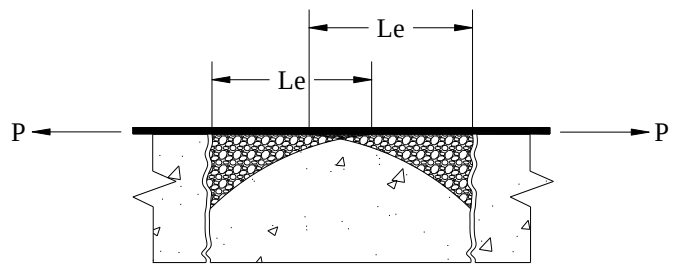

(b) Crack Spacing Less than 2Le

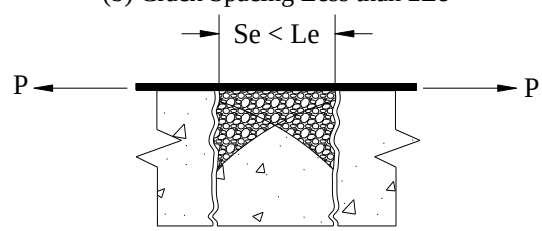

(c) Crack Spacing Less than Le

Figure A 5.117 Shear Crack and Debonding Models

With the assumptions for the suggested models, when the crack spacing is greater than $2L_e$ (Case (a) in Figure A 5.117), which was the case for the Type 4 girders, the area of debonded concrete cover is relatively small as compared to the total area of the compression strut. Therefore, web crushing failure did not occur. In this case, Equation A5-8 is still applicable or τ_{max} can be replaced with the tensile strength of concrete ($4\sqrt{f_c^{'}}$ for normal weight concrete). Meanwhile, the moderately reinforced (stirrups spaced at 12 inches) Type 3 girders exhibited much tighter crack spacings, and the bond behavior of FRP and concrete can be treated as Cases (b) and (c) in Figure A 5.117. In these cases, the loss of concrete due to FRP debonding in the concrete strut cannot be ignored and thus web crushing is likely to occur. For Case (b) where crack spacing is less than $2L_e$, the maximum debonding force can be determined in order to account for the overlapped effective bond length as:

$$P_u = \tau_{\max} b_f (S_e - L_e) \text{ or } P_u = 4\sqrt{f_c^{'}} b_f (S_e - L_e) \qquad \text{(A5-9)}$$

where, S_e = crack spacing.

For Case (c) where the crack spacing is smaller than the effective bond length L_e, the maximum debonding force can be determined using the crack spacing instead of the bond length as follows:

$$P_u = \tau_{\max} b_f S_e \quad \text{or} \quad P_u = 4\sqrt{f_c^{'}} b_f S_e \qquad \text{(A5-10)}$$

For the MoDOT Type 3 specimens under low transverse steel reinforcement conditions (stirrups spaced at 18 inches), ultimate failure was always characterized by diagonal shear-tension failure (failure mode – DT) preceded by some level of debonding (failure mode – D) when FRP reinforcement was present. The debonding behavior of FRP for this series of girders was somewhat different from that of previously observed debonding mechanisms. The primary difference was characterized by a pseudo-ductile behavior in the overall response as a result of the progressive spread of debonding. This pseudo-ductile behavior is reflected in the load-displacement responses depicted in Figure A 5.111. With each stage of debonding comes a release of stresses which must be redistributed among the remaining fibers. This is observed as a sudden drop in the applied shear force in the load-displacement response. As more load was applied to the girder, the applied shear force increases towards its previous state prior to initial debonding. Meanwhile, the remaining fibers begin approaching their bond critical stress, initiating more debonding and, again, a loss in applied shear force as stresses are redistributed. This process continued throughout failure, thus inhibiting substantial increase in shear strength beyond that at which debonding first initiated. Although the sandwich discontinuous mechanical anchorage system (T3-18-S90-SDMA) did result in the highest shear strength of the FRP strengthened girders in this group, it was apparent that the mechanical anchors created a plane of weakness along which the critical cracks were observed to propagate. This may explain the lower shear strength as compared to the control specimen (T3-18-Control).

A5.3.8.3 Contribution of Various Shear Components

To better understand the shear resistance mechanisms and to better quantify the FRP contribution to the ultimate shear capacity, it is necessary to decouple the individual components contributing to the total shear resistance. In this case, the primary components contributing to the shear resistance are the concrete (V_c), steel stirrups (V_s), and externally bonded FRP (V_f). A shear component analysis was conducted on the experimental data to identify the contribution of each component throughout the loading history of the test girders. The results of this analysis are presented graphically in Figure A 5.118 and Figure A 5.119. This analysis is based on the understanding that the internal shear resistance must be equal to the applied shear force as indicated by a 45° line originating from the origin. The internal shear resistance is comprised of three individual components (V_c, V_s, and V_f) which were evaluated from crack-based free body diagrams of a portion of the test girders along the critical shear cracks. The shear resistance provided by the steel stirrups (V_s) and FRP (V_f) were determined from strain gage measurements along the stirrups and FRP strips within the test regions. Only those strain gage measurements closest to the critical shear crack were used for such analysis. From equilibrium, the shear resistance provided by concrete (V_c) is simply the difference between the applied shear force (V_n) and the contributions coming from the stirrups and FRP ($V_s + V_f$).

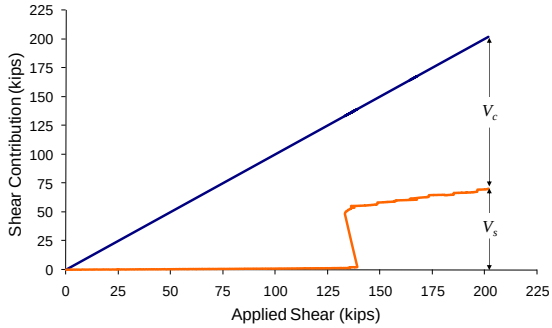

(a) T4-12-Control

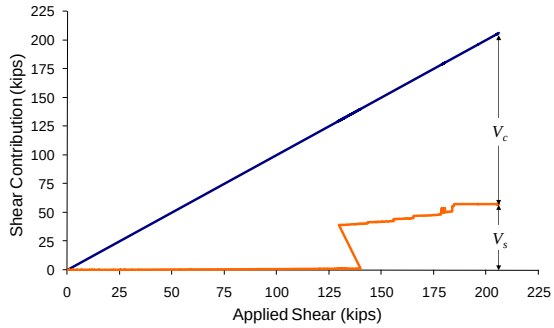

(b) T4-18-Control

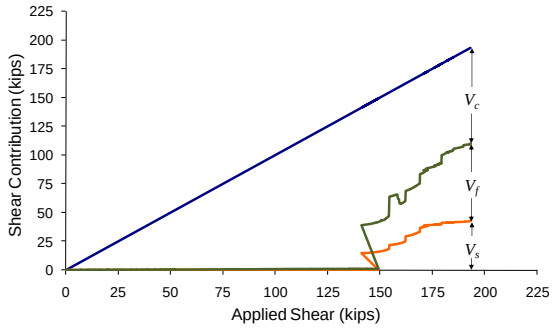

(c) T4-18-S90-NA

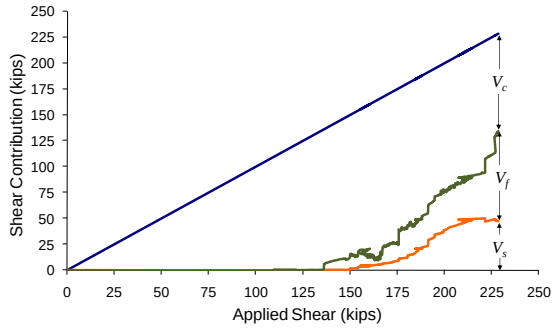

(d) T4-18-S90-CMA

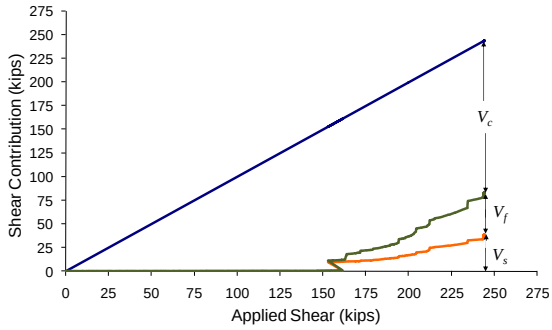

(e) T4-18-S90-DMA

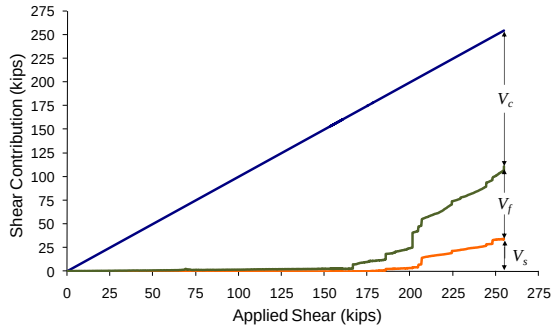

(f) T4-18-S45-DMA

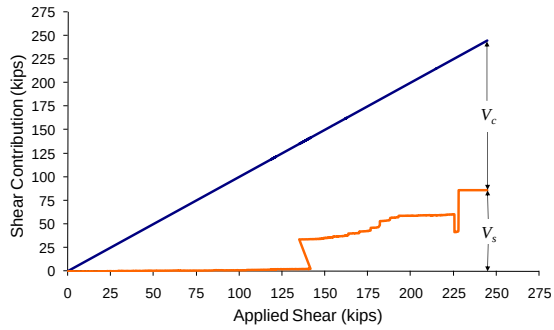

(g) T4-12-Control-Deck

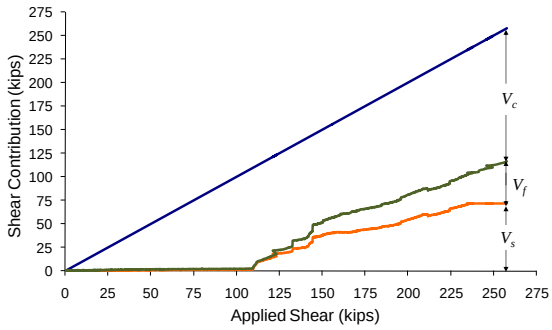

(h) T4-12-S90-SDMA

Figure A 5.118 Shear Components for Type 4 MoDOT Specimens

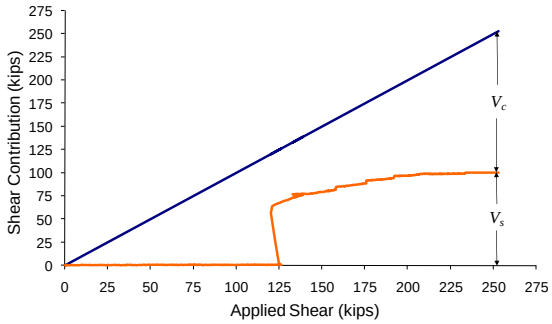

(a) T3-12-Control

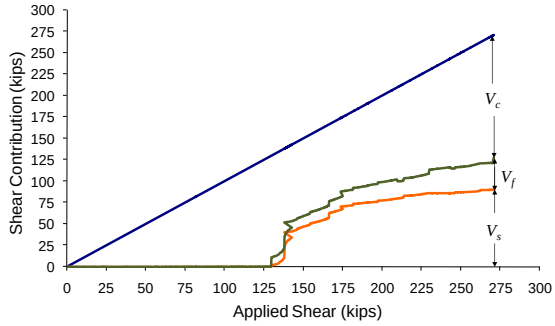

(b) T3-12-S90-NA

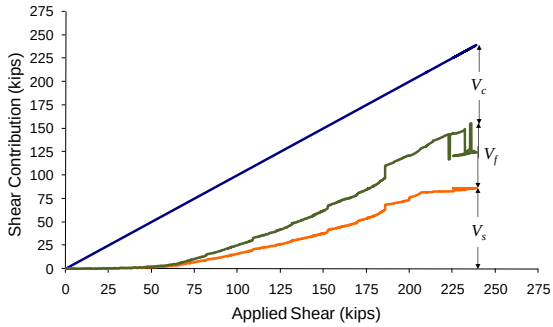

(c) T3-12-S90-NA-PC

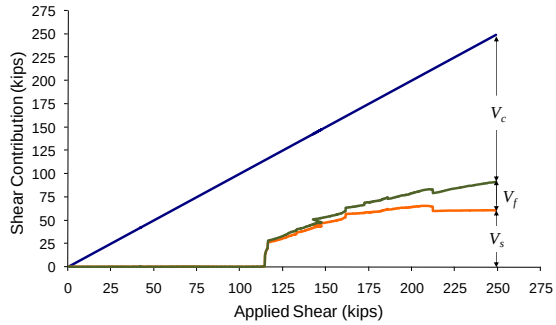

(d) T3-12-S90-DMA

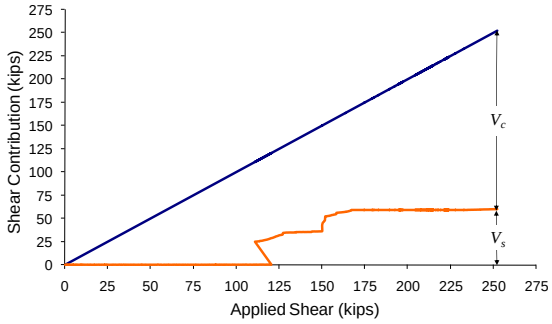

(e) T3-18-Control

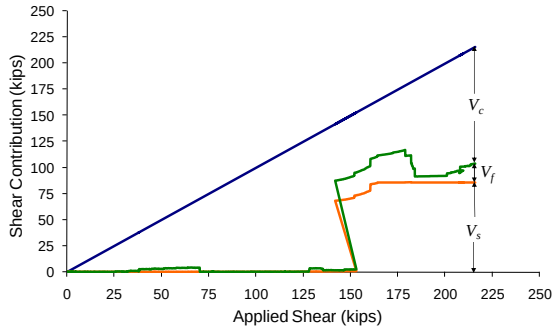

(f) T3-18-S90-NA

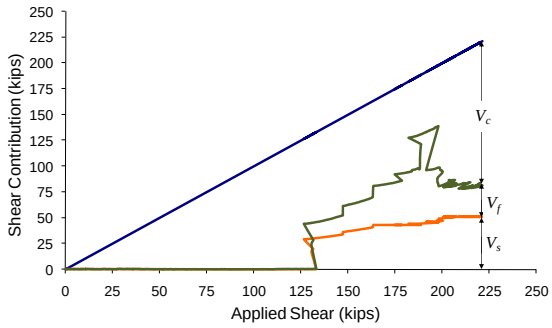

(g) T3-18-S90-HS

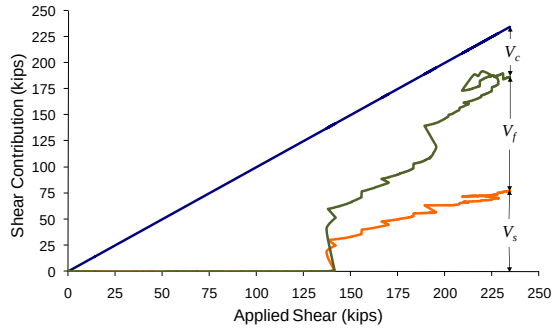

(h) T3-18-S90-SDMA

Figure A 5.119 Shear Components for Type 3 MoDOT Specimens

As shown in Figure A 5.118 and Figure A 5.119, it was found that prior to inclined shear cracking, the applied shear force was carried primarily by concrete (V_c). This concrete contribution can be considered as coming from the shear resistance of concrete in the compression zone (V_{cz}), shear resistance due to dowel action (V_{cd}), and shear resistance due to aggregate interlocking (V_{ci}). The contributions provided by the transverse reinforcement (stirrups and FRP) was minimal to non-existent prior to web shear cracking. At cracking, a portion of the applied shear forces are transferred to the steel stirrups and FRP strips as shown by the sudden jump in the shear contribution responses. The stirrups and FRP strips continue to take load, as shown by the gradual increase in shear contribution response, until yielding of the stirrups or debonding of the FRP strips occurs. Yielding of the stirrups is shown as a plateau in the shear contribution response for the stirrups (V_s). Sudden or gradual drops in the FRP contribution responses signify debonding of the FRP strips. The severity of the drop in shear contribution reflects the magnitude of debonding occurring along the load history.

The values of the shear contributions coming from concrete, steel, and FRP are summarized in Table A 5.18 at the stages corresponding to yielding of the steel stirrups and ultimate load. As shown in Table A 5.18, despite the abnormalities in the overall behavior, the shear component analysis shows that the FRP does in fact have a significant contribution in the total shear resistance of a PC girder.

Table A 5.18 Summary of Shear Contributions

MoDOT Standard	Test I.D.	Cross Section Type	Shear Crack Angle (deg.)	At Yielding of Steel Stirrups			At Ultimate Load		
				V_{cy} (kips)	V_{sy} (kips)	V_{fy} (kips)	V_{cu} (kips)	V_{su} (kips)	V_{fu} (kips)
Type 4	T4-12-Control	I	32.0	N/A	N/A	N/A	131	71	N/A
	T4-18-Control	I	26.0	127	57	N/A	149	57	N/A
	T4-18-S90-NA	I	21.0	83	43	67	83	43	67
	T4-18-S90-CMA	II	25.0	N/A	N/A	N/A	95	47	87
	T4-18-S90-DMA	II	24.0	N/A	N/A	N/A	161	39	44
	T4-18-S45-DMA	II	32.0	N/A	N/A	N/A	144	34	77
	T4-12-Control-Deck	II	26.0	142	86	N/A	159	86	N/A
	T4-12-S90-SDMA	II	30.0	113	57	35	134	57	67
Type 3	T3-12-Control	III	23.0	133	100	N/A	153	100	N/A
	T3-12-S90-NA	III	22.0	120	86	23	143	90	38
	T3-12-S90-NA-PC	III	21.0	110	86	41	115	86	39
	T3-12-S90-DMA	III	25.0	N/A	N/A	N/A	158	60	31
	T3-18-Control	IV	21.0	108	59	N/A	192	60	N/A
	T3-18-S90-NA	IV	15.0	52	86	26	112	86	18
	T3-18-S90-HS	IV	26.0	82	43	38	140	51	31
	T3-18-S90-SDMA	IV	33.0	48	77	110	48	77	110

A5.3.9 Summary and Conclusions

The results of the PC girder testing has raised suspicion that the effectiveness of FRP shear strengthening is greatly affected by the cross-sectional shape of the strengthened member. These thin webbed members can be negatively affected when debonding of FRP is accompanied by peeling off of the concrete cover. In extreme cases, web crushing failure can occur which is a failure mode that cannot benefit from FRP strengthening. However, this theory cannot be verified with the limited test results from this study. The use of FRP systems properly anchored with mechanical anchorage was found to yield better performance by minimizing the extent of debonding. Despite abnormalities in the experimental test results, strain gage measurements prove that externally bonded FRP does in fact provide a significant contribution to the total shear resistance of a PC girder. Thus it is more appropriate to evaluate these results through a shear component analysis. In this case, the shear resistance mechanisms can be better understood. A deeper investigation into the suspected shape effect is recommended inorder to provide greater insight on the PC girder test results.

A5.4 Behavior of Anchorage Systems

A5.4.1 General

The previous sections focused on presenting the effectiveness of FRP shear strengthening. This section presents in detail the performance of the anchorage systems used in the RC T-beam and PC girder testing of this project.

A5.4.2 Performance of Anchorage Systems

A5.4.2.1 Continuous Mechanical Anchorage System with Anchor Bolts

The mechanical anchorage used on specimen T4-18-S90-CMA consisted of continuous CFRP plates, 108 inches long, bonded to the FRP strips with FRP resin. The plates were anchored firmly in place with concrete wedge anchors, each ½ inch in diameter with 2 inches of embedment length. The anchor bolt system used in this specimen was ineffective. At failure, the plate exhibited a buckling type of failure mode, but debonding of FRP sheets was not observed, as shown in Figure A 5.120. This buckling failure was due to the large space between anchor bolts and the continuity of the plate; however, the specimen failed prematurely due to the splitting of the top flange, preventing the FRP strips from reaching their ultimate strength. Therefore, to monitor the behavior of this anchorage system, the girder was loaded beyond its ultimate load capacity to induce greater deformations. As a result of further loading, the anchor bolts were pulled out from the concrete due to the short embedment length and severe debonding. In addition, bearing failure of the CFRP plate was found at the first and last anchors of the top CFRP plate.

Figure A 5.120 Failure of Mechanical Anchorage in T4-18-S90-CMA

A5.4.2.2 Discontinuous Mechanical Anchorage System with Thru Bolts

This mechanical anchorage configuration was designed to overcome the short embedment length of members with thin webs. Three specimens were tested to observe the performance of the system. The first specimen was T4-18-S90-DMA, which used a mechanical anchorage consisting of two 12 inch long CFRP plates. The plates were anchored firmly in place with steel bolts running through the web, each with a diameter of 3/8 inch. This mechanical anchorage system was designed to prevent buckling of the FRP plate and anchor pull-out issues experienced during testing of specimen T4-18-S90-CMA. The thru-bolt system did not fail severely until the test girder reached its maximum shear capacity. Although slight debonding occurred, the bolt remained intact. This specimen was loaded beyond maximum shear capacity so that the ultimate failure mode of the thru-bolt system could be observed. The ultimate failure of the thru-bolt system was located near the bottom flange of the specimen, as a result of bending of the CFRP plate along the line of the thru bolts, as shown in Figure A 5.121.

Figure A 5.121 Failure of Mechanical Anchorage in T4-18-S90-DMA

The thru-bolt system used for T4-18-S45-DMA performed very well. It did not fail severely until the test girder reached its maximum shear capacity. Although slight debonding occurred, as shown in Figure A 5.122, the thru-bolt system remained intact. The same bolt diameter was used as in T4-18-S90-DMA; the length of the plates was increased to 17.5 inches, but not enough to stop debonding at the edge of the FRP strips.

Figure A 5.122 Debonding of FRP in T4-18-S45-DMA

Specimen T4-18-S45-DMA was also loaded beyond the maximum shear capacity so that the ultimate failure mode of the thru-bolt system could be observed. Figure A 5.123(a) shows the rupture of the FRP while the connection bolt and plate were intact even at ultimate failure. Rupture of the FRP occurred at multiple locations, as shown in Figure A 5.123(b).

(a) Due to failure of top flange (b) Due to web crushing

Figure A 5.123 FRP Rupture in T4-18-S45-DMA

In specimen T4-18-S90-DMA, the FRP plates used for mechanical anchorage were bent along the line of the bolt holes, resulting in splitting of the plate. This situation did not occur in this test, but a bearing failure of the plate was found, as shown in Figure A 5.124. As reported in previous research (Rizzo et al., 2005) related to the use and application of CFRP plates, larger-diameter drill holes in the plates caused the bearing failure, which is more desirable than failure of the anchors. This factor must be considered when using this anchorage system.

Figure A 5.124 Bearing Failure of Mechanical Anchorage in T4-18-S45-DMA

The thru-bolt system used in T3-12-S90-DMA was slightly different than that used in T4-18-S90-DMA. The length of the plates was increased to protect the edges of the FRP strip. In addition, a bigger bolt was used (½ inch), and four bolts were used instead of three. The size increment of the bolts was due to spacing limitations that depend on the diameter of the anchor. Two bolts were located outside of the strip, and the other two located inside to distribute the load uniformly. The failure of this specimen was located near the loading point, as shown in Figure A 5.125. The FRP sheets and mechanical anchorage were not damaged until failure.

Figure A 5.125 View of Girder T3-12-S90-DMA at failure

A5.4.2.3 Discontinuous Mechanical Anchorage System with Anchor Bolts

This anchoring system was used in the RC T-beam specimens where drilling through the web was not feasible. The anchor bolt system used in test specimen RC-8-S90-DMA was less effective than the thru-bolt system implemented in the previous PC girder tests. Debonding started at a shear force of 170 kips at the bottom of the CFRP plate in Strip 3. The debonded area was monitored manually by tapping the surface in the region beneath the plate. As the load was increased, debonding developed in Strip 3 at mid-height of the web due to the presence of the anchorage system. Strip 3 debonded completely at a shear force of 191 kips. As the load increased, debonding also began in Strip 4; this strip was almost completely debonded at a shear force of 198 kips. Failure of the beam occurred at a shear force of 212 kips as the critical crack

width became severe near Strip 2, inducing debonding failure as shown in Figure A 5.126(a). At failure, the FRP sheets slipped from the anchor plates, as shown in Figure A 5.126(b).

(a) Detail of Strips 3 and 4

(b) Slipping of the FRP sheets

Figure A 5.126 Failure Modes in RC-8-S90-DMA

However, specimen RC-8-S90-MA failed before the FRP strips reached their ultimate strength. As shown in Figure A 5.127, the FRP sheet was pulled in shear resulting in bearing failure of the FRP sheet along the holes drilled for the mechanical anchorage. The slippage of the FRP sheets occurred mainly because the epoxy used to bond the CFRP plate and the FRP sheet was not fully cured. This behavior was not observed in the previous PC tests, and the anchor bolts did not fail. Thus, the bond between the CFRP plates and the FRP sheets is critical for this type of mechanical anchorage system.

Figure A 5.127 Bearing Failure of the FRP Sheet

The anchor bolt system used in RC-12-S90-DMA was the same as that implemented in RC-8-S90-DMA. Debonding occurred first in Strip 3 at a shear force of 161 kips. At a shear force of 180 kips, debonding was found along the right edge of Strip 4. As the load increased, debonding increased in Strips 3 and 4. Strip 5 also started to debond at a shear force of 198 kips. Once the critical crack reached the compression flange and propagated horizontally, debonding occurred along the left edge of Strip 5. Failure occurred at a shear force of 205 kips, along with complete debonding of Strips 4 and 5 due to the large crack openings, as shown in Figure A 5.128.

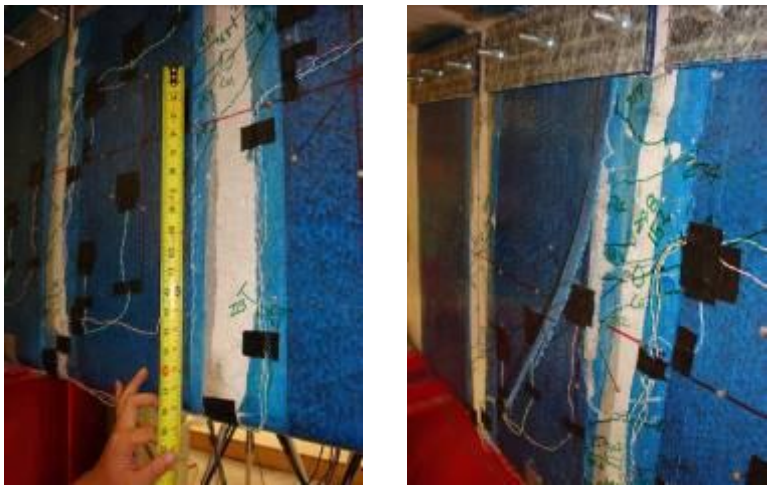

(a) Detail of strip 4 (b) Rupture of strip 5

Figure A 5.128 Failure Modes in RC-12-S90-DMA

As in the case of RC-8-S90-DMA, the use of mechanical anchorage delayed the initiation of debonding at a higher load than that carried by the specimen with no anchorage. As a result, slipping between the CFRP plates and FRP sheets was significantly reduced, as shown in Figure A 5.129. The FRP sheets ruptured at the edge of one strip as shown in Figure A 5.130. More attention should be given to increasing the bond between the CFRP plates and FRP sheets to increase the effect of the FRP strengthening.

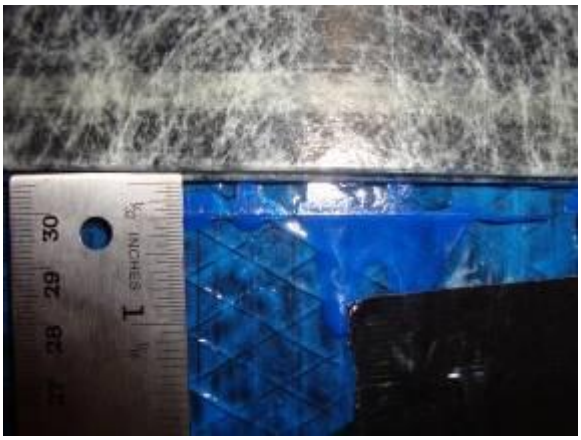

Figure A 5.129 Behavior of Mechanical Anchorage System in RC-12-S90-DMA

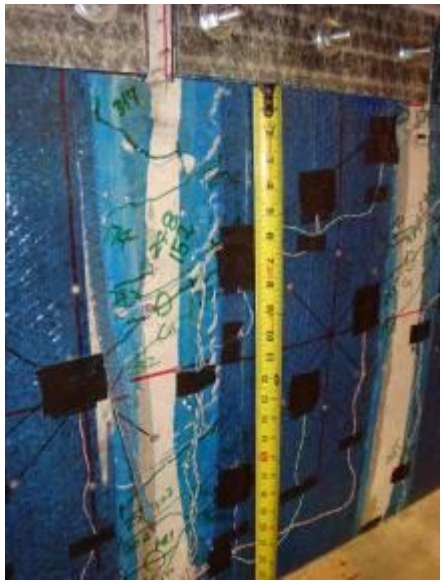

Figure A 5.130 Rupture of FRP in RC-12-S90-DMA

A5.4.2.4 Sandwich Panel Discontinuous Mechanical Anchorage

This mechanical anchorage system was designed as an alternative for those that exhibited slipping failure. The main objective of the modified anchor bolt system used in specimen RC-12-S90-SDMA-PC was to prevent slipping of the FRP sheet observed in the RC specimens with discontinuous mechanical anchorage. By wrapping the FRP composite around the first plate and overlapping it with the second plate to form a three-layer connection, as shown in Figure A 5.22, the slipping failure mode observed in the previous specimen was prevented. Debonding first occurred in Strip 4 at a shear force of 163 kips. At a shear force of 205 kips, debonding was found along both edges of the Strip 3, as shown in Figure A 5.131(a). Once the diagonal cracks reached the compression flange and propagated horizontally, debonding occurred along the edge of Strip 5. Failure occurred at a shear force of 214 kips, along with debonding of Strips 4 and 5 due to the large crack openings, as shown in Figure A 5.131(b).

(a) Detail of strip 3

(b) Detail of strip 5

Figure A 5.131 Debonding Propagation in RC-12-S90-SDMA-PC

No slipping failure of the sheets was observed in this specimen, indicating that the sandwich panel system worked properly. The anchor bolts did not fail. Figure A 5.132 shows the specimen at failure. The FRP sheets ruptured at the edge of one strip, as shown in Figure A 5.133. The shear capacity of the specimen increased over that of specimen RC-12-S90-DMA, from 198 kips to 214 kips, but the FRP sheets did not reach full capacity due to shear compression in the top flange before FRP ruptured.

Figure A 5.132 View of Specimen RC-12-S90-SDMA-PC at Failure

Figure A 5.133 FRP Rupture in RC-12-S90-SDMA-PC

The performance of this mechanical anchorage configuration in specimen RC-12-S45-SDMA was excellent, and FRP rupture occurred at several locations in various FRP strips. The anchorage system delayed FRP debonding until the shear force reached 182 kips, at which point delamination was found at the edges of Strips 3, 4, and 5. At a shear force of 195 kips, FRP rupture was found along both edges of Strip 4, as shown in Figure A 5.134(a). At a shear force of 198 kips, FRP rupture was also found along the left edge of Strip 5, as shown in Figure A 5.134(b). When the shear force reached 200 kips, both Strips 4 and 5 exhibited FRP rupture and

extensive debonding. Figure A 5.135 shows this specimen at failure. The anchorage system was intact until the specimen failed, and the anchorage system never reached its ultimate capacity.

(a) FRP rupture in strip 4

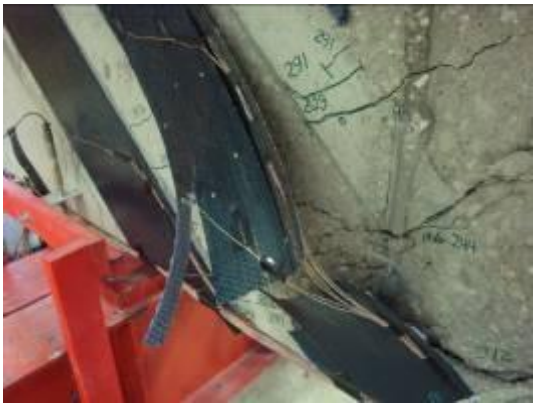

(b) FRP rupture in strip 5

Figure A 5.134 FRP Rupture in RC-12-S45-SDMA

(a) Full view at failure

(b) Detail of strips 4 and 5 at failure

Figure A 5.135 View of Beam RC-12-S45-SDMA at Failure

The performance of the mechanical anchorage system in specimen RC-12-S90-SDMA-NM showed similar behavior to that of specimen RC-12-S45-SDMA, and FRP rupture occurred at the edges of Strips 1 and 2. The anchorage system delayed FRP debonding until the shear force reached 185 kips, at which point delamination was found at the edge of Strip 3. At a shear force of 192 kips, delamination was found in Strips 2 and 4. At a shear force of 201 kips, delamination increased along both edges of Strip 2. At a shear force of 216 kips, delamination increased along both edges of Strip 3. At a shear force of 229 kips, delamination was found along the edge of Strip 1. At failure, Strips 1 and 2 exhibited FRP rupture and extensive debonding, as shown in Figure A 5.136. Figure A 5.137 shows this specimen at failure. The anchorage system remained intact throughout failure of the specimen and never reached its ultimate capacity.

(a) Detail of strip 1

(b) Detail of strip 2

Figure A 5.136 FRP Rupture in Specimen RC-12-S90-SDMA-NM

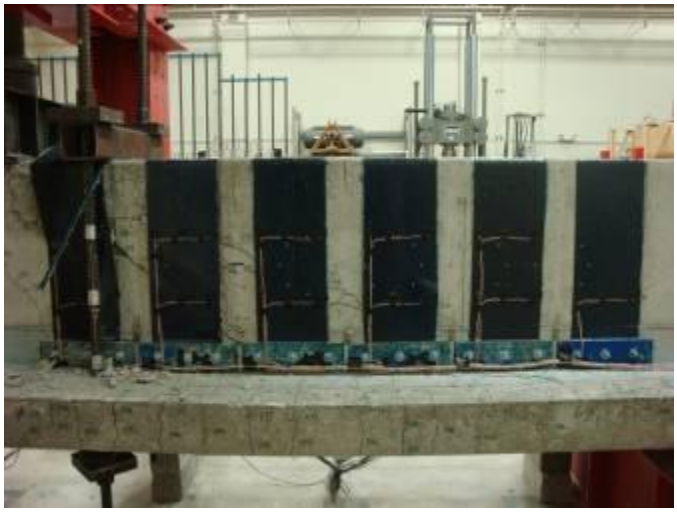

Figure A 5.137 View of Specimen RC-12-S90-SDMA-NM at failure

The mechanical anchorage system in Specimen RC-12-S90-SDMA-COR allowed the FRP sheets to reach their ultimate capacity, and FRP rupture occurred at the edges of Strips 4 and 5. The anchorage system delayed FRP debonding until the shear force reached 224 kips, at which point delamination was found at the edges of Strips 3 and 4. At a shear force of 246 kips, delamination was found in Strip 5 and increased along the edge in Strip 3. At this load step, Strip 4 exhibited FRP rupture. At a shear force of 265 kips, FRP rupture increased along the edge of strip 4, as shown in Figure A 5.138(a). At failure Strips 4 and 5 exhibited FRP rupture and extensive debonding, as shown in Figure A 5.138(b). Figure A 5.139 shows this specimen at failure. The anchorage system remained intact throughout failure of the specimen and never reached its ultimate capacity.

(a) Detail of strip 4 at 265 kips

(b) Detail of strip 4 at failure

Figure A 5.138 FRP Rupture in RC-12-S90-SDMA-COR

Figure A 5.139 View of RC-12-S90-SDMA-COR at Failure

This anchorage configuration was also implemented in the PC girders. Girder T3-18-S90-SDMA was the first PC specimen tested using this anchorage configuration. The debonding effect was delayed, allowing the FRP to give a higher shear contribution to the girder, but there was no gain in shear strength. Ultimate failure of this girder resulted from a diagonal tension crack that propagated upward towards the top flange then turned and ran horizontally along the row of mechanical anchors, as shown in Figure A 5.140. The mechanical anchors clearly created a plane of weakness along which the critical crack propagated. This weakness reduced the shear strength in comparison with the control girder. The anchorage system failed when the plates were bent along the line of the thru-bolts, as shown in Figure A 5.141.

Figure A 5.140 View of Girder T3-18-S90-SDMA after Failure

Figure A 5.141 Failure of Mechanical Anchorage in T3-18-S90-SDMA

Similar behavior was observed in Girder T4-12-S90-SDMA. No debonding occurred, but the shear strength did not increase beyond that of the control girder. This girder failed prematurely due to shear compression failure in the top flange. Although the girder was loaded beyond failure, the anchorage system did not reach its ultimate capacity and remained intact throughout failure of the girder, as shown in Figure A 5.142. Thus, the failure of the anchorage system could not be observed.

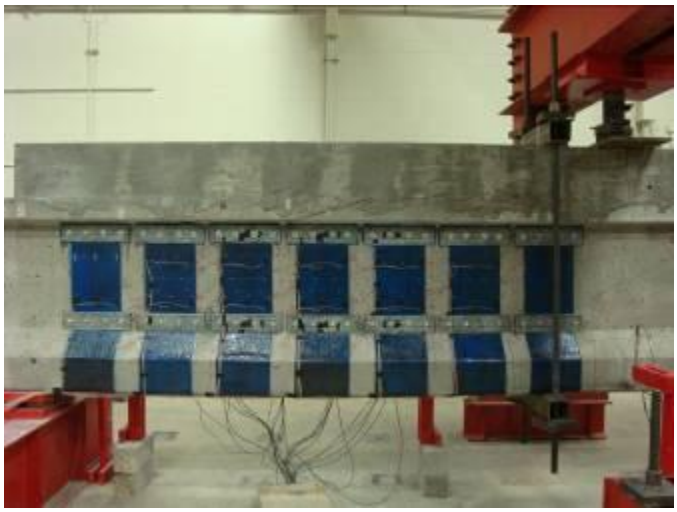

Figure A 5.142 View of Girder T4-12-S90-SDMA at failure

A5.4.2.5 Additional Horizontal FRP Strips

This horizontal strip emerged as a quick and easy solution, but it does not offer the same benefits as a mechanical anchorage system because it depends on the bond strength between the FRP and concrete. This anchorage system was applied first to beam RC-12-S90-HS-PC, which was also precracked prior to application of FRP sheets.

In Specimen RC-12-S90-HS-PC, debonding started at the edges of the horizontal strip in the upper portion of Strip 4 at a shear force of 119 kips, as shown in Figure A 5.143(a). At a shear force of 151 kips, debonding was found along both edges of Strip 3. The horizontal strip continued to debond at the edge all the way to Strip 3 as the shear force reached 151 kips. As a consequence of this debonding in the anchorage system, Strips 4 and 5 fully debonded at a shear force of 176 kips. Further, a buckling failure of the horizontal strip occurred at the upper portion of strip 5, as shown in Figure A 5.143(b). This failure caused the debonding of Strip 5, and this phenomenon continued until Strip 4 was also completely debonded. Failure occurred at a shear force of 187 kips, along with the full debonding of Strips 4 and 5. This specimen reached a shear force of 187 kips at failure, showing less shear capacity than Specimen RC-12-S90-SDMA-PC. Figure A 5.144 shows the beam at failure.

(a) Detail of horizontal strip (b) Buckling failure mode

Figure A 5.143 Failure Modes in RC-12-S90-HS-PC

Figure A 5.144 View of Specimen RC-12-S90-HS-PC at Failure

This anchorage system was also applied to a different FRP configuration in Specimen RC-12-S45-HS. Debonding started at the edges of the horizontal strip in the upper portion of Strip 3 at a shear force of 147 kips, as shown in Figure A 5.145(a). Debonding was also found along the right edge of Strip 3. At a shear force of 158 kips, debonding was found along the left edge of Strip 4. The horizontal strip continued to debond at the edge all the way to Strip 4, when the shear force reached a peak of 172 kips. As a consequence of this debonding in the anchorage system, Strip 4 completely debonded. As in the previous specimen, a buckling failure of the horizontal strip occurred at the upper portion between Strips 3 and 4, as shown in Figure A 5.145(b). This failure caused the debonding of Strip 4, and this phenomenon continued until Strip 3 was also affected. Failure occurred at a shear force of 172 kips along with the full debonding of Strips 3 and 4. This specimen reached a lower shear force at failure, showing less shear capacity than specimen RC-12-S45-SDMA, in which sandwich panel system was implemented. Figure A 5.146 shows the specimen at failure.

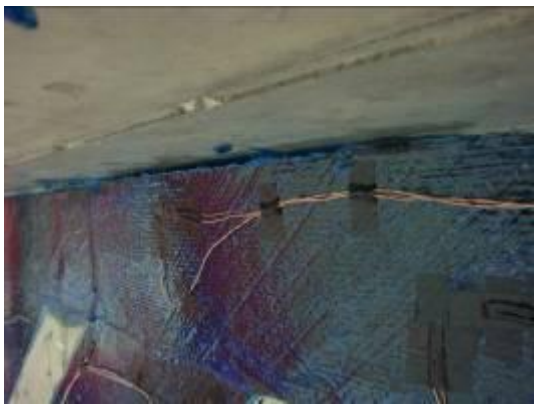

(a) Detail of horizontal strip

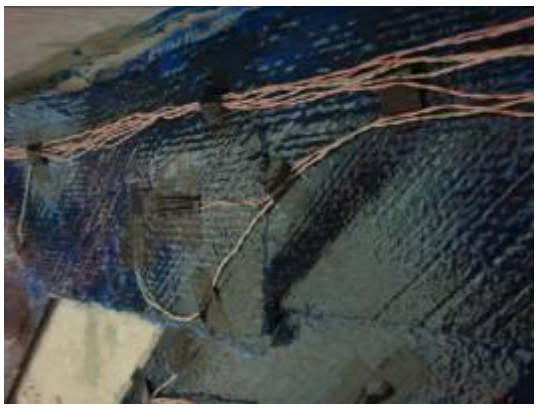

(b) Buckling failure mode

Figure A 5.145 Failure Modes in RC-12-S45-HS

(a) Detail of strip 4

(b) Full view

Figure A 5.146 View of Specimen RC-12-S45-HS at failure

Similar behavior was observed in Girder T3-18-S90-HS. Debonding began at the top edge of the top horizontal strip in the upper portion of Strip 5 at a shear force of 129 kips. At a shear force of 160 kips, debonding was found along the top edge of the top horizontal strip right in the middle of Strip 3, as shown in Figure A 5.147(a). The top horizontal strip continued to debond at the edge up to a point between Strips 2 and 4, at which point the shear force had reached 185 kips. At a shear force of 194 kips, the other two horizontal strips started to debond at the intersection between the web and the bottom chamfer in Strip 7, as shown in Figure A 5.147(b). At a shear force of 203 kips, the horizontal strip was totally debonded at the edge between Strips 2 and 5.

(a) Debonding in top horizontal strip

(b) Debonding in bottom horizontal strip

Figure A 5.147 Debonding of Horizontal Strip in T3-18-S90-HS

A buckling failure occurred in the top and bottom horizontal strips, as shown in Figure A 5.148. In the top horizontal FRP strip, this failure caused the debonding of Strip 6. Failure occurred at a shear force of 221 kips, with the debonding of Strips 2 through 6. This specimen reached a lower shear force than girder T3-18-S90-SDMA, showing the anchorage system to be less effective. Figure A 5.149 shows the beam at failure.

(a) Buckling of top horizontal strip

(b) Buckling of bottom horizontal strip

Figure A 5.148 Buckling Failure Mode in T3-18-S90-HS

Figure A 5.149 View of Girder T3-18-S90-HS at Failure

A5.4.3 Recommendations for Anchorage Installation and Design

This section addresses the design considerations for concrete beams strengthened in shear with FRP in cases when mechanical anchorage systems are used. These considerations include the design procedure for the discontinuous mechanical anchorage system used in this study, limitations on the material properties of FRP plates used for the anchorage system, and detailing requirements.

A5.4.3.1 Design Procedure

The design of the discontinuous mechanical anchorage system used in this study was based on the bearing failure of the anchorage system as observed in the tests. Thus, the capacity of a discontinuous mechanical anchorage, consisting of a thick plate and multiple anchor bolts or thru bolts, can be determined as:

$$P_{u\_anchor} = n_a P_{bearing} \qquad \text{(A5-11)}$$

where n_a is the number of anchor bolts, and $P_{bearing}$ is the bearing capacity of the plate. This calculated bearing capacity should be greater that the force exerted by the FRP sheets attached to the FRP plate (F_{fu}). The force exerted by the FRP can be determined as:

$$\sigma_{fu} = E_f \varepsilon_{fu} \qquad \text{(A5-12)}$$

$$F_{fu} = \sigma_{fu} A_f = \sigma_{fu} w_f t_f \qquad \text{(A5-13)}$$

where E_f and ε_{fu} are the elasticity modulus and the ultimate strain of the FRP, respectively; A_f is the area of the FRP calculated based on w_f and t_f which are the width and thickness of the strip, respectively.

Since the mechanical anchorage should maintain its integrity until the FRP sheet reaches its full capacity, Equation A5-12 uses the ultimate strain of FRP to calculate the force exerted by the FRP.

For beams with an irregular cross-section such as the PC I-girders tested in this study, the pull-out capacity of the anchor bolts should be investigated. In the case of the PC girders, there exists an outward force generated by the tensile forces in the FRP sheets near the web-flange interface, as shown in Figure A 5.133. Based on the force previously calculated using Equation A5-13 and the geometry of the cross-section, the tensile force is calculated as:

$$F_{res} = 2F_{fu}\cos\beta_g \qquad \text{(A5-14)}$$

Thus, the horizontal force to be used for the pull-out capacity design can be determined as:

$$P_{pull\_out} = F_{res}\cos\left(\beta_g - \beta_H\right) \qquad \text{(A5-15)}$$

The pull-out capacity of an anchor bolt (P_{pull_out}) is usually provided by the manufacturer. The shear strength of the anchor bolts used in a mechanical anchorage system should be measured to ensure that it is greater than the force exerted by the FRP sheet attached to the mechanical anchorage system.

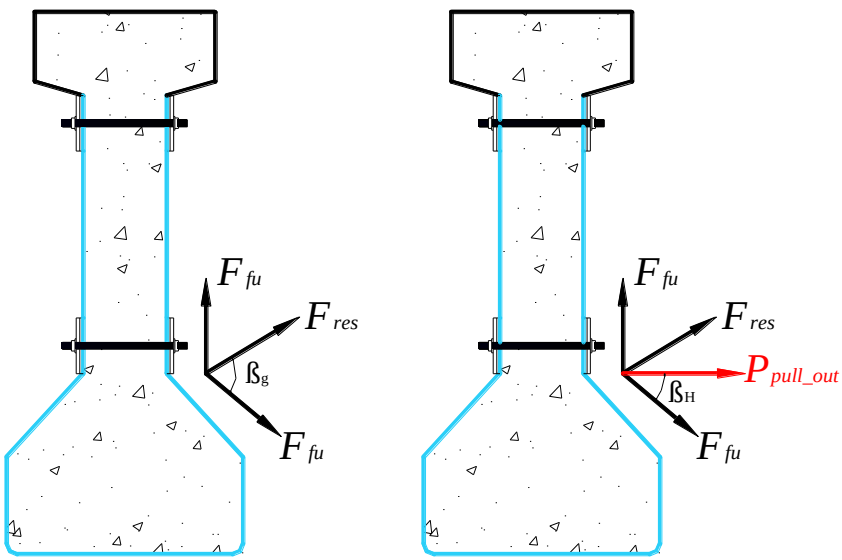

Figure A 5.150 Anchor Tensile Force in I-Sections

A5.4.3.2 Material Properties

The FRP plate for mechanical anchors should have a proper bearing capacity. The FRP plate used in this study was originally developed to have a bearing capacity of 8.99 kips when the diameter of the holes is 3/8 inch. However, Rizzo et al (2005) reported that the maximum bearing stresses in the longitudinal and transverse direction do not depend on the size of the anchor. The longitudinal bearing capacity is 34.1 ksi in the longitudinal direction and 23.2 ksi in the transverse direction. The bearing capacity of the FRP plate should be obtained from the manufacturers or determined experimentally. The design ultimate tensile stress of the FRP sheets must also be given by the manufacturer.

For the anchor bolts and thru bolts, the shear capacity and pull-out capacity should be considered in the design of the mechanical anchorage. The shear and pull-out capacity of the anchor bolts used in this study were considerably higher than the predicted force exerted by the FRP sheets. In addition, the tests reported here indicate that the embedment length of the anchor bolts should be greater than 4 inches.

A5.4.3.3 Detailing Requirements

The FRP plate for mechanical anchorage must meet specific requirements for maximum spacing between anchors and minimum edge distance. These parameters were initially determined based on limits provided in the literature, and their validity was evaluated during this study. Tests showed that the maximum spacing between anchors should not be greater than twelve times the diameter. A larger diameter ensures bearing failure and allows a larger spacing. The edge distance should not be lower than 2 inches from the edge of the plate to the center of the first hole to avoid rupture of the FRP plate.

A5.4.4 Summary and Conclusions

The performance of various anchorage systems were evaluated in this section, including horizontal additional FRP strips (HA), continuous mechanical anchorage system (CMA), discontinuous mechanical anchorage system (DMA), and sandwich discontinuous mechanical anchorage systems (SDMA). The following conclusions can be drawn:

Continuous anchorage systems, including both the continuous mechanical anchorage (CMA) and additional horizontal strips (HA), were found to be ineffective compared to discontinuous mechanical anchorage (DMA) because buckling failure accelerates the debonding of the strips in the vicinity of the buckling.

Discontinuous mechanical anchorage (DMA) used in the RC T-beams produced slipping failure in the FRP sheets. Curing time plays an important role in the bond strength of this connection; it is crucial to the capacity of the anchorage system.

The sandwich discontinuous mechanical anchorage (SDMA) configuration performed better than the DMA because the FRP sheets did not slip.

The DMA configuration seems to be the best anchorage configuration in terms of both practicality and performance. However, the SDMA configuration was found to provide the best overall performance and requires only slightly more effort in application. The additional horizontal strip is an easy and quick solution, but it is less effective than mechanical anchorage configurations.

The failure of DMA and SDMA configurations was bearing failure of the FRP plates. The strain recorded by the strain gauges in the plates of the mechanical anchorage system was found to be much smaller than the ultimate strain at failure, demonstrating that the plates did not reach their ultimate tensile capacity.

Design recommendations based on this research include design equations, material properties, and detailing requirements for the mechanical anchorage systems investigated in this study.

A5.5 Suggestions for Future Research

Although the effective strain concepts adopted for design guidelines and codes provide a simple but practical estimation of the shear contribution of FRP, non-uniform FRP distribution should be investigated further to predict realistic strain levels of FRP and thus to develop more reliable design equations.

Parameters affecting the shear behavior of RC beams were identified through analysis of the existing database. Some of these parameters have not been fully investigated. Parameters of primary interest include various strengthening schemes, different FRP materials, shear span to depth ratio, and the effects of pre-cracking. The interactions among transverse steel reinforcement, longitudinal reinforcement, and FRP shear reinforcement demand immediate investigation.

Other types of mechanical anchorage systems should be studied to improve the effectiveness of FRP shear strengthening. The size effect may be more evident through testing of large-scale members without transverse steel reinforcement.

According to the experimental results of the PC girders, an actual shear gain due to the application of FRP strengthening was hardly obverved. However, it was found that FRP strengthening contributed some of the total shear resistance according to the shear component analysis performed in this project. It is believed that PC girders will obtain shear strength gain due to FRP strengthening if the failure modes are properly controlled, which may be related to the shape of the cross-sections. Therefore, a comphrehensive parametric study is needed to evaluate the effectiveness of FRP shear strengthening based on different cross-sectional shapes (i.e., different aspect ratios of web thickness to effective depth or flange thickness to effective depth of the girders).

Most of the experimental studies have involved short-term loading histories until failure of the specimen. However, long-term performance under service load conditions would provide a better measure of realistic behavior. The combination of long-term and short-term performance can be used to develop valid equations for strength and serviceability.

The embedment length of the anchor bolt, and spacing are an important issue in the design of mechanical anchorage systems. The embedment length should be sufficient to avoid a pull-out failure while the bolts should also be arranged so that a weak plane is not developed along the bolts. Although some research has investigated this issue, a comprehensive parametric study is necessary.

A6. FINITE ELEMENT MODEL ANALYSIS

A6.1 Development of Finite Element Model

Nonlinear finite element analyses were carried out and corresponding FE models have been developed during the project period. The two main objectives of FEM simulations were to: (1) predict the behavior of the test girders prior to experimental testing, (2) investigate the effects of additional parameters not considered in the experimental test matrix, and (3) monitor the global and local behavior of test girders not being observed from experimental measurements such as interface behavior between concrete and FRP sheets. The commercial FE program DIsplacement ANAlyzer (DIANA) was chosen to achieve these objectives. DIANA is a powerful program that not only has its own large library of structural elements and constitutive material models, but also includes a user-defined option where users, if necessary, may add specific elements and constitutive models to the program. This capability allows maximum flexibility for FE modeling. This is a very important aspect for FE models of RC and PC girders strengthened with FRP since they are mainly governed by many significant parameters which need to be accounted for such as aggregate interlock, dowel action, and softening effect of concrete. Specifically, when FRP material is applied to concrete structures as a strengthening material, more complicated modeling techniques are required. With the progress of the experimental studies, the calibration of the FE models was conducted with respect to both mechanical and technical aspects. Accordingly, a well-established FE model capable of simulating the global and local behavior of the RC and PC girders strengthened with FRP in shear was developed. Substantial improvements during the project period are explained in detail in this report.

A6.1.1 Important FE Modeling Techniques

Besides the calibration of FE models with respect to mechanical properties, FE simulations for concrete structures strengthened with FRP require several significant modeling techniques due to their specific configurations. In addition, one more technique is also needed for PC girders to simulate the prestressing process of the pretensioning method.

The most important technique of FE modeling in this project is the phased analysis of FE models which makes it possible to predict the response with respect to the time-dependent behavior of elements or materials. The software DIANA, has a special built-in option for phased analysis which highlights the suitability of this program for this project because the other software programs do not have this option. To demonstrate the different loading conditions of test girders under construction or loading history, a phased analysis technique is usually employed in the FE simulation. Between each phase, the finite element model is updated by addition or removal of elements and constraints. In each phase a separate analysis is performed, in which the results from the previous phases are automatically used as initial values. As illustrated in Figure A 6.1, the typical three phases of PC girder strengthened with FRP are: (a) a prestressing phase, (b) a pre-cracking phase, and (c) a loading phase which includes a step of FRP strengthening.

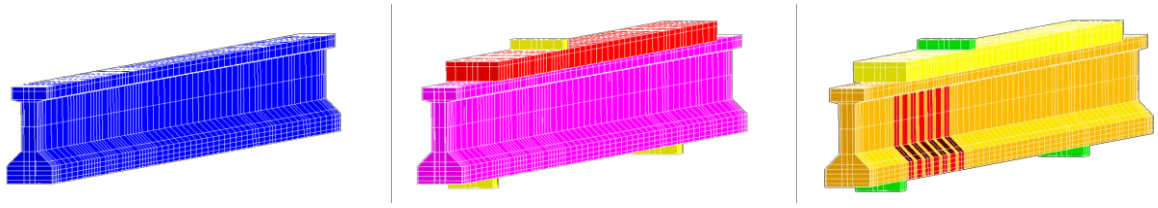

(a) Phase I: Prestressing (b) Phase II: Pre-Cracking (c) Phase III: Loading state

Figure A 6.1 Finite element models in each phase

The FE modeling of the FRP material itself and interfaces between two layers is another important technique. Besides the interface between concrete and FRP, the interface between two FRP layers can exist in some test girders due to the usage of FRP sheet as an anchorage system. In this case, the orthotropic material property of FRP requires a careful modeling technique. Composite structures are generally characterized by a sequence of layers with different material properties. In DIANA, the family of layered shell elements is particularly suited for the global analysis of composite structures. The orthotropic material can be modeled with orthotropic elasticity and an orthotropic plasticity model. In addition, the delamination of composite materials can be modeled accurately via a strategy in which the layers have an orthotropic linear elastic material behavior and the interface between the layers is connected by interface elements with nonlinear behavior. This technique enables the developed FE model to simulate the debonding failure of FRP explicitly as well as to investigate the insight behavior of interface regions which is impossible to do in experiments.

The prestressing process of tendons also requires a specified FE modeling technique. In the initial stage of the prestressing process, tendons are free from the mother specimen, followed by bonding to the specimen in the next stage. This process is actually a part of the phased analysis. Thus, the FE software should satisfy these two special options for proper simulation of test girders. DIANA has a special built-in option capable of simulating the unbonded state of embedded reinforcement. That is, in this state, the stiffness of the reinforcements does not contribute to the stiffness of the mother elements, nor do the reinforcement strains and stresses change with deformation of the mother element. When a prestress is specified for the reinforcements, then DIANA applies the prestressing force as an external loading to the mother elements with subsequent full bonding between tendons and the mother specimen. After bonding, the reinforcement contributes to the stiffness of the mother elemen,t and the reinforcement strains and stresses change upon deformation of the mother element.

The background theories and detailed application of the mentioned techniques will be explained in the corresponding sections.

A6.1.2 Substantial Improvements of Finite Element Analysis

Continuous improvements of FE analyses have been conducted during the project period with respect to significant aspects needed for simulating the actual structural behavior of test girders. In addition, geometries of test girders and corresponding test set-ups have been changed several times. Accordingly, substantial improvements of FE analyses have been achieved. Detailed improvements are explained in this section according to the time sequence of improvements.

A6.1.2.1 Initial State of FE Analysis with Three-Dimensional FE Models (DIANA) and Two-Dimensional FE Models (FEAP)

Preliminary analyses had been carried out at the initial state of the FE analysis via two- and three-dimensional FE models before experimental results were available. These analyses focused on the modeling aspects of the FE model rather than considering the reliable mechanical behavior of the test girders. Despite the coarse analyses of these initial FE models, the results helped predict behavior of test girders and possible weakness of test set-up which was not the typically adopted method in girder tests.

In the first step of the development of FE model, an additional Finite Element Analysis Program (FEAP) was also used to backup the results of the initial FE models simulated by DIANA. At this time, DIANA was used to analyze three-dimensional models for the test girders and FEAP was used for two-dimensional models, respectively. Due to the fine meshes of the FE model by DIANA, it was discovered that DIANA required a great deal of time to generate reliable non-linear analysis results. For example, the required time to run a non-linear finite element model for a test girder strengthened with FRP was found to be 36 hours with only a small number of loading steps. Thus, two-dimensional models for the test girders were also augmented using the finite element program FEAP (Finite Element Analysis Program) developed by R.L. Taylor at UC-Berkeley. FEAP is a general purpose finite element analysis program which is designed for research and educational use. User functions can be developed and added to the program. The FEAP program includes options for defining one, two, and three dimensional meshes, along with a wide range of linear and nonlinear solution algorithms. In addition, the running time for an analysis by FEAP was found to be much smaller than that of DIANA, which allowed the MST research team to obtain an immediate overview of the behavior of the girders while designing them. Although the results obtained by FEAP analysis are not as accurate as those obtained by DIANA analysis, the quick results obtained from FEAP were very useful during the design process.

At this state, four analysis cases were considered for DIANA and FEAP as shown in Table A 6.1. The analysis cases were divided according to the spacing between stirrups and whether or not FRP strengthening was used. Only cases 1 and 2 had been analyzed by DIANA due to the current time limitations, while all four cases were analyzed by FEAP. However, FEAP used a continuous wrapping scheme instead of strips of FRP for modeling due to its modeling capability limitations. Due to this shortcoming , FEAP was only used at this stage, namely, the design stage of test girders. Figure A 6.2 shows the DIANA FE model at this stage. Detailed configurations of DIANA FE models are explained in the corresponding section including information for used elements, material properties, constraints, and loading conditions, etc.

Table A 6.1 Analysis Cases of the Initial FE Models

Cases	Stirrup Spacing	FRP Strengthening Types	Corresponding Test Girders and IDs
1	12 in.	No FRP Strengthening	T4-12-Control
2		Strip/90	T4-12-S90-NA (not exist in test matrix)
3	18 in.	No FRP Strengthening	T4-18-Control
4		Strip/90	T4-18-S90-NA

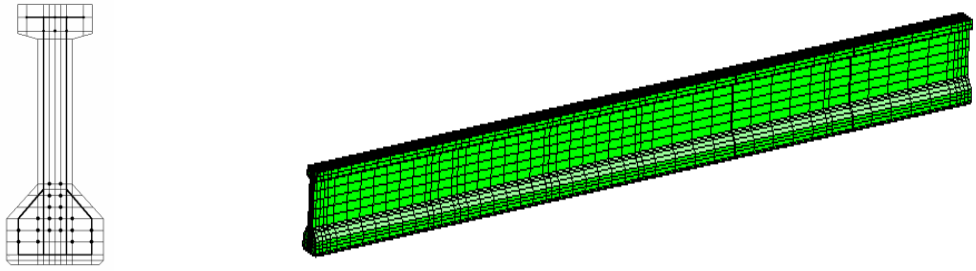

(a) Cross section (b) Longitudinal section

Figure A 6.2 FE Model of DIANA at the Initial State

Shear force-displacement relations obtained from FEAP and DIANA are presented in Figure A 6.3 and analytical shear strengths are compared with the calculated values of two specifications, ACI (ACI 318, 2008) and AASHTO LRFD (AASHTO, 2008), in Table A 6.2. Because FEAP cannot take into account the shear behavior in the FE models, there are no significant ultimate shear failure points in the shear force-displacement diagram as shown in Figure A 6.3(a). Therefore, the failure load of FEAP was assumed to occur at the same ultimate displacement of the DIANA model.

As shown in Figure A 6.3(b), there are apparent peak points in both analysis cases simulated by DIANA. In case 1, a sudden failure occurred in the shear region at the peak point, which was considered as shear strength, and no plastic deformations were observed. Contrary to case 1, it can be seen that after the peak point, plastic deformations are observed in analysis case 2. This post-peak behavior is caused by gradual concrete crushing at the support region with load increase. The corresponding crack patterns at the peak point as shown in Figure A 6.4 can supplement the failure mechanisms of both analyses cases as explained above.

DIANA predictions for the shear strength of analysis case 1 are almost the same as the ACI (ACI 318, 2008) calculations and 1.13 times greater than the AASHTO LRFD (AASHTO, 2008) calculations, while in the case of analysis case 2, 0.87 times smaller than the ACI (ACI 318, 2008) calculations, and 1.05 times greater than the AASHTO LRFD (AASHTO, 2008) calculations, respectively. FEAP results are always greater than ACI (ACI 318, 2008) and AASHTO LRFD (AASHTO, 2008) calculations. For analysis case 1, FEAP predictions are 1.45 and 1.61 times greater than ACI (ACI 318, 2008) and AASHTO LRFD (AASHTO, 2008) calculations, respectively. For analysis case 2, which considered the effect of FRP strengthening, FEAP predictions are 1.04 and 1.26 times greater than ACI (ACI 318, 2008) and AASHTO LRFD (AASHTO, 2008) calculations. Similar observations can be made in Cases 3 and 4.

From these preliminary analyses, the accuracy of DIANA was roughly confirmed on predicting the behavior of the three dimensional finite element models of the test specimens. Based on these analyses, further improvements of FE models have been conducted.

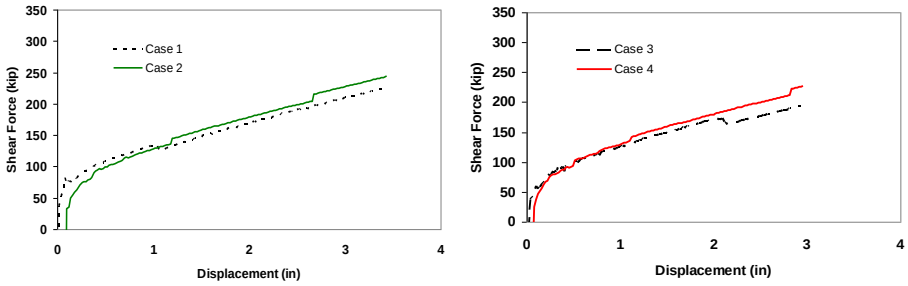

(a) FEAP

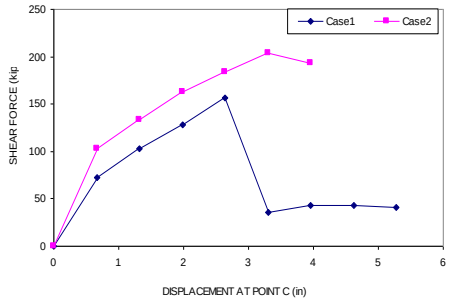

(b) DIANA

Figure A 6.3 Shear Force-Displacement Relations Simulated by FEAP & DIANA

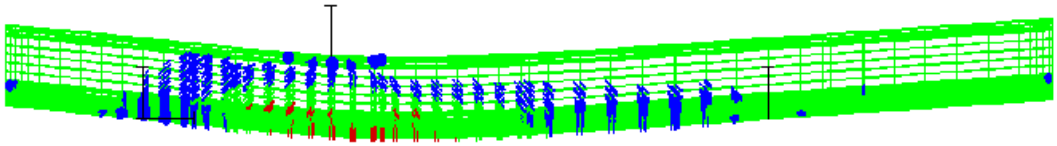

(a) Analysis Case 1

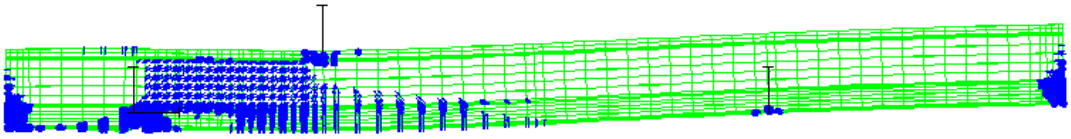

(b) Analysis Case 2

Figure A 6.4 Crack Patterns at the Ultimate State

Table A 6.2 Comparison of Shear Strengths between FEAP, DIANA, ACI (ACI 318, 2008), and AASHTO LRFD (AASHTO, 2008)

Cases	Shear Strength (kips)				Ratio			
	FEAP	DIANA	ACI	LRFD	FEAP /ACI	FEAP /LRFD	DIANA /ACI	DIANA /LRFD
1	225	157.5	155.2	139.9	1.45	1.61	1.01	1.13
2	244	204	235.5	194.2	1.04	1.26	0.87	1.05
3	194	-	141.6	120.8	1.37	1.60	-	-
4	228	-	211.9	176.4	1.10	1.30	-	-

A6.1.2.2 Two- and Three Dimensional FE Analyses with DIANA

The purpose of conducting two-dimensional FE analysis was to better investigate the behavior of concrete under a combined state of stress, which had been calibrated in the literature versus experimentally tested two-dimensional concrete panel elements. The parameters of the concrete constitutive law used in the three-dimensional FE model were not calibrated versus experimental data since no such data existed in the literature. The results of the two-dimensional FE analysis were therefore used to refine the input parameters of the three-dimensional model in order to improve the accuracy of the solution. Only representative analysis cases related with concrete material properties, namely control girders, are presented in this report and summarized in Table A 6.3.

Table A 6.3 Analysis Cases of Two- and Three-Dimensional FE Analysis

Cases	Model Dimensions	Stirrup Spacing	Corresponding Test Girders and IDs
1	2D	12 in.	T4-12-Control
2		18 in.	T4-18-Control
3	3D	12 in.	T4-12-Control
4		18 in.	T4-18-Control

Figure A 6.5 shows the configurations of two- and three-dimensional FE models, and the shear strengths obtained from these models are summarized and compared with the corresponding specifications in Table A 6.4. In these analyses, wider bearing plates were assumed to avoid bearing failure at the support regions observed in the initial FE analyses due to insufficient bearing area. Accordingly, the bearing plates in the real test also had the same geometries assumed in these FE models. These wide bearing plates prevented the bearing failure at the supporting regions and simultaneously induced a perfect shear failure on the web of girders resulting in an increase of shear strengths as compared with the initial FE analyses. As summarized in Table A 6.4, the shear strengths of three-dimensional FE models are higher than those of two-dimensional FE models. Specifically, girders with 12 in. stirrups are more affected by dimensionality, while girders with 18 in. stirrups are not. This phenomenon can be related with the lateral strain effects of concrete which depend on the confinement and softening effects.

Figure A 6.6 shows the principal compressive stress contours for analysis cases 1 and 2 at the ultimate state. At this state, the maximum compressive stress of concrete struts is around 2.75 ksi and 2.5 ksi for the two cases, respectively. These values are smaller by a factor of 0.39 and 0.35 respectively than the original concrete strength used of 7 ksi. From these results, it is clear that a considerable amount of concrete softening has taken place in the shear dominant region. Based on these results, the softening effect of concrete was taken into account in the following FE analyses in order to better calibrate the model parameters. Background theories and application of the softening effect are explained in the corresponding section.

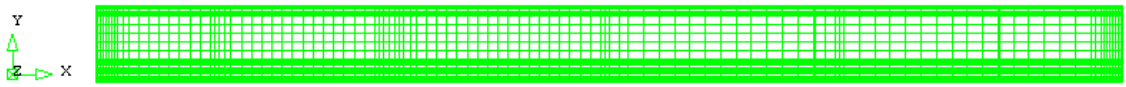

(a) Two-Dimensional FE Model

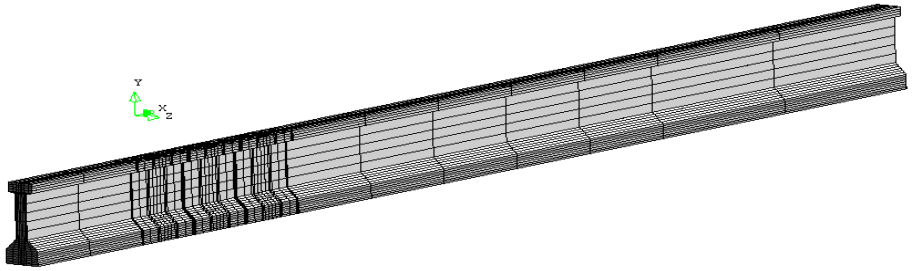

(b) Three-Dimensional FE Model

Figure A 6.5 Two- and Three-Dimensional FE Models by DIANA

Table A 6.4 Comparison of Shear Strengths between Two- and Three-Dimensional DIANA Models, ACI, and AASHTO LRFD

Cases	Shear Strength (kips)			Ratio	
	DIANA	ACI 440 2R-02	AASHTO LRFD	DIANA/ACI	DIANA/LRFD
1	209	155.2	139.9	1.35	1.49
2	204	141.6	120.8	1.44	1.69
3	227	155.2	139.9	1.46	1.62
4	208	141.6	120.8	1.47	1.72

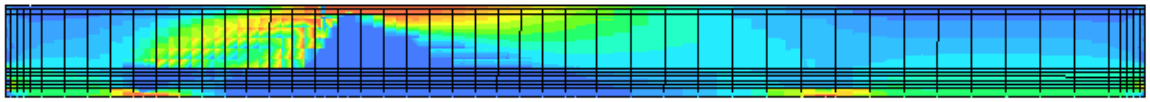

(a) Case 1

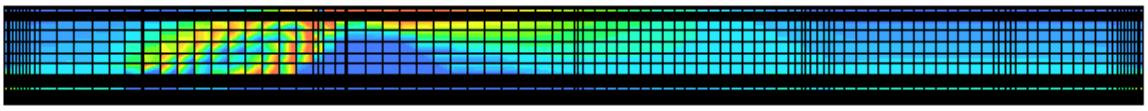

(b) Case 2

Figure A 6.6 Principal Compressive Stress Contour at the Ultimate State

A6.1.2.3 Reduction of Mesh Density

Fine meshes of FE models required an excessive running time for nonlinear analysis and made it difficult to examine the trial parameters being considered in this project. Accordingly, proper reduction of mesh density was performed.

Figure A 6.7 shows the change of the cross-sectional finite element mesh used in the three-dimensional modeling. Figure A 6.7(a) shows the cross-sectional mesh used in the initial three-dimensional FE models. In this model, all reinforcements were modeled as embedded reinforcement elements supported by DIANA at each location. To reduce the number of FE meshes, reinforcements located in the same heights were lumped as shown Figure A 6.7(b). This cross-sectional mesh was used for the following FE models. Besides the change of cross-

sectional mesh, the mesh in the longitudinal direction also changed according to the purpose of each FE model. After reducing the mesh density, the running time had been significantly reduced, and final results were almost the same between the two models.

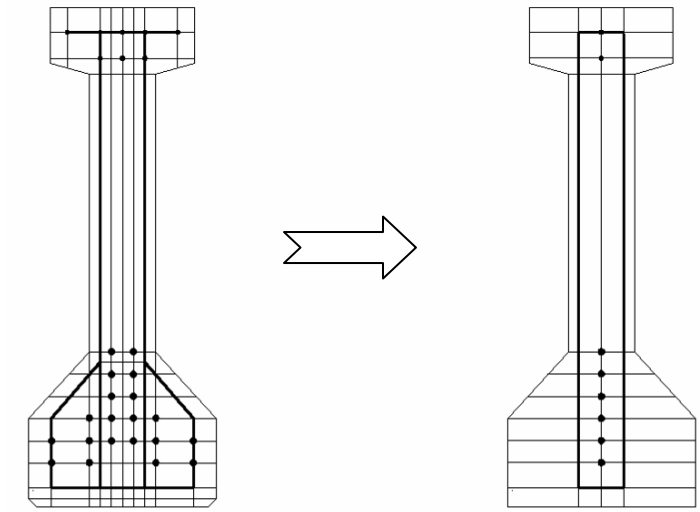

(a) Initial FE Model (b) Updated FE Model

Figure A 6.7 Change of Cross Sectional Mesh

A6.1.2.4 Calibration of Concrete Properties – Softening Effect

Softening effect of concrete is a very important factor that affects the shear behavior of RC structures. Well known truss models, such as the MCFT and STM, are also based on the concept of softening effect of concrete. As observed in two- and three-dimensional FE analyses, the principal compressive stresses at the ultimate state were significantly lower than the concrete strength. Thus, the softening effect of concrete should be included in FE models. To examine the softening effect of concrete on shear behavior, trial analyses were carried out and compared with test results of both PC control girders, namely, T4-12-control and T4-18-control, respectively.

The shear force-displacement relationships for both control girders, with or without the softening effect, are depicted in Figure A 6.8. As shown in Figure A 6.8(a), the FE model taking into account the softening effect showed better prediction than the FE model disregarding the softening effect in terms of the ultimate shear strength and the entire behavior compared with the experimental result of test girder, T4-12-control. Specifically, the FE model taking into account the softening effect almost exactly predicted the post-peak behavior of the experimental results. Although there were small discrepancies between the prediction of the FE model and experimental results in test girder T4-18-control as shown in Figure A 6.8(b), the overall tendency was well captured by the FE model, especially in the post-peak behavior. An interesting phenomena was observed from both figures. The initial stiffness of the FE models was typically larger than the initial stiffness of the experimental results, especially in Figure A 6.8(b). There seemed to be several reasons such as the settlement of the test set-up at the initial loading period and the effect of upward loading, etc. Nevertheless, as observed in these analyses, the softening effect of concrete significantly affected not only the ultimate shear strength but also the overall behavior, especially the post-peak behavior. Thus, the softening effect had been taken into account in the subsequent FE models.

A6.1.2.5 Modeling of Interface Regions and Anchorages

Due to the fact that structural strengthening is achieved by the interfacial normal and shear stresses transferred from the FRP sheets to the concrete surface through the adhesive layer, the overall structural behavior of FRP strengthened structures is strongly dependant on the mechanical behavior of the adhesive layer between the concrete and FRP sheets, denoted by the interface region.

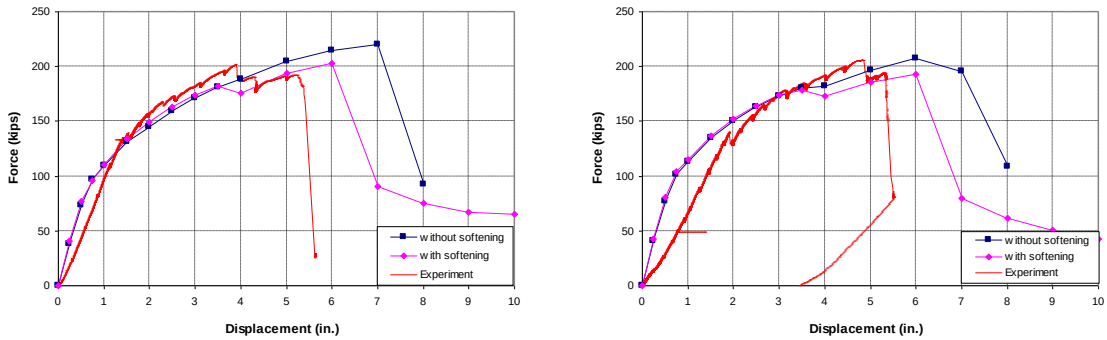

(a) T4-12-control (b) T4-18-control

Figure A 6.8 Shear Force vs. Displacement of FE Models with or without Softening Effect

The initial two- and three-dimensional FE models in this project disregarded the modeling of the interface regions similar to most other research work in this area. It meant that the interface regions between the concrete and FRP sheets were assumed to be perfectly bonded resulting in perfect composite action between FRP sheets and the corresponding concrete surface. The two-dimensional FE models usually adopted this assumption due to the dimensional restriction and the simplicity of modeling. This assumption can give a reasonable result in the elastic region but cannot in the plastic region. The boundary of elastic and plastic regions can be distinguished from the moment of delamination of FRP sheets. Thus, sophisticated modeling strategies are required in modeling the interface region to simulate more realistic behavior of FRP strengthened structures.

Throughout careful review of the literature, proper interface elements and material models in three-dimensional FE models were adopted in the developed FE models. In addition, several attempts to simulate the mechanical anchorages have been also made. Figure A 6.10 shows an initial FE model representing the configurations of strengthened FRP having mechanical anchorages. In this model, the mechanical anchorage was modeled with 2-node interface elements at the location of steel anchors to represent the mechanical anchorage itself. The material properties for these anchorages followed the specifications provided by the steel anchor manufacturer. The effect of anchorage plates used in test was disregarded in this model. To encompass possible factors of anchorage systems, more detailed modeling techniques for the anchorage systems were introduced as shown in Figure A 6.10. An anchorage system by means of horizontal strips was modeled with a layer by layer approach as shown in Figure A 6.10(a). That is, the interface elements were applied in each layer which was a layer between the concrete surface and 45° FRP strips and a layer between 45° FRP strips and horizontal strips, respectively. Mechanical anchorage systems are modeled by adjusting the material properties of interface elements located in the anchorage plates according to averaged stress distribution under the plate as shown in Figure A 6.10(b). Averaged normal and shear traction stresses were derived from the

capacity of anchors provided by manufacturers and geometrical conditions of plates. All background theories and modeling methods related to the interface and mechanical anchorages are explained in the corresponding sections.

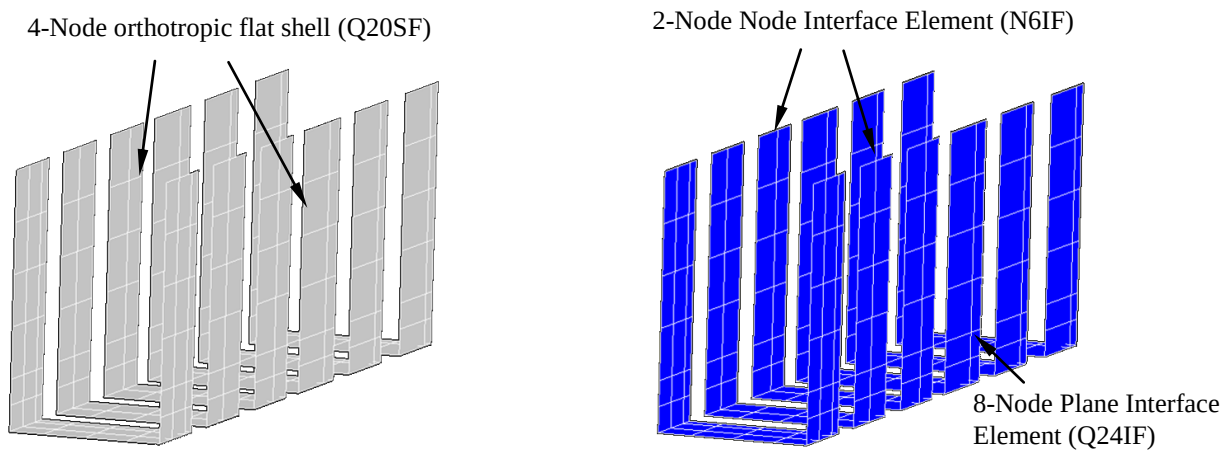

(a) FRP Sheets (b) Interface and Mechanical Anchorage

Figure A 6.9 Initial FE models of FRP sheets, Interface and Mechanical Anchorage

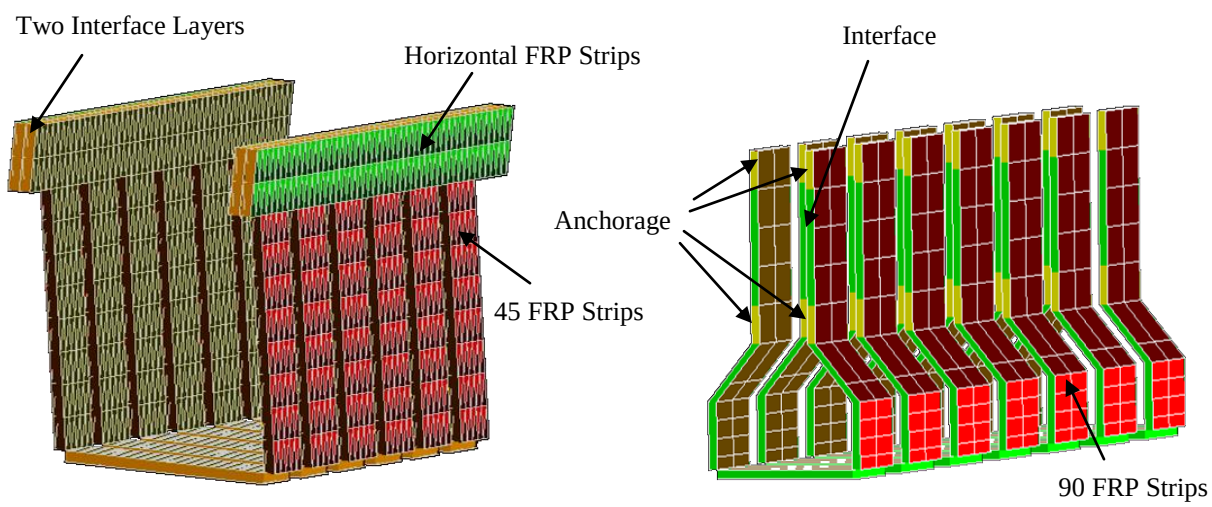

(a) Horizontal FRP (b) Mechanical Anchorage

Figure A 6.10 Updated FE models of Anchorage Systems

A6.1.2.6 Improvement of Elements

Usage of proper elements capable of rationally simulating the behavior of components is the most important part in FE modeling. In this project, improvements of elements in FE models have been made to the FRP sheets and the concrete due to the variable configurations of FRP strengthening scheme. When FRP sheets were orthogonally applied in the test girders, quadrilateral elements were used for modeling of FRP sheets and interface, brick elements for the concrete as shown in Figure A 6.11. However, it was impossible to use these elements on test girders diagonally strengthened with FRP sheets due to the restriction of their geometries.

Accordingly, triangular elements were used for FRP sheets and interface, and edge elements for the concrete as shown in Figure A 6.12.

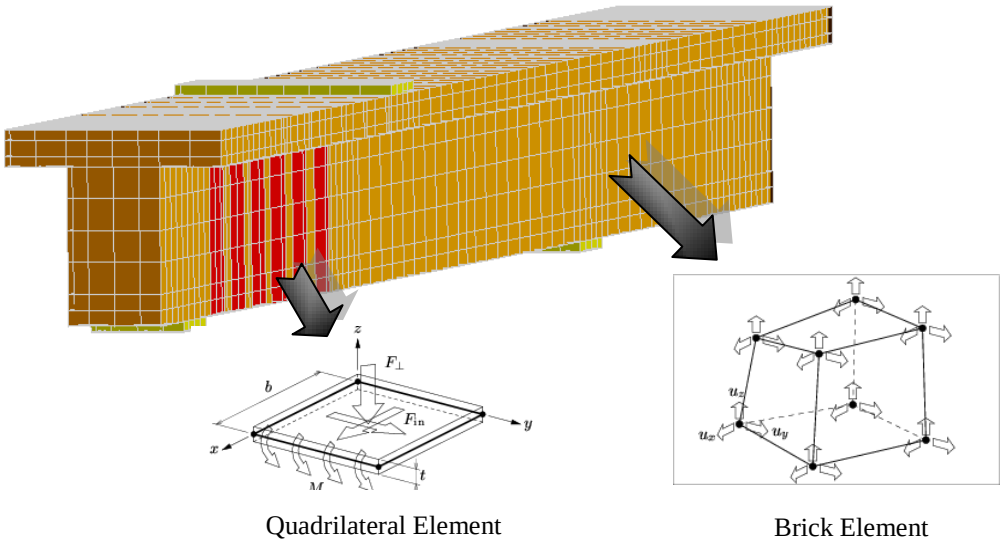

Figure A 6.11 FE Models Strengthened with Orthogonal FRP Sheets

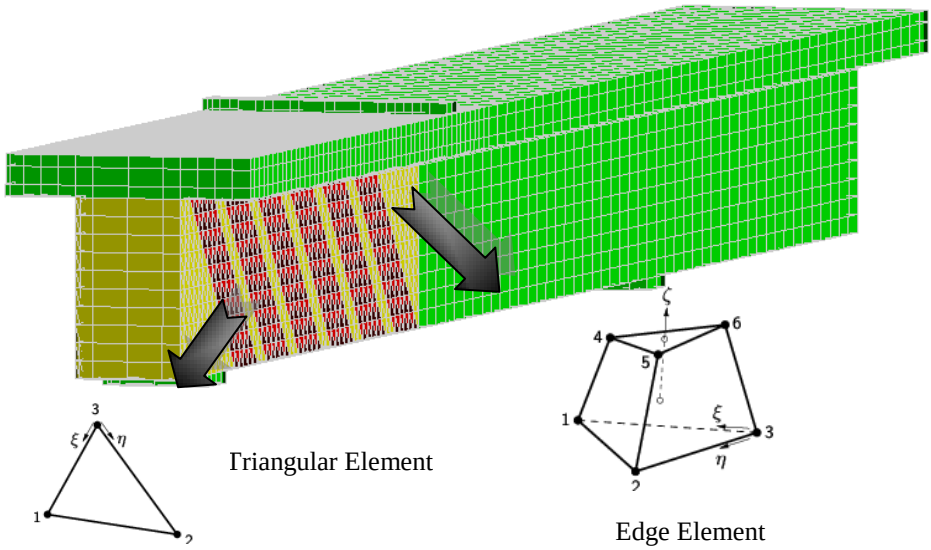

Figure A 6.12 FE Models Strengthened with Orthogonal FRP Sheets

A6.2 Configuration of FE Models and Background Theories

General configurations of FE models with respect to RC and PC girders are described in the first section followed by detailed background theories for the elements and material models used.

A6.2.1 Configurations of FE Models for RC and PC Girders

Based on modeling techniques and improvements explained in the previous sections, the configurations of the finalized FE models for RC and PC girders are briefly explained next.

A6.2.1.1 FE Models for RC Girders

Two representative FE models for test girders, test I.D. RC-12-S45-HA and RC-12-S90-SDMA-PC, are chosen to show general configurations of FE model because these models are representative ones, employing all elements and modeling techniques used in the other FE models.

Figure A 6.13 shows both FE models. As explained in the previous section, different elements are introduced in the FE model for test girder RC-12-S45-HA due to the diagonal strengthening scheme of FRP sheets as shown in Figure A 6.13(a). Except for different strengthening regions which needed the use of different elements for concrete, FRP sheets and interface region, most other configurations are identical in terms of geometries and material properties.

The eight-node isoparametric solid brick element (HX24L in DIANA) has been chosen for modeling the concrete in the un-strengthened regions and loading plates in both FE models, while a six-node isoparametric solid wedge element (TP18L in DIANA) was used for the concrete of the test region in test girder RC-12-S45-HA. Except for test specimens strengthened with 45° FRP strips, most FRP sheets were modeled with four-node quadrilateral orthotropic flat shell elements (Q20SF in DIANA) also taking into account the wrinkling effect, which is characterized by the fact that compression stresses cannot be resisted by FRP, while a three-node triangular isoparametric flat shell element (T15SF in DIANA) was used for test girder RC-12-S45-SDMA. Accordingly, the interface elements in both FE models were also different as an eight-node quadrilateral interface element (Q24IF in DIANA) was used along with the brick element, while a six-node triangular interface element (T18IF in DIANA) was used with the wedge element. Because the concept of zero thickness of interface had been applied in the FE models, the interface regions could not be observed in the final FE models as shown in the upper parts of Figure A 6.13. Thus, the figure of interfaces and FRP sheets illustrated in Figure A 6.13(a) is the one obtained during the process of FE modeling.

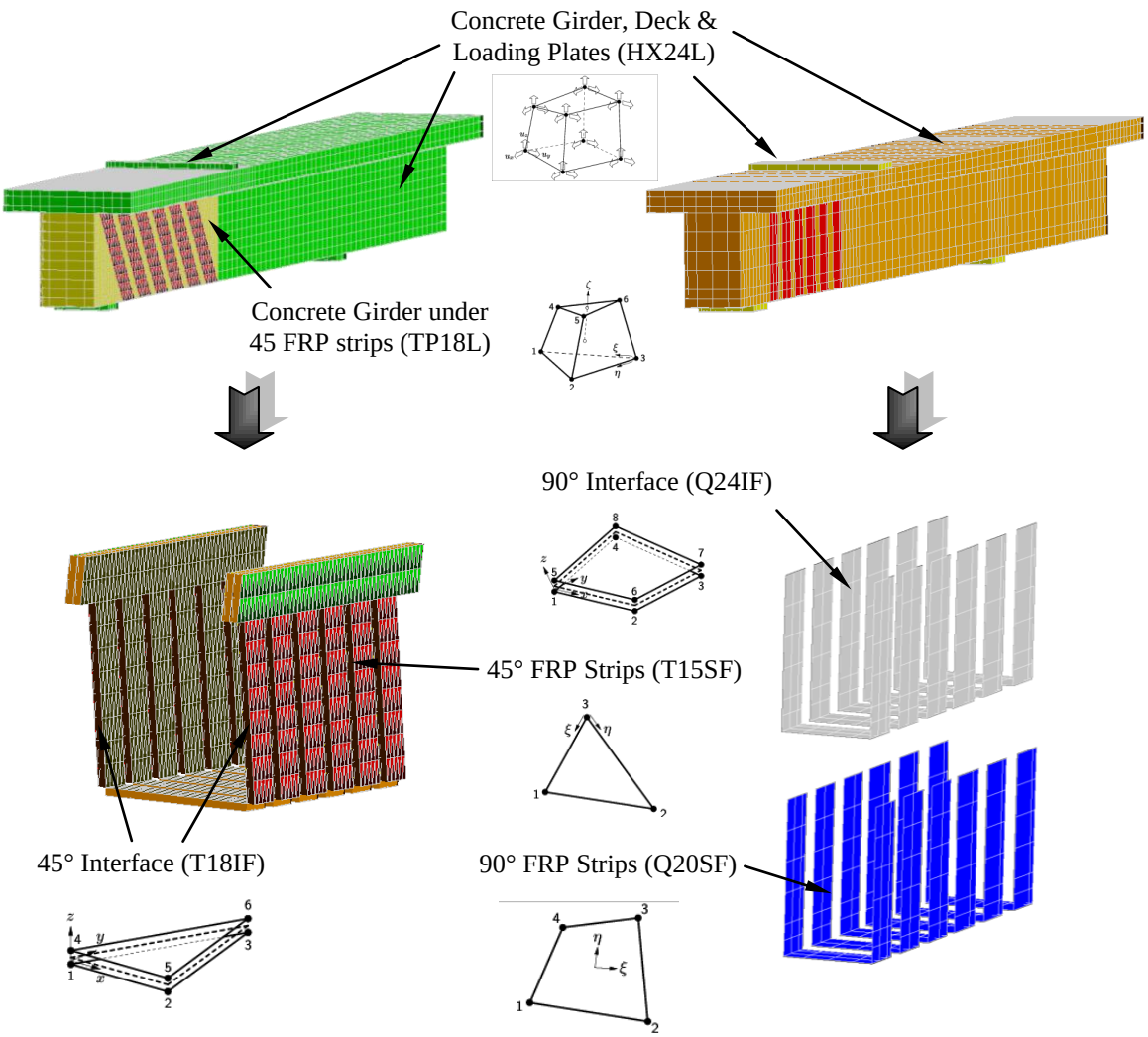

(a) RC-12-S45-HA (b) RC-12-S90-SDMA-PC

Figure A 6.13 Configurations of FE Models for RC Test Girders

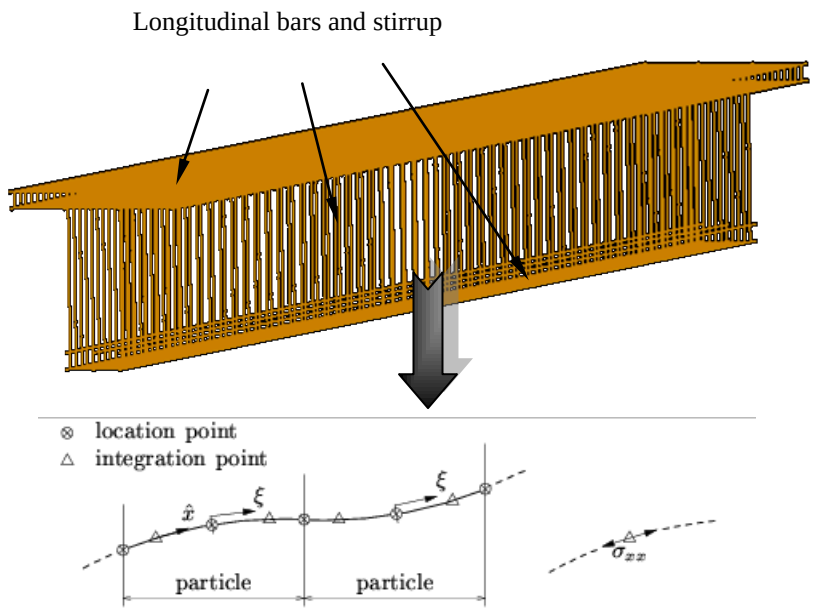

Figure A 6.14 Reinforcement of RC Test Girder

The reinforcing steel was modeled as embedded bar elements specialized by DIANA as shown in Figure A 6.14. Their main characteristics are as follows:

- Reinforcements are embedded in structural elements, the so-called mother elements.
- Reinforcements do not have degrees of freedom of their own.
- By default, reinforcement strains are computed from the displacement field of the mother elements. This implies perfect bond between the reinforcement and the surrounding material.

For nonlinear analyses, the embedded formulation with perfect bond may be too coarse. For such cases, employing separate truss elements for the reinforcement and connecting them to the surrounding structural elements via interface elements makes them capable of representing the bond stress-slip relations between reinforcement and concrete. However, this method requires an excessive computational effort especially for the three-dimensional FE model. Thus, developed FE models in this project assume perfect bond between concrete and reinforcing steel.

A6.2.1.2 FE Models for PC Girders

Figure A 6.15 shows a representative FE model for PC test girder, T3-18-S90-SDMA. Most features of this model are similar to the FE models of RC test girders except for considering the prestressing process of strands. In addition, this model illustrates an updated modeling method for the mechanical anchorages as mentioned above. This method does not affect the choice of the element representing the mechanical anchorage region but the material properties of the selected elements.

Elements used in this model are similar to the FE models for RC test girders. The eight-node isoparametric solid brick element (HX24L in DIANA) has been chosen for modeling the girder concrete, deck concrete, and loading plate. The four-node quadrilateral orthotropic flat shell element (Q20SF in DIANA) was used for the FRP sheets while the eight-node quadrilateral

interface element (Q24IF in DIANA) was used for the interface regions. The figure of interfaces and FRP sheets illustrated in Figure A 6.15 is also obtained during the process of FE modeling.

The most important and interesting feature of FE modeling for PC girders is the simulation of the process of prestressing. This simulation was possible to carry on by a special built-in input option in DIANA. Reinforcing steels and tendons in PC girders, can be unbonded to the embedding elements, namely the mother elements, during the prestressing process using this option. After the prestressing process, tendons are assumed to be perfectly bonded to the embedding elements similar to the other reinforcing steels. Because this simulation requires a time-dependent analysis, the phased analysis technique is considered as a fundamental analytical method for modeling the prestressing process. Figure A 6.16 shows the reinforcements of the FE model for PC girders. All reinforcing steels including tendons are also modeled as embedded bar elements specialized by DIANA with different geometrical and material properties. Thus, it can be said that the unbonded state of tendons is just a part of the physical conditions of reinforcing steels. Accordingly, the first diagram of Figure A 6.16 illustrates the reinforcement arrangement at the prestressing phase. At this stage, the tendons are unbonded to the embedding elements. After this stage, the tendons are bonded to the embedding elements and additional reinforcements are added in the FE model with the addition of the concrete deck as shown in the second figure.

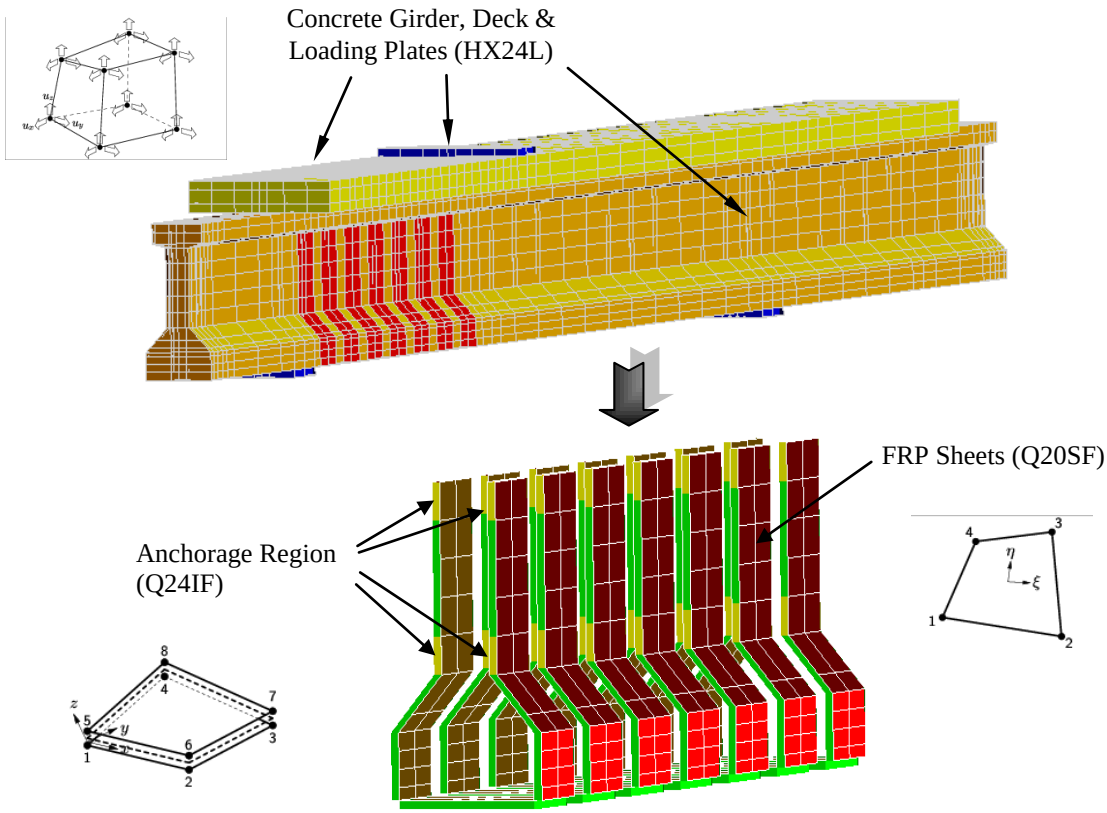

Figure A 6.15 Configurations of FE Models for PC Test Girders

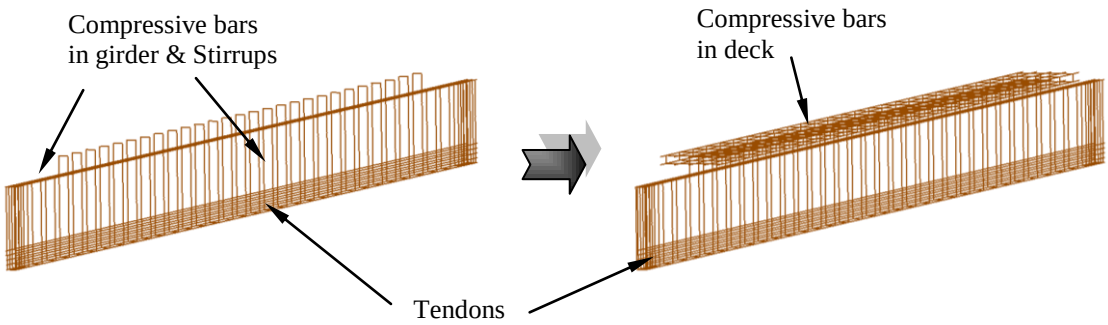

Figure A 6.16 Reinforcement of PC Test Girder

A6.2.2 Background Theory of Used Elements

This section summarizes the background theory of the elements used in the developed FE models.

A6.2.2.1 Flat Shell Elements (FRP Sheet) - Q20SF (4 nodes, quadrilateral) & T15SF (3 nodes, triangular)

Flat shell elements basically are a combination of plane stress elements and plate bending elements as shown in Figure A 6.17. But unlike the plane stress elements, the basic variables are forces rather than Cauchy stresses. Flat shell elements must fulfill the following conditions with respect to shape and loading:

They must be plane, i.e., the coordinates of the element nodes must be in one flat plane, the *xy* plane of the element, otherwise the curved shell elements must be used. They must be thin, i.e., the thickness *t* must be small in relation to the dimension *b* in the plane of the element. Force loads F may act in any direction between perpendicular to the plane and in the plane. Moment loads M must act in the plane of the element.

Flat shell elements are characterized by the following facts. The normal of the element plane remains straight after deformation, but by definition, they do not have to be perpendicular to the element plane. The displacement perpendicular to the plane does not vary in the direction of the thickness.

As mentioned above, the flat shell elements basically are combinations of a plane stress element and a plate bending element, and there is no coupling between membrane and bending behavior. Generally, the membrane behavior is based on its corresponding plane stress element except the primary stresses which are defined in terms of moments and forces rather than Cauchy stresses. The bending behavior is based on the Mindlin-Reissner theory and its corresponding Mindlin plate bending element. For all flat shell elements, the numerical integration is only performed in the reference surface.

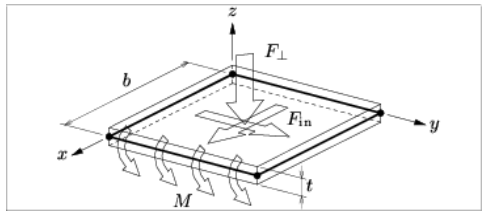

Figure A 6.17 Characteristics of Flat Shell Element

Two regular flat shell elements were used in the developed FE models depending on the FRP strengthening scheme. One is a four-node quadrilateral isoparametric flat shell element, Q20SF, and the other is a three-node triangular isoparametric flat shell element, T15SF, as shown in Figure A 6.18.

In both elements, the plate bending is based on the Mindlin-Reissner theory with an adapted transverse shear interpolation. The geometry and the displacements are interpolated by bi-linear functions. The integration perpendicular to the element face is direct. The polynomials for the translations u and the rotations φ with respect to both elements can be expressed as follows:

For Q20SF :

$$u_i(\xi,\eta) = a_0 + a_1\xi + a_2\eta + a_3\xi\eta \qquad \text{(A6-1)}$$

$$\varphi_i(\xi,\eta) = b_0 + b_1\xi + b_2\eta + b_3\xi\eta \qquad \text{(A6-2)}$$

For T15SF :

$$u_i(\xi,\eta) = a_0 + a_1\xi + a_2\eta \qquad \text{(A6-3)}$$

$$\varphi_i(\xi,\eta) = b_0 + b_1\xi + b_2\eta \qquad \text{(A6-4)}$$

(a) Q20SF (b) T15SF

Figure A 6.18 Used Flat Shell Elements in FE Models

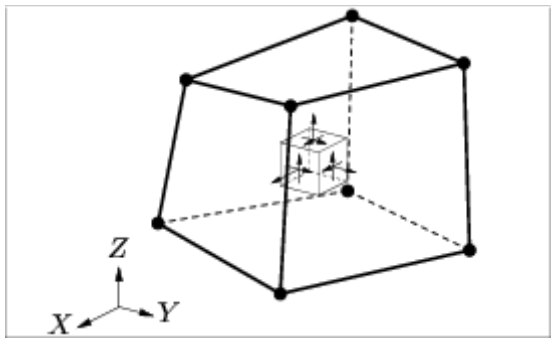

Figure A 6.19 Characteristics of Solid Element

A6.2.2.2 Solid Elements (Concrete) – HX24L (8 nodes, brick) & TP18L (6 nodes, wedge)
Figure A 6.19 shows the characteristics of solid elements which are general purpose elements. However, because of their tendency to produce large systems of equations, these elements are usually applied only when other elements are unsuitable or would produce inaccurate analysis results. Solid elements are characterized by the following properties. The stress situation is three-dimensional; the loading may be arbitrary, and the dimensions exist in three axial directions X, Y and Z are of the same order of magnitude. Typical applications of solid elements are the analysis of voluminous structures like concrete foundations and off-shore structures, thick walls and floors, and soil masses.

Two regular solid elements were used in the developed FE models. One is an eight-node isoparametric solid brick element, HX24L, and the other is a six-node isoparametric solid wedge element, TP18L, as shown in Figure A 6.20.

The HX24L element is based on linear interpolation and Gauss integration. The polynomials for the translations u_{xyz} can be expressed as Equation A6-5. Typically, a rectangular brick element approximates the following strain and stress distribution over the element volume. The strain ε_{xx} and stress σ_{xx} are constant in the *x* direction and vary linearly in the *y* and *z* directions. The strain ε_{yy} and stress σ_{yy} are constant in the *y* direction and vary linearly in the *x* and *z* directions. The strain ε_{zz} and stress σ_{zz} are constant in the z direction and vary linearly in the x and y direction.

$$u_i(\xi,\eta,\zeta) = a_0 + a_1\xi + a_2\eta + a_3\zeta + a_4\xi\eta + a_5\eta\zeta + a_6\zeta\xi + a_7\xi\eta\zeta \qquad \text{(A6-5)}$$

The TP18L element is based on linear area interpolation in the triangular domain and a linear isoparametric interpolation in the ζ direction. The polynomials for the translations u_{xyz} can be expressed as Equation A6-6. These polynomials yield a constant strain and stress distribution over the element volume.

$$u_i(\xi,\eta,\zeta) = a_0 + a_1\xi + a_2\eta + a_3\zeta + a_4\xi\eta + a_5\eta\zeta \qquad \text{(A6-6)}$$

(a) HX24L (b) TP18L

Figure A 6.20 Used Solid Elements in FE Models

A6.2.2.3 Interface Elements (Interface & Anchorage) – Q24IF (4+4 nodes, plane quadrilateral), T18IF (3+3 nodes, plane triangular) & N6IF (1+1 nodes)

The interface elements describe the interface behavior in terms of a relationship between the normal and shear tractions and the normal and shear relative displacements across the interface. Typical applications for interface elements are elastic bedding, nonlinear-elastic bedding (for instance, no-tension bedding), discrete cracking, bond-slip along reinforcement, friction between surfaces, joints in rock, masonry, etc. With respect to shape and connectivity, there are three types of interface elements. Because the line interface element is out of interest, only nodal and plane interface elements are illustrated in Figure A 6.21 in terms of topology and displacements.

- **Nodal interface element (N61F)**
  This element should be placed between two nodes. With this element, the interface surface and directions are user-specified. However, this element cannot be applied in geometric nonlinear analysis.
- **Line interface element**
  This element should be placed between truss elements, beam elements or edges of two-dimensional and shell elements. With these elements the interface surface and directions are evaluated automatically from the geometry of the element itself. This element to shell element cannot be applied in geometric nonlinear analysis.
- **Plane interface elements (T18IF & Q24IF)**
  This element should be placed between faces of three-dimensional elements. With these elements, the interface surface and directions are also evaluated automatically from the geometry of the element itself.

The formulation of the line and plane interface elements is fully isoparametric. This means that the quadratic line interface elements may be straight as well as curved, and that the plane interface elements may be flat as well as curved.

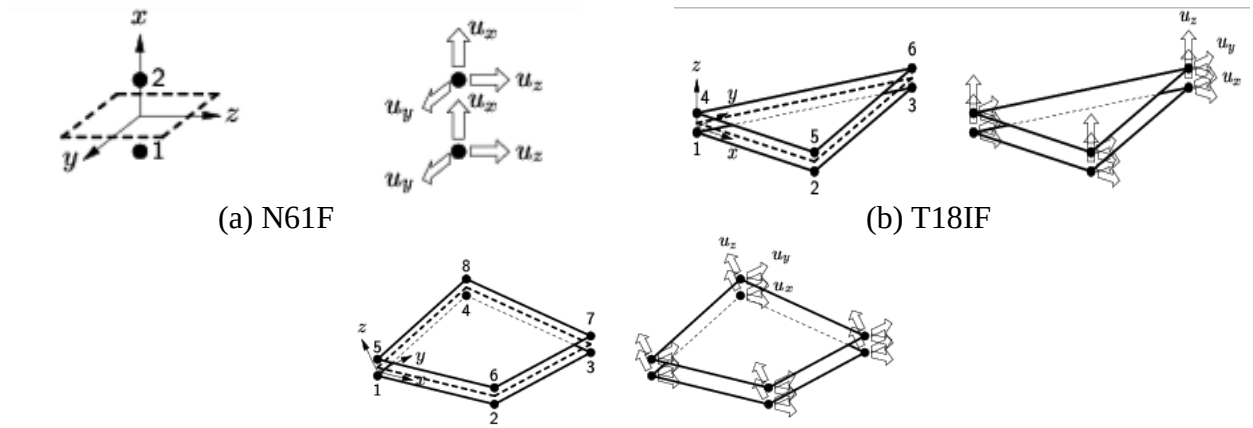

Figure A 6.21 Used Interface Elements in FE Models

The basic variables for interfaces are the nodal displacements Δu_e. The derived values are the relative displacements Δu and the tractions t. The interface elements describe a relation between Δu and t across the interface. The actual set of variables depends on the dimensionality of the interface element as follows.

<u>Two-dimensional</u>

Variables of two-dimensional interfaces are oriented in the local *xy* axes and expressed as Equation A6-7.

$$u_e = \begin{Bmatrix} u_x \\ u_y \end{Bmatrix} \qquad \Delta u = \begin{Bmatrix} \Delta u_x \\ \Delta u_y \end{Bmatrix} \qquad t = \begin{Bmatrix} t_x \\ t_y \end{Bmatrix} \tag{A6-7}$$

The normal traction t_x is perpendicular to the interface while the shear traction t_y is tangential to the interface as shown in Figure A 6.22.

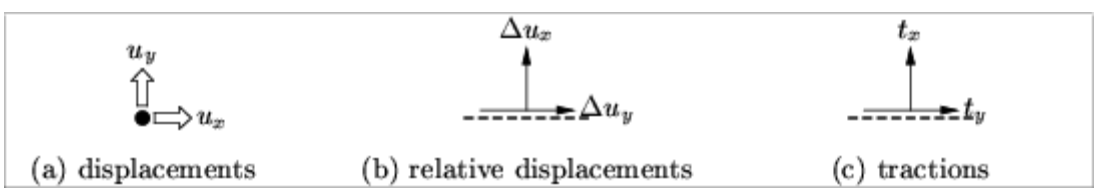

Figure A 6.22 Variables of Two-Dimensional Interfaces

<u>Interfaces to shells</u>

Variables of interfaces to shell elements are oriented in the local *xyz* axes. Compared to the two-dimensional interface elements, these elements additionally have a translational degree of freedom u_z and a rotational degree of freedom ϕ_x which give compatibility to curved shell elements.

$$u_e = \begin{Bmatrix} u_x \\ u_y \\ u_z \\ \phi_x \end{Bmatrix} \qquad \Delta u = \begin{Bmatrix} \Delta u_x \\ \Delta u_y \\ \Delta u_z \end{Bmatrix} \qquad t = \begin{Bmatrix} t_x \\ t_y \\ t_z \end{Bmatrix} \tag{A6-8}$$

The normal traction t_x is perpendicular to the interface while the shear tractions t_y and t_z are tangential to the interface as shown in Figure A 6.23.

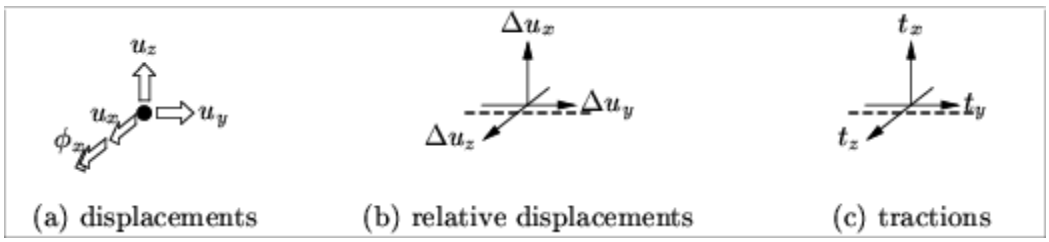

Figure A 6.23 Variables of Interface Elements to Shells

<u>Three-dimensional Interfaces</u>

Variables of three-dimensional interfaces are oriented in the local *xyz* axes.

$$u_e = \begin{Bmatrix} u_x \\ u_y \\ u_z \end{Bmatrix} \qquad \Delta u = \begin{Bmatrix} \Delta u_x \\ \Delta u_y \\ \Delta u_z \end{Bmatrix} \qquad t = \begin{Bmatrix} t_x \\ t_y \\ t_z \end{Bmatrix} \tag{A6-9}$$

Similar to interface elements to shells, the normal traction t_x is perpendicular to the interface while the shear tractions t_y and t_z are tangential to the interface as shown in Figure A 6.24.

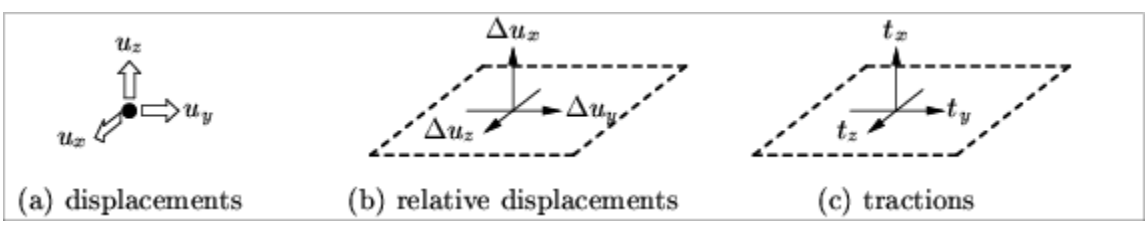

Figure A 6.24 Variables of Three-Dimensional Interfaces

A6.2.3 Background Theory of Material Properties & Modeling Method

This chapter addresses the overview of material models with respect to concrete, reinforcements, FRP sheets and interfaces. Besides fundamental background theories of material properties, literature reviews related to this subject are also included.

A6.2.3.1 Concrete

The constitutive model of concrete follows the total strain concept, also called the "Total Strain crack model," which describes the tensile and compressive behavior of the material with a uniaxial stress-strain relationship affected by lateral strains. This makes the modes very well suited for Serviceability Limit State (SLS) and Ultimate Limit State (ULS) analyses in either two- or three-dimensional models which are predominantly governed by cracking or crushing of the material. A constitutive model based on total strain describes the stress as a function of the strain. One commonly used approach is the coaxial stress-strain concept, in which the stress-strain relationships are evaluated in the principal directions of the strain vector. This approach, also known as the Rotating Crack model, is applied to the constitutive modeling of reinforced concrete and has shown that it is well suited for reinforced concrete structures. More appealing to the physical nature of cracking is the fixed stress-strain concept in which the stress-strain relationships are evaluated in a fixed coordinate system which is fixed upon cracking. Both approaches are easily described in the same framework where the crack directions are either fixed or continuously rotating with the principal directions of the strain vector. The basic concept of the Total Strain crack models is that the stress is evaluated in the directions given by the crack directions. The FE model developed in this report adopted the Rotating Crack model concept with Thorenfeldt et al. (1987) uniaxial model for the concrete compressive behavior and an exponential softening relation for the concrete tensile behavior based on fracture energy related to a crack bandwidth as commonly adopted in smeared crack models.

In cracked concrete, large tensile strains perpendicular to the principal compressive direction reduce the concrete compressive strength. The compressive strength is consequently not only a function of the uni-axial compressive strain ε_1, but also a function of the lateral strains governing the tensile damage in the lateral directions, ε_2 and ε_3. Accordingly, the softening effect for concrete compressive stresses caused by lateral cracking perpendicular to the principal compressive direction was also considered by adoption of the softening coefficient in the modified compression field theory (MCFT) proposed by Vecchio and Collins (1993). However, MCFT is derived and calibrated for two-dimensional problems, that is, the relation between ε_1 and ε_2. The three-dimensional extension to this theory was proposed by Selby and Vecchio (1993) assuming the average lateral strain given by $\varepsilon_{lat} = \sqrt{\varepsilon_2^2 + \varepsilon_3^2}$.

A6.2.3.2 Reinforcement and FRP Sheets

The constitutive behavior of the reinforcement was modeled by an elasto-plastic material model with hardening. Accordingly, both reinforcing steel and prestressing tendons in the FE models were assumed to be elastic-perfectly plastic disregarding the hardening effect.

Composite structures, like graphite-epoxy laminates, are generally characterized by a sequence of layers with different material properties. That is, the orthotropic material can be modeled with orthotropic elasticity and an orthotropic plasticity model. Accordingly, the FRP sheets in FE models were assumed linear elastic up to failure along the orthotropic directions of FRP sheets.

A6.2.3.3 Interface Regions

Due to the fact that structural strengthening is achieved by the interfacial normal and shear stresses transferred from the FRP sheets to the concrete surface through the adhesive layer, there

has been a concentration of research efforts on characterization and modeling of debonding failure in recent years.

Figure A 6.25 Types of Debonding in FRP Strengthened RC Members

Theoretically, debonding in FRP strengthened members can take place within or at the interfaces of materials that form the strengthening system. To date, six failure modes have been identified from experimental investigation as shown in Figure A 6.25: (1) FRP delamination, (2) adhesive/FRP interfacial failure, (3) adhesive failure, (4) concrete/adhesive interfacial failure, (5) concrete substrate failure, and (6) concrete cover delamination failure along the main bar. A majority of the debonding failures reported in the literature took place in the concrete substrate. However, depending on the geometric and material properties, other debonding mechanisms can also be observed. Parallel with the experimental research efforts taking into account various parameters affecting the debonding failures, considerable progress on the theoretical models and numerical analysis has been achieved. Research studies on the theoretical models are classified in general terms by their approach to the problem as strength and fracture approaches. In addition to these, a number of researchers have proposed relatively simple semi-empirical and empirical models that avoid the complexities of stresses and fracture analyses and can be relatively easily implemented in design calculations. These are well summarized by Chen and Teng (2001) and Buyukozturk et al. (2004).

Meanwhile, two numerical approaches, which are macro and micro level FE analysis with respect to two- and three-dimensional FE models have been used for simulating several debonding failure modes based on the developed theoretical models. In the FE model, the interface element is located between the concrete element and the FRP element. In the unloaded stage, the interface element exists between two nodes that have identical coordinates. However, when the load is applied, the nodes behave independently based on the response of the interface element. At this time, the bond stress-slip relationship is the most important factor in assessing the behavior of the interface element. It depends on the compressive strength of concrete as well as the bond materials, such as the type of FRP and epoxy. Lu et al. (2005a) examined the existing representative theoretical bond stress-slip models classified with three categories addressed in the previous paragraph and finally proposed three bond stress-slip models from a meso-scale finite element model which was developed by Lu et al. (2005b). These models have been widely incorporated into the interface elements of FE models by many researchers. However, there are some minor issues related to the use of these models in numerical modeling of FRP shear-strengthened RC beams due to the difficulties of defining some of the variables

related to the geometrical conditions of the FRP and concrete. Sato and Vecchio (2003) proposed the bond stress-slip model considering the crack formation and the tension stiffening of tension chords with FRP sheets. This model was developed based on the concept of the distributed stress field model (DSFM, Vecchio, 2000), as an expanded model of the modified compression field theory (MCFT, Vecchio and Collins, 1986) and validated against test results (Kim and Vecchio, 2008). This model is not only free from the geometrical conditions of materials but is also applicable to the various types of FE models for FRP strengthened concrete members. In addition, the finite element analysis package DIANA used in this project is also based on the MCFT. With the advantages mentioned above, this bond stress-slip model was suitable to apply to the FE models in this project.

$$\tau_{bFy} = (54 f_c')^{0.19} \quad \text{(A6-10)}$$

$$G_f = (\tau_{bFy} / 6.6)^2 \quad \text{(A6-11)}$$

$$s_{Fy} = 0.057 G_f^{0.5} \quad \text{(A6-12)}$$

$$s_{Fu} = 2G_f / \tau_{bFy} \quad \text{(A6-13)}$$

Where τ_{bFy} = maximum bond shear stress; f_c' = compressive strength of the concrete; s_{Fy} = bond slip at the maximum bond shear stress; s_{Fu} = ultimate bond slip.

Most numerical studies have been conducted with the aim of verifying the proposed theoretical models or of comparing with test results. Depending on their specified purposes, various FE modeling techniques have been introduced for two- and three-dimensional FE models with respect to micro- and macro-level structures. According to careful review of these techniques, the most suitable one was chosen to improve the capacity of the FE models in this project.

In finite-element analysis, simulation of debonding is possible using two approaches as mentioned above. In the first approach, debonding is simulated by modeling the cracking and failure of the concrete elements adjacent to the adhesive layer based on fracture mechanics principals. This approach, referred to as a mesoscale model, utilizes a very fine mesh with small element sizes and generally requires large computational resources. This method is usually used to simulate and characterize the local debonding failure in the interface region by using two-dimensional FE models with the assumption of concrete substrate failure (Wu and Yin, 2003; Lu et al., 2005c; Coronado and Lopez, 2007; Lu et al., 2007). In the second approach, interface elements are utilized to predict the overall nonlinear behavior between the FRP and concrete regardless of the specific debonding failure modes. In other words, it can be said that this method can simulate the global debonding failure in the structural system. Most numerical analysis studies related with FRP strengthened concrete members incorporate this method by means of an FE software package used in their work. In literature, three approaches have been proposed to simulate debonding modes at the macro-level analysis and to predict the associated debonding loads. One approach involves simulating cracking and failure of the concrete adjacent to the adhesive layer using a relatively fine finite-element mesh similar to micro level analysis (Pham and Al-Mahaidi, 2005). In this approach, a smeared crack model that treats cracked concrete as a continuum is adopted. The second approach uses the discrete crack model to represent discontinuities due to major cracks, and a smeared crack model to represent the behavior

between cracks (Yang et al., 2003; Kishi et al., 2005; Niu and Wu, 2005). In the third approach, interface elements having a predefined bond-slip relation are used to link the FRP and concrete elements (Wong and Vecchio, 2003; Baky et al., 2007; Godat et al., 2007).

All of these approaches incorporate two types of elements, which are interface and bond elements respectively, into their FE models depending on the FE software package. Two appropriate bond element types are the link element and the one-dimensional contact element as shown in Figure A 6.26. The link element is more popular than the contact element due to its simplicity and therefore is more commonly used in two- and three-dimensional FE modeling for FRP strengthened RC members (Yang et al., 2003; Wong and Vecchio, 2003; Baky et al., 2007; Godat et al., 2007). This element allows relative displacements to take place between the two adherents. The difference in relative displacement between the concrete and FRP represents the slip at the interface. It is necessary to emphasize that these line elements do not directly represent the adhesive. They represent the overall concrete/FRP interfacial response, which depends on the concrete, the FRP, as well as the adhesive. This concept of interface elements is very similar to that of bond elements. That is, interface elements, which have pairs of overlapping nodes and a zero thickness, also do not directly represent the response of the adhesive as shown in Figure A 6.27. Depending on the dimensionality, a variety of element types are available and incorporated in many research studies (Pham and Al-Mahaidi, 2005; Kishi et al., 2005; Niu and Wu, 2005; Perez et al., 2005).

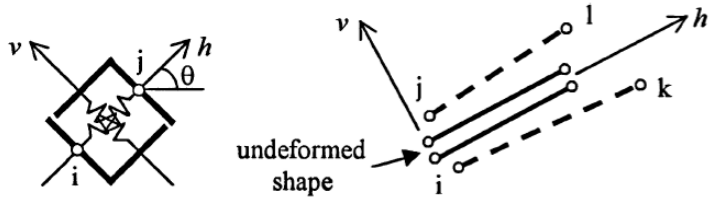

(a) Link Element (b) One-dimensional Contact Element

Figure A 6.26 Bond Elements

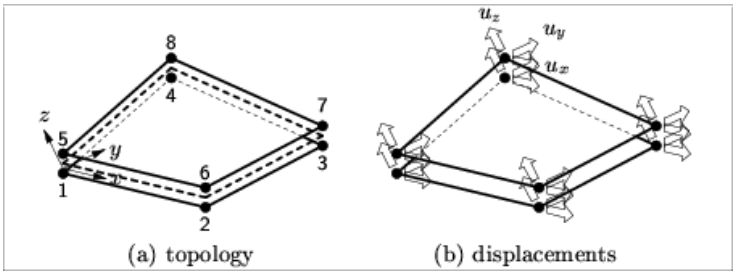

Figure A 6.27 3-Dimensioanl Interface Element

Because the micro approach is much more computationally expensive especially for three-dimensional statistical analysis, and since bridge engineers are more familiar with the local bond stress-slip constitutive characterization of the interfacial behavior used in conjunction with macro models, the macro approaches incorporated with the theories mentioned above were applied to the FE models in this project.

A6.3 Results and Discussions

Substantial analytical results such as overall behavior, shear strength, failure modes, and stress variations on each component are summarized and compared with test results with respect to RC and PC girders. The efficiency of the developed FE models is validated through these comparisons.

A6.3.1 Comparison between FEM and Experimental Results for PC Girders

A6.3.1.1 Shear Strength and Behavior

The experimental shear force-displacement relations are compared with FEM results with respect to all test girders except for test girder, T4-18-S45-DMA, as shown in Figure A 6.28, and the comparison of ultimate strengths is summarized in Table A 6.5.

Most FE results show a reasonable agreement with test results regarding the overall behavior shown in Figure A 6.28, while all experimental results were more ductile than the FE analytical results. There are several reasons for this phenomenon. For external environmental reasons, external prestressing in the vertical direction by Dywidag bars along the non-test regions was ignored in the FE model. In addition, there was an initial settlement of the test-set up during the test as a result of the upward loading system. These types of external effects with respect to experimental conditions cannot be considered as primary factors in the FE simulation. In other words, these particular effects can be easily removed when typical tests in shear are performed. In contrast to external effects, mechanical assumptions adopted in the FE modeling have a significant meaning for FE simulations regardless of external conditions. In this context, the smeared crack model used for concrete in FE simulations is the most important feature affecting the shear force-displacement relationships. The reason for this is the differences in crack patterns between test girders, which show some major discrete cracks, and the FE simulations. However, overall crack patterns were very similar between the simulations and the test results. In spite of these discrepancies, there are explicit evidences to prove the efficiency of the FE analysis in terms of simulating the global behavior, such as, accurate simulation of the cracking load and the ultimate strength, and consistent predictions of differences in ductility, as well as in terms of local behavior through strain and stress variations in each component.

As summarized in Table A 6.5, the average ratio of shear strength (V_{exp} /V_{FE}) is 1.04 with max ratio of 1.22 and min ratio of 0.95. Accordingly, the variance (VAR), standard deviation (STDEV) and coefficient of variance (COV) are calculated as 0.01, 0.07 and 0.07 respectively. Therefore, it can be said that the FE models can accurately predict the ultimate strength.

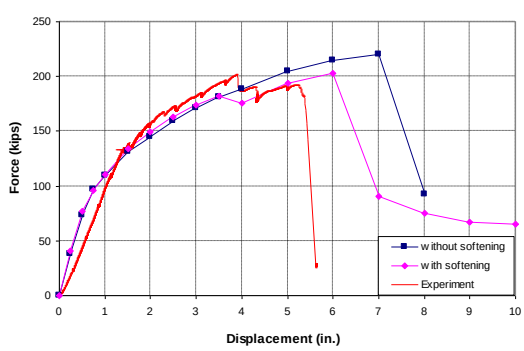

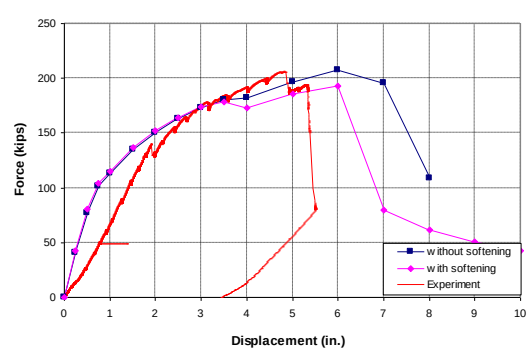

(a) T4-12-Control

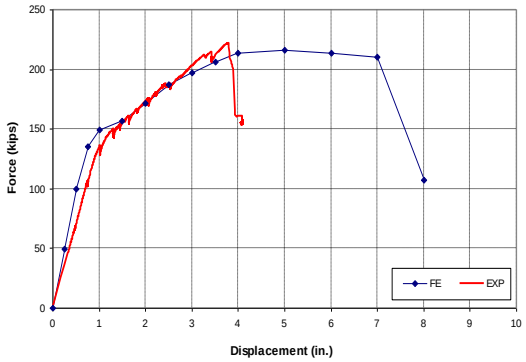

(b) T4-18-Control

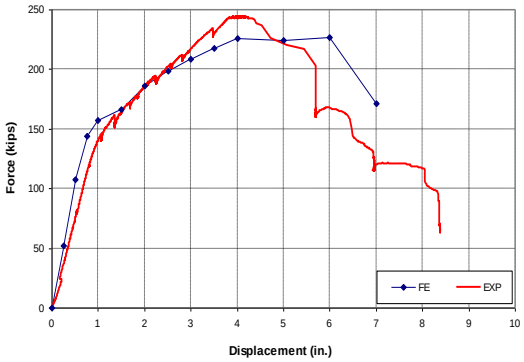

(c) T4-18-S90-NA

(d) T4-18-S90-CMA

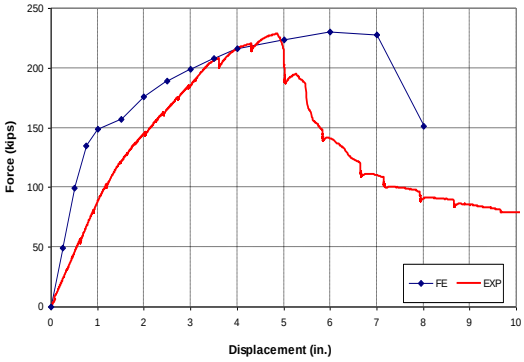

(e) T4-18-S90-DMA

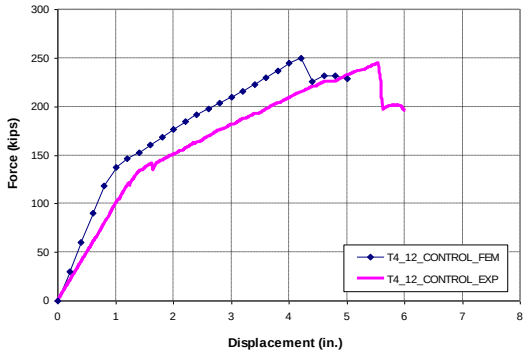

(f) T4-12-Control-Deck

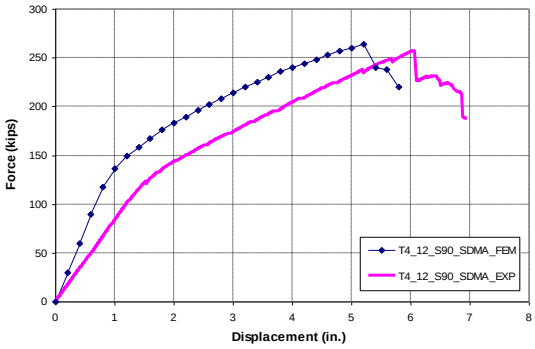

(g) T4-12-S90-SDMA

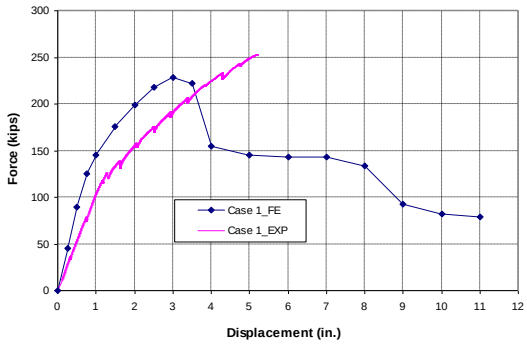

(h) T3-12-Control

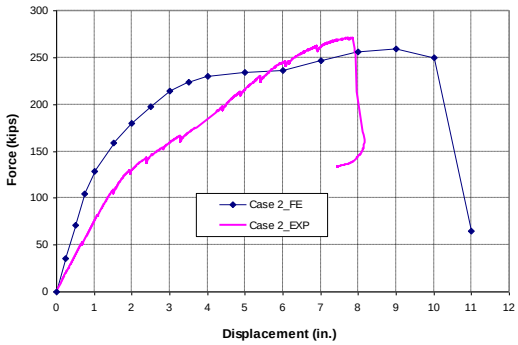

(i) T3-12-S90-NA

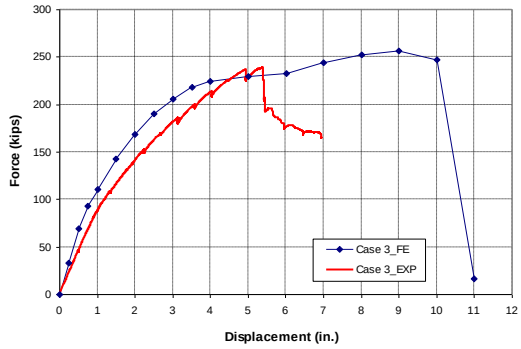

(j) T3-12-S90-NA-PC

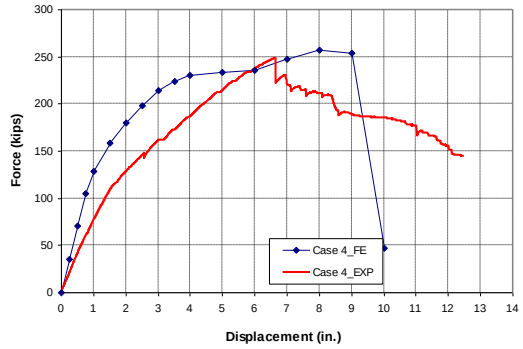

(k) T3-12-S90-DMA

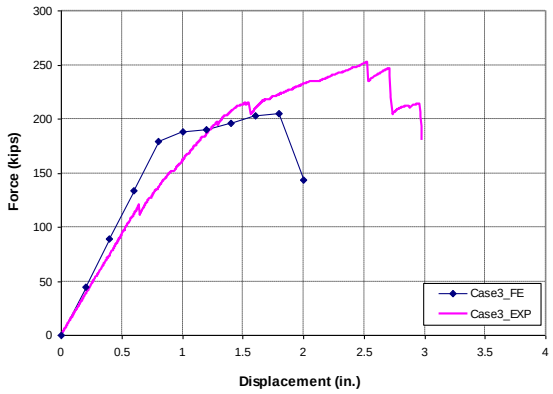

(l) T3-18-Control

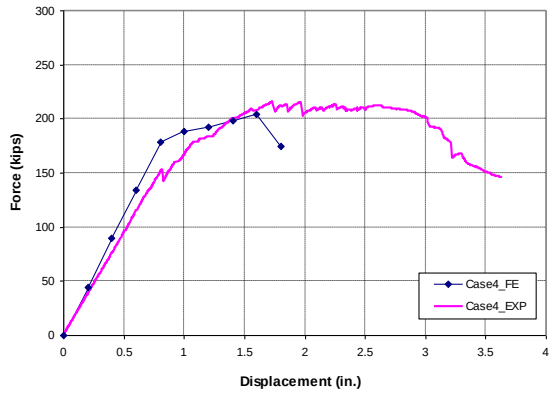

(m) T3-18-S90-NA

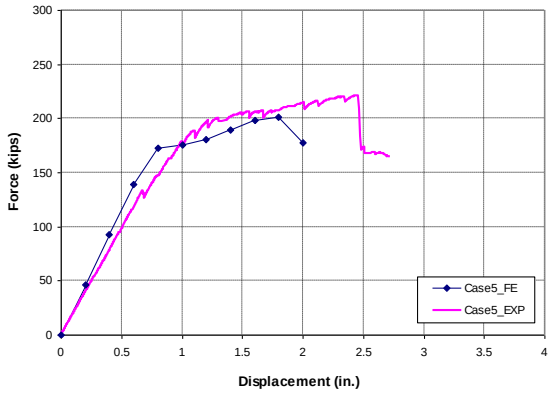

(n) T3-18-S90-HS

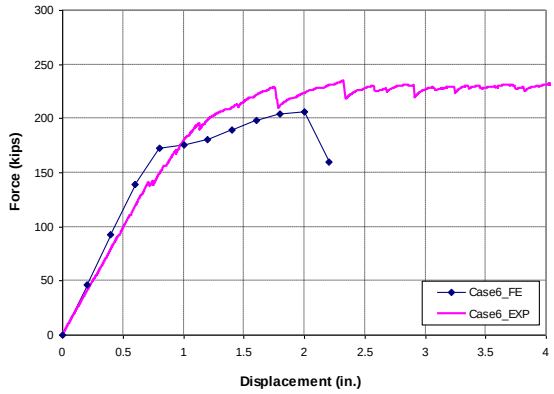

(o) T3-18-S90-SDMA

Figure A 6.28 Shear Force vs. Displacement at the Loading Point of PC Girders

Table A 6.5 Comparison of Shear Strengths of PC Girders

Test I.D.	Corresponding Figures	Shear Strength (kips)		Exp/FE
		Experiment	FE Analysis	
T4-12-Control	Figure A 6.28 (a)	201	203	0.99
T4-18-Control	Figure A 6.28 (b)	205	193	1.06
T4-18-S90-NA	Figure A 6.28 (c)	221	216	1.02
T4-18-S90-CMA	Figure A 6.28 (d)	244	227	1.07
T4-18-S90-DMA	Figure A 6.28 (e)	226	230	0.98
T4-12-Control-Deck	Figure A 6.28 (f)	245	250	0.98

T4-12-S90-SDMA	Figure A 6.28 (g)	256	264	0.98
T3-12-Control	Figure A 6.28 (h)	252	228	1.10
T3-12-S90-NA	Figure A 6.28 (i)	270	259	1.04
T3-12-S90-NA-PC	Figure A 6.28 (j)	244	257	0.95
T3-12-S90-DMA	Figure A 6.28 (k)	249	257	0.97
T3-18-Control	Figure A 6.28 (l)	252	205	1.22
T3-18-S90-NA	Figure A 6.28 (m)	212	204	1.04
T3-18-S90-HS	Figure A 6.28 (n)	220	201	1.09
T3-18-S90-SDMA	Figure A 6.28 (o)	235	204	1.15
AVERAGE	**-**	**-**	**-**	**1.04**
VAR	**-**	**-**	**-**	**0.01**
STDEV	**-**	**-**	**-**	**0.07**
COV	**-**	**-**	**-**	**0.07**

A6.3.1.2 Failure Modes

Comparison of the final failure modes can be another explicit evidence of the efficiency of the FE models as well. Because the developed FE models adopt the concept of smeared cracks, FE models cannot depict the exact crack patterns of test girders at the failure state which are usually governed by a few, critical, primary cracks—the so-called discrete cracks—but can give a glance of the overall failure modes. Crack patterns of test girders at the ultimate state are summarized in Table A 6.6 with respect to the experimental and FE analytical results.

Table A 6.6 Crack Patterns at the Ultimate State of PC Girders

Test I.D.	Experiment	FE Simulation
T4-12-Control	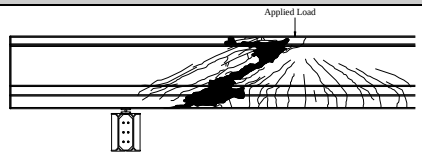	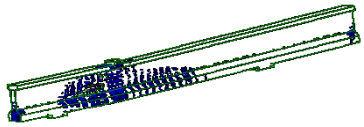
T4-18-Control	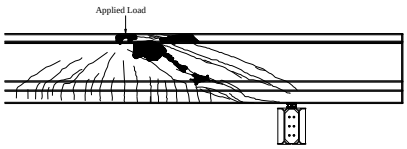	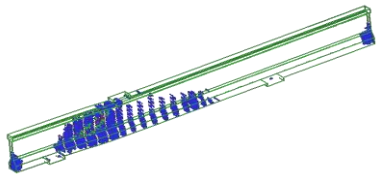
T4-18-S90-NA	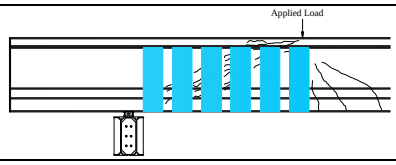	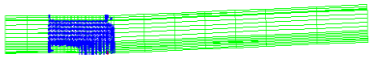
T4-18-S90-CMA	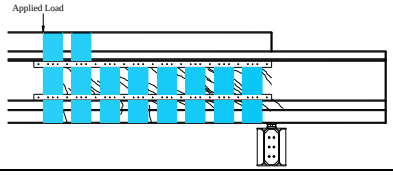	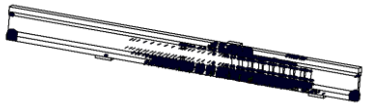

T4-18-S90-DMA	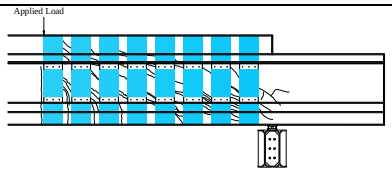	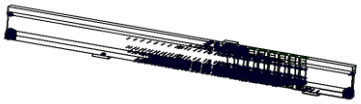
T4-12-Control-Deck	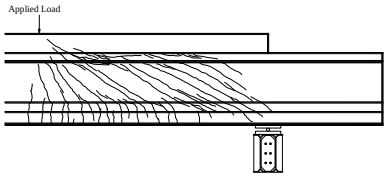	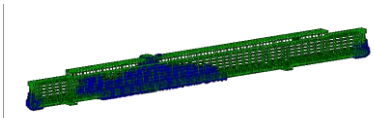
T4-12-S90-SDMA	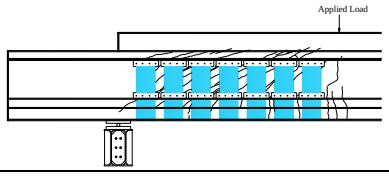	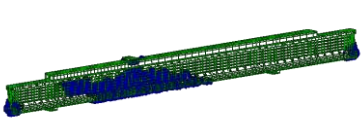
T3-12-Control	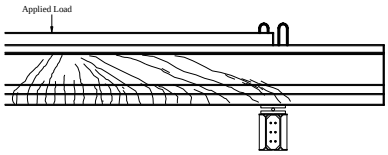	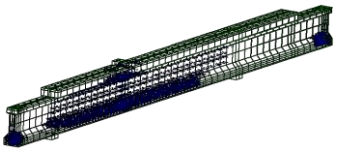
T3-12-S90-NA	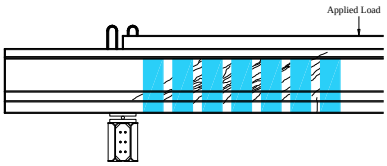	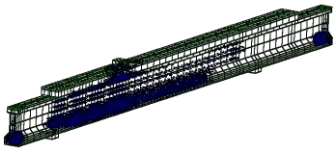
T3-12-S90-NA-PC	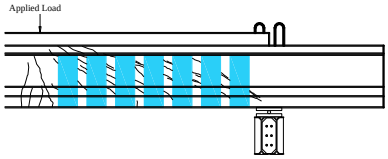	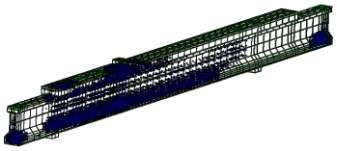
T3-12-S90-DMA	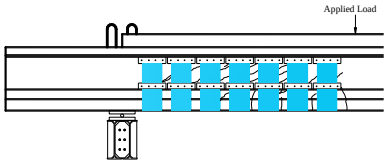	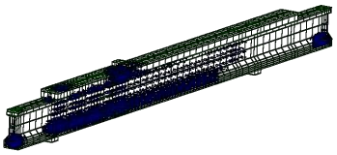
T3-18-Control	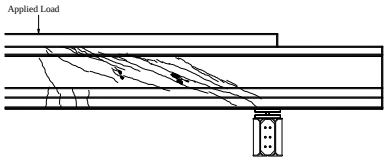	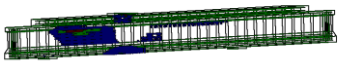
T3-18-S90-NA	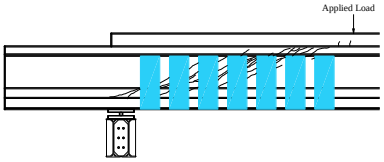	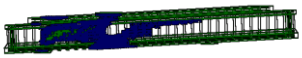

T3-18-S90-HS	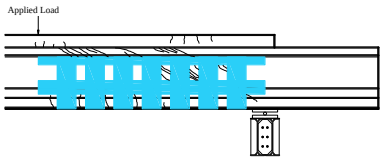	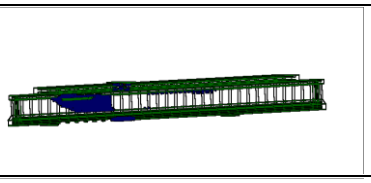
T3-18-S90-SDMA	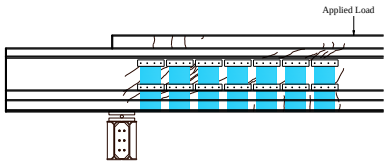	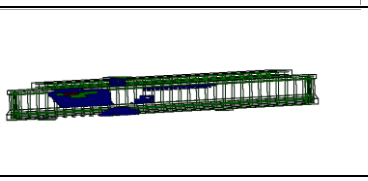

A6.3.1.3 Stress & Strain Variations on Each Component

The most beneficial aspect of FE analysis is its feasibility for investigating the detailed local behaviors of each component which are impossible to examine through experiments alone. In particular, there is no way to investigate the interface behavior between concrete and FRP sheets experimentally. This section describes detailed information about the local behavior of each component with respect to stress and strain variations. This supplementary information can also enhance the evidence for the efficiency of FE models. Due to a vast amount of information, a representative test girder, T3-12-S90-NA, is selected for this purpose.

Stress Variations on Concrete (Von Mises Stress and Principal Stress)

Figure A 6.29 shows various stress variations on concrete. These results can provide supplementary information for the final failure mode as well as a glance at the role of each component. In particular, the out-of-plane principal tensile stress contours shown in Figure A 6.29(d) have a special meaning. These stress variations indicate the role of interface along the out-of-plane normal direction, that is, they represent the normal traction of epoxy layer. Since it is impossible to measure these stresses in experiments, the investigation of these types of stresses is a substantial advantage of FE analysis.

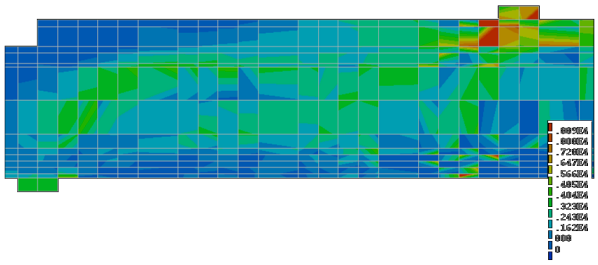

(a) Von Mises Stress

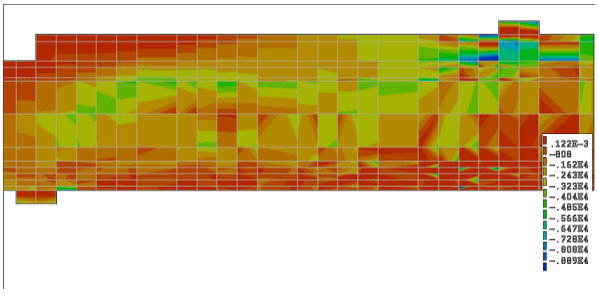

(b) Principal Compressive Stress

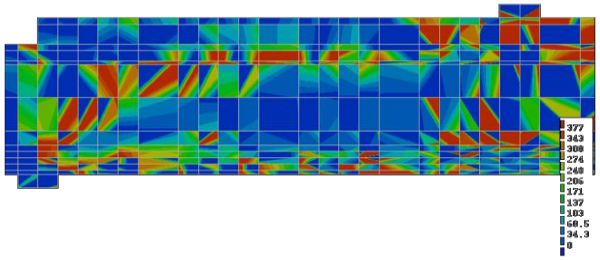

(c) Principal Tensile Stress

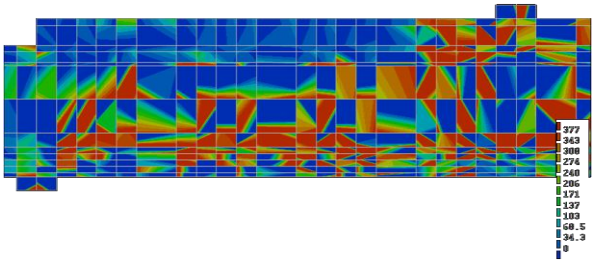

(d) Out of Plane Principal Tensile Stress

Figure A 6.29 Stress Variations on Concrete of PC Gider

Stress Variations on Steel (Von Mises Stress and Principal Stress)

Von Mises and principal stress variations on reinforcing steels are illustrated in Figure A 6.30. From these results, participating portions of reinforcing steels on the failure mechanism of a given structural system can be observed. In addition, relative stress variations on steel to FRP sheets provide the interaction relationship between the two materials. Similar to the out-of-plane stresses of concrete, it is also difficult to measure the stress variations on tendons during an experiment, which confirms another advantage of FE simulations.

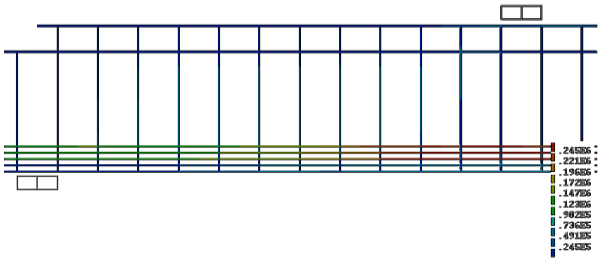

(a) Von Mises Stress on Reinforcing Steel

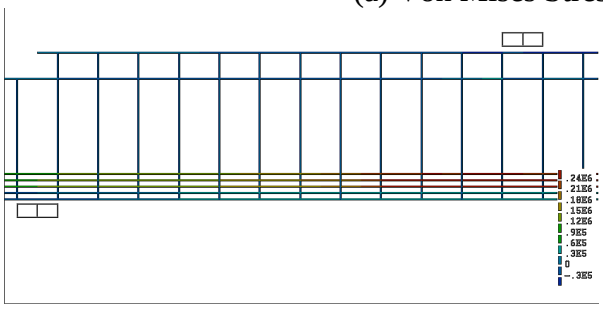

(b) Principal Tensile Stress on Tendons

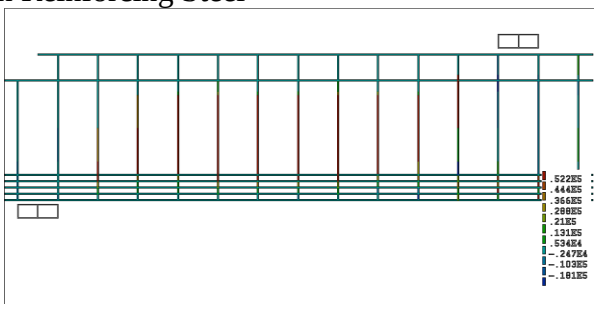

(c) Principal Tensile Stress on Stirrup

Figure A 6.30 Stress Variations on Reinforcements of PC Girder

Stress Variations on FRP (Von Mises Stress and Principal Stress)

Figure A 6.31 shows important stress variations on FRP sheets. Due to the effect of delamination caused by debonding of interface regions, stress concentrations of FRP sheets are observed in the figure. From Figure A 6.29(d) and Figure A 6.31(d), the region of delamination can be observed. Based on this information, it can be seen that the second FRP strip from the loading point is under severe local stress concentration as represented in the other stress variations.

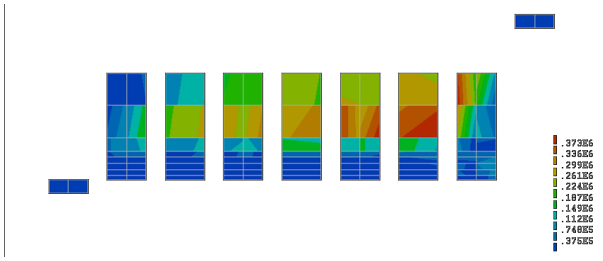

(a) Von Mises Stress

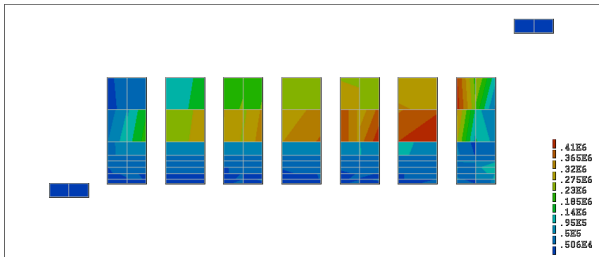

(b) Principal Tensile Stress

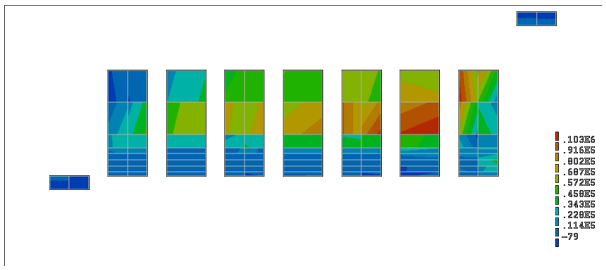

(c) Lateral Principal Tensile Stress

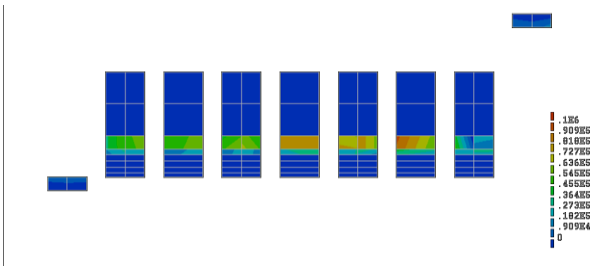

(d) Out-of-Plane Stress

Figure A 6.31 Stress Variations on FRP Sheets of PC Girder

Deformation of FRP Sheet

Relative displacement of FRP sheets is illustrated with respect to geometrical deformations and vectors represented in Figure A 6.32. This result signifies a visible behavior of FRP sheets resulting in an explicit evidence for the other results. In addition, strain variations along the principal direction of a critical FRP sheet with various loading states such as cracking, ultimate, and yielding of the steel depicted in the legend are illustrated in Figure A 6.33. Because most codes and specifications for designing FRP sheets for shear adopt the concept of effective strain of FRP sheets, this information is very important for further studies. As shown in the figure, when the test beam reaches the ultimate state, the maximum strains in the FRP reach only 54%, (0.0091) of the rupture strain (0.017), and even this value does not significantly change after the ultimate state due to debonding failure. This is a very interesting result permitting visualization of the effective strain concept for a given FRP sheet. It is desirable that the concept of effective strain be scrutinized more from further parametric studies using the developed FE models.

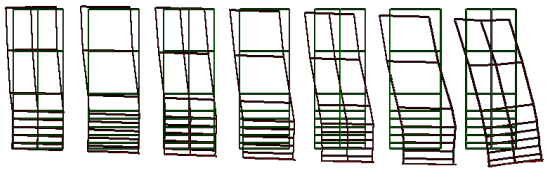

(a) Relative Deformation of FRP Sheets

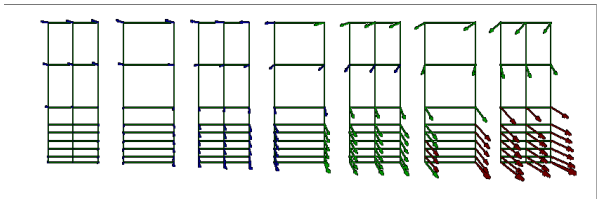

(b) Vectors of Deformation

Figure A 6.32 Deformation of FRP Sheet of PC Girder

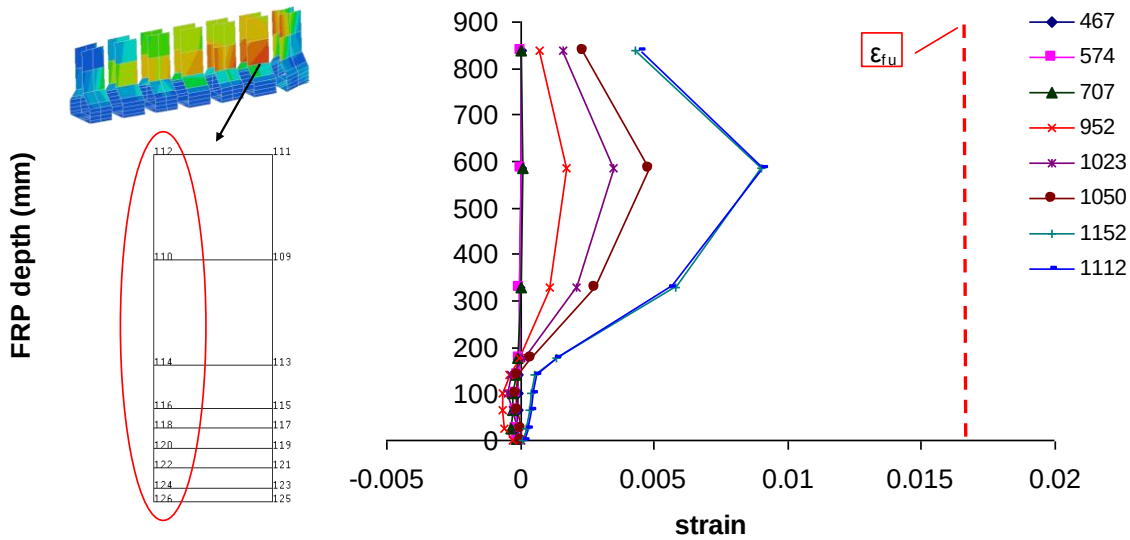

Figure A 6.33 Strain Variations along Principal Direction of Critical FRP Sheet

A6.3.2 Comparison between FEM and Experimental Results for RC Girders

A6.3.2.1 Shear Strength and Behavior

The experimental shear force-displacement relations are compared with FEM results with respect to all test girders except for test girders, RC-12-S90-SDMA-Cor and RC-12-S90-NA-Ftg, as shown in Figure A 6.34, and the comparison of ultimate strengths is summarized in Table A 6.7. In addition, FE models of un-tested girders are added in the test matrix to supplement the missing information of control girders which are not available in the experiment. Because there were significant differences in concrete strengths between the control girders and strengthened girders, it was necessary to predict the behavior of the control girders having the same concrete strength with the corresponding strengthened test girders. These are RC-8-Control-FE-Add, RC-12-Control-FE-Add1, RC-12-Control-FE-Add2 and RC-12-Control-HM-FE-Add.

Similar to the comparison of PC girders, all FE analyses show stiffer behavior than experiments, even much stiffer than PC girders. Besides the effects of external environment such as diwidag bars or initial settlement of test set-up, there is one more specific reason for this phenomenon. Relatively, a larger amount of tensile reinforcements were used in RC girders than PC girders due to the larger cross section of RC girders. The enhancement of tensile reinforcements eventually reduces the effect of flexural cracks in either test region or non-test region in the FE models resulting in stiffer behavior. From a mechanical point of view, this phenomenon is strongly related with the concept of smeared crack model. Except for the difference of stiffness, most analytical results show a reasonable agreement with test results. Moreover, there is explicit evidence to prove the efficiency of FE analysis, such as, accurate simulation of the cracking load and ultimate strength, and the consistent difference in ductility.

As summarized in Table A 6.7, the average ratio of shear strength (V_{exp} /V_{FE}) is 0.98 with a max ratio of 1.11 and min ratio of 0.90. Accordingly, the variance (VAR), standard deviation (STDEV) and coefficient of variance (COV) are calculated as 0.00, 0.07 and 0.07 respectively. Similar to the PC girders, FE analyses show a good agreement with test results with respect to

the ultimate strength. Thus, it can be said that the developed FE models are sufficiently accurate for the prediction of the ultimate strength with respect to both PC and RC girders.

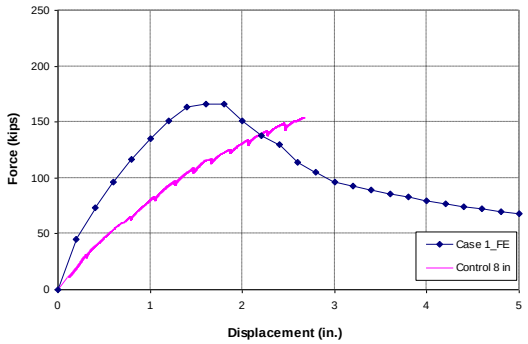

(a) RC-8-Control

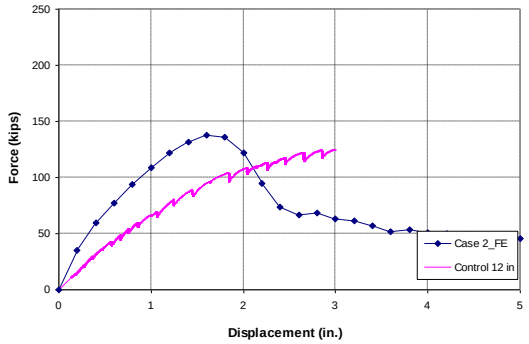

(b) RC-12-Control

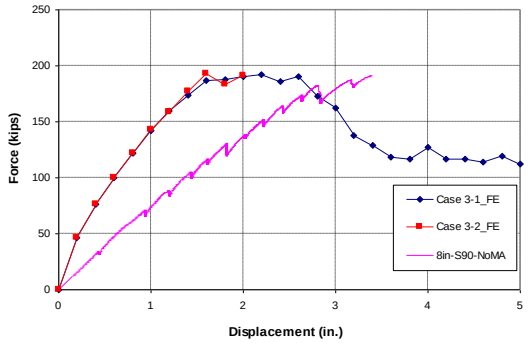

(c) RC-8-S90-NA

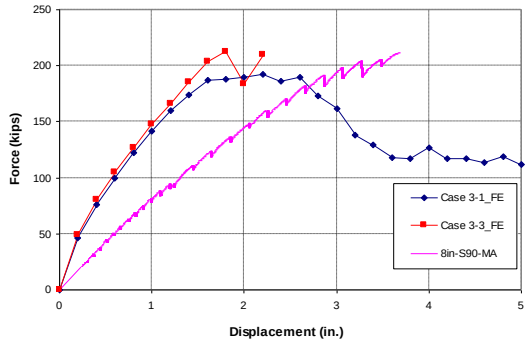

(d) RC-8-S90-DMA

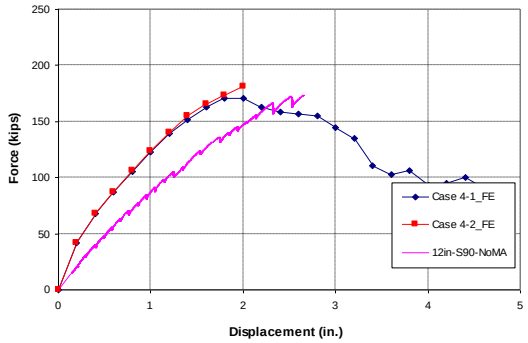

(e) RC-12-S90-NA

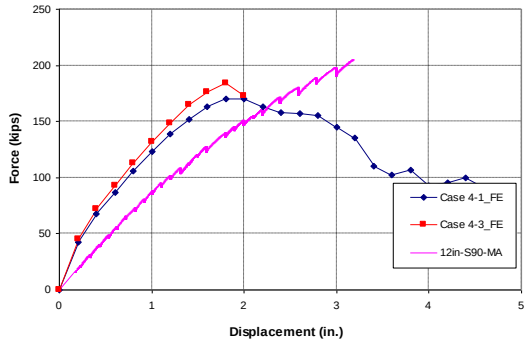

(f) RC-12-S90-DMA

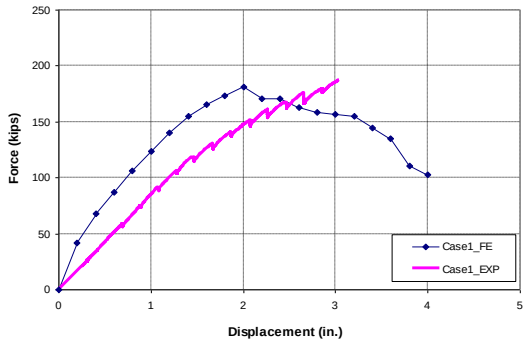

(g) RC-12-S90-HA-PC

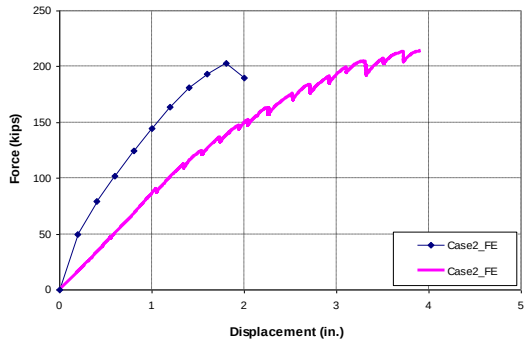

(h) RC-12-S90-SDMA-PC

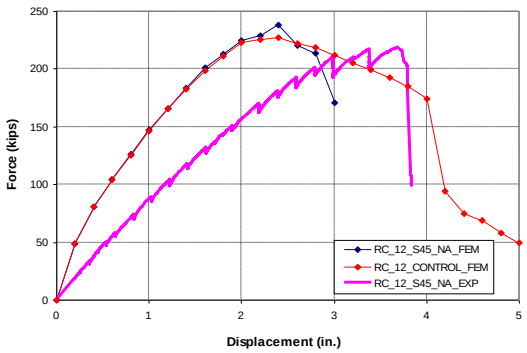

(i) RC-12-S45-NA

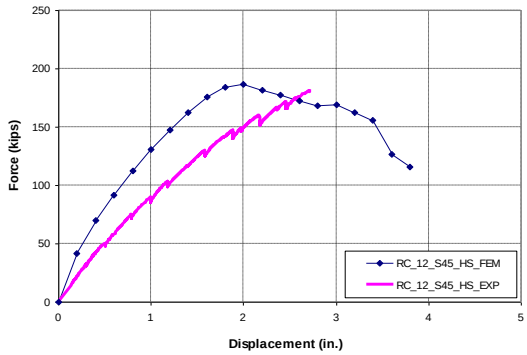

(j) RC-12-S45-HA

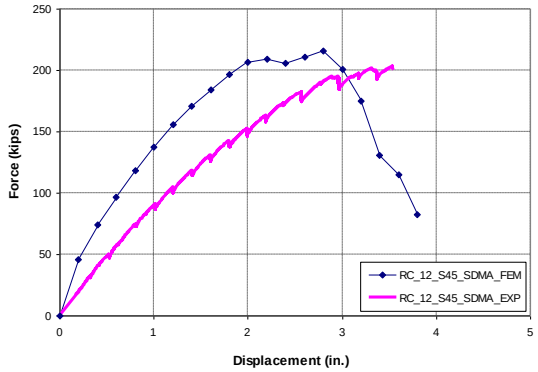

(k) RC-12-S45-SDMA

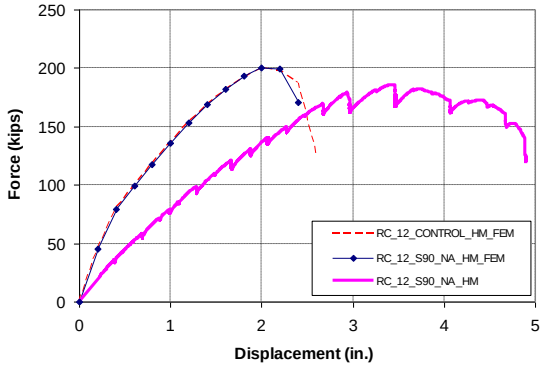

(l) RC-12-S90-NA-HA

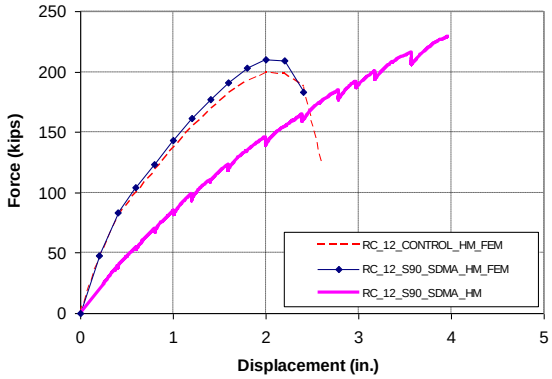

(m) RC-12-S90-SDMA-HA

Figure A 6.34 Shear Force vs. Displacement at the Loading Point of RC Girders
Table A 6.7 Comparison of Shear Strengths of RC Girders

Test I.D.	Corresponding Figures	Shear Strength (kips)		Exp/FE
		Experiment	FE Analysis	
RC-8-Control	Figure A 6.34 (a)	153	166	0.92
RC-12-Control	Figure A 6.34 (b)	124	138	0.90
RC-8-Control-FE-Add	-	-	192	
RC-8-S90-NA	Figure A 6.34 (c)	191	193	0.99
RC-8-S90-DMA	Figure A 6.34 (d)	212	212	1.00
RC-12-Control-FE-Add1	-	-	170	
RC-12-S90-NA	Figure A 6.34 (e)	172	181	0.95
RC-12-S90-DMA	Figure A 6.34 (f)	205	184	1.11
RC-12-S90-HA-PC	Figure A 6.34 (g)	187	181	1.03
RC-12-S90-SDMA-PC	Figure A 6.34 (h)	214	203	1.05
RC-12-Control-FE-Add2	-	-	227	-
RC-12-S45-NA	Figure A 6.34 (i)	219	238	0.92
RC-12-S45-HA	Figure A 6.34 (j)	181	187	0.97
RC-12-S45-SDMA	Figure A 6.34 (k)	203	216	0.94
RC-12-Control-HM-FE-Add	-	-	199	-
RC-12-S90-NA-HM	Figure A 6.34 (l)	186	200	0.93
RC-12-S90-SDMA-HM	Figure A 6.34 (m)	229	210	1.09
AVERAGE	**-**	**-**	**-**	**0.98**
VAR	**-**	**-**	**-**	**0.00**
STDEV	**-**	**-**	**-**	**0.07**
COV	**-**	**-**	**-**	**0.07**

A6.3.2.2 Failure Modes

Crack patterns of RC test girders at the ultimate state are summarized in Table A 6.8 with respect to both experimental and FE analytical results. Although FE analyses cannot exactly capture the primary discrete cracks seen in the experiment, the tendency of crack propagations can be observed. Finally, the final failure modes can be induced from these crack patterns.

Table A 6.8 Crack Patterns at the Ultimate State of RC Girders

Test I.D.	Experiment	FE Simulation
RC-8-Control	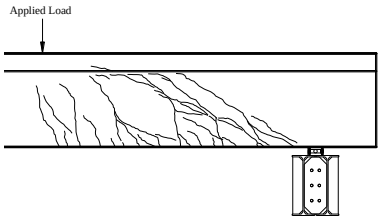	
RC-12-Control	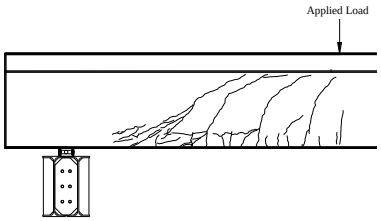	
RC-8-S90-NA	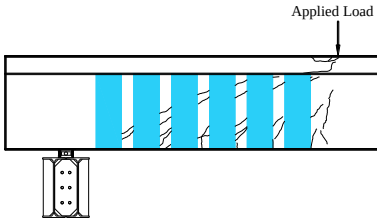	
RC-8-S90-DMA	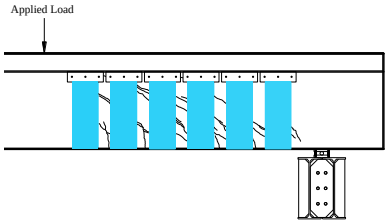	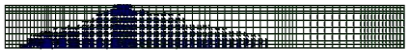
RC-12-S90-NA	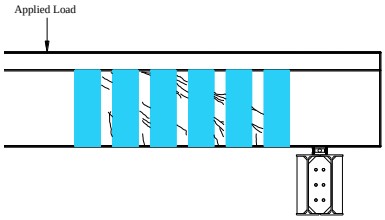	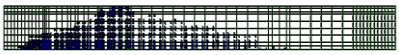
RC-12-S90-DMA	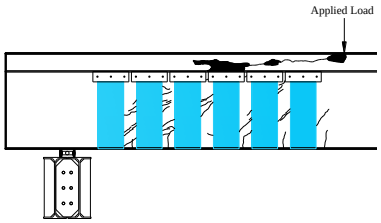	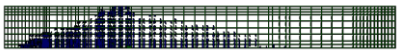

RC-12-S90-HA-PC	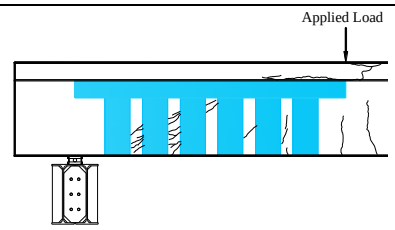	
RC-12-S90-SDMA-PC	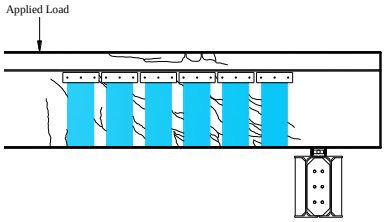	
RC-12-S45-NA	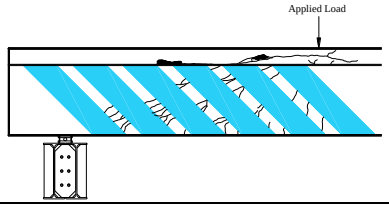	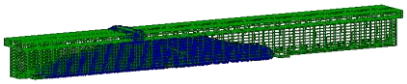
RC-12-S45-HA	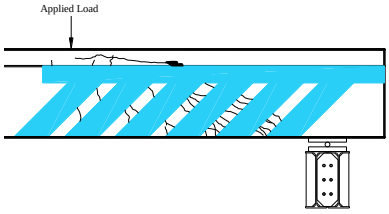	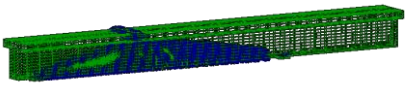
RC-12-S45-SDMA	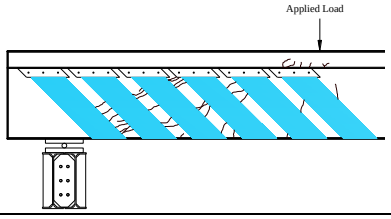	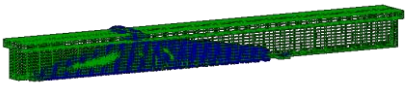
RC-12-S90-NA-HM	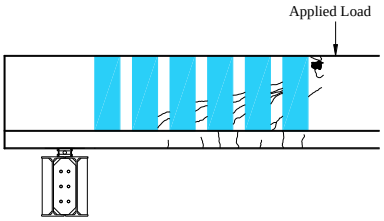	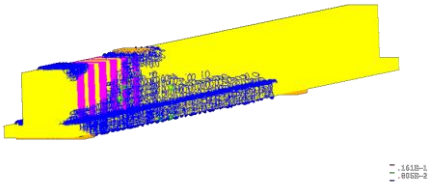
RC-12-S90-SDMA-HM	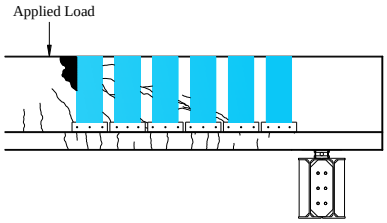	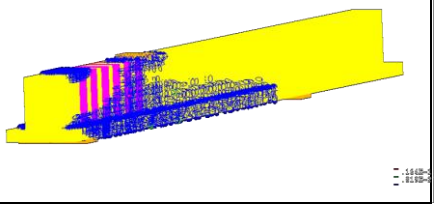

A6.3.2.3 Stress & Strain Variations on Each Component

More valuable information obtained from FE analyses is presented for a representative test girder, RC-8-S90-NA.

Stress Variations on Each Component (Von Mises Stress)

Von Mises stress variations make it easy to recognize the critical local region under severe conditions. In addition, relative stress variations on each component, as shown in Figure A 6.35, can also provide interaction relations between each of these components. Figure A 6.35(c) shows the stress variations on FRP at the ultimate state and the final failure state. From this figure, the behavior of FRP sheets around the final failure state can be observed.

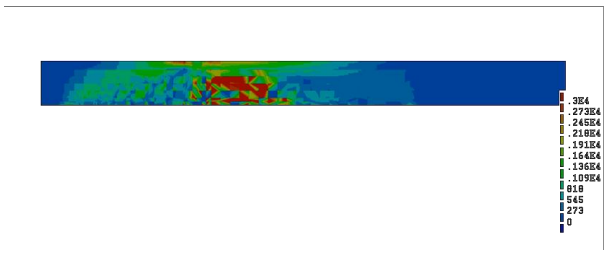

(a) Concrete

(b) Stirrup

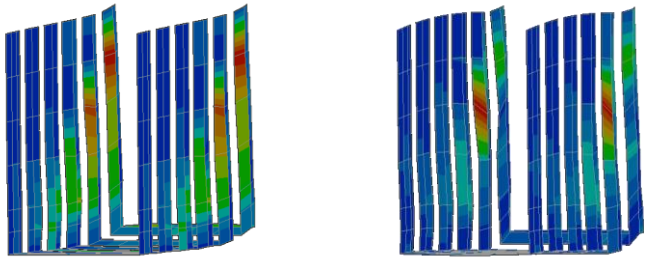

(c) FRP at the Ultimate State and after the Ultimate State

Figure A 6.35 Von Mises Stress Variations on Each Component of RC-8-S90-NA

Relative displacement of FRP

Relative displacements of FRP to concrete surfaces at the ultimate state are illustrated in Figure A 6.36. They are comprised of three displacements with respect to the XYZ axes respectively and one total combined displacement. The X axis represents the out of plane direction, while the Y axis represents the vertical direction and principal direction of FRP sheets, and the Z axis the longitudinal direction, lateral direction of FRP sheets. Displacement along the X axis is exaggerated compared with the other displacements. This displacement can simulate the normal direction behavior of FRP and show the final debonding failure. Displacements along the Y and Z axes are representative of the shear slip with respect to each direction. From these displacements, debonding failure by shear slip can be observed. Finally, the combined displacements are added at the end of the figure as Figure A 6.36(d). This combined displacement can show the critical FRP sheet inducing the final failure of the system, which also corresponds to the stress variations on FRP sheets.

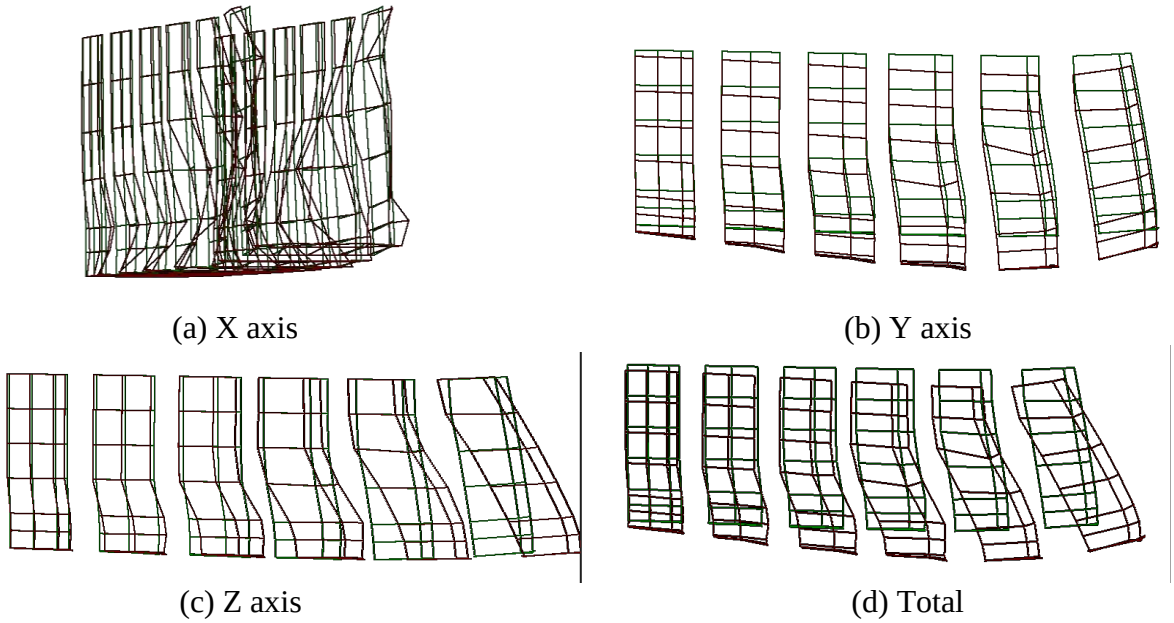

(a) X axis (b) Y axis

(c) Z axis (d) Total

Figure A 6.36 Relative Displacement of FRP for RC-8-S90-NA

A6.4 Conclusions and Future Recommendations

A6.4.1 Concluding Remarks

In order to investigate the strengthening effect of FRP for the PC and RC girders in shear, numerical simulation was carried out by developing a three-dimensional non-linear finite element model incorporating the rational material laws and elements using a powerful commercial FE program DIANA (DIsplacement ANAlyzer). This program has prominent, special, built-in options for simulating various conditions of structures. In particular, the phased analysis option and the simulation of prestressing process differentiate its capability from the other commercial FE software programs. The efficiency of the developed FE models had been validated against the experimental results, and a reasonable agreement was obtained. Especially, the interfacial behavior between concrete and FRP, which is difficult to measure from experiments, could be successfully simulated from the developed FE models. Moreover, a phased analysis technique adopted in the developed FE model made it possible to simulate the strengthening effect of FRP according to the damage levels of deteriorated PC girders.

Thus, the following conclusions can be made about the development of three-dimensional non-linear finite element (FE) model.

- Differences between two- and three-dimensional FE analysis:
  Because simulation with two-dimensional FE models has a restriction about modeling the interface regions between concrete and FRP sheet, development of three-dimensional FE models has been carried out in this project with respect to geometrical and mechanical aspects.
- Modification of FE models:

Fine meshes of FE models required an excessive running time for nonlinear analysis and made it difficult to examine trial parameters being considered in this project. Accordingly, proper reduction of mesh density was performed and did not cause a significant difference in results compared to the FE models with fine meshes.

- Phased Analysis:
  Different stages of test girders such as prestressing, construction, pre-cracking and loading stages could be successfully simulated by the phased analysis technique. Since the prestressing process is basically one type of the phased analysis, FE models simulating the PC girders should incorporate the phased analysis. Unlike other commercial software, DIANA has special built-in options for the phased analysis and the prestressing operation. Thus, it was possible to simulate various aspects of test girders in terms of time-dependent mechanical behaviors.
- Softening Effect of Concrete:
  It was observed that the softening effect of concrete was significant for the behavior of test girders from the trial simulations. In particular, FE models considering the softening effect could exactly predict the post-peak behavior. From this conclusion, assumptions for the three-dimensional extension of the MCFT were also validated.
- Interface between Concrete and FRP Sheet:
  The overall behavior of FRP sheets could be successfully simulated through proper modeling techniques and using rational bond-slip model selected from careful review of the literature. In addition, detailed behavior of interfaces which were impossible to measure from the experiments could be observed by the FE simulations. This information is very important to further expand this type of research.

Thus, this study can enhance the weak archival data in this field as well as be helpful in developing a simplified design tool by FE simulation taking into account various parameters affecting the shear capacity of FRP strengthened PC beams.

A6.4.2 Recommendations for Future Research

The following research is recommended as an extension to this work:

- Parametric Study:
  Only a few limited parameters were considered in this project. There are substantial parameters affecting the shear behavior of concrete structures strengthened with FRP. These can be concrete strength, steel strength, shear span, shear span to depth ratio, steel ratios (stirrup and longitudinal steel), prestressing force, and strengthening scheme of FRP sheets etc. Thus, it is difficult to generalize the shear behavior of FRP strengthened concrete structures with limited parameters. Rather than conducting experiments, the developed FE models can resolve this problem with little effort.
- Statistical Approach:
  It is possible to enhance the weak archival data for shear behavior of FRP strengthened concrete structures with FEM simulations. Hence, a statistical approach and reliability analysis can be performed based on accumulated data to support the development of simplified design specifications or tools.
- Interaction between Components:

Most shear design equations adopt the supposition method in designing FRP sheets for shear, disregarding the interaction relationships between each component. However, FRP sheets are externally added to the mother specimen, and their effect on the response is strongly dependent on the behavior of the other components. Therefore, interaction between each component should be considered in design of shear strengthening using FRP sheets.

- Effective Strain of FRP Sheets:
  Effective strains in FRP sheets used in the design of externally bonded FRP for shear are calculated based on empirical equations adopted in most design codes or specifications. Because these equations are also derived from simplified supposition methods using limited experimental results, it is necessary to update these equations considering the interaction relationships between each component through a parametric study.
- Simulation of Fatigue:
  With the developed FE models, it is possible to simulate the fatigue behavior of FRP strengthened concrete structures with consideration of various parameters.

A7. RELIABILITY STUDY

A7.1 Introduction

The proposed design procedure described in Section A7 was developed based on review of procedures reported in the literature and assessment of these procedures in light of experimental results from tests conducted as part of this study as well as many others that were obtained from the literature. As stated earlier, the proposed design method was chosen to result in acceptable predictions of the FRP contribution to the shear strength (V_f) over the wide range of parameters covered in the experimental database. This section presents a calibration of the design procedure using structural reliability methodology similar to that used in the development of the AASHTO LRFD (AASHTO, 1994) which is reported in NCHRP Report 368 (Nowak, 1999). After the introduction of LRFD philosophy to AASHTO design procedures, several projects investigated various aspects of bridge design and rating using the same philosophy (Moses, 2001; Kulicki et al., 2006). The same procedure (Nowak and Szerszen, 2003; Szerszen and Nowak 2003) was also used more recently in the calibration of the building specifications for the construction of concrete buildings (ACI 318-02, 2002) by the American Concrete Institute (ACI).

This section first identifies a design space that covers a wide range of the main parameters that were determined to have the largest impact on the shear strength. The variabilities in all design parameters to be used in the calibration process are then established. Two reliability approaches; namely Monte Carlo simulations and First Order Reliability Method (FORM), are then used to calibrate the design coefficient such that a pre-specified target reliability index results from the proposed design procedure.

A7.2 Design Space

The purpose of identifying a design space is to ensure that the calibrated design equation delivers acceptable reliability levels over a wide range of design scenarios. Three bridges that vary in span length (L = 45 feet, 60 feet, and 80 feet) were chosen for this purpose. All bridges share a typical reinforced concrete girder cross section consisting of five girders spaced at seven feet and supporting a 7.5 inch reinforced concrete deck. The bridge is designed following AASHTO LRFD specifications (AASHTO, 2008), which yielded the dimensions shown in Figure A 7.1. A concrete compressive strength of 5 ksi and Grade 60 steel was assumed for all bridges. A modulus of elasticity (E_f) equal to 33,500 ksi and a rupture strength (f_{fu}) equal to 335 ksi was assumed for FRP strengthening material.

The shear demands on this bridge were calculated by following AASHTO LRFD specifications (AASHTO, 2008) for wearing surface dead loads (V_{DW}), component dead loads (V_{DC}), and live loads including impact (HL-93 loads) as given in Table A 7.1. It can be seen that the live-to-dead load shear demand ratio for the chosen bridges covers a range from 0.83 to 2.32. This range, plus the various parameter ranges, will provide information about the reliability of the proposed design equations over a wide range of design scenarios that the code addresses. The table also lists the factored ultimate shear demand at the critical section ($V_{u,cr}$).

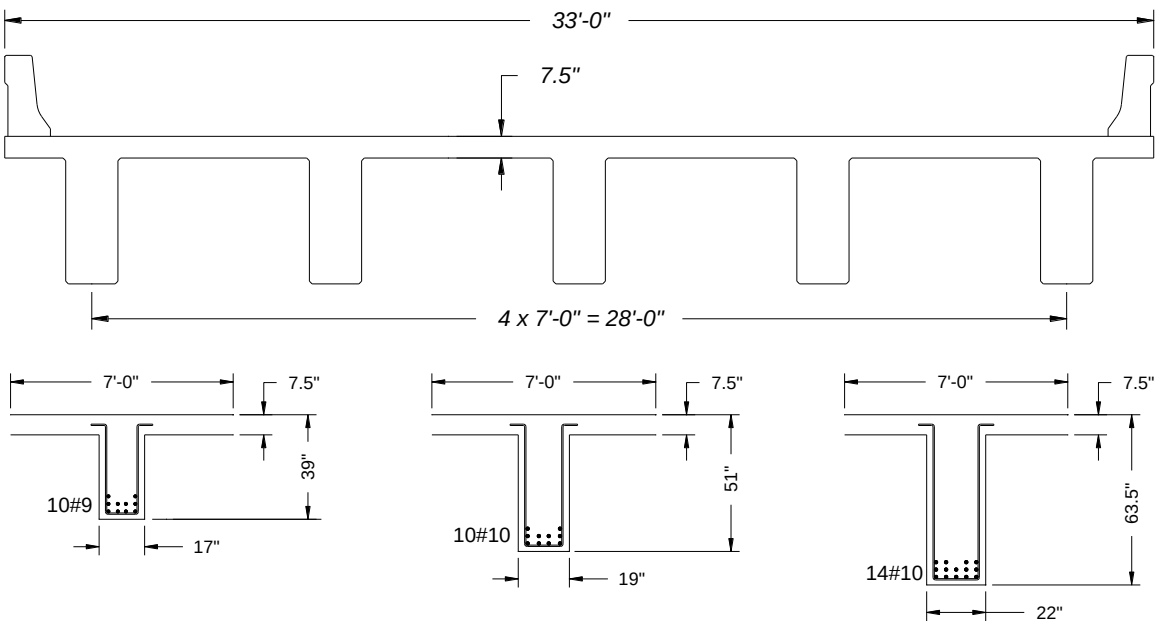

(a) Span Length = 45 feet (b) Span Length = 60 feet (c) Span Length = 75 feet

Figure A 7.1 Details of Bridge Used to Cover Identified Design Space

Table A 7.1 Shear Demands on Design Space Bridges

Bridge		V_{DW}	V_{DC}	V_{LL+IM}	$\frac{V_{LL+IM}}{V_{DW}+V_{DC}}$	$V_{u,cr}$
Span Length	Girder	(kips)	(kips)	(kips)		(kips)
45 ft	Interior	3.26	23.41	61.88	2.32	142.44
	Exterior	3.03	31.55	55.69	1.61	141.43
60 ft	Interior	4.34	38.94	68.65	1.59	175.31
	Exterior	4.03	49.77	61.78	1.15	176.37
75 ft	Interior	5.41	62.08	73.91	1.10	215.06
	Exterior	5.02	75.59	66.52	0.83	218.44

Each of the chosen bridges was then assumed to have three levels of steel shear reinforcement. All three levels were chosen such that the resulting factored nominal shear resistance without the FRP contribution, $\phi(V_c + V_s)$, is less than the ultimate shear demand at the critical section ($V_{u,cr}$) and that the FRP shear reinforcement would resist the remaining shear demand. Arbitrary steel and FRP configurations were chosen to deliver the chosen steel (V_s) and FRP (V_f) contributions to shear capacity. Each of the FRP configurations was considered twice. The first was based on the assumption that an FRP anchoring system was present, while the second assumes that no such anchoring system exists. The FRP contribution to the shear strength (V_f) was calculated using using the strain reduction factor, R_f, given in Equations A7-1 and A7-2 for the anchored and non-anchored cases, respectively.

$$R_f = 0.143(\rho_f E_f)^{-0.67} \quad \text{(GPa units)} \qquad \text{(A7-1a)}$$

$$R_f = 4(\rho_f E_f)^{-0.67} \quad \text{(ksi units)} \qquad \text{(A7-1b)}$$

$$R_f = 0.107\left(\rho_f E_f\right)^{-0.67} \qquad \text{(GPa units)} \qquad \text{(A7-2a)}$$

$$R_f = 3\left(\rho_f E_f\right)^{-0.67} \qquad \text{(ksi units)} \qquad \text{(A7-2b)}$$

Table A 7.2 lists the final design configurations and resulting shear capacity contribution for each component (i.e. V_c, V_s, and V_f). Also listed is the ratio of the FRP contribution to the combined contribution of concrete (V_c) and steel (V_s) to illustrate that the chosen design space covers a wide range of strengthening levels. Figure A 7.2 illustrates the different contribution levels for each of the bridges in the design space.

Table A 7.2 Shear Resistance Components for Design Space Bridges

Bridge		Case	$A_v d_v / s$ (in^2)	w_f (in)	s_f (in)	t_f (in)		V_c (kips)	V_s (kips)	V_f (kips)	$\frac{V_f}{V_c + V_s}$
Span Length	Girder					Rupture (Eq. A7-1)	Debond (Eq. A7-2)				
45 ft	Interior	L45F1I	0.847	4.0	12.0	0.00774	0.01863	73.57	50.82	33.88	0.272
		L45F2I	0.730		10.0	0.01142	0.02749		43.79	40.91	0.349
		L45F3I	0.613		8.0	0.01477	0.03556		36.76	47.94	0.435
	Exterior	L45F1E	0.697		12.0	0.01461	0.03519		41.79	41.79	0.362
		L45F2E	0.532		10.0	0.02315	0.05575		31.92	51.66	0.490
		L45F3E	0.368		8.0	0.03146	0.07576		22.05	61.53	0.643
60 ft	Interior	L60F1I	0.696		14.0	0.00644	0.01023	111.24	41.77	41.77	0.273
		L60F2I	0.580		12.0	0.00644	0.01402		34.78	48.76	0.334
		L60F3I	0.463		10.0	0.00728	0.01753		27.79	55.76	0.401
	Exterior	L60F1E	0.565		14.0	0.01461	0.01855		33.89	50.84	0.350
		L60F2E	0.468		12.0	0.02315	0.02210		28.06	56.67	0.407
		L60F3E	0.371		10.0	0.03146	0.02477		22.23	62.49	0.468
75 ft	Interior	L75F1I	0.501		16.0	0.00596	0.00596	163.81	30.06	45.09	0.233
		L75F2I	0.319		14.0	0.00648	0.00776		19.12	56.03	0.306
		L75F3I	0.136		12.0	0.00664	0.01142		8.18	66.97	0.389
	Exterior	L75F1E	0.394		16.0	0.00730	0.00849		23.67	55.23	0.295
		L75F2E	0.214		14.0	0.00764	0.01277		12.86	66.04	0.374
		L75F3E	0.034		12.0	0.00762	0.01734		2.05	76.85	0.463

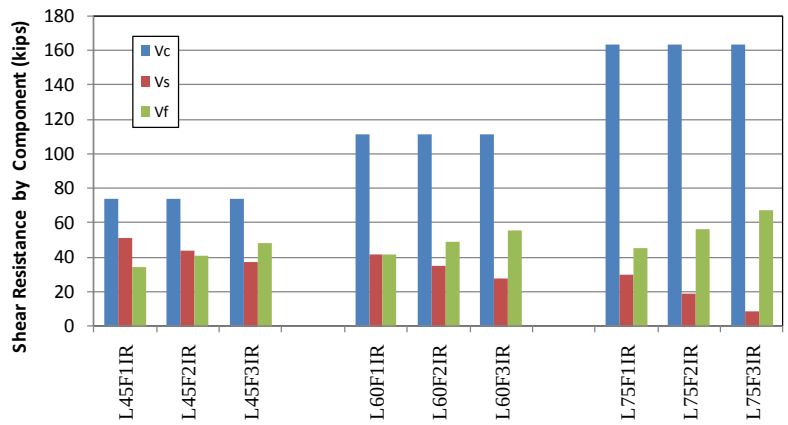

(a) Interior Griders

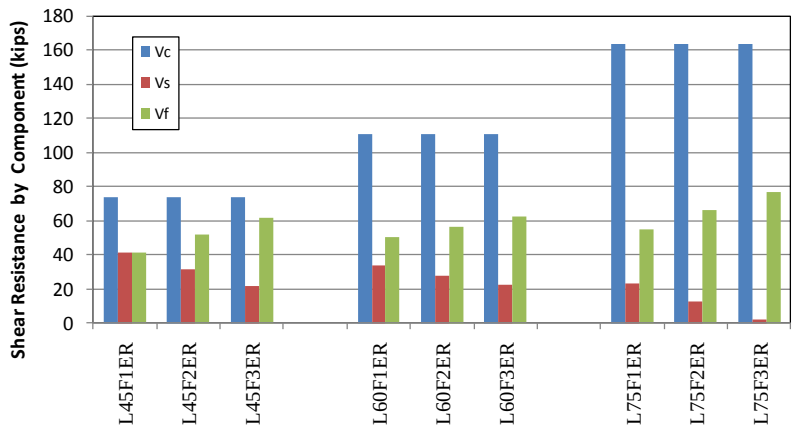

(b) Exterior Griders

Figure A 7.2 Shear Resistance Contributions by Component

A7.3 Statistical Properties of Load and Resistance Parameters

All load and resistance parameters that cannot be considered to be deterministic will be treated as random variables. The variability in these parameters will be described in terms of three statistical descriptors: the bias, coefficient of variations, and distribution type. The bias (λ) is a measure of the ratio between the mean value of the parameter (μ) and its nominal value used in the design process. The coefficient of variation (COV) is a measure of the data scatter and is given as the ratio between the standard deviation (σ) of the random variable and its mean value. Finally, the distribution type is the best mathematical fit of the frequency diagram of collected data for each parameter and is determined using statistical tests that compare the closeness of several distribution types such as Gaussian, Lognormal, and Extreme Event distributions. In the current study, the statistical descriptors of many of the load and resistance parameters will be taken from the literature, while others will be determined using data generated, or collected, as part of this study.

The following sections present the variability used in the current study. For each parameter that will be treated as a random variable, a bias, coefficient of variation, and distribution type are

given. The bias (λ_X) is defined as the ratio between of the mean value of the random variable (X) for any parameter to its nominal value. The coefficient of variation ($COV(X)$) is the ratio between the standard deviation and the mean value.

$$\lambda_X = \frac{\mu_X}{X_n} \tag{A7-3}$$

$$COV(X) = \frac{\sigma_X}{\mu_X} \tag{A7-4}$$

A7.3.1 Loads

The proposed provisions for shear strengthening are recommended for adoption into AASHTO LRFD (AASHTO, 2008). Therefore, the same load models used in the calibration of AASHTO LRFD (Nowak, 1999) will be used in this study.

A7.3.1.1 Dead Load

AASHTO-LRFD treats component dead loads—i.e. gravity loads due to self weight of bridge members—in a different way than wearing surface dead loads—i.e. gravity loads due to self weight of asphalt layer. This separation was introduced in AASHTO LRFD (AASHTO, 1994) to account for the different levels of variability inherent in them. As part of the calibration of AASHT LRFD (Nowak, 1999), a survey was conducted to assess the bias and coefficient of variation for dead loads. It was found that the variabilities differ based on the component type. Table A 7.3 lists these values for the main dead load components; namely factory-made (precast), cast-in place, and wearing surface. These statistical descriptors are incorporated in the reliability analyses.

Table A 7.3 Bias and COV for Bridge Dead Loads (Nowak, 1999)

Component	λ_{DL}	$COV(DL)$
Factory-made Members	1.03	0.08
Cast-in-place Members	1.05	0.10
Asphalt	1.00	0.25

A7.3.1.2 Live Load

The statistical characteristics of the HL-93 live load model are well documented in the literature (Nowak, 1999). The bias for single-lane bridges as determined using simulations is given in Table A 7.4 for different maximum design life values. AASHTO LRFD (AASHTO, 2008) was calibrated for a 75-year maximum truck. For typical two-lane bridges, the maximum shear forces develop from two side-by-side trucks. Each of the side-by-side trucks is a two month maximum truck, which is about 85% of the 75 year maximum truck. It should be noted that the preceding values are for an average daily truck traffic (ADTT) equal to 1000.

Table A 7.4 Bias for HL-93 Shear Forces in Simply Supported Bridges (Nowak, 1999)

Span (feet)	1 (year)	5 (years)	50 (years)	75 (years)
10	1.09	1.13	1.19	1.20
20	1.12	1.16	1.22	1.23
30	1.15	1.19	1.24	1.25
40	1.14	1.16	1.22	1.23
50	1.14	1.16	1.22	1.22
60	1.15	1.19	1.22	1.23
70	1.16	1.19	1.24	1.25
80	1.18	1.21	1.26	1.27
90	1.19	1.22	1.27	1.28
100	1.18	1.22	1.27	1.28
110	1.17	1.21	1.25	1.26
120	1.14	1.18	1.22	1.22
130	1.12	1.15	1.19	1.20
140	1.12	1.15	1.20	1.20
150	1.12	1.15	1.20	1.20
160	1.11	1.14	1.19	1.20
170	1.10	1.14	1.19	1.19
180	1.10	1.13	1.18	1.19
190	1.08	1.12	1.17	1.17
200	1.08	1.11	1.16	1.17

Based on the previous discussion, the live load model bias used in this study was taken equal to:

$$\lambda_{V_{LL}} = 0.85 \times 1.225 = 1.041 \qquad \text{(for } L \text{ = 45 feet)} \qquad \text{(A7-5a)}$$

$$\lambda_{V_{LL}} = 0.85 \times 1.230 = 1.046 \qquad \text{(for } L \text{ = 60 feet)} \qquad \text{(A7-5b)}$$

$$\lambda_{V_{LL}} = 0.85 \times 1.260 = 1.071 \qquad \text{(for } L \text{ = 75 feet)} \qquad \text{(A7-5c)}$$

The coefficient of variation for the live load is given for the collective action of the live load and dynamic impact, which is discussed in the next section.

A7.3.1.3 Dynamic Allowance

The dynamic load effect is taken as 33% of the design truck in AASHTO LRFD (AASHTO, 2008). For calibration purposes, it was estimated that the bias is about 10% of the total maximum 75-year live load effect for two-lane bridges and 15% for single-lane bridges. The coefficient of variation for the live load and dynamic impact effect is between 19% and 20.5% for single-lane bridges. The corresponding value for two-lane bridges is 18% and 19%. Therefore a value of 18% is used in this study for the coefficient of variation of the total live load effect including impact.

A7.3.2 Resistance Model

Three sources of uncertainty affect the variability of resistance models, namely material variability (*M*), fabrication tolerances (*F*), and professional factor (*P*). All three sources are treated as random variables and are accounted for in this study. The random variable (*R*) for the resistance can be expressed as:

$$R = R_n \; M \; F \; P \qquad \text{(A7-6)}$$

where: R_n is the nominal resistance as obtained from the proposed design expression.

The details of each source of uncertainty are described next.

A7.3.2.1 Material Variability (*M*)

The present study requires a description of the variability in three materials: (1) compressive strength of concrete, (2) yield strength of reinforcing steel, and (3) rupture strength of FRP. No tests were conducted for that purpose as the literature has adequate information about the statistics of each of the materials that is also relatively recent.

Table A 7.5 lists the bias and coefficient of variation for the compressive strength of ordinary concrete over a range of typical concrete strengths. Nowak and Szerzsen (2003) used a concrete compressive strength coefficient of variation of 10% in the calibration of ACI 318 (ACI 318, 2008) and developed an expression for the bias:

$$\lambda_{f_c^{'}} = -0.0081 f_c^{'3} + 0.1509 f_c^{'2} - 0.9338 f_c^{'} + 3.0649 \qquad \text{(A7-7)}$$

Table A 7.5 Bias and COV for concrete compressive strength (Nowak and Szerszen, 2003)

a- Ordinary ready-mix concrete			b- Ordinary plant-cast concrete		
$f_c^{'}$ (psi)	$\lambda_{f_c^{'}}$	$COV(f_c^{'})$	$f_c^{'}$ (psi)	$\lambda_{f_c^{'}}$	$COV(f_c^{'})$
3000	1.35	0.102	5000	1.38	0.120
3500	1.21	0.079	5500	1.19	0.101
4000	1.235	0.145	6000	1.16	0.090
4500	1.14	0.042	6500	1.14	0.081
5000	1.15	0.058			
6000	1.12	0.042			

The yield strength of reinforcing steel bars was also recently investigated by Nowak and Szerzsen (2003) for the calibration of ACI 318 (ACI 318, 2008). Based on the results of recent data, it was concluded that a bias, $\lambda_{f_y} = 1.145$, and a coefficient of variation, $COV(f_y) = 0.05$, are representative of actual data.

Composite materials have an inherent low variability due to the manufacturing process by which they are produced at the fiber level. The literature lists coefficient of variation values that are as low as 2.2% for Carbon FRP products (Bakht et al. 2000), which is lower than most classical civil engineering materials; e.g. concrete and steel. Nevertheless, the nature of applications in civil infrastructure has prompted the use of more realistic in-situ properties. A survey conducted by ACI Committee 440 of six commercially available FRP products used in strengthening of concrete structures was conducted by a Task Group (TG) of which Dr. Okeil was a member. The TG concluded that a bias, $\lambda_{f_{fu}} = 1.10$, and a coefficient of variation, $COV(f_{fu}) = 0.083$ is

appropriate for the rupture strength of FRP laminates (f_{fu}). The bias (λ_{E_f}) and coefficient of variation ($COV(E_f)$) for the modulus of elasticity of FRP laminates (E_f) were estimated to be 1.04 and 0.058, respectively. These values will be used in the current reliability study. The literature has extensive evidence that the best distribution type to represent composite materials is the Weibull (Extreme Type III) distribution (Kaminski, 1973; Bullock, 1974; Harlow and Phoenix, 1981; Batdorf and Ghaffarian, 1984; Zureick et al., 2006). Since both parameters (f_{fu} and E_f) are not independent, a correlation coefficient ($\rho_{E_f, f_{fu}}$) of 0.6945 will be used. This coefficient was also determined as part of the TG for ACI Committee 440 effort.

A7.3.2.2 Fabrication Variability (*F*)

Fabrication tolerances account for inaccuracies in measured dimensions and sizes. This source of uncertainty has improved with the development of better, more rigorous quality control (QC) and quality assurance (QA) procedures. Nevertheless, recent research on structural reliability still takes into account small variations caused by fabrication tolerances. In this study, dimensions as well as cross-sectional areas of bars and FRP laminates were included as random variables with the statistical properties given in Table A 7.6. It was assumed that these random variables were normally distributed.

Table A 7.6 Bias and COV for fabrication tolerances

Parameter		λ	*COV*
Dimensions	Web Width, b	1.01	0.04
	Effective Depth, d, d_f	0.99	0.04
	FRP Width, w_f	1.00	0.02
	FRP Thickness, t_f	1.00	0.02
	FRP/Stirrup Spacing, s_f, s	1.00	0.02
Cross-sectional Area (A_v)		1.00	0.015

A7.3.2.3 Professional Factor, (P)

The analysis model was used to predict the shear capacity of laboratory tested beams in the compiled database (see Section A2.5 and Additional Material B to Appendix). The results were compared with the experimental capacities reported in the literature and the statistics of the ratio between the predicted (V_{Anal}) to the experimental shear (V_{Exp}) capacities. The bias (λ_p) and coefficient of variation (*COV(P)*) of the ratio V_{Anal}/V_{Exp} were then determined from the statistics of the data using the following equations:

$$\lambda_P = \mu\left(\frac{V_{\text{Anal}}}{V_{\text{Exp}}}\right) \tag{A7-8}$$

$$COV(P) = \frac{\sigma\left(\frac{V_{\text{Anal}}}{V_{\text{Exp}}}\right)}{\mu\left(\frac{V_{\text{Anal}}}{V_{\text{Exp}}}\right)} \tag{A7-9}$$

The results show that λ_P and $COV(P)$ vary based on the failure mode. Table A 7.7 lists the values for the two major classifications; namely failure by FRP rupture, and failure by other failure modes including FRP debonding.

Table A 7.7 Statistical Parameters for Analysis Model

Failure Mode	λ_P	$COV(P)$
FRP Rupture	1.680	0.330
FRP Debonding / Other	1.410	0.269

A7.3.2.4 Monte Carlo Simulations of Material *(M)* and Fabrication *(F)* Variabilities

The resistance model uncertainty due to material and fabrication tolerances were assessed collectively using Monte Carlo simulations. Random values were generated for the variables in the design equation related to the material properties or dimensions according to the statistical properties given in Sections A7.2.2.1 and A7.2.2.2. Figure A 7.3 shows the histograms for some of the key variables involved in determining the shear strength of the FRP-strengthened concrete girders. The histograms are for one of the Monte Carlo simulations conducted on a sample beam in the experimental database (Beam BS2 by Taerwe et al., 1997).

One million random values were generated for each random variable. The shear strength was then calculated for each of the simulated cases using the proposed equations. Figure A7.2 is a plot of the histograms for the shear strength of the aforementioned Beam BS2. The figure shows the histogram for each component contribution, i.e. concrete (V_c), steel stirrups (V_s), and FRP composite (V_f) as well as the total shear strength ($V_{total} = V_c + V_s + V_f$). The histogram of the total shear strength is shown to have a mean value of 53.70 kips and a standard deviation of 3.22 kips. The nominal value according to the proposed equations is calculated to be 49.02 kips. These results indicate that the bias (λ_{MF}) and coefficient of variation ($COV(MF)$) due to material and fabrication tolerances are determined to be:

$$\lambda_{MF} = \frac{53.07}{49.02} = 1.095 \qquad \text{(A7-10)}$$

$$COV(MF) = \frac{3.22}{53.07} = 0.06 \qquad \text{(A7-11)}$$

The distribution type that best fits the total shear strength was examined using the Chi-square statistical test. Since normal, lognormal, and Weibull distributions are represented in the material and fabrication parameters, they were considered as possible distributions. The results of the Chi-square test showed that the normal distribution passes the statistical test for a confidence level of 5%. Details about the Chi-square statistical test procedure are provided in Additional Material P to Appendix. Figure A 7.5 shows a normal probability paper plot of the total shear strength (V_{total}). The linearity of the plot shows that a normal distribution is a good fit for the material and fabrication tolerances on the total shear strength. Monte Carlo simulations were carried out for each of the bridge girders identified in the design space (see Section A7.2) following the same procedure. The results are summarized in Table A 7.8.

Table A 7.8 Statistical Parameters for Material and Fabrication Tolerances

Bridge		Case	Rupture		Debonding	
Span Length	Girder		λ_{MF}	$COV(MF)$	λ_{MF}	$COV(MF)$
45 ft	Interior	L45F1I	1.096	0.0590	1.096	0.0590
		L45F2I	1.093	0.0600	1.093	0.0600
		L45F3I	1.090	0.0613	1.090	0.0613
	Exterior	L45F1E	1.092	0.0603	1.092	0.0603
		L45F2E	1.088	0.0623	1.088	0.0623
		L45F3E	1.083	0.0648	1.084	0.0648
60 ft	Interior	L60F1I	1.096	0.0600	1.091	0.0611
		L60F2I	1.090	0.0614	1.089	0.0620
		L60F3I	1.086	0.0632	1.086	0.0631
	Exterior	L60F1E	1.086	0.0618	1.088	0.0622
		L60F2E	1.086	0.0631	1.086	0.0631
		L60F3E	1.084	0.0642	1.084	0.0642
75 ft	Interior	L75F1I	1.092	0.0629	1.091	0.0631
		L75F2I	1.089	0.0642	1.084	0.0657
		L75F3I	1.087	0.0659	1.081	0.0673
	Exterior	L75F1E	1.090	0.0636	1.085	0.0650
		L75F2E	1.088	0.0652	1.082	0.0665
		L75F3E	1.079	0.0676	1.079	0.0682

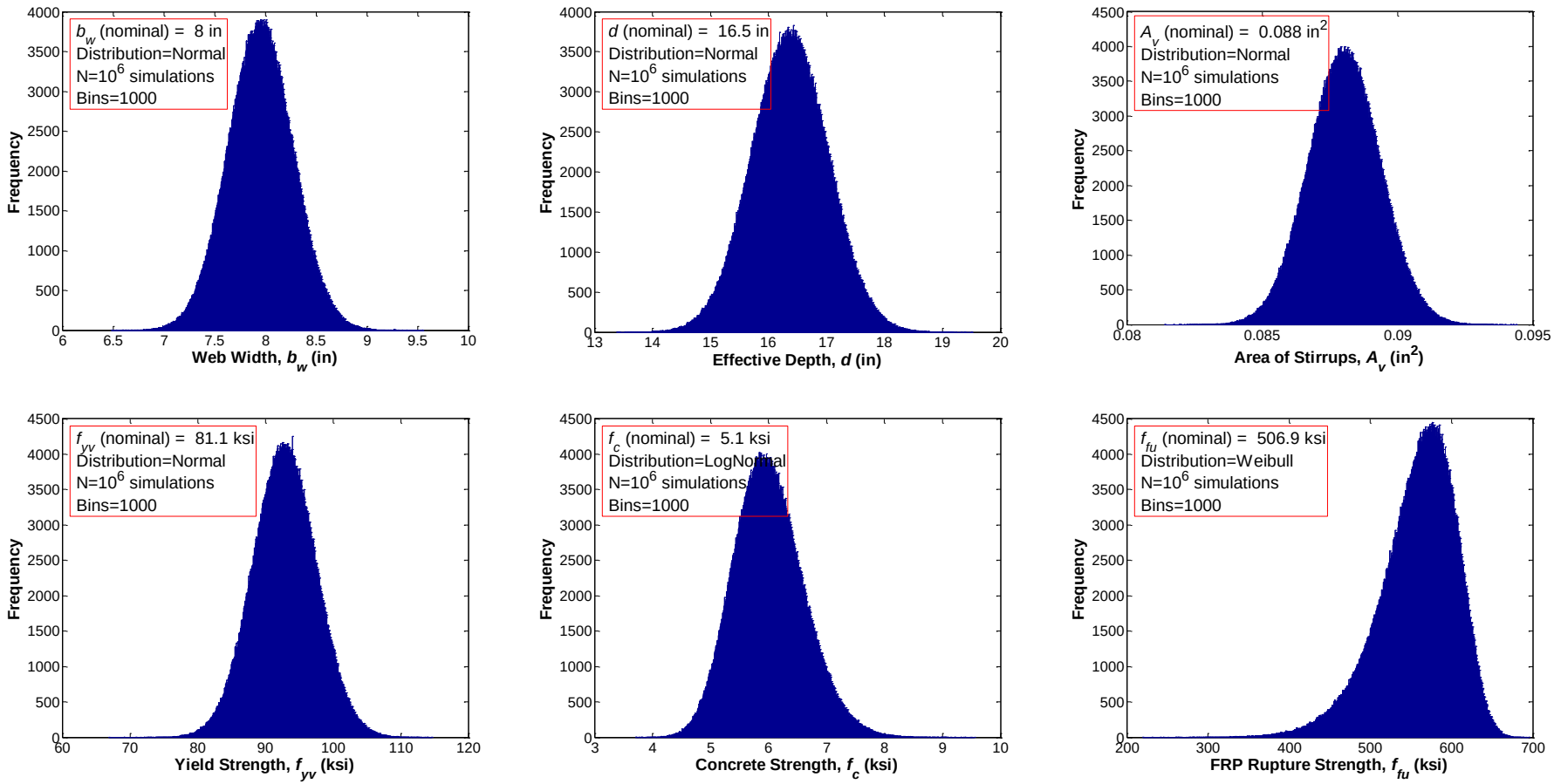

Figure A 7.3 Histograms of randomly generated numbers for key variables

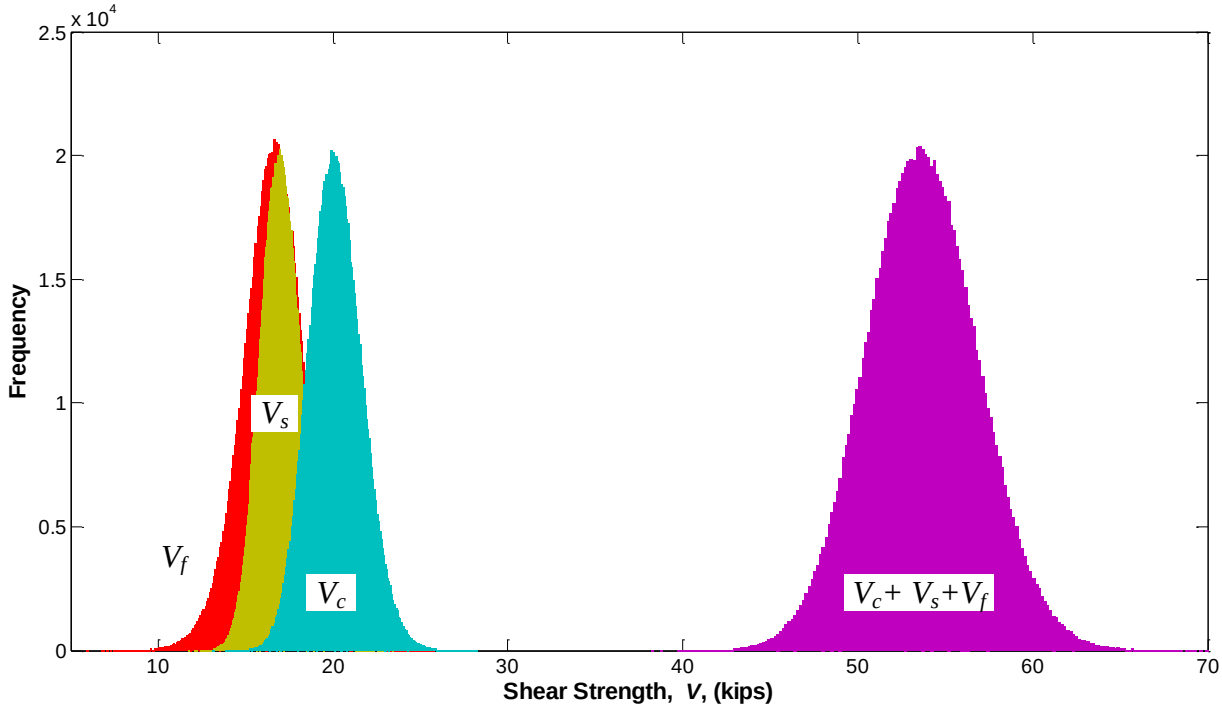

Figure A 7.4 Histograms of shear strength from Monte Carlo simulations

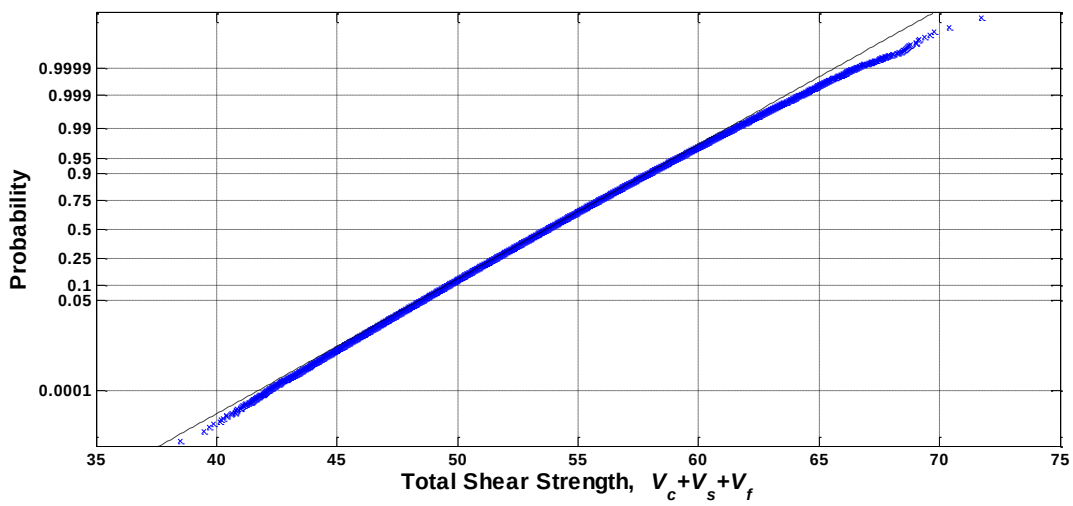

Figure A 7.5 Normal Probability Paper Plot of the Total Shear Strength

A7.3.3 Girder Distribution Factor

Girder distribution factors (g) have been the subject of many studies. NCHRP sponsored two recent studies for the development of girder distribution factors to succeed the $S/$constant expressions that were adopted in AASHTO AASHTO Standard Specifications (AASHTO, 2007) for a long time. NCHRP Project 12-26 developed the expressions currently in AASHTO LRFD (AASHTO, 2008). NCHRP 12-62 (BridgeTech Inc et al., 2007), investigated the development of simplified equations for girder distribution factors. The final report from NCHRP Project 12-62 (BridgeTech Inc et al., 2007) provides valuable information about the variability in the girder distribution factors currently adopted in AASHTO LRFD (AASHTO, 2008). The bias (λ_g) and

coefficient of variation (*COV(g)*) are given for different girder bridge types, number of loaded lanes, girder location (exterior or interior), and straining action (shear and moment). They are defined as:

$$\lambda_g = \mu\left(\frac{g_{\text{simplified}}}{g_{\text{rigorous}}}\right) \tag{A7-12}$$

$$COV(g) = \frac{\sigma\left(\frac{g_{\text{simplified}}}{g_{\text{rigorous}}}\right)}{\mu\left(\frac{g_{\text{simplified}}}{g_{\text{rigorous}}}\right)} \tag{A7-13}$$

where: $g_{\text{simplified}}$ is the girder distribution factor as determined using AASHTO LRFD (AASHTO, 2008) equations, and g_{rigorous} is the girder distribution factor obtained from a refined grillage analysis model.

Of interest for the current study is the variability in shear distribution factors for reinforced concrete decks on girder bridges. Table A 7.9 lists the values extracted from NCHRP Report 592 (BridgeTech Inc et al., 2007). It can be seen that the simplified approach overestimates the shear distribution factor on average by values that range from 13.4% to 41.5%. The coefficient of variation also varies from 7.2% to 25%. Since this study is mainly concerned with an ultimate limit state, a multiple lane loading condition will most probably control the shear design. Therefore, a bias of 1.134 and a coefficient of variation of 15.7% will be used in the reliability calibration.

The distribution type was not provided in the report. A normal distribution was assumed which is often conservative since it covers negative values over the entire domain from $-\infty$ to $+\infty$.

Table A 7.9 Shear Bias and COV in Girder Distribution Factor Equations (BridgeTech Inc et al., 2007)

Girder Location	HL-93 Loading	System	Bias	COV
Exterior	Single Lane	RC	1.415	20.4%
		PSC	1.305	13.2%
	Multiple Lanes	RC	1.337	25.0%
		PSC	1.307	23.9%
Interior	Single Lane	RC	1.312	9.1%
		PSC	1.296	7.2%
	Multiple Lanes	RC	1.134	15.7%
		PSC	1.134	13.6%

A7.4 Limit State Function

A limit state function that accounts for the variability of all nondeterministic parameters will now be established. The complexity of the limit state function depends on the level of detail for which the results will be used. In this study, the variability of material properties and fabrication tolerances will be represented with one random variable whose statistical properties have been determined in Section A7.3.2.4. Other random variables will be introduced to account for variability in the design load models and the theoretical model proposed in this study. Equation A7-14 gives the limit state function used in this study.

$$Z = \alpha_{MF}\ \xi_P\ V_{\mathrm{n}} - (\zeta_{\mathrm{WS}} V_{\mathrm{WS}} + \zeta_{\mathrm{DC}} V_{\mathrm{DC}} + \frac{\zeta_{\mathrm{LL+IM}} V_{\mathrm{LL}}}{\eta_{\mathrm{GDF}}}) \qquad \text{(A7-14)}$$

The limit state function (Z) accounts for variability in the material and fabrication tolerances through the random variable (α_{MF}) which has a bias (λ_{MF}) and coefficient of variation ($COV(MF)$), whose values are taken from Table A 7.8. The analysis model uncertainty is represented by the random variable (ξ_p) which has been established using the compiled database. The bias (λ_P) and coefficient of variation ($COV(P)$) for ξ_p were found to be different for each mode of failure. The reliability study was assumed to address girder strengthening where U-wrapping is feasible. Thus, the uncertainty in the girder distribution factor (which affects the live load moment calculations) had to be accounted for through the random variable (η_{GDF}) which has a bias ($\lambda_{g_{v,Int}}$) and COV ($g_{v,Int}$) equal to 1.134 and 0.157, respectively, for reinforced concrete interior girders. The corresponding values for exterior reinforced concrete girders are 1.307 and 23.9%. Table A 7.10 summarizes the statistical characteristics of all the random variables used in the study.

Table A 7.10 Summary of Bias and COV Values Used in Calibration Study

Random Variable		Bias	COV	Distribution
Material and Fabrication Tolerances, α_{MF}		Varies (Table A 7.7)		Normal
Analysis Model, ξ_P	FRP Rupture	1.680	0.330	LogNormal
	Other	1.410	0.269	LogNormal
Wearing Surface DL, ζ_{WS}		1.000	0.250	Normal
Component DL, ζ_{DC}		1.050	0.100	Normal
Highway LL (including impact), $\zeta_{\mathrm{LL+IM}}$	L=45 ft	1.041	0.180	Normal
	L=60 ft	1.046	0.180	Normal
	L=75 ft	1.071	0.180	Normal
LRFD Girder Distribution Factor, η_{GDF}	Interior	1.134	0.157	Normal
	Exterior	1.307	0.239	Normal

A7.5 Reliability Analysis

The goal of structural reliability analysis is to quantitatively assess the probability of failure (P_f) for a given design procedure knowing the uncertainties associated with relevant parameters. Quantifying P_f is performed on a limit state function ($Z()$) that describes the mode of failure. The simplest form of the limit state function is:

$$Z(R,Q) = R - Q \tag{A7-15}$$

where: R is the random variable representing the resistance of the member and Q is the random variable representing the load effect acting on the member.

Based on that formulation, a failure is defined as a condition where the resistance (R) of the member falls below the applied load demand (Q); i.e. $Z()$ is negative. Figure A 7.6 shows a graphical representation of the three random variables in the given LSF; namely $Z()$, R, and Q. In general, $Z()$ is more complex and involves a number of random variables, $X_1, X_2, \cdots, X_n$, representing dimensions, material properties, loads …etc.

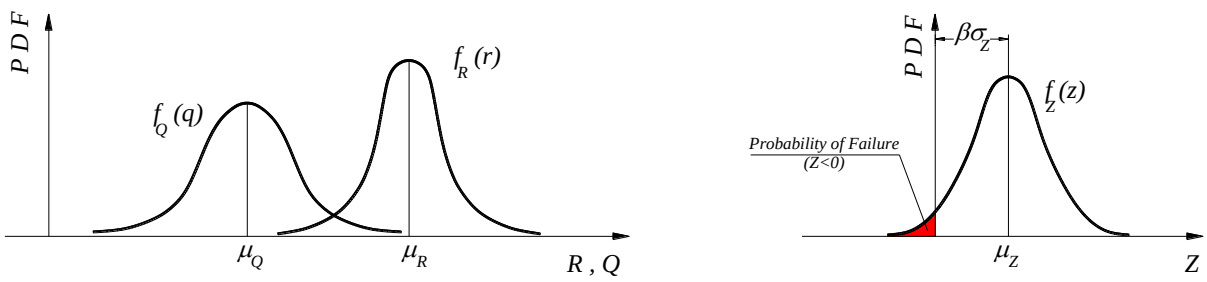

Figure A 7.6 Graphical illustration of *R, Q,* and *Z(R,Q)*

The probability of failure (P_f) is often expressed in terms of the *Reliability Index* (β_r). The relationship between β_r and P_f is:

$$P_f = \Phi(-\beta_r) \tag{A7-16}$$

where: $\Phi(\cdot)$ is a Cumulative Distribution Function (CDF) for a limit state function ($Z()$) that represents the loading action in question; e.g. shear, flexure, … etc.

The reliability index is also defined as the ratio between the mean and standard deviation of the LSF, which can be seen in Figure A 7.6.

$$\beta_r = \frac{\mu_Z}{\sigma_Z} \tag{A7-17}$$

The relationship between P_f and β_r is given numerically in Table A 7.9 for a few key values that cover the range often encountered in structural engineering problems.

Table A 7.11 Relationship Between the Reliability Index (β_r) and the Probability of Failure (P_f)

P_f	β_r
0.1	1.28155
0.01	2.32635
0.001	3.09023
0.0001	3.71902
0.00001	4.26489
0.000001	4.75342
0.0000001	5.19934
0.00000001	5.61200

β_r	P_f
0	0.500000000000
1	0.158655253931
2	0.022750131948
3	0.001349898032
4	0.000031671242
5	0.000000286652
6	0.000000000987
7	0.000000000001

The reliability index (β_r) which represents the risk level of any design component, can be calculated using various methods. In most cases, the limit state function can be simplified into two random variables representing the structural resistance (R) and the collective load effects (Q). If a lognormal distribution is assumed for the resistance (R) and a normal distribution is assumed for the load effects (Q), one can calculate the reliability index using an approximate formula (Nowak and Collins, 2000) for the reliability index (β_r) which is given as:

$$\beta_r = \frac{\lambda_R R_n A[1-\ln(A)] - \lambda_Q Q_n}{\sqrt{(\sigma_R A)^2 + (\sigma_Q)^2}} \qquad \text{(A7-18)}$$

where:

$$A = 1 - k\,COV(R) \qquad \text{(A7-19)}$$

in which: k measures the shift of the design point from the mean value and is typically taken equal to 2.0.

The previous expression was used in several calibration studies including AASHTO LRFD specifications for highway bridges (Nowak, 1999) and horizontally curved steel girder bridges (Kulicki et al., 2006). One of the limitations of the expression given in Equation A7-18 is that it returns good results when the coefficient of variation of the resistance ($COV(R)$) is less than 20%. In the current study, higher $COV(R)$ values were determined. Therefore, utilizing the previous expression was deemed unacceptable, and hence, a more exact analysis was used.

The First Order Reliability Method (FORM) is often used by researchers (El-Tawil and Okeil, 2002; Okeil et al., 2002) for calculating β_r. In FORM, the closest point (also known as the design point) on failure surface as defined by the limit state function to the origin of the design space is determined, and β_r is defined as the distance between those two points (Nowak and Collins, 2000). FORM expands the limit state function using a first order Taylor series expansion which approximates the failure surface by a tangent plane at the point of interest. An iterative process executed on transformed standard normally distributed random vectors is employed to find the design point. A detailed description of this process (Estes and Frangopol, 1998) can be found in and is summarized in Additional Material O to Appendix. A MATLAB computer program was

developed to solve the structural reliability problem using FORM and was used to determine the β_r values reported in this study.

A7.6 Target Reliability Index ($\beta_{r,\text{target}}$)

The main goal of code writing committees is to ensure that components designed using any proposed provision will have a probability of failure (P_f) that is below the expectations of users, owners, designers and all parties involved. Design codes calibrated roughly within the past decade, have come to converge on a range of P_f that if translated to β_r values it would be between 3.0 and 4.5 for strength limit states. The first step in conducting any calibration is to identify a target reliability index ($\beta_{r,target}$). A $\beta_{r,target}$ value of 3.5 was adopted during the calibration of AASHTO LRFD provisions (AASHTO, 2008). This target value corresponds to a probability of failure equal to 2.3263×10^{-4}. Therefore, a similar target value (i.e. 3.50) will be used in the calibration of the design provisions in this study.

A7.7 Calibration of Proposed Design Equation

The proposed design equation was calibrated during its development through iterations of reliability assessments of the aforementioned design space. Earlier versions of the expressions produced low β_r values and were adjusted to improve their performance over the design space covered by the chosen bridges. The final version of the design equation is the one used in the final design presented in this report. The reliability of each of the 36 bridges in the chosen design space was calculated using the procedures described in this Appendix. The results from these analyses can be seen in Table A 7.12.

It can be seen that the proposed design equation results in β_r values close to the target reliability index ($\beta_{r,target}$) of 3.5. The bridges with the lowest reliability index are L60F3ID where $\beta_r = 3.12$. The probability of failure corresponding to this reliability index is 9.13508×10^{-4}. It should be noted that despite the fact that this reliability index is lower than what the target value is, it still is within the realm of low P_f values. Furthermore, the calibration procedure followed in this study is identical to that used in the calibration of specifications used in the design of new structures. The nature of this study is slightly different in the sense that it addresses strengthening of existing structures. Existing structures undergo many inspections to identify their actual properties (materials, dimensions, …etc.) before executing any strengthening techniques. These inspections substantially reduce or even eliminate part of the uncertainties incorporated in this study. Furthermore, a 75-year design life may be needed for newly constructed bridges. Conversely, aging deficient bridges may be strengthened to extend their service life by 10 or 20 years. This implicit shorter design life goal leads to lower predicted highway loads, which was not utilized in the calibration. In summary, it can be said that the calibrated design equations produce acceptable designs.

Table A 7.12 Reliability Index (β_r) Results From Calibration Study

Bridge		Case	β_r	
Span Length	Girder		Rupture	Debond
45 ft	Interior	L45F1I	3.482	3.502
		L45F2I	3.473	3.491
		L45F3I	3.463	3.480
	Exterior	L45F1E	3.248	3.132
		L45F2E	3.241	3.125
		L45F3E	3.232	3.117
60 ft	Interior	L60F1I	3.259	3.278
		L60F2I	3.249	3.251
		L60F3I	3.241	3.230
	Exterior	L60F1E	3.257	3.155
		L60F2E	3.256	3.151
		L60F3E	3.252	3.146
75 ft	Interior	L75F1I	3.403	3.399
		L75F2I	3.401	3.393
		L75F3I	3.394	3.385
	Exterior	L75F1E	3.218	3.147
		L75F2E	3.211	3.138
		L75F3E	3.186	3.129

To demonstrate the performance of the design equation over a wider range of parameters, the following procedure is followed:

1. For assumed load values (e.g. V_{LL+IM}) and load ratios (e.g. $V_{LL+IM}/(V_{DW}+V_{DC})$), determine the required nominal strength using the LRFD design equation.

$$V_n = \frac{1.50V_{DW} + 1.25V_{DC} + 1.75V_{LL+IM}}{\phi} \qquad \text{(A7-20)}$$

2. Determine the mean and standard deviation values for each random variable using the nominal values from Step 1 and the bias and COV values established in this study.
3. Calculate the reliability index using the limit state function (Z) given in Equation A7-14.
4. Repeat the previous steps after varying the initial assumption for any parameter of interest; e.g. LL-to-DL ratio.

This procedure was used to demonstrate the performance of the proposed design procedure for two main parameters; namely span length and girder spacing. Span lengths from 20 feet to 90 feet were covered in this parametric study. The lower bound of this range represents the shortest span length of a bridge covered by AASHTO LRFD (AASHTO, 2008), while the upper bound represents a practical limit of the feasibility of reinforced concrete girder bridges. Three girder spacings were considered. They also reflect practical values for reinforced concrete bridges, namely 5 feet, 7 feet, and 9 feet. The results from this parametric study are presented and discussed next.

Figure A 7.7 shows a plot of the results from one of these parametric studies. Three curves are shown in the plot. Each represents one of the girder spacings covered in this parametric study. It can be seen from the plot that the reliability index exceeds 3.50 for shorter span lengths. The plot also shows that as the span length increases, a decrease in β_r values are to be expected, which is consistent with other calibration studies (NCHRP Report 368). In all cases, the lowest β_r values did not drop below 3.1 which corresponds to a probability of failure (P_f) equal to 9.676x10^{-4}.

The effect of girder spacing can also be seen in Figure A 7.7. For shorter girder span lengths, the reliability index values are almost identical with very small differences between the β_r values obtained for each girder spacing case. Differences between β_r values become distinguishable for longer span lengths. Nevertheless, the differences are still considered small (less than 0.05) and do not call for conducting more thorough investigations. It should be noted that the kink in the plots seen in Figure A 7.7 occur at a span length of about 30 feet. This is due to the introduction of the third axle of the design truck load with an assumed distance between the rear axles (i.e. 14 feet). In such a case, the distance between the front and rear axle is 28 feet, which leads to an abrupt change in the LL-to-DL ratio.

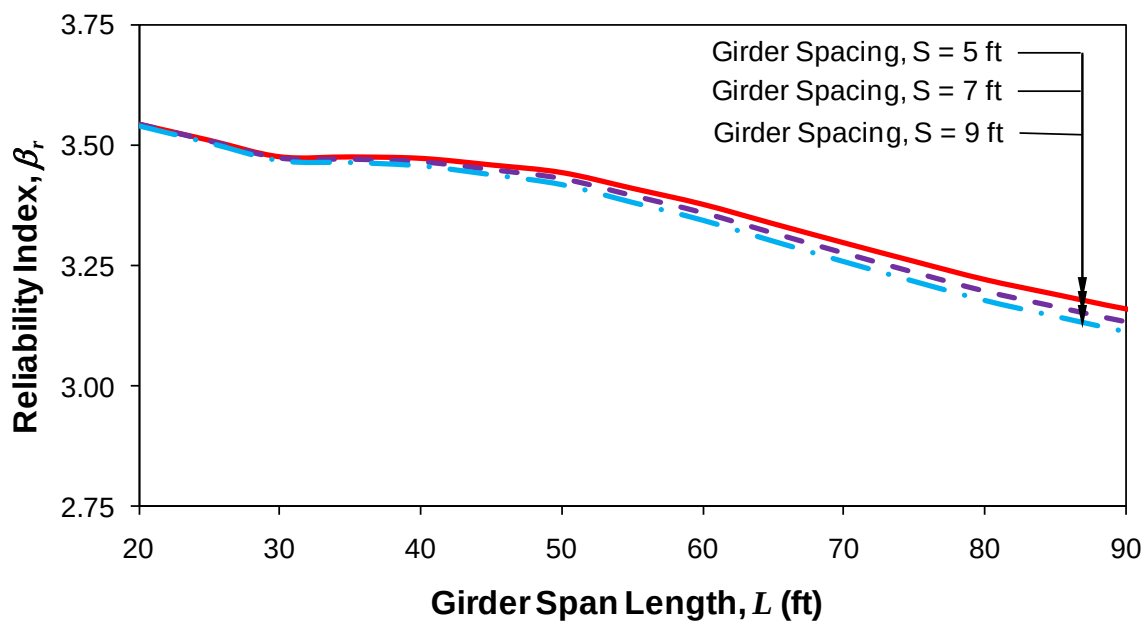

Figure A 7.7 Reliability Results of Proposed Design Equation for Different Span Lengths and Girder Spacings

In addition to the reliability results shown in Figure A 7.7, the proposed strain reduction factor, R_f, expressions were also investigated for different coefficient values. For the anchored FRP expression, the coefficient was varied between 2.8 and 4.0. The corresponding coefficient for the non-anchored R_f expression were varied between 2.1 and 3.0. Figure A 7.8 shows a comparison of the reliability results for each of the considered coefficients.

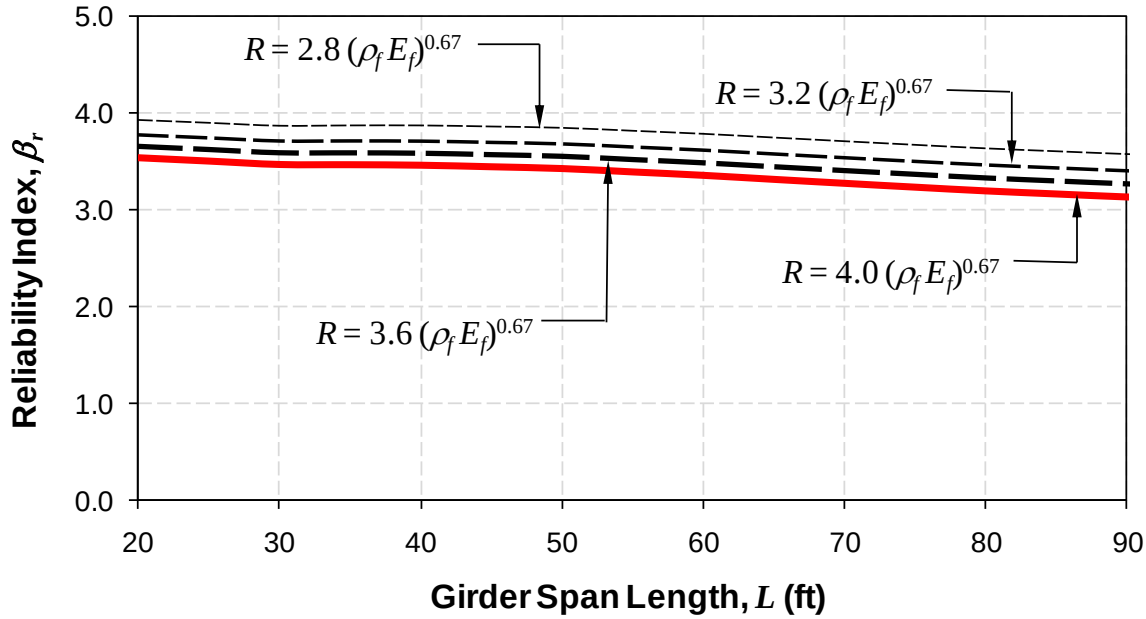

(a) Proposed Expressions (Anchored FRP)

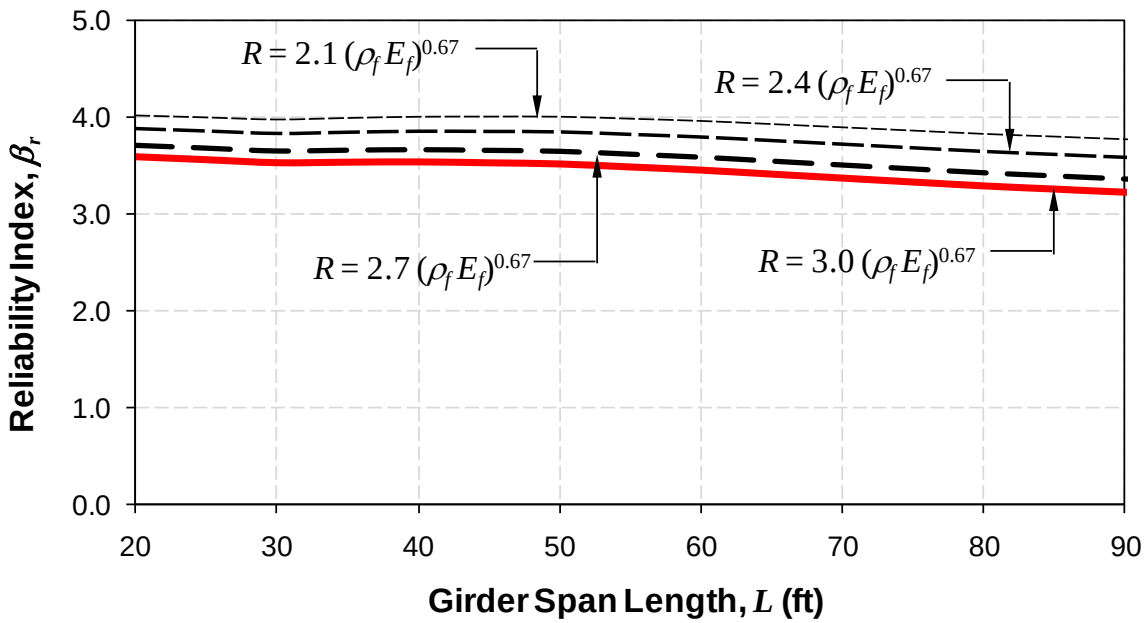

(b) Proposed Expressions (Non-anchored FRP)

Figure A 7.8 Reliability indices for reinforced concrete bridge girders.

As expected, the reliability index β_r increases as more conservative; i.e. smaller, R_f values are used. For example, an R_f coefficient of 2.8 for the anchored FRP case and 2.1 for the non-anchored FRP case yield β_r values that are consistently higher than 3.50. The proposed coefficients yield β_r values higher than 3.50 for short span lengths which drop for longer span lengths to values that are below 3.50 with a minimum value of 3.12. It is believed that the

proposed expressions ($R_f = 4(\rho_f E_f)^{-0.67}$ for anchored FRP and $R_f = 3(\rho_f E_f)^{-0.67}$ for non-anchored FRP) achieve adequate reliability for the purpose of strengthening deficient girders as a result of the fact that the reliability study used a much larger database than any other databases used in similar calibration exercises. Qualitatively, this more extensive database has the ability to uncover unforeseen uncertainties that may be missed if a smaller sample is used. Quantitatively, the larger database produces a higher confidence level in the statistical results from which they were extracted.

A7.8 Verification of Reliability Results Using Monte Carlo Simulations

In this section, results of reliability index calculations using Monte Carlo simulations are presented. The purpose of this study is to verify the results obtained using FORM and ensure that the solution converged to a global design point rather than a local one. The case of L45F1IR is chosen as the validation case. Random values for all the random variables represented in the limit state function were generated based on the statistical characteristics given in Table A 7.10. Histograms of the random values generated for each of the random variables in Equation A7-14 are plotted in Figure A 7.9, which only shows values generated from 10 million simulations. The limit state function was then evaluated for each of the simulated randomly generated values.

$$z_i = \alpha_{MF,i}\, \xi_{P,i}\, V_{\mathrm{n}} - (\zeta_{\mathrm{WS},i} V_{\mathrm{WS}} + \zeta_{\mathrm{DC},i} V_{\mathrm{DC}} + \frac{\zeta_{\mathrm{LL+IM},i} V_{\mathrm{LL}}}{\eta_{\mathrm{GDF},i}}) \qquad \text{(A7-21)}$$

Each of the evaluations (z_i) was tested for failure. The summation of all the cases where z_i fell below zero, indicates the number of simulated failure cases (N_f). The ration between N_f and the total number of simulations (N) is a measure of the probability of failure (P_f) which can be used to calculate the reliability index (β_r). Table A 7.13 lists the results obtained from analyses conducted using different numbers of simulations. The purpose of trying different numbers of simulations is to ensure that the results are stable and the chosen number of simulations is sufficient.

It can be seen from the results in Table A 7.13 that the reliability index (β_r) obtained using 100,000,000 Monte Carlo simulations (3.443) is almost identical to that obtained using FORM (3.482). This result validates the approach used in this study and justifies using it instead of the approximate expression which is deemed not applicable for the current study.

Table A 7.13 Reliability Index (β_r) Results From Monte Carlo Simulations

N	N_f	P_f	β_r
5,000	1	0.00020000	3.5401
10,000	6	0.00060000	3.2389
50,000	18	0.00036000	3.3818
100,000	26	0.00026000	3.4702
500,000	138	0.00027600	3.4542
1,000,000	283	0.00028300	3.4474
5,000,000	1,418	0.00028360	3.4468
10,000,000	2,876	0.00028760	3.4430
20,000,000	5,750	0.00028750	3.4431
100,000,000	28,804	0.00028804	3.4426

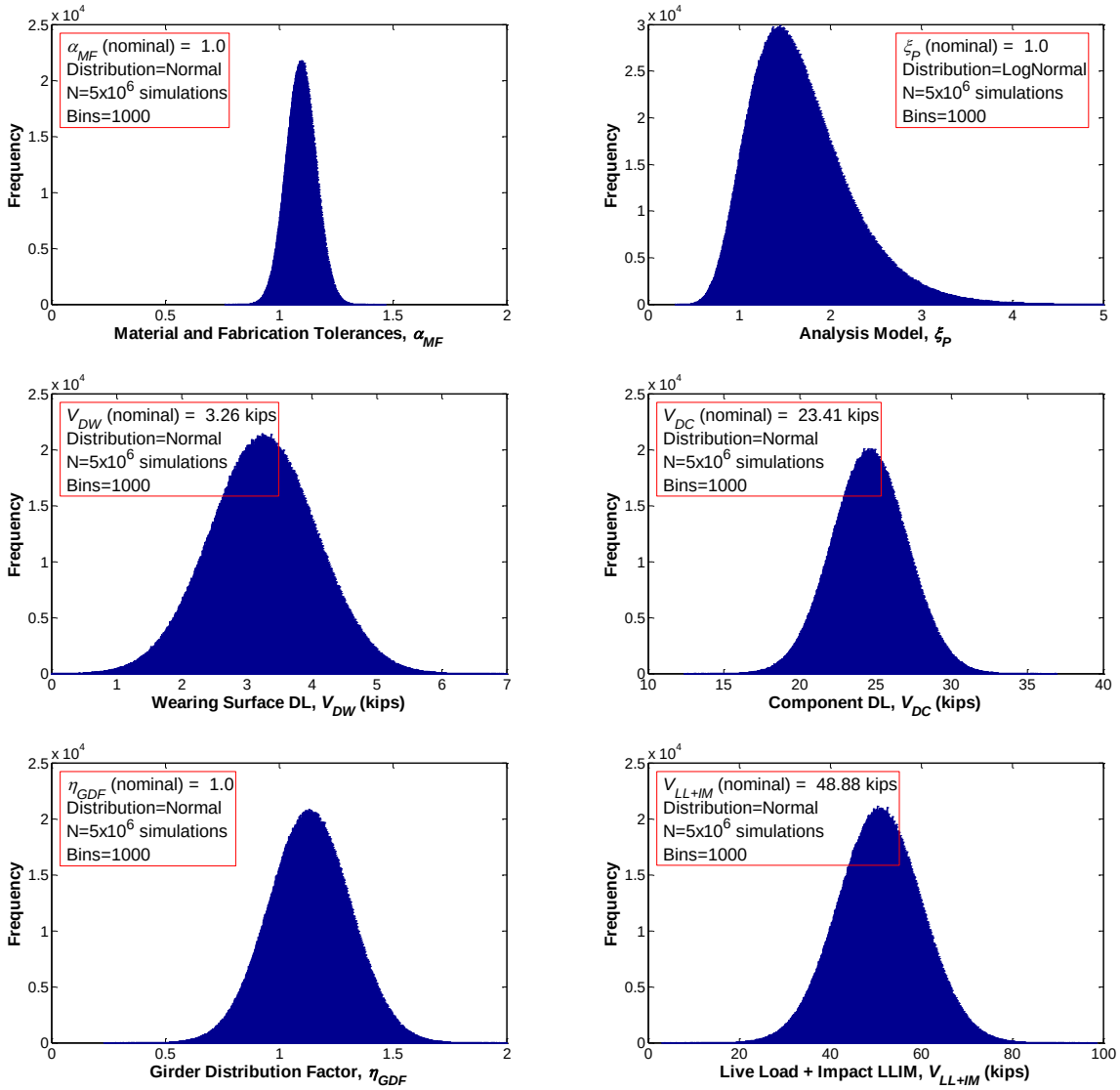

Figure A 7.9 Histograms of Randomly Generated Numbers for Random Variables in Limit State Function

A7.9 Summary of Reliability Study

A study was conducted to assess the performance of the proposed design equation after calibrating them using theory of structural reliability. The variabilities inherent in both resistance and demand sides of the design equation were incorporated to assess the reliability of the proposed design approach. Thirty-six bridges were used in the calibration study. The bridges covered different span lengths, FRP contribution levels, interior and exterior girders, and use of anchorage or lack thereof.

The statistical characteristics of the random variables were obtained from the literature for most cases, except for some that needed to be assessed for this study, such as the accuracy of the analysis model, and the material and fabrication tolerances. The high scatter nature of the results in the database prohibited the use of simplified approximate reliability index expressions. Therefore, the First Order Reliability Method (FORM) was utilized. The iterative solution procedure converges on the design point whose distance from the origin in the transformed domain is equal to the reliability index (β_r). A validation study was conducted to ensure that the FORM results represent the global minimum and not a local minimum. The reliability index for one case was evaluated using 100,000,000 Monte Carlo simulations. The β_r value obtained from the simulations was almost identical to that obtained from FORM.

The reliability study shows that the proposed design expressions yield components that have a reliability index (β_r) in the range of 3.15-3.55. This range was deemed acceptable for strengthening applications were the design life is less than the 75-year design life targeted for new structures. Furthermore, inspections and evaluations of existing structures in need of strengthening reduce or eliminate many of the uncertainties and variabilities incorporated in this study.

REFERENCES

AASHTO (1994), *AASHTO LRFD Bridge Design Specifications*, 1st edition, Washington, DC, USA.

AASHTO (2002), *Standard Specifications for Highway Bridges*, 17th edition, Washington, DC, USA.

AASHTO (2007), *AASHTO LRFD Bridge Design Specifications*, 3rd edition, Washington, DC, USA.

AASHTO (2008), *AASHTO LRFD Bridge Design Specifications*, 4th edition, Washington, DC, USA.

Abdelrahman, A. A., El-Dieb, A. S., Gewaily, T. H., and Okba, S. H. (2009), "Bond Behavior of Carbon Fiber Sheets to Cracked Concrete," *Proceedings*, 9th International RILEM Symposium on Non-Metalic (FRP) Reinforcement for Concrete Structures (FRPRCS-9), Sidney, Australia, 4 pp.

ACI-ASCE Committee 445 (1998), "Recent Approaches to Shear Design of Structural Concrete," *Journal of Structural Engineering*, Vol. 124, No. 12, pp. 1375-1417.

ACI Committee 318 (1999), *Building Code Requirements for Structural Concrete and Commentary (ACI 318-99)*, Farmington Hills, MI, USA.

ACI Committee 318 (2002), *Building Code Requirements for Structural Concrete and Commentary (ACI 318-02)*, Farmington Hills, MI, USA.

ACI Committee 318 (2008), *Building Code Requirements for Structural Concrete and Commentary (ACI 318-08)*, Farmington Hills, MI, USA.

ACI Committee 440 (2002), *Guide for the Design and Construction of Externally Bonded FRP Systems for Strengthening Concrete Structures (ACI 440.2R-02)*, Farmington Hills, MI, USA.

ACI Committee 440 (2008), *Guide for the Design and Construction of Externally Bonded FRP Systems for Strengthening Concrete Structures (ACI 440.2R-08)*, Farmington Hills, MI, USA.

Adey, B., San-Román, J. D. C., and Brühwiller, E. (1998), "Carbon Fiber Shear Strengthening of Rectangular Concrete Beams," Final Report 97.02, École Polythechnique de Lausanne, Lausanne, Switzerland, 28 pp.

Adhikary, B. B., Mutsuyoshi, H., and Ashraf, M. (2004), "Shear Strengthening of Reinforced Concrete Beams Using Fiber-Reinforced Polymer Sheets with Bonded Anchorage," *ACI Structural Journal*, Vol. 101, No. 5, pp. 660-668.

Aidoo, J., Harries, K. A., and Petrou, M. F. (2004), "Fatigue Behavior of Carbon Fiber Reinforced Polymer-Strengthened Reinforced Concrete Bridge Girders," *Journal of Composites for Construction*, Vol. 8, No. 6, pp. 501-509.

Aiello, M. A., and Ombres, L. (2004), "Cracking and Deformability Analysis of Reinforced Concrete Beams Strengthened with Externally Bonded Carbon Fiber Reinforced Polymer Sheet," *Journal of Materials in Civil Engineering*, Vol. 16, No. 5, pp. 392-399.

Al-Sulaimani, G. J., Shariff, A., Basanbul, I. A., Baluch, M. H, and Ghaleb, B. N. (1994), "Shear Repair of Reinforced Concrete by Fiber Glass Plate Bonding," *ACI Structural Journal*, Vol. 91, No. 4, pp. 458-464.

Alexander, J. G. S., and Cheng, J. J. R. (1997), "Shear Rehabilitation of G-Girder Bridges Using CFRP Sheets," Structural Engineering Report No. 218, Department of Civil and Environmental Engineering, University of Alberta, Edmonton, Canada, 181 pp.

Alrousan, R. Z., Issa, M. A., and Issa, M. A. (2009), "Size Effect of Reinforced Concrete Beams on Shear Contribution of CFRP Composites," *Proceedings*, 9th International RILEM Symposium on Non-Metalic (FRP) Reinforcement for Concrete Structures (FRPRCS-9), Sidney, Australia, 4 pp.

Antonopoulos, C. P. (1996), "Shear Strengthening of Reinforced Concrete Structures Using Composite Materials," Diploma Thesis, Department of Civil Engineering, University of Patras, Patras, Greece.

Aprile, A., and Benedetti, A. (2004), "Coupled Flexural-Shear Design of RC Beams Strengthened with FRP," *Composites Part B: Engineering*, Vol. 35, No. 1, pp. 1-25.

Araki, N., Matsuzaki, Y., Nakano, K., Kataoka, T., and Fukuyama, H. (1997), "Shear Capacity of Retrofitted RC Members with Continuous Fiber Sheets," *Proceedings*, 3rd International RILEM Symposium on Non-Metallic (FRP) Reinforcement for Concrete Structures (FRPRCS-3), Sapporo, Japan, pp. 515-522.

Arteaga, A., Alzate, A., De Diego, A., Gutierrez, J. P., Lopez, C., Perera, R., and Barchin, M. (2009), "Experimental Study on FRP Shear Strengthened Full-Scale Concrete Beams," *Proceedings*, 9th International RILEM Symposium on Non-Metalic (FRP) Reinforcement for Concrete Structures (FRPRCS-9), Sidney, Australia, 4 pp.

Arya, C., Ofori-Darko, F. K., and Pirethapon, G. (1995), "FRP Rebars and the Elimination of Reinforcement Corrosion in Concrete Structures," *Proceedings*, 2nd International RILEM Symposium on Non-Metallic (FRP) Reinforcement for Concrete Structures (FRPRCS-2), Ghent, Belgium, pp. 227-234.

Asplund, S. O. (1949), "Strengthening Bridge Slabs with Grouted Reinforcement," *American Concrete Institute Journal*, Vol. 20, No. 5, pp. 397-406.

ASTM A370-08a (2008), *Standard Test Methods and Definitions for Mechanical Testing of Steel Products*, American Society for Testing Materials (ASTM International).

ASTM C 39/C 39M-05 (2005), *Standard Test Method for Compressive Strength of Cylindrical Concrete Specimens*, American Society for Testing Materials (ASTM International).

ASTM D4541-03 (2003), *Standard Test Method for Pull-Off Strength of Coatings Using Portable Adhesion Testers*, American Society for Testing Materials (ASTM International).

Bakht, B., Al-Bazi, G., Banthia, N., Cheung, M., Erki, M. A., Faoro, M., Machida, A., Mufti, A. A., Neale, K. W., and Tadros, G. (2000), "Canadian Bridge Design Code Provisions for Fiber-Reinforced Structures," *Journal of Composites for Construction*, Vol. 4, No. 1, pp. 3-15.

Bakis, C. E., Bank, L. C., Brown, V. L., Cosenza, E., Davalos, J. F., Lesko, J. J., Machida, A., Rizkalla, S. H., and Trianatfillou, T. C. (2002), "Fiber-Reinforced Polymer Composites for Construction – State of the Art Review," *Journal of Composites for Construction*, Vol. 6, No. 2, pp. 73-87.

Baky, H. A., Ebead, U. A., and Neale K. W. (2007), "Flexural and Interfacial Behavior of FRP Strengthened Reinforced Concrete Bemas," *Journal of Composites for Construction*, Vol. 11, No. 6, pp. 629-639.

Balazs, G. L. (1991), "Fatigue of Bond," *ACI Materials Journal*, Vol. 88, No. 6, pp. 620-629

Bank, L. C., Borowicz, D. T., Arora, D., and Lamanna, A. J. (2004), "Strengthening of Concrete Beams with Fasteners and Composite Material Strips-Scaling and Anchorage Issues," Technical Report ERDC/GSL TR-04-5, U.S. Army Corps of Engineers, Washington, DC.

Barnes, A. R., and Mays, C. G. (1999), "Fatigue Performance of Concrete Beams Strengthened with CFRP Plates", *Journal of Composites for Construction*, Vol. 3, No. 2, pp. 63-72.

Barros, J., and Dias, S. (2003), "Shear Strengthening of Reinforced Concrete Beams with Laminate Strips of CFRP," *Proceedings*, International Conference on Composites in Constructions (CCC2003), Italy, pp. 289-294.

Barros, J. A. O., and Dias, S. J. E. (2006), "Near Surface Mounted CFRP Laminates for Shear Strengthening of Concrete Beams," *Cement & Concrete Composites*, Vol. 28, No. 3, pp. 276-292.

Barros, J. A. O., and Dias, S. J. E. (2008), "Shear Strengthening of T Cross Section Reinforced Concrete Beams by Near Surface Mounted Technique," *Journal of Composites for Construction*, Vol. 12, No. 3, pp. 300-311.

Batdorf, S. B., and Ghaffarian, R. (1984), "Size Effect and Strength Variability of Unidirectional Composites," *International Journal of Fracture*, Vol. 26, No. 2, pp. 113-123.

Beber, A. J. (2003), "Comportamento Estrutural de Vigas de Concreto Armado Reforcadas com Compositos de Fibra de Carbono," Ph.D. Thesis, Universidade Federal do Rio Grande do Sul, Porto Alegre, Brasil.

Ben Ouezdou, M., Bae, S., and Belarbi, A. (2008), "Effective Bond Length of Externally Bonded FRP Sheets," *Proceedings*, 4th International Conference on FRP Composites in Civil Engineering (CICE-2008), Zurich, Switzerland.

Berset, J. D. (1992), "Strengthening of Reinforced Concrete Beams for Shear Using FRP Composites," M.S. Thesis, Department of Civil and Environmental Engineering, MIT, Boston, MA, USA.

Bilotta, A., Di Ludovico, M., and Nigro, E. (2009a), "FRP Debonding on Concrete Members. Part I: Experimental Investigation," *Proceedings*, 9th International RILEM Symposium on Non-Metalic (FRP) Reinforcement for Concrete Structures (FRPRCS-9), Sidney, Australia, 4 pp.

Bilotta, A., Di Ludovico, M., and Nigro, E. (2009b), "FRP Debonding on Concrete Members. Part II: Capacity Model Calibration," *Proceedings*, 9th International RILEM Symposium on Non-Metalic (FRP) Reinforcement for Concrete Structures (FRPRCS-9), Sidney, Australia, 4 pp.

Bizindavyi, L., and Neale, K. W. (1997), "Experimental and Theoretical Investigation of Transfer Lengths for Composite Laminates Bonded to Concrete," *Proceedings*, Annual Conference of the Canadian Society for Civil Engineering, pp. 51-60.

Bizindavyi, L., and Neale, K. W. (1999), "Transfer Lengths and Bond Strengths for Composites Bonded to Concrete," *Journal of Composites for Construction*, Vol. 3, No. 4, pp. 153-160.

Bousselham, A., and Chaallal, O. (2004), "Shear Strengthening Reinforced Concrete Beams with Fiber-Reinforced Polymer: Assessment of Influencing Parameters and Required Research," *ACI Structural Journal*, Vol. 101, No. 2, pp. 219-227.

Bousselham, A., and Chaallal, O. (2006a), "Behavior of Reinforced Concrete T-Beams Strengthened in Shear with Carbon Fiber-Reinforced Polymer-An Experimental Study," *ACI Structural Journal*, Vol. 103, No.3, pp. 339-347.

Bousselham, A., and Chaallal, O. (2006b), "Effect of Transverse Steel and Shear Span on the Performance of RC Beams Strengthened in Shear with CFRP," *Composites Part B: Engineering*, Vol. 37, No. 1, pp. 37-46.

Bousselham, A., and Chaallal, O. (2006c), "Influence of the Beam Size on the Shear Strength of RC T-Beams Retrofitted in Shear with CFRP Fabrics," *ACI Structural Journal*.

Breña, S. F., and Gussenhoven, R. (2005), "Fatigue Behaviour of Reinforced Concrete Beams Strengthened with Different FRP Laminate Configurations," *Proceedings*, 7th International RILEM Symposium on Non-Metallic (FRP) Reinforcement for Concrete Structures (FRPRCS-7), Kansas City, Missouri, USA.

BridgeTech Inc, Tennessee Technological University, and Mertz, D. R. (2007), *NCHRP Report 592: Simplified Live Load Distribution Factor Equations*, Transportation Research Board, Washington, D.C., USA.

Brosens, K., and Van Gemert, D. (1997), "Anchoring Stresses between Concrete and Carbon Fiber Reinforced Laminates," *Proceedings*, 3rd International RILEM Symposium on Non-Metallic (FRP) Reinforcement for Concrete Structures (FRPRCS-3), Sapporo, Japan, pp. 271-278.

Budek, A., Taylor, J., and Nash, P. (2007), "The Effect of Fatigue on Understrength Shear-Critical Reinforced Concrete Beams Reinforced with External CFRP Stirrups," CIES Report, University Transportation Center Program at the University of Missouri-Rolla, Rolla, MO, USA.

Bullock, R. E. (1974), "Strength Ratios of Composite-Materials in Flexure and in Tension," *Journal of Composite Materials*, Vol. 8, pp. 200-206.

Buyukozturk, O., Gunes, O., and Karaca, E. (2004), "Progress on Understanding Debonding Problems in Reinforced Concrete and Steel Members Strengthened Using FRP Composites," *Construction and Building Materials*, Vol. 18, No. 1, pp. 9-19.

CAN/CSA A23.3-94 (1994), *Design of Concrete Structures for Buildings*, Canadian Standards Association, Rexdale, Ontario, Canada.

CAN/CSA A23.3-04 (2004), *Design of Concrete Structures for Buildings*, Canadian Standards Association, Rexdale, Ontario, Canada.

CAN/CSA S6-06 (2006), *Canadian Highway Bridge Design Code*, Canadian Standard Association, Rexdale, Ontario, Canada.

CAN/CSA S806-02 (2002), *Design and Construction of Building Components with Fiber-Reinforced Polymer*, Canadian Standard Association, Rexdale, Ontario, Canada.

Cao, S. Y., Chen, J. F., Teng, J. G., Hao, Z., and Chen, J. (2005), "Debonding in RC Beams Strengthened with Complete FRP Wraps," *Journal of Composites for Construction*, Vol. 9, No. 5, pp. 417-428.

Carolin, A., and Taljsten, B. (2005a), "Experimental Study of Strengthening for Increased Shear Bearing Capacity," *Journal of Composites for Construction*, Vol. 9, No. 6, pp. 488-496.

Carolin, A., and Taljsten, B. (2005b), "Theoretical Study of Strengthening for Increased Shear Bearing Capacity," *Journal of Composites for Construction*, Vol. 9, No. 6, pp. 497-506.

Casas, J. R., and Pascual, J. (2007), "Debonding of FRP in Bending: Simplified Model and Experimental Validation," *Construction and Building Materials*, Vol. 21, pp. 1940-1949.

Ceroni, F., and Pecce, M. (2009), "Performance of Anchorage Systems for Elements Strengthened with FRP Sheets," *Proceedings*, 9th International RILEM Symposium on Non-Metalic (FRP) Reinforcement for Concrete Structures (FRPRCS-9), Sidney, Australia, 4 pp.

Chaallal, O., Nollet, M. J., and Perraton, D. (1998a), "Shear Strengthening of RC Beams by Externally Bonded Side CFRP Strips," *Journal of Composites for Construction*, Vol. 2, No. 2, pp. 111-113.

Chaallal, O., Nollet, M. J., and Perraton, D. (1998b), "Strengthening of RC Beams with Externally Bonded Fiber-Reinforced-Plastic Plates: Design Guidelines for Shear and Flexure," *Canadian Journal of Civil Engineers*, Vol. 25, No. 4, pp. 692-704.

Chaallal, O., Nollet, M. J., and Perraton, D. (1998c), "Use of CFRP Strips for Flexure and Shear Strengthening of RC Members," *Proceedings*, 2nd International Conference on Composites in Infrastructure, Tucson, AZ, USA, pp. 249-260.

Chaallal, O., Shahawy, M., and Hassan, M. (2002), "Performance of Reinforced Concrete T-Girders Strengthened in Shear with Carbon Fiber Reinforced Polymer Fabrics," *ACI Structural Journal*, Vol. 99, No. 3, pp. 335-343.

Chaallal, O., Boussaha, F., Bousselham, A., Nollet, M. J., Masmoudi, R., and Benmokrane, B. (2009), "Fatigue Behaviour of Reinforced Concrete Beams Strengthened in Shear with Advanced Composite," *Proceedings*, 9th International RILEM Symposium on Non-Metalic (FRP) Reinforcement for Concrete Structures (FRPRCS-9), Sidney, Australia, 4 pp.

Chajes, M. J., Jansuska, T. F., Mertz, D. R., Thomson, T. A., and Finch, W. W. (1995), "Shear Strength of RC Beams using Externally Applied Composite Fabrics," *ACI Structural Journal*, Vol. 92, No. 3, pp. 295-303.

Chajes, M. J., Finch, W. W., Januzka, T. F., and Thompson, T. A. (1996), "Bond and Force Transfer of Composite Material Plates Bonded to Concrete," *ACI Structural Journal*, Vol. 93, No. 2, pp. 208-217.

Chang, T. S., and Kesler, C. E. (1958), "Fatigue Behavior of Reinforced Concrete Beams," *ACI Journal*, Vol. 55, pp. 245-254.

Chen, J. F., and Teng, J. G. (2001), "Anchorage Strength Models for FRP and Steel Plates Bonded to Concrete," *Journal of Structural Engineering*, Vol. 127, No. 7, pp. 784-791.

Chen, J. F., and Teng, J. G. (2003a), "Shear Capacity of FRP Strengthened RC Beams: FRP Debonding," *Construction Building Materials*, Vol. 17, No. 1, pp. 27-41.

Chen, J. F., and Teng, J. G. (2003b), "Shear Capacity of Fiber-Reinforced Polymer-Strengthened Reinforced Concrete Beams: Fiber Reinforced Polymer Rupture," *Journal of Structural Engineering*, Vol. 129, No. 5, pp. 615-625.

CNR-DT 200/2004 (2004), *Guide for the Design and Construction of Externally Bonded Systems for Strengthening Existing Structures – Materials, RC and PC Structures, Masonry Structures*, CNR – Advisory Committee on Technical Recommendations for Construction, National Research Council, Rome, Italy.

Collins, M. P., and Mitchell, D. (1997), *Prestressed Concrete Structures*, Response Publications, Canada.

Concrete Society (2004), *Design Guidance on Strengthening Concrete Structures using Fibre Composite Materials: Technical Report 55*, Second Edition, The Concrete Society, London, UK.

Corley, W. G., Hanson, J. M., Helgason, T. (1978), "Design of Reinforced Concrete for Fatigue," *ASCE Journal of Structural Division*,

Coronado, C. A., and Lopez, M. M. (2007), "Damage Approach for the Prediction of Debonding Failure on concrete Elements Strengthened with FRP", *Journal of Composites for Construction*, Vol. 11, No. 4, pp. 391-400.

Czaderski, C. (2002), "Shear Strengthening with Prefabricated CFRP L-Shaped plates. Test Beams S1 to S6," EMPA. Report No. 116/7, Switzerland.

Czaderski, C. and Motavalli, M. (2004), "Fatigue Behavior of CFRP L-Shaped Plates for Shear Strengthening of RC T-Beams," *Composites: Part B*, Elsevier.

Dai, J. G., Saito, Y., Ueda, T., and Sato, Y. (2005), "Static and Fatigue Bond Characteristics of Interfaces between CFRP Sheets and Frost Damage Experienced Concrete," *Proceedings*, 7th International RILEM Symposium on Non-Metallic (FRP) Reinforcement for Concrete Structures (FRPRCS-7), Kansas City, Missouri, USA.

De Lorenzis, L., and Nanni, A. (2001a), "Shear Strengthening of Reinforced Concrete Beams with Near-Surface Mounted Fiber-Reinforced Polymer Rods," *ACI Structural Journal*, Vol. 98, No. 1, pp. 60-68.

De Lorenzis, L., and Nanni, A. (2001b), "Characterization of NSM FRP Rods as Near Surface Mounted Reinforcement," *Journal of Composites for Construction*, Vol. 4, pp. 114-121.

De Lorenzis, L. (2002), "Strengthening of RC Structures with Near-Surface Mounted FRP Rods," Ph.D. Thesis, Department of Innovation Engineering, University of Lecce, Lecce, Italy, 2002.

Deniaud, C., and Cheng, J. J. R. (2001), "Shear Behavior of Reinforced Concrete T-Beams with Externally Bonded Fiber-Reinforced Polymer Sheets," *ACI Structural Journal*, Vol. 98, No. 3, pp. 386-394.

Deniaud, C., and Cheng, J. J. R. (2003), "Reinforced Concrete T-Beams Strengthened in Shear with Fiber Reinforced Polymer Sheets," *Journal of Composites for Construction*, Vol. 7, No. 4, pp. 302-310.

Deniaud, C., and Cheng, J. J. R. (2004), "Simplified Shear Design Method for Concrete Beams Strengthened with Fiber Reinforced Polymer Sheets," *Journal of Composites for Construction*, Vol. 8, No. 5, pp. 425-433.

Denton, S. R., Shave, J. D., and Porter, A. D. (2004), "Shear Strengthening of Reinforced Concrete Structures using FRP Composites," *Proceedings*, International Conference on Advanced Polymer composites for Structural applications in Constructions, Cambridge, UK, pp. 134-143.

Diab, H., and Wu, Z. (2009), "Bond Behaviour of Different FRP Sheets," *Proceedings*, 9th International RILEM Symposium on Non-Metalic (FRP) Reinforcement for Concrete Structures (FRPRCS-9), Sidney, Australia, 4 pp.

Diagana, C., Li, A., Gedalia, B., and Delmas, Y. (2003), "Shear Strengthening Effectiveness with CFF Strips," *Engineering Structures*, Elsevier, Vol. 25, No. 4, pp. 507-516.

Dolan, C. W., Rider, W., Chajes, M. J., and DeAscanis, M. (1992), "Prestressed Concrete Beams Using Non-Metallic Tendons and External Shear Reinforcement," *ACI SP 138-29*, pp. 475-495.

Drimoussis, E. H., and Cheng, J. J. R. (1994), "Shear Strengthening of Concrete Girders using Carbon Fiber Reinforced Plastic Sheets," Structural Engineering Report No. 205, Univ. of Alberta, Edmonton, Alta., Canada.

Ekenel, M., and Myers, J. J. (2005), "Effect of Environmental Conditioning & Sustained Loading on the Fatigue Performance of RC Beams Strengthened with Bonded CFRP Fabrics," *Proceedings*, 7th International RILEM Symposium on Non-Metallic (FRP) Reinforcement for Concrete Structures (FRPRCS-7), Kansas City, Missouri, USA, pp. 1571-1592.

El-Sayed, W. E., Ebead, U. A., and Neale, K. W. (2009), "Studies on Mechanically Fastened Fiber-Reinforced Polymer Strengthening Systems," *ACI Structural Journal*, Vol. 106, No. 1, pp. 49-59.

El-Tawil, S., and Okeil, A. M. (2002), "LRFD Flexural Provisions for Prestressed Concrete Bridge Girders Strengthened With Carbon Fiber-Reinforced Polymer Laminates," *ACI Structural Journal*, Vol. 99, No. 2, pp. 181-190.

Emberson, N. K. and Mays, G. C. (1996), "Significance of Property Mismatch in the Patch Repair of Structural Concrete: Part 3: Reinforced concrete members in flexure," *Magazine of Concrete Research*, Vol. 48, No. 174, pp. 45-57.

EN 1990 (2002), *Eurocode: Basis of Structural Design*, CEN.

Eshwar, N., Nanni, A., and Ibell, T. (2003), "CFRP Strengthening of Concrete Bridges with Curved Soffits," *Proceedings*, Proceedings of the International Conference on Structural Faults and Repairs, Montreal, Quebec.

Eshwar, N., Nanni, A., and Ibell, T.J. (2008), "Performance of Two Anchor Systems of Externally Bonded Fiber-Reinforced Polymer Laminates," *ACI Materials Journal*, Vol. 105, No. 1, pp. 72-80.

Estes, A. C., and Frangopol, D. M. (1998), "RELSYS: A Computer Program for Structural System Reliability," *Structural Engineering and Mechanics*, Vol. 6, No. 8, pp. 901-919.

Eurocode No. 2 (1992), *Design of Concrete Structures*, Comité Européén International du Béton, Lausanne.

Eurocode 8-3 (2004), "Design of Structures for Earthquake Resistance; Part 3: Assessment and Retrofitting of Buildings," *European Standard*, EN 1998-3m Brussels, Belgium.

fib-TG9.3 (2001), "Design and Use of Externally Bonded Fiber Polymer Reinforcement (FRP EBR) for Reinforced Concrete Structures," Technical Report Prepared by EBR Task Group 9.3, Bulletin 14, Lausanne, Swiss.

Foster, S. J., and Khomwan, N. (2005), "Determination of Bond Stress versus Slip for Externally Bonded FRP from Standardized Bond Strength Tests," *Proceedings*, International Symposium on Bond Behavior of FRP Structures, Hong Kong, China, pp. 85-90.

Funakawa, I., Shimono, K., Watanabe, T., Asada, S., and Ushijima, S. (1997), "Experimental Study on Shear Strengthening with Continuous Fiber Reinforcement Sheet and Methyl Methacrylate Resin," *Proceedings*, 3rd International RILEM Symposium on Non-Metallic (FRP) Reinforcement for Concrete Structures (FRPRCS-3), Sapporo, Japan, pp. 491-498.

Gamino, A. L., Sousa, J. L. A. O., and Bittencourt, T. N. (2009), "Application of Carbon Fiber Reinforced Polymer in Strengthening to Shear R/C T Beams," *Proceedings*, 9th International RILEM Symposium on Non-Metalic (FRP) Reinforcement for Concrete Structures (FRPRCS-9), Sidney, Australia, 4 pp.

Godat, A., Neale, K. W., and Labossiere, P. (2007), "Numerical Modeling of FRP Shear Strengthened Reinforced Concrete Beams", *Journal of Composites for Construction*, Vol. 11, No. 6, pp. 640-649.

Hag-Elsafi, O., Kunin, J., Alampalli, S., and Conway, T. (2001a), "Strengthening of Route 378 Bridge Over Wynantskill Creek in New York Using FRP Laminates," New York State Department of Transportation, Special Repot 135.

Hag-Elsafi, O., Kunin, J., and Alampalli, S. (2001b), "In-Service Evaluation of a Concrete Bridge FRP Strengthening System," New York State Department of Transportation, Special Repot 139.

Halgason, T. and Hanson, J.M. (1974), "Investigation of Design Factors Affecting Fatigue Strength of Reinforcing Bars-Statistical Analysis," *Proceedings*, Proceedings Abeles Symp. On Fatigue of Concrete, ACI, Detroit, USA, pp. 107-138.

Harlow, D. G., and Phoenix, S. L. (1981), "Probability-Distributions for the Strength of Composite-Materials II: A Convergent Sequence of Tight Bounds," *International Journal of Fracture*, Vol. 17, No. 6, pp. 601-630.

Harries, K. (2005), "Fatigue Behavior of Bonded FRP Used for Flexural Retrofit," *Proceedings*, International Symposium on Bond Behavior of FRP in Structures (BBFS 2005), International Institute for FRP in Construction, pp. 547-552.

Harries, K., and Aidoo, J. (2005), "Deterioration of FRP-to-Concrete Bond under Fatigue Loading," *Proceedings*, International Symposium on Bond Behavior of FRP in Structures (BBFS 2005), International Institute for FRP in Construction, pp. 553-558.

Harries, K., and Aidoo, J. (2006), "Debonding- and Fatigue-Related Strain Limits for Externally Bonded FRP," *Journal of Composites for Construction*, Vol. 10, No. 1, pp. 87-90.

Hassan Dirar, S. M. O., Hoult, N. A., Morley, C. T., and Lees, J. M. (2006), "Shear Strengthening of Pre-cracked Reinforced Concrete Beams Using CFRP Straps," *Proceedings*, 2nd International Congress, Fédération Internationale de Béton (FIB), Naples, Italy, ID 10-70.

Hawkins, N. M. (1974), "Fatigue Characteristics in Bond and Shear of Reinforced Concrete Beams," *ACI Publication SP-41-10*, pp. 203-235.

Holzemkampfer, O. (1994), "Ingenieurmodelle des Verbundes Gekleber Bewehrung fur Betonbauteile," Dissertation, TU Braunschweig, Germany.

Horiguchi, T., and Saeki, N. (1997), "Effect of Test Methods and Quality of Concrete on Bond Strength of CFRP Sheet," *Proceedings*, 3rd International RILEM Symposium on Non-Metallic (FRP) Reinforcement for Concrete Structures (FRPRCS-3), Sapporo, Japan, pp. 475-482.

Hoult, N., and Lees, J. (2005), "Long-Term Performance of a CFRP Strap Shear Retrofitting System," 7th International RILEM Symposium on Non-Metallic (FRP) Reinforcement for Concrete Structures (FRPRCS-7), Kansas City, Missouri, USA, pp. 685-704.

Hsu, C. T. T., Bian, H. T. and Jia, Y. X. (1997), "Research for Bond-Slip Using Sika's CorboDur System," A report to Sika Corporation, New Jersey, USA.

Hsu, C. T. T., Punurai, W., and Zhang, Z. (2003), "Flexural and Shear Strengthening of RC Beams using Carbon Fiber Reinforced Polymer Laminate," *ACI SP-211-5*, Farminton Hills, MI, pp. 89-113.

Hutchinson, R. L., and Rizkalla, S. H. (1999), "Shear Strengthening of AASHTO Bridge Girders Using Carbon Fiber Reinforced Polymer Sheets," *ACI Special Publications (SP-188)*, Vol. 188, pp. 945-958.

ICRI Technical Guideline No. 03732 (1997), *Selecting and Specifying Concrete Surface Preparation for Coatings, Sealers, and Polymer Overlays*, International Concrete Repair Institute (ICRI.

ISIS Design Manual 4 (2001), *Strengthening Reinforced Concrete Structures with Externally-Bonded Fiber Reinforced Polymers*, Intelligent Sensing for Innovative Structures, Winnipeg, Canada, 2001.

Iwashita, K., Wu, Z., Ishikawa, T., Hamaguchi, Y., and Suzuki, T. (2007), "Bonding and Debonding Behavior of FRP Sheets under Fatigue Loading," *Advanced Composite Materials*, Vol. 16, No. 1, pp. 31-44.

JCI (2003), "International Symposium on Latest Achievement of Technology and Research on Retrofitting Concrete Structures," *Proceedings*, Proceedings and Technical Report on JCI Technical Committee, Sapporo, Japan.

Jinno, Y., and Tsukagishi, H. (1998), "Structural Properties of RC Walls Strengthened by Carbon Fiber Sheets," *Proceedings*, Architectural Institute of Japan Annual Conference, Fukuoka, Japan, pp. 209-210.

JSCE (2001), *Recommendations for Upgrading of Concrete Structures with Use of Continuous Fiber Sheets*, Concrete Engineering Series 41, Japan Society of Civil Engineers, Tokyo, Japan.

Kachlakev, D. I, and Barnes, W. A. (1999a), "Flexural and Shear Performance of Concrete Beams Strengthened with Fiber Reinforced Polymer Laminates," *Composites-Part B: Engineering*, Vol. 31, pp. 445-452.

Kachlakev, D. I, and Barnes, W. A. (1999b), "Flexural and Shear Performance of Concrete Beams Strengthened with Fiber Reinforced Polymer Laminates," *Proceedings*, 4th International RILEM Symposium on Non-Metallic (FRP) Reinforcement for Concrete Structures (FRPRCS-4), Baltimore, Maryland, pp. 959-972.

Kage, T., Abe, M., Lee, H. S., Tomosawa F. (1997), "Effect of CFRP Sheets on Shear Strengthening of RC Beams Damaged by Corrosion of Stirrup," *Proceedings*, 3rd International RILEM Symposium on Non-Metallic (FRP) Reinforcement for Concrete Structures (FRPRCS-3), Sapporo, Japan, pp. 443-450.

Kamel, A. S., Elwi, A. E., and Cheng, J. J. R. (2000), "Experimental Study on the Behavior of CFRP Sheets Bonded to Concrete," *Proceedings*, 3rd International Conference on Advanced Composite Materials in Bridges and Structures, Canadian Society for Civil Engineering, Ottawa, Canada, pp. 61–68.

Kamiharako, A., Maruyama, K., Takada, K., and Shimomura, T. (1997), "Evaluation of Shear Contribution of FRP Sheets Attached to Concrete Beams," *Non-Metallic (FRP) Reinforcement for Concrete Structures*, Vol. 1, pp. 467-474.

Kaminski, B. E. (1973), "Effects of Specimen Geometry on the Strength of Composite Materials," *Analysis of the Test Methods for High Modulus Fibers and Composites, ASTM*, West Conshohocken, PA, pp. 181-191.

Kanakubo, T., Furuta, T., and Fukuyama, H. (2003), "Bond Strength between Fiber-Reinforced Polymer Laminates and Concrete," *Proceedings*, 6th International RILEM Symposium on Non-Metallic (FRP) Reinforcement for Concrete Structures (FRPRCS-6), World Scientific, Singapore, pp. 134-143.

Karbhari, V. M., and Engineer, M. (1996), "Investigation of Bond between Concrete and Composites: Use of a Peel Test," *Journal of Reinforced Plastics and Composites*, Vol. 15, No. 2, pp. 208-227.

Khalifa, A., Gold, W., Nanni, A., and Abdel Aziz, M. I. (1998), "Contribution of Externally Bonded FRP to Shear Capacity of RC Flexural Members," *Journal of Composites for Construction*, Vol. 2, No. 4, pp. 195-202.

Khalifa, A. (1999), "Shear Performance of Reinforced Concrete Beams Strengthened with Advanced Composites," Ph.D. Thesis, Department of Structural Engineering, University of Alexandria, Alexandria, Egypt, 148 pp.

Khalifa, A., Tumialan, G., Nanni, A., and Belarbi, A. (1999a), "Shear Strengthening of Continuous Reinforced Concrete Beams using Externally Bonded Carbon Fiber Reinforced Polymer Sheets," *Proceedings*, 4th International RILEM Symposium on Non-Metallic (FRP) Reinforcement for Concrete Structures (FRPRCS-4), Baltimore, Maryland, pp. 995-1008.

Khalifa, A., Alkhrdaji, T., Nanni, A., and Lansburg, S. (1999b), "Anchorage of Surface Mounted FRP Reinforcement," *Concrete International: Design and Construction*, Vol. 21, No. 10, pp. 49-54.

Khalifa, A., and Nanni, A. (2000), "Improving Shear Capacity of Existing RC T-Section Beams using CFRP Composites," *Cement & Concrete Composites*, Vol. 22, pp. 165-174.

Khalifa, A., Belarbi, A., and Nanni, A. (2000a), "Shear Perfomance of RC Members Strengthened with Externally Bonded FRP Wraps," *Proceedings*, 12th World Conference on Earthquake Engineering, Auckland, New Zealand.

Khalifa, A., Nanni, A., and De Lorenzis, L. (2000b), "FRP Composites for Shear Strengthening of RC Beams," *Proceedings*, 3rd International Conference on Advanced Composite Materials in Bridges and Structures, Ottawa, Canada, pp. 137- 144.

Kim, S. J., and Smith, S. T. (2009), "Shear Strength and Behaviour of FRP Spike Anchors in Cracked Concrete," *Proceedings*, 9th International RILEM Symposium on Non-Metalic (FRP) Reinforcement for Concrete Structures (FRPRCS-9), Sidney, Australia, 4 pp.

Kim, S. W., and Vecchio, F. J. (2008), "Modeling of Shear Critical Reinforced Concrete Structures Repaired with Fiber Reinforced Polymer Composites", *Journal of Structural Engineering*, Vol. 134, No. 8, pp. 1288-1299.

Kishi, N., Zhang, G., and Mikami, H. (2005), "Numerical Cracking and Debonding Analysis of RC beams Reinforced with FRP Sheet", *Journal of Composites for Construction*, Vol. 9, No. 6, pp. 507-514.

Kreger, M. E., Bachman, P. M., and Breen, J. E. (1989), "An Exploratory Study of Shear Fatigue Behavior of Pretensioned Concrete Girders," *Journal of the Prestressed Concrete Institute*, Vol. 34, No. 4, pp. 104-125.

Kulicki, J. M., Wassef, W. G., Kleinhans, D. D., Yoo, C. H., Nowak, A. S., and Grubb, M. (2006), "Development of LRFD Specifications for Horizontally Curved Steel Girder Bridges," NCHRP Report 563, Transportation Research Board, Washington, DC, USA.

Kwak, K. H., and Park, J. G. (2001), "Shear-Fatigue Behavior of High-Strength Reinforced Concrete Beams under Repeat Loading," *Journal of Structural Engineering Mechanics*, Vol. 2, No. 3, pp. 301-314.

Lamanna, A. J. (2002), "Flexural Strengthening of Reinforced Concrete Beams with Mechanically Fastened Fiber Reinforced Polymer Strips," Ph.D. Thesis, Department of Civil and Environmental Engineering, University of Wisconsin-Madison.

Lees, J. M., Winistöfer, A. U., and Meier, U. (2002), "External Prestressed Carbon Fiber-Reinforced Polymer Straps for Shear Enhancement of Concrete," *Journal of Composites for Construction*, Vol. 6, No. 4, pp. 249-256.

Leung, C. (2001), "Delamination Failure in Concrete Beams Retrofitted with a Bonded Plate," *Journal of Materials in Civil Engineering*, Vol. 13, No. 2, pp. 106-113.

Leung, C., Chen, Z., Lee, S., Mandy, N., Ming, X., and Tang, J. (2007), "Effect of Size on the Failure of Geometrically Similar Concrete Beams Strengthened in Shear with FRP Strips," *Journal of Composites for Construction*, Vol. 11, No. 5, pp. 487-496.

Li, A., Assih, J., and Delmas, Y. (2001), "Shear Strengthening of RC Beams with Externally Bonded CFRP Sheets," *Journal of Structural Engineering*, Vol. 127, No. 4, pp. 374-380.

Li, A., Diagana, C., and Delmas Y. (2002), "Shear Strengthening Effect by Bonded Composite Fabrics on RC Beams," *Composites Part B: Engineering*, Vol. 33, No.3, pp. 225-239.

Lopez-Anido, R., Kwon, S. C., Dutta, P. K., and Kim, Y. H. (2003), "Comparison of the Fatigue Behaviors of FRP Bridge Decks and Reinforced Concrete Conventional Decks under

Extreme Environmental Conditions," *KSME International Journal*, Vol. 17, No. 1, pp. 1-10.

Lu, X. Z., Teng, J. G., Ye, L. P., and Jiang, J. J. (2005a), "Bond-Slip Models for FRP Sheets/Plates Bonded to Concrete," *Engineering Structures*, Vol. 27, No. 6, pp. 920-937.

Lu, X. Z., Teng, J. G., Ye, L. P., and Jiang, J. J. (2005b), "Meso-scale Finite Element Model for FRP Sheets/Plates Bonded to Concrete," *Engineering Structures*, Vol. 27, pp. 564-575.

Lu, X. Z., Chen, J. F., Ye, L. P., Teng, J. G., and Rotter J. M. (2005c), "Theoretical Analysis of Stress Distributions in FRP Side Bonded to RC Beams for Shear Strengthening", *Proceedings*, International Symposium on Bond Behavior of FRP in Structures (BBFS2005), pp. 363-370.

Lu, X. Z., Teng, J. G., Ye, L. P., and Jiang, J. J. (2007), "Intermediate Crack Debonding in FRP Strengthened RC Beams: FE Analysis and Strength Model", *Journal of Composites for Construction*, Vol. 11, No. 2, pp. 161-174.

Maeda, T., Asano, Y., and Sato, Y. (1997), "A Study on Bond Mechanism of Carbon Fiber Sheet," *Proceedings*, 3rd International RILEM Symposium on Non-Metallic (FRP) Reinforcement for Concrete Structures (FRPRCS-3), Sapporo, Japan, pp. 279-286.

Mahmoudabadi, E., and Mostofinejad, D. (2009), "An Alternative Method to Surface Preparation to Postpone Debonding of FRP Laminates," *Proceedings*, 9th International RILEM Symposium on Non-Metalic (FRP) Reinforcement for Concrete Structures (FRPRCS-9), Sidney, Australia, 4 pp.

Malek, A. M., and Saadatmanesh, H. (1998), "Analytical Study of Reinforced Concrete Beams Strengthened with Web-Bonded Fiber Reinforced Plastics or Fabrics," *ACI Structural Journal*, Vol. 95, No. 3, pp. 343-351.

Malvar, L. J. (1995), "Tensile and Bond Properties of GFRP Reinforcing Bars," *ACI Materials Journal*, Vol. 92, No. 3, pp. 276-285.

Matthys, S. (2000), "Structural Behavior and Design of Concrete Members Strengthened with Externally Bonded FRP Reinforcement," Ph.D. Thesis, Department of Structural Engineering, University of Ghent, Belgium.

Mattock, A. H. (1979), "Flexural Strength of Prestressed Concrete Sections by Programmable Calculator," *PCI Journal*, Vol. 24, No. 1, pp. 32-54.

Mbrace (1998), *Mbrace Composite Strengthening System Engineering Design Guidelines, 2nd Edition*, Master Builders Inc. and Structural Preservation Systems.

Micelli, F., Annaiah, R., and Nanni, A. (2002), "Strengthening of Short Shear Span RC-T Joists with FRP Composites," *Journal of Composites for Construction*, Vol. 6, No. 4, pp. 264-271.

Miller, B. (1999), "Bond between Carbon Fiber Reinforced Polymer Sheets and Concrete," M.S. Thesis, Department of Civil, Architectural, and Environmental Engineering, University of Missouri-Rolla, Rolla, MO, USA.

Miller, B., and Nanni, A. (1999), "Bond between CFRP Sheets and Concrete," *Proceedings*, ASCE 5th Materials Congress, Cincinnati, OH, USA, pp 240-247.

Mitsui, Y., Murakami, K., Takeda, K., and Sakai, H. (1998), "A Study on Shear Reinforcement of Reinforced Concrete Beams Externally Bonded with Carbon Fiber Sheets," *Composites Interfaces*, Vol. 5, No. 4, pp. 285-295.

Miyajima, H., Kosa, K., Tasaki, K., and Matsumoto, S. (2005), "Shear Strengthening of RC Beams Using Carbon Fiber Sheets and its Resistance Mechanism," *Proceedings*, 5th

Workshop on Safety and Stability of Infrastructures against Environmental Impacts, Manila, Phillipines, pp. 114-125.

Miyauchi, K., Inoue, S., Nishibayashi, S., and Tanka, Y. (1997), "Shear Behavior of Reinforced Concrete Beam Strengthened with CFRP Sheet," *Transactions of the Japan Concrete Institute*, Vol. 19, pp. 97-104.

Modena, C., Pellegrino, C., and Golfetto, G. (1999), "Shear Strengthening of Concrete Beams with FRP Laminates," *Proceedings*, 2nd International RILEM Symposium on Adhesion between Polymers and Concrete, ISAP '99, Reunion Internanaionale des Laoboratories d'Essais et de Recherches sur les Materiaux et les Constructions, Cachan, Cedex, France, pp. 375-386.

Monti, G., and Liotta, M. A. (2005), "FRP-Strengthening in Shear: Tests and Design Equations," *Proceedings*, 7th International RILEM Symposium on Non-Metallic (FRP) Reinforcement for Concrete Structures (FRPRCS-7), Kansas City, Missouri, USA, pp. 543-562.

Monti, G., and Liotta, M. A. (2007), "Tests and Design Equations for FRP-Strengthening in Shear," *Construction and Building Materials*, Vol. 21, No. 24, pp. 799-809.

Moses, F. (2001), "Calibration of Load Factors for LRFR Bridge Evaluation," NCHRP Report 454, Transportation Research Board, Washington, DC, USA.

Muszynski, L. C., and Sierakowski, R. L. (1996), "Fatigue Strength of Externally Reinforced Concrete Beams," *Proceedings*, Materials for the New Millennium, Materials Engineering Conference, Washington, DC, USA, Vol. 2, pp. 648-656.

Mutsuyoshi, H., Ishibashi, T., Okano, M., and Katsuki, F. (1999), "New design method for seismic retrofit of bridge columns with continuous fiber sheet – performance-based design," *Proceedings*, 4th International RILEM Symposium on Non-Metallic (FRP) Reinforcement for Concrete Structures (FRPRCS-4), Baltimore, Maryland, pp. 229-241.

Nakaba, K., Kanakubo, T., Furuta, T., and Yoshizawa, H. (2001), "Bond Behavior between Fiber-Reinforced Polymer Laminates and Concrete," *ACI Structural Journal*, Vol. 98, No. 3, pp. 359-367.

Neale, K. W. (2000), "FRPs for Structural Rehabilitation: a Survey of Recent Progress," *Progress in Structural Engineering and Materials*, Vol. 2, No. 2, pp.133- 138.

Neubauer, U., and Rostasy, F. S. (1997), "Design Aspects of Concrete Structures Strengthened with Externally Bonded CFRP Plates," *Proceedings*, 7th International Conference on Structural Faults and Repairs, pp. 109-118.

Niedermeier, R. (1996), "Stellungnahme zur Richtlinie fur das Verkleben von Beton-Bauteilen durch Ankleben von Stahllaschen – Entwurf Marz 1996," Schreiben Nr 1390 vom 30.10.1996 des Lehrstuhls fur Massivbau, TU Munchen, Germany.

Nielsen, M. P., and Braestrup, M. W. (1975), "Plastic Shear Strength of Reinforced Concrete Beams," *Bygningsstatiske Meddelelser*, Vol. 46, No. 3, pp. 61-99.

Niemitz, C.W. (2008), "Anchorage of Carbon Fiber Reinforced Polymers to Reinforced Concrete in Shear Applications," M.S. Thesis, Department of Civil and Environmental Engineering, University of Massachusetts-Amherst.

Nigro, E., and Savoia, M. (2005), "Strutture di conglomerato cementizio armato," Il fenomeno della delaminazione nel placcaggio con FRP, L'Edilizia, No. 139.

Niu, H., and Wu, Z. S. (2000), "Study on Debonding Failure Load of RC Beams Strengthened with FRP Sheets," *Journal of Structural Engineering*, Vol. 46A, pp. 1431-1441.

Niu, H., and Wu, Z. (2005), "Numerical Analysis of Debonding Mechanisms in FRP-Strengthened RC Beams," *Computer-Aided Civil & Infrastructure Engineering*, Vol. 20, No. 5, pp. 354-368.

Norris, T. (1994), "Improving the Serviceaility of Concrete Beams Using Carbon Fiber Reinforced Polymer (CFRP) Sheets," Report, Department of Civil Engineering and Engineering Mechanics, University of Arizona, Tucson, AZ, USA, 285 pp.

Norris, T., Saddatmanesh, H., and Ehsani, M.R. (1997), "Shear and Flexural Strengthening of R/C Beams with Carbon Fiber Sheets," *Journal of Structural Engineering*, Vol. 123, No.7, pp. 903-911.

Nowak, A. S. (1999), "Calibration of LRFD Bridge Design Code," NCHRP Report No. 368, Transportation Research Board, Washington, DC, USA.

Nowak, A. S., and Collins, K. R. (2000), *Reliability of Structures*, McGraw Hill, USA.

Nowak, A. S., and Szerszen, M. M. (2003), "Calibration of Design Code for Buildings (ACI 318): Part 1 - Statistical Models for Resistance," *ACI Structural Journal*, Vol. 100, No. 3, pp. 377-382.

Ohuchi, H., Ohno, S., Katsumata, H., Kobatake, Y., Meta, T., Yamagata, K., Inokuma, Y., and Ogata, N. (1994), "Seismic Strengthening Design Technique for Existing Bridge Columns with CFRP," *Proceedings*, Proceedings of the 2nd International Workshop on Seismic Design and Retrofitting of Reinforced Concrete Bridges, Queenstown, New Zealand, pp. 495-514.

Okeil, A.M., El-Tawil, S., and Shahawy, M. (2002), "Flexural Reliability of RC Bridge Girders Strengthened With CFRP Laminates," *Journal of Bridge Engineering*, Vol. 7, No. 5, pp. 290-299.

O'Neill, A., Harries, K. A., and Minnaugh, P. L. (2007), "Fatigue Behavior of Adhesive Systems Used For Externally-Bonded FRP Applications," *Proceedings*, 3rd international conference on durability & field applications of frp composites for construction, Quebec , Canada, pp. 1-8.

Ono, K., Matsumura, M., Sakanishi, S., and Miyata, K. (1997), "Strength Improvement of RC Bridge Piers with Carbon Fiber Sheet," *Proceedings*, 3rd International RILEM Symposium on Non-Metallic (FRP) Reinforcement for Concrete Structures (FRPRCS-3), Sapporo, Japan, pp. 563-570.

Orton, S.L. (2007), "Development of a CFRP System to Provide Continuity in Existing Reinforced Concrete Buildings Vulnerable to Progressive Collapse," Dissertation, Department of Civil, Architectural, and Environmental Engineering, University of Austin-Texas, Austin, Texas, USA.

Papakonstantinou, C. G., Petrou, M. F. and Harries, K. A. (2001), "Fatigue of Reinforced Concrete Beams Strengthened with GFRP Sheets", *ASCE Journal of Composites in Construction*, Vol. 5, No. 4, pp. 246-253.

Park, S. Y., Naaman, A. E., Lopez, M. M., and Till, R. D. (2001), "Shear strengthening effect of R/C beams using glued CFRP sheets," *Proceedings*, International Conference on FRP Composites in Civil Engineering, Hong Kong, China, pp. 669-676.

Pellegrino, C., and Modena, C. (2002), "Fiber Reinforced Polymer Shear Strengthening of Reinforced Concrete Beams with Transverse Steel Reinforcement," *Journal of Composites for Construction*, Vol. 6, No. 2, pp. 104-111.

Pellegrino, C., and Modena, C. (2006), "Fiber-Reinforced Polymer Shear Strengthening of Reinforced Concrete Beams: Experimental Study and Analytical Modeling," *ACI Structural Journal*, Vol. 103, No. 5, pp. 720-728.

Pellegrino, C., Tinazzi, D., and Modena, C. (2008), "Experimental Study on Bond Behavior between Concrete and FRP Reinforcement," *Journal of Composites for Construction*, Vol. 12, No. 2, pp. 180-189.

Perez, J. J., Zhao, L., and O'Riordan-Adjah, C. A. (2005), "Finite Element Evaluation of The Effects of Lateral Anchorage Strips on the Behavior of CFRP Strengthened RC Beams", *Proceedings*, Proceedings of International Symposium on Bond Behavior of FRP in Structures (BBFS2005), pp. 303-308.

Pham, H. B., and Al-Mahaidi, R. (2005), "Finite Element Modelling of RC Beams Retrofitted with CFRP Fabrics", *Proceedings*, 7th International RILEM Symposium on Non-Metallic (FRP) Reinforcement for Concrete Structures (FRPRCS-7), Kansas City, Missouri, USA, pp. 499-514.

Popovics, S. (1973), "A Numerical Approach to the Complete Stress-Strain Relation for Concrete," *Cement and Concrete Research*, Vol. 3, No. 5, pp. 583-599.

Priestley, M., Seible, F., and Calvi, G. (1996), "Seismic Design and Retrofit of Bridges," John Wiley and Sons, New York, NY, USA, 704 pp.

Rasheed, H. A., Larson, K. H., and Peterman, R. J. (2006), "Analysis and Design Procedure for FRP-Strengthened Prestressed Concrete T-Girders Considering Strength and Fatigue." *Journal of Composites for Construction*, Vol. 10, No. 5, pp. 419-432.

Rehm G., and Eligehausen R. (1979), "Bond of Ribbed Bars Under High Cycle Repeated Loads," *ACI Journal*, Vol. 76, No. 2, pp. 297-309.

Rizkalla, S., Hassan, T., and Hassan, N. (2003), "Design Recommendations for the Use of FRP for Reinforcement and Strengthening of Concrete Structures," *Progress in Structural Engineering Materials*, Wiley, pp. 16-28.

Rizzo, A., Galati, N., Nanni, A. (2005), "Strengthening of Off-System Bridges with Mechanically Fastened Pre-Cured FRP Laminates," *ACI Special Publication (SP-230)*, pp. 1157-1176.

Rosenboom, O. A., and Rizkalla, S. H. (2005), "Fatigue Behavior of Prestressed Concrete Bridge Girders Strengthened with Various CFRP Systems," *Proceedings*, 7th International RILEM Symposium on Non-Metallic (FRP) Reinforcement for Concrete Structures (FRPRCS-7), Kansas City, Missouri, USA, pp. 597-612.

Sato, Y., Ueda, T., Kakuta, Y., and Tanaka, T. (1996), "Shear Reinforcing Effect of Carbon Fiber Sheet Attached to the Side of Reinforced Concrete Beams," *Proceedings*, 3rd International Conference on Advanced Composite Materials in Bridges and Structures, Montreal, Canada, pp. 621-628.

Sato, Y., Ueda, T., Kakuta, Y., and Ono, S. (1997a), "Ultimate Shear Capacity of Reinforced Concrete Beams with Carbon Fiber Sheet," *Proceedings*, 3rd International RILEM Symposium on Non-Metallic (FRP) Reinforcement for Concrete Structures (FRPRCS-3), Sapporo, Japan, pp. 499-506.

Sato, Y., Katsumata, H., and Kobatake, Y. (1997b), "Shear Strengthening of Existing Reinforced Concrete Beams by CFRP Sheet," *Proceedings*, 3rd International RILEM Symposium on Non-Metallic (FRP) Reinforcement for Concrete Structures (FRPRCS-3), Sapporo, Japan, pp. 507-514.

Sato, Y., and Vecchio, F. J. (2003), “Tension Stiffening and Crack Formation in Reinforced Concrete Members with Fiber-Reinforced Polymer Sheets”, *Journal of Structural Engineering*, Vol. 129, No. 6, pp. 717-724.

Schnerch, A. (2001), “Shear Behavior of Large-Scale Concrete Beams Strengthened with Fibre Reinforced Polymer (FRP) Sheets,” M.S. Thesis, Department of Civil Engineering, University of Manitoba.

Schuman, P., and Karbhari, V. M. (2004a), “Local Response of Anchored and Unanchored CFRP Shear Stirrups to Crack Opening,” *Proceedings*, International SAMPE Symposium and Exhibition, Long Beach, CA, USA, pp. 2897-2911.

Schuman, P., and Karbhari, V. M. (2004b), “Local Response of Anchored and Unanchored CFRP Shear Stirrups to Crack Opening,” *Proceedings*, International SAMPE Technical Conference SAMPE, Long Beach, CA, USA, pp. 2915-2929.

Schuman, P. M. (2004c), “Mechanical Anchorage for Shear Rehabilitation of Reinforced Concrete Structures with FRP: An Appropriate Design Approach,” Ph.D. Thesis, Department of Structural Engineering, University of California, UCSD, San Diego, CA,USA.

Selby, R. G., and Vecchio, F. J. (1993), “Three-dimensional Constitutive Relations for Reinforced Concrete”, Technical Report 93-02, University of Toronto, Toronto, Canada.

Senthilnath, P., Belarbi, A., and Myers, J. J. (2001), "Performance of CFRP Strengthened Reinforced Concrete (RC) Beams in the Presence of Delaminations and Lap Splices Under Fatigue Loading," *Proceedings*, International Conference on Composites in Construction (CCC-2001), Porto, Portugal, pp. 323-328.

Siafas, D., and Donchev, T. (2009), “Strengthening of Reinforced Concrete Beams with CFRP Laminates – Modes of Failure,” *Proceedings*, 9th International RILEM Symposium on Non-Metalic (FRP) Reinforcement for Concrete Structures (FRPRCS-9), Sidney, Australia, 4 pp.

Sika CarboDur (2003), *FRP Composites for Repair and Strengthening of Structures*, www.sika.com.

Sim, J., Kim, G., Park, C., and Ju, M. (2005), “Shear Strengthening Effects with Varying Types of FRP Materials and Strengthening Methods,” *Proceedings*, 7th International RILEM Symposium on Non-Metallic (FRP) Reinforcement for Concrete Structures (FRPRCS-7), Kansas City, Missouri, USA, pp. 1665-1680.

Szerszen, M. M., and Nowak, A. S. (2003), “Calibration of Design Code for Buildings (ACI 318): Part 2 - Reliability Analysis and Resistance Factors,” *ACI Structural Journal*, Vol. 100, No. 3, pp. 383-391.

Taerwe, L., Khalil, H., and Matthys, S. (1997), “Behavior of RC Beams Strengthened in Shear by External CFRP Sheets,” *Proceedings*, 3rd International RILEM Symposium on Non-Metallic (FRP) Reinforcement for Concrete Structures (FRPRCS-3), Sapporo, Japan, pp. 483-490.

Taljsten, B. (1994), “Plate Debonding Strengthening of Existing Concrete Structures with Epoxy Bonded Plates of Steel or Fibre Reinforced Plastics,” Ph.D. Thesis, Department of Civil, Mining, Environmental Engineering, Lulea University of Technology, Sweden.

Taljsten, B. (1997), “Strengthening of Concrete Structures for Shear with Bonded CFRP Fabrics,” *Proceedings*, US-Canada-Europe Workshop on Bridge Engineering, Zurich, Switzerland, pp. 67-74.

Taljsten, B. (2003), "Strengthening for Concrete Beam for Shear with CFRP Sheets," *Construction and Building Materials*, Vol. 17, No. 1, pp. 15-26.

Teng, J. G., Chen, J. F., and Smith, S. T. (2001), "Debonding Failures in FRP-Strengthened RC Beams: Failure Modes, Existing Research and Future Challenges," *Proceedings*, Composites in Constructions: A reality, Capri, Italy, pp. 139-148.

Teng, J. G., Lam, L., and Chen, J. F. (2004), "Shear Strengthening of RC Beams with FRP Composites," *Progress in Structural Engineering Materials*, Vol. 6, pp. 173-184.

Teng, S., Tan, K. H., Kong, F. K., and Ma, W., (1998), "Fatigue Tests of Reinforced Concrete Deep Beams," *Structural Engineer*, Vol. 76, No. 18, pp. 347-352.

Thorenfeldt, E., Tomaszewicz, A., and Jensen, J. J. (1987), "Mechanical Properties of High Strength Concrete and Application in Design," *Proceedings*, Symposium on Utilization of High Strength Concrete and Application in Design, Stavanger, Norway, Tapir, Trondheim, pp. 149-159.

Tozser, O., and Loov, R. (1999), "Shear Design of Prestressed Beams using Shear Friction," *Proceedings*, Annual Conference of the Canadian Society for Civil Engineering (CSCE), Regina, Canada, pp. 195-204.

Triantafillou, T. C. (1997), "Shear Strengthening of Concrete Members using Composites," *Proceedings*, 3rd International RILEM Symposium on Non-Metallic (FRP) Reinforcement for Concrete Structures (FRPRCS-3), Sapporo, Japan, pp. 523-530.

Triantafillou, T. C. (1998a), "Shear Strengthening of Reinforced Concrete Beams Using Epoxy-Bonded FRP Composites," *ACI Structural Journal*, Vol. 95, No. 2, pp. 107-115.

Triantafillou, T. C. (1998b), "Strengthening of Structures with Advanced FRPs," *Progress in Structural Engineering and Materials*, Vol. 1, No. 2, pp.126-134.

Triantafillou, T. C., and Antonopoulos, C. P. (2000), "Design of Concrete Flexural Members Strengthened in Shear with FRP," *Journal of Composites for Construction*, Vol. 4, No. 4, pp. 198-205.

Tumialan, R. P. (2007), "Performance Evaluation of Existing Analytical Methods to Compute the Shear Contribution Provided by Externally Bonded FRP Sheets in Concrete Structures," M.S. Thesis, Department of Civil, Architectural, and Environmental Engineering, University of Missouri-Rolla, MO.

Ueda, T., Okamura, H., and Farghaly, A. (1981), "Behaviors of Reinforced Concrete Beams with Stirrups Failing in Shear under Fatigue Loading," *Proceedings*, JSCE, No. 308, Japan, pp. 109-122.

Ueda, T., and Okamura, H. (1983), "Behavior in Shear of Reinforced Concrete Beams under Fatigue Loading," *Journal of the Faculty of Engineering*, The University of Tokyo (B), Vol. 37, No. 1, pp. 17-48.

Ueda, T., and Dai, J. G. (2004), "New Shear Bond Model for FRP-Concrete Interface-from Modeling to Application," *Proceedings*, 2nd International Conference on FRP Composites in Civil Engineering-CICE 2004, Adelaide, Australia, pp. 69-81.

Uji, K. (1992), "Improving the Shear Capacity of Existing Reinforced Concrete Members by Applying Carbon Sheets," *Transactions of the Japan Concrete Institute*, Vol. 14, pp. 253-266.

Umezu, K., Fujita, M., Nakai, H., and Tamaki, K. (1997), "Shear Behavior of RC Beams with Aramid Fiber Sheet," *Proceedings*, 3rd International RILEM Symposium on Non-Metallic (FRP) Reinforcement for Concrete Structures (FRPRCS-3), Sapporo, Japan, pp. 491-498.

Vecchio, F. J. (2000), “Disturbed stress field model for reinforced concrete: Formulation.” *Journal of Structural Engineering*, Vol. 126, No. 9, pp. 1070–1077.

Vecchio, F. J., and Collins, M. P. (1986), “The modified compression field theory for reinforced concrete elements subjected to shear.” *ACI Journal*, Vol. 83, No. 2, pp. 219–231

Vecchio, F. J., and Collins, M. P. (1993), “Compression Response of Cracked Reinforced Concrete,” *Journal of Structural Engineering*, Vol. 119, No. 12, pp. 3590-3610.

Volnyy, V. A., and Pantelides, C. P. (1999), “Bond Length of CFRP Composites Attached to Precast Concrete Walls,” *Journal of Composites for Construction*, Vol. 3, No. 4, pp. 168-176.

Wong, R. S. Y., and Vecchio, F. J. (2003), “Towards Modeling of Reinforced Concrete Members with Externally Bonded Fiber Reinforced Polymer Composites”, *ACI Structural Journal*, Vol. 100, No. 1, pp. 47-55.

Wu, Z., and Yin, J. (2003), “Fracturing Behaviors of FRP Strengthened Concrete Structure”, *Engineering Fracture Mechanics*, Vol. 70, pp. 1339-1355.

Williams, G., and Higgins, C. (2008), “Fatigue of Diagonally Cracked RC Girders Repaired with CFRP,” *Journal of Bridge Engineering*, Vol. 13, No. 1, pp. 24-33.

Xue Song, F., Jie, L., and Zhong Fan, C. (2004), “Experimental Research on Shear Strengthening of Reinforced Concrete Beams with Externally Bonded CFRP Sheets.” *Proceedings*, 3rd International Conference on Earthquake Engineering, Nanjing, China.

Yang, Y. X., Yue, Q. R., and Hu, Y. C. (2001), “Experimental Study on Bond Performance between Carbon Fiber Sheets and Concrete,” *Journal of Building Structures*, Vol. 22, No. 3, pp. 36-42.

Yang, Z. J., Chen, J. F., and Proverbs, D. (2003), “Finite Element Modelling of Concrete Cover Separation Failure in FRP plated RC beams”, *Construction and Building Materials*, Vol. 17, pp3-13.

Yuan, H., and Wu, Z. (1999), “Interfacial Fracture Theory in Structures Strengthened with Composite of Continuous Fiber,” *Proceedings*, Proceedings of Symposium of China and Japan, Science and Technology of 21st Century, Tokyo, Japan, pp. 142-155.

Yuan, H., Teng, J. G., Seracino, R., Wu, Z. S., and Yao, J. (2003), “Full-Range Behaviour of FRP-to-Concrete Bonded Joints: A Closed-Form Analytical Solution,” *Engineering Structures*, Vol. 26, pp. 553-565.

Yun, Y., Wu, Y. F., and Tang, W. C. (2008), “Performance of FRP Bonding Systems under Fatigue Loading.” *Engineering Structures*, Vol. 30, pp. 3129-3140.

Zhang, Z., Hsu, C. T., and Moren, J. (2004), “Shear Strengthening of Reinforced Concrete Deep Beams Using Carbon Fiber Reinforced Polymer Laminates,” *Journal of Composites for Construction*, Vol. 8, No. 5, pp. 403-414.

Zhang, Z., and Hsu, C.T. (2005), “Shear Strengthening of Reinforced Concrete Beams Using Carbon-Fiber-Reinforced Polymer Laminates,” *Journal of Composites for Construction*, Vol. 9, No. 2, pp. 158-169.

Zureick, A. H., Bennett, R. M., and Ellingwood, B. R. (2006), "Statistical Characterization of Fiber-Reinforced Polymer Composite Material Properties for Structural Design," *Journal of Structural Engineering*, Vol. 132, No. 8, pp. 1320-1327.

ABBREVIATIONS

AASHTO	American Association of State Highway and Transportation Officials
ACI	American Concrete Institute
AFRP	Aramid Fiber Reinforced Polymer
ASTM	American Society for Testing and Materials
CFRP	Carbon Fiber Reinforced Polymer
GFRP	Glass Fiber Reinforced Polymer
FHWA	Federal Highway Administration
fib	fédération internationale du béton
FRP	Fiber Reinforced Polymer
IC	Intermediate Crack
JCI	Japan Concrete Institute
JSCE	Japan Society of Civil Engineers
LEFM	Linear Elastic Fracture Mechanics
LRFD	Load and Resistance Factor Design
MF-FRP	Mechanically Fastened FRP
NCHRP	National Cooperative Highway Research Program
NLFM	Nonlinear Fracture Mechanics
NSM	Near Surface Mounted
PC	Prestressed Concrete
RC	Reinforced Concrete

NOTATIONS

Symbol	Description
a	Softening zone length
a_g	Maximum aggregate size
$\{a_i\}$	Generalized translational degree of freedom (also known as generalized translational coordinates)
a/d	Shear span-to-depth ratio
A_c	Area of the cross-section
A_f, A_{fv}	Cross-sectional area of FRP
A_s, A_{sx}	Area of longitudinal steel reinforcement
A_{ps}, A_{px}	Area of longitudinal prestressed steel reinforcement
A_{sv}, A_v	Area of transverse steel reinforcement
A_{sw}, A_w	Area of shear reinforcement
B	Interfacial ductility factor
$b_f/b_c, b_p/b_c$	Width ratio of bonded plate to concrete member
b_v	Effective web [AASHTO LRFD]
b_w	Minimum width of cross-section over effective depth
$\{b_i\}$	Generalized rotational degree of freedom (also known as generalized rotational coordinates)
c	Clear concrete cover
c_v	Clear distance from transverse reinforcement to longitudinal axis of beam
c_x	Clear distance from longitudinal reinforcement to center of cross-section
d	Effective depth of cross-section
D_A	FRP anchor diameter
d_b	Bar diameter
d_{bv}	Stirrup diameter
d_{bx}	Diameter of longitudinal steel reinforcement
d_f	Effective depth of FRP reinforcement
$d_{f,t}$	Distance from beam compression face to upper edge of FRP
D_f	FRP stress distribution factor
D_{frp}	Strain distribution factor [Chen and Teng, 2003]
$D_{f\theta}$	Modified FRP strain distribution factor = D_{frp}/θ [Cao et al., 2005]
d_s	Stirrup height
d_v	Effective shear depth [AASHTO LRFD]
E_c	Elastic modulus of concrete

E_f, E_{frp}	Elastic modulus of FRP
E_s	Elastic modulus of steel reinforcement
f_c'	Concrete compressive strength
f_{cm}	Mean cylindrical compressive strength of concrete
f_{ct}	Concrete splitting tensile strength
f_{ctk}	Peel-off shear strength of concrete
f_{ctm}	Mean tensile strength of concrete surface
f_{cu}	Cubic concrete compressive strength
f_f	Stress in FRP composite materials
f_{fdd}	Debonding FRP strength
f_{fe}	Effective tensile stress in FRP sheet in the direction of the principal fibers
f_{fed}	Effective FRP debonding strength
f_{frp}	Strength of FRP sheet [Chen and Teng, 2003]
$f_{frp,e}$	Average/effective stress of FRP intersected by shear crack at beam failure
$f_{frp,ed}$	Average/effective design stress of FRP intersected by shear crack at beam failure
F_{fu}	Force exerted by FRP sheet
f_{fu}	FRP ultimate tensile strength
f_{fud}	Design strength of FRP composite materials
F_p	Force in the composite plate
F_{res}	Outward tensile force in FRP sheets
f_t	Direct tensile strength of concrete
f_y, f_{yv}	Yield strength of steel reinforcement
G_a, G_r	Shear modulus of adhesive bond layer
g_b	Shear joint stiffness of concrete plus adhesive resin
G_c	Shear modulus of concrete
g_c	Shear joint stiffness of concrete
G_f	Interfacial fracture energy
g_r	Shear joint stiffness of adhesive resin
h, h_{frp}	Height of RC/PC member
h_{fe}	Effective FRP height
h_w	Height of beam web
K	Shear reinforcing efficiency [JSCE Recommendations]
k	Experimental constant describing the gradient of the effective bond length [Khalifa et al., 1998]
k_a	Coefficient describing anchorage considerations [Deniaud and Cheng, 2003]
k_b	Covering coefficient for FRP sheets

k_e	Integer describing number of debonding ends
k_1	Coefficient that characterizes bond properties of bars
k_2	Coefficient to account for strain gradient
L_b	Development length
L_e, L_{eff}	Effective bond length
$L_{\max}$	Maximum bond length
M_d	Design bending moment
M_o	Decompression moment
M_u	Factored moment
n, n_p	Number of FRP plies
n	Ratio of elastic modulus between FRP reinforcement and transverse steel reinforcement [Chaallal et al., 2002]
n_a	Number of anchor bolts
$P_{bearing}$	Bearing capacity of anchor bolt
$P_{\max}$	Ultimate load capacity of the FRP sheet
P_{pull_out}	Pull-out capacity of anchor bolt
P_u	Maximum normal force carried by an FRP sheet
P_{u_anchor}	Capacity of a discontinuous mechanical anchorage system
R	Ratio of effective stress/strain in the FRP sheet to its ultimate strength/strain [Khalifa et al., 1998]
r_f	Factor depending on the FRP strengthening scheme
R_L	Remaining bonded width over initial width ratio [Deniaud and Cheng, 2004]
R^*	Additional reduction factor for debonding failures of beams with steel web reinforcement [Pellegrino and Modena, 2002]
s, s_v	Spacing of stirrups
s_A	FRP anchor splay diameter
s_e, s_m	Crack spacing
s_f	Deflection at maximum shear stress [Yuan et al., 2003]
s_f, s_{frp}	Spacing of FRP strips
S_f, S_{frp}	FRP laminate spacing
s_{mv}	Horizontal crack spacing due to transverse tension
s_{mx}	Vertical crack spacing due to axial tension
$s_{m\theta}$	Inclined crack spacing due to shear
s_o	Deflection at failure
s_x	Spacing of longitudinal steel reinforcement
	Thickness of adhesive bond layer
	Thickness of concrete prism

t_f, t_{frp}	FRP thickness
T_f	Tension force in FRP
t_p	Nominal thickness of FRP sheet or bonded plate
T_v	Tension force in stirrups
{u}	Vector of displacement, $\{u\} = \begin{bmatrix} u & v & w \end{bmatrix}^T$
V_c, V_{cd}	Shear contribution of concrete
$V_{\exp}$	Experimental shear capacity
$V_f, V_{f,\max}$	Shear contribution of FRP
V_{frp}	Design shear capacity provided by FRP [Chen and Teng, 2003]
V_n	Total shear capacity
	Component in the direction of the applied shear of the effective prestressing force
V_{ped}	Shear resistance contributed by prestressing reinforcement
V_{Rd1}	Shear resistance without web reinforcement [fib TG9.3]
$V_{Rd2,\max}$	Web crushing shear force based on plasticity theory [fib TG9.3]
V_{Rd3}	Shear resistance of the members with shear reinforcement [fib TG9.3]
V_{rg}	Nominal shear strength [CSA A23.3-94]
V_s	Shear contribution of stirrups
V_u	Factored shear force
w_f, w_{frp}	Width of FRP strip
w_{fe}	Effective width of FRP strip
z	Distance from the extreme concrete compression surface to the centroid of tension reinforcement [JSCE, 2000]
z_b	Coordinate of lower edge of effective FRP
z_t	Coordinate of upper edge of effective FRP
α	Ratio of bond force that effective bond area can bear
α	Angle of transverse steel reinforcement to the longitudinal axis [Deniaud and Cheng, 2003]
α_f	Angle between principal direction of FRP sheets and the longitudinal axis of the beam [Hutchinson and Rizkalla, 1999]
β	Angle of inclination of FRP fibers to longitudinal axis of member
β_g	Angle of outward tensile force in FRP sheets
β_H	Angle of pull-out force of anchor bolt
β_l	Bond length factor
β_p, β_w	Width ratio factor
ε_{cr}	Critical FRP strain
$\varepsilon_{f,ave}$	Average strain in FRP at failure [Hutchinson and Rizkalla, 1999]

$\varepsilon_{f,\max}$	Maximum strain in FRP sheet [Cao et al., 2005]
$\varepsilon_{fe}, \varepsilon_{f,e}$	Effective tensile strain of FRP
$\varepsilon_{frp,e}$	Effective FRP strain [Triantafillou, 1998]
ε_{fu}	Ultimate tensile strain of FRP
$\varepsilon_{\max}$	Maximum strain in FRP sheet [Chen and Teng, 2003]
εv_{cu}	Ultimate vertical tensile strain of the concrete taken as 0.005 [Chajes et al., 1995]
γ_b	Partial safety factor for FRP debonding [Triantafillou, 1998]
Γ_{Fk}	Specific fracture energy of the FRP-concrete bond interface
η	Average FRP fiber utilization
λ	Shear span-to-effective depth ratio
λ_f	Bond length index
λ_{frp}	Normalized FRP bond length = $L_{\max}/L_e$
λ_1, λ_2	Parameters related to sizes and properties of materials and interface
θ	Shear crack angle
ρ, ρ_s, ρ_x	Longitudinal steel reinforcement ratio
ρ_{ef}	Ratio of area of steel to area of effective embedment zone of concrete
ρ_f, ρ_{frp}	FRP reinforcement ratio
$\rho_{s,f}$	Stiffness ratio between the transverse steel shear reinforcement and FRP shear reinforcement [Pellegrino and Modena, 2002]
ρ_{tot}	Total shear reinforcement ratio [Chaallal et al., 2002]
ρ_v	Transverse steel reinforcement ratio
σ_{fd}	Tensile stress
$\sigma_{frp,\max}$	Maximum stress in FRP intersected by shear crack [Chen and Teng, 2003]
$\sigma_{frp,\max,d}$	Maximum stress in FRP intersected by shear crack for design [Chen and Teng, 2003]
σ_{fu}	Maximum tensile stress in FRP
τ_{ave}	Average shear stress
τ_{bu}	Bond strength between the FRP and concrete
τ_f	Bond stress
$\tau_{\max}$	Maximum shear stress
τ_{ult}	Interface shear strength
ψ_f	Additional reduction factor applied to the FRP shear contribution
ξ, η, ζ	Reference coordinates of isoparametric elements